UCRL-ID-119564 Vol 3 Rev 1.

JUNE 30, 1998

Engineered Materials Characterization Report Volume 3

Corrosion Data and Modeling Update for Viability Assessment

by R. Daniel McCright

Lawrence Livermore National Laboratory
Livermore, California 94551

Work performed under the auspices of the U S Department of Energy by Lawrence Livermore National Laboratory under Contract W-7405-ENG-48 This work is supported by the Yucca Mountain Site Characterization Project, LLNL

About the cover This 200× photograph shows the microstructure of a polarized Alloy C-22 specimen The etchant was 4% nital electrolytic

Contents

Acronyms and Abbreviations

AFM	atomic force microscopy
ALHR	apparent local homogeneous rate
AOD	argon–oxygen decarb
AP	aqueous phase
APC	aqueous-phase corrosion
APW	artificial pore water
ASTM	American Society for Testing and Materials
BC	boundary conditions
CAM	corrosion-allowance material
CCD	charge-coupled device
CDF	cumulative (probability) distribution function
CPP	cyclic potentiodynamic polarization
CRM	corrosion-resistant material
DCB	double-cantilever beam
DEF	delayed ettringite formation
DST	Drift-Scale Test
EBS	Engineered Barrier System
EDAX	energy-dispersive x-ray analysis
EEP	Expert Elicitation Panel
El	elongation
EMCR	*Engineered Materials Characterization Report*
ESF	Exploratory Studies Facility
ESR	electroslag remelt
Fe-Ni-Cr-Mo	iron–nickel–chromium–molybdenum alloy
HAC	humid air corrosion
HAZ	heat-affected zones
HE	hydrogen embrittlement
HVOF	high-velocity oxygenated fuel
IC	ion chromatography
ICP	inductively coupled plasma (atomic emission spectroscopy)
INEEL	Idaho National Engineering and Environmental Laboratory
ISE	ion-selective electrode
LC	localized corrosion
LDRD	Laboratory Directed Research and Development
LEED	low-energy electron diffraction
LEFM	linear elastic fracture mechanics
LLNL	Lawrence Livermore National Laboratory
LRO	long-range ordering
LTCT	long-term corrosion test
LTCTF	Long-Term Corrosion Test Facility

MIC	microbially induced corrosion
NACE	National Association of Corrosion Engineers
NFE	near-field environment
PDE	partial differential equation
PGR	pit-generation rate
PLFA	phospholipid fatty acid
QCM	quartz–crystal microbalance
RA	reduction in area
SAW	simulated acidified well water
SCC	stress corrosion cracking
SCE	saturated calomel electrode
SCMW	simulated cement-modified water
SCW	simulated concentrated well water
SDW	simulated dilute well water
SEM	scanning electron microscope
SHE	standard hydrogen electrode
SIP	Scientific Investigation Plan
SNF	spent nuclear fuel
SSR	slow strain rate
SSRT	slow strain rate testing
STM	scanning tunneling microscopy
TE	thermal embrittlement
TEM	transmission electron microscopy
TGA	thermogravimetric analyzer
TIP	Technical Implementation Plan
TSPA	Total System Performance Assessment
TSPA-VA	Total System Performance Assessment–Viability Assessment
TTF	total time to failure
UNS	unified numbering system
UHV	ultra-high vacuum
VA	Viability Assessment
VIM	vacuum induction melt
VP	vapor phase
WBS	work breakdown structure
WL	water line
WP	waste package
XPS	x-ray photoelectron spectroscopy
XRD	x-ray diffraction
YM	Yucca Mountain
YMP	Yucca Mountain Project
YMSCP	Yucca Mountain Site Characterization Project

Commonly Used Terms

E	electrochemical potential
E_{corr}	corrosion potential
E_{crit}	pitting potential
E_{pit}	critical potential for initiation of pitting
E_{pass}	repassivation potential
E_{prot}	repassivation or protection potential
F	Faraday's constant
K	stress intensity factor
K_I	crack-tip stress intensity factor
R	universal gas constant
RH	relative humidity
ρ	density
T	temperature (°C)

Executive Summary

by R. Daniel McCright

This *Engineered Materials Characterization Report* (EMCR), Volume 3, discusses in considerable detail the work of the past 18 months on testing the candidate materials proposed for the waste-package (WP) container and on modeling the performance of those materials in the Yucca Mountain (YM) repository setting This report was prepared as an update of information and serves as one of the supporting documents to the Viability Assessment (VA) of the Yucca Mountain Project. Previous versions of the EMCR have provided a history and background of container-materials selection and evaluation (Volume 1), a compilation of physical and mechanical properties for the WP design effort (Volume 2), and corrosion-test data and performance-modeling activities (Volume 3) Because the information in Volumes 1 and 2 is still largely current, those volumes are not being revised. As new information becomes available in the testing and modeling efforts, Volume 3 is periodically updated to include that information.

The purpose of this executive summary is to give an overall assessment of where the materials-testing and modeling work stands. Pointers are given to the various sections of the report where much more detailed information is available for the interested reader This section will indicate the significance of this work to other elements of the Yucca Mountain Project (YMP)—in particular, the parts of the project concerned with the design aspects of the repository and the WP and the performance assessment of the engineered barrier system

Report Organization

The general organization of the report is according to the types of degradation modes that affect each or both of the metal barriers under consideration in the two-barrier VA design for the WP, which is a thick, outer, corrosion-allowance material barrier surrounding a thinner, inner, corrosion-resistance material barrier. A 10-cm-thick outer barrier of carbon steel (ASTM A516 Grade 55) surrounds a 2-cm-thick inner barrier of Ni–Cr–Mo Alloy C-22 in the VA design. Testing and modeling of other candidate container materials are also discussed in the report. Section 2 of the report is devoted to the corrosion testing and performance modeling for the container. Section 2 is the longest section in the report, and is divided into eight subsections, each dealing with an area of investigation to support one or more of the degradation modes. Section 3 of the report discusses the work to date on ceramic coatings on a steel substrate, which are being considered to prolong the lifetime of the outer barrier. Sections 2 and 3, therefore, are directly related to issues centered on substantially complete containment of the waste.

Sections 4 and 5 of the report deal with other materials issues but not primarily containment issues. Section 4 discusses work on the "basket" of internal elements that separate the fuel assemblies from one another in spent-fuel WPs Some of these components contain boron to control the neutron flux and prevent criticality of the mass of spent nuclear fuel. The main performance issue with these materials is how they will react with water, and what will happen to the criticality control, once the WP is breached. Section 5 discusses work on concrete used to line the drift wall and for construction of the invert and much of the pier structure upon which the WP will rest. There is concern about structural, mechanical, and chemical changes that will occur in the concrete in the heated environment surrounding the WP and what effect the degrading concrete will have on the water chemistry that ultimately

contacts the WP. Because concretes are mildly alkaline materials, it is believed that the effect on the WP will not be detrimental.

Waste Package Degradation: Outer Barrier

The composite of results so far indicate a mixed performance for the outer barrier. Analysis in the previous EMCR Volume 3 showed that the oxidation of the carbon steel during the so-called "thermal period," when the surface of the container is well above 100°C and the humidity of the surrounding atmosphere is low, results in negligible wastage of the 10-cm thick barrier. Percolating water is expected to vaporize in the drift above the WP because of the heat. As the container surface temperature drops, water approaches the surface, and drips from the fractured rock will strike the container surface Because the container is still hot, the water evaporates and leaves behind a salt residue reflecting the ionic content of the vadose water at the repository site

Humid Air Corrosion on Carbon Steel

The ionic content of the salt residue has an important influence on the time at which aqueous corrosion effects begin. The experimental work and analyses in Section 2 1 on humid air corrosion address this issue Results so far indicate that the mix of ionic salts present in vadose waters typical of the site are not particularly hygroscopic, so high relative humidities are needed (~80–85%) to sustain a water film and to initiate corrosion on a carbon-steel surface (see Section 2.1.4) Laboratory tests are being performed over a range of temperatures and humidity levels, and the surfaces of the steel specimens are coated with different mixtures of salts. The chemical composition of the electrolyte and salt deposits is being measured in an experiment that simulates drips contacting a warm WP in a humid environment The solubility and, in some cases, the thermal stability of the ionic species vary, so their ratio in a concentrated electrolyte on the surface is not the same as their ratio in the more dilute vadose water The actual ionic concentration and ratios are important to the corrosion rates, because some species stimulate corrosive dissolution of the metal (e g , chloride ion), but others have a definite mitigating effect on corrosion reactions (e g , bicarbonate). Carbon-steel specimens have been emplaced in field studies at the YM site to complement the work being performed under laboratory conditions. This work is discussed in Section 2.1.8. These are longer-term tests, and specimens are still in test

Carbon Steel General Aqueous Corrosion

It is not surprising that the carbon-steel outer barrier will corrode once it is wet, but the rates of corrosion, and the fractional area of the container surface that is wetted, are unknown. The corrosion rate of carbon steel is sensitive to the water chemistry; this is evident from results presented in Section 2 2.4 from the long-term corrosion test Results indicate that concentration of salts substantially reduces the corrosion rate of carbon steel because of a pH buffering effect and reduced solubility of oxygen. Reduced oxygen solubility at higher temperatures is also an important factor in mitigating corrosion of carbon steel. However, there are some important effects that appear to increase the rate. High rates of corrosion were observed in water-saturated vapor (dripping conditions) where high carbon-dioxide levels were measured. Also, higher corrosion rates were measured at lower test temperatures and in more dilute electrolyte, conditions that favor higher oxygen solubility. These results indicate that a wide range of corrosion rates will occur on carbon steel under repository conditions. It is imagined that a wet container surface will eventually be pocked with areas of high corrosion surrounded by areas exhibiting little attack

The 6-month and 1-year data for corrosion of carbon steel in Section 2.2 6 show a significant decrease in the rate for all conditions. These results are consistent with the results of other rate measurement (not YM work), in which several years were needed before a steady-state corrosion rate was observed. The decrease in corrosion rates with time is attributed to formation of protective corrosion products (mostly oxides), and work has begun to characterize these corrosion products This work is discussed in more detail in Section 2.7.3. After 1 year of exposure, average general-corrosion rates of A516 steel varied from 6 to 76 μm/yr when fully immersed in waters of different concentrations and at different temperatures This range of rates is attributed to O_2 solubility and pH buffering, the lowest rates being measured in 90°C high ionic strength water (~1000× the ionic content of J-13 well water). The comparable corrosion rates of this same material varied from 27 to 227 μm/yr under exposure to condensing water in the vapor space above the water This range of rates is attributed to high CO_2 contents, the highest rates being measured at 90°C above the high ionic strength water More details of these analyses are presented in Section 2 2.7. These long-term corrosion tests are expected to last a minimum of 5 years

A mathematical model for predicting corrosion rates of carbon steel has been developed by linear regression analysis of the same long-term corrosion data This analysis is presented in Section 2.8 2 2 and gives the corrosion rate in terms of temperature, pH, and equivalent chloride concentrations The positive and negative coefficients in this regression analysis show that the maximum corrosion rate occurs at 75–80°C under immersion conditions, which agrees well with many other results in the technical literature

Because the dripping-water scenario is assumed to be the most plausible water-contact mode, the nature of the drip formation is important in determining how long a carbon-steel barrier will last before penetration. Usually, development of drip scenarios belongs to hydrological and geochemical studies, but, from a corrosion viewpoint, it is important whether drips issue continually from a given fracture or whether a given fracture eventually plug up and percolating water moves elsewhere. In the current Total System Performance Assessment (TSPA), the container surface is divided up into a large number of patches. If high and low corrosion-rate events alternate on a given patch of the container, then a long-lived outer barrier is forecast, and its wastage is determined mostly by the slow general-corrosion rate in an atmosphere becoming progressively more humid. If (as is imagined under the very conservative approach made in TSPA-VA) a given patch becomes wet and stays wet, because the water-admitting fracture does not seal, then corrosive attack proceeds in a drill-like penetration over relatively small areas of the container. The nonuniformity of the environment depicted in this type of approach is a major problem in predicting the performance of steel (or any other corrosion-allowance material). Obviously, more analyses are needed, and these analyses must involve people from other areas in the project besides the engineered barrier materials group, to better determine the details of the water-contact mode with the outer barrier.

Corrosion Localization Effects on Carbon Steel

Localization of the corrosion attack on carbon steel was one of the important technical issues discussed during the past year with the various expert panel groups convened by YMP (see the final section of this executive summary). Reports in the technical literature on long-term exposure (on the order of several years) of carbon steels under immersion conditions indicate that, in addition to the general corrosion, pits form on the steel. These pits tend to be shallow and broad, as opposed to the very deep but narrow pits that occur on susceptible corrosion-resistant metals. Quantification of the corrosion-localization factor (ratio of depth

of localized penetrations to the depth of generalized attack) has not been completed for the carbon-steel specimens. These measurements are tedious. However, analyses from the technical literature suggests localized penetration will be about 2× as deep after several years of exposure, and this factor appears to decrease with time as the general corrosion penetration grows deeper.

Microbiological activity (bacteria and fungi) is a possible corrosion-enhancing scenario on a wet carbon-steel surface. Section 2.5 of the report describes the work in progress to evaluate the potential for microbiologically influenced corrosion (MIC) Microbial activity requires aqueous conditions for sustenance It is believed that the repository environment is somewhat "starved" for nutrients that promote microbiological activity. However, results from the microcosm experiments indicate that MIC on carbon steel will occur once aqueous conditions are present on the surface even under very limited nutrient-availability conditions Acid-forming bacteria appear to propagate under limited nutrient availability, and these bacterial strains are corrosive to carbon steel (see Section 2 5.4). Comparison of the measurements of the corrosion rates of carbon steel in sterile media and in bacteria-inoculated media indicates that the general-corrosion rates increase by 5 to 7 times, depending on the particular bacteria strains used in the test The test environment was ~10× the ionic content of J-13 well water Also, the corrosion potential decreases in the inoculated environment, indicative of a lowered pH (see Section 2.5 7) Work is underway to better characterize the nature of this attack in terms of the corrosion products and whether there are any localization factors

Other Degradation Modes on Carbon Steel

Environmentally accelerated cracking of carbon steel, whether by an anodic path or cathodic path, has not been considered an important degradation mode, and no experimental work has been undertaken. Some analyses of temper embrittlement of carbon steel have been undertaken, and are discussed in Sections 2 6 and 2 8 of the report The conclusion from these analyses is that the residual element content in A516 steel and the container-surface temperatures in the repository are too low to cause precipitation of nonmetallic inclusions that are responsible for this type of degradation

Waste Package Degradation: Outer Barrier/Inner Barrier Interface

Once the 10-cm-thick carbon steel has been penetrated, our attention shifts to corrosion at the interface. Several concurrent effects occur at the interface, and these concurrent effects are the focus of much of the WP performance model, discussed in Section 2.8. These concurrent effects include a crevice geometry, galvanic coupling between the two electrochemically dissimilar metals, and residual stress from the container fabrication and welding processes.

Crevice and Galvanic Effects at the Interface

Depending on how the individual barriers are fabricated and assembled, a crevice may be formed between the two barriers. The shrink-fit process, which has been used to produce scaled-down prototypes of the WP (see Section 2.6.4), will result in crevice formation between the outer steel layer and inner Ni-base alloy layer. Nonconcentricity of the two cylindrical sections, used to make the outer shell of the container, prevents complete contact as the two barriers press together. Designers have been concerned about the kind of environment that would develop in this creviced region, and, specifically, whether it is enriched in ferric chloride. Work has been undertaken to determine the corrosion performance in environments

simulating the crevice (see Section 2 3.2) As expected, Alloy C-22 exhibited much greater resistance to localized corrosion effects than the other Ni-base alloys tested, as indicated in determinations of the pitting potentials and repassivation potentials In general, these critical potentials are considerably more positive than the corrosion potential for Alloy C-22, indicating a very strong resistance to localized attack such as crevice corrosion or pitting corrosion Even when a specimen of this alloy was held at an applied potential some 900 mV above the corrosion potential for 4 days, no localized attack was observed and only some discoloration of the specimen occurred It would require addition of a very strong oxidant to the environment to cause such a shift in the corrosion potential, and this type of event is thought highly unlikely in the repository By the time the steel has corroded to expose the underlying Alloy C-22 (this is expected to be at least several hundred years), the gamma radiation will have decayed many orders of magnitude (the half-lives of the significant gamma emitters are ~30 yr), so that no source of strong oxidant is present

Analysis of the YM experimental work, along with work reported in the corrosion literature, indicate that extremely aggressive conditions are required to initiate crevice and pitting corrosion on Alloy C-22. This is discussed under corrosion modeling in Section 2.8 3 The crevice-corrosion model predicts a pH of ~2.8 for Ni–Cr–Mo alloys, such as Alloy C-22, with corresponding electromigration of chloride and other anions into the crevice At this pH value, the solubility of $FeCl_3$ is very low. The predicted environmental conditions in the crevice are not severe compared to the performance of Alloy C-22, so this alloy is expected to resist attack when creviced The remaining steel will also tend to reduce the common corrosion potential for the two metals in galvanic contact, so the critical potentials for Alloy C-22 are even further removed from the corrosion potential. Galvanic effects are further discussed in Section 2 3 5, where potentials and currents have been measured for different combinations of metals and in different area ratios All of these results show a strong shift in the coupled metals toward the corrosion potential of the steel Work is underway to perform microchemical analyses in actual crevices to determine whether the calculated chemical conditions are in fact the correct conditions This work is described in Section 2 8 3.9

Stress Effects at the Interface

Residual stresses left from the container fabrication and welding processes can contribute to the degradation of the inner barrier by making the material susceptible to either anodic-path stress corrosion cracking (SCC) or cathodic-path hydrogen embrittlement The residual stress is expected to be highest near welds; if this is coupled with a susceptible microstructure, then perhaps cracking can occur. Analysis of the stress in the weld region indicates that it can be near the yield strength of the material (see Section 2.8.5.5). Ni–Cr–Mo alloys are normally very resistant to SCC even in acidic chloride environments, which could be produced in creviced areas. Some work has been initiated using precracked, self-loaded, fracture-mechanics types of specimens (see Section 2.4 2) Some of these results appear to show elongation of the existing crack when exposed to pH 2.7 chloride solutions, but these results must await additional exposure time for more definitive results. Other types of SCC tests are planned for the near future to ascertain whether Alloy C-22 is susceptible to this cracking. Also, work is planned to determine whether hydrogen effects exist on Alloy C-22 when it is in the more hydrogen-sensitive ordered microstructural condition and simultaneously cathodically polarized by being coupled to the steel. More on this subject can be found in Sections 2.6.2 and 2.4.3. Additional sources of stress at the outer barrier/inner barrier interface are residual stresses from the shrink-fit process and the possible wedging effect caused by formation of voluminous iron-rich corrosion products in the restricted

crevice geometry. Stress-analysis models are being developed to evaluate whether these sources are particularly damaging. These are discussed in both Sections 2.6 3 and 2.8 5.

Waste Package Degradation: Inner Barrier

Once enough of the carbon-steel outer barrier is mostly corroded away (so that galvanic effects are minimal), the inner barrier must stand on its own. The main environment-related concern is whether a localized form of stress corrosion would menace the performance The degradation model development indicates that even if pits were initiated on the surface of the exposed Alloy C-22, their propagation will be the stifled. This argument is based on the formation of film-forming compounds, which in turn is based on solubility and hydrolysis considerations for the various corrosion products (see Section 2.8.3). Because of the stability of Mo and W compounds at very low pH values, and the stability of Cr and Ni in the middle and upper pH ranges, the stability of passive films on Alloy C-22 has a remarkably broad pH range. As indicated in the previous discussion on crevice and pitting corrosion initiation, these degradation modes require the presence of a strong oxidant to destabilize the passive film Even if such an event were to occur and initiate localized corrosion, the broad range of chemical stability of this film would tend to restore the passivity and slow down the propagation.

A further mitigating factor in slowing localized-corrosion propagation is the ever-decreasing temperature of the container surface The critical temperatures for the Alloy C-22 are above 100°C (except in strongly oxidizing solutions), and when the carbon steel has finally corroded through, the temperature at the inner barrier surface should be well below any critical condition Localized corrosion of the inner barrier material therefore seems very remote Stress corrosion perhaps a possibility, but the decreasing temperature should help to mitigate against this phenomenon as well Hydrogen embrittlement should completely cease as a degradation mode, once the steel is corroded away

Microstructural Effects in Alloy C-22

However, one potential degradation phenomenon remains. the phase instability of the alloy under certain conditions In the multiple component Alloy C-22, the possibility exists that brittle intermetallic phases will form, particularly sigma and mu phases. Normally, these phases are not a problem in the base alloy, because they can be controlled by alloy composition, fabrication processing, and heat treatment. Some ordering of the structure may occur over long times at moderately elevated temperatures, but this reaction results only in a small reduction of mechanical properties. Brittle intermetallic phases may occur, however, in the welded region (see Section 2.6.2), because of nonequilibrium conditions and possible temperature excursions in the 600–800°C range, where these phases readily form. Working arrangements have been established with nickel producers who have made available some material that has been previously thermally aged. Transmission electron microscopy reveals that none of the harmful brittle phases occurs in Alloy C-22 aged for more than 5 yr at 427°C, but some intermetallic phases were observed on samples aged for 1.8 yr at 760°C. In addition to reduction of the mechanical properties, formation of brittle intermetallic phases also denudes localized areas around the phases in Cr, Mo, and W, making these areas more prone to localized attack, often along grain boundaries.

Passive Corrosion of Alloy C-22

In the absence of pitting corrosion, crevice corrosion, stress corrosion cracking, hydrogen embrittlement, or embrittlement by phase instability, the default degradation mode of Alloy C-22 is the low rate of general corrosion on the passivated surface. Results from the long-term corrosion test (Sections 2.2 6 and 2 2.7) and a linear regression analysis (Section 2.8 2.4) indicate that the rates are indeed quite low (in the range of 0.01 to 0 10 μm/yr) in the aqueous environments that are relevant to the repository In fact, many of these rates are experimentally barely measurable after 6-month and 1-year exposure periods. Projection of these rates indicates that the 2-cm thick Alloy C-22 barrier would survive for a very long time

Alloy C-22 was developed in the early 1980s, but its parent material, Alloy C or Hastelloy C, has been commercially available since the 1930s A panel of Alloy C has been exposed at Kure Beach, NC, since 1941 and is shown in Figure 1 4-1. During the more than 50 years of exposure, the specimen has been subjected to a range of temperatures, humidities, alternate wetting and drying cycles, periodic flooding, and abundant salt spray, because the exposure location is 250 m from shore. The original mirror finish on the specimen is still intact after all the years of exposure This observation indicates that the material is quite corrosion resistant (Alloy C differs from C-22 in having a much higher carbon content, considerably lower chromium content, and higher iron content If there are any effects in the seacoast exposure, Alloy C-22 would be expected to be even more resistant)

Figure 0-1. **Specimen of Hastelloy C exposed at Kure Beach, North Carolina, 250 m from shore. The specimen retains its original mirror finish after more than 50 years of exposure.** *(Photo courtesy of Ralph Moller, Nickel Development Institute.)*

Ceramic Coatings

Because of the need to demonstrate that a very long-lived WP could be designed and fabricated, the use of ceramic coatings are being explored as a means to prolong the time until water contacts the outer steel barrier. One practical way of coating the steel is thermally spraying the ceramic. The different materials and different thermal-spray processes under consideration are discussed in Sections 3 1 and 3.2, and the various test methods for evaluating the performance of these coatings are discussed in Section 3 3. Of the materials under consideration, a magnesia–alumina spinel appears most promising because it avoids the undesirable phase transformation problem in pure alumina, and low porosity coatings can be made. Of the various thermal spray processes evaluated to date, the high-velocity oxygenated fuel (HVOF) process appears to be the most successful. So far, ceramic coatings on steel appear to greatly prolong the service lifetime over that of the bare metal

Carbon-steel specimens coated with different materials applied by different processes are being exposed in the Long-Term Corrosion Test Facility (LTCTF; see Section 2 2) with periodic withdrawal of specimens for evaluation. Coating porosity was also a test variable, and pretest metalographic and microscopic evaluation of the coatings was performed. To date, the high-density (low-porosity) coatings have held up well in the test environments with no apparent penetration by the fluid to the steel surface. As expected, the highly porous coatings showed water penetration and spalling of the coating from the steel substrate. A major concern is interconnected porosity leading to a pathway for water penetration, and ac impedance spectroscopy is being used to evaluate this phenomenon. Some otherwise high integrity coatings have been intentionally slotted to allow easy water entry to the steel surface

and to determine whether and how undermining of the coating will occur It appears that steel corrosion products may stifle further corrosion and damage to the coating The exposure period has so far only been a few months, and obviously longer periods are needed.

A preliminary mathematical model has also been advanced for projecting fluid flow through interconnected porosity, assuming different regimes of pores filled or partially filled with water. Also, ways of mitigating porosity effects, essentially by adding sacrificial anodic materials (Zn and Al metal) to the coating, are discussed (see Section 3 5).

Other EBS Materials

A large amount of concrete or other cementitious material will be placed around the WP. These materials will be used as part of the invert and pier structure to support the WP and to line the drift walls above the WP The degradation of the concrete by its reaction with heat, moisture, carbon dioxide, and microbial activity will, in turn, affect the performance of the WP. The concrete is expected to degrade long before the metal WP, so it is assumed that water eventually contacting the WP will first be conditioned by contact with the degraded concrete One of the bounding environments used in the long-term corrosion test corresponds to the expected composition of this conditioned water The work, which is presented in Section 5 of the report, focuses on the hydrothermal and environmental degradation of concrete and cements Section 5 also discusses steel reinforcement materials (rebar) and their expected reaction with concrete and aqueous environments

One of the important functions of the internal structure in spent-fuel WPs is to provide criticality control once the packages are breached and allowed to fill with water Neutron-absorbing materials are used for some components in this structure A survey of these materials was discussed in the previous EMCR Volume 3 Since that time, additional studies show that borated aluminum material, even in the anodized condition, corrodes rapidly (Section 4 0) Boron-containing stainless steels are under test in the LTCTF (Section 2 2). Electrochemical evaluation is also being performed on these materials, and results to date indicate that the boride phase is cathodic and would be left behind (and still function as a neutron-absorber material) in an aggressive water-chemistry scenario.

Expert Panels

During the past year a number of review panels have been formed under various auspices to lend additional professional and expert judgment and opinion to the project technical staff on the direction of the work and interpretation of results available to date. The purpose of these panels was to bring in experts in the field of metal corrosion and degradation. One important review panel was the one formed specifically for WP degradation (the Waste Package Degradation Expert Elicitation, or WPDEE, Panel). This panel consisted of two panel members from within YMP and four outside members. Several parts of the discussion in Section 2 8 on corrosion modeling and supporting references were drawn from the WPDEE Panel One of the functions of that panel was to help fill information gaps where repository-relevant data is not yet available The panel members also worked closely with the WP performance-assessment group and supplied information that is being used in the Waste Package Degradation code. Individual and consensus elicitations from the panel indicate that the VA-design carbon steel-over-Alloy C-22 WP will endure for a considerable amount of time, and even with very conservative (that is, high corrosion rates) estimates of degradation modes and very conservative estimates of the water contact (that is,

once water begins to drip on the package, it never ceases), at least 8,000 years will elapse before the two layers of the WP are breached

Other panels were formed with a much broader scope These include the TSPA panel and the Repository Consulting Board, but in each case the panel or board included at least one member with expertise in metallic corrosion The work of these panels also helps to guide and critique the work reported here Their work will continue past the VA

Engineered Materials Characterization Report, Volume 3 Corrosion Data and Modeling Update for Viability Assessment

1. Introduction

by R. Daniel McCright

The *Engineered Materials Characterization Report* (EMCR) serves as a source of information on the properties of materials proposed as elements in the engineered barrier system (EBS) for the potential Yucca Mountain nuclear waste repository The Yucca Mountain site is being characterized to determine whether it is a suitable location to house the nation's commercial spent nuclear fuel and high-level reprocessed waste The initial version of this report was compiled in December 1994 In the initial version (Revision 0), the report was divided into three volumes Volume 1 covered the background and history of the materials effort Volume 2 covered the physical and mechanical properties of paramount interest to the waste package design effort Volume 3 covered the corrosion data and modeling effort A revision (Revision 1) to Volume 3 was prepared in April 1997 and included corrosion test data up to that date as well as the performance modeling for the various candidate materials under consideration

This update is an extension of Revision 1, and includes test data and progress on performance modeling through May 1998 This update is not intended to be a revision of the April 1997 version of the EMCR Volume 3, but rather a supplement to that report Volumes 1 and 2 of the December 1994 issue of the EMCR (McCright, 1996) were not revised in April 1997 (Van Konynenburg et al , 1997) and are not being revised or updated at this time because the information contained within them is still current

This update to Volume 3 is being prepared as a companion document for the project-wide Viability Assessment (VA) report. As such, this update contains test information relative to the VA design for the waste package and EBS and details on the models for performance of the waste package that are being used for the Total System Performance Assessment for this Viability Assessment (TSPA-VA)

The EMCR also serves as a companion document to comparable reports prepared on the near-field environment (WBS 1 2 3 12) and the waste form (1 2 2 4) technical area (Wilder, 1997, Stout and Leider, 1997) These reports are also periodically revised and updated

1.1 Waste Package Design and Emplacement

The emphasis of this report is on the waste package container materials being evaluated as part of the VA design namely, a thick outer barrier of carbon steel, specifically American Society for Testing and Materials (ASTM) A516 Grade 55 surrounding a thinner inner barrier of a high-performance Ni–Cr–Mo alloy, specifically Alloy C-22 These materials are also identified by their ASTM-SAE Unified Numbering System (UNS) designations· K01800 for the A516 carbon steel, and N06022 for Alloy C-22 The proposed thickness dimensions are 10 cm for the outer barrier and 2 cm for the inner barrier. The total thickness of the two barriers strongly attenuates the amount of gamma radiation that can penetrate the container, so that radiolysis effects on the environment are very small, if not negligible The thick carbon-steel layer provides considerable structural strength to the waste package and makes

it robust with regard to handling and emplacement operations. All of the waste packages have the common configuration of the carbon-steel outer and Alloy C-22 inner barriers Other candidate materials are under consideration for different waste package designs and configurations of the individual barriers that will be evaluated in the future These materials are discussed at different places in this report

The overall strategy in the selection of material for the VA design is that the carbon steel will slowly oxidize during the hot and dry thermal period, when heat from the waste package keeps the container surface temperature well above the boiling point of water. Any incoming water is vaporized As the temperature cools, the atmosphere around the waste package becomes more humid, and aqueous corrosion processes can begin once the humidity attains a "critical" level Eventually, water will drip from the drift ceiling and will strike the waste package Depending on the water chemistry, such water will corrode the steel at low to moderate rates The steel is viewed as a corrosion-allowance material (CAM), and it is assumed that it will eventually be consumed by the corrosion processes Depending on our models for hydrology in the heat-disturbed environment in the repository drift and nearby rock, water access to the container surface will not occur until many hundreds of years after emplacement. As the steel is penetrated, areas of the underlying Alloy C-22 are exposed to the environment. This material is a highly corrosion resistant material (CRM) in a very wide range of environmental chemistries It is believed that this material will provide thousands of years of containment before it is eventually breached Several scenarios for possible corrosion of the C-22 are the focus of much of the work discussed in Section 2 of this report

Other nickel-base alloys have been evaluated in the past as inner barrier materials, with particular focus on Alloy 825 and Alloy 625 After much discussion within the Yucca Mountain Project and the larger corrosion community, Alloy C-22 was selected for the waste package VA design because of its superior corrosion resistance, even in very aggressive environments (Pasupathi, 1997)

Figure 1-1 is a schematic of a large spent nuclear fuel (SNF) waste package This particular design accommodates 21 PWR assemblies or 44 BWR assemblies The outer diameter of this two-barrier container is approximately 1 8 m Figure 1-2 is a schematic of a similar, but smaller, SNF waste package designed to accommodate 12 PWR or 24 BWR assemblies The outer diameter of this smaller package is approximately 1 5 m The length of the waste package container varies to accommodate the lengths of the fuel rods, most waste packages are 5 7 m in length Special spent fuel from DOE experimental reactors and that from non-light-water reactor commercial power plants will be accommodated in appropriately sized containers The cut-away sections in Figures 1-1 and 1-2 show the internal structure of the waste package The internal structure consists of an interlocking series of plates or grids to support and separate the individual fuel rod assemblies and to provide a conduit for heat transfer from the fuel rods to the waste package container The system of grids is often called the basket Long-term criticality control is important. Borated stainless steel is used for many elements in the grid structure, the boron addition acting to capture neutrons from the decaying spent fuel Carbon steel is also used for many of the internal supporting structural members (corner guides and slide guides), which also serve to dissipate heat from the fuel to the container The largest spent fuel waste packages weigh approximately 34 metric tonnes unloaded, and approximately 50 metric tonnes loaded

Figure 1-1. **Schematic of the large spent nuclear fuel waste package. This package can accommodate 21 PWR or 44 BWR assemblies. The schematic shows the outer A516 carbon steel barrier and the inner Alloy C-22 barrier. Internal support and criticality control components are also shown.**

Figure 1-2. **Schematic of the small spent nuclear fuel waste package. This package can accommodate 12 PWR or 24 BWR assemblies. The schematic shows the outer A516 carbon steel barrier and the inner Alloy C-22 barrier. Internal support and criticality control components are also shown.**

Figure 1-3 shows the waste package design for vitrified high-level waste for both defense waste currently being processed at the Savannah River and Hanford sites and for the small amount of commercially reprocessed waste processed at the West Valley site The waste is encapsulated in a borosilicate glass that is melted and poured into Type 304L stainless-steel pour canisters at the respective sites In the current design for the vitrified waste package, five or these pour canisters will be placed inside the two-barrier carbon-steel/alloy C-22 container. The diameter of the vitrified waste package is 1 8 m, and its length is 3 6 m In contrast to the spent fuel package, the smaller radionuclide inventory in the vitrified waste packages results in lower surface temperatures

Figure 1-3. **Schematic of the waste package containing high-level reprocessed, vitrified waste. The waste is contained in the stainless-steel pour canisters, which are enclosed in the outer A516 carbon steel and inner Alloy C-22 two-barrier disposal container.**

Waste packages will be emplaced horizontally in drifts A schematic of such emplacement is shown in Figure 1-4 The waste packages will be supported initially by a system of steel piers that raise them off the floor of the emplacement drift The piers will eventually corrode away, and the package will slide to the floor The floor is made of a concrete invert segment The drift walls are lined with concrete The concrete will degrade with time, and its degradation affects water coming into the repository, which will then affect the waste package The current plan is to co-mingle the vitrified waste packages among the spent fuel waste packages (also shown in Figure 1-4) to maintain a more even temperature in the repository emplacement drifts. This is important for performance considerations of the waste package container material The drifts may eventually be filled with a backfilled material, most likely the crushed tuff rock removed during repository excavation. The backfill serves to cushion the waste packages from falling rock It also could retard water entry into the drift by maintaining a higher drift temperature

Figure 1-4. **Schematic showing emplacement of spent nuclear fuel and high-level reprocessed waste in the repository drift. The schematic shows commingling of the two kinds of waste packages. The invert and support structure for the waste packages are also shown.**

Much more detailed reports on the waste package design, configuration of barrier, and emplacement descriptions and options are available (see, for example, CRWMS M&O, 1997)

Different fabrication processes are under evaluation for producing the waste package It is expected that much of the assembly of the shell of the waste package will be performed away from the repository, but the spent fuel or pour canister waste-loading operations will be done at a surface facility to be built at the base of Yucca Mountain The lids of the waste package

container will be welded onto the container shell at the surface facility after the container is loaded with waste. A container fabrication process that has received a great deal of attention is shrink fitting the steel over the nickel-base alloy The steel piece is heated, slipped past the cold nickel-alloy piece, and then allowed to cool Contraction of the steel ensures a tight fit against the nickel alloy, so that a "monolithic" shell is created The fabrication process has important implications on the container material performance, as is discussed in different sections of this report. The shell itself will likely be made of two (or more) rolled and welded plates The welding process and resulting microstructure have important performance implications on the container, and this topic is discussed in appropriate sections of this report

The waste package and EBS have recently received considerable attention in terms of demonstrating that the repository will indeed be able to contain and isolate the waste for very long time periods Because of the attention, a very long-lived waste package is sought, and various ways of enhancing the performance are under evaluation Testing of several highly corrosion resistant metals is underway, and perhaps different combinations of these metals could be used with or without a steel barrier Thermally sprayed ceramic coatings on steel (or other metals) is another way to enhance performance by keeping water away from the metal surface Backfilled materials will increase the container temperature and therefore keep the waste package hotter and drier for an extended period of time. Although most of the corrosion testing and modeling work supporting this report has been performed with the carbon steel over Alloy C-22 configuration as the goal, some testing and evaluation of other options have proceeded, as discussed in this report

1.2 Organization of This Report

This report discusses the progress on predicting the performance of the two-barrier waste package and the other components of the EBS Section 2—the longest section of the report—focuses on the waste package, both the current inner and outer barrier materials for the VA design and other metallic materials being considered in alternative design options Section 3 deals with ceramic coatings, which are one of the options under investigation for prolonging the container life Section 4 is devoted to the basket materials for maintaining criticality control inside the waste package Section 5 covers work on concretes used for the drift invert and liner material

The arrangement of this report corresponds to the formal work breakdown structure (WBS) of the project. The metallic barriers work described in Section 2 is WBS 1.2 2 5.1 The ceramic coating work described in Section 3 is WBS 1 2 2 5.6 The work on criticality control materials in Section 4 is WBS 1 2 2.5 2. The invert materials work in Section 5 is WBS 1 2 2 5 5

1.3 References for Section 1

CRWMS M&O (1997). *Reference Design Description for a Geological Repository* (B00000000-01717-5707-00002, Rev 1) Las Vegas, NV Civilian Radioactive Waste Management System Management and Operating Contractor TRW Environmental Safety Systems, Inc [MOL.19980127 0313]

McCright, R D (1996) *Engineered Materials Characterization Report* (UCRL-ID-119564, Rev 0) Livermore, CA· Lawrence Livermore National Laboratory [MOL 19961022 0024]

Pasupathi, V. (1997) *Design Analysis Report—Waste Package Materials Selection Analysis* (BBA00000000-0717-0200-00020 Rev. 01) Las Vegas, NV: Civilian Radioactive Waste Management System Management and Operating Contractor TRW Environmental Safety Systems, Inc

Stout, R.B , and H R Leider (1997) *Waste Form Characteristics Report* (UCRL-ID-108314, Rev 1 2) Livermore, CA Lawrence Livermore National Laboratory [MOL 19971210 0027]

Van Konynenburg, R.A , R.D McCright, A K Roy, and D Jones (1997) *Engineered Materials Characterization Report* (UCRL-ID-119564, Rev 1) Livermore, CA. Lawrence Livermore National Laboratory [MOL 19960402 0552]

Wilder, D.G (1997) *Near-Field and Altered-Zone Environment Report, Volume I Technical Bases for EBS Design* (UCRL-LR-124998, Vol I) Livermore, CA Lawrence Livermore National Laboratory [MOL 19980127 0120]

2. Metallic Barriers Testing and Modeling

Overview

This section of the report discusses in detail the work that is being performed on developing models to predict the performance of a dual-barrier container It also discusses the experimental work that provides the physical, chemical, mechanical, and structural support for the models The current design concept consists of an outer barrier made from a corrosion-allowance material (CAM) and an inner barrier made from a corrosion resistant material (CRM) The Viability Assessment (VA) design focuses on an A516 Grade 55 carbon-steel outer barrier and a Ni–Cr–Mo Alloy C-22 inner barrier, however, experimental work on other candidate materials is also presented here

The major planning document for both the testing and modeling activities for the metal barriers (WBS 1 2 2 5 1) is the Scientific Investigation Plan (SIP) (McCright, 1996) The SIP divides the work into four areas

1 Degradation-mode surveys
2 Corrosion testing and physical properties evaluation
3 Model development of performance behavior
4 Materials recommendations

The degradation-mode surveys were discussed in the 1997 revision of the EMCR, Volume 3, and the list of references is repeated because these documents furnish a considerable amount of information on the expected performance of the materials in environments relative to the repository (Farmer et al , 1986, Gdowski, 1991, Vinson et al , 1995, Vinson and Bullen, 1995, Roy and Jones , 1996) Since 1997, an additional degradation-mode survey has been prepared on titanium-base alloys (Gdowski, 1997) Progress made on the corrosion testing and physical properties evaluation will be the subject of Sections 2 1 through 2 6 of this report, model development is discussed in detail in Section 2 8 Materials recommendation for the license application design is a longer-range activity and will not be addressed in this update

The principle of the two-barrier configuration is that the different types of barrier materials will respond quite differently to the changes of environments that will occur over the very long time periods of concern for waste containment Stated another way, the two materials are different from one another in the electrochemical sense, so it is quite unlikely that they will fail (fail in the sense of a through-wall breach) by the same cause. Scenarios have been advanced to describe how and when the waste package container will degrade and to identify the most likely forms of corrosion (and in some cases embrittlement) Figure 2-1 shows a sequence of degradation events This sequence forms the framework of a brief discussion here, more detail is provided in the subsections that follow.

Figure 2-1. **Schematic of a degraded waste package container showing the different *possible* degradation modes occurring on the two barriers. The extent of each degradation mode depends strongly on the materials chosen for each barrier and many aspects of the environment and water chemistry contacting each barrier.**

Corrosion of the Outer Barrier

As shown in Figure 2-1 (see item 1), the first mode sequentially is oxidation and eventual aqueous corrosion of the outer barrier An important part of the waste-isolation strategy at Yucca Mountain is to design the waste package repository so that the environment surrounding the waste packages remains warm and dry for a lengthy period. Depending on many details of the repository layout and the thermal output of the waste packages, estimates of peak temperatures near 200°C on the surface of the container have been made for the waste packages in the center of the repository Waste packages at the repository periphery will develop lower peak temperatures. The peak temperatures are obtained shortly after emplacement, then the temperatures slowly drop. The thick outer barrier of the waste package (on the order of 10 cm thick) is expected to slowly oxidize under these conditions

As the temperature decreases and conditions become progressively more humid, a point is reached at which aqueous-corrosion effects may develop Depending on the repository design and the location within the array of waste packages, such effects may take several hundred to well over a thousand years until the container surface cools to the boiling point (97°C for pure water at the elevation of Yucca Mountain, however, dissolved salts will raise this temperature by a few degrees) Water drips from the drift wall would contact the container near the top or roll around the surface and accumulate near the bottom, so both areas are shown in Figure 2-1 It is generally believed that large areas of the container surface would not be immersed because of the abundance of rock fractures both above and below the repository horizon In addition, the overall flux of water averaged over the long containment period is expected to be low However, the uncertainty that some high pluvial event coupled with a juxtaposition of water entry with slow drainage (such as by a plugged network of fractures below the repository) occurring at some location in the repository layout requires consideration of aqueous corrosion effects Corrosion-allowance materials, such as carbon steel, are proposed for the outer barrier These materials would withstand the low-temperature oxidation and would corrode at moderate rates once they are wet A considerable amount of work on determining corrosion rates of carbon steel in atmospheres of varying humidity has been undertaken and is reported in Section 2 1

The corrosion rate of carbon steel depends on the chemical composition of the water, and on the oxygen content in particular. The fracture network in the rock ensures air exchange, and the water is expected to be oxygen-saturated at whatever temperature is occurring Water chemistries of groundwaters and vadose waters of the site have been measured and discussed (McCright, 1996) The pH of these waters is close to neutral or slightly alkaline Passage of water past the concrete liner is expected to leach calcium compounds and saturate the water in calcium carbonate. This event is expect of provide some mitigation to the corrosiveness of the water Measurements of the corrosion rates of carbon steel in waters of different composition has been performed in the Long Term Corrosion Test Facility (LTCTF) This work is reported in Section 2.2.

On the other hand, microbial activity could enhance the aggressivity of water (Figure 2-1, item 3) In much the same way that the appearance of a water film on a metal surface exposed in a sufficiently humid atmosphere marks the beginning of the electrolytic processes of aqueous corrosion, the water film also supports microbiological life In the hot, dry repository, microbiologically influenced corrosion (MIC) seems an impossibility, but as temperatures cool and humidities rise, MIC becomes a possibility Several different types of microbial species attack CAMs like carbon steel. Native colonies of the corrosion-enhancing bacteria are found in Yucca Mountain, however, the low organic carbon content and the

virtual absence of phosphate in waters associated with the site suggest unfavorable conditions for continued propagation of microbial species In contrast, human intrusion during repository construction and operation can introduce more favorable conditions for microbiological activity Work in evaluating the propensity of microbiological activity in the vicinity of the waste package and its effect on the container performance (particularly that of steel) is discussed in Section 2 5

Corrosion at the Outer-Barrier/Inner-Barrier Interface

Several galvanic effects are possible between the outer-barrier and inner-barrier materials, once the thick outer barrier has been penetrated and the inner barrier is exposed (Figure 2-1, item 4). The inner barrier is proposed to be made from a highly corrosion resistant material (CRM) The most obvious galvanic effect is that the remaining carbon steel will corrode at a somewhat faster rate while the inner barrier materials is protected However, soluble ferric corrosion products are aggressive towards many of the nickel-base alloys. In this particular configuration, the possibility of a creviced region between the two metals (resulting from a less-than-perfect fit when the container is fabricated) favors a lower pH and high anion concentrations where the detrimental effects of the ferric ion would be greatest Insoluble corrosion products from the outer barrier can also create under-deposit types of crevices, affecting the inner barrier Work on galvanic effects between the two barriers is discussed in Sections 2 2 and 2 3

Exposed areas of the inner barrier are subject to localized corrosion attack (Figure 2-1, item 5), which is the usual degradation mode for CRMs Once again, depending on the severity of the water chemistry and choice of material, corrosive attack may be extremely modest and provide for a very long life One of the major candidate materials, Alloy C-22, is extremely resistant to pitting, crevice, and intergranular corrosion, including environments containing some ferric chloride Higher concentrations (several wt%) of $FeCl_3$ with a trace of Alloy C-22 Even if the salts present in the ground water concentrate on the warm metal surface, the net effect may produce an environment that is not highly aggressive The high bicarbonate content of the ground water tends to act as an effective pH buffer, maintaining water in the moderately alkaline range such that corrosion effects tend to be mitigated for many metals. Solubility limitations will prevent all the salts from concentrating to the same degree In the absence of localized corrosion and stress-accelerated corrosion effects (discussed next), the "default" corrosion mode for Alloy C-22 is slow, general corrosion on the passive metal Localized corrosion of the inner-barrier material is discussed in Section 2 3 (electrochemical approaches) and Section 2 7 (advanced techniques) General corrosion of the inner-barrier material is discussed in Section 2 2 (Long-Term Corrosion Test Facility work)

The next group of concerns (Figure 2-1, item 6) is centered on stress Although ponderous, the weight of the waste package will not produce high stress in the container walls, but residual stress may be left from the shrink-fit fabrication and welding processes, if not annealed out Areas around the welds are believed to be the most vulnerable. Another potential source of stress is the wedging effect caused by formation of voluminous corrosion product, particularly at the interface between the two materials Once again, depending on the particular alloy used and the galvanic configuration between the barriers, one or both of the barriers may be subject to anodic-path stress corrosion cracking (SCC) or cathodically induced hydrogen embrittlement (HE) Many of the candidate materials for the inner barrier are quite resistant to SCC even in highly aggressive solutions, such as acidic chlorides However, such materials may have some susceptibility to HE effects if they are cathodic to carbon steel. Work on stress corrosion is discussed in Section 2.4

Another group of potential problems (Figure 2-1, item 2) is also related to residual stress to welded areas Although an extensive container-inspection program is planned before waste packages are emplaced, a very small number of containers may have undetected cracks that propagate after emplacement. In addition, some candidate materials show some tendency to form brittle intermetallic phases that are undetected when the container is freshly fabricated but that propagate during the lengthy exposure to modestly high temperatures These types of failures can occur throughout the containment period Unlike the corrosion degradation modes, their occurrence does not depend on water entry and access to the waste package container surface Work on microstructural analysis, particularly such analysis of the Alloy C-22 inner barrier, is described in Section 2.6

Thus, several different scenarios for waste package container degradation are possible over the long containment period, several hundreds to thousands of years An active testing program has been initiated to resolve the rates of degradation and to determine whether or not the various corrosion and other metallurgical degradation modes really will occur in the repository setting. One substantial difficulty in making these kinds of analyses and establishing a testing program is that the environment certainly will change with time and likely will change with location within the repository. In addition, the environment varies from place to place on the container surface because most aqueous effects result from dripping and ground water salt accumulations. The testing program must therefore bracket the ranges of environmental conditions, and it must also include conditions corresponding to "what-if" scenarios—events believed to be unlikely but still credible and usually limited to situations involving only a few containers

Modeling of Corrosion Performance

Presentation of the modeling work in this report follows much the same organization as that described above First, models are described for performance of the outer barrier Then, models to predict the performance at the breached outer-barrier/inner-barrier interface are presented Finally, the models for predicting eventual degradation of the inner barrier are discussed Modeling of the waste package container is discussed in Section 2 8

List of Candidate Materials

The VA design concept for the waste package consists of an inner CRM surrounded by a much thicker layer of a CAM Specifically for the VA design, the focus is on an inner barrier of Alloy C-22 and an outer barrier of A516 Grade 55 carbon steel. The chemical compositions of these materials, along with those of other candidate materials, are shown in Table 2-1

Several of the candidate materials continue to be tested because their comparative behaviors are used in corrosion model development This is especially true for the CRMs, where the less-alloyed (in the sense of the Cr + Mo content) Alloy 825 is expected to suffer more extensive localized corrosion than the more highly alloyed Alloy C-22. Previous container design efforts have focused on Alloys 825 and 625, hence their incorporation in the testing activities. The other Ni-base materials, Alloys G-3 and C-4, have been retained in the testing program because they have some potential advantages. Two grades of titanium are also being tested because some additional future design work may focus on a multiple corrosion-resistant-barrier design

Different grades of steels are being investigated for the outer barrier. A wrought hypoeutectoid steel (A516) and a cast steel (A27) of similar carbon content are being tested to allow some diversity in product forms. Whereas rolled and welded plate has generally been

the choice of starting material for fabricating the container, some consideration has been given to cast material Both steels have carbon contents similar to AISI 1020 steel (UNS G10200), which may be more familiar to some readers. The Cr–Mo alloy steel is included because of its better oxidation resistance at elevated temperatures. Depending on details of the repository design and layout, oxidation resistance may be a more important issue for some waste package repository configurations

Copper-bearing materials, specifically Alloy 400 (Monel 400) and CDA 70/30 copper-nickel, have been retained in the testing activities as possible outer barrier materials They are intermediate in corrosion performance between CAMs like carbon steel and CRMs like the Ni-base and Ti-base alloys

The chemical compositions for all of these materials are those from the American Society for Testing and Materials (ASTM) product specifications for plate material If another product form is used, some of the compositions may vary slightly from those given here For the carbon-steel materials, the compositions are those for 4-inch-thick (10-cm-thick) plate because the permitted compositions can vary somewhat according to size

The mechanical properties for many of these candidate materials have been compiled in EMCR Volume 2 (Van Konynenburg et al , 1995)

In some cases during the experimental discussion that follows, other materials (usually Ni–Cr–Mo alloys) have been tested, generally for purposes of comparison

Table 2-1. Candidate materials for multi-barrier containers.

UNS number	Common or commercial name	ASTM designation	Nominal composition
Corrosion resistant materials (CRMs)			
Nickel-rich stainless alloys (Ni-Cr-Fe-Mo alloys)			
N08825	Alloy 825 Incoloy 825	B 424 (plate)	Ni 38 0–46 0, Cr 19 5–23 5, Mo 2 5–3 5, Fe balance, Cu 1 5–3 0, Ti 0 6–1 2, Mn 1 0 max, C 0 05 max, Si 0 5 max, S 0 03 max, Al 0 2 max
N06030	Alloy G-30, Hastelloy G-30	B 582 (plate)	Ni balance, Cr 28 0–31 5, Mo 4 0–6 0, Fe 13 0–17 0, W 1 5–4 0, Co 5 0 max, Cu 1 0–2 4, Nb + Ta 0 3–1 5, Mn 1 5 max, C 0 03 max, Si 0 8 max, S 0 02 max, P 0 04 max
Nickel-base alloys (Ni-Cr-Mo alloys)			
N06625	Alloy 625 Inconel 625	B 443 (plate)	Ni balance, Cr 20 0–23 0, Mo 8 0–10 0, Fe 5 0 max, Nb 3 15–4 15, Mn 0 5 max, Al 0 40 max, Ti 0 40 max, C 0 10 max, Si 0 50 max, P 0 015 max, P 0 015 max
N06022	Alloy C-22, Hastelloy C-22, Inconel 622, Alloy 22	B 575 (plate)	Ni balance, Cr 20 0–22 0, Mo 12 5–14 5, Fe 2 0–6 0, W 2 5–3 5, Co 2 5 max, Mn 0 5 max, C 0 015 max, Si 0 08 max, V 0 35 max, S 0 02 max, P 0 02 max
N06455	Alloy C-4 Hastelloy C-4	B 575 (plate)	Ni balance, Cr 14 0–18 0, Mo 14 0–17 0, Fe 3 0 max, Co 2 0 max, Mn 1 0 max, C 0 015 max, Si 0 08 max, Ti 0 7 max, S 0 03 max, P 0 04 max
Titanium			
R53400	Ti-Grade 12	B 265 Grade 12 (plate)	Ni 0 6–0 9, Mo 0 2–0 4, N 0 03 max, C 0 08 max, H 0 015 max, Fe 0 3 max, O 0 25 max, Ti balance
R52402	Ti-Grade 16	B265 Grade 16 (plate)	0 05 Pd, Ti balance
Corrosion-allowance materials (CAMs)			
Carbon and alloy steels			
K01800	Carbon steel	A 516 (Grade 55)	C 0 22 max, Mn 0 6–1 20, P 0 035 max, S 0 04 max, Si 0 15–0 40, Fe remainder
J02501	Centrifugally cast steel	A 27 (Grade 70-40)	C 0 25 max, Mn 1 20 max, P 0 50 max, S 0 060 max, Si 0 80 max, Fe remainder
K21590	2 Cr – 1 Mo Alloy steel	A 387 (Grade 22)	C 0 15 max, Mn 0 3–0 6, P 0 035 max, S 0 035 max, Si 0 5 max, Cr 2 00–2 50, Mo 0 90–1 10, Fe remainder
Moderately corrosion resistant or "intermediate" materials (performance between corrosion allowance and corrosion resistant)			
Copper and nickel alloys			
N04400	Alloy 400, Monel 400	B 127 (plate)	Ni 63 0 min, Cu 28 0–34 0, Fe 2 5 max, Mn 2 0 max, C 0 03 max, Si 0 5 max, Si 0 5 max, S 0 024 max
C71500	70-30 copper nickel, CDA 715	B 171 (plate)	Ni 29 0–33 0, Cu balance, Mn 1 0 max, Pb 0 02 max, Fe 0 4–1 0, Zn 0 5 max, C 0 05 max, P 0 02 max, S 0 02 max

References for Section 2.0

Farmer, J C , R D McCright, and J N Kass (1988). *Survey of Degradation Modes of Candidate Materials for High-Level Radioactive Waste Disposal Containers*, Volumes 1–8, Lawrence Livermore National Laboratory, Livermore, CA, UCID-21362 [NNA 19891222 0305]

Gdowski, G E (1997) *Degradation Mode Survey Candidate Titanium-Base Alloys for Yucca Mountain Project Waste Package Materials*, Lawrence Livermore National Laboratory, Livermore, CA, UCRL-ID-121191, Rev 1 [MOL 19980120 0053]

Gdowski, G E (March 1991) *Survey of Degradation Modes of Four Nickel–Chromium–Molybdenum Alloys*, Lawrence Livermore National Laboratory, Livermore, CA, UCRL-ID-108330 [NNA 19910521 0010]

McCright, R D. (1996) *Metallic Barriers Selection and Testing Scientific Investigation Plan (SIP)*, SIP-CM-01, Rev 3, Lawrence Livermore National Laboratory, Livermore, CA [Draft. MOL 19960708.0470]

Roy, A K and D. A Jones (November 1996) *Degradation Mode Survey Galvanic Corrosion of Candidate Metallic Materials for High-Level Radioactive Waste Disposal Containers*, Lawrence Livermore National Laboratory, Livermore, CA, UCRL-ID-125645 [MOL.19970121 0087]

Van Konynenburg, R A , R D McCright, A K Roy, and D A Jones (1995) *Engineered Materials Characterization Report*, Volume 2 , Lawrence Livermore National Laboratory, Livermore, CA, UCRL-ID-119564 [MOL 19960402 0547]

Vinson, D W and D B Bullen (September 1995) *Survey of Degradation Modes of Candidate Materials for High-Level Radioactive Waste Disposal Container—Nickel-Copper Alloys*, Lawrence Livermore National Laboratory, Livermore, CA, UCRL-CR-122862 [MOL 19960418 0094]

Vinson, D. W , W M. Nutt, and D B Bullen (June 1995). *Survey of the Degradation Modes of Candidate Materials for High Level Radioactive Waste Disposal Containers, Iron-Base Corrosion-Allowance Materials*, Lawrence Livermore National Laboratory, Livermore, CA, UCRL-CR-120464 [MOL.19960418 0201]

2.1 Water Films

by G.E. Gdowski

The water chemistry that develops on the surface of a waste package (WP) is important because the corrosion or degradation processes of the WPs are strongly dependent on water chemistry This section discusses aspects of the development of thin film aqueous solutions on the surfaces of WPs Parameters considered include relative humidity (*RH*), temperature (*T*), water composition, and gas phase composition

Water adsorption on metal surfaces can be enhanced by several factors, such as adsorbed salts, corrosion products, gaseous contaminants, and crevices formed with the surfaces The effects of these factors will be discussed in following sections

2.1.1 Drift Characteristics

2.1.1.1 Drifts before Emplacement

The potential repository at Yucca Mountain, Nevada (YM), is located in the unsaturated zone, which is, by definition, located above the local water table The rock, however, has 10–20% water by volume This water is primarily trapped in pores and microfractures Unperturbed (that is, unventilated) ambient relative humidity within the Exploratory Studies Facility (ESF) at the YM site is at least 98% At the elevation of the potential repository, the ambient atmospheric pressure is nominally 0 091 MPa Due to the fractured nature of the repository rock, it is expected that the gas pressure in the drifts after emplacement will remain near this pressure, therefore, the repository is an open system with respect to gas transport As a consequence of the potential repository's elevation above sea level, the unconstrained boiling point of pure water is about 97°C

2.1.1.2 Drifts after Emplacement

The heat generated by the radioactive decay of the nuclear waste will raise the temperature of the rock surrounding the drifts. However, the temperature of the WP will still be higher than that of the surrounding rock (Buscheck et al , 1997). The elevated temperatures of the rock surrounding the drifts will liberate and mobilize the water contained in the pores and microfractures As the rock temperature rises, the water-vapor pressure will also rise Water is initially expected to be transported away from the hotter regions, decreasing the water content of the rock surrounding the drifts and decreasing the *RH* at the waste package for *T*s above approximately 100°C. After the thermal pulse, the temperature of the rock around the emplacement drifts will decrease, the water content of the rock surrounding the drifts will rise, and the *RH* at the WP will increase

Episodic water contact with the WPs is considered possible This contact could take the form of water dripping or of large volumes of water flowing down fractures Either case would result in aqueous salt solutions contacting the WP. I assum that the liquid water contacting the WPs will contain salts typical of the YM site , the term "salts" refers to those chemical compounds that have a measurable solubility in water.

To define typical YM salts, the compositions of YM waters are listed in Table 2.1-1. Well J-13 water is considered to be a representative water (Harrar et al., 1990); it is ground water from the same rock horizon as the potential repository. The major cations are Na^+, Ca^{2+}, K^+, and Mg^{2+}, and the major anions are HCO_3^-, SO_4^{2-}, Cl^-, NO_3^-, and F^-. The bicarbonate

concentration is determined from total inorganic carbon Silicon is present in solution as silicic ions

Table 2.1-1 Composition of well J-13 water.

Constituent	Well J-13 (mg/l)
Na	45.8
Si	28.5
Ca	13.0
K	5.04
Mg	2.01
F	2.18
Cl	7.14
NO_3	8.78
SO_4	18.4
HCO_3	128.9
pH	7.41

2.1.2 Relative Humidity Considerations

Relative humidity is the ratio of actual water-vapor pressure to the equilibrium water-vapor pressure at a given *T*. Figure 2 1-1 is a plot of equilibrium water-vapor pressure as a function of *T* (Weast and Astle, 1981) Figure 2 1-2 is a plot of the maximum *RH* obtainable versus *T* assuming a total gas pressure of 0 101 MPa, the mean sea-level atmospheric pressure (Because the expected maximum pressure in the emplacement drifts is 0 091 MPa, the maximum *RH* obtainable would decrease at *Ts* greater than 97°C, a curve for this case is also plotted in Figure 2 1-2)

Figure 2.1-1. Equilibrium water vapor pressure versus temperature.

Figure 2.1-2. Maximum relative humidity versus temperature.

Pure water condensation—that is, bulk liquid water formation—occurs at 100% *RH* However, Section 3 presents studies that have demonstrated the formation of very thin water films ($<10^{-6}$ g/cm^2) on clean metal and oxide surfaces at *RH* < 100%

2.1.2.1 Relative Humidity at a Waste-Package Surface

Because of the radioactive decay heat, the temperature of a WP will be higher than the temperature of the surrounding local drift walls. Further, the local water-vapor pressure in a drift is determined by the coldest local surface that is in contact with the air. The consequence is that the *RH* at the WP will always be less than that at the surrounding drift wall and will always be less than 100%.

With episodic water infiltration that contacts a WP, there will be a net evaporation of water from the WP until the thermodynamic state of the water is in equilibrium with the vapor-phase water (Van Konynenburg et al (1993) and Buscheck et al (1996) have previously made similar arguments.) This argument depends on the amount of the episodic

water being small If large quantities of water contact the WP, then nonequilibrium conditions could result

2.1.3 Water-Film or Liquid-Water Formation on Metal or Oxide Surfaces

This section discusses the formation of aqueous films on clean metal or oxide surfaces, including a discussion of water condensation in pores or crevices. The effect of hygroscopic salts on water adsorption is discussed in Section 4

By definition, when *RH* is greater than 100%, the air is super-saturated with water Water condensation will occur on any accessible surface, assuming all surfaces are at a constant temperature.

2.1.3.1 Clean Surfaces when RH < 100%

Several studies have investigated the adsorption of water on metal surfaces for a range of *RHs* and *Ts* For a completely inert surface there would be no adsorbed water, however, for real surfaces water molecules can be chemisorbed and physisorbed (Thiel, 1987) Chemisorbed water is limited to those water molecules that strongly interact with the surface and therefore form some type of chemical bond with the surface Additional water multilayers are physisorbed The physical forces that hold the molecules are a combination of van der Waals force and hydrogen bonding between water molecules These forces are much weaker than the chemisorption forces

The van der Waals force decreases rapidly with distance from the metal or oxide surface, the relation is the inverse square of the distance

In a recent study, Lee and Staehle (1997) determined the amount of water adsorbed on clean nickel, copper, and iron as a function of *T* and *RH* using a quartz-crystal microbalance (QCM) The effect of air or nitrogen as the carrier gas was investigated, and the maximum *T* investigated was 85°C Figure 2 1-3 shows their data for iron As a matter of interest, the amount of water adsorbed is not a strong function of *T* over the range of conditions investigated

Figure 2.1-3. Amount of water adsorbed on iron as a function of relative humidity and temperature. (a) under humidified nitrogen. (b) under humidified air.

On iron, the maximum amount of adsorbed water was less than 5×10^{-7} g/cm^2 (calculated film thickness less than 0 002 μm) in nitrogen, maximum adsorbed water was less than 3.7×10^{-7} g/cm^2 (thickness < 0 0015 μm) in air On copper, the maximum amount of adsorbed water was less than 6×10^{-7} g/cm^2 (thickness < 0 0025 μm) in nitrogen and about 6×10^{-7} g/cm^2 (thickness about 0.0025 μm) in air (*RHs* investigated for both metals ranged up to about 93%) The calculated film thickness (present author's calculation) assumes a uniformly flat surface; however, Lee and Staehle showed that their surfaces contained pores and cracks The calculated film thicknesses therefore overestimate the actual film thicknesses

Lee and Staehle suggested that the reduced water adsorption in air was due to formation of an oxide layer, which is less able to polarize the adsorbed water than an unoxidized surface Hence there is a decrease in the physisorption force between the adsorbed water and the surface (Suhrmann, 1968)

Eichhorn and Forker (1988) also determined that between 90 and 95% *RH* and at 25°C, the thickness of the adsorbed water layer on iron is between 0.002 and 0 003 μm

Sharma (1979), using the QCM technique, studied water adsorption of copper and copper oxide in the temperature range 18 to 45°C. The maximum amount of water adsorption was less than 10 monolayers at about 90% *RH*, these results did not vary significantly as a function of *T*. About 50% more water was adsorbed on the copper oxide than on the copper metal This contrasts with the results of Lee and Staehle

Dante and Kelly (1993) investigated the adsorption of water on copper using a QCM In clean air at 90% *RH* and 30°C, an average film thickness of about 18 monolayers of water was adsorbed on copper About 30 minutes was required to reach steady state

On polished iron, Tomashov (1966) reported water film thicknesses of 15 monolayers (0 004 μm, estimated) at 55% *RH* and 90 monolayers (0 028 μm, estimated) at just below 100% *RH*

2.1.3.2 Effect of Crevices and Pores on Water Condensation at RH < 100%

Water condensation will also occur in crevices and microfractures at *RH*s less than 100% The extent of this water condensation can be estimated by calculating the radii of pores in which water will condense as a function of *RH* and *T* This relation is expressed by the Thompson or Kelvin equation $P = P_o 2\gamma M/r\rho RT$, where

P is vapor pressure,

P_o is equilibrium vapor pressure,

γ is surface tension,

r is pore radius,

r is density, and

R is the gas constant

Note that P/P_o is the relative humidity

Table 2 1-2 lists the calculated radius for various values of *T* and *RII* (Values for the surface tension of water/air and water density were taken from Weast and Astle, 1981) Fyfe (1994) has also performed this calculation, but, unfortunately, the temperature was not given In general, however, there is good agreement between the present results and his results, which are also given in Table 2 1-2 for comparison

Table 2.1-2 Calculated pore radius in which water will condense as a function of *T* and *RH*.

RH (%)	Pore radius (μm)					Capillary radius (from Fyfe)	
	100°C	90°C	80°C	70°C	60°C	Å	μm
99	0 071	0 075	0 079	0 083	0 087		
98	0 035	0 037	0 039	0 041	0 043	360	0 036
95	0 014	0 015	0 015	0 016	0 017		
90	0 007	0 007	0 008	0 008	0 008	94	0 009
85	0 004	0 005	0 005	0 005	0 005		
80	0 003	0 003	0 004	0 004	0 004	47	0 005
75	0 003	0 003	0 003	0 003	0 003		
70	0 002	0 002	0 002	0 002	0 003	30	0 003
60						21	0 002
50						15	0 001

For *RH* < 90%, the characteristic dimension of the adsorbed water is of the same order of magnitude as for water adsorption at very high *RH*s At 98% *RH*, the characteristic thickness is 10 to 30 times larger

2.1.4 Hygroscopic Salts and the Equilibrium *RH* of Aqueous Salt Solutions

The equilibrium *RH*s versus *T* of several saturated salt solutions (Greenspan, 1977) and the boiling points of several saturated salt solutions (Washburn, 1928) are plotted in Figure 2 1-3. The solid line is the maximum *RH* that is obtainable with the total pressure limited to 0.101 MPa, that is, the mean sea-level atmospheric pressure

Figure 2.1-3. Equilibrium relative humidities versus temperature, and boiling points, for various aqueous salt solutions.

There are some general trends in how effective certain ions are at lowering the water-vapor pressure Among anions, sulfates (SO_4) have higher equilibrium *RH*s (are less hygroscopic) than chlorides (Cl) and nitrates (NO_3) have

For some salts, such as sodium chloride (NaCl), there is little change in the equilibrium *RH* as a function of *T*. This is probably because the solubility of NaCl does not change much with temperature. For other salts, such as magnesium nitrate [$Mg(NO_3)_2$], there is almost a 20% change in the equilibrium *RH* as a function of *T* greater than 50°C This is probably because the solubility of $Mg(NO_3)_2$ doubles between 25 and 100°C

The lower water-vapor pressure of an aqueous salt solution results in the elevation of the boiling point of the solution. (The boiling point of water is the temperature at which the water-vapor pressure of the solution equals atmospheric pressure at mean sea level) The boiling points of several saturated salt solutions at 0.101 MPa pressure (normal atmospheric pressure) are also shown in Figure 2 1-3. Extension of the equilibrium *RH* versus *T* curves should intersect the maximum *RH* curve at the boiling points of the corresponding saturated solutions

The implication of the elevated boiling points is that aqueous solutions of saturated salts such as $CaCl_2$ can exist at *T*s as high as 166°C. In terms of metallic corrosion, such salts permit

aqueous electrochemical corrosion processes at these $Ts \geq 100°C$ for susceptible materials, provided that there is an oxidant available

At *RH* values less than the equilibrium value for saturated salt solutions, bulk aqueous salt solutions will not form from the dry salt. At *RH* values greater than the equilibrium value for saturated salt solutions, more dilute aqueous solutions will form. The amount of water that is taken up by hygroscopic salts, such as NaCl, has been determined previously as a function of *RH* (Washburn, 1928). Table 2 1-3 lists the equilibrium *RH* as a function of salt concentration for various salts As can be seen, as the *RH* increases, the salt concentration decreases For the salts listed, very concentrated solutions (> 1M) exist at *RH*s less than 95%

Corrosion of susceptible metal alloys has been noted at *RH* values less than the equilibrium *RH* for saturated salt solutions (Duly, 1950)

Table 2.1-3 Aqueous solution concentrations for some salts in various environments.

NaCl			NaCl			NaCl			Na_2SO_4			Na_2CO_3		
20–25°C			80°C			100°C			100°C			100°C		
ppm	M	*RH*	ppm	M	*RH*	ppm	M	*RH*	ppm	M	*RH*	ppm	M	*RH*
5844	0 1	0 997	233771	4 0	0 854	146107	2 5	0 913	142041	1 0	0 983	74192	0 7	0 973
11689	0 2	0 993	292214	5 0	0 811	204550	3 5	0 875	639185	4 5	0 967	105379	1 0	0 954
23377	0 4	0 987	350657	6 0	0 765	233771	4 0	0 855	781227	5 5	0 951	201379	1 9	0 910
35066	0 6	0 980				292214	5 0	0 812	923268	6 5	0 935	233176	2 2	0 896
46754	0 8	0 974				368190	6 3	0 754	994288	7 0	0 919	317967	3 0	0 859
58443	1 0	0 967				391567	6 7	0 739	$1\ 6\times10^6$	11 5	0 902	413357	3 9	0 839
116886	2 0	0 932												
163640	2 8	0 901												
292214	5 0	0 807												
350657	6 0	0 761												

ppm = parts per million; M = molarity; *RH* = relative humidity

2.1.5 Gaseous Components and Relative Humidity

Nitric and sulfuric acids form aqueous solutions with equilibrium *RH*s less than the saturation value However, a partial pressure of these gases is required to maintain these solutions Table 2 1-4 lists the *RH*s and gaseous partial pressures as a function of *T* for a 20 wt% HNO_3 (nitric acid) aqueous solution (Perry and Chilton, 1973)

Table 2.1-4 *RH*, water partial pressure, and nitric acid partial pressure for 20 wt% HNO_3 aqueous solution.

T (°C)	Pure H_2O partial pressure (mm Hg)	20 wt% NHO_3		
		H_2O partial pressure (mm Hg)	*RH* (%)	HNO_3 partial pressure (mm Hg)
55	118 0	100	85	0 09
60	149 4	128	86	0 13
65	187 5	162	86	0 19
70	233 7	200	86	0 27
75	289 1	250	86	0 38
80	355 1	307	86	0 53
85	433 6	378	87	0 74
90	525 8	458	87	1 01
95	633 9	555	88	1 37
100	760 0	675	89	1 87
105	906 1	800	88	2 50

No data were found for dilute solutions It would be interesting to know what partial pressures of nitric and sulfuric acids and *RH*s are necessary to maintain solutions of pH 4 (0 49 and 0 63 wt% of sulfuric and nitric acid, respectively), and pH 5 (0 05 and 0 06 wt% of sulfuric and nitric acid, respectively)

Gaseous sulfur dioxide, SO_2, is known to cause enhanced corrosion of carbon steel at *RH*s greater than 60% at ambient temperatures and SO_2 concentration on the order of 1 ppm One of the steps in the corrosion process is the oxidation of the sulfur dioxide to form sulfuric acid, H_2SO_4 Sulfuric acid is hygroscopic and will readily form aqueous solutions, which facilitate the electrochemical corrosion of the carbon steel.

Although SO_2 is important in atmospheric corrosion because it is present in urban atmospheres as an industrial pollutant, it may not be present in significant concentration in the drifts of the potential YM repository There are, however, naturally occurring gaseous sulfur species (H_2S and COS) that will corrode iron (Graedel and McGill, 1986)

Nitric acid and ammonia have been shown to form in air containing water vapor under gamma irradiation, and the quantities formed are dose dependent (Reed, 1991, p 58) The effect these would have on the degradation of the WPs would depend on the amounts that form and their residence time on a WP surface Gaseous nitric acid could be neutralized by the near-neutral–to–alkaline water characteristic of YM waters, the water at the YM site is strongly influenced by the calcite mineral deposits throughout the mountain

2.1.6 CO_2 and Cement-Modified Water

Water that has been in contact with cement may attain pH 12.4 This is the result of the reaction of CaO with water to produce $Ca(OH)_2$, and the dissolution of $Ca(OH)_2$ A saturated solution of $Ca(OH)_2$ has pH 12 4 in the absence of gaseous CO_2 (20°C) (Drever, 1982).

$$CaO + H_2O \rightarrow Ca(OH)_2 \qquad (2\ 1\text{-}1)$$

The carbonation of cement is the result of the reaction of gaseous CO_2 with the aqueous calcium hydroxide solutions, thus

$$CO_2 + H_2O \rightarrow H_2CO_3 \rightarrow H^+ + HCO_3^- \quad , \qquad (2\ 1\text{-}2)$$

$$Ca(OH)_2 \rightarrow Ca_2^+ + {}_2OH^- \quad , \qquad (2\ 1\text{-}3)$$

$$H^+ + OH^- \rightarrow H_2O \quad , \qquad (2\ 1\text{-}4)$$

and

$$Ca_2^+ + {}_2HCO_3^- \rightarrow CaCO_3 + CO_2 + H_2O \qquad (2\ 1\text{-}5)$$

A $CaCO_3$ solution has pH 8 2 when in contact with normal atmospheric CO_2 content air (Drever, 1982) Mean carbon dioxide partial pressure of air is 0 00033 atm

This same reaction would occur in aqueous calcium hydroxide solutions on the surface of a metal in contact with air containing CO_2 The amount of gaseous CO_2 obviously is a contributing factor to the pH of the aqueous solutions

2.1.7 Oxygen Solubility in Aqueous Solutions

In atmospheric corrosion of metals, the reduction of oxygen is an important step in the electrochemical corrosion process The availability of oxygen can therefore influence on the rate of corrosion of a metal Oxygen solubility in water and in numerous aqueous salt solutions, in contact with water-vapor-saturated air, has been determined by Cramer (1974) Those solubilities are reproduced in Figure 2 1-4

Figure 2.1-4. Solubility of oxygen in water and in brines, from air saturated with water vapor at a total pressure of 1 atm (101.3 kPa).

With increasing salt concentrations, the solubility of oxygen at a given temperature decreases, this process is called the salting-out effect With increasing temperature, the solubility of oxygen in a given aqueous solution decreases This is in part because of the decreasing oxygen content of vapor in contact with the solution For example, for water-vapor-saturated air at 25°C, the partial pressure of oxygen is 0 020 MPa, while at 95 and 100°C it is 0.003 and 0 000 MPa, respectively. At 100°C, the vapor is 100% water

Cramer has also determined the change in oxygen solubility with changes in T (in a brine solution exposed to a constant partial pressure of oxygen). about a 20–30% decrease in oxygen solubility with a temperature change from 25 to 100°C for oxygen partial pressure of both 0 07 and 0 20 atm (0 0071 and 0 021 MPa) It is important to note that oxygen content in water, even at 100°C, can be substantial, depending on the oxygen content of the gas in contact with the water

Oxygen diffusion in water will also influence the rate of the electrochemical reactions, if the oxygen diffusion limits the reaction rates Fick's first law describes the flux J of a solute in a solvent in terms of the solute's concentration gradient, dC/dx, and diffusion coefficient, D,

thus $J = -D(dC/dx)$. The diffusion coefficient for oxygen in water is 2 2 × 10^{-5} cm^2/sec at room temperature

It is illustrative to make the following simplifying assumption to Fick's first law: $dC/dx = \Delta C/\Delta x$, where ΔC is the difference between the oxygen concentration at the air–film interface and the film–metal interface, and Δx is equal to the film thickness This equation implies that for every order of magnitude decrease in the film thickness, there is consequent order of magnitude increase in the oxygen flux

2.1.8 Summary

Appreciable water adsorption will occur on a surface if any of the following conditions are met·

- The relative humidity at the surface is ≥ 100%
- Hygroscopic salts are deposited on the surface and the local *RH* is equal to or greater than the equilibrium *RH* for the saturated salt solution
- Certain hygroscopic gases, such as sulfur dioxide, are present, and the *RH* exceeds a certain value

Thin water films are adsorbed on clean metal or oxide surfaces when the *RH* < 100% These films have thicknesses of less than 0 1 μm (and probably less than 0 01 μm) Oxygen flux through films of such thicknesses is relatively fast

Crevices and micropores can hold somewhat more water than free surfaces However, *RH* > 90% is required before crevices or micropores of large diameter will hold water

Acknowledgements

Kirk Staggs, Scott Doughty, Ken King, Steve Gordon, John Estill, Rich Green, and Stan Edson are acknowledged for their significant contributions to these studies

2.1.9 References

Buscheck, T A , J J. Nitao, and L D Ramspott (1996). "Near-Field Thermal-Hydrological Behavior for Alternative Repository Designs at Yucca Mountain " In proceedings from *XX International Symposium Science Basis Nuclear Waste Management* Boston, MA Dec 2, 1996 Mater Res Soc (Also UCRL-JC-124629, Livermore, CA Lawrence Livermore National Laboratory) [MOL.19961014 0031]

Cramer, S D (1974) "The Solubility of Oxygen in Geothermal Brines " C. S Tedmon, Jr , ed *Corrosion Problems in Energy Conversion and Generation* Princeton, NJ: Corrosion Division, Electrochemical Society. pp. 251-262

Dante, J F , and R. G Kelly (1993). "The Evolution of the Adsorbed Solution Layer during Atmospheric Corrosion and its Effect on the Corrosion Rate of Copper " *J Electrochem Soc* **140:**1890

Drever, J. I (1982) *Geochemistry of Natural Water* Englewood Cliffs, NJ. Prentice-Hall

Duly, S J (1950). "The Corrosion of Steel by Sea Salt of Given Moisture Content " *J Soc Chem Ind* **69:**304.

Eichhorn, K J., and W. Forker (1988) "The Properties of Oxide and Water Films Formed during the Atmospheric Exposure of Iron and Low-Alloy Steels " *Corros Sci* **28**(8) 745–758.

Fyfe, D (1994) "The Atmosphere " L L Shreir, R A. Jarman, and G T. Burstein, eds *Corrosion Metal/Environments* Third edition Oxford, U K . Butterworth Heinemann Ltd

Graedel, T E , and R. McGill (1986) "Degradation of Materials in the Atmosphere," *Environmental Science & Technology* **20**.1093

Greenspan, L (1977) "Humidity Fixed-Points of Binary Saturated Aqueous-Solutions " *J Res Natl Bur Stand* **81**(1A) 89–96

Harrar, J , J F Carley, W F Isherwood, and E Raber (1990). *Report of the Committee to Review the Use of J-13 Well Water in Nevada Nuclear Waste Storage Investigations* (UCRL-ID-21867) Livermore, CA Lawrence Livermore National Laboratory [NNA.910131.0274]

Lee, S , and R W Staehle (1997) "Adsorption of Water on Copper, Nickel, and Iron," *Corrosion* **53** 33-42

Perry, R H , and C. H. Chilton, eds (1973) *Chemical Engineers' Handbook* Fourth edition New York, NY· McGraw-Hill

Reed, D T (1991) "Progress in Assessing the Effect of Ionizing Radiation on the Anticipated Waste Package Environment at the Yucca Mountain Potential Repository Site " In proceedings of *Topical Meeting on Nuclear Waste Packaging Focus '91* La Grange Park, IL American Nuclear Society, Inc p 58

Suhrmann, R , J M Heras, L V de Heras, and G Wedler (1968) "Chemisorption und Zerfall der Wassermolekel an reinen Eisen- und Kupferoberflächen bei niedrigen Temperaturen." *Ber Bunsenges Physik Chem* **72** 854

Sharma, S P (1979) "Adsorption of Water on Copper and Cuprous Oxide," *J Vacuum Sci Tech* **16**(5) 1557

Thiel, P. A , and T E Madey (1987) "The Interaction of Water with Solid Surfaces Fundamental Aspects." *Surface Science Reports*. 7:211-385

Tomashov, N D (1964) "Development of the Electrochemical Theory of Metallic Corrosion " *Corrosion* **20** 7t-14t.

Van Konynenburg, R. A , W G Halsey, R. D McCright, W L. Clarke, Jr , and G E Gdowski (1993) *Selection of Candidate Container Materials for the Conceptual Waste Package Design for a Potential High Level Nuclear Waste Repository at Yucca Mountain* (UCRL-ID-112058) Livermore, CA· Lawrence Livermore National Laboratory

Washburn, E W , editor-in-chief (1928) *International Critical Tables of Numerical Data, Physics, Chemistry and Technology*. New York, NY: McGraw-Hill

Weast, R C., and M. J. Astle, eds (1981) *CRC Handbook of Chemistry and Physics* Boca Raton, FL CRC Press

2.2 Long-Term Corrosion Studies

by John C. Estill, Francis Wang, Steven Gordon, Kenneth King, and Larry Logoteta

2.2.1 Facility

A corrosion test facility has been constructed and operational for nearly two years The facility was constructed to house large vessels that contain several thousand test specimens, which are being studied to determine the corrosion properties of candidate materials for construction of containers to be used for long-term storage of high-level radioactive waste at Yucca Mountain, Nevada The Long-Term Corrosion Test Facility (LTCTF) currently has 24 vessels on line containing various chemical solutions, specimen configurations, and alloys, encompassing a range of possible environments and design considerations for a multibarrier containment package The test program described herein is being conducted according to the requirements set forth in Metallic Barriers Scientific Investigation Plan Activity E-20-50, revision 4 (Gdowski, 1998)

The test vessel construction was described in a previous *Engineered Materials Characterization Report* (EMCR) (McCright, 1997, vol 3) Each vessel contains a thermocouple in the vapor and aqueous phase, and the temperature is logged for the test duration A level-sensor package is installed in each vessel so that the water level remains constant, drawing on a reservoir of deionized water as needed A condenser is placed on the top of the vessel to minimize water loss The vessel also contains a mixer motor attached to the top of vessel with a Teflon-coated stainless-steel shaft to provide mild agitation of the water Approximately 60% of the vessel is filled with the test solution so that a rack has specimens exposed in the aqueous phase, in the vapor phase, and at the water line

Each vessel contains spacing for up to six specimen racks Sufficient numbers of replicate specimens are placed in each vessel, and we plan to remove specimen sets at fixed intervals An examination and evaluation of a specimen set is planned after six months, one year, two years, four years, and five years Many of the vessels have a full compliment of specimens to accomplish the planned interval evaluation, whereas other vessels only have one or two racks of specimens for removal at a selected interval Budgetary considerations did not make it possible to completely fill all vessels with a full compliment of specimens As the budget allows, more specimen racks will be added to those vessels with available space The facility plan view drawing is presented in Figure 2 2-1, and Table 2 2 -1 lists the contents of each vessel as well as the start date and removal date for each specimen rack.

Figure 2.2-1. Plan of ICF B-435, Room 1020.

Table 2.2-1. Test facility schedule.

Materials	Sample Rack	Start	Remove
Vessel 9: 60°C SCW galvanic corrosion	9-1	04-10-98	10-10-98
	9-2	NA	NA
	9-3	NA	NA
	9-4	NA	NA
	9-5	09-25-97	09-25-02
	9-6	NA	NA
Vessel 10 90°C SCW galvanic corrosion	10-1	04-10-98	10-10-98
	10-2	NA	NA
	10-3	NA	NA
	10-4	NA	NA
	10-5	09-25-97	09-25-02
	10-6	NA	NA
Vessel 11: 60°C SCW intermediate corrosion-resistant	11-1	03-19-98	09-19-98
	11-2	03-20-98	03-20-98
	11-3	03-22-98	03-22-00
	11-4	03-23-98	03-23-01
	11-5	09-25-97	09-25-02
	11-6	NA	NA
Vessel 12: 90°C SCW intermediate corrosion-resistant	12-1	03-27-98	09-27-98
	12-2	03-27-98	03-27-99
	12-3	03-26-98	02-26-00
	12-4	03-26-98	03-26-01
	12-5	09-26-97	09-25-02
	12-6	NA	NA
Vessel 13 60°C SDW intermediate corrosion-resistant	13-1	03-31-98	09-31-98
	13-2	03-31-98	03-31-99
	13-3	03-31-98	03-31-00
	13-4	03-30-98	03-30-01
	13-5	09-24-97	09-24-02
	13-6	NA	NA
Vessel 14: 90°C SDW intermediate corrosion-resistant	14-1	04-02-98	10-02-98
	14-2	04-02-98	04-02-99
	14-3	04-02-98	04-02-00
	14-4	04-02-98	04-02-01
	14-5	09-24-97	09-24-02
	14-6	NA	NA

Vessel 17: 60°C SDW galvanic corrosion	17-1	04-08-98	10-08-98
	17-2	NA	NA
	17-3	NA	NA
	17-4	NA	NA
	17-5	09-15-97	09-15-02
	17-6	NA	NA
Vessel 18· 90°C SAW intermediate corrosion-resistant	18-1	12-09-96	06-09-97
	18-2	12-09-96	12-09-97
	18-3	12-09-96	12-09-98
	18-4	12-09-96	12-09-99
	18-5	12-09-96	12-09-01
	18-6	NA	NA
Vessel 19 60°C SAW intermediate corrosion-resistant	19-1	11-26-96	05-26-97
	19-2	11-26-96	11-26-97
	19-3	11-26-96	11-26-98
	19-4	11-26-96	11-26-99
	19-5	11-26-96	11-26-01
	19-6	NA	NA
Vessel 20· 90°C SCW corrosion-allowance	20-1	11-15-96	05-15-97
	20-2	11-15-96	11-15-97
	20-3	11-15-96	11-15-97
	20-4	11-15-96	11-15-99
	20-5	11-15-96	11-15-01
	20-6	NA	NA
Vessel 21: 60°C SCW corrosion-allowance	21-1	10-28-96	04-28-97
	21-2	10-28-96	10-28-97
	21-3	10-28-96	10-28-98
	21-4	10-28-96	10-28-99
	21-5	10-28-96	10-28-01
	21-6	NA	NA
Vessel 22: 90°C SDW corrosion-allowance	22-1	10-10-96	04-10-97
	22-2	10-10-96	10-10-97
	22-3	10-10-96	19-19-98
	22-4	10-10-96	10-10-99
	22-5	10-10-96	10-10-01
	22-6	NA	NA
Vessel 23: 60°C SDW corrosion-allowance	23-1	09-24-96	03-24-97
	23-2	09-24-96	09-24-97
	23-3	09-24-96	09-24-98
	23-4	09-24-96	09-24-01
	23-5	09-24-96	09-24-01
	23-6	NA	NA

Vessel 24: 90°C SDW galvanic corrosion	24-1	04-09-98	10-09-98
	24-2	NA	NA
	24-3	NA	NA
	24-4	NA	NA
	24-5	09-18-97	09-18-02
	24-6	NA	NA
Vessel 25: 60°C SAW corrosion-resistant	25-1	02-06-97	08-06-97
	25-2	02-06-97	02-06-98
	25-3	02-06-97	02-06-99
	25-4	02-06-97	02-06-02
	25-5	02-06-97	02-06-02
	25-6	NA	NA
Vessel 26: 90°C SAW corrosion-resistant	26-1	02-21-97	08-21-97
	26-2	02-21-97	02-21-98
	26-3	02-21-97	02-21-99
	26-4	02-21-97	02-21-00
	26-5	02-21-97	02-21-02
	26-6	NA	NA
Vessel 27: 60°C SCW corrosion-resistant	27-1	03-10-97	09-10-97
	27-2	03-10-97	03-10-98
	27-3	03-10-97	03-10-99
	27-4	03-10-97	03-10-00
	27-5	03-10-97	03-10-02
	27-6	NA	NA
Vessel 28 90°C SCW corrosion-resistant	28-1	04-10-97	10-10-97
	28-2	04-10-97	04-10-98
	28-3	04-10-97	04-10-99
	28-4	04-10-97	04-10-00
	28-5	04-10-97	04-10-02
	28-6	NA	NA
Vessel 29: 60°C SDW corrosion-resistant	29-1	04-14-97	10-14-97
	29-2	04-14-97	04-14-98
	29-3	04-14-97	04-14-99
	29-4	04-14-97	04-14-00
	29-5	04-14-97	04-14-02
	29-6	NA	NA
Vessel 30: 90°C SDW corrosion-resistant/Westinghouse	30-1	06-05-97	12-05-97
	30-2	06-05-97	06-05-98
	30-3	06-05-97	06-05-99
	30-4	06-05-97	06-05-00
	30-5	04-17-97	04-17-02
	30-6	10-24-97	10-24-98

Vessel 31. 60°C SCMW galvanic corrosion	31-1	04-07-98	10-07-98
	31-2	NA	NA
	31-3	NA	NA
	31-4	NA	NA
	31-5	09-17-97	09-17-02
	31-6	NA	NA
Vessel 32: 90°C SCMW galvanic corrosion	32-1	04-17-98	10-07-98
	32-2	NA	NA
	32-3	NA	NA
	32-4	NA	NA
	32-5	09-17-97	09-17-02
	32-6	NA	NA
Vessel 33: 60°C SCMW corrosion-allowance	33-1	03-10-98	09-10-98
	33-2	03-08-98	03-08-99
	33-3	03-01-98	03-01-00
	33-4	02-27-98	02-27-01
	33-5	09-22-97	09-22-02
	33-6	NA	NA
Vessel 34 90°C SCMW corrosion-allowance	34-1	03-15-98	09-15-98
	34-2	03-15-98	03-15-99
	34-3	03-13-98	03-13-00
	34-4	03-13-98	03-13-01
	34-5	09-22-97	09-22-02
	34-6	NA	NA

2.2.2 Materials

An earlier EMCR discussed in detail the materials being tested (McCright, 1997), however, two additional alloys have since been added to the test matrix

The first of these alloys is Inconel 625 (UNS N06625, with nominal composition 20 0–23 0 Cr, 5 0 max. Fe, 8.0–10 0 Mo, 3 15–4 14 Cb + Ta, 0 10 max C, 0.50 max Mn, 0.50 max Si, 0 015 max P, 0.015 max S, 0 40 max Al, 0 40 max. Ti, 1 0 max Co, 58 0 min Ni) Weight-loss, crevice, U-bend, and galvanic specimens were fabricated from this alloy

The second material added to the alloy matrix was Inconel 686 (UNS N06686, with nominal composition 19 0–23.0 Cr, 5 0 max Fe, 15 0–17 0 Mo, 0 01 max C, 0 75 max. Mn, 0.08 max Si, 0 04 max P, 0 02 max S, 0 02–0 25 Ti, 3 0–4 4 W, remainder Ni). Only galvanic specimens were fabricated from this alloy This alloy was added to the test matrix because in the manufacturer's testing of Inconel 686, increased resistance to $FeCl_3$-induced corrosion was realized $FeCl_3$ is thought to be an aggressive species present during crevice corrosion of stainless steels and is considered contributory to crevice corrosion

2.2.3 Specimens

Three specimen types used for studying general corrosion (weight-loss specimen), crevice corrosion (crevice-corrosion specimen), and stress-corrosion cracking (U-bend specimen) have been discussed in a previous EMCR (McCright, 1997) These specimens are exposed in the aqueous phase, in the vapor phase, and at the water line A typical rack loaded with these specimen types is presented in Figure 2 2-2

Figure 2.2-2. Typical single metal specimen rack.

Galvanic corrosion testing has been underway for nearly six months and is expected to provide a ranking of the galvanic corrosion resistance of alloys Hastelloy C22, Inconel 686, Inconel 625, Incoloy 825, and titanium grade 12 coupled directly to alloys A516 and A387, using weight-loss data for corrosion-rate calculations, and pitting analysis using optical profiling Flat specimens are weighed and measured before and after testing to determine corrosion rates, these specimens were 1 × 2 × 0 125 in , 2 × 2 × 0 125 in , or 1 5 × 1 5 × 0 125 in Both welded and unwelded specimens are tested from alloys Hastelloy C22, Inconel 686, Inconel 625, and titanium grade 12 An optical profiler system is used to determine maximum pit depth and other surface characteristics

In addition to providing a relative ranking of materials based on corrosion rates and pitting data, galvanic corrosion testing may provide some clues to the presence or nature of hydrogen charging effects, especially in titanium materials coupled to carbon and low-alloy steels Post-test chemical analysis to determine hydrogen absorption will be conducted on selected materials As in the single metal tests, test exposures are in the aqueous and vapor phase as well as at the water line A typical specimen rack containing the galvanic specimens is pictured in Figure 2 2-3

Figure 2.2-3. Typical galvanic metal specimen rack.

The galvanic specimen assembly is constructed of two different metal systems coupled to provide intimate electrical contact between specimens and is designed to simulate the interaction of bounding environments with the multibarrier conceptual design components The galvanic assembly is actually a sandwich of materials consisting of a corrosion-resistant material placed between two corrosion-allowance specimens Intimate contact between specimens is mediated via multiple Belleville spring washers providing axial force at the metal interfaces. The galvanic study also includes the effect of different surface-area ratios with respect to the corrosion-resistant and corrosion-allowance materials. For the galvanic study, two distinct specimen assemblies, type I and type II, will be studied, each representing a galvanic-corrosion scenario

The type I galvanic specimen has a large anode-to-cathode ratio (20 1) and is representative of a large area of corrosion-allowance material (anode) and small area of corrosion-resistant material (cathode) exposed to the environment While the anode material will corrode preferentially to the cathode material, the corrosion can be spread over a larger area This particular scenario is possible if a breach of the outer container occurs, thus exposing a small area of the underlying corrosion-resistant material. The type I test will provide clues as to what degree the corrosion-allowance material offers protection to the corrosion-resistant material should such a breach occur in the repository

The type II galvanic specimen has an anode-to-cathode ratio of 1 1. The type II specimen is representative of equal areas of corrosion-allowance material (anode) and corrosion-

resistant materials (cathode) exposed to the environment The reduced area of the anode, compared to the type I specimen, is expected to have a focusing effect of the corrosion attack on the smaller area, thus the extent of attack to the corrosion-allowance material is expected to be more substantial than in the type I test Figure 2.2-4 shows both type I and type II galvanic assemblies

Figure 2.2-4. Galvanic specimen assemblies.

The corrosion rates and pitting data generated from the galvanic study will be compared to the data generated from the single-metal weight-loss and crevice-corrosion experiments

2.2.4 Test Environments

There are currently four test environments used for long-term corrosion studies The solution makeup is governed by Technical Implementing Procedures (TIP) CM-06, CM-07, CM-08, and CM-11 These are bounding environments thought to be plausible given the ionic species present in well J-13 water and the possible interaction of water with the near-field environment over extended periods An earlier EMCR discussed the environments described in TIPs CM-06, CM-07, and CM-08 (McCright, 1997)

The environment described in TIP CM-11, "Formulation and Make-Up of Simulated Cement Modified Water," was calculated to simulate J-13 water coming into contact with aged cement (Gdowski, 1997) Due to the extreme thermal loading of the repository during the early part of the waste package storage life, water is not expected to move into the near field for many years, thus, any cementitious contact with water will be with aged cement Aged cement is cement that is expected to undergo some change in chemical composition due to extended exposure to high temperature and CO_2 The makeup of this environment was determined using the EQ3/6 software program

The test environments include four aqueous solutions that may simulate a range of environments to which the container materials may be exposed The environments are briefly described as follows

- TIP CM-06, Simulated Dilute Well (SDW) J-13 water at 10× concentration Well J-13 water is thought to be typical of the vadose water in the repository The slight concentration is intended to represent the effects of water evaporation and boiling in the repository environment, which concentrates the salts in the water
- TIP CM-07, Simulated Concentrated Well (SCW) J-13 water at 1000×. The extreme concentration of water is intended to represent the long-term concentration effects brought on by evaporation and boiling of water in the repository
- TIP CM-08, Simulated Acidified Well (SAW) J-13 water concentrated and acidified to pH between 2.0 and 3.0 This environment is intended to simulate the effect of possible microbial metabolic products, which tend to lower the pH of water. Water pH was lowered using reagent-grade acids
- TIP CM-11, Simulated Cement-Modified Water (SCMW). This environment is intended to simulate the effect of water contact with aged cementitious materials that may be used in the repository construction.

Table 2 2-2 through Table 2 2-5 describe the actual solution chemistry results for each vessel as well as the target values pursuant to the applicable TIP.

Table 2.2-2 Simulated Dilute Well Water (SDW).

	60°C					90°C				
	Target values	Vessel 13	Vessel 17	Vessel 23	Vessel 29	Target values	Vessel 14	Vessel 22	Vessel 24	Vessel 30
vspd		9/23/97	9/12/97	9/20/96	3/21/97		9/23/97	10/3/96	9/16/97	3/21/97
iasd		9/24/97	9/15/97	9/24/96	4/15/97		9/24/97	10/28/96	11/17/97	4/18/97
Na^+	409	434	421	463	440	409	437	456	380	430
Si^+	27	25	25	28	20	49	36	21	15	21
Ca^+	0 5	24	12	21	3	0 5	10	2	0 4	0 6
K^+	34	34	33	36	36	34	34	38	42	36
Mg^+	1	22	32	20	13	1	13	0 2	0 3	0 7
Fl^-	14	14	13	14	25	14	14	15	35	25
Cl^-	67	68	46	71	67	67	75	74	78	68
NO_3^-	64	61	63	62	78	64	62	64	55	78
SO_4^-	167	175	173	167	166	167	170	175	154	172
HCO_3	947	864	788	849	763	947	798	701	513	671
pH	equilibrium	8 5	8 4	8 6	9 0	equilibrium	8 6	9 6	9 9	9 3

vspd = vessel solution preparation date, iasd = ion analysis sample date

Table 2.2-3 Simulated Concentrated Well Water (SCW).

	60°C					90°C				
	Target values	Vessel 9	Vessel 11	Vessel 21	Vessel 27	Target values	Vessel 10	Vessel 12	Vessel 20	Vessel 28
vspd		9/24/97	9/24/97	10/23/96	3/7/97		9/24/97	9/23/97	11/13/96	3/11/97
iasd		9/25/97	9/25/97	10/28/96	3/10/97		9/25/97	9/25/97	11/15/96	4/11/97
Na^+	40,900	36,500	37,000	28,500	38,000	40,900	38,100	42,500	45,000	45,000
Si^+	27	47	44	10	52	49	48	52	57	55
Ca^+	<1	28	8	4	0 6	<1	24	138	4	2
K^+	3,400	3,490	3,500	2,700	3,600	3,400	3,500	3,580	4,600	3,700
Mg^+	<1	7	1	89	0 1	<1	4	48	nd	0 3
Fl^-	1,400	1,240	1,340	84	2,520	1,400	1,270	1,580	1,390	2,510
Cl^-	6,700	6,820	7,300	6,570	6,790	6,700	7,190	7,200	7,720	6,960
NO_3^-	6,400	6,180	6,490	6,570	8,090	6,400	6,500	6,440	7,380	7,870
SO_4^-	16,700	12,600	12,900	12,500	13,700	16,700	13,100	13,000	13,300	14,600
HCO_3	70,000	21,762	75,564	36,448	61,229	70,000	76,631	21,827	37,759	57,569
pH	equilibrium	8 3	8 3	8 4	8 5	equilibrium	8 5	8 9	8 9	9 7

Table 2.2-4 Simulated Acidified Well Water (SAW).

	60°C			90°C		
	Target values	Vessel 19	Vessel 25	Target values	Vessel 18	Vessel 26
vspd		11/26/96	2/5/97		12/9/96	2/20/97
iasd		11/27/96	2/6/97		12/10/96	2/21/97
Na^+	40,900	43,000	43,000	40,900	43,000	42,000
Si^+	27	32	27	49	54	44
Ca^+	<1	60	55	<1	59	55
K^+	3,400	4,300	3,700	3,400	4,300	3,500
Mg^+	<1	53	52	<1	54	51
Fl^-	1,400	<10	<10	1,400	<10	<10
Cl^-	6,700	25,000	27,500	6,700	26,300	26,900
NO_3^-	6,400	22,900	24,300	6,400	22,500	24,000
SO_4^-	16,700	39,800	42,400	16,700	41,100	41,000
HCO_3	–	–	–	–	–	–
pH	2 8	2 7	2 7	2 8	2 7	2 7

Table 2.2-5 Simulated Cement-Modified Water (SCMW).

	60°C			90°C		
	Target values	Vessel 31	Vessel 33	Target values	Vessel 32	Vessel 34
vspd		9/15/97	9/18/97		9/15/97	9/18/97
iasd		9/17/97	9/22/97		9/18/97	9/22/97
Na^+	11 0	13	12	14 0	17	16
Si^+	12 8	5	5	22 7	9	8 5
Ca^+	452 8	478	473	197 5	214	210
K^+	86 9	95	91	309	339	331
Mg^+	3 6	4	4	0 3	<0 1	0 4
Fl^-	1 3	<0 1	<0 3	1 3	<0 3	<0 3
Cl^-	4 1	11	<0 5	4 3	<0 5	<0 5
NO_3^-	4 9	10	<0 9	5 2	<0 9	<0 9
SO_4^-	1,201 6	1,220	1,110	864 7	845	824
HCO_3	9 0	10	15	6 4	10	15
pH	7 65	7 67	7 53	7 75	7 84	7 60

In addition to the chemical environment, there are some important considerations with regard to dissolved oxygen and carbon dioxide (produced from the decomposition of HCO_3^-),

both of which may play a large part in the corrosion process in both the aqueous and vapor phase

The concentration of dissolved oxygen in test solutions may be a factor for aqueous-phase corrosion The oxygen concentrations are 7 0 ppm in SDW and 5 2 ppm in SCW at 24°C Cramer (1974) reported the solubility of oxygen, as a function of temperature, in distilled water, NaCl solutions, and geothermal brines. Cramer shows that oxygen is less soluble in a solution with higher dissolved salts at the same temperature, but the difference in oxygen solubility among the solutions is smaller at higher temperature

Dissolved oxygen is an important factor in the long-term corrosion study When dissolved oxygen is in limited supply, the oxygen-reduction reaction may be limiting the overall corrosion process, stifling corrosion Thus, reduced levels of oxygen play an important part in corrosion inhibition We think that the concentrated solutions of SAW and SCW may be inhibiting in the aqueous phase due to the excessive levels of HCO_3^- or NO_3^- or other anions Due to budgetary and manpower constraints, dissolved oxygen measurements were not obtained for the various test solutions at test start-up However, baseline data were established from off-line experiments using a glass reactor that has all the features of the large vessels in the LTCTF, e g , heater, stirrer, air inlet, and reflux-condenser One liter of solution was used in each experiment Table 2 2-6 presents the baseline dissolved-oxygen content representative of test solution content at start-up

Table 2.2-6 Dissolved-oxygen content.

Environment	Distilled water		SDW		SCW		SAW		SCMW	
Temperature (°C)	60	90	60	90	60	90	60	90	60	90
Dissolved oxygen (ppm)	7 0	3 4	5 4	2 9	4 5	0 8	5 1	2 5	5 6	3 0

These preliminary data show that as the temperature of the test solutions increases, the dissolved oxygen decreases In addition, as the dissolved salt content increases (in SCW and SAW), the dissolved oxygen decreases Furthermore, we hypothesize that the elevated HCO_3^- concentration present in SCW is probably decomposing to evolve CO_2, which purges the oxygen out of solution Thus, it would be expected that the aqueous-phase environment in SCW is the least aggressive environment, based on the little oxygen (0.8 ppm) available to take part in the oxygen reduction reaction

A monitoring apparatus was constructed to measure the dissolved oxygen from the test vessels directly Solution is forced to flow through a condenser by a diaphragm pump As the solution passes through the condenser, it is cooled to room temperature and then circulated through a sensor channel. Dissolved oxygen, pH, and temperature are measured using probes that are placed in the sensor channel The solution is then returned to the reactor or vessel. The apparatus does not allow the solution to be exposed to air, and is used to measure the dissolved oxygen of the test solutions in situ A laptop personal computer is used to record the data.

Another important consideration for the long-term corrosion studies is the CO_2 content present in the vapor phase above the test solutions, which comes from the decomposition of the HCO_3^- ions present in the SCW and SDW environments We hypothesize that CO_2 is the dominant reason for the high corrosion rates of carbon steels exposed in the vapor phase above the SCW at both 60° and 90°C Off-line experiments, using the mini reactor system

described previously, were conducted to measure the concentration of CO_2 above the SCW and SDW solutions at 60° and 90°C A quadrupole gas analyzer (model 201), manufactured by Hilden Analytical Ltd , was used to measure the partial pressure of CO_2 in room air and in the atmosphere above the solution. The results are shown in Table 2 2-7 as the ratio of CO_2 concentration above a solution versus the CO_2 in room air

Table 2.2-7 Ratio of CO_2 concentration.

	SCW 90°C	SCW 60°C	SDW 90°C	SDW 60°C
$\frac{CO_2 \text{ above solution}}{CO_2 \text{ in air}}$	70	3	17	11

These preliminary data show that the most aggressive environment in the vapor phase should be the one above the SCW 90°C environment The elevated CO_2 levels in the vapor phase can react with condensed water on the surface of specimens and lower the pH of the condensate, thus accelerating corrosion of specimens in the vapor phase

2.2.5 Test Procedures

Weight-Loss Specimens Nominal 1- × 2- × 0 125-in specimens were cleaned in acetone, weighed, and measured before testing The weighing of specimens was performed according to the requirements of TIP CM-04 (Estill, 1996) The specimen length, width, and thickness were measured for surface-area calculation according to the requirements of TIP CM-05 (Estill, 1996) After testing, the specimens were cleaned according to the specific chemical and mechanical methods required in American Society for Testing and Materials (ASTM) G1-90 (ASTM, 1987) The methodology varies with each particular alloy system The samples were then weighed after cleaning according to the requirements of TIP CM-04 The corrosion rates were calculated from weight-loss data, surface area, time-in-test, and alloy density, in accordance with the calculation requirements described in ASTM G1-90

Crevice-Corrosion Specimens Nominal 2- × 2- × 0 125-in specimens were cleaned in acetone, weighed, and measured for surface area calculation before testing Weighing and measuring of specimens were performed according to the requirements of TIP CM-04 and TIP CM-05 The specimens were assembled with a 0 75-in Teflon washer forced against both faces of specimen to provide a tight crevice between the Teflon and specimen using a ten-high stack of Belleville washers. After testing, the specimens were cleaned according to the requirements described in ASTM G1-90, they were then weighed according to the requirements of TIP CM-04. The corrosion rate was calculated from weight-loss data, surface area, time-in-test, and alloy density, according to the calculation requirements described in ASTM G1-90. An optical profile interferometer has been purchased for pitting evaluation of test surfaces, especially the area bound by the Teflon washer

U-bend Specimens U-bend specimens were constructed according to the requirements of ASTM G30 (ASTM, 1987), and were cleaned in acetone prior to mounting on the specimen rack. After testing, the corrosion-resistant and intermediate-corrosion-resistant specimens were cleaned in a mild detergent and rinsed in deionized water, followed by a rinse in isopropyl alcohol The carbon, cast, and low alloy steel were bead-blasted for 20–30 seconds to remove extensive corrosion product The samples were then examined under a low-power light microscope (>50×) for evidence of cracking

Galvanic Specimens Nominal 2- × 2- × 0 125-in , 1- × 2- × 0.125-in , and 1 5- × 1 5- × 0 125-in specimens were cleaned in acetone, weighed, and measured before testing Weighing and measuring were performed according to the requirements of TIP CM-04 and TIP CM-05 The specimens were configured in two different assembly modes to provide the requisite surface-area ratios being evaluated. They were assembled to create a tight interface between differing materials using a ten-high stack of Belleville spring washers to provide axial force (see Figure 2 2-4) No samples have been removed from test yet, but the post-test cleaning and examination methodology will follow in much the same manner as for the crevice specimens, according to the requirements described in ASTM G1-90 and TIP CM-04 An optical profile interferometer has been purchased for pitting evaluation of test surfaces, especially the area at the interface of the differing alloy systems

2.2.6 Results

Weight-Loss and Crevice-Corrosion Specimens Corrosion rates have been calculated for all the specimens on the six-month and one-year racks from vessels 18–23, 25, and 26, and for all the specimens on the six-month racks from vessels 27–30 Specimens from the one-year racks from vessels 27, 28, and 29 have been removed from test and will be cleaned, weighed, and examined in the near future Comprehensive listings of the corrosion rates of the weight-loss and crevice-corrosion test specimens are provided in Supplement 1 and Supplement 2, respectively

Summary test results presented in Table 2 2-8, Table 2 2-9, and Table 2 2-10 display the average corrosion rate of the corrosion-resistant, corrosion-allowance, and copper–nickel materials, respectively There was little or no notable difference in the corrosion resistance between welded and unwelded specimens, nor between weight-loss and crevice specimens, so the average corrosion rates presented in these tables are representative of the average corrosion rates of the welded and unwelded weight-loss and crevice specimens

Table 2.2-8 Corrosion rate (μm/yr) of corrosion-resistant materials.

		Environment					
	Solution and	Aqueous		Vapor		Water line	
Material	temperature	6 mo.	1 yr	6 mo	1 yr	6 mo	1 yr
Alloy 825	SAW, 60°C	0 58	1 13	0 03	0	–0 03	
Alloy G3		0 01	0 1	0 02	0	–0 02	
Alloy C22		0 04	0 03	0.06	0 03	0	
Alloy C4		0 08	0 04	0 06	0 02	–0 03	
Alloy 625		–0 01	0 02	0 05	0 01	–0 04	
Ti grade 12		4 48	0	7 97	–0 02	15 3	
Ti grade 16		2 05	–0 01	5 49	–0 03	0 08	

Alloy 825	SAW, 90°C	1 33	1 64	0 08	0	0 05	
Alloy G3		0 12	0 02	0 04	0	0 05	
Alloy C22		0 02	0	0 06	–0 01	0 02	
Alloy C4		0 13	0 05	0 06	0 02	0 06	
Alloy 625		–0 01	–0 04	0 03	–0 01	0 03	
Ti grade 12		3 96	–0 22	7 78	–0 06	2 79	
Ti grade 16		2 3	–0 18	4 43	–0 04	2 78	
Alloy 825	SDW, 60°C	0 06		0 06		0	
Alloy G3		0 06		0 06		–0 02	
Alloy C22		0 06		0 07		0 01	
Alloy C4		0 04		0 05		0	
Alloy 625		0 03		0 02		0 01	
Ti grade 12		5 67		5 23		5 54	
Ti grade 16		4 63		4 81		6 87	
Alloy 825	SDW, 90°C	0 06		0 05		0 02	
Alloy G3		0 08		0 07		0 05	
Alloy C22		0 07		0 06		0 05	
Alloy C4		0 06		0 08		0 08	
Alloy 625		0 04		0 03		0 04	
Ti grade 12		6 2		7 47		5 55	
Ti grade 16		5 55		7 43		4 15	
Alloy 825	SCW, 60°C	0 07		0 05		0 06	
Alloy G3		0 08		0 06		0 04	
Alloy C22		0 08		0 06		0 06	
Alloy C4		0 1		0 06		0 03	
Alloy 625		0 08		0 06		0 08	
Ti grade 12		7 07		7 38		6 77	
Ti grade 16		3 64		4 67		4 27	
Alloy 825	SCW, 90°C	0 07		0 05		0 04	
Alloy G3		0 07		0 02		–0 03	
Alloy C22		0 08		0 07		0 03	
Alloy C4		0 09		0 02		0 09	
Alloy 625		0 08		0 02		0 04	
Ti grade 12		11 79		5 86		9 65	
Ti grade 16		6 6		6 67		4 2	

Table 2.2-9 Corrosion rate (μm/yr) of corrosion-allowance material.

Material	Solution and temperature	Environment					
		Aqueous		Vapor		Water line	
		6 mo.	1 yr	6 mo.	1 yr	6 mo.	1 yr
A387	SDW, 60°C	45	91	31	18	130	158
A516		93	76	46	27	220	194
Cast carbon steel		94	78	51	37	190	208
A387	SDW, 90°C	100	73	36	36	210	165
A516		100	54	77	56	240	111
Cast carbon steel		80	50	72	39	240	119
A387	SCW, 60°C	25	7	110	132	170	135
A516		66	10	210	194	210	134
Cast carbon steel		72	11	200	114	210	190
A387	SCW, 90°C	12	4	210	287	85	99
A516		12	6	240	227	16	58
Cast carbon steel		14	7	180	148	94	89

Table 2.2-10 Corrosion rate (μm/yr) of Monel 400 and CDA 715.

Material	Solution and temperature	Environment					
		Aqueous		Vapor		Water line	
		6 mo	1 yr	6 mo	1 yr	6 mo	1 yr
Monel 400	SAW, 60°C	118	61	1	1	87	54
CDA 715		219	117	4	3	403	216
Monel 400	SAW, 90°C	92	52	4	2	59	38
CDA 715		282	215	11	9	285	221

U-bend Specimens Specimens from vessels 18–23 and 25–30 are currently being examined for possible stress corrosion cracking There is currently no documented evidence of stress corrosion cracking on any of the specimens examined to date, however, a few specimens may indicate some degree of attack. They will be examined in more detail with metallography and other suitable methods to determine the pattern and extent of attack, including possible cracking

2.2.7 Discussion

2.2.7.1 Corrosion-Resistant Metals

Summary test results presented in Table 2 2-8, Table 2 2-9, and Table 2 2-10 display the average corrosion rate of the corrosion-resistant, corrosion-allowance, and copper–nickel materials, respectively There was little or no notable difference in the corrosion resistance between welded and unwelded specimens, nor between weight-loss and crevice specimens, so the average corrosion rates presented in these tables are representative of the average corrosion rates of the welded and unwelded weight-loss and crevice specimens

Table 2 2-8 summarizes the corrosion rates for the corrosion-resistant materials to date These rates are negligible, however, the titanium grade 12 and titanium grade 16 showed elevated corrosion rates at the six-month interval in the SAW, SCW, and SDW environments when compared to the other corrosion-resistant materials in the same environment and time interval These anomalous data are considered to be a result of the acid-cleaning procedure employed for the six-month titanium specimens, because the chemical cleaning method was found to be responsible for removing base metal instead of corrosion product There was no prescribed method for cleaning titanium-based materials in the ASTM G1-90 specification, so the methodology initially adopted for cleaning titanium was the same as that used for the other corrosion-resistant materials, i.e , the cleaning method described for stainless-steel alloys There was no corrosion product on the titanium alloys at either the six-month or one-year interval, but there was a very thin and seemingly tightly bound oxide layer We have decided that the titanium specimens can be adequately cleaned by using deionized water and brushing with a nylon brush The one-year titanium samples were cleaned using this method, and it will be used for the other titanium specimens coming out of test in the future. The corrosion rates of titanium specimens were found to be negligible using this cleaning method

Alloy 825 coupons exposed to the aqueous phase in 60° and 90°C SAW had some small pits in the crevice area Pitting analysis of the affected areas will be performed after installation of optical profile instrumentation.

2.2.7.2 Corrosion-Allowance Steels

The corrosion rates for the corrosion-allowance specimens are presented in Table 2 2-9 For both weight-loss and crevice specimens, visual inspection and weight-loss data provide no clear evidence to differentiate corrosion resistance between the welded or unwelded specimens Because the corrosion of welded and unwelded weight-loss and crevice specimens are quite similar in the six-month data, the data from these sample sets were grouped together to obtain an average corrosion rate for a given material The corrosion rate of the water-line specimens is the average of one welded and one unwelded weight-loss specimen For the aqueous- and vapor-phase specimens in the SAW and SCW environments, the corrosion rate is an average of 12 specimens three welded weight-loss, three unwelded weight-loss, three welded crevice, and three unwelded crevice For the aqueous- and vapor-phase specimens in the SDW environments, the corrosion rate is an average of eight specimens one welded weight-loss, one unwelded weight-loss, three welded crevice, and three unwelded crevice

The data in Table 2.2-9 understate the actual penetration of the corrosion into the specimens for two reasons In some cases, portions of a specimen were only lightly attacked, whereas other portions of the same specimen suffered significant corrosion attack. In addition, the depth of penetration was not uniform in the attacked area, that is, the surface was roughened on a macroscopic scale The roughening was primarily broad pits A more detailed study, using an optical profiling system, will be begun to determine the characteristics of the penetration front into the specimens.

As indicated in Table 2.2-9, no single candidate of the three steels appears superior to others in the six- and twelve-month corrosion data. In the test environments of SCW, the vapor-phase specimens have higher corrosion rates than the aqueous-phase specimens. This is probably caused by the higher CO_2 concentration in the atmosphere generated from the HCO_3^- in the test solution. CO_2 released to the atmosphere inside a chamber will be redissolved in the condensate on the surfaces of vapor-phase specimens, forming carbonic acid, which, similar to any acid reaction with iron, can accelerate the corrosion of iron The

lower corrosion rates of the water-line specimens in SCW at 90°C, especially alloy A516, may be a result of the vertical specimen mounting, where less condensate is collected on the surface As stated previously, the CO_2 content is indeed higher above the bicarbonate-rich SCW solution versus the SDW solution The corrosion-rate results clearly show an increased degree of attack on the specimens exposed in the vapor phase above the SCW solution for all three alloys

The low corrosion rate of aqueous-phase specimens in SCW is likely due to the passivation of steels by high concentration of anions, especially bicarbonate Brasher (1969) reported that anions can contribute to the destruction of the oxide film, but they can also provide inhibition by being adsorbed onto the metal surface at weak points in the oxide film, suppressing anodic dissolution of the metal Brasher also shows that less aggressive anions are likely to be able to passivate at lower concentration than more aggressive ones In the test solutions used for this study, bicarbonate is the least aggressive anion of the concentrated species This reasoning explains the observed reduction in corrosion rates for specimens exposed to SCW aqueous phase versus SDW aqueous phase

For coupons mounted at the water line, the corrosion condition of the vapor-phase portion of a specimen is similar to that of vapor-phase specimens The aqueous-phase portion of a specimen is usually worse than that of aqueous-phase specimens The worst corrosion is always located directly below the water line, probably due to slight water-line level fluctuations Characterization of the water/vapor interface will be examined closely with the optical profiler system to characterize the extent and pattern of attack

Oxidation of iron leads to the generation of distinct layers of iron oxides Preliminary x-ray diffraction patterns of corrosion products from a specimen exposed in the vapor phase above the SCW solution revealed oxides of Fe_2O_3, FeO, and Fe_3O_4 A more detailed study of corrosion products will be begun soon

2.2.7.3 *Intermediate-Resistant Metals*

The corrosion-rate results of the copper–nickel materials are presented in Table 2 2-10 The pH 2–3 acidified environment (SAW) is intended to simulate the effect of possible microbial production of acid After the Monel 400 and CDA 715 specimens were placed in the SAW environment, the pH values of water gradually increased from 2 7 to 5 3 in three months (pH was not monitored during this period) More sulfuric acid was added to both solutions of 60° and 90°C to lower the pH to ~3. The solution pH values were monitored and reached pH 5 5 in two weeks During this time, the solutions were also sampled and analyzed for Cu and Ni ionic concentrations The concentration of Cu and Ni were 170 and 130 ppm, respectively, at 60°C The concentration of Cu and Ni were 180 and 170 ppm, respectively, at 90°C immediately after the addition of acid As the pH increased, the Ni concentrations increased, but Cu decreased The results indicate the specimens were dissolving in acidic solutions

We have found that the corrosion rates of aqueous-phase specimens were 1 to 2 orders of magnitude greater than those of vapor-phase specimens. The specimens exposed to the vapor phase are relatively resistant to general corrosion in this environment, with corrosion rates varying from 1 to 11 μm/yr The corrosion rates for CDA 715 are two to four times that of Monel 400.

The large weight loss of aqueous-phase specimens is due to both dissolution (i.e , $M + 2H^+ \rightarrow M_2^+ + H_2$) and corrosion. We think that dissolution is the dominant factor causing weight loss in samples exposed in the aqueous phase. This hypothesis is supported by the rapid

change of pH values from ~3 to ~5 in two weeks (i e , equivalent to ~0.5 mole of divalent metals dissolved in 1,000 L of solution) To continue the long-term corrosion study of intermediate-resistant materials in SAW, we have decided to carry out the study under equilibrium pH values (presently at pH 5–6)

Pitting evaluation of selected specimens will be performed using the optical profile system Many of the samples are pitted, especially those exposed in the aqueous phase

2.2.8 Future Work

Many specimen racks are scheduled for test removal in FY 99 Samples in those racks will undergo the comprehensive post-test characterization regimen, including photography, metallography, chemical and mechanical cleaning, post-test weighing, corrosion-rate calculations, and specimen archival.

A large volume of work is planned using the optical profiler system to characterize the pattern and extent of pitting attack on specimens removed from test The new analysis tool is due at LLNL August 1998 and will have to be qualified to be used on Yucca Mountain Project Training of operators is scheduled for early FY 99

Metallography and other methods will be used on selected U-bend specimens removed from test that are tagged as having a notable surface attack present

Dissolved-oxygen measurements will be performed on the solutions currently being used in the LTCTF Confirmation of carbon dioxide measurements made earlier will be performed

Long-term corrosion-potential measurements of specimens exposed to the bounding environments described earlier are planned for FY99 In addition, long-term corrosion-potential measurements are planned in particularly aggressive environments, such as saturated J-13 ionic species and $FeCl_3$ at 30°, 60°, and 90°C

A planned-interval approach of long-term testing is being planned for materials in solutions containing selected J-13 ions (saturated) at 30°, 60°, and 90°C

2.2.9 References

ASTM (1987a) *Standard Practice for Making and Using U-Bend Stress Corrosion Test Specimens* (Standard G30-79, reapproved 1994) Philadelphia, PA American Society for Testing and Materials (Book of Standards, Vol 3 02) [NNA 19891005 0117]

ASTM (1987b) *Standard Practice for Preparing, Cleaning, and Evaluating Corrosion Test Specimens* (Standard G1-90, reapproved 1994) Philadelphia, PA American Society for Testing and Materials (Book of Standards, Vol 3.02)

Brasher, D M. (1969) "Stability of the Oxide Film on Metals in Relation to Inhibition of Corrosion: Part II. Dual Role of the Anion in the Inhibition of the Corrosion of Mild Steel " *Br Corros J* **2**:122

Cramer, S D (1974) "The Solubility of Oxygen in Geothermal Brines." C S Tedmon, Jr., ed *Corrosion Problems in Energy Conversion and Generation* Princeton, N J Corrosion Division, Electrochemical Society.

Estill, J. (1996a) *Yucca Mountain Project Technical Implementation Plan, User Calibration of Fowler Ultra Cal Mark III Digital Caliper* (TIP-CM-05, Rev 1) Livermore, CA Lawrence Livermore National Laboratory. [MOL.19961021 0119]

Estill, J (1996b) *Yucca Mountain Project Technical Implementation Plan, User Calibration of Mettler AT200 Analytical Balance* (TIP-CM-04) Livermore, CA. Lawrence Livermore National Laboratory. [MOL 19960814 0257]

Gdowski, G E (1997) *Yucca Mountain Project Technical Implementation Plan, Formulation and Make-Up of Simulated Cement Modified Water* (TIP-CM-11) Livermore, CA Lawrence Livermore National Laboratory [MOL 19980109 0292]

Gdowski, G E (1998) *Yucca Mountain Project Activity Plan, Long-Term Corrosion Studies* (MB SIP Activity E-20-50, Rev 4) Livermore, CA Lawrence Livermore National Laboratory [MOL 19980105 0583]

McCright, R D (1997) *Engineered Materials Characterization Report* Milestone report for the CRWMS Management and Operating Contractor, U S Department of Energy (TR251FB9, Rev 1) Livermore, CA· Lawrence Livermore National Laboratory (Also UCRL-ID-119564, Rev 1) [MOL 19980105 0616]

EMCR Section 2.2.6 Supplement 1: Weight-loss results.

Sample identification	Alloy	Density (g/cc)	Exposure time (hours)	Surface area (sq cm)	Weight loss (g)	Corrosion rate (μm/y)	Vessel number-rack number	Test environment
AWA 001	I825	8 14	4296	28 30	–0 0005	–0 04	25-1A	60°C vapor SAW
AWA 002	I825	8 14	4296	28 37	0 0000	0 00	25-1A	60°C vapor SAW
AWA 003	I825	8 14	4296	28 34	0 0003	0 03	25-1A	60°C vapor SAW
AWA 004	I825	8 14	4296	28 26	–0 0002	–0 02	25-1B	60°C aqueous SAW
AWA 005	I825	8 14	4296	28 21	–0 0003	–0 03	25-1B	60°C aqueous SAW
AWA 006	I825	8 14	4296	27 81	0 0015	0 14	25-1B	60°C aqueous SAW
AWA 007	I825	8 14	8376	28 13	–0 0001	0 00	25-2A	60°C vapor SAW
AWA 008	I825	8 14	8376	28 16	–0 0005	–0 02	25-2A	60°C vapor SAW
AWA 009	I825	8 14	8376	28 26	–0 0003	–0 01	25-2A	60°C vapor SAW
AWA 010	I825	8 14	8376	28 26	0 0000	0 00	25-2B	60°C aqueous SAW
AWA 011	I825	8 14	8376	28 31	0 0026	0 12	25-2B	60°C aqueous SAW
AWA 012	I825	8 14	8376	27 99	–0 0003	–0 01	25-2B	60°C aqueous SAW
AWA 031	I825	8 14	4296	28 15	–0 0002	–0 02	25-1A	60°C water line SAW
AWA 032	I825	8 14	8376	28 27	0 0001	0 00	25-2A	60°C water line SAW
AWA 036	I825	8 14	4344	27 94	0 0005	0 04	26-1A	90°C water line SAW
AWA 037	I825	8 14	8784	28 34	0 0000	0 00	26-2A	90°C water line SAW
AWA 041	I825	8 14	4344	28 29	0 0011	0 10	26-1A	90°C vapor SAW
AWA 042	I825	8 14	4344	28 24	0 0016	0 14	26-1A	90°C vapor SAW
AWA 043	I825	8 14	4344	28 12	0 0008	0 07	26-1A	90°C vapor SAW
AWA 044	I825	8 14	4344	28 44	0 0019	0 17	26-1B	90°C aqueous SAW
AWA 045	I825	8 14	4344	28 04	0 0013	0 11	26-1B	90°C aqueous SAW
AWA 046	I825	8 14	4344	28 35	0 0018	0 16	26-1B	90°C aqueous SAW
AWA 047	I825	8 14	8784	28 18	0 0002	0 01	26-2A	90°C vapor SAW
AWA 048	I825	8 14	8784	27 93	0 0004	0 02	26-2A	90°C vapor SAW
AWA 049	I825	8 14	8784	28 22	0 0005	0 02	26-2A	90°C vapor SAW
AWA 050	I825	8 14	8784	28 28	0 0109	0 47	26-2B	90°C aqueous SAW
AWA 051	I825	8 14	8784	28 30	0 0105	0 45	26-2B	90°C aqueous SAW
AWA 052	I825	8 14	8784	28 31	0 0061	0 26	26-2B	90°C aqueous SAW
AWA 071	I825	8 14	4392	28 34	–0 0001	–0 01	27-1A	60°C vapor SCW
AWA 072	I825	8 14	4392	28 13	0 0004	0 03	27-1A	60°C vapor SCW
AWA 073	I825	8 14	4392	28 30	0 0003	0 03	27-1A	60°C vapor SCW
AWA 074	I825	8 14	4392	28 16	0 0007	0 06	27-1B	60°C aqueous SCW
AWA 075	I825	8 14	4392	28 18	0 0006	0 05	27-1B	60°C aqueous SCW
AWA 076	I825	8 14	4392	28 20	0 0006	0 05	27-1B	60°C aqueous SCW
AWA 101	I825	8 14	4392	28 14	0 0006	0 05	27-1A	60°C water line SCW
AWA 106	I825	8 14	4464	28 20	0.0007	0 06	28-1A	90°C water line SCW
AWA 111	I825	8 14	4464	28 25	0 0002	0 02	28-1A	90°C vapor SCW
AWA 112	I825	8 14	4464	28 12	0 0005	0 04	28-1A	90°C vapor SCW

2.2 Long-Term Corrosion Studies

Sample identification	Alloy	Density (g/cc)	Exposure time (hours)	Surface area (sq cm)	Weight loss (g)	Corrosion rate (μm/y)	Vessel number-rack number	Test environment
AWA 113	I825	8 14	4464	27 89	0 0003	0 03	28-1A	90°C vapor SCW
AWA 114	I825	8 14	4464	28 11	0.0002	0 02	28-1B	90°C aqueous SCW
AWA 115	I825	8 14	4464	28 43	0 0000	0 00	28-1B	90°C aqueous SCW
AWA 116	I825	8 14	4464	28 13	0 0004	0 03	28-1B	90°C aqueous SCW
AWA 141	I825	8 14	4464	28 37	–0 0002	–0 02	29-1A	60°C vapor SDW
AWA 142	I825	8 14	4464	28 02	–0 0001	–0 01	29-1B	60°C aqueous SDW
AWA 151	I825	8.14	4464	28 41	–0 0003	–0 03	29-1A	60°C water line SDW
AWA 164	I825	8 14	4392	28 06	0 0002	0 02	30-1A	90°C water line SDW
AWA 168	I825	8 14	4392	28 28	0 0003	0 03	30-1A	90°C vapor SDW
AWA 169	I825	8 14	4392	28 22	0 0006	0 05	30-1B	90°C aqueous SDW
AWB 001	I825	8 14	4296	27 74	–0 0004	–0 04	25-1A	60°C vapor SAW
AWB 002	I825	8 14	4296	26 75	0 0010	0 09	25-1A	60°C vapor SAW
AWB 003	I825	8 14	4296	27 53	0 0004	0 04	25-1A	60°C vapor SAW
AWB 004	I825	8 14	4296	27 56	–0 0003	–0 03	25-1B	60°C aqueous SAW
AWB 005	I825	8 14	4296	27 53	0 0001	0 01	25-1B	60°C aqueous SAW
AWB 006	I825	8 14	4296	27 54	–0 0011	–0 10	25-1B	60°C aqueous SAW
AWB 007	I825	8 14	8376	27 66	–0 0004	–0 02	25-2A	60°C vapor SAW
AWB 008	I825	8 14	8376	27 71	0 0000	0 00	25-2A	60°C vapor SAW
AWB 009	I825	8 14	8376	27 68	–0 0004	–0 02	25-2A	60°C vapor SAW
AWB 010	I825	8 14	8376	27 84	–0 0002	–0 01	25-2B	60°C aqueous SAW
AWB 011	I825	8 14	8376	27 91	0 0001	0 00	25-2B	60°C aqueous SAW
AWB 012	I825	8 14	8376	27 69	–0 0003	–0 01	25-2B	60°C aqueous SAW
AWB 031	I825	8 14	4296	27 56	–0 0006	–0 05	25-1B	60°C water line SAW
AWB 032	I825	8 14	8376	27 43	–0 0001	0 00	25-2B	60°C water line SAW
AWB 036	I825	8 14	4344	27 45	0 0006	0 05	26-1B	90°C water line SAW
AWB 037	I825	8 14	8784	27 65	0 0003	0 01	26-2B	90°C water line SAW
AWB 041	I825	8 14	4344	27 83	0 0009	0 08	26-1A	90°C vapor SAW
AWB 042	I825	8 14	4344	27 68	0 0006	0 05	26-1A	90°C vapor SAW
AWB 043	I825	8 14	4344	27 49	0 0007	0 06	26-1A	90°C vapor SAW
AWB 044	I825	8 14	4344	27 48	0 0055	0 50	26-1B	90°C aqueous SAW
AWB 045	I825	8 14	4344	27 72	0 0016	0 14	26-1B	90°C aqueous SAW
AWB 046	I825	8 14	4344	27 64	0 0040	0 36	26-1B	90°C aqueous SAW
AWB 047	I825	8 14	8784	27 07	0 0005	0 02	26-2A	90°C vapor SAW
AWB 048	I825	8 14	8784	27 88	0 0006	0 03	26-2A	90°C vapor SAW
AWB 049	I825	8 14	8784	27 70	0 0005	0 02	26-2A	90°C vapor SAW
AWB 050	I825	8 14	8784	27 88	0 0006	0 03	26-2B	90°C aqueous SAW
AWB 051	I825	8 14	8784	27 70	0 0003	0 01	26-2B	90°C aqueous SAW
AWB 052	I825	8 14	8784	27 60	0 0154	0 68	26-2B	90°C aqueous SAW
AWB 071	I825	8 14	4392	27 63	0 0002	0 02	27-1A	60°C vapor SCW
AWB 072	I825	8 14	4392	27 83	0 0010	0 09	27-1A	60°C vapor SCW

Sample identification	Alloy	Density (g/cc)	Exposure time (hours)	Surface area (sq cm)	Weight loss (g)	Corrosion rate (μm/y)	Vessel number-rack number	Test environment
AWB 073	I825	8 14	4392	27 75	0 0005	0 04	27-1A	60°C vapor SCW
AWB 074	I825	8 14	4392	27 90	0 0003	0 03	27-1B	60°C aqueous SCW
AWB 075	I825	8 14	4392	27 37	0 0007	0 06	27-1B	60°C aqueous SCW
AWB 076	I825	8 14	4392	27 25	0 0001	0 01	27-1B	60°C aqueous SCW
AWB 101	I825	8 14	4392	27 55	0 0007	0 06	27-1B	60°C water line SCW
AWB 106	I825	8 14	4464	27 44	0 0001	0 01	28-1B	90°C water line SCW
AWB 111	I825	8 14	4464	27 29	0 0003	0 03	28-1A	90°C vapor SCW
AWB 112	I825	8 14	4464	27 35	0 0003	0 03	28-1A	90°C vapor SCW
AWB 113	I825	8 14	4464	27 59	0 0004	0 03	28-1A	90°C vapor SCW
AWB 114	I825	8 14	4464	27 48	0 0005	0 04	28-1B	90°C aqueous SCW
AWB 115	I825	8 14	4464	27 49	0 0007	0 06	28-1B	90°C aqueous SCW
AWB 116	I825	8 14	4464	27 60	0 0002	0 02	28-1B	90°C aqueous SCW
AWB 141	I825	8 14	4464	27 03	0 0003	0 03	29-1A	60°C vapor SDW
AWB 142	I825	8 14	4464	27 38	0 0005	0 04	29-1B	60°C aqueous SDW
AWB 151	I825	8 14	4464	27 70	0.0004	0 03	29-1B	60°C water line SDW
AWB 164	I825	8 14	4392	27 75	0 0002	0 02	30-1B	90°C water line SDW
AWB 168	I825	8 14	4392	27 87	0 0004	0 04	30-1A	90°C vapor SDW
AWB 169	I825	8 14	4392	27 90	0 0002	0 02	30-1B	90°C aqueous SDW
BWA 001	G3	8 27	4296	28 31	–0 0003	–0 03	25-1A	60°C vapor SAW
BWA 002	G3	8 27	4296	28 32	–0 0006	–0 05	25-1A	60°C vapor SAW
BWA 003	G3	8 27	4296	28 55	–0 0002	–0 02	25-1A	60°C vapor SAW
BWA 004	G3	8 27	4296	28 74	–0 0007	–0 06	25-1B	60°C aqueous SAW
BWA 005	G3	8 27	4296	28 26	–0 0001	–0 01	25-1B	60°C aqueous SAW
BWA 006	G3	8 27	4296	28 45	–0 0023	–0 20	25-1B	60°C aqueous SAW
BWA 007	G3	8 27	8376	28 51	–0 0002	–0 01	25-2A	60°C vapor SAW
BWA 008	G3	8 27	8376	28 64	–0 0006	–0 03	25-2A	60°C vapor SAW
BWA 009	G3	8 27	8376	28 55	–0 0005	–0 02	25-2A	60°C vapor SAW
BWA 010	G3	8 27	8376	28 46	0 0005	0 02	25-2B	60°C aqueous SAW
BWA 011	G3	8 27	8376	28 49	–0 0001	0 00	25-2B	60°C aqueous SAW
BWA 012	G3	8 27	8376	28 38	0 0000	0 00	25-2B	60°C aqueous SAW
BWA 031	G3	8 27	4296	28 55	–0 0004	–0 03	25-1A	60°C water line SAW
BWA 032	G3	8 27	8376	28 39	–0 0008	–0 04	25-2A	60°C water line SAW
BWA 036	G3	8 27	4344	28 61	0 0002	0 02	26-1A	90°C water line SAW
BWA 037	G3	8.27	8784	28 71	0 0002	0 01	26-2A	90°C water line SAW
BWA 041	G3	8 27	4344	28 76	0 0000	0 00	26-1A	90°C vapor SAW
BWA 042	G3	8 27	4344	28 31	0 0003	0 03	26-1A	90°C vapor SAW
BWA 043	G3	8 27	4344	28 35	0 0000	0 00	26-1A	90°C vapor SAW
BWA 044	G3	8 27	4344	28 61	–0 0004	–0 03	26-1B	90°C aqueous SAW
BWA 045	G3	8 27	4344	28 41	0 0000	0 00	26-1B	90°C aqueous SAW
BWA 046	G3	8 27	4344	28 48	–0 0003	–0 03	26-1B	90°C aqueous SAW

2.2 Long-Term Corrosion Studies

Sample identification	Alloy	Density (g/cc)	Exposure time (hours)	Surface area (sq cm)	Weight loss (g)	Corrosion rate (μm/y)	Vessel number-rack number	Test environment
BWA 047	G3	8 27	8784	28 34	0 0006	0 03	26-2A	90°C vapor SAW
BWA 048	G3	8 27	8784	28 63	0 0003	0 01	26-2A	90°C vapor SAW
BWA 049	G3	8 27	8784	28 69	0 0006	0 03	26-2A	90°C vapor SAW
BWA 050	G3	8 27	8784	28 64	–0 0005	–0 02	26-2B	90°C aqueous SAW
BWA 051	G3	8 27	8784	28 62	–0 0006	–0 03	26-2B	90°C aqueous SAW
BWA 052	G3	8 27	8784	28 41	0 0004	0 02	26-2B	90°C aqueous SAW
BWA 071	G3	8 27	4392	28 56	0 0001	0 01	27-1A	60°C vapor SCW
BWA 072	G3	8 27	4392	28 55	0 0006	0 05	27-1A	60°C vapor SCW
BWA 073	G3	8 27	4392	28 44	0 0002	0 02	27-1A	60°C vapor SCW
BWA 074	G3	8 27	4392	28 70	0 0003	0 03	27-1B	60°C aqueous SCW
BWA 075	G3	8 27	4392	28 72	0 0008	0 07	27-1B	60°C aqueous SCW
BWA 076	G3	8 27	4392	28 78	0 0002	0 02	27-1B	60°C aqueous SCW
BWA 101	G3	8 27	4392	28 42	0 0005	0 04	27-1A	60°C water line SCW
BWA 106	G3	8 27	4464	28 53	–0 0008	–0 07	28-1A	90°C water line SCW
BWA 111	G3	8 27	4464	28 20	–0 0003	–0 03	28-1A	90°C vapor SCW
BWA 112	G3	8 27	4464	28 74	–0 0003	–0 02	28-1A	90°C vapor SCW
BWA 113	G3	8 27	4464	28 54	0 0000	0 00	28-1A	90°C vapor SCW
BWA 114	G3	8 27	4464	28 60	–0 0001	–0 01	28-1B	90°C aqueous SCW
BWA 115	G3	8 27	4464	28 58	–0 0003	–0 02	28-1B	90°C aqueous SCW
BWA 116	G3	8 27	4464	28 62	0 0003	0 02	28-1B	90°C aqueous SCW
BWA 141	G3	8 27	4464	28 57	0 0006	0 05	29-1A	60°C vapor SDW
BWA 142	G3	8 27	4464	28 68	0 0005	0 04	29-1B	60°C aqueous SDW
BWA 151	G3	8 27	4464	28 38	–0 0002	–0 02	29-1A	60°C water line SDW
BWA 164	G3	8 27	4392	27 82	0 0010	0 09	30-1A	90°C water line SDW
BWA 168	G3	8 27	4392	27 79	0 0016	0 14	30-1A	90°C vapor SDW
BWA 169	G3	8 27	4392	27 87	0 0014	0 12	30-1B	90°C aqueous SDW
BWC 001	G3	8 27	4296	28 35	–0 0004	–0 03	25-1A	60°C vapor SAW
BWC 002	G3	8 27	4296	27 94	0 0000	0 00	25-1A	60°C vapor SAW
BWC 003	G3	8 27	4296	28 26	–0 0005	–0 04	25-1A	60°C vapor SAW
BWC 004	G3	8 27	4296	28 15	–0 0005	–0 04	25-1B	60°C aqueous SAW
BWC 005	G3	8 27	4296	27 94	–0 0002	–0 02	25-1B	60°C aqueous SAW
BWC 006	G3	8 27	4296	28 29	–0 0002	–0 02	25-1B	60°C aqueous SAW
BWC 007	G3	8 27	8376	27 95	–0 0010	–0 05	25-2A	60°C vapor SAW
BWC 008	G3	8 27	8376	28 16	–0 0004	–0 02	25-2A	60°C vapor SAW
BWC 009	G3	8 27	8376	28 22	0 0000	0 00	25-2A	60°C vapor SAW
BWC 010	G3	8 27	8376	28 07	0 0000	0 00	25-2B	60°C aqueous SAW
BWC 011	G3	8 27	8376	28 32	–0 0003	–0 01	25-2B	60°C aqueous SAW
BWC 012	G3	8 27	8376	27.84	–0 0008	–0 04	25-2B	60°C aqueous SAW
BWC 031	G3	8 27	4296	28 30	–0 0002	–0 02	25-1B	60°C water line SAW
BWC 032	G3	8 27	8376	28 29	0 0002	0 01	25-2B	60°C water line SAW

Sample identification	Alloy	Density (g/cc)	Exposure time (hours)	Surface area (sq cm)	Weight loss (g)	Corrosion rate (μm/y)	Vessel number-rack number	Test environment
BWC 036	G3	8 27	4344	28 34	0 0009	0 08	26-1B	90°C water line SAW
BWC 037	G3	8 27	8784	28 23	0 0001	0 00	26-2B	90°C water line SAW
BWC 041	G3	8 27	4344	28 25	0 0008	0 07	26-1A	90°C vapor SAW
BWC 042	G3	8 27	4344	28 30	0 0003	0 03	26-1A	90°C vapor SAW
BWC 043	G3	8 27	4344	27 85	0 0003	0 03	26-1A	90°C vapor SAW
BWC 044	G3	8 27	4344	28 32	–0 0005	–0 04	26-1B	90°C aqueous SAW
BWC 045	G3	8 27	4344	28 31	0 0011	0 09	26-1B	90°C aqueous SAW
BWC 046	G3	8 27	4344	28 33	–0 0001	–0 01	26-1B	90°C aqueous SAW
BWC 047	G3	8 27	8784	28 26	0 0002	0 01	26-2A	90°C vapor SAW
BWC 048	G3	8 27	8784	28 37	0 0013	0 06	26-2A	90°C vapor SAW
BWC 049	G3	8 27	8784	28 30	0 0013	0 06	26-2A	90°C vapor SAW
BWC 050	G3	8 27	8784	28 42	–0 0003	–0 01	26-2B	90°C aqueous SAW
BWC 051	G3	8 27	8784	28 27	–0 0005	–0 02	26-2B	90°C aqueous SAW
BWC 052	G3	8 27	8784	28 37	–0 0005	–0 02	26-2B	90°C aqueous SAW
BWC 071	G3	8 27	4392	28 31	0 0005	0 04	27-1A	60°C vapor SCW
BWC 072	G3	8 27	4392	27 89	0 0001	0 01	27-1A	60°C vapor SCW
BWC 073	G3	8 27	4392	28 26	0 0021	0 18	27-1A	60°C vapor SCW
BWC 074	G3	8 27	4392	28 41	0 0006	0 05	27-1B	60°C aqueous SCW
BWC 075	G3	8 27	4392	28 51	0 0000	0 00	27-1B	60°C aqueous SCW
BWC 076	G3	8 27	4392	28 28	0 0002	0 02	27-1B	60°C aqueous SCW
BWC 101	G3	8 27	4392	27 69	0 0005	0 04	27-1B	60°C water line SCW
BWC 106	G3	8 27	4464	28 29	0 0001	0 01	28-1B	90°C water line SCW
BWC 111	G3	8 27	4464	28 28	0 0003	0 03	28-1A	90°C vapor SCW
BWC 112	G3	8 27	4464	28 18	0 0002	0 02	28-1A	90°C vapor SCW
BWC 113	G3	8 27	4464	28 38	0 0004	0 03	28-1A	90°C vapor SCW
BWC 114	G3	8 27	4464	28 22	0 0004	0 03	28-1B	90°C aqueous SCW
BWC 115	G3	8 27	4464	28 02	0 0004	0 03	28-1B	90°C aqueous SCW
BWC 116	G3	8 27	4464	28 37	0 0003	0 03	28-1B	90°C aqueous SCW
BWC 141	G3	8 27	4464	28 24	0 0001	0 01	29-1A	60°C vapor SDW
BWC 142	G3	8 27	4464	28 35	0 0002	0 02	29-1B	60°C aqueous SDW
BWC 151	G3	8 27	4464	28 28	–0 0001	–0 01	29-1B	60°C water line SDW
BWC 164	G3	8 27	4392	27 92	0 0001	0 01	30-1B	90°C water line SDW
BWC 168	G3	8 27	4392	27 84	0 0000	0 00	30-1A	90°C vapor SDW
BWC 169	G3	8 27	4392	27 90	0 0011	0 10	30-1B	90°C aqueous SDW
CWA 001	C4	8 60	4296	28 01	0 0002	0 02	25-1A	60°C vapor SAW
CWA 002	C4	8 60	4296	27 87	0 0000	0 00	25-1A	60°C vapor SAW
CWA 003	C4	8 60	4296	27 96	0 0001	0 01	25-1A	60°C vapor SAW
CWA 004	C4	8 60	4296	27 81	0 0005	0 04	25-1B	60°C aqueous SAW
CWA 005	C4	8 60	4296	27 82	0 0004	0 03	25-1B	60°C aqueous SAW
CWA 006	C4	8 60	4296	28 08	0 0005	0 04	25-1B	60°C aqueous SAW

2.2 Long-Term Corrosion Studies

Sample identification	Alloy	Density (g/cc)	Exposure time (hours)	Surface area (sq cm)	Weight loss (g)	Corrosion rate (μm/y)	Vessel number-rack number	Test environment
CWA 007	C4	8 60	8376	28 32	–0 0004	–0 02	25-2A	60°C vapor SAW
CWA 008	C4	8 60	8376	27 81	–0 0003	–0 01	25-2A	60°C vapor SAW
CWA 009	C4	8 60	8376	28 09	–0 0005	–0 02	25-2A	60°C vapor SAW
CWA 010	C4	8 60	8376	28 03	0 0000	0 00	25-2B	60°C aqueous SAW
CWA 011	C4	8 60	8376	28 01	0 0002	0 01	25-2B	60°C aqueous SAW
CWA 012	C4	8 60	8376	28 09	0 0007	0 03	25-2B	60°C aqueous SAW
CWA 031	C4	8 60	4296	28 34	0 0002	0 02	25-1A	60°C water line SAW
CWA 032	C4	8 60	8376	27 97	0 0003	0 01	25-2A	60°C water line SAW
CWA 036	C4	8 60	4344	27 81	0 0004	0 03	26-1A	90°C water line SAW
CWA 037	C4	8 60	8784	28 00	0 0010	0 04	26-2A	90°C water line SAW
CWA 041	C4	8 60	4344	28 00	–0 0001	–0 01	26-1A	90°C vapor SAW
CWA 042	C4	8 60	4344	27 86	0 0008	0 07	26-1A	90°C vapor SAW
CWA 043	C4	8 60	4344	27 94	0 0004	0 03	26-1A	90°C vapor SAW
CWA 044	C4	8 60	4344	27 98	0 0006	0 05	26-1B	90°C aqueous SAW
CWA 045	C4	8 60	4344	28 20	0 0008	0 07	26-1B	90°C aqueous SAW
CWA 046	C4	8 60	4344	28 07	0 0007	0 06	26-1B	90°C aqueous SAW
CWA 047	C4	8 60	8784	28 00	0 0006	0 02	26-2A	90°C vapor SAW
CWA 048	C4	8 60	8784	27 72	0 0008	0 03	26-2A	90°C vapor SAW
CWA 049	C4	8 60	8784	28 03	0 0008	0 03	26-2A	90°C vapor SAW
CWA 050	C4	8 60	8784	28 21	0 0011	0 05	26-2B	90°C aqueous SAW
CWA 051	C4	8 60	8784	28 06	0 0012	0 05	26-2B	90°C aqueous SAW
CWA 052	C4	8 60	8784	27 87	0 0010	0 04	26-2B	90°C aqueous SAW
CWA 071	C4	8 60	4392	27 83	0 0005	0 04	27-1A	60°C vapor SCW
CWA 072	C4	8 60	4392	28 40	0 0002	0 02	27-1A	60°C vapor SCW
CWA 073	C4	8 60	4392	27 62	0 0007	0 06	27-1A	60°C vapor SCW
CWA 074	C4	8 60	4392	28 07	0 0008	0 07	27-1B	60°C aqueous SCW
CWA 075	C4	8 60	4392	27 72	0 0011	0 09	27-1B	60°C aqueous SCW
CWA 076	C4	8 60	4392	28 23	0 0008	0 07	27-1B	60°C aqueous SCW
CWA 101	C4	8 60	4392	28 32	0 0005	0 04	27-1A	60°C water line SCW
CWA 106	C4	8 60	4464	27 90	0 0001	0 01	28-1A	90°C water line SCW
CWA 111	C4	8 60	4464	28 31	0 0001	0 01	28-1A	90°C vapor SCW
CWA 112	C4	8 60	4464	28 20	0 0003	0 02	28-1A	90°C vapor SCW
CWA 113	C4	8 60	4464	28 05	–0 0001	–0 01	28-1A	90°C vapor SCW
CWA 114	C4	8 60	4464	27 96	0 0008	0 07	28-1B	90°C aqueous SCW
CWA 115	C4	8 60	4464	27 90	0 0003	0 02	28-1B	90°C aqueous SCW
CWA 116	C4	8 60	4464	28 17	0 0011	0 09	28-1B	90°C aqueous SCW
CWA 141	C4	8 60	4464	28 36	0 0006	0 05	29-1A	60°C vapor SDW
CWA 142	C4	8 60	4464	28.10	0 0002	0 02	29-1B	60°C aqueous SDW
CWA 151	C4	8 60	4464	27 92	0 0000	0 00	29-1A	60°C water line SDW
CWA 164	C4	8 60	4392	28 15	0 0011	0 09	30-1A	90°C water line SDW

Sample identification	Alloy	Density (g/cc)	Exposure time (hours)	Surface area (sq cm)	Weight loss (g)	Corrosion rate (μm/y)	Vessel number-rack number	Test environment
CWA 168	C4	8 60	4392	28 15	0 0016	0 13	30-1A	90°C vapor SDW
CWA 169	C4	8 60	4392	28 11	0 0012	0 10	30-1B	90°C aqueous SDW
CWB 001	C4	8 60	4296	27 78	0 0001	0 01	25-1A	60°C vapor SAW
CWB 002	C4	8 60	4296	27 12	0 0001	0 01	25-1A	60°C vapor SAW
CWB 003	C4	8 60	4296	27 44	0 0007	0 06	25-1A	60°C vapor SAW
CWB 004	C4	8 60	4296	28 02	–0 0001	–0 01	25-1B	60°C aqueous SAW
CWB 005	C4	8 60	4296	27 77	0 0006	0 05	25-1B	60°C aqueous SAW
CWB 006	C4	8 60	4296	27 73	–0 0003	–0 03	25-1B	60°C aqueous SAW
CWB 007	C4	8 60	8376	27 93	0 0001	0 00	25-2A	60°C vapor SAW
CWB 008	C4	8 60	8376	27 62	0 0001	0 00	25-2A	60°C vapor SAW
CWB 009	C4	8 60	8376	27 49	–0 0003	–0 01	25-2A	60°C vapor SAW
CWB 010	C4	8 60	8376	27 63	–0 0001	0 00	25-2B	60°C aqueous SAW
CWB 011	C4	8 60	8376	27.69	0 0001	0 00	25-2B	60°C aqueous SAW
CWB 012	C4	8 60	8376	27 87	–0 0001	0 00	25-2B	60°C aqueous SAW
CWB 031	C4	8 60	4296	27 70	–0 0003	–0 03	25-1B	60°C water line SAW
CWB 032	C4	8 60	8376	27 48	–0 0003	–0 01	25-2B	60°C water line SAW
CWB 036	C4	8 60	4344	26 92	0 0010	0 09	26-1B	90°C water line SAW
CWB 037	C4	8 60	8784	27 77	0 0010	0 04	26-2B	90°C water line SAW
CWB 041	C4	8 60	4344	27 64	0 0006	0 05	26-1A	90°C vapor SAW
CWB 042	C4	8 60	4344	27 85	0 0006	0 05	26-1A	90°C vapor SAW
CWB 043	C4	8 60	4344	27 15	0 0008	0 07	26-1A	90°C vapor SAW
CWB 044	C4	8 60	4344	27 77	0 0004	0 03	26-1B	90°C aqueous SAW
CWB 045	C4	8 60	4344	27 76	0 0002	0 02	26-1B	90°C aqueous SAW
CWB 046	C4	8 60	4344	27 90	0 0002	0 02	26-1B	90°C aqueous SAW
CWB 047	C4	8 60	8784	28 00	0 0010	0 04	26-2A	90°C vapor SAW
CWB 048	C4	8 60	8784	28 07	0 0012	0 05	26-2A	90°C vapor SAW
CWB 049	C4	8 60	8784	28 24	0 0011	0 05	26-2A	90°C vapor SAW
CWB 050	C4	8 60	8784	27 89	0 0010	0 04	26-2B	90°C aqueous SAW
CWB 051	C4	8 60	8784	28 12	0 0010	0 04	26-2B	90°C aqueous SAW
CWB 052	C4	8 60	8784	27 94	0 0010	0 04	26-2B	90°C aqueous SAW
CWB 071	C4	8 60	4392	28 07	0 0005	0 04	27-1A	60°C vapor SCW
CWB 072	C4	8 60	4392	27 83	0 0010	0 08	27-1A	60°C vapor SCW
CWB 073	C4	8 60	4392	27 85	0 0007	0 06	27-1A	60°C vapor SCW
CWB 074	C4	8 60	4392	27 83	0 0007	0 06	27-1B	60°C aqueous SCW
CWB 075	C4	8 60	4392	27 67	0 0010	0 08	27-1B	60°C aqueous SCW
CWB 076	C4	8 60	4392	27 35	0 0014	0 12	27-1B	60°C aqueous SCW
CWB 101	C4	8 60	4392	27 44	0 0012	0 10	27-1B	60°C water line SCW
CWB 106	C4	8 60	4464	27 56	0 0008	0 07	28-1B	90°C water line SCW
CWB 111	C4	8 60	4464	27 65	0 0001	0 01	28-1A	90°C vapor SCW
CWB 112	C4	8 60	4464	27 73	0 0000	0 00	28-1A	90°C vapor SCW

2.2 Long-Term Corrosion Studies

Sample identification	Alloy	Density (g/cc)	Exposure time (hours)	Surface area (sq cm)	Weight loss (g)	Corrosion rate (μm/y)	Vessel number-rack number	Test environment
CWB 113	C4	8 60	4464	27 68	–0 0001	–0 01	28-1A	90°C vapor SCW
CWB 114	C4	8 60	4464	28 03	0 0005	0 04	28-1B	90°C aqueous SCW
CWB 115	C4	8 60	4464	27 86	0 0004	0 03	28-1B	90°C aqueous SCW
CWB 116	C4	8 60	4464	27 77	0 0004	0 03	28-1B	90°C aqueous SCW
CWB 141	C4	8 60	4464	27 87	0 0004	0 03	29-1A	60°C vapor SDW
CWB 142	C4	8 60	4464	27 99	0 0003	0 02	29-1B	60°C aqueous SDW
CWB 151	C4	8 60	4464	28 19	0 0000	0 00	29-1B	60°C water line SDW
CWB 164	C4	8 60	4392	28 03	0 0008	0 07	30-1B	90°C water line SDW
CWB 168	C4	8 60	4392	27 79	0 0004	0 03	30-1A	90°C vapor SDW
CWB 169	C4	8 60	4392	27 61	0 0011	0 09	30-1B	90°C aqueous SDW
DWA 001	C22	8 60	4296	28 17	0 0003	0 03	25-1A	60°C vapor SAW
DWA 002	C22	8 60	4296	28 15	–0 0006	–0 05	25-1A	60°C vapor SAW
DWA 003	C22	8 60	4296	28 04	0 0006	0 05	25-1A	60°C vapor SAW
DWA 004	C22	8 60	4296	28 02	–0 0007	–0 06	25-1B	60°C aqueous SAW
DWA 005	C22	8 60	4296	28 03	–0 0004	–0 03	25-1B	60°C aqueous SAW
DWA 006	C22	8 60	4296	28 22	–0 0003	–0 03	25-1B	60°C aqueous SAW
DWA 007	C22	8 60	8376	28 30	0 0004	0 02	25-2A	60°C vapor SAW
DWA 008	C22	8 60	8376	28 12	0 0003	0 01	25-2A	60°C vapor SAW
DWA 009	C22	8 60	8376	28 16	0 0006	0 03	25-2A	60°C vapor SAW
DWA 010	C22	8 60	8376	27 99	0 0001	0 00	25-2B	60°C aqueous SAW
DWA 011	C22	8 60	8376	28 25	0 0004	0 02	25-2B	60°C aqueous SAW
DWA 012	C22	8 60	8376	28 04	0 0005	0 02	25-2B	60°C aqueous SAW
DWA 031	C22	8 60	4296	27 78	–0 0004	–0 03	25-1A	60°C water line SAW
DWA 032	C22	8 60	8376	28 10	0 0003	0 01	25-2A	60°C water line SAW
DWA 036	C22	8 60	4344	27 89	0 0002	0 02	26-1A	90°C water line SAW
DWA 041	C22	8 60	4344	28 14	0 0000	0 00	26-1A	90°C vapor SAW
DWA 042	C22	8 60	4344	28 11	0 0006	0 05	26-1A	90°C vapor SAW
DWA 043	C22	8 60	4344	28 08	0 0010	0 08	26-1A	90°C vapor SAW
DWA 044	C22	8 60	4344	28 11	–0 0004	–0 03	26-1B	90°C aqueous SAW
DWA 045	C22	8 60	4344	28 07	–0 0005	–0 04	26-1B	90°C aqueous SAW
DWA 046	C22	8 60	4344	28 08	0 0001	0 01	26-1B	90°C aqueous SAW
DWA 047	C22	8 60	8784	28 28	0 0005	0.02	26-2A	90°C vapor SAW
DWA 049	C22	8 60	8784	27 84	0 0005	0 02	26-2A	90°C vapor SAW
DWA 050	C22	8 60	8784	28 04	0 0004	0 02	26-2B	90°C aqueous SAW
DWA 052	C22	8 60	8784	28 22	0 0002	0 01	26-2B	90°C aqueous SAW
DWA 071	C22	8 60	4392	28 20	0.0003	0 02	27-1A	60°C vapor SCW
DWA 072	C22	8 60	4392	28 18	0 0004	0 03	27-1A	60°C vapor SCW
DWA 073	C22	8 60	4392	28 05	0 0010	0 08	27-1A	60°C vapor SCW
DWA 074	C22	8 60	4392	28 12	0 0011	0 09	27-1B	60°C aqueous SCW
DWA 075	C22	8 60	4392	28 14	0 0009	0 07	27-1B	60°C aqueous SCW

Sample identification	Alloy	Density (g/cc)	Exposure time (hours)	Surface area (sq cm)	Weight loss (g)	Corrosion rate (μm/y)	Vessel number-rack number	Test environment
DWA 076	C22	8 60	4392	28 29	0 0005	0 04	27-1B	60°C aqueous SCW
DWA 101	C22	8 60	4392	28 37	0 0006	0 05	27-1A	60°C water line SCW
DWA 106	C22	8 60	4464	28 12	0 0004	0 03	28-1A	90°C water line SCW
DWA 111	C22	8 60	4464	28 13	0 0003	0 02	28-1A	90°C vapor SCW
DWA 112	C22	8 60	4464	28 36	0 0002	0 02	28-1A	90°C vapor SCW
DWA 113	C22	8 60	4464	28 23	0 0002	0 02	28-1A	90°C vapor SCW
DWA 114	C22	8 60	4464	28 24	–0 0002	–0 02	28-1B	90°C aqueous SCW
DWA 115	C22	8 60	4464	28 12	0 0002	0 02	28-1B	90°C aqueous SCW
DWA 116	C22	8 60	4464	28 07	0 0004	0 03	28-1B	90°C aqueous SCW
DWA 141	C22	8 60	4464	28 20	–0 0001	–0 01	29-1A	60°C vapor SDW
DWA 142	C22	8 60	4464	28 21	–0 0002	–0 02	29-1B	60°C aqueous SDW
DWA 151	C22	8 60	4464	28 14	0 0001	0 01	29-1A	60°C water line SDW
DWA 164	C22	8 60	4392	28 19	0 0010	0 08	30-1A	90°C water line SDW
DWA 168	C22	8 60	4392	28 07	0 0004	0 03	30-1A	90°C vapor SDW
DWA 169	C22	8 60	4392	27 99	0 0009	0 07	30-1B	90°C aqueous SDW
DWB 001	C22	8 60	4296	27 39	0 0013	0 11	25-1A	60°C vapor SAW
DWB 002	C22	8 60	4296	27 44	0 0019	0 16	25-1A	60°C vapor SAW
DWB 003	C22	8 60	4296	27 54	0 0007	0 06	25-1A	60°C vapor SAW
DWB 004	C22	8 60	4296	27 49	0 0000	0 00	25-1B	60°C aqueous SAW
DWB 005	C22	8 60	4296	27 46	0 0004	0 03	25-1B	60°C aqueous SAW
DWB 006	C22	8 60	4296	27 32	0 0004	0 03	25-1B	60°C aqueous SAW
DWB 007	C22	8 60	8376	27 50	0 0004	0 02	25-2A	60°C vapor SAW
DWB 008	C22	8 60	8376	27 32	0 0003	0 01	25-2A	60°C vapor SAW
DWB 009	C22	8 60	8376	27 47	0 0000	0 00	25-2A	60°C vapor SAW
DWB 010	C22	8 60	8376	27 34	–0 0003	–0 01	25-2B	60°C aqueous SAW
DWB 011	C22	8 60	8376	27 22	–0 0002	–0 01	25-2B	60°C aqueous SAW
DWB 012	C22	8 60	8376	27 31	–0 0001	0 00	25-2B	60°C aqueous SAW
DWB 031	C22	8 60	4296	27 60	–0 0004	–0 03	25-1B	60°C water line SAW
DWB 032	C22	8 60	8376	27 60	0 0002	0 01	25-2B	60°C water line SAW
DWB 036	C22	8 60	4344	27.55	0 0001	0 01	26-1B	90°C water line SAW
DWB 037	C22	8 60	8784	27 43	–0 0010	–0 04	26-2B	90°C water line SAW
DWB 041	C22	8 60	4344	27 37	0 0005	0 04	26-1A	90°C vapor SAW
DWB 042	C22	8 60	4344	27.13	0 0014	0 12	26-1A	90°C vapor SAW
DWB 043	C22	8 60	4344	27 64	0 0002	0 02	26-1A	90°C vapor SAW
DWB 044	C22	8 60	4344	27 35	–0 0001	–0 01	26-1B	90°C aqueous SAW
DWB 045	C22	8 60	4344	27 12	–0 0001	–0 01	26-1B	90°C aqueous SAW
DWB 046	C22	8 60	4344	26 87	–0 0002	–0 02	26-1B	90°C aqueous SAW
DWB 047	C22	8 60	8784	27 59	–0 0001	0 00	26-2A	90°C vapor SAW
DWB 048	C22	8 60	8784	27 03	0 0000	0 00	26-2A	90°C vapor SAW
DWB 049	C22	8 60	8784	27 69	0 0001	0 00	26-2A	90°C vapor SAW

2.2 Long-Term Corrosion Studies

Sample identification	Alloy	Density (g/cc)	Exposure time (hours)	Surface area (sq cm)	Weight loss (g)	Corrosion rate (μm/y)	Vessel number-rack number	Test environment
DWB 050	C22	8 60	8784	27 61	–0 0003	–0 01	26-2B	90°C aqueous SAW
DWB 051	C22	8 60	8784	27 63	–0 0003	–0 01	26-2B	90°C aqueous SAW
DWB 052	C22	8 60	8784	27 75	–0 0010	–0 04	26-2B	90°C aqueous SAW
DWB 071	C22	8 60	4392	27 47	0 0003	0 03	27-1A	60°C vapor SCW
DWB 072	C22	8 60	4392	27 61	0 0003	0 03	27-1A	60°C vapor SCW
DWB 073	C22	8 60	4392	27 48	0 0004	0 03	27-1A	60°C vapor SCW
DWB 074	C22	8 60	4392	27 44	0 0005	0 04	27-1B	60°C aqueous SCW
DWB 075	C22	8 60	4392	27 57	0 0004	0 03	27-1B	60°C aqueous SCW
DWB 076	C22	8 60	4392	27 43	0 0008	0 07	27-1B	60°C aqueous SCW
DWB 101	C22	8 60	4392	27 46	0 0008	0 07	27-1B	60°C water line SCW
DWB 106	C22	8 60	4464	27 64	0 0004	0 03	28-1B	90°C water line SCW
DWB 111	C22	8 60	4464	27 45	0 0005	0 04	28-1A	90°C vapor SCW
DWB 112	C22	8 60	4464	27 33	0 0007	0 06	28-1A	90°C vapor SCW
DWB 113	C22	8 60	4464	27 47	0 0004	0 03	28-1A	90°C vapor SCW
DWB 114	C22	8 60	4464	27 06	0 0009	0 08	28-1B	90°C aqueous SCW
DWB 115	C22	8 60	4464	27 04	0 0007	0 06	28-1B	90°C aqueous SCW
DWB 116	C22	8 60	4464	27 44	0 0008	0 07	28-1B	90°C aqueous SCW
DWB 141	C22	8 60	4464	27 73	0 0003	0 02	29-1A	60°C vapor SDW
DWB 142	C22	8 60	4464	27 44	0 0001	0 01	29-1B	60°C aqueous SDW
DWB 151	C22	8 60	4464	27 67	0 0001	0 01	29-1B	60°C water line SDW
DWB 164	C22	8 60	4392	27 61	0 0002	0 02	30-1B	90°C water line SDW
DWB 168	C22	8 60	4392	27 76	0 0008	0 07	30-1A	90°C vapor SDW
DWB 169	C22	8 60	4392	27 24	0 0003	0 03	30-1B	90°C aqueous SDW
EWA 001	Ti Grade 12	4 43	4296	28 24	0 0308	5 02	25-1A	60°C vapor SAW
EWA 002	Ti Grade 12	4 43	4296	28 93	0 0310	4 93	25-1A	60°C vapor SAW
EWA 003	Ti Grade 12	4 43	4296	28 64	0 0278	4 47	25-1A	60°C vapor SAW
EWA 004	Ti Grade 12	4 43	4296	28 30	0 0230	3 74	25-1B	60°C aqueous SAW
EWA 005	Ti Grade 12	4 43	4296	28 72	0 0254	4 07	25-1B	60°C aqueous SAW
EWA 006	Ti Grade 12	4 43	4296	28 56	0 0230	3 71	25-1B	60°C aqueous SAW
EWA 007	Ti Grade 12	4 43	8376	28 31	–0 0007	–0 06	25-2A	60°C vapor SAW
EWA 008	Ti Grade 12	4 43	8376	28 35	–0 0004	–0 03	25-2A	60°C vapor SAW
EWA 009	Ti Grade 12	4 43	8376	28 42	–0 0004	–0 03	25-2A	60°C vapor SAW
EWA 010	Ti Grade 12	4 43	8376	28 54	–0 0005	–0 04	25-2B	60°C aqueous SAW
EWA 011	Ti Grade 12	4 43	8376	28 92	–0 0008	–0 07	25-2B	60°C aqueous SAW
EWA 012	Ti Grade 12	4 43	8376	28 39	–0 0005	–0 04	25-2B	60°C aqueous SAW
EWA 031	Ti Grade 12	4 43	4296	28 31	0 0303	4 93	25-1A	60°C water line SAW
EWA 032	Ti Grade 12	4 43	8376	28 69	–0 0004	–0 03	25-2A	60°C water line SAW
EWA 036	Ti Grade 12	4 43	4344	27 84	0 0158	2 58	26-1A	90°C water line SAW
EWA 037	Ti Grade 12	4 43	8784	28 36	–0 0004	–0 03	26-2A	90°C water line SAW
EWA 041	Ti Grade 12	4 43	4344	28 05	0 0551	8 94	26-1A	90°C vapor SAW

Sample identification	Alloy	Density (g/cc)	Exposure time (hours)	Surface area (sq cm)	Weight loss (g)	Corrosion rate (μm/y)	Vessel number-rack number	Test environment
EWA 042	Ti Grade 12	4 43	4344	28 40	0 0212	3 40	26-1A	90°C vapor SAW
EWA 043	Ti Grade 12	4 43	4344	28 61	0 0550	8 75	26-1A	90°C vapor SAW
EWA 044	Ti Grade 12	4 43	4344	28 76	0 0270	4 27	26-1B	90°C aqueous SAW
EWA 045	Ti Grade 12	4 43	4344	29 08	0 0357	5 59	26-1B	90°C aqueous SAW
EWA 046	Ti Grade 12	4 43	4344	28 43	0 0150	2 40	26-1B	90°C aqueous SAW
EWA 047	Ti Grade 12	4 43	8784	28 90	–0 0001	–0 01	26-2A	90°C vapor SAW
EWA 048	Ti Grade 12	4 43	8784	28 54	–0 0007	–0 06	26-2A	90°C vapor SAW
EWA 049	Ti Grade 12	4 43	8784	28 74	–0 0010	–0 08	26-2A	90°C vapor SAW
EWA 050	Ti Grade 12	4 43	8784	28 69	–0 0021	–0 16	26-2B	90°C aqueous SAW
EWA 051	Ti Grade 12	4 43	8784	28 24	–0 0013	–0 10	26-2B	90°C aqueous SAW
EWA 052	Ti Grade 12	4 43	8784	28 24	–0 0022	–0 18	26-2B	90°C aqueous SAW
EWA 071	Ti Grade 12	4 43	4392	28 32	0 0404	6 42	27-1A	60°C vapor SCW
EWA 072	Ti Grade 12	4 43	4392	28 51	0 0527	8 32	27-1A	60°C vapor SCW
EWA 073	Ti Grade 12	4 43	4392	28 60	0 0539	8 49	27-1A	60°C vapor SCW
EWA 074	Ti Grade 12	4 43	4392	28 14	0 0532	8 51	27-1B	60°C aqueous SCW
EWA 075	Ti Grade 12	4 43	4392	28 50	0 0440	6 95	27-1B	60°C aqueous SCW
EWA 076	Ti Grade 12	4 43	4392	28 63	0 0470	7 39	27-1B	60°C aqueous SCW
EWA 077	Ti Grade 12	4 43	8760	28 60	–0 0003	–0 02	27-2A	60°C vapor SCW
EWA 078	Ti Grade 12	4 43	8760	28 23	–0 0001	–0 01	27-2A	60°C vapor SCW
EWA 079	Ti Grade 12	4 43	8760	28 43	–0 0002	–0 02	27-2A	60°C vapor SCW
EWA 080	Ti Grade 12	4 43	8760	28 66	0 0022	0 17	27-2B	60°C aqueous SCW
EWA 081	Ti Grade 12	4 43	8760	28 54	0 0012	0 09	27-2B	60°C aqueous SCW
EWA 082	Ti Grade 12	4 43	8760	28 35	0 0020	0 16	27-2B	60°C aqueous SCW
EWA 101	Ti Grade 12	4 43	4392	29 06	0 0491	7 61	27-1A	60°C water line SCW
EWA 102	Ti Grade 12	4 43	8760	29 18	0 0011	0 09	27-2A	60°C water line SCW
EWA 106	Ti Grade 12	4 43	4464	28 10	0 0376	5 93	28-1A	90°C water line SCW
EWA 111	Ti Grade 12	4 43	4464	28 34	0 0207	3 24	28-1A	90°C vapor SCW
EWA 112	Ti Grade 12	4 43	4464	28 58	0 0261	4 04	28-1A	90°C vapor SCW
EWA 113	Ti Grade 12	4 43	4464	28 60	0 0309	4 79	28-1A	90°C vapor SCW
EWA 114	Ti Grade 12	4 43	4464	27 98	0 0397	6 29	28-1B	90°C aqueous SCW
EWA 115	Ti Grade 12	4 43	4464	28 65	0 0495	7 65	28-1B	90°C aqueous SCW
EWA 116	Ti Grade 12	4 43	4464	28 65	0 0406	6 28	28-1B	90°C aqueous SCW
EWA 141	Ti Grade 12	4 43	4464	28 37	0 0296	4 62	29-1A	60°C vapor SDW
EWA 142	Ti Grade 12	4 43	4464	29 04	0 0236	3 60	29-1B	60°C aqueous SDW
EWA 151	Ti Grade 12	4 43	4464	29 12	0 0327	4 98	29-1A	60°C water line SDW
EWA 164	Ti Grade 12	4 43	4392	27 80	0 0349	5 65	30-1A	90°C water line SDW
EWA 168	Ti Grade 12	4 43	4392	27 72	0 0377	6 12	30-1A	90°C vapor SDW
EWA 169	Ti Grade 12	4 43	4392	27 65	0 0328	5 34	30-1B	90°C aqueous SDW
EWD 001	Ti Grade 12	4 43	4296	28 96	0 0688	10 93	25-1A	60°C vapor SAW
EWD 002	Ti Grade 12	4 43	4296	29 03	0 1822	28 89	25-1A	60°C vapor SAW

2.2 Long-Term Corrosion Studies

Sample identification	Alloy	Density (g/cc)	Exposure time (hours)	Surface area (sq cm)	Weight loss (g)	Corrosion rate (μm/y)	Vessel number-rack number	Test environment
EWD 003	Ti Grade 12	4 43	4296	29 05	0 0433	6 86	25-1A	60°C vapor SAW
EWD 004	Ti Grade 12	4 43	4296	29 19	0 0123	1 94	25-1B	60°C aqueous SAW
EWD 005	Ti Grade 12	4 43	4296	28 99	0 0369	5 86	25-1B	60°C aqueous SAW
EWD 006	Ti Grade 12	4 43	4296	29 22	0 0384	6 05	25-1B	60°C aqueous SAW
EWD 007	Ti Grade 12	4 43	8376	29 08	0 0001	0 01	25-2A	60°C vapor SAW
EWD 008	Ti Grade 12	4 43	8376	28 99	–0 0004	–0 03	25-2A	60°C vapor SAW
EWD 009	Ti Grade 12	4 43	8376	29 08	0 0003	0 02	25-2A	60°C vapor SAW
EWD 010	Ti Grade 12	4 43	8376	29 17	–0 0004	–0 03	25-2B	60°C aqueous SAW
EWD 011	Ti Grade 12	4 43	8376	29 11	–0 0004	–0 03	25-2B	60°C aqueous SAW
EWD 012	Ti Grade 12	4 43	8376	28 77	–0 0004	–0 03	25-2B	60°C aqueous SAW
EWD 031	Ti Grade 12	4 43	4296	29 25	0 1630	25 65	25-1B	60°C water line SAW
EWD 032	Ti Grade 12	4 43	8376	29 22	–0 0005	–0 04	25-2B	60°C water line SAW
EWD 036	Ti Grade 12	4 43	4344	29 09	0 0192	3 00	26-1B	90°C water line SAW
EWD 037	Ti Grade 12	4 43	8784	28 78	–0 0011	–0 09	26-2B	90°C water line SAW
EWD 041	Ti Grade 12	4 43	4344	29 24	0 0211	3 28	26-1A	90°C vapor SAW
EWD 042	Ti Grade 12	4 43	4344	29 16	0 0678	10 58	26-1A	90°C vapor SAW
EWD 043	Ti Grade 12	4 43	4344	29 22	0 0468	7 29	26-1A	90°C vapor SAW
EWD 044	Ti Grade 12	4 43	4344	29 23	0 0237	3 69	26-1B	90°C aqueous SAW
EWD 045	Ti Grade 12	4 43	4344	29 22	0 0178	2 77	26-1B	90°C aqueous SAW
EWD 046	Ti Grade 12	4 43	4344	29 10	0 0240	3 75	26-1B	90°C aqueous SAW
EWD 047	Ti Grade 12	4 43	8784	29 14	–0 0012	–0 09	26-2A	90°C vapor SAW
EWD 048	Ti Grade 12	4 43	8784	29 21	0 0000	0 00	26-2A	90°C vapor SAW
EWD 049	Ti Grade 12	4 43	8784	29 15	–0 0006	–0 05	26-2A	90°C vapor SAW
EWD 050	Ti Grade 12	4 43	8784	29 09	–0 0028	–0 22	26-2B	90°C aqueous SAW
EWD 051	Ti Grade 12	4 43	8784	28 67	–0 0019	–0 15	26-2B	90°C aqueous SAW
EWD 052	Ti Grade 12	4 43	8784	29 20	–0 0020	–0 15	26-2B	90°C aqueous SAW
EWD 071	Ti Grade 12	4 43	4392	28 95	0 0434	6 75	27-1A	60°C vapor SCW
EWD 072	Ti Grade 12	4 43	4392	29 13	0 0370	5 72	27-1A	60°C vapor SCW
EWD 073	Ti Grade 12	4 43	4392	29 19	0 0428	6 60	27-1A	60°C vapor SCW
EWD 074	Ti Grade 12	4 43	4392	29 09	0 0325	5 03	27-1B	60°C aqueous SCW
EWD 075	Ti Grade 12	4 43	4392	29 12	0 0489	7 56	27-1B	60°C aqueous SCW
EWD 076	Ti Grade 12	4 43	4392	28 97	0 0371	5 77	27-1B	60°C aqueous SCW
EWD 077	Ti Grade 12	4 43	8760	29 21	0 0003	0 02	27-2A	60°C vapor SCW
EWD 078	Ti Grade 12	4 43	8760	29 14	–0 0002	–0 02	27-2A	60°C vapor SCW
EWD 079	Ti Grade 12	4 43	8760	29 21	–0 0002	–0 02	27-2A	60°C vapor SCW
EWD 080	Ti Grade 12	4 43	8760	29 17	0 0009	0 07	27-2B	60°C aqueous SCW
EWD 081	Ti Grade 12	4 43	8760	29 10	0 0007	0 05	27-2B	60°C aqueous SCW
EWD 082	Ti Grade 12	4 43	8760	29 11	0 0010	0 08	27-2B	60°C aqueous SCW
EWD 101	Ti Grade 12	4 43	4392	29 12	0 0445	6 88	27-1B	60°C water line SCW
EWD 102	Ti Grade 12	4 43	8760	29 12	0 0008	0 06	27-2B	60°C water line SCW

Sample Identification	Alloy	Density (g/cc)	Exposure time (hours)	Surface area (sq cm)	Weight loss (g)	Corrosion rate (μm/y)	Vessel number-rack number	Test environment
EWD 106	Ti Grade 12	4 43	4464	29 08	0 0815	12 41	28-1B	90°C water line SCW
EWD 111	Ti Grade 12	4 43	4464	28 82	0 0316	4 86	28-1A	90°C vapor SCW
EWD 112	Ti Grade 12	4 43	4464	29 21	0 0411	6 23	28-1A	90°C vapor SCW
EWD 113	Ti Grade 12	4 43	4464	28 96	0 0244	3 73	28-1A	90°C vapor SCW
EWD 114	Ti Grade 12	4 43	4464	28 95	0 0426	6 52	28-1B	90°C aqueous SCW
EWD 115	Ti Grade 12	4 43	4464	28 71	0 2063	31 84	28-1B	90°C aqueous SCW
EWD 116	Ti Grade 12	4 43	4464	29 11	0 0631	9 60	28-1B	90°C aqueous SCW
EWD 141	Ti Grade 12	4 43	4464	29 04	0 0260	3 97	29-1A	60°C vapor SDW
EWD 142	Ti Grade 12	4 43	4464	28 93	0 0617	9 45	29-1B	60°C aqueous SDW
EWD 151	Ti Grade 12	4 43	4464	28 99	0 0399	6 10	29-1B	60°C water line SDW
EWD 164	Ti Grade 12	4 43	4392	27 37	0 0331	5 44	30-1B	90°C water line SDW
EWD 168	Ti Grade 12	4 43	4392	27 66	0 0338	5 50	30-1A	90°C vapor SDW
EWD 169	Ti Grade 12	4 43	4392	37 86	0 0386	4 59	30-1B	90°C aqueous SDW
FWA 001	Ti Grade 16	4 52	4296	27 27	0 0188	3 11	25-1A	60°C vapor SAW
FWA 002	Ti Grade 16	4 52	4296	27 46	0 0222	3 65	25-1A	60°C vapor SAW
FWA 003	Ti Grade 16	4 52	4296	27 35	0 0259	4 27	25-1A	60°C vapor SAW
FWA 004	Ti Grade 16	4 52	4296	27 68	–0 0001	–0 02	25-1B	60°C aqueous SAW
FWA 005	Ti Grade 16	4 52	4296	27 25	0 0000	0 00	25-1B	60°C aqueous SAW
FWA 006	Ti Grade 16	4 52	4296	27 36	–0 0002	–0 03	25-1B	60°C aqueous SAW
FWA 007	Ti Grade 16	4 52	8376	27 58	–0 0004	–0 03	25-2A	60°C vapor SAW
FWA 008	Ti Grade 16	4 52	8376	27 68	–0 0002	–0 02	25-2A	60°C vapor SAW
FWA 009	Ti Grade 16	4 52	8376	27 62	–0 0003	–0 03	25-2A	60°C vapor SAW
FWA 010	Ti Grade 16	4 52	8376	27 43	–0 0002	–0 02	25-2B	60°C aqueous SAW
FWA 011	Ti Grade 16	4 52	8376	27 44	–0 0003	–0 03	25-2B	60°C aqueous SAW
FWA 012	Ti Grade 16	4 52	8376	26 96	–0 0003	–0 03	25-2B	60°C aqueous SAW
FWA 031	Ti Grade 16	4 52	4296	27 68	0 0001	0 02	25-1A	60°C water line SAW
FWA 032	Ti Grade 16	4 52	8376	27 35	–0 0003	–0 03	25-2A	60°C water line SAW
FWA 036	Ti Grade 16	4 52	4344	27 65	0 0166	2 68	26-1A	90°C water line SAW
FWA 037	Ti Grade 16	4 52	8784	27 60	–0 0025	–0 20	26-2A	90°C water line SAW
FWA 041	Ti Grade 16	4 52	4344	27.58	0 0198	3 20	26-1A	90°C vapor SAW
FWA 042	Ti Grade 16	4 52	4344	27.50	0 0187	3 03	26-1A	90°C vapor SAW
FWA 043	Ti Grade 16	4 52	4344	27.62	0 0223	3 60	26-1A	90°C vapor SAW
FWA 044	Ti Grade 16	4 52	4344	27 48	0 0143	2 32	26-1B	90°C aqueous SAW
FWA 045	Ti Grade 16	4 52	4344	27 47	0 0148	2 40	26-1B	90°C aqueous SAW
FWA 046	Ti Grade 16	4 52	4344	27 58	0 0127	2 05	26-1B	90°C aqueous SAW
FWA 047	Ti Grade 16	4 52	8784	27 60	–0 0005	–0 04	26-2A	90°C vapor SAW
FWA 048	Ti Grade 16	4 52	8784	27 56	–0 0006	–0 05	26-2A	90°C vapor SAW
FWA 049	Ti Grade 16	4 52	8784	27 63	–0 0004	–0 03	26-2A	90°C vapor SAW
FWA 050	Ti Grade 16	4 52	8784	27 55	–0 0017	–0 14	26-2B	90°C aqueous SAW
FWA 051	Ti Grade 16	4 52	8784	27.75	–0 0020	–0.16	26-2B	90°C aqueous SAW

Sample identification	Alloy	Density (g/cc)	Exposure time (hours)	Surface area (sq cm)	Weight loss (g)	Corrosion rate (μm/y)	Vessel number-rack number	Test environment
FWA 052	Ti Grade 16	4 52	8784	27 64	–0 0016	–0 13	26-2B	90°C aqueous SAW
FWA 071	Ti Grade 16	4 52	4392	27 70	0 0177	2 82	27-1A	60°C vapor SCW
FWA 072	Ti Grade 16	4 52	4392	27 37	0 0310	5 00	27-1A	60°C vapor SCW
FWA 073	Ti Grade 16	4 52	4392	27 51	0 0196	3 14	27-1A	60°C vapor SCW
FWA 074	Ti Grade 16	4 52	4392	27 77	0 0214	3 40	27-1B	60°C aqueous SCW
FWA 075	Ti Grade 16	4 52	4392	27 68	0 0147	2 34	27-1B	60°C aqueous SCW
FWA 076	Ti Grade 16	4 52	4392	26 73	0 0181	2 99	27-1B	60°C aqueous SCW
FWA 077	Ti Grade 16	4 52	8760	27 69	–0 0007	–0 06	27-2A	60°C vapor SCW
FWA 078	Ti Grade 16	4 52	8760	27 65	0 0000	0 00	27-2A	60°C vapor SCW
FWA 079	Ti Grade 16	4 52	8760	27 96	–0 0004	–0 03	27-2A	60°C vapor SCW
FWA 080	Ti Grade 16	4 52	8760	27 76	–0 0002	–0 02	27-2B	60°C aqueous SCW
FWA 081	Ti Grade 16	4 52	8760	27 71	0 0002	0 02	27-2B	60°C aqueous SCW
FWA 082	Ti Grade 16	4 52	8760	27 53	0 0002	0 02	27-2B	60°C aqueous SCW
FWA 101	Ti Grade 16	4 52	4392	27 76	0 0238	3 78	27-1A	60°C water line SCW
FWA 102	Ti Grade 16	4 52	8760	27 66			27-2A	60°C water line SCW
FWA 106	Ti Grade 16	4 52	4464	27 80	0 0241	3 76	28-1A	90°C water line SCW
FWA 111	Ti Grade 16	4 52	4464	27 80	0 0290	4 53	28-1A	90°C vapor SCW
FWA 112	Ti Grade 16	4 52	4464	27 63	0 0640	10 06	28-1A	90°C vapor SCW
FWA 113	Ti Grade 16	4 52	4464	27 59	0 0295	4 64	28-1A	90°C vapor SCW
FWA 114	Ti Grade 16	4 52	4464	27 46	0 0361	5 71	28-1B	90°C aqueous SCW
FWA 115	Ti Grade 16	4 52	4464	27 53	0 0314	4 95	28-1B	90°C aqueous SCW
FWA 116	Ti Grade 16	4 52	4464	27 64	0 0343	5 39	28-1B	90°C aqueous SCW
FWA 141	Ti Grade 16	4 52	4464	27 81	0 0249	3 89	29-1A	60°C vapor SDW
FWA 142	Ti Grade 16	4 52	4464	27 63	0 0238	3 74	29-1B	60°C aqueous SDW
FWA 151	Ti Grade 16	4 52	4464	27 72	0 0608	9 52	29-1A	60°C water line SDW
FWA 164	Ti Grade 16	4 52	4392	27 44	0 0262	4 21	30-1A	90°C water line SDW
FWA 168	Ti Grade 16	4 52	4392	27 24	0 0245	3 97	30-1A	90°C vapor SDW
FWA 169	Ti Grade 16	4 52	4392	27 44	0 0236	3 79	30-1B	90°C aqueous SDW
FWE 001	Ti Grade 16	4 52	4296	27 42	0 0362	5 96	25-1A	60°C vapor SAW
FWE 002	Ti Grade 16	4 52	4296	27 62	0 0425	6 94	25-1A	60°C vapor SAW
FWE 003	Ti Grade 16	4 52	4296	28 13	0 0322	5 16	25-1A	60°C vapor SAW
FWE 004	Ti Grade 16	4 52	4296	28 10	0 0110	1 77	25-1B	60°C aqueous SAW
FWE 005	Ti Grade 16	4 52	4296	27 93	0 0099	1 60	25-1B	60°C aqueous SAW
FWE 006	Ti Grade 16	4 52	4296	28 01	0 0128	2 06	25-1B	60°C aqueous SAW
FWE 007	Ti Grade 16	4 52	8376	28 06	–0 0003	–0 02	25-2A	60°C vapor SAW
FWE 008	Ti Grade 16	4 52	8376	28 20	–0 0007	–0 06	25-2A	60°C vapor SAW
FWE 009	Ti Grade 16	4 52	8376	28 02	–0 0006	–0 05	25-2A	60°C vapor SAW
FWE 010	Ti Grade 16	4 52	8376	28 14	–0 0004	–0 03	25-2B	60°C aqueous SAW
FWE 011	Ti Grade 16	4 52	8376	27 91	–0 0006	–0 05	25-2B	60°C aqueous SAW
FWE 012	Ti Grade 16	4 52	8376	28 04	–0 0005	–0 04	25-2B	60°C aqueous SAW

Sample identification	Alloy	Density (g/cc)	Exposure time (hours)	Surface area (sq cm)	Weight loss (g)	Corrosion rate (μm/y)	Vessel number-rack number	Test environment
FWE 031	Ti Grade 16	4 52	4296	27 84	0 0008	0 13	25-1B	60°C water line SAW
FWE 032	Ti Grade 16	4 52	8376	27 63	–0 0007	–0 06	25-2B	60°C water line SAW
FWE 036	Ti Grade 16	4 52	4344	28 06	0 0181	2 88	26-1B	90°C water line SAW
FWE 037	Ti Grade 16	4 52	8784	27 54	–0 0027	–0 22	26-2B	90°C water line SAW
FWE 041	Ti Grade 16	4 52	4344	27 89	0 0212	3 39	26-1A	90°C vapor SAW
FWE 042	Ti Grade 16	4 52	4344	27 74	0 0331	5 32	26-1A	90°C vapor SAW
FWE 043	Ti Grade 16	4 52	4344	27 99	0 0204	3 25	26-1A	90°C vapor SAW
FWE 044	Ti Grade 16	4 52	4344	28 01	–0 0011	–0 18	26-1B	90°C aqueous SAW
FWE 045	Ti Grade 16	4 52	4344	28 01	0 0110	1 75	26-1B	90°C aqueous SAW
FWE 046	Ti Grade 16	4 52	4344	27 79	0 0111	1 78	26-1B	90°C aqueous SAW
FWE 047	Ti Grade 16	4 52	8784	27 49	0 0009	0 07	26-2A	90°C vapor SAW
FWE 048	Ti Grade 16	4 52	8784	27 99	–0 0006	–0 05	26-2A	90°C vapor SAW
FWE 049	Ti Grade 16	4 52	8784	27 98	–0 0002	–0 02	26-2A	90°C vapor SAW
FWE 050	Ti Grade 16	4 52	8784	28 09	–0 0016	–0 13	26-2B	90°C aqueous SAW
FWE 051	Ti Grade 16	4 52	8784	27 73	–0 0018	–0 14	26-2B	90°C aqueous SAW
FWE 052	Ti Grade 16	4 52	8784	27 77	–0 0021	–0 17	26-2B	90°C aqueous SAW
FWE 071	Ti Grade 16	4 52	4392	27 73	0 0201	3 20	27-1A	60°C vapor SCW
FWE 072	Ti Grade 16	4 52	4392	27 91	0 0216	3 42	27-1A	60°C vapor SCW
FWE 073	Ti Grade 16	4 52	4392	27 66	0 0311	4 96	27-1A	60°C vapor SCW
FWE 074	Ti Grade 16	4 52	4392	28 15	0 0240	3 76	27-1B	60°C aqueous SCW
FWE 075	Ti Grade 16	4 52	4392	27 99	0 0214	3 37	27-1B	60°C aqueous SCW
FWE 076	Ti Grade 16	4 52	4392	27 51	0 0187	3 00	27-1B	60°C aqueous SCW
FWE 077	Ti Grade 16	4 52	8760	27 68			27-2A	60°C vapor SCW
FWE 078	Ti Grade 16	4 52	8760	28 05	–0 0007	–0 06	27-2A	60°C vapor SCW
FWE 079	Ti Grade 16	4 52	8760	27 94	0 0001	0 01	27-2A	60°C vapor SCW
FWE 080	Ti Grade 16	4 52	8760	27 99	0 0001	0 01	27-2B	60°C aqueous SCW
FWE 081	Ti Grade 16	4 52	8760	28 16	0 0003	0 02	27-2B	60°C aqueous SCW
FWE 082	Ti Grade 16	4 52	8760	27 85	0 0009	0 07	27-2B	60°C aqueous SCW
FWE 101	Ti Grade 16	4 52	4392	27 72	0 0299	4 76	27-1B	60°C water line SCW
FWE 102	Ti Grade 16	4 52	8760	27 95	0 0010	0 08	27-2B	60°C water line SCW
FWE 106	Ti Grade 16	4 52	4464	27 49	0 0294	4 64	28-1B	90°C water line SCW
FWE 111	Ti Grade 16	4 52	4464	28 21	0 0292	4 49	28-1A	90°C vapor SCW
FWE 112	Ti Grade 16	4 52	4464	27 85	0 0192	2 99	28-1A	90°C vapor SCW
FWE 113	Ti Grade 16	4 52	4464	28 11	0 0289	4 46	28-1A	90°C vapor SCW
FWE 114	Ti Grade 16	4 52	4464	28 03	0 0326	5 05	28-1B	90°C aqueous SCW
FWE 115	Ti Grade 16	4.52	4464	27 74	0 0831	13 01	28-1B	90°C aqueous SCW
FWE 116	Ti Grade 16	4 52	4464	28 00	0 0362	5 61	28-1B	90°C aqueous SCW
FWE 141	Ti Grade 16	4 52	4464	27 67	0 0158	2 48	29-1A	60°C vapor SDW
FWE 142	Ti Grade 16	4 52	4464	27 57	0 0267	4 20	29-1B	60°C aqueous SDW
FWE 151	Ti Grade 16	4 52	4464	27 87	0 0271	4 22	29-1B	60°C water line SDW

Sample identification	Alloy	Density (g/cc)	Exposure time (hours)	Surface area (sq cm)	Weight loss (g)	Corrosion rate (μm/y)	Vessel number-rack number	Test environment
FWE 164	Ti Grade 16	4 52	4392	27 38	0 0253	4 08	30-1B	90°C water line SDW
FWE 168	Ti Grade 16	4 52	4392	27 60	0 0177	2 83	30-1A	90°C vapor SDW
FWE 169	Ti Grade 16	4 52	4392	27 57	0 0472	7 55	30-1B	90°C aqueous SDW
GWA 001	Monel 400	8 80	4536	28 49	0 0061	0 47	19-1A	60°C vapor SAW
GWA 002	Monel 400	8 80	4536	28 20	0 0117	0 91	19-1A	60°C vapor SAW
GWA 003	Monel 400	8 80	4536	28 39	0 0153	1 18	19-1A	60°C vapor SAW
GWA 004	Monel 400	8 80	4536	28 40	1 4796	114 33	19-1B	60°C aqueous SAW
GWA 005	Monel 400	8 80	4536	27 93	1 4297	112 33	19-1B	60°C aqueous SAW
GWA 006	Monel 400	8 80	4536	28 38	1 5462	119 57	19-1B	60°C aqueous SAW
GWA 007	Monel 400	8 80	8760	28 04	0 0110	0 45	19-2A	60°C vapor SAW
GWA 008	Monel 400	8 80	8760	27 98	0 0119	0 48	19-2A	60°C vapor SAW
GWA 009	Monel 400	8 80	8760	28 43	0 0108	0 43	19-2A	60°C vapor SAW
GWA 010	Monel 400	8 80	8760	28 53	1 6761	66 76	19-2B	60°C aqueous SAW
GWA 011	Monel 400	8 80	8760	28 51	1 6655	66 39	19-2B	60°C aqueous SAW
GWA 012	Monel 400	8 80	8760	27 99	1 6915	68 68	19-2B	60°C aqueous SAW
GWA 031	Monel 400	8 80	4536	27 71	1 0818	85 69	19-1A	60°C water line SAW
GWA 032	Monel 400	8 80	8760	27 75	1 3017	53 30	19-2A	60°C water line SAW
GWA 036	Monel 400	8 80	4392	28 02	0 7423	60 05	18-1A	90°C water line SAW
GWA 037	Monel 400	8 80	8760	27 93	0 8876	36 11	18-2A	90°C water line SAW
GWA 041	Monel 400	8 80	4392	28 75	0 0487	3 84	18-1A	90°C vapor SAW
GWA 042	Monel 400	8 80	4392	28 73	0 0568	4 48	18-1A	90°C vapor SAW
GWA 043	Monel 400	8 80	4392	27 94	0 0522	4 23	18-1A	90°C vapor SAW
GWA 044	Monel 400	8 80	4392	28 67	0 9861	77 96	18-1B	90°C aqueous SAW
GWA 045	Monel 400	8 80	4392	27 60	1 0208	83 84	18-1B	90°C aqueous SAW
GWA 046	Monel 400	8 80	4392	28 37	1 0802	86 29	18-1B	90°C aqueous SAW
GWA 047	Monel 400	8 80	8760	28 42	0 0491	1 96	18-2A	90°C vapor SAW
GWA 048	Monel 400	8 80	8760	28 26	0 0504	2 03	18-2A	90°C vapor SAW
GWA 049	Monel 400	8 80	8760	27 91	0 0580	2 36	18-2A	90°C vapor SAW
GWA 050	Monel 400	8 80	8760	28 61	1 1329	45 00	18-2B	90°C aqueous SAW
GWA 051	Monel 400	8 80	8760	27 84	1 1457	46 76	18-2B	90°C aqueous SAW
GWA 052	Monel 400	8 80	8760	28 66	1 1759	46 63	18-2B	90°C aqueous SAW
GWF 001	Monel 400	8 80	4536	27 17	0 0107	0 86	19-1A	60°C vapor SAW
GWF 002	Monel 400	8 80	4536	27 77	0 0143	1 13	19-1A	60°C vapor SAW
GWF 003	Monel 400	8 80	4536	27 77	0 0129	1 02	19-1A	60°C vapor SAW
GWF 004	Monel 400	8 80	4536	27 53	1 4721	117 34	19-1B	60°C aqueous SAW
GWF 005	Monel 400	8 80	4536	27 49	1 5264	121 87	19-1B	60°C aqueous SAW
GWF 006	Monel 400	8 80	4536	27 18	1 5832	127 84	19-1B	60°C aqueous SAW
GWF 007	Monel 400	8 80	8760	27 29	0 0185	0 77	19-2A	60°C vapor SAW
GWF 008	Monel 400	8 80	8760	27 80	0 0337	1 38	19-2A	60°C vapor SAW
GWF 009	Monel 400	8 80	8760	27 76	0 0319	1 31	19-2A	60°C vapor SAW

Sample identification	Alloy	Density (g/cc)	Exposure time (hours)	Surface area (sq cm)	Weight loss (g)	Corrosion rate (μm/y)	Vessel number-rack number	Test environment
GWF 010	Monel 400	8 80	8760	27 85	1 5732	64 19	19-2B	60°C aqueous SAW
GWF 011	Monel 400	8 80	8760	27 38	1 5294	63 47	19-2B	60°C aqueous SAW
GWF 012	Monel 400	8 80	8760	27 16	1 5600	65 26	19-2B	60°C aqueous SAW
GWF 031	Monel 400	8 80	4536	27 12	1 0996	88 97	19-1A	60°C water line SAW
GWF 032	Monel 400	8 80	8760	27 97	1 3393	54 42	19-2A	60°C water line SAW
GWF 036	Monel 400	8 80	4392	26 95	0 6858	57 68	18-1A	90°C water line SAW
GWF 037	Monel 400	8 80	8760	27 38	0 9459	39 26	18-2A	90°C water line SAW
GWF 041	Monel 400	8 80	4392	27 64	0 0480	3 94	18-1A	90°C vapor SAW
GWF 042	Monel 400	8 80	4392	27 49	0 0518	4 27	18-1A	90°C vapor SAW
GWF 043	Monel 400	8 80	4392	27 69	0 0424	3 47	18-1A	90°C vapor SAW
GWF 044	Monel 400	8 80	4392	26 87	1 0116	85 33	18-1B	90°C aqueous SAW
GWF 045	Monel 400	8 80	4392	27 40	1 0926	90 38	18-1B	90°C aqueous SAW
GWF 046	Monel 400	8 80	4392	27 27	1 1571	96 15	18-1B	90°C aqueous SAW
GWF 047	Monel 400	8 80	8760	27 29	0 0560	2 33	18-2A	90°C vapor SAW
GWF 048	Monel 400	8 80	8760	26 90	0 0460	1 94	18-2A	90°C vapor SAW
GWF 049	Monel 400	8 80	8760	27 30	0 0526	2 19	18-2A	90°C vapor SAW
GWF 050	Monel 400	8 80	8760	27 65	1 1954	49 14	18-2B	90°C aqueous SAW
GWF 051	Monel 400	8 80	8760	27 66	1 2342	50 70	18-2B	90°C aqueous SAW
GWF 052	Monel 400	8 80	8760	27 27	1 2562	52 35	18-2B	90°C aqueous SAW
HWA 001	CDA 715	8 94	4536	27 51	0 0402	3 16	19-1A	60°C vapor SAW
HWA 002	CDA 715	8 94	4536	27 58	0 0543	4 25	19-1A	60°C vapor SAW
HWA 003	CDA 715	8 94	4536	28 22	0 0618	4 73	19-1A	60°C vapor SAW
HWA 004	CDA 715	8 94	4536	27 84	3 2743	254 02	19-1B	60°C aqueous SAW
HWA 005	CDA 715	8 94	4536	27 87	3 4426	266 83	19-1B	60°C aqueous SAW
HWA 006	CDA 715	8 94	4536	27 91	3 7590	290 90	19-1B	60°C aqueous SAW
HWA 007	CDA 715	8 94	8760	27 71	0 0814	3 29	19-2A	60°C vapor SAW
HWA 008	CDA 715	8 94	8760	27 80	0 0895	3 60	19-2A	60°C vapor SAW
HWA 009	CDA 715	8 94	8760	27 77	0 0993	4 00	19-2A	60°C vapor SAW
HWA 010	CDA 715	8 94	8760	27 99	3 3825	135 18	19-2B	60°C aqueous SAW
HWA 011	CDA 715	8 94	8760	27 33	3 3421	136 77	19-2B	60°C aqueous SAW
HWA 012	CDA 715	8 94	8760	27 57	3 5737	144 97	19-2B	60°C aqueous SAW
HWA 031	CDA 715	8 94	4536	27 48	4 7230	371 32	19-1A	60°C water line SAW
HWA 032	CDA 715	8 94	8760	27 65	5 4566	220 73	19-2A	60°C water line SAW
HWA 036	CDA 715	8 94	4392	27 79	3 5809	287 50	18-1A	90°C water line SAW
HWA 037	CDA 715	8 94	8760	27 95	6 1186	244 87	18-2A	90°C water line SAW
HWA 041	CDA 715	8 94	4392	27 79	0 2227	17 88	18-1A	90°C vapor SAW
HWA 042	CDA 715	8 94	4392	27 64	0 1531	12 36	18-1A	90°C vapor SAW
HWA 043	CDA 715	8 94	4392	27 72	0 1116	8 98	18-1A	90°C vapor SAW
HWA 044	CDA 715	8 94	4392	28 26	3 2813	259 03	18-1B	90°C aqueous SAW
HWA 045	CDA 715	8 94	4392	27 98	3 2059	255 62	18-1B	90°C aqueous SAW

Sample identification	Alloy	Density (g/cc)	Exposure time (hours)	Surface area (sq cm)	Weight loss (g)	Corrosion rate (μm/y)	Vessel number-rack number	Test environment
HWA 046	CDA 715	8 94	4392	27.48	3.6026	292 46	18-1B	90°C aqueous SAW
HWA 047	CDA 715	8 94	8760	27 86	0 3061	12 29	18-2A	90°C vapor SAW
HWA 048	CDA 715	8 94	8760	27 94	0 2586	10 35	18-2A	90°C vapor SAW
HWA 049	CDA 715	8 94	8760	28 22	0 1936	7 67	18-2A	90°C vapor SAW
HWA 050	CDA 715	8 94	8760	28 12	4 2182	167 79	18-2B	90°C aqueous SAW
HWA 051	CDA 715	8 94	8760	27 78	6 0110	242 05	18-2B	90°C aqueous SAW
HWA 052	CDA 715	8 94	8760	27 54	3 8218	155 24	18-2B	90°C aqueous SAW
HWG 001	CDA 715	8 94	4536	26 81	0 0435	3 50	19-1A	60°C vapor SAW
HWG 002	CDA 715	8 94	4536	26 89	0 0484	3 89	19-1A	60°C vapor SAW
HWG 003	CDA 715	8 94	4536	26 88	0 0660	5 30	19-1A	60°C vapor SAW
HWG 004	CDA 715	8 94	4536	26 74	2 5337	204 66	19-1B	60°C aqueous SAW
HWG 005	CDA 715	8 94	4536	26 66	2 7715	224 56	19-1B	60°C aqueous SAW
HWG 006	CDA 715	8 94	4536	26 53	3 1442	255 99	19-1B	60°C aqueous SAW
HWG 007	CDA 715	8 94	8760	26 72	0 0562	2 35	19-2A	60°C vapor SAW
HWG 008	CDA 715	8 94	8760	26 74	0 0939	3 93	19-2A	60°C vapor SAW
HWG 009	CDA 715	8 94	8760	26 81	0 1004	4 19	19-2A	60°C vapor SAW
HWG 010	CDA 715	8 94	8760	26 56	2 6060	109 74	19-2B	60°C aqueous SAW
HWG 011	CDA 715	8 94	8760	26 83	2 7953	116 54	19-2B	60°C aqueous SAW
HWG 012	CDA 715	8 94	8760	26 73	3 0622	128 13	19-2B	60°C aqueous SAW
HWG 031	CDA 715	8 94	4536	26 83	5 3929	434 28	19-1A	60°C water line SAW
HWG 032	CDA 715	8 94	8760	26 89	5 0582	210 41	19-2A	60°C water line SAW
HWG 036	CDA 715	8 94	4392	26 83	3 3935	282 14	18-1A	90°C water line SAW
HWG 037	CDA 715	8 94	8760	26 77	4 7066	196 68	18-2A	90°C water line SAW
HWG 041	CDA 715	8 94	4392	26 82	0 1346	11 20	18-1A	90°C vapor SAW
HWG 042	CDA 715	8 94	4392	26 92	0 1047	8 68	18-1A	90°C vapor SAW
HWG 043	CDA 715	8 94	4392	26 82	0 0953	7 93	18-1A	90°C vapor SAW
HWG 044	CDA 715	8 94	4392	26 75	3 4887	290 97	18-1B	90°C aqueous SAW
HWG 045	CDA 715	8 94	4392	26 91	3 6809	305 21	18-1B	90°C aqueous SAW
HWG 046	CDA 715	8 94	4392	26 84	3 7686	313 24	18-1B	90°C aqueous SAW
HWG 047	CDA 715	8 94	8760	26 89	0 2696	11 21	18-2A	90°C vapor SAW
HWG 048	CDA 715	8 94	8760	26 61	0 2005	8 43	18-2A	90°C vapor SAW
HWG 049	CDA 715	8 94	8760	26 35	0 1964	8 34	18-2A	90°C vapor SAW
HWG 050	CDA 715	8 94	8760	26 78	5 2821	220 62	18-2B	90°C aqueous SAW
HWG 051	CDA 715	8 94	8760	26 84	5 4112	225 50	18-2B	90°C aqueous SAW
HWG 052	CDA 715	8 94	8760	26 79	5 4941	229 43	18-2B	90°C aqueous SAW
IWA 001	A387 Grade 22	7 86	4536	28 68	0 2073	17 76	23-1A	60°C vapor SDW
IWA 002	A387 Grade 22	7 86	4536	28 86	0 2647	22 54	23-1A	60°C vapor SDW
IWA 003	A387 Grade 22	7 86	4536	29 18	0 5066	42 65	23-1A	60°C vapor SDW
IWA 004	A387 Grade 22	7 86	4536	28 43	0 5857	50 62	23-1B	60°C aqueous SDW
IWA 005	A387 Grade 22	7 86	4536	29 02	0 2817	23 85	23-1B	60°C aqueous SDW

Sample identification	Alloy	Density (g/cc)	Exposure time (hours)	Surface area (sq cm)	Weight loss (g)	Corrosion rate (μm/y)	Vessel number-rack number	Test environment
IWA 006	A387 Grade 22	7 86	4536	29 03	1 4452	122 30	23-1B	60°C aqueous SDW
IWA 007	A387 Grade 22	7 86	8760	29 05	0 2910	12 74	23-2A	60°C vapor SDW
IWA 008	A387 Grade 22	7 86	8760	28 52	0 3327	14 84	23-2A	60°C vapor SDW
IWA 009	A387 Grade 22	7 86	8760	28 95	0 6259	27 51	23-2A	60°C vapor SDW
IWA 010	A387 Grade 22	7 86	8760	28 54	2 0178	89 95	23-2B	60°C aqueous SDW
IWA 011	A387 Grade 22	7 86	8760	28 30	2 2737	102 23	23-2B	60°C aqueous SDW
IWA 012	A387 Grade 22	7 86	8760	28 95	2 7486	120 79	23-2B	60°C aqueous SDW
IWA 031	A387 Grade 22	7 86	4536	29 01	1 6293	138 02	23-1A	60°C water line SDW
IWA 032	A387 Grade 22	7.86	8760	28 97	3 6390	159 84	23-2A	60°C water line SDW
IWA 036	A387 Grade 22	7 86	4632	28 87	2 4882	207 41	22-1A	90°C water line SDW
IWA 037	A387 Grade 22	7 86	8832	28 97	3 8451	167 51	22-2A	90°C water line SDW
IWA 041	A387 Grade 22	7 86	4632	28 86	0 5304	44 22	22-1A	90°C vapor SDW
IWA 042	A387 Grade 22	7 86	4632	28 88	0 5403	45 02	22-1A	90°C vapor SDW
IWA 043	A387 Grade 22	7 86	4632	28 94	0 4968	41 31	22-1A	90°C vapor SDW
IWA 044	A387 Grade 22	7 86	4632	28 80	1 3652	114 06	22-1B	90°C aqueous SDW
IWA 045	A387 Grade 22	7 86	4632	28 69	1 2959	108 68	22-1B	90°C aqueous SDW
IWA 046	A387 Grade 22	7 86	4632	28 79	0 9445	78 94	22-1B	90°C aqueous SDW
IWA 047	A387 Grade 22	7 86	8832	28 81	0 8075	35 36	22-2A	90°C vapor SDW
IWA 048	A387 Grade 22	7 86	8832	28 96	0 8414	36 67	22-2A	90°C vapor SDW
IWA 049	A387 Grade 22	7 86	8832	29 08	0 9785	42 46	22-2A	90°C vapor SDW
IWA 050	A387 Grade 22	7 86	8832	28 92	1 7311	75 54	22-2B	90°C aqueous SDW
IWA 051	A387 Grade 22	7 86	8832	28 96	1 8040	78 59	22-2B	90°C aqueous SDW
IWA 052	A387 Grade 22	7 86	8832	28 87	1 8432	80 56	22-2B	90°C aqueous SDW
IWA 071	A387 Grade 22	7 86	4392	27 26	0 9572	89 10	21-1A	60°C vapor SCW
IWA 072	A387 Grade 22	7 86	4392	28 96	1 5336	134 36	21-1A	60°C vapor SCW
IWA 073	A387 Grade 22	7.86	4392	29 05	1 9986	174 56	21-1A	60°C vapor SCW
IWA 074	A387 Grade 22	7 86	4392	29 07	0 2220	19 38	21-1B	60°C aqueous SCW
IWA 075	A387 Grade 22	7 86	4392	28 77	0 1779	15 69	21-1B	60°C aqueous SCW
IWA 076	A387 Grade 22	7 86	4392	28 91	0 2982	26 17	21-1B	60°C aqueous SCW
IWA 077	A387 Grade 22	7 86	8760	29 06	1 5731	68 87	21-2A	60°C vapor SCW
IWA 078	A387 Grade 22	7 86	8760	28 96	3 1742	139 42	21-2A	60°C vapor SCW
IWA 079	A387 Grade 22	7 86	8760	28 77	4 0826	180 52	21-2A	60°C vapor SCW
IWA 080	A387 Grade 22	7 86	8760	28 75	0 1690	7 48	21-2B	60°C aqueous SCW
IWA 081	A387 Grade 22	7 86	8760	28 55	0 1672	7 45	21-2B	60°C aqueous SCW
IWA 082	A387 Grade 22	7 86	8760	27 30	0 1270	5 92	21-2B	60°C aqueous SCW
IWA 101	A387 Grade 22	7 86	4392	28 80	1 8391	162 02	21-1A	60°C water line SCW
IWA 102	A387 Grade 22	7 86	8760	28 71	3 3904	150 23	21-2A	60°C water line SCW
IWA 106	A387 Grade 22	7 86	4344	29 08	0 6845	60 39	20-1A	90°C water line SCW
IWA 107	A387 Grade 22	7 86	8736	28 84	2 6919	119 08	20-2A	90°C water line SCW
IWA 111	A387 Grade 22	7.86	4344	28 71	1 0126	90 49	20-1A	90°C vapor SCW

Sample identification	Alloy	Density (g/cc)	Exposure time (hours)	Surface area (sq cm)	Weight loss (g)	Corrosion rate (μm/y)	Vessel number-rack number	Test environment
IWA 112	A387 Grade 22	7 86	4344	29 01	1 3432	118 80	20-1A	90°C vapor SCW
IWA 113	A387 Grade 22	7 86	4344	29 10	2 0452	180 31	20-1A	90°C vapor SCW
IWA 114	A387 Grade 22	7 86	4344	28 95	0 1481	13 12	20-1B	90°C aqueous SCW
IWA 115	A387 Grade 22	7 86	4344	28 84	0 1323	11 77	20-1B	90°C aqueous SCW
IWA 116	A387 Grade 22	7 86	4344	28 75	0 1594	14 23	20-1B	90°C aqueous SCW
IWA 117	A387 Grade 22	7 86	8736	28 82	5 6546	250 33	20-2A	90°C vapor SCW
IWA 118	A387 Grade 22	7 86	8736	28 74	8 2820	367 59	20-2A	90°C vapor SCW
IWA 119	A387 Grade 22	7 86	8736	28 88	6 9939	308 92	20-2A	90°C vapor SCW
IWA 120	A387 Grade 22	7 86	8736	28 81	0 1424	6 31	20-2B	90°C aqueous SCW
IWA 121	A387 Grade 22	7 86	8736	27.46	0 1594	7 41	20-2B	90°C aqueous SCW
IWA 122	A387 Grade 22	7 86	8736	28 84	0 1769	7 83	20-2B	90°C aqueous SCW
IWH 001	A387 Grade 22	7 86	4536	29 12	0 2385	20 12	23-1A	60°C vapor SDW
IWH 002	A387 Grade 22	7 86	4536	27 94	0 3676	32 33	23-1A	60°C vapor SDW
IWH 003	A387 Grade 22	7 86	4536	29 37	0 6853	57 34	23-1A	60°C vapor SDW
IWH 004	A387 Grade 22	7 86	4536	29 10	0 4067	34 34	23-1B	60°C aqueous SDW
IWH 005	A387 Grade 22	7 86	4536	29 05	0 3622	30 64	23-1B	60°C aqueous SDW
IWH 006	A387 Grade 22	7 86	4536	29 18	0 4538	38 21	23-1B	60°C aqueous SDW
IWH 007	A387 Grade 22	7 86	8760	29 24	0 4200	18 27	23-2A	60°C vapor SDW
IWH 008	A387 Grade 22	7 86	8760	29 15	0 5590	24 40	23-2A	60°C vapor SDW
IWH 009	A387 Grade 22	7 86	8760	28 94	0 8521	37 46	23-2A	60°C vapor SDW
IWH 010	A387 Grade 22	7 86	8760	29 11	2 6131	114 20	23-2B	60°C aqueous SDW
IWH 011	A387 Grade 22	7 86	8760	28 78	2 4676	109 08	23-2B	60°C aqueous SDW
IWH 012	A387 Grade 22	7 86	8760	29 17	0 4248	18 53	23-2B	60°C aqueous SDW
IWH 031	A387 Grade 22	7 86	4536	28 99	1 6319	138 31	23-1A	60°C water line SDW
IWH 032	A387 Grade 22	7 86	8760	29 28	3 5821	155 67	23-2A	60°C water line SDW
IWH 036	A387 Grade 22	7 86	4632	28 04	2 5592	219 58	22-1A	90°C water line SDW
IWH 037	A387 Grade 22	7 86	8832	28 86	3 7071	162 12	22-2A	90°C water line SDW
IWH 041	A387 Grade 22	7 86	4632	29 11	0 6336	52 37	22-1A	90°C vapor SDW
IWH 042	A387 Grade 22	7 86	4632	29 23	0 6235	51 33	22-1A	90°C vapor SDW
IWH 043	A387 Grade 22	7 86	4632	29 16	0 6283	51 85	22-1A	90°C vapor SDW
IWH 044	A387 Grade 22	7 86	4632	29 21	1 3804	113 72	22-1B	90°C aqueous SDW
IWH 045	A387 Grade 22	7 86	4632	29 18	1 2912	106 46	22-1B	90°C aqueous SDW
IWH 046	A387 Grade 22	7 86	4632	29 06	1 5030	124 44	22-1B	90°C aqueous SDW
IWH 047	A387 Grade 22	7 86	8832	29 00	1 1770	51 21	22-2A	90°C vapor SDW
IWH 048	A387 Grade 22	7 86	8832	29 04	0 9553	41 51	22-2A	90°C vapor SDW
IWH 049	A387 Grade 22	7 86	8832	28 43	0 9245	41 04	22-2A	90°C vapor SDW
IWH 050	A387 Grade 22	7 86	8832	28 96	1 7169	74 80	22-2B	90°C aqueous SDW
IWH 051	A387 Grade 22	7 86	8832	29 07	2 0195	87 66	22-2B	90°C aqueous SDW
IWH 052	A387 Grade 22	7 86	8832	29 17	1 6894	73 07	22-2B	90°C aqueous SDW
IWH 071	A387 Grade 22	7 86	4392	29 21	1 2434	108 02	21-1A	60°C vapor SCW

Sample identification	Alloy	Density (g/cc)	Exposure time (hours)	Surface area (sq cm)	Weight loss (g)	Corrosion rate (μm/y)	Vessel number-rack number	Test environment
IWH 072	A387 Grade 22	7 86	4392	29 18	1 3570	118 02	21-1A	60°C vapor SCW
IWH 073	A387 Grade 22	7 86	4392	29 19	1 9149	166 45	21-1A	60°C vapor SCW
IWH 074	A387 Grade 22	7 86	4392	29 12	0 3411	29 72	21-1B	60°C aqueous SCW
IWH 075	A387 Grade 22	7 86	4392	29 26	0 3521	30 54	21-1B	60°C aqueous SCW
IWH 076	A387 Grade 22	7 86	4392	29 17	0 3025	26 31	21-1B	60°C aqueous SCW
IWH 077	A387 Grade 22	7 86	8760	29 13	2 8172	123 03	21-2A	60°C vapor SCW
IWH 078	A387 Grade 22	7 86	8760	29 33	3 6720	159 31	21-2A	60°C vapor SCW
IWH 079	A387 Grade 22	7 86	8760	29 12	3 5753	156 21	21-2A	60°C vapor SCW
IWH 080	A387 Grade 22	7 86	8760	27 94	0 1572	7 16	21-2B	60°C aqueous SCW
IWH 081	A387 Grade 22	7 86	8760	29 46	0 1446	6 25	21-2B	60°C aqueous SCW
IWH 082	A387 Grade 22	7 86	8760	29 05	0 1588	6 95	21-2B	60°C aqueous SCW
IWH 101	A387 Grade 22	7 86	4392	29 14	2 0023	174 36	21-1A	60°C water line SCW
IWH 102	A387 Grade 22	7 86	8760	28 84	2 7097	119 53	21-2A	60°C water line SCW
IWH 106	A387 Grade 22	7 86	4344	29 03	1 2430	109 85	20-1A	90°C water line SCW
IWH 107	A387 Grade 22	7 86	8736	28 91	1 7789	78 50	20-2A	90°C water line SCW
IWH 111	A387 Grade 22	7 86	4344	29 12	2 5059	220 76	20-1A	90°C vapor SCW
IWH 112	A387 Grade 22	7 86	4344	29 00	5 0985	451 11	20-1A	90°C vapor SCW
IWH 113	A387 Grade 22	7 86	4344	29 14	0 5900	51 94	20-1A	90°C vapor SCW
IWH 114	A387 Grade 22	7 86	4344	29 29	0 1525	13 36	20-1B	90°C aqueous SCW
IWH 115	A387 Grade 22	7 86	4344	29 12	0 1673	14 74	20-1B	90°C aqueous SCW
IWH 116	A387 Grade 22	7 86	4344	29 04	0 1841	16 27	20-1B	90°C aqueous SCW
IWH 117	A387 Grade 22	7 86	8736	28 96	5 3066	233 79	20-2A	90°C vapor SCW
IWH 118	A387 Grade 22	7 86	8736	29 16	9 3263	407 97	20-2A	90°C vapor SCW
IWH 119	A387 Grade 22	7 86	8736	29 31	13 9834	608 57	20-2A	90°C vapor SCW
IWH 120	A387 Grade 22	7 86	8736	29 04	0 0718	3 15	20-2B	90°C aqueous SCW
IWH 121	A387 Grade 22	7 86	8736	29 17	0 0735	3 21	20-2B	90°C aqueous SCW
IWH 122	A387 Grade 22	7 86	8736	29 04	0 0672	2 95	20-2B	90°C aqueous SCW
JWA 001	A516 Grade 55	7 86	4536	28 70	0 3233	27 68	23-1A	60°C vapor SDW
JWA 002	A516 Grade 55	7 86	4536	28 86	0 2539	21 62	23-1A	60°C vapor SDW
JWA 003	A516 Grade 55	7 86	4536	28 66	0 4892	41 94	23-1A	60°C vapor SDW
JWA 004	A516 Grade 55	7 86	4536	28 40	1 1677	101 01	23-1B	60°C aqueous SDW
JWA 005	A516 Grade 55	7 86	4536	28 32	1 2497	108 43	23-1B	60°C aqueous SDW
JWA 006	A516 Grade 55	7 86	4536	28 81	1 2349	105 33	23-1B	60°C aqueous SDW
JWA 007	A516 Grade 55	7 86	8760	28 70	0 4950	21 94	23-2A	60°C vapor SDW
JWA 008	A516 Grade 55	7 86	8760	28 49	0 5526	24 67	23-2A	60°C vapor SDW
JWA 009	A516 Grade 55	7 86	8760	28 13	0 8404	38 00	23-2A	60°C vapor SDW
JWA 010	A516 Grade 55	7 86	8760	28 79	1 8102	80 00	23-2B	60°C aqueous SDW
JWA 011	A516 Grade 55	7 86	8760	28 66	1 5038	66 75	23-2B	60°C aqueous SDW
JWA 012	A516 Grade 55	7 86	8760	28 61	1 7383	77 31	23-2B	60°C aqueous SDW
JWA 031	A516 Grade 55	7 86	4536	29 19	2 6075	219 46	23-1A	60°C water line SDW

Sample identification	Alloy	Density (g/cc)	Exposure time (hours)	Surface area (sq cm)	Weight loss (g)	Corrosion rate (μm/y)	Vessel number-rack number	Test environment
JWA 032	A516 Grade 55	7 86	8760	28 39	3 7620	168 61	23-2A	60°C water line SDW
JWA 036	A516 Grade 55	7 86	4632	27 77	2 4751	214 42	22-1A	90°C water line SDW
JWA 037	A516 Grade 55	7 86	8832	28 50	1 9016	84 19	22-2A	90°C water line SDW
JWA 041	A516 Grade 55	7 86	4632	28 84	0 8489	70 83	22-1A	90°C vapor SDW
JWA 042	A516 Grade 55	7 86	4632	28 57	0 7100	59 79	22-1A	90°C vapor SDW
JWA 043	A516 Grade 55	7 86	4632	28 36	0 7533	63 91	22-1A	90°C vapor SDW
JWA 044	A516 Grade 55	7 86	4632	29 06	1 0797	89 41	22-1B	90°C aqueous SDW
JWA 045	A516 Grade 55	7 86	4632	28 40	0 8133	68 90	22-1B	90°C aqueous SDW
JWA 046	A516 Grade 55	7 86	4632	29 48	1 0294	84 02	22-1B	90°C aqueous SDW
JWA 047	A516 Grade 55	7 86	8832	27 71	1 0232	46 59	22-2A	90°C vapor SDW
JWA 048	A516 Grade 55	7 86	8832	29 19	1 0397	44 95	22-2A	90°C vapor SDW
JWA 049	A516 Grade 55	7 86	8832	29 06	1 0305	44 75	22-2A	90°C vapor SDW
JWA 050	A516 Grade 55	7 86	8832	28.86	0 9982	43 65	22-2B	90°C aqueous SDW
JWA 051	A516 Grade 55	7 86	8832	28 72	1 0286	45 19	22-2B	90°C aqueous SDW
JWA 052	A516 Grade 55	7.86	8832	28 31	1 0836	48 30	22-2B	90°C aqueous SDW
JWA 071	A516 Grade 55	7 86	4392	28 56	2 2380	198 86	21-1A	60°C vapor SCW
JWA 072	A516 Grade 55	7 86	4392	27 26	2 8459	264 87	21-1A	60°C vapor SCW
JWA 073	A516 Grade 55	7 86	4392	27 46	3 1926	295 00	21-1A	60°C vapor SCW
JWA 074	A516 Grade 55	7 86	4392	28 59	0 6150	54 59	21-1B	60°C aqueous SCW
JWA 075	A516 Grade 55	7 86	4392	28 71	0 6219	54 97	21-1B	60°C aqueous SCW
JWA 076	A516 Grade 55	7 86	4392	28 42	0 5627	50 25	21-1B	60°C aqueous SCW
JWA 077	A516 Grade 55	7 86	8760	29 30	3 6173	157 05	21-2A	60°C vapor SCW
JWA 078	A516 Grade 55	7 86	8760	28 52	4 6929	209 38	21-2A	60°C vapor SCW
JWA 079	A516 Grade 55	7 86	8760	28 72	4 8081	213 02	21-2A	60°C vapor SCW
JWA 080	A516 Grade 55	7 86	8760	29 55	0 1842	7 93	21-2B	60°C aqueous SCW
JWA 081	A516 Grade 55	7 86	8760	28 55	0 2510	11 19	21-2B	60°C aqueous SCW
JWA 082	A516 Grade 55	7 86	8760	29 15	0 1841	8 03	21-2B	60°C aqueous SCW
JWA 101	A516 Grade 55	7 86	4392	29 65	2 3122	197 90	21-1A	60°C water line SCW
JWA 102	A516 Grade 55	7 86	8760	28 90	2 9941	131 80	21-2A	60°C water line SCW
JWA 106	A516 Grade 55	7 86	4344	28 74	0 2115	18 88	20-1A	90°C water line SCW
JWA 107	A516 Grade 55	7 86	8736	28 65	1 5234	67 85	20-2A	90°C water line SCW
JWA 111	A516 Grade 55	7 86	4344	29 28	2 7599	241 82	20-1A	90°C vapor SCW
JWA 112	A516 Grade 55	7 86	4344	28 25	3 5412	321 66	20-1A	90°C vapor SCW
JWA 113	A516 Grade 55	7 86	4344	29 19	2 9348	257 97	20-1A	90°C vapor SCW
JWA 114	A516 Grade 55	7 86	4344	29 37	0 1467	12 81	20-1B	90°C aqueous SCW
JWA 115	A516 Grade 55	7 86	4344	29 54	0 1598	13 88	20-1B	90°C aqueous SCW
JWA 116	A516 Grade 55	7 86	4344	28.64	0 1219	10 92	20-1B	90°C aqueous SCW
JWA 117	A516 Grade 55	7 86	8736	29.59	7 9562	342 99	20-2A	90°C vapor SCW
JWA 118	A516 Grade 55	7 86	8736	28 80	8 2022	363 36	20-2A	90°C vapor SCW
JWA 120	A516 Grade 55	7 86	8736	28 62	0 1562	6 96	20-2B	90°C aqueous SCW

Sample identification	Alloy	Density (g/cc)	Exposure time (hours)	Surface area (sq cm)	Weight loss (g)	Corrosion rate (μm/y)	Vessel number-rack number	Test environment
JWA 121	A516 Grade 55	7 86	8736	28 77	0 1297	5 75	20-2B	90°C aqueous SCW
JWA 122	A516 Grade 55	7 86	8736	27 78	0 0803	3 69	20-2B	90°C aqueous SCW
JWI 001	A516 Grade 55	7 86	4536	27 50	0 4384	39 16	23-1A	60°C vapor SDW
JWI 002	A516 Grade 55	7 86	4536	27 76	0 4193	37 11	23-1A	60°C vapor SDW
JWI 003	A516 Grade 55	7 86	4536	27 42	0 6981	62 56	23-1A	60°C vapor SDW
JWI 004	A516 Grade 55	7 86	4536	28 09	1 0079	88 15	23-1B	60°C aqueous SDW
JWI 005	A516 Grade 55	7 86	4536	27 49	1 1405	101 95	23-1B	60°C aqueous SDW
JWI 006	A516 Grade 55	7 86	4536	27 89	1 3384	117 92	23-1B	60°C aqueous SDW
JWI 007	A516 Grade 55	7 86	8760	27 84	0 4071	18 60	23-2A	60°C vapor SDW
JWI 008	A516 Grade 55	7 86	8760	27 64	0 4418	20 34	23-2A	60°C vapor SDW
JWI 009	A516 Grade 55	7 86	8760	27 52	0 8367	38 69	23-2A	60°C vapor SDW
JWI 010	A516 Grade 55	7 86	8760	27 84	1 5283	69 84	23-2B	60°C aqueous SDW
JWI 011	A516 Grade 55	7 86	8760	27 68	1 8222	83 74	23-2B	60°C aqueous SDW
JWI 012	A516 Grade 55	7 86	8760	27 47	1 7121	79 29	23-2B	60°C aqueous SDW
JWI 031	A516 Grade 55	7 86	4536	27 85	2 5852	228 06	23-1A	60°C water line SDW
JWI 032	A516 Grade 55	7 86	8760	28 02	4 8260	219 11	23-2A	60°C water line SDW
JWI 036	A516 Grade 55	7 86	4632	28 05	3 1770	272 52	22-1A	90°C water line SDW
JWI 037	A516 Grade 55	7 86	8832	27 80	3 0561	138 74	22-2A	90°C water line SDW
JWI 041	A516 Grade 55	7 86	4632	27 90	0 8859	76 41	22-1A	90°C vapor SDW
JWI 042	A516 Grade 55	7 86	4632	27 94	1 0990	94 64	22-1A	90°C vapor SDW
JWI 043	A516 Grade 55	7 86	4632	28 12	1 2261	104 93	22-1A	90°C vapor SDW
JWI 044	A516 Grade 55	7 86	4632	28 12	1 0243	87 65	22-1B	90°C aqueous SDW
JWI 045	A516 Grade 55	7 86	4632	27 66	1 2352	107 46	22-1B	90°C aqueous SDW
JWI 046	A516 Grade 55	7 86	4632	28 40	1 5348	130 02	22-1B	90°C aqueous SDW
JWI 047	A516 Grade 55	7 86	8832	28 09	1 1352	51 00	22-2A	90°C vapor SDW
JWI 048	A516 Grade 55	7 86	8832	28 26	1 3274	59 26	22-2A	90°C vapor SDW
JWI 049	A516 Grade 55	7 86	8832	28 02	1 3047	58 76	22-2A	90°C vapor SDW
JWI 050	A516 Grade 55	7 86	8832	28 12	1 2473	55 97	22-2B	90°C aqueous SDW
JWI 051	A516 Grade 55	7 86	8832	28 25	1 4235	63 58	22-2B	90°C aqueous SDW
JWI 052	A516 Grade 55	7 86	8832	28 29	1 1245	50 17	22-2B	90°C aqueous SDW
JWI 071	A516 Grade 55	7 86	4392	28 00	1 7925	162 43	21-1A	60°C vapor SCW
JWI 072	A516 Grade 55	7 86	4392	28 02	1 7055	154 47	21-1A	60°C vapor SCW
JWI 073	A516 Grade 55	7 86	4392	28 02	2 1305	192 96	21-1A	60°C vapor SCW
JWI 074	A516 Grade 55	7 86	4392	27 74	0 7498	68 58	21-1B	60°C aqueous SCW
JWI 075	A516 Grade 55	7 86	4392	27 90	0 9368	85 21	21-1B	60°C aqueous SCW
JWI 076	A516 Grade 55	7 86	4392	28 10	1 0138	91 55	21-1B	60°C aqueous SCW
JWI 077	A516 Grade 55	7 86	8760	28 24	4 4491	200 47	21-2A	60°C vapor SCW
JWI 078	A516 Grade 55	7 86	8760	28 04	5 8348	264 75	21-2A	60°C vapor SCW
JWI 079	A516 Grade 55	7 86	8760	28 12	5 7048	258 15	21-2A	60°C vapor SCW
JWI 080	A516 Grade 55	7 86	8760	27 94	0 2074	9 45	21-2B	60°C aqueous SCW

Sample Identification	Alloy	Density (g/cc)	Exposure time (hours)	Surface area (sq cm)	Weight loss (g)	Corrosion rate (μm/y)	Vessel number-rack number	Test environment
JWI 081	A516 Grade 55	7 86	8760	28 06	0 2438	11 05	21-2B	60°C aqueous SCW
JWI 082	A516 Grade 55	7 86	8760	27 75	0 1986	9 10	21-2B	60°C aqueous SCW
JWI 101	A516 Grade 55	7 86	4392	27 86	2 5297	230 40	21-1A	60°C water line SCW
JWI 102	A516 Grade 55	7 86	8760	27 85	2 9865	136 42	21-2A	60°C water line SCW
JWI 106	A516 Grade 55	7 86	4344	27 93	0 1359	12 48	20-1A	90°C water line SCW
JWI 107	A516 Grade 55	7 86	8736	28 07	1 0687	48 57	20-2A	90°C water line SCW
JWI 111	A516 Grade 55	7 86	4344	28 53	2 6476	238 11	20-1A	90°C vapor SCW
JWI 112	A516 Grade 55	7 86	4344	27 73	2 1105	195 23	20-1A	90°C vapor SCW
JWI 113	A516 Grade 55	7 86	4344	27 90	2 0883	192 02	20-1A	90°C vapor SCW
JWI 114	A516 Grade 55	7 86	4344	28 25	0 2101	19 08	20-1B	90°C aqueous SCW
JWI 115	A516 Grade 55	7 86	4344	27 95	0 1526	14 01	20-1B	90°C aqueous SCW
JWI 116	A516 Grade 55	7 86	4344	27 86	0 1759	16 20	20-1B	90°C aqueous SCW
JWI 117	A516 Grade 55	7 86	8736	28 04	7 8826	358 68	20-2A	90°C vapor SCW
JWI 118	A516 Grade 55	7 86	8736	28 25	9 3670	423 06	20-2A	90°C vapor SCW
JWI 119	A516 Grade 55	7 86	8736	27 51	4 1127	190 72	20-2A	90°C vapor SCW
JWI 120	A516 Grade 55	7 86	8736	27 91	0 2045	9 35	20-2B	90°C aqueous SCW
JWI 121	A516 Grade 55	7 86	8736	27 76	0 1405	6 46	20-2B	90°C aqueous SCW
JWI 122	A516 Grade 55	7 86	8736	27 98	0 1502	6 85	20-2B	90°C aqueous SCW
KWA 001	A27 Grade 70-40	7 82	4536	28 34	0 4362	38 01	23-1A	60°C vapor SDW
KWA 002	A27 Grade 70-40	7 82	4536	28 17	0 2313	20 28	23-1A	60°C vapor SDW
KWA 003	A27 Grade 70-40	7 82	4536	28 23	0 4351	38 06	23-1A	60°C vapor SDW
KWA 004	A27 Grade 70-40	7 82	4536	28 06	1 3262	116 72	23-1B	60°C aqueous SDW
KWA 005	A27 Grade 70-40	7 82	4536	28 09	0 4700	41 31	23-1B	60°C aqueous SDW
KWA 006	A27 Grade 70-40	7 82	4536	28 15	1 0919	95 78	23-1B	60°C aqueous SDW
KWA 007	A27 Grade 70-40	7 82	8760	28 17	0 7855	35 66	23-2A	60°C vapor SDW
KWA 008	A27 Grade 70-40	7 82	8760	28 16	0 5552	25 21	23-2A	60°C vapor SDW
KWA 009	A27 Grade 70-40	7 82	8760	28 15	0 7363	33 45	23-2A	60°C vapor SDW
KWA 010	A27 Grade 70-40	7 82	8760	28 00	1 9919	90 97	23-2B	60°C aqueous SDW
KWA 011	A27 Grade 70-40	7 82	8760	28 12	1 8306	83 26	23-2B	60°C aqueous SDW
KWA 012	A27 Grade 70-40	7 82	8760	28 21	1 6387	74 29	23-2B	60°C aqueous SDW
KWA 031	A27 Grade 70-40	7 82	4536	28 22	2 3064	201 84	23-1A	60°C water line SDW
KWA 032	A27 Grade 70-40	7 82	8760	28 26	5 1990	235 24	23-2A	60°C water line SDW
KWA 036	A27 Grade 70-40	7 82	4632	28 15	3 1445	270 15	22-1A	90°C water line SDW
KWA 037	A27 Grade 70-40	7 82	8832	28 14	2 3383	105 38	22-2A	90°C water line SDW
KWA 041	A27 Grade 70-40	7 82	4632	28 16	1 0636	91 35	22-1A	90°C vapor SDW
KWA 042	A27 Grade 70-40	7 82	4632	28 28	0 5573	47 65	22-1A	90°C vapor SDW
KWA 043	A27 Grade 70-40	7 82	4632	27 84	0 7197	62 53	22-1A	90°C vapor SDW
KWA 044	A27 Grade 70-40	7.82	4632	28.30	0 8423	71 97	22-1B	90°C aqueous SDW
KWA 045	A27 Grade 70-40	7 82	4632	28 19	0 9280	79 61	22-1B	90°C aqueous SDW
KWA 046	A27 Grade 70-40	7 82	4632	28.02	1 1289	97 43	22-1B	90°C aqueous SDW

Sample identification	Alloy	Density (g/cc)	Exposure time (hours)	Surface area (sq cm)	Weight loss (g)	Corrosion rate (μm/y)	Vessel number-rack number	Test environment
KWA 047	A27 Grade 70-40	7 82	8832	28 03	0 9801	44 36	22-2A	90°C vapor SDW
KWA 048	A27 Grade 70-40	7 82	8832	28 12	0 6153	27 75	22-2A	90°C vapor SDW
KWA 049	A27 Grade 70-40	7 82	8832	28 21	0 5048	22 69	22-2A	90°C vapor SDW
KWA 050	A27 Grade 70-40	7 82	8832	28 18	1 0395	46 79	22-2B	90°C aqueous SDW
KWA 051	A27 Grade 70-40	7 82	8832	28 00	1 5213	68 91	22-2B	90°C aqueous SDW
KWA 052	A27 Grade 70-40	7 82	8832	27 89	1 0273	46 72	22-2B	90°C aqueous SDW
KWA 071	A27 Grade 70-40	7 82	4392	28 13	1 9195	174 02	21-1A	60°C vapor SCW
KWA 072	A27 Grade 70-40	7 82	4392	28 06	2 4878	226 13	21-1A	60°C vapor SCW
KWA 073	A27 Grade 70-40	7 82	4392	28 18	3 9854	360 78	21-1A	60°C vapor SCW
KWA 074	A27 Grade 70-40	7 82	4392	28 40	0 8134	73 05	21-1B	60°C aqueous SCW
KWA 075	A27 Grade 70-40	7 82	4392	28 36	0 8716	78 39	21-1B	60°C aqueous SCW
KWA 076	A27 Grade 70-40	7 82	4392	27 83	0 7729	70 84	21-1B	60°C aqueous SCW
KWA 077	A27 Grade 70-40	7 82	8760	27 87	1 6645	76 38	21-2A	60°C vapor SCW
KWA 078	A27 Grade 70-40	7 82	8760	28 01	1 9880	90 77	21-2A	60°C vapor SCW
KWA 079	A27 Grade 70-40	7 82	8760	28 27	2 8218	127 64	21-2A	60°C vapor SCW
KWA 080	A27 Grade 70-40	7 82	8760	28 30	0 2362	10 67	21-2B	60°C aqueous SCW
KWA 081	A27 Grade 70-40	7 82	8760	27 88	0 2180	10 00	21-2B	60°C aqueous SCW
KWA 082	A27 Grade 70-40	7 82	8760	27 93	0 1620	7 42	21-2B	60°C aqueous SCW
KWA 101	A27 Grade 70-40	7 82	4392	28 22	2 0872	188 62	21-1A	60°C water line SCW
KWA 102	A27 Grade 70-40	7 82	8760	28 20	3 9143	177 53	21-2A	60°C water line SCW
KWA 106	A27 Grade 70-40	7 82	4344	28 37	1 4599	132 71	20-1A	90°C water line SCW
KWA 107	A27 Grade 70-40	7 82	8736	28 16	2 6998	122 94	20-2A	90°C water line SCW
KWA 111	A27 Grade 70-40	7 82	4344	28 16	1 8152	166 22	20-1A	90°C vapor SCW
KWA 112	A27 Grade 70-40	7 82	4344	28 29	2 8697	261 61	20-1A	90°C vapor SCW
KWA 113	A27 Grade 70-40	7 82	4344	28 21	2 2235	203 28	20-1A	90°C vapor SCW
KWA 114	A27 Grade 70-40	7 82	4344	28 11	0 1252	11 48	20-1B	90°C aqueous SCW
KWA 115	A27 Grade 70-40	7 82	4344	28 04	0 1487	13 67	20-1B	90°C aqueous SCW
KWA 116	A27 Grade 70-40	7 82	4344	27 88	0 0976	9 03	20-1B	90°C aqueous SCW
KWA 117	A27 Grade 70-40	7 82	8736	28 35	4 7050	212 81	20-2A	90°C vapor SCW
KWA 118	A27 Grade 70-40	7 82	8736	28 32	4 2686	193 28	20-2A	90°C vapor SCW
KWA 119	A27 Grade 70-40	7 82	8736	27 93	5 9267	272 06	20-2A	90°C vapor SCW
KWA 120	A27 Grade 70-40	7 82	8736	28 27	0 1435	6 51	20-2B	90°C aqueous SCW
KWA 121	A27 Grade 70-40	7 82	8736	28 44	0 1582	7 13	20-2B	90°C aqueous SCW
KWA 122	A27 Grade 70-40	7 82	8736	28 24	0 1171	5 32	20-2B	90°C aqueous SCW
KWI 001	A27 Grade 70-40	7 82	4536	28 54	0 7067	61 16	23-1A	60°C vapor SDW
KWI 002	A27 Grade 70-40	7 82	4536	28 45	0 5307	46 07	23-1A	60°C vapor SDW
KWI 003	A27 Grade 70-40	7 82	4536	28 09	0 8026	70 57	23-1A	60°C vapor SDW
KWI 004	A27 Grade 70-40	7 82	4536	28 26	1 1524	100 69	23-1B	60°C aqueous SDW
KWI 005	A27 Grade 70-40	7 82	4536	27 89	1 0008	88 62	23-1B	60°C aqueous SDW
KWI 006	A27 Grade 70-40	7 82	4536	28 53	1 2701	109 93	23-1B	60°C aqueous SDW

Sample identification	Alloy	Density (g/cc)	Exposure time (hours)	Surface area (sq cm)	Weight loss (g)	Corrosion rate (μm/y)	Vessel number-rack number	Test environment
KWI 007	A27 Grade 70-40	7 82	8760	27 81	0 7467	34 34	23-2A	60°C vapor SDW
KWI 008	A27 Grade 70-40	7 82	8760	28 04	0 8135	37 10	23-2A	60°C vapor SDW
KWI 009	A27 Grade 70-40	7 82	8760	28 06	0 9692	44 17	23-2A	60°C vapor SDW
KWI 010	A27 Grade 70-40	7 82	8760	28 52	1 6251	72 87	23-2B	60°C aqueous SDW
KWI 011	A27 Grade 70-40	7 82	8760	28 39	1 6309	73 47	23-2B	60°C aqueous SDW
KWI 012	A27 Grade 70-40	7 82	8760	27 95	1 8289	83 66	23-2B	60°C aqueous SDW
KWI 031	A27 Grade 70-40	7 82	4536	27 37	2 2139	199 75	23-1A	60°C water line SDW
KWI 032	A27 Grade 70-40	7 82	8760	28 04	3 9510	180 21	23-2A	60°C water line SDW
KWI 036	A27 Grade 70-40	7 82	4632	28 26	2 4648	210 93	22-1A	90°C water line SDW
KWI 037	A27 Grade 70-40	7 82	8832	27 28	2 8428	132 17	22-2A	90°C water line SDW
KWI 041	A27 Grade 70-40	7 82	4632	27 66	1 1642	101 81	22-1A	90°C vapor SDW
KWI 042	A27 Grade 70-40	7 82	4632	28 21	0 7152	61 30	22-1A	90°C vapor SDW
KWI 043	A27 Grade 70-40	7 82	4632	27 71	0 8577	74 85	22-1A	90°C vapor SDW
KWI 044	A27 Grade 70-40	7 82	4632	28 02	0 8749	75 50	22-1B	90°C aqueous SDW
KWI 045	A27 Grade 70-40	7 82	4632	28 16	0 7917	67 99	22-1B	90°C aqueous SDW
KWI 046	A27 Grade 70-40	7 82	4632	28 14	1 0459	89 88	22-1B	90°C aqueous SDW
KWI 047	A27 Grade 70-40	7 82	8832	28 16	0 8939	40 26	22-2A	90°C vapor SDW
KWI 048	A27 Grade 70-40	7 82	8832	28 08	0 6022	27 20	22-2A	90°C vapor SDW
KWI 049	A27 Grade 70-40	7 82	8832	28 39	0 6925	30 94	22-2A	90°C vapor SDW
KWI 050	A27 Grade 70-40	7 82	8832	28 16	1 0281	46 31	22-2B	90°C aqueous SDW
KWI 051	A27 Grade 70-40	7 82	8832	28 40	0 8144	36 38	22-2B	90°C aqueous SDW
KWI 052	A27 Grade 70-40	7 82	8832	27 93	1 4508	65 88	22-2B	90°C aqueous SDW
KWI 071	A27 Grade 70-40	7 82	4392	28 30	1 9898	179 32	21-1A	60°C vapor SCW
KWI 072	A27 Grade 70-40	7 82	4392	27 66	2 2157	204 34	21-1A	60°C vapor SCW
KWI 073	A27 Grade 70-40	7 82	4392	28 16	2 7674	250 65	21-1A	60°C vapor SCW
KWI 074	A27 Grade 70-40	7 82	4392	28 37	0 5969	53 66	21-1B	60°C aqueous SCW
KWI 075	A27 Grade 70-40	7 82	4392	27 71	0 6270	57 72	21-1B	60°C aqueous SCW
KWI 076	A27 Grade 70-40	7 82	4392	28 10	0 6101	55 38	21-1B	60°C aqueous SCW
KWI 077	A27 Grade 70-40	7 82	8760	28 53	1 7246	77 30	21-2A	60°C vapor SCW
KWI 078	A27 Grade 70-40	7 82	8760	28 33	1 7060	77 01	21-2A	60°C vapor SCW
KWI 079	A27 Grade 70-40	7 82	8760	28 20	2 1671	98 26	21-2A	60°C vapor SCW
KWI 080	A27 Grade 70-40	7 82	8760	28 47	0 1801	8 09	21-2B	60°C aqueous SCW
KWI 081	A27 Grade 70-40	7 82	8760	28 08	0 2266	10 32	21-2B	60°C aqueous SCW
KWI 082	A27 Grade 70-40	7 82	8760	28 61	0 2424	10 83	21-2B	60°C aqueous SCW
KWI 101	A27 Grade 70-40	7 82	4392	27 43	2 5415	236 28	21-1A	60°C water line SCW
KWI 102	A27 Grade 70-40	7 82	8760	28 07	4 4400	202 28	21-2A	60°C water line SCW
KWI 106	A27 Grade 70-40	7 82	4344	27 97	0 6114	56 36	20-1A	90°C water line SCW
KWI 107	A27 Grade 70-40	7 82	8736	28 27	1 2315	55 86	20-2A	90°C water line SCW
KWI 111	A27 Grade 70-40	7 82	4344	27.75	1 6176	150 33	20-1A	90°C vapor SCW
KWI 112	A27 Grade 70-40	7 82	4344	28 57	2 3328	210 60	20-1A	90°C vapor SCW

Sample identification	Alloy	Density (g/cc)	Exposure time (hours)	Surface area (sq cm)	Weight loss (g)	Corrosion rate (μm/y)	Vessel number-rack number	Test environment
KWI 113	A27 Grade 70-40	7 82	4344	27 30	3 3143	313 05	20-1A	90°C vapor SCW
KWI 114	A27 Grade 70-40	7 82	4344	27 19	0 1775	16 84	20-1B	90°C aqueous SCW
KWI 115	A27 Grade 70-40	7 82	4344	27 35	0 2339	22 06	20-1B	90°C aqueous SCW
KWI 116	A27 Grade 70-40	7 82	4344	27 60	0 1933	18 06	20-1B	90°C aqueous SCW
KWI 117	A27 Grade 70-40	7 82	8736	28 23	1 7647	80 15	20-2A	90°C vapor SCW
KWI 118	A27 Grade 70-40	7 82	8736	27 79	2 6178	120 81	20-2A	90°C vapor SCW
KWI 119	A27 Grade 70-40	7 82	8736	28 02	3 6868	168 75	20-2A	90°C vapor SCW
KWI 120	A27 Grade 70-40	7 82	8736	27 82	0 1330	6 13	20-2B	90°C aqueous SCW
KWI 121	A27 Grade 70-40	7 82	8736	28 32	0 1305	5 91	20-2B	90°C aqueous SCW
KWI 122	A27 Grade 70-40	7 82	8736	27 48	0 1756	8 20	20-2B	90°C aqueous SCW
LWA 001	Inconel 625	8 44	4296	28 22	–0 0004	–0 03	25-1A	60°C vapor SAW
LWA 002	Inconel 625	8 44	4296	28 26	–0 0002	–0 02	25-1A	60°C vapor SAW
LWA 003	Inconel 625	8 44	4296	28 14	–0 0005	–0 04	25-1A	60°C vapor SAW
LWA 004	Inconel 625	8 44	4296	28 29	–0 0016	–0 14	25-1B	60°C aqueous SAW
LWA 005	Inconel 625	8 44	4296	28 23	–0 0017	–0 15	25-1B	60°C aqueous SAW
LWA 006	Inconel 625	8 44	4296	28 18	–0 0018	–0 15	25-1B	60°C aqueous SAW
LWA 007	Inconel 625	8 44	8376	28.25	0 0000	0 00	25-2A	60°C vapor SAW
LWA 008	Inconel 625	8 44	8376	28 27	–0 0004	–0 02	25-2A	60°C vapor SAW
LWA 009	Inconel 625	8 44	8376	28 27	–0 0002	–0 01	25-2A	60°C vapor SAW
LWA 010	Inconel 625	8 44	8376	28 17	–0 0004	–0 02	25-2B	60°C aqueous SAW
LWA 011	Inconel 625	8 44	8376	28 21	–0 0004	–0 02	25-2B	60°C aqueous SAW
LWA 012	Inconel 625	8 44	8376	28 20	–0 0006	–0 03	25-2B	60°C aqueous SAW
LWA 031	Inconel 625	8 44	4296	28 32	–0 0005	–0 04	25-1A	60°C water line SAW
LWA 032	Inconel 625	8 44	8376	28 37	–0 0001	0 00	25-2A	60°C water line SAW
LWA 036	Inconel 625	8 44	4344	27 81	0 0004	0 03	26-1A	90°C water line SAW
LWA 037	Inconel 625	8 44	8784	28 29	0 0000	0 00	26-2A	90°C water line SAW
LWA 041	Inconel 625	8 44	4344	28 32	0 0002	0 02	26-1A	90°C vapor SAW
LWA 042	Inconel 625	8 44	4344	28 43	0 0001	0 01	26-1A	90°C vapor SAW
LWA 043	Inconel 625	8 44	4344	28 37	0 0005	0 04	26-1A	90°C vapor SAW
LWA 044	Inconel 625	8 44	4344	28 30	–0 0004	–0 03	26-1B	90°C aqueous SAW
LWA 045	Inconel 625	8 44	4344	28 24	–0 0010	–0 08	26-1B	90°C aqueous SAW
LWA 046	Inconel 625	8 44	4344	28 20	–0 0006	–0 05	26-1B	90°C aqueous SAW
LWA 047	Inconel 625	8 44	8784	28 18	0 0002	0 01	26-2A	90°C vapor SAW
LWA 048	Inconel 625	8 44	8784	28.14	0 0004	0 02	26-2A	90°C vapor SAW
LWA 049	Inconel 625	8 44	8784	28 08	0 0004	0 02	26-2A	90°C vapor SAW
LWA 050	Inconel 625	8 44	8784	28 23	–0.0003	–0 01	26-2B	90°C aqueous SAW
LWA 051	Inconel 625	8 44	8784	28 24	0 0000	0 00	26-2B	90°C aqueous SAW
LWA 052	Inconel 625	8 44	8784	28 23	0 0005	0 02	26-2B	90°C aqueous SAW
LWA 071	Inconel 625	8 44	4392	28 27	0 0011	0 09	27-1A	60°C vapor SCW
LWA 072	Inconel 625	8 44	4392	28 24	0 0008	0 07	27-1A	60°C vapor SCW

Sample identification	Alloy	Density (g/cc)	Exposure time (hours)	Surface area (sq cm)	Weight loss (g)	Corrosion rate (μm/y)	Vessel number-rack number	Test environment
LWA 073	Inconel 625	8 44	4392	28 25	0 0010	0 08	27-1A	60°C vapor SCW
LWA 074	Inconel 625	8 44	4392	28 26	0 0009	0 08	27-1B	60°C aqueous SCW
LWA 075	Inconel 625	8 44	4392	28 27	0 0006	0 05	27-1B	60°C aqueous SCW
LWA 076	Inconel 625	8 44	4392	28 45	0 0012	0 10	27-1B	60°C aqueous SCW
LWA 101	Inconel 625	8 44	4392	28 25	0 0013	0 11	27-1A	60°C water line SCW
LWA 106	Inconel 625	8 44	4464	28 33	0 0005	0 04	28-1A	90°C water line SCW
LWA 111	Inconel 625	8 44	4464	28 10	0 0004	0 03	28-1A	90°C vapor SCW
LWA 112	Inconel 625	8 44	4464	28 27	0 0004	0 03	28-1A	90°C vapor SCW
LWA 113	Inconel 625	8 44	4464	28 25	0 0004	0 03	28-1A	90°C vapor SCW
LWA 114	Inconel 625	8 44	4464	28 17	0 0006	0 05	28-1B	90°C aqueous SCW
LWA 115	Inconel 625	8 44	4464	28 21	0 0009	0 07	28-1B	90°C aqueous SCW
LWA 116	Inconel 625	8 44	4464	28 12	0 0005	0 04	28-1B	90°C aqueous SCW
LWA 141	Inconel 625	8 44	4464	28 31	0 0009	0 07	29-1A	60°C vapor SDW
LWA 142	Inconel 625	8 44	4464	28 34	0 0006	0 05	29-1B	60°C aqueous SDW
LWA 151	Inconel 625	8 44	4464	28 25	0 0002	0 02	29-1A	60°C water line SDW
LWA 164	Inconel 625	8 44	4392	28 25	0 0007	0 06	30-1A	90°C water line SDW
LWA 168	Inconel 625	8 44	4392	28 20	0 0005	0 04	30-1A	90°C vapor SDW
LWA 169	Inconel 625	8 44	4392	28 11	0 0012	0 10	30-1B	90°C aqueous SDW
LWJ 001	Inconel 625	8 44	4296	27 60	–0 0004	–0 04	25-1A	60°C vapor SAW
LWJ 002	Inconel 625	8 44	4296	27 71	–0 0012	–0 10	25-1A	60°C vapor SAW
LWJ 003	Inconel 625	8 44	4296	27 72	0 0000	0 00	25-1A	60°C vapor SAW
LWJ 004	Inconel 625	8 44	4296	27 74	–0 0001	–0 01	25-1B	60°C aqueous SAW
LWJ 005	Inconel 625	8 44	4296	27 68	0 0004	0 03	25-1B	60°C aqueous SAW
LWJ 006	Inconel 625	8 44	4296	27 71	–0 0004	–0 03	25-1B	60°C aqueous SAW
LWJ 007	Inconel 625	8 44	8376	27 79	0 0000	0 00	25-2A	60°C vapor SAW
LWJ 008	Inconel 625	8 44	8376	27 70	0 0000	0 00	25-2A	60°C vapor SAW
LWJ 009	Inconel 625	8 44	8376	27 77	–0 0001	0 00	25-2A	60°C vapor SAW
LWJ 010	Inconel 625	8 44	8376	27 62	0 0001	0 00	25-2B	60°C aqueous SAW
LWJ 011	Inconel 625	8 44	8376	27 76	0 0002	0 01	25-2B	60°C aqueous SAW
LWJ 012	Inconel 625	8 44	8376	27 74	–0 0002	–0 01	25-2B	60°C aqueous SAW
LWJ 031	Inconel 625	8 44	4296	27 62	–0 0004	–0 03	25-1B	60°C water line SAW
LWJ 032	Inconel 625	8 44	8376	27 54	–0 0002	–0 01	25-2B	60°C water line SAW
LWJ 036	Inconel 625	8 44	4344	27 58	0 0002	0 02	26-1B	90°C water line SAW
LWJ 037	Inconel 625	8 44	8784	27 63	–0 0001	0 00	26-2B	90°C water line SAW
LWJ 041	Inconel 625	8 44	4344	27 47	0 0001	0 01	26-1A	90°C vapor SAW
LWJ 042	Inconel 625	8 44	4344	27 66	0 0001	0 01	26-1A	90°C vapor SAW
LWJ 043	Inconel 625	8 44	4344	27 77	0 0012	0 10	26-1A	90°C vapor SAW
LWJ 044	Inconel 625	8 44	4344	27 68	0 0011	0 09	26-1B	90°C aqueous SAW
LWJ 045	Inconel 625	8 44	4344	27 79	–0 0005	–0 04	26-1B	90°C aqueous SAW
LWJ 046	Inconel 625	8 44	4344	27 67	0 0001	0 01	26-1B	90°C aqueous SAW

Sample identification	Alloy	Density (g/cc)	Exposure time (hours)	Surface area (sq cm)	Weight loss (g)	Corrosion rate (μm/y)	Vessel number-rack number	Test environment
LWJ 047	Inconel 625	8 44	8784	27 67	0 0005	0 02	26-2A	90°C vapor SAW
LWJ 048	Inconel 625	8 44	8784	27 71	0 0004	0 02	26-2A	90°C vapor SAW
LWJ 049	Inconel 625	8 44	8784	27 84	0 0004	0 02	26-2A	90°C vapor SAW
LWJ 050	Inconel 625	8 44	8784	27 75	–0 0003	–0 01	26-2B	90°C aqueous SAW
LWJ 051	Inconel 625	8 44	8784	27 77	–0 0003	–0 01	26-2B	90°C aqueous SAW
LWJ 052	Inconel 625	8 44	8784	27 69	0 0000	0 00	26-2B	90°C aqueous SAW
LWJ 071	Inconel 625	8 44	4392	27 89	0 0004	0 03	27-1A	60°C vapor SCW
LWJ 072	Inconel 625	8 44	4392	27 50	0 0009	0 08	27-1A	60°C vapor SCW
LWJ 073	Inconel 625	8 44	4392	27 67	0 0006	0 05	27-1A	60°C vapor SCW
LWJ 074	Inconel 625	8 44	4392	27 85	0 0012	0 10	27-1B	60°C aqueous SCW
LWJ 075	Inconel 625	8 44	4392	27 50	0 0010	0 09	27-1B	60°C aqueous SCW
LWJ 076	Inconel 625	8 44	4392	27 64	0 0007	0 06	27-1B	60°C aqueous SCW
LWJ 101	Inconel 625	8 44	4392	27 75	0 0006	0 05	27-1B	60°C water line SCW
LWJ 106	Inconel 625	8 44	4464	27 73	0 0003	0 03	28-1B	90°C water line SCW
LWJ 111	Inconel 625	8 44	4464	27 65	0 0003	0 03	28-1A	90°C vapor SCW
LWJ 112	Inconel 625	8 44	4464	27 56	–0 0002	–0 02	28-1A	90°C vapor SCW
LWJ 113	Inconel 625	8 44	4464	27 78	0 0002	0 02	28-1A	90°C vapor SCW
LWJ 114	Inconel 625	8 44	4464	27 63	0 0005	0 04	28-1B	90°C aqueous SCW
LWJ 115	Inconel 625	8 44	4464	27 59	0 0005	0 04	28-1B	90°C aqueous SCW
LWJ 116	Inconel 625	8 44	4464	27 81	0 0003	0 03	28-1B	90°C aqueous SCW
LWJ 141	Inconel 625	8 44	4464	27 76	0 0002	0 02	29-1A	60°C vapor SDW
LWJ 142	Inconel 625	8 44	4464	27 77	0 0002	0 02	29-1B	60°C aqueous SDW
LWJ 151	Inconel 625	8 44	4464	27 86	0 0000	0 00	29-1B	60°C water line SDW
LWJ 164	Inconel 625	8 44	4392	27 77	0 0002	0 02	30-1B	90°C water line SDW
LWJ 168	Inconel 625	8 44	4392	27 75	0 0008	0 07	30-1A	90°C vapor SDW
LWJ 169	Inconel 625	8 44	4392	27 75	0 0004	0 03	30-1B	90°C aqueous SDW
AWA 001	I825	8 14	4296	28 30	–0 0005	–0 04	25-1A	60°C vapor SAW
AWA 002	I825	8 14	4296	28 37	0 0000	0 00	25-1A	60°C vapor SAW
AWA 003	I825	8 14	4296	28 34	0 0003	0 03	25-1A	60°C vapor SAW
AWA 004	I825	8 14	4296	28 26	–0 0002	–0 02	25-1B	60°C aqueous SAW
AWA 005	I825	8 14	4296	28 21	–0 0003	–0 03	25-1B	60°C aqueous SAW
AWA 006	I825	8 14	4296	27 81	0 0015	0 14	25-1B	60°C aqueous SAW
AWA 007	I825	8 14	8376	28 13	–0 0001	0 00	25-2A	60°C vapor SAW
AWA 008	I825	8 14	8376	28 16	–0 0005	–0 02	25-2A	60°C vapor SAW
AWA 009	I825	8 14	8376	28 26	–0 0003	–0 01	25-2A	60°C vapor SAW
AWA 010	I825	8 14	8376	28 26	0 0000	0 00	25-2B	60°C aqueous SAW
AWA 011	I825	8 14	8376	28 31	0 0026	0 12	25-2B	60°C aqueous SAW
AWA 012	I825	8 14	8376	27 99	–0 0003	–0 01	25-2B	60°C aqueous SAW
AWA 031	I825	8 14	4296	28 15	–0 0002	–0 02	25-1A	60°C water line SAW
AWA 032	I825	8 14	8376	28 27	0 0001	0 00	25-2A	60°C water line SAW

Sample identification	Alloy	Density (g/cc)	Exposure time (hours)	Surface area (sq cm)	Weight loss (g)	Corrosion rate (μm/y)	Vessel number-rack number	Test environment
AWA 036	I825	8 14	4344	27 94	0 0005	0 04	26-1A	90°C water line SAW
AWA 037	I825	8 14	8784	28 34	0 0000	0 00	26-2A	90°C water line SAW
AWA 041	I825	8 14	4344	28 29	0 0011	0 10	26-1A	90°C vapor SAW
AWA 042	I825	8 14	4344	28 24	0 0016	0 14	26-1A	90°C vapor SAW
AWA 043	I825	8 14	4344	28 12	0 0008	0 07	26-1A	90°C vapor SAW
AWA 044	I825	8 14	4344	28 44	0 0019	0 17	26-1B	90°C aqueous SAW
AWA 045	I825	8 14	4344	28 04	0 0013	0 11	26-1B	90°C aqueous SAW
AWA 046	I825	8 14	4344	28 35	0 0018	0 16	26-1B	90°C aqueous SAW
AWA 047	I825	8 14	8784	28 18	0 0002	0 01	26-2A	90°C vapor SAW
AWA 048	I825	8 14	8784	27 93	0 0004	0 02	26-2A	90°C vapor SAW
AWA 049	I825	8 14	8784	28 22	0 0005	0 02	26-2A	90°C vapor SAW
AWA 050	I825	8 14	8784	28 28	0 0109	0 47	26-2B	90°C aqueous SAW
AWA 051	I825	8 14	8784	28 30	0 0105	0 45	26-2B	90°C aqueous SAW
AWA 052	I825	8 14	8784	28 31	0 0061	0 26	26-2B	90°C aqueous SAW
AWA 071	I825	8 14	4392	28 34	–0 0001	–0 01	27-1A	60°C vapor SCW
AWA 072	I825	8 14	4392	28 13	0 0004	0 03	27-1A	60°C vapor SCW
AWA 073	I825	8 14	4392	28 30	0 0003	0 03	27-1A	60°C vapor SCW
AWA 074	I825	8 14	4392	28 16	0 0007	0 06	27-1B	60°C aqueous SCW
AWA 075	I825	8 14	4392	28 18	0 0006	0 05	27-1B	60°C aqueous SCW
AWA 076	I825	8 14	4392	28 20	0 0006	0 05	27-1B	60°C aqueous SCW
AWA 101	I825	8 14	4392	28 14	0 0006	0 05	27-1A	60°C water line SCW
AWA 106	I825	8 14	4464	28 20	0 0007	0 06	28-1A	90°C water line SCW
AWA 111	I825	8 14	4464	28 25	0 0002	0 02	28-1A	90°C vapor SCW
AWA 112	I825	8 14	4464	28 12	0 0005	0 04	28-1A	90°C vapor SCW
AWA 113	I825	8 14	4464	27 89	0 0003	0 03	28-1A	90°C vapor SCW
AWA 114	I825	8 14	4464	28 11	0 0002	0 02	28-1B	90°C aqueous SCW
AWA 115	I825	8 14	4464	28 43	0 0000	0 00	28-1B	90°C aqueous SCW
AWA 116	I825	8 14	4464	28 13	0 0004	0 03	28-1B	90°C aqueous SCW
AWA 141	I825	8 14	4464	28 37	–0 0002	–0 02	29-1A	60°C vapor SDW
AWA 142	I825	8 14	4464	28 02	–0 0001	–0 01	29-1B	60°C aqueous SDW
AWA 151	I825	8 14	4464	28 41	–0 0003	–0 03	29-1A	60°C water line SDW
AWA 164	I825	8 14	4392	28 06	0 0002	0 02	30-1A	90°C water line SDW
AWA 168	I825	8 14	4392	28 28	0 0003	0 03	30-1A	90°C vapor SDW
AWA 169	I825	8 14	4392	28 22	0 0006	0 05	30-1B	90°C aqueous SDW
AWB 001	I825	8 14	4296	27 74	–0 0004	–0 04	25-1A	60°C vapor SAW
AWB 002	I825	8 14	4296	26 75	0 0010	0 09	25-1A	60°C vapor SAW
AWB 003	I825	8 14	4296	27 53	0 0004	0 04	25-1A	60°C vapor SAW
AWB 004	I825	8 14	4296	27 56	–0 0003	–0 03	25-1B	60°C aqueous SAW
AWB 005	I825	8 14	4296	27 53	0 0001	0 01	25-1B	60°C aqueous SAW
AWB 006	I825	8 14	4296	27 54	–0 0011	–0 10	25-1B	60°C aqueous SAW

Sample identification	Alloy	Density (g/cc)	Exposure time (hours)	Surface area (sq cm)	Weight loss (g)	Corrosion rate (μm/y)	Vessel number-rack number	Test environment
AWB 007	I825	8 14	8376	27 66	–0 0004	–0 02	25-2A	60°C vapor SAW
AWB 008	I825	8 14	8376	27 71	0 0000	0 00	25-2A	60°C vapor SAW
AWB 009	I825	8 14	8376	27 68	–0 0004	–0 02	25-2A	60°C vapor SAW
AWB 010	I825	8 14	8376	27 84	–0 0002	–0 01	25-2B	60°C aqueous SAW
AWB 011	I825	8 14	8376	27 91	0 0001	0 00	25-2B	60°C aqueous SAW
AWB 012	I825	8 14	8376	27 69	–0 0003	–0 01	25-2B	60°C aqueous SAW
AWB 031	I825	8 14	4296	27 56	–0 0006	–0 05	25-1B	60°C water line SAW
AWB 032	I825	8 14	8376	27 43	–0 0001	0 00	25-2B	60°C water line SAW
AWB 036	I825	8 14	4344	27 45	0 0006	0 05	26-1B	90°C water line SAW
AWB 037	I825	8 14	8784	27 65	0 0003	0 01	26-2B	90°C water line SAW
AWB 041	I825	8 14	4344	27 83	0 0009	0 08	26-1A	90°C vapor SAW
AWB 042	I825	8 14	4344	27 68	0 0006	0 05	26-1A	90°C vapor SAW
AWB 043	I825	8 14	4344	27 49	0 0007	0 06	26-1A	90°C vapor SAW
AWB 044	I825	8 14	4344	27 48	0 0055	0 50	26-1B	90°C aqueous SAW
AWB 045	I825	8 14	4344	27 72	0 0016	0 14	26-1B	90°C aqueous SAW
AWB 046	I825	8 14	4344	27 64	0 0040	0 36	26-1B	90°C aqueous SAW
AWB 047	I825	8 14	8784	27 07	0 0005	0 02	26-2A	90°C vapor SAW
AWB 048	I825	8 14	8784	27 88	0 0006	0 03	26-2A	90°C vapor SAW
AWB 049	I825	8 14	8784	27 70	0 0005	0 02	26-2A	90°C vapor SAW
AWB 050	I825	8 14	8784	27 88	0 0006	0 03	26-2B	90°C aqueous SAW
AWB 051	I825	8 14	8784	27 70	0 0003	0 01	26-2B	90°C aqueous SAW
AWB 052	I825	8 14	8784	27 60	0 0154	0 68	26-2B	90°C aqueous SAW
AWB 071	I825	8 14	4392	27 63	0 0002	0 02	27-1A	60°C vapor SCW
AWB 072	I825	8 14	4392	27 83	0 0010	0 09	27-1A	60°C vapor SCW
AWB 073	I825	8 14	4392	27 75	0 0005	0 04	27-1A	60°C vapor SCW
AWB 074	I825	8 14	4392	27 90	0 0003	0 03	27-1B	60°C aqueous SCW
AWB 075	I825	8 14	4392	27 37	0 0007	0 06	27-1B	60°C aqueous SCW
AWB 076	I825	8 14	4392	27 25	0 0001	0 01	27-1B	60°C aqueous SCW
AWB 101	I825	8 14	4392	27 55	0 0007	0 06	27-1B	60°C water line SCW
AWB 106	I825	8 14	4464	27 44	0 0001	0 01	28-1B	90°C water line SCW
AWB 111	I825	8 14	4464	27 29	0 0003	0 03	28-1A	90°C vapor SCW
AWB 112	I825	8 14	4464	27 35	0 0003	0 03	28-1A	90°C vapor SCW
AWB 113	I825	8 14	4464	27 59	0 0004	0 03	28-1A	90°C vapor SCW
AWB 114	I825	8 14	4464	27 48	0 0005	0 04	28-1B	90°C aqueous SCW
AWB 115	I825	8 14	4464	27 49	0 0007	0 06	28-1B	90°C aqueous SCW
AWB 116	I825	8 14	4464	27 60	0 0002	0 02	28-1B	90°C aqueous SCW
AWB 141	I825	8 14	4464	27 03	0 0003	0 03	29-1A	60°C vapor SDW
AWB 142	I825	8 14	4464	27 38	0 0005	0 04	29-1B	60°C aqueous SDW
AWB 151	I825	8 14	4464	27 70	0 0004	0 03	29-1B	60°C water line SDW
AWB 164	I825	8 14	4392	27 75	0 0002	0 02	30-1B	90°C water line SDW

Sample Identification	Alloy	Density (g/cc)	Exposure time (hours)	Surface area (sq cm)	Weight loss (g)	Corrosion rate (μm/y)	Vessel number-rack number	Test environment
AWB 168	I825	8 14	4392	27 87	0 0004	0 04	30-1A	90°C vapor SDW
AWB 169	I825	8 14	4392	27 90	0 0002	0 02	30-1B	90°C aqueous SDW
BWA 001	G3	8 27	4296	28 31	–0 0003	–0 03	25-1A	60°C vapor SAW
BWA 002	G3	8 27	4296	28 32	–0 0006	–0 05	25-1A	60°C vapor SAW
BWA 003	G3	8 27	4296	28 55	–0 0002	–0 02	25-1A	60°C vapor SAW
BWA 004	G3	8 27	4296	28 74	–0 0007	–0 06	25-1B	60°C aqueous SAW
BWA 005	G3	8 27	4296	28 26	–0 0001	–0 01	25-1B	60°C aqueous SAW
BWA 006	G3	8 27	4296	28 45	–0 0023	–0 20	25-1B	60°C aqueous SAW
BWA 007	G3	8 27	8376	28 51	–0 0002	–0 01	25-2A	60°C vapor SAW
BWA 008	G3	8 27	8376	28 64	–0 0006	–0 03	25-2A	60°C vapor SAW
BWA 009	G3	8 27	8376	28 55	–0 0005	–0 02	25-2A	60°C vapor SAW
BWA 010	G3	8 27	8376	28 46	0 0005	0 02	25-2B	60°C aqueous SAW
BWA 011	G3	8 27	8376	28 49	–0 0001	0 00	25-2B	60°C aqueous SAW
BWA 012	G3	8 27	8376	28 38	0 0000	0 00	25-2B	60°C aqueous SAW
BWA 031	G3	8 27	4296	28 55	–0 0004	–0 03	25-1A	60°C water line SAW
BWA 032	G3	8 27	8376	28 39	–0 0008	–0 04	25-2A	60°C water line SAW
BWA 036	G3	8 27	4344	28 61	0 0002	0 02	26-1A	90°C water line SAW
BWA 037	G3	8 27	8784	28 71	0 0002	0 01	26-2A	90°C water line SAW
BWA 041	G3	8 27	4344	28 76	0 0000	0 00	26-1A	90°C vapor SAW
BWA 042	G3	8 27	4344	28 31	0 0003	0 03	26-1A	90°C vapor SAW
BWA 043	G3	8 27	4344	28 35	0 0000	0 00	26-1A	90°C vapor SAW
BWA 044	G3	8 27	4344	28 61	–0 0004	–0 03	26-1B	90°C aqueous SAW
BWA 045	G3	8 27	4344	28 41	0 0000	0 00	26-1B	90°C aqueous SAW
BWA 046	G3	8 27	4344	28 48	–0 0003	–0 03	26-1B	90°C aqueous SAW
BWA 047	G3	8 27	8784	28 34	0 0006	0 03	26-2A	90°C vapor SAW
BWA 048	G3	8 27	8784	28 63	0 0003	0 01	26-2A	90°C vapor SAW
BWA 049	G3	8 27	8784	28 69	0 0006	0 03	26-2A	90°C vapor SAW
BWA 050	G3	8 27	8784	28 64	–0 0005	–0 02	26-2B	90°C aqueous SAW
BWA 051	G3	8 27	8784	28 62	–0 0006	–0 03	26-2B	90°C aqueous SAW
BWA 052	G3	8 27	8784	28 41	0 0004	0 02	26-2B	90°C aqueous SAW
BWA 071	G3	8 27	4392	28 56	0 0001	0 01	27-1A	60°C vapor SCW
BWA 072	G3	8 27	4392	28 55	0 0006	0 05	27-1A	60°C vapor SCW
BWA 073	G3	8 27	4392	28 44	0 0002	0 02	27-1A	60°C vapor SCW
BWA 074	G3	8 27	4392	28 70	0 0003	0 03	27-1B	60°C aqueous SCW
BWA 075	G3	8 27	4392	28 72	0 0008	0 07	27-1B	60°C aqueous SCW
BWA 076	G3	8 27	4392	28 78	0 0002	0 02	27-1B	60°C aqueous SCW
BWA 101	G3	8 27	4392	28 42	0 0005	0 04	27-1A	60°C water line SCW
BWA 106	G3	8 27	4464	28 53	–0 0008	–0 07	28-1A	90°C water line SCW
BWA 111	G3	8 27	4464	28 20	–0 0003	–0 03	28-1A	90°C vapor SCW
BWA 112	G3	8 27	4464	28 74	–0 0003	–0 02	28-1A	90°C vapor SCW

Sample identification	Alloy	Density (g/cc)	Exposure time (hours)	Surface area (sq cm)	Weight loss (g)	Corrosion rate (μm/y)	Vessel number-rack number	Test environment
BWA 113	G3	8 27	4464	28 54	0 0000	0 00	28-1A	90°C vapor SCW
BWA 114	G3	8 27	4464	28 60	–0 0001	–0 01	28-1B	90°C aqueous SCW
BWA 115	G3	8 27	4464	28 58	–0 0003	–0 02	28-1B	90°C aqueous SCW
BWA 116	G3	8 27	4464	28 62	0 0003	0 02	28-1B	90°C aqueous SCW
BWA 141	G3	8 27	4464	28 57	0 0006	0 05	29-1A	60°C vapor SDW
BWA 142	G3	8 27	4464	28 68	0 0005	0 04	29-1B	60°C aqueous SDW
BWA 151	G3	8 27	4464	28 38	–0 0002	–0 02	29-1A	60°C water line SDW
BWA 164	G3	8 27	4392	27 82	0 0010	0 09	30-1A	90°C water line SDW
BWA 168	G3	8 27	4392	27 79	0 0016	0 14	30-1A	90°C vapor SDW
BWA 169	G3	8 27	4392	27 87	0 0014	0 12	30-1B	90°C aqueous SDW
BWC 001	G3	8 27	4296	28 35	–0 0004	–0 03	25-1A	60°C vapor SAW
BWC 002	G3	8 27	4296	27 94	0 0000	0 00	25-1A	60°C vapor SAW
BWC 003	G3	8 27	4296	28 26	–0 0005	–0 04	25-1A	60°C vapor SAW
BWC 004	G3	8 27	4296	28 15	–0 0005	–0 04	25-1B	60°C aqueous SAW
BWC 005	G3	8 27	4296	27 94	–0 0002	–0 02	25-1B	60°C aqueous SAW
BWC 006	G3	8 27	4296	28 29	–0 0002	–0 02	25-1B	60°C aqueous SAW
BWC 007	G3	8 27	8376	27 95	–0 0010	–0 05	25-2A	60°C vapor SAW
BWC 008	G3	8 27	8376	28 16	–0 0004	–0 02	25-2A	60°C vapor SAW
BWC 009	G3	8 27	8376	28 22	0 0000	0 00	25-2A	60°C vapor SAW
BWC 010	G3	8 27	8376	28 07	0 0000	0 00	25-2B	60°C aqueous SAW
BWC 011	G3	8 27	8376	28 32	–0 0003	–0 01	25-2B	60°C aqueous SAW
BWC 012	G3	8 27	8376	27 84	–0 0008	–0 04	25-2B	60°C aqueous SAW
BWC 031	G3	8 27	4296	28 30	–0 0002	–0 02	25-1B	60°C water line SAW
BWC 032	G3	8 27	8376	28 29	0 0002	0 01	25-2B	60°C water line SAW
BWC 036	G3	8 27	4344	28 34	0 0009	0 08	26-1B	90°C water line SAW
BWC 037	G3	8 27	8784	28 23	0 0001	0 00	26-2B	90°C water line SAW
BWC 041	G3	8 27	4344	28 25	0 0008	0 07	26-1A	90°C vapor SAW
BWC 042	G3	8 27	4344	28 30	0 0003	0 03	26-1A	90°C vapor SAW
BWC 043	G3	8 27	4344	27 85	0 0003	0 03	26-1A	90°C vapor SAW
BWC 044	G3	8 27	4344	28 32	–0 0005	–0 04	26-1B	90°C aqueous SAW
BWC 045	G3	8 27	4344	28 31	0 0011	0 09	26-1B	90°C aqueous SAW
BWC 046	G3	8 27	4344	28 33	–0 0001	–0 01	26-1B	90°C aqueous SAW
BWC 047	G3	8 27	8784	28 26	0 0002	0 01	26-2A	90°C vapor SAW
BWC 048	G3	8 27	8784	28 37	0 0013	0 06	26-2A	90°C vapor SAW
BWC 049	G3	8 27	8784	28 30	0 0013	0 06	26-2A	90°C vapor SAW
BWC 050	G3	8 27	8784	28 42	–0 0003	–0 01	26-2B	90°C aqueous SAW
BWC 051	G3	8 27	8784	28 27	–0 0005	–0 02	26-2B	90°C aqueous SAW
BWC 052	G3	8 27	8784	28 37	–0 0005	–0 02	26-2B	90°C aqueous SAW
BWC 071	G3	8 27	4392	28 31	0 0005	0 04	27-1A	60°C vapor SCW
BWC 072	G3	8 27	4392	27 89	0 0001	0 01	27-1A	60°C vapor SCW

Sample identification	Alloy	Density (g/cc)	Exposure time (hours)	Surface area (sq cm)	Weight loss (g)	Corrosion rate (μm/y)	Vessel number-rack number	Test environment
BWC 073	G3	8 27	4392	28 26	0 0021	0 18	27-1A	60°C vapor SCW
BWC 074	G3	8 27	4392	28 41	0 0006	0 05	27-1B	60°C aqueous SCW
BWC 075	G3	8 27	4392	28 51	0 0000	0 00	27-1B	60°C aqueous SCW
BWC 076	G3	8 27	4392	28 28	0 0002	0 02	27-1B	60°C aqueous SCW
BWC 101	G3	8 27	4392	27 69	0 0005	0 04	27-1B	60°C water line SCW
BWC 106	G3	8 27	4464	28 29	0 0001	0 01	28-1B	90°C water line SCW
BWC 111	G3	8 27	4464	28 28	0 0003	0 03	28-1A	90°C vapor SCW
BWC 112	G3	8 27	4464	28 18	0 0002	0 02	28-1A	90°C vapor SCW
BWC 113	G3	8 27	4464	28 38	0 0004	0 03	28-1A	90°C vapor SCW
BWC 114	G3	8 27	4464	28 22	0 0004	0 03	28-1B	90°C aqueous SCW
BWC 115	G3	8 27	4464	28 02	0 0004	0 03	28-1B	90°C aqueous SCW
BWC 116	G3	8 27	4464	28 37	0 0003	0 03	28-1B	90°C aqueous SCW
BWC 141	G3	8 27	4464	28 24	0 0001	0 01	29-1A	60°C vapor SDW
BWC 142	G3	8 27	4464	28 35	0 0002	0 02	29-1B	60°C aqueous SDW
BWC 151	G3	8 27	4464	28 28	–0 0001	–0 01	29-1B	60°C water line SDW
BWC 164	G3	8 27	4392	27 92	0 0001	0 01	30-1B	90°C water line SDW
BWC 168	G3	8 27	4392	27 84	0 0000	0 00	30-1A	90°C vapor SDW
BWC 169	G3	8 27	4392	27 90	0 0011	0 10	30-1B	90°C aqueous SDW
CWA 001	C4	8 60	4296	28 01	0 0002	0 02	25-1A	60°C vapor SAW
CWA 002	C4	8 60	4296	27 87	0 0000	0 00	25-1A	60°C vapor SAW
CWA 003	C4	8 60	4296	27 96	0 0001	0 01	25-1A	60°C vapor SAW
CWA 004	C4	8 60	4296	27 81	0 0005	0 04	25-1B	60°C aqueous SAW
CWA 005	C4	8 60	4296	27 82	0 0004	0 03	25-1B	60°C aqueous SAW
CWA 006	C4	8 60	4296	28 08	0 0005	0 04	25-1B	60°C aqueous SAW
CWA 007	C4	8 60	8376	28 32	–0 0004	–0 02	25-2A	60°C vapor SAW
CWA 008	C4	8 60	8376	27 81	–0 0003	–0 01	25-2A	60°C vapor SAW
CWA 009	C4	8 60	8376	28 09	–0 0005	–0 02	25-2A	60°C vapor SAW
CWA 010	C4	8 60	8376	28 03	0 0000	0 00	25-2B	60°C aqueous SAW
CWA 011	C4	8 60	8376	28 01	0 0002	0 01	25-2B	60°C aqueous SAW
CWA 012	C4	8 60	8376	28 09	0 0007	0 03	25-2B	60°C aqueous SAW
CWA 031	C4	8 60	4296	28 34	0 0002	0 02	25-1A	60°C water line SAW
CWA 032	C4	8 60	8376	27 97	0 0003	0 01	25-2A	60°C water line SAW
CWA 036	C4	8 60	4344	27 81	0 0004	0 03	26-1A	90°C water line SAW
CWA 037	C4	8 60	8784	28 00	0 0010	0 04	26-2A	90°C water line SAW
CWA 041	C4	8 60	4344	28 00	–0 0001	–0 01	26-1A	90°C vapor SAW
CWA 042	C4	8 60	4344	27 86	0 0008	0 07	26-1A	90°C vapor SAW
CWA 043	C4	8 60	4344	27 94	0 0004	0 03	26-1A	90°C vapor SAW
CWA 044	C4	8 60	4344	27 98	0 0006	0 05	26-1B	90°C aqueous SAW
CWA 045	C4	8 60	4344	28 20	0 0008	0 07	26-1B	90°C aqueous SAW
CWA 046	C4	8 60	4344	28 07	0 0007	0 06	26-1B	90°C aqueous SAW

Sample identification	Alloy	Density (g/cc)	Exposure time (hours)	Surface area (sq cm)	Weight loss (g)	Corrosion rate (μm/y)	Vessel number-rack number	Test environment
CWA 047	C4	8 60	8784	28 00	0 0006	0 02	26-2A	90°C vapor SAW
CWA 048	C4	8 60	8784	27 72	0 0008	0 03	26-2A	90°C vapor SAW
CWA 049	C4	8 60	8784	28 03	0 0008	0 03	26-2A	90°C vapor SAW
CWA 050	C4	8 60	8784	28 21	0 0011	0 05	26-2B	90°C aqueous SAW
CWA 051	C4	8 60	8784	28 06	0 0012	0 05	26-2B	90°C aqueous SAW
CWA 052	C4	8 60	8784	27 87	0 0010	0 04	26-2B	90°C aqueous SAW
CWA 071	C4	8 60	4392	27 83	0 0005	0 04	27-1A	60°C vapor SCW
CWA 072	C4	8 60	4392	28 40	0 0002	0 02	27-1A	60°C vapor SCW
CWA 073	C4	8 60	4392	27 62	0 0007	0 06	27-1A	60°C vapor SCW
CWA 074	C4	8 60	4392	28 07	0 0008	0 07	27-1B	60°C aqueous SCW
CWA 075	C4	8 60	4392	27 72	0 0011	0 09	27-1B	60°C aqueous SCW
CWA 076	C4	8 60	4392	28 23	0 0008	0 07	27-1B	60°C aqueous SCW
CWA 101	C4	8 60	4392	28 32	0 0005	0 04	27-1A	60°C water line SCW
CWA 106	C4	8 60	4464	27 90	0 0001	0 01	28-1A	90°C water line SCW
CWA 111	C4	8 60	4464	28 31	0 0001	0 01	28-1A	90°C vapor SCW
CWA 112	C4	8 60	4464	28 20	0 0003	0 02	28-1A	90°C vapor SCW
CWA 113	C4	8 60	4464	28 05	–0 0001	–0 01	28-1A	90°C vapor SCW
CWA 114	C4	8 60	4464	27 96	0 0008	0 07	28-1B	90°C aqueous SCW
CWA 115	C4	8 60	4464	27 90	0 0003	0 02	28-1B	90°C aqueous SCW
CWA 116	C4	8 60	4464	28 17	0 0011	0 09	28-1B	90°C aqueous SCW
CWA 141	C4	8 60	4464	28 36	0 0006	0 05	29-1A	60°C vapor SDW
CWA 142	C4	8 60	4464	28 10	0 0002	0 02	29-1B	60°C aqueous SDW
CWA 151	C4	8 60	4464	27 92	0 0000	0 00	29-1A	60°C water line SDW
CWA 164	C4	8 60	4392	28 15	0 0011	0 09	30-1A	90°C water line SDW
CWA 168	C4	8 60	4392	28 15	0 0016	0 13	30-1A	90°C vapor SDW
CWA 169	C4	8 60	4392	28 11	0 0012	0 10	30-1B	90°C aqueous SDW
CWB 001	C4	8 60	4296	27 78	0 0001	0 01	25-1A	60°C vapor SAW
CWB 002	C4	8 60	4296	27 12	0 0001	0 01	25-1A	60°C vapor SAW
CWB 003	C4	8.60	4296	27 44	0 0007	0 06	25-1A	60°C vapor SAW
CWB 004	C4	8 60	4296	28 02	–0 0001	–0 01	25-1B	60°C aqueous SAW
CWB 005	C4	8 60	4296	27 77	0 0006	0 05	25-1B	60°C aqueous SAW
CWB 006	C4	8 60	4296	27 73	–0 0003	–0 03	25-1B	60°C aqueous SAW
CWB 007	C4	8 60	8376	27 93	0 0001	0 00	25-2A	60°C vapor SAW
CWB 008	C4	8 60	8376	27 62	0 0001	0 00	25-2A	60°C vapor SAW
CWB 009	C4	8 60	8376	27 49	–0 0003	–0 01	25-2A	60°C vapor SAW
CWB 010	C4	8 60	8376	27 63	–0 0001	0 00	25-2B	60°C aqueous SAW
CWB 011	C4	8 60	8376	27 69	0 0001	0 00	25-2B	60°C aqueous SAW
CWB 012	C4	8 60	8376	27 87	–0 0001	0 00	25-2B	60°C aqueous SAW
CWB 031	C4	8 60	4296	27 70	–0 0003	–0 03	25-1B	60°C water line SAW
CWB 032	C4	8 60	8376	27 48	–0 0003	–0 01	25-2B	60°C water line SAW

Sample identification	Alloy	Density (g/cc)	Exposure time (hours)	Surface area (sq cm)	Weight loss (g)	Corrosion rate (μm/y)	Vessel number-rack number	Test environment
CWB 036	C4	8 60	4344	26 92	0 0010	0 09	26-1B	90°C water line SAW
CWB 037	C4	8 60	8784	27 77	0 0010	0 04	26-2B	90°C water line SAW
CWB 041	C4	8 60	4344	27 64	0 0006	0 05	26-1A	90°C vapor SAW
CWB 042	C4	8 60	4344	27 85	0 0006	0 05	26-1A	90°C vapor SAW
CWB 043	C4	8 60	4344	27 15	0 0008	0 07	26-1A	90°C vapor SAW
CWB 044	C4	8 60	4344	27 77	0 0004	0 03	26-1B	90°C aqueous SAW
CWB 045	C4	8 60	4344	27 76	0 0002	0 02	26-1B	90°C aqueous SAW
CWB 046	C4	8 60	4344	27 90	0 0002	0 02	26-1B	90°C aqueous SAW
CWB 047	C4	8 60	8784	28 00	0 0010	0 04	26-2A	90°C vapor SAW
CWB 048	C4	8 60	8784	28 07	0 0012	0 05	26-2A	90°C vapor SAW
CWB 049	C4	8 60	8784	28 24	0 0011	0 05	26-2A	90°C vapor SAW
CWB 050	C4	8 60	8784	27 89	0 0010	0 04	26-2B	90°C aqueous SAW
CWB 051	C4	8 60	8784	28 12	0 0010	0 04	26-2B	90°C aqueous SAW
CWB 052	C4	8 60	8784	27 94	0 0010	0 04	26-2B	90°C aqueous SAW
CWB 071	C4	8 60	4392	28 07	0 0005	0 04	27-1A	60°C vapor SCW
CWB 072	C4	8 60	4392	27 83	0 0010	0 08	27-1A	60°C vapor SCW
CWB 073	C4	8 60	4392	27 85	0 0007	0 06	27-1A	60°C vapor SCW
CWB 074	C4	8 60	4392	27 83	0 0007	0 06	27-1B	60°C aqueous SCW
CWB 075	C4	8 60	4392	27 67	0 0010	0 08	27-1B	60°C aqueous SCW
CWB 076	C4	8 60	4392	27 35	0 0014	0 12	27-1B	60°C aqueous SCW
CWB 101	C4	8 60	4392	27 44	0 0012	0 10	27-1B	60°C water line SCW
CWB 106	C4	8 60	4464	27 56	0 0008	0 07	28-1B	90°C water line SCW
CWB 111	C4	8 60	4464	27 65	0 0001	0 01	28-1A	90°C vapor SCW
CWB 112	C4	8 60	4464	27 73	0 0000	0 00	28-1A	90°C vapor SCW
CWB 113	C4	8 60	4464	27 68	–0 0001	–0 01	28-1A	90°C vapor SCW
CWB 114	C4	8 60	4464	28 03	0 0005	0 04	28-1B	90°C aqueous SCW
CWB 115	C4	8 60	4464	27 86	0 0004	0 03	28-1B	90°C aqueous SCW
CWB 116	C4	8 60	4464	27 77	0 0004	0 03	28-1B	90°C aqueous SCW
CWB 141	C4	8 60	4464	27 87	0 0004	0 03	29-1A	60°C vapor SDW
CWB 142	C4	8 60	4464	27 99	0 0003	0 02	29-1B	60°C aqueous SDW
CWB 151	C4	8 60	4464	28 19	0 0000	0 00	29-1B	60°C water line SDW
CWB 164	C4	8 60	4392	28 03	0 0008	0 07	30-1B	90°C water line SDW
CWB 168	C4	8 60	4392	27 79	0 0004	0 03	30-1A	90°C vapor SDW
CWB 169	C4	8 60	4392	27 61	0 0011	0 09	30-1B	90°C aqueous SDW
DWA 001	C22	8 60	4296	28 17	0 0003	0 03	25-1A	60°C vapor SAW
DWA 002	C22	8 60	4296	28 15	–0 0006	–0 05	25-1A	60°C vapor SAW
DWA 003	C22	8 60	4296	28 04	0 0006	0 05	25-1A	60°C vapor SAW
DWA 004	C22	8 60	4296	28 02	–0 0007	–0 06	25-1B	60°C aqueous SAW
DWA 005	C22	8 60	4296	28 03	–0 0004	–0 03	25-1B	60°C aqueous SAW
DWA 006	C22	8 60	4296	28 22	–0 0003	–0 03	25-1B	60°C aqueous SAW

Sample identification	Alloy	Density (g/cc)	Exposure time (hours)	Surface area (sq cm)	Weight loss (g)	Corrosion rate (μm/y)	Vessel number-rack number	Test environment
DWA 007	C22	8 60	8376	28 30	0 0004	0 02	25-2A	60°C vapor SAW
DWA 008	C22	8 60	8376	28 12	0 0003	0 01	25-2A	60°C vapor SAW
DWA 009	C22	8 60	8376	28 16	0 0006	0 03	25-2A	60°C vapor SAW
DWA 010	C22	8 60	8376	27 99	0 0001	0 00	25-2B	60°C aqueous SAW
DWA 011	C22	8 60	8376	28 25	0 0004	0 02	25-2B	60°C aqueous SAW
DWA 012	C22	8 60	8376	28 04	0 0005	0 02	25-2B	60°C aqueous SAW
DWA 031	C22	8 60	4296	27 78	–0 0004	–0 03	25-1A	60°C water line SAW
DWA 032	C22	8 60	8376	28 10	0 0003	0 01	25-2A	60°C water line SAW
DWA 036	C22	8 60	4344	27 89	0 0002	0 02	26-1A	90°C water line SAW
DWA 041	C22	8 60	4344	28 14	0 0000	0 00	26-1A	90°C vapor SAW
DWA 042	C22	8 60	4344	28 11	0 0006	0 05	26-1A	90°C vapor SAW
DWA 043	C22	8 60	4344	28 08	0 0010	0 08	26-1A	90°C vapor SAW
DWA 044	C22	8 60	4344	28 11	–0 0004	–0 03	26-1B	90°C aqueous SAW
DWA 045	C22	8 60	4344	28 07	–0 0005	–0 04	26-1B	90°C aqueous SAW
DWA 046	C22	8 60	4344	28 08	0 0001	0 01	26-1B	90°C aqueous SAW
DWA 047	C22	8 60	8784	28 28	0 0005	0 02	26-2A	90°C vapor SAW
DWA 049	C22	8 60	8784	27 84	0 0005	0 02	26-2A	90°C vapor SAW
DWA 050	C22	8 60	8784	28 04	0 0004	0 02	26-2B	90°C aqueous SAW
DWA 052	C22	8 60	8784	28 22	0 0002	0 01	26-2B	90°C aqueous SAW
DWA 071	C22	8 60	4392	28 20	0 0003	0 02	27-1A	60°C vapor SCW
DWA 072	C22	8 60	4392	28 18	0 0004	0 03	27-1A	60°C vapor SCW
DWA 073	C22	8 60	4392	28 05	0 0010	0 08	27-1A	60°C vapor SCW
DWA 074	C22	8 60	4392	28 12	0 0011	0 09	27-1B	60°C aqueous SCW
DWA 075	C22	8 60	4392	28 14	0 0009	0 07	27-1B	60°C aqueous SCW
DWA 076	C22	8 60	4392	28 29	0 0005	0 04	27-1B	60°C aqueous SCW
DWA 101	C22	8 60	4392	28 37	0 0006	0 05	27-1A	60°C water line SCW
DWA 106	C22	8 60	4464	28 12	0 0004	0 03	28-1A	90°C water line SCW
DWA 111	C22	8 60	4464	28 13	0 0003	0 02	28-1A	90°C vapor SCW
DWA 112	C22	8 60	4464	28 36	0 0002	0 02	28-1A	90°C vapor SCW
DWA 113	C22	8 60	4464	28 23	0 0002	0 02	28-1A	90°C vapor SCW
DWA 114	C22	8 60	4464	28 24	–0 0002	–0 02	28-1B	90°C aqueous SCW
DWA 115	C22	8 60	4464	28 12	0 0002	0 02	28-1B	90°C aqueous SCW
DWA 116	C22	8 60	4464	28 07	0 0004	0 03	28-1B	90°C aqueous SCW
DWA 141	C22	8 60	4464	28 20	–0 0001	–0 01	29-1A	60°C vapor SDW
DWA 142	C22	8 60	4464	28 21	–0 0002	–0 02	29-1B	60°C aqueous SDW
DWA 151	C22	8 60	4464	28 14	0 0001	0 01	29-1A	60°C water line SDW
DWA 164	C22	8 60	4392	28 19	0 0010	0 08	30-1A	90°C water line SDW
DWA 168	C22	8 60	4392	28 07	0 0004	0.03	30-1A	90°C vapor SDW
DWA 169	C22	8 60	4392	27 99	0 0009	0 07	30-1B	90°C aqueous SDW
DWB 001	C22	8 60	4296	27 39	0 0013	0 11	25-1A	60°C vapor SAW

Sample identification	Alloy	Density (g/cc)	Exposure time (hours)	Surface area (sq cm)	Weight loss (g)	Corrosion rate (μm/y)	Vessel number-rack number	Test environment
DWB 002	C22	8 60	4296	27 44	0 0019	0 16	25-1A	60°C vapor SAW
DWB 003	C22	8 60	4296	27 54	0 0007	0 06	25-1A	60°C vapor SAW
DWB 004	C22	8 60	4296	27 49	0 0000	0 00	25-1B	60°C aqueous SAW
DWB 005	C22	8 60	4296	27 46	0 0004	0 03	25-1B	60°C aqueous SAW
DWB 006	C22	8 60	4296	27 32	0 0004	0 03	25-1B	60°C aqueous SAW
DWB 007	C22	8 60	8376	27 50	0 0004	0 02	25-2A	60°C vapor SAW
DWB 008	C22	8 60	8376	27 32	0 0003	0 01	25-2A	60°C vapor SAW
DWB 009	C22	8 60	8376	27 47	0 0000	0 00	25-2A	60°C vapor SAW
DWB 010	C22	8 60	8376	27 34	–0 0003	–0 01	25-2B	60°C aqueous SAW
DWB 011	C22	8 60	8376	27 22	–0 0002	–0 01	25-2B	60°C aqueous SAW
DWB 012	C22	8 60	8376	27 31	–0 0001	0 00	25-2B	60°C aqueous SAW
DWB 031	C22	8 60	4296	27 60	–0 0004	–0 03	25-1B	60°C water line SAW
DWB 032	C22	8 60	8376	27 60	0 0002	0 01	25-2B	60°C water line SAW
DWB 036	C22	8 60	4344	27 55	0 0001	0 01	26-1B	90°C water line SAW
DWB 037	C22	8 60	8784	27 43	–0 0010	–0 04	26-2B	90°C water line SAW
DWB 041	C22	8 60	4344	27 37	0 0005	0 04	26-1A	90°C vapor SAW
DWB 042	C22	8 60	4344	27 13	0 0014	0 12	26-1A	90°C vapor SAW
DWB 043	C22	8 60	4344	27 64	0 0002	0 02	26-1A	90°C vapor SAW
DWB 044	C22	8 60	4344	27 35	–0 0001	–0 01	26-1B	90°C aqueous SAW
DWB 045	C22	8 60	4344	27 12	–0 0001	–0 01	26-1B	90°C aqueous SAW
DWB 046	C22	8 60	4344	26 87	–0 0002	–0 02	26-1B	90°C aqueous SAW
DWB 047	C22	8 60	8784	27 59	–0 0001	0 00	26-2A	90°C vapor SAW
DWB 048	C22	8 60	8784	27 03	0 0000	0 00	26-2A	90°C vapor SAW
DWB 049	C22	8 60	8784	27 69	0 0001	0 00	26-2A	90°C vapor SAW
DWB 050	C22	8 60	8784	27 61	–0 0003	–0 01	26-2B	90°C aqueous SAW
DWB 051	C22	8 60	8784	27 63	–0 0003	–0 01	26-2B	90°C aqueous SAW
DWB 052	C22	8 60	8784	27 75	–0 0010	–0 04	26-2B	90°C aqueous SAW
DWB 071	C22	8 60	4392	27 47	0 0003	0 03	27-1A	60°C vapor SCW
DWB 072	C22	8 60	4392	27 61	0 0003	0 03	27-1A	60°C vapor SCW
DWB 073	C22	8 60	4392	27 48	0 0004	0 03	27-1A	60°C vapor SCW
DWB 074	C22	8 60	4392	27 44	0 0005	0 04	27-1B	60°C aqueous SCW
DWB 075	C22	8 60	4392	27 57	0 0004	0 03	27-1B	60°C aqueous SCW
DWB 076	C22	8 60	4392	27 43	0 0008	0 07	27-1B	60°C aqueous SCW
DWB 101	C22	8 60	4392	27 46	0 0008	0 07	27-1B	60°C water line SCW
DWB 106	C22	8 60	4464	27 64	0 0004	0 03	28-1B	90°C water line SCW
DWB 111	C22	8 60	4464	27 45	0 0005	0 04	28-1A	90°C vapor SCW
DWB 112	C22	8 60	4464	27 33	0 0007	0 06	28-1A	90°C vapor SCW
DWB 113	C22	8 60	4464	27 47	0 0004	0 03	28-1A	90°C vapor SCW
DWB 114	C22	8 60	4464	27 06	0 0009	0 08	28-1B	90°C aqueous SCW
DWB 115	C22	8 60	4464	27 04	0 0007	0 06	28-1B	90°C aqueous SCW

Sample identification	Alloy	Density (g/cc)	Exposure time (hours)	Surface area (sq cm)	Weight loss (g)	Corrosion rate (μm/y)	Vessel number-rack number	Test environment
DWB 116	C22	8 60	4464	27 44	0 0008	0 07	28-1B	90°C aqueous SCW
DWB 141	C22	8 60	4464	27 73	0 0003	0 02	29-1A	60°C vapor SDW
DWB 142	C22	8 60	4464	27 44	0 0001	0 01	29-1B	60°C aqueous SDW
DWB 151	C22	8 60	4464	27 67	0 0001	0 01	29-1B	60°C water line SDW
DWB 164	C22	8 60	4392	27 61	0 0002	0 02	30-1B	90°C water line SDW
DWB 168	C22	8 60	4392	27 76	0 0008	0 07	30-1A	90°C vapor SDW
DWB 169	C22	8 60	4392	27 24	0 0003	0 03	30-1B	90°C aqueous SDW
EWA 001	Ti Grade 12	4 43	4296	28 24	0 0308	5 02	25-1A	60°C vapor SAW
EWA 002	Ti Grade 12	4 43	4296	28 93	0 0310	4 93	25-1A	60°C vapor SAW
EWA 003	Ti Grade 12	4 43	4296	28 64	0 0278	4 47	25-1A	60°C vapor SAW
EWA 004	Ti Grade 12	4 43	4296	28 30	0 0230	3 74	25-1B	60°C aqueous SAW
EWA 005	Ti Grade 12	4 43	4296	28 72	0 0254	4 07	25-1B	60°C aqueous SAW
EWA 006	Ti Grade 12	4 43	4296	28 56	0 0230	3 71	25-1B	60°C aqueous SAW
EWA 007	Ti Grade 12	4 43	8376	28 31	–0 0007	–0 06	25-2A	60°C vapor SAW
EWA 008	Ti Grade 12	4 43	8376	28 35	–0 0004	–0 03	25-2A	60°C vapor SAW
EWA 009	Ti Grade 12	4 43	8376	28 42	–0 0004	–0 03	25-2A	60°C vapor SAW
EWA 010	Ti Grade 12	4 43	8376	28 54	–0 0005	–0 04	25-2B	60°C aqueous SAW
EWA 011	Ti Grade 12	4 43	8376	28 92	–0 0008	–0 07	25-2B	60°C aqueous SAW
EWA 012	Ti Grade 12	4 43	8376	28 39	–0 0005	–0 04	25-2B	60°C aqueous SAW
EWA 031	Ti Grade 12	4 43	4296	28 31	0 0303	4 93	25-1A	60°C water line SAW
EWA 032	Ti Grade 12	4 43	8376	28 69	–0 0004	–0 03	25-2A	60°C water line SAW
EWA 036	Ti Grade 12	4 43	4344	27 84	0 0158	2 58	26-1A	90°C water line SAW
EWA 037	Ti Grade 12	4 43	8784	28 36	–0 0004	–0 03	26-2A	90°C water line SAW
EWA 041	Ti Grade 12	4 43	4344	28 05	0 0551	8 94	26–1A	90°C vapor SAW
EWA 042	Ti Grade 12	4 43	4344	28 40	0 0212	3 40	26-1A	90°C vapor SAW
EWA 043	Ti Grade 12	4 43	4344	28 61	0 0550	8 75	26-1A	90°C vapor SAW
EWA 044	Ti Grade 12	4 43	4344	28 76	0 0270	4 27	26-1B	90°C aqueous SAW
EWA 045	Ti Grade 12	4 43	4344	29 08	0 0357	5 59	26-1B	90°C aqueous SAW
EWA 046	Ti Grade 12	4 43	4344	28 43	0 0150	2 40	26-1B	90°C aqueous SAW
EWA 047	Ti Grade 12	4 43	8784	28 90	–0 0001	–0 01	26-2A	90°C vapor SAW
EWA 048	Ti Grade 12	4 43	8784	28 54	–0 0007	–0 06	26-2A	90°C vapor SAW
EWA 049	Ti Grade 12	4 43	8784	28 74	–0 0010	–0 08	26-2A	90°C vapor SAW
EWA 050	Ti Grade 12	4 43	8784	28 69	–0 0021	–0 16	26-2B	90°C aqueous SAW
EWA 051	Ti Grade 12	4 43	8784	28 24	–0 0013	–0 10	26-2B	90°C aqueous SAW
EWA 052	Ti Grade 12	4 43	8784	28 24	–0 0022	–0 18	26-2B	90°C aqueous SAW
EWA 071	Ti Grade 12	4 43	4392	28 32	0 0404	6 42	27-1A	60°C vapor SCW
EWA 072	Ti Grade 12	4 43	4392	28 51	0 0527	8 32	27-1A	60°C vapor SCW
EWA 073	Ti Grade 12	4 43	4392	28 60	0 0539	8 49	27-1A	60°C vapor SCW
EWA 074	Ti Grade 12	4 43	4392	28 14	0.0532	8 51	27-1B	60°C aqueous SCW
EWA 075	Ti Grade 12	4 43	4392	28 50	0 0440	6 95	27-1B	60°C aqueous SCW

Sample identification	Alloy	Density (g/cc)	Exposure time (hours)	Surface area (sq cm)	Weight loss (g)	Corrosion rate (μm/y)	Vessel number-rack number	Test environment
EWA 076	Ti Grade 12	4 43	4392	28 63	0 0470	7 39	27-1B	60°C aqueous SCW
EWA 077	Ti Grade 12	4 43	8760	28 60	-0 0003	–0 02	27-2A	60°C vapor SCW
EWA 078	Ti Grade 12	4 43	8760	28 23	–0 0001	–0 01	27-2A	60°C vapor SCW
EWA 079	Ti Grade 12	4 43	8760	28 43	–0 0002	–0 02	27-2A	60°C vapor SCW
EWA 080	Ti Grade 12	4 43	8760	28 66	0 0022	0 17	27-2B	60°C aqueous SCW
EWA 081	Ti Grade 12	4 43	8760	28 54	0 0012	0 09	27-2B	60°C aqueous SCW
EWA 082	Ti Grade 12	4 43	8760	28 35	0 0020	0 16	27-2B	60°C aqueous SCW
EWA 101	Ti Grade 12	4 43	4392	29 06	0 0491	7 61	27-1A	60°C water line SCW
EWA 102	Ti Grade 12	4 43	8760	29 18	0 0011	0 09	27-2A	60°C water line SCW
EWA 106	Ti Grade 12	4 43	4464	28 10	0 0376	5 93	28-1A	90°C water line SCW
EWA 111	Ti Grade 12	4 43	4464	28 34	0 0207	3 24	28-1A	90°C vapor SCW
EWA 112	Ti Grade 12	4 43	4464	28 58	0 0261	4 04	28-1A	90°C vapor SCW
EWA 113	Ti Grade 12	4 43	4464	28 60	0 0309	4 79	28-1A	90°C vapor SCW
EWA 114	Ti Grade 12	4 43	4464	27 98	0 0397	6 29	28-1B	90°C aqueous SCW
EWA 115	Ti Grade 12	4 43	4464	28 65	0 0495	7 65	28-1B	90°C aqueous SCW
EWA 116	Ti Grade 12	4 43	4464	28 65	0 0406	6 28	28-1B	90°C aqueous SCW
EWA 141	Ti Grade 12	4 43	4464	28 37	0 0296	4 62	29-1A	60°C vapor SDW
EWA 142	Ti Grade 12	4 43	4464	29 04	0 0236	3 60	29-1B	60°C aqueous SDW
EWA 151	Ti Grade 12	4 43	4464	29 12	0 0327	4 98	29-1A	60°C water line SDW
EWA 164	Ti Grade 12	4 43	4392	27 80	0 0349	5 65	30-1A	90°C water line SDW
EWA 168	Ti Grade 12	4 43	4392	27 72	0 0377	6 12	30-1A	90°C vapor SDW
EWA 169	Ti Grade 12	4 43	4392	27 65	0 0328	5 34	30-1B	90°C aqueous SDW
EWD 001	Ti Grade 12	4 43	4296	28 96	0 0688	10 93	25-1A	60°C vapor SAW
EWD 002	Ti Grade 12	4 43	4296	29 03	0 1822	28 89	25-1A	60°C vapor SAW
EWD 003	Ti Grade 12	4 43	4296	29 05	0 0433	6 86	25-1A	60°C vapor SAW
EWD 004	Ti Grade 12	4 43	4296	29 19	0 0123	1 94	25-1B	60°C aqueous SAW
EWD 005	Ti Grade 12	4 43	4296	28 99	0 0369	5 86	25-1B	60°C aqueous SAW
EWD 006	Ti Grade 12	4 43	4296	29 22	0 0384	6 05	25-1B	60°C aqueous SAW
EWD 007	Ti Grade 12	4 43	8376	29 08	0 0001	0 01	25-2A	60°C vapor SAW
EWD 008	Ti Grade 12	4 43	8376	28 99	–0 0004	–0 03	25-2A	60°C vapor SAW
EWD 009	Ti Grade 12	4 43	8376	29 08	0 0003	0 02	25-2A	60°C vapor SAW
EWD 010	Ti Grade 12	4 43	8376	29 17	–0 0004	–0 03	25-2B	60°C aqueous SAW
EWD 011	Ti Grade 12	4 43	8376	29 11	–0 0004	–0 03	25-2B	60°C aqueous SAW
EWD 012	Ti Grade 12	4 43	8376	28 77	–0 0004	–0 03	25-2B	60°C aqueous SAW
EWD 031	Ti Grade 12	4 43	4296	29 25	0 1630	25 65	25-1B	60°C water line SAW
EWD 032	Ti Grade 12	4 43	8376	29 22	–0 0005	–0 04	25-2B	60°C water line SAW
EWD 036	Ti Grade 12	4 43	4344	29 09	0 0192	3 00	26-1B	90°C water line SAW
EWD 037	Ti Grade 12	4 43	8784	28 78	–0 0011	–0 09	26-2B	90°C water line SAW
EWD 041	Ti Grade 12	4 43	4344	29 24	0 0211	3 28	26-1A	90°C vapor SAW
EWD 042	Ti Grade 12	4 43	4344	29 16	0 0678	10 58	26-1A	90°C vapor SAW

Sample identification	Alloy	Density (g/cc)	Exposure time (hours)	Surface area (sq cm)	Weight loss (g)	Corrosion rate (μm/y)	Vessel number-rack number	Test environment
EWD 043	Ti Grade 12	4 43	4344	29 22	0 0468	7 29	26-1A	90°C vapor SAW
EWD 044	Ti Grade 12	4 43	4344	29 23	0 0237	3 69	26-1B	90°C aqueous SAW
EWD 045	Ti Grade 12	4 43	4344	29 22	0 0178	2 77	26-1B	90°C aqueous SAW
EWD 046	Ti Grade 12	4 43	4344	29 10	0 0240	3 75	26-1B	90°C aqueous SAW
EWD 047	Ti Grade 12	4 43	8784	29 14	–0 0012	–0 09	26-2A	90°C vapor SAW
EWD 048	Ti Grade 12	4 43	8784	29 21	0 0000	0 00	26-2A	90°C vapor SAW
EWD 049	Ti Grade 12	4 43	8784	29 15	–0 0006	–0 05	26-2A	90°C vapor SAW
EWD 050	Ti Grade 12	4 43	8784	29 09	–0 0028	–0 22	26-2B	90°C aqueous SAW
EWD 051	Ti Grade 12	4 43	8784	28 67	–0 0019	–0 15	26-2B	90°C aqueous SAW
EWD 052	Ti Grade 12	4 43	8784	29.20	–0 0020	–0 15	26-2B	90°C aqueous SAW
EWD 071	Ti Grade 12	4 43	4392	28 95	0 0434	6 75	27-1A	60°C vapor SCW
EWD 072	Ti Grade 12	4 43	4392	29 13	0 0370	5 72	27-1A	60°C vapor SCW
EWD 073	Ti Grade 12	4 43	4392	29.19	0 0428	6 60	27-1A	60°C vapor SCW
EWD 074	Ti Grade 12	4 43	4392	29 09	0 0325	5 03	27-1B	60°C aqueous SCW
EWD 075	Ti Grade 12	4 43	4392	29 12	0 0489	7 56	27-1B	60°C aqueous SCW
EWD 076	Ti Grade 12	4 43	4392	28 97	0 0371	5 77	27-1B	60°C aqueous SCW
EWD 077	Ti Grade 12	4 43	8760	29 21	0 0003	0 02	27-2A	60°C vapor SCW
EWD 078	Ti Grade 12	4 43	8760	29 14	–0 0002	–0 02	27-2A	60°C vapor SCW
EWD 079	Ti Grade 12	4 43	8760	29 21	–0 0002	–0 02	27-2A	60°C vapor SCW
EWD 080	Ti Grade 12	4 43	8760	29 17	0 0009	0 07	27-2B	60°C aqueous SCW
EWD 081	Ti Grade 12	4 43	8760	29 10	0 0007	0 05	27-2B	60°C aqueous SCW
EWD 082	Ti Grade 12	4 43	8760	29 11	0 0010	0 08	27-2B	60°C aqueous SCW
EWD 101	Ti Grade 12	4 43	4392	29 12	0 0445	6 88	27-1B	60°C water line SCW
EWD 102	Ti Grade 12	4 43	8760	29 12	0 0008	0 06	27-2B	60°C water line SCW
EWD 106	Ti Grade 12	4 43	4464	29 08	0 0815	12 41	28-1B	90°C water line SCW
EWD 111	Ti Grade 12	4 43	4464	28 82	0 0316	4 86	28-1A	90°C vapor SCW
EWD 112	Ti Grade 12	4 43	4464	29 21	0 0411	6 23	28-1A	90°C vapor SCW
EWD 113	Ti Grade 12	4 43	4464	28 96	0 0244	3 73	28-1A	90°C vapor SCW
EWD 114	Ti Grade 12	4 43	4464	28 95	0 0426	6 52	28-1B	90°C aqueous SCW
EWD 115	Ti Grade 12	4 43	4464	28 71	0 2063	31 84	28-1B	90°C aqueous SCW
EWD 116	Ti Grade 12	4 43	4464	29 11	0 0631	9 60	28-1B	90°C aqueous SCW
EWD 141	Ti Grade 12	4 43	4464	29 04	0 0260	3 97	29-1A	60°C vapor SDW
EWD 142	Ti Grade 12	4 43	4464	28 93	0 0617	9 45	29-1B	60°C aqueous SDW
EWD 151	Ti Grade 12	4 43	4464	28 99	0 0399	6 10	29-1B	60°C water line SDW
EWD 164	Ti Grade 12	4 43	4392	27 37	0 0331	5 44	30-1B	90°C water line SDW
EWD 168	Ti Grade 12	4 43	4392	27 66	0 0338	5 50	30-1A	90°C vapor SDW
EWD 169	Ti Grade 12	4 43	4392	37 86	0 0386	4 59	30-1B	90°C aqueous SDW
FWA 001	Ti Grade 16	4.52	4296	27 27	0 0188	3 11	25-1A	60°C vapor SAW
FWA 002	Ti Grade 16	4 52	4296	27 46	0 0222	3 65	25-1A	60°C vapor SAW
FWA 003	Ti Grade 16	4 52	4296	27 35	0 0259	4.27	25-1A	60°C vapor SAW

Sample identification	Alloy	Density (g/cc)	Exposure time (hours)	Surface area (sq cm)	Weight loss (g)	Corrosion rate (μm/y)	Vessel number-rack number	Test environment
FWA 004	Ti Grade 16	4 52	4296	27 68	–0 0001	–0 02	25-1B	60°C aqueous SAW
FWA 005	Ti Grade 16	4 52	4296	27 25	0 0000	0 00	25-1B	60°C aqueous SAW
FWA 006	Ti Grade 16	4 52	4296	27 36	–0 0002	–0 03	25-1B	60°C aqueous SAW
FWA 007	Ti Grade 16	4 52	8376	27 58	–0 0004	–0 03	25-2A	60°C vapor SAW
FWA 008	Ti Grade 16	4 52	8376	27 68	–0 0002	–0 02	25-2A	60°C vapor SAW
FWA 009	Ti Grade 16	4 52	8376	27 62	–0 0003	–0 03	25-2A	60°C vapor SAW
FWA 010	Ti Grade 16	4 52	8376	27 43	–0 0002	–0 02	25-2B	60°C aqueous SAW
FWA 011	Ti Grade 16	4 52	8376	27 44	–0 0003	–0 03	25-2B	60°C aqueous SAW
FWA 012	Ti Grade 16	4 52	8376	26 96	–0 0003	–0 03	25-2B	60°C aqueous SAW
FWA 031	Ti Grade 16	4 52	4296	27 68	0 0001	0 02	25-1A	60°C water line SAW
FWA 032	Ti Grade 16	4 52	8376	27 35	–0 0003	–0 03	25-2A	60°C water line SAW
FWA 036	Ti Grade 16	4 52	4344	27 65	0 0166	2 68	26-1A	90°C water line SAW
FWA 037	Ti Grade 16	4 52	8784	27 60	–0 0025	–0 20	26-2A	90°C water line SAW
FWA 041	Ti Grade 16	4 52	4344	27 58	0 0198	3 20	26-1A	90°C vapor SAW
FWA 042	Ti Grade 16	4 52	4344	27 50	0 0187	3 03	26-1A	90°C vapor SAW
FWA 043	Ti Grade 16	4 52	4344	27 62	0 0223	3 60	26-1A	90°C vapor SAW
FWA 044	Ti Grade 16	4 52	4344	27 48	0 0143	2 32	26-1B	90°C aqueous SAW
FWA 045	Ti Grade 16	4 52	4344	27 47	0 0148	2 40	26-1B	90°C aqueous SAW
FWA 046	Ti Grade 16	4 52	4344	27 58	0 0127	2 05	26-1B	90°C aqueous SAW
FWA 047	Ti Grade 16	4 52	8784	27 60	–0 0005	–0 04	26-2A	90°C vapor SAW
FWA 048	Ti Grade 16	4 52	8784	27 56	–0 0006	–0 05	26-2A	90°C vapor SAW
FWA 049	Ti Grade 16	4 52	8784	27 63	–0 0004	–0 03	26-2A	90°C vapor SAW
FWA 050	Ti Grade 16	4 52	8784	27 55	–0 0017	–0 14	26-2B	90°C aqueous SAW
FWA 051	Ti Grade 16	4 52	8784	27 75	–0 0020	–0 16	26-2B	90°C aqueous SAW
FWA 052	Ti Grade 16	4 52	8784	27 64	–0 0016	–0 13	26-2B	90°C aqueous SAW
FWA 071	Ti Grade 16	4 52	4392	27 70	0 0177	2 82	27-1A	60°C vapor SCW
FWA 072	Ti Grade 16	4 52	4392	27 37	0 0310	5 00	27-1A	60°C vapor SCW
FWA 073	Ti Grade 16	4 52	4392	27 51	0 0196	3 14	27-1A	60°C vapor SCW
FWA 074	Ti Grade 16	4 52	4392	27 77	0 0214	3 40	27-1B	60°C aqueous SCW
FWA 075	Ti Grade 16	4 52	4392	27 68	0 0147	2 34	27-1B	60°C aqueous SCW
FWA 076	Ti Grade 16	4 52	4392	26 73	0 0181	2 99	27-1B	60°C aqueous SCW
FWA 077	Ti Grade 16	4 52	8760	27 69	–0 0007	–0 06	27-2A	60°C vapor SCW
FWA 078	Ti Grade 16	4 52	8760	27 65	0 0000	0 00	27-2A	60°C vapor SCW
FWA 079	Ti Grade 16	4 52	8760	27 96	–0 0004	–0 03	27-2A	60°C vapor SCW
FWA 080	Ti Grade 16	4 52	8760	27 76	–0 0002	–0 02	27-2B	60°C aqueous SCW
FWA 081	Ti Grade 16	4 52	8760	27 71	0 0002	0 02	27-2B	60°C aqueous SCW
FWA 082	Ti Grade 16	4 52	8760	27 53	0 0002	0 02	27-2B	60°C aqueous SCW
FWA 101	Ti Grade 16	4 52	4392	27 76	0 0238	3 78	27-1A	60°C water line SCW
FWA 102	Ti Grade 16	4 52	8760	27 66			27-2A	60°C water line SCW
FWA 106	Ti Grade 16	4 52	4464	27 80	0 0241	3 76	28-1A	90°C water line SCW

Sample identification	Alloy	Density (g/cc)	Exposure time (hours)	Surface area (sq cm)	Weight loss (g)	Corrosion rate (μm/y)	Vessel number-rack number	Test environment
FWA 111	Ti Grade 16	4 52	4464	27 80	0 0290	4 53	28-1A	90°C vapor SCW
FWA 112	Ti Grade 16	4 52	4464	27 63	0 0640	10 06	28-1A	90°C vapor SCW
FWA 113	Ti Grade 16	4 52	4464	27 59	0 0295	4 64	28-1A	90°C vapor SCW
FWA 114	Ti Grade 16	4 52	4464	27 46	0 0361	5 71	28-1B	90°C aqueous SCW
FWA 115	Ti Grade 16	4 52	4464	27 53	0 0314	4 95	28-1B	90°C aqueous SCW
FWA 116	Ti Grade 16	4 52	4464	27 64	0 0343	5 39	28-1B	90°C aqueous SCW
FWA 141	Ti Grade 16	4 52	4464	27 81	0 0249	3 89	29-1A	60°C vapor SDW
FWA 142	Ti Grade 16	4 52	4464	27 63	0 0238	3 74	29-1B	60°C aqueous SDW
FWA 151	Ti Grade 16	4 52	4464	27 72	0 0608	9 52	29-1A	60°C water line SDW
FWA 164	Ti Grade 16	4 52	4392	27 44	0 0262	4 21	30-1A	90°C water line SDW
FWA 168	Ti Grade 16	4 52	4392	27 24	0 0245	3 97	30-1A	90°C vapor SDW
FWA 169	Ti Grade 16	4 52	4392	27 44	0 0236	3 79	30-1B	90°C aqueous SDW
FWE 001	Ti Grade 16	4 52	4296	27 42	0 0362	5 96	25-1A	60°C vapor SAW
FWE 002	Ti Grade 16	4 52	4296	27 62	0 0425	6 94	25-1A	60°C vapor SAW
FWE 003	Ti Grade 16	4 52	4296	28 13	0 0322	5 16	25-1A	60°C vapor SAW
FWE 004	Ti Grade 16	4 52	4296	28 10	0 0110	1 77	25-1B	60°C aqueous SAW
FWE 005	Ti Grade 16	4 52	4296	27 93	0 0099	1 60	25-1B	60°C aqueous SAW
FWE 006	Ti Grade 16	4 52	4296	28 01	0 0128	2 06	25-1B	60°C aqueous SAW
FWE 007	Ti Grade 16	4 52	8376	28 06	–0 0003	–0 02	25-2A	60°C vapor SAW
FWE 008	Ti Grade 16	4 52	8376	28 20	–0 0007	–0 06	25-2A	60°C vapor SAW
FWE 009	Ti Grade 16	4 52	8376	28 02	–0 0006	–0 05	25-2A	60°C vapor SAW
FWE 010	Ti Grade 16	4 52	8376	28 14	–0 0004	–0 03	25-2B	60°C aqueous SAW
FWE 011	Ti Grade 16	4 52	8376	27 91	–0 0006	–0 05	25-2B	60°C aqueous SAW
FWE 012	Ti Grade 16	4 52	8376	28 04	–0 0005	–0 04	25-2B	60°C aqueous SAW
FWE 031	Ti Grade 16	4 52	4296	27 84	0 0008	0 13	25-1B	60°C water line SAW
FWE 032	Ti Grade 16	4 52	8376	27 63	–0 0007	–0 06	25-2B	60°C water line SAW
FWE 036	Ti Grade 16	4 52	4344	28 06	0 0181	2 88	26-1B	90°C water line SAW
FWE 037	Ti Grade 16	4 52	8784	27 54	–0 0027	–0 22	26-2B	90°C water line SAW
FWE 041	Ti Grade 16	4 52	4344	27 89	0 0212	3 39	26-1A	90°C vapor SAW
FWE 042	Ti Grade 16	4.52	4344	27 74	0 0331	5 32	26-1A	90°C vapor SAW
FWE 043	Ti Grade 16	4 52	4344	27 99	0 0204	3 25	26-1A	90°C vapor SAW
FWE 044	Ti Grade 16	4 52	4344	28 01	–0 0011	–0 18	26-1B	90°C aqueous SAW
FWE 045	Ti Grade 16	4 52	4344	28 01	0 0110	1 75	26-1B	90°C aqueous SAW
FWE 046	Ti Grade 16	4 52	4344	27 79	0 0111	1 78	26-1B	90°C aqueous SAW
FWE 047	Ti Grade 16	4 52	8784	27 49	0 0009	0 07	26-2A	90°C vapor SAW
FWE 048	Ti Grade 16	4 52	8784	27 99	–0 0006	–0 05	26-2A	90°C vapor SAW
FWE 049	Ti Grade 16	4 52	8784	27 98	–0 0002	–0 02	26-2A	90°C vapor SAW
FWE 050	Ti Grade 16	4 52	8784	28 09	–0 0016	–0 13	26-2B	90°C aqueous SAW
FWE 051	Ti Grade 16	4 52	8784	27 73	–0 0018	–0 14	26-2B	90°C aqueous SAW
FWE 052	Ti Grade 16	4 52	8784	27 77	–0 0021	–0 17	26-2B	90°C aqueous SAW

Sample identification	Alloy	Density (g/cc)	Exposure time (hours)	Surface area (sq cm)	Weight loss (g)	Corrosion rate (μm/y)	Vessel number-rack number	Test environment
FWE 071	Ti Grade 16	4 52	4392	27 73	0 0201	3 20	27-1A	60°C vapor SCW
FWE 072	Ti Grade 16	4 52	4392	27 91	0 0216	3 42	27-1A	60°C vapor SCW
FWE 073	Ti Grade 16	4 52	4392	27 66	0 0311	4 96	27-1A	60°C vapor SCW
FWE 074	Ti Grade 16	4 52	4392	28 15	0 0240	3 76	27-1B	60°C aqueous SCW
FWE 075	Ti Grade 16	4 52	4392	27 99	0 0214	3 37	27-1B	60°C aqueous SCW
FWE 076	Ti Grade 16	4 52	4392	27 51	0 0187	3 00	27-1B	60°C aqueous SCW
FWE 077	Ti Grade 16	4 52	8760	27 68			27-2A	60°C vapor SCW
FWE 078	Ti Grade 16	4 52	8760	28 05	–0 0007	–0 06	27-2A	60°C vapor SCW
FWE 079	Ti Grade 16	4 52	8760	27 94	0 0001	0 01	27-2A	60°C vapor SCW
FWE 080	Ti Grade 16	4 52	8760	27 99	0 0001	0 01	27-2B	60°C aqueous SCW
FWE 081	Ti Grade 16	4 52	8760	28 16	0 0003	0 02	27-2B	60°C aqueous SCW
FWE 082	Ti Grade 16	4 52	8760	27 85	0 0009	0 07	27-2B	60°C aqueous SCW
FWE 101	Ti Grade 16	4 52	4392	27 72	0 0299	4 76	27-1B	60°C water line SCW
FWE 102	Ti Grade 16	4 52	8760	27 95	0 0010	0 08	27-2B	60°C water line SCW
FWE 106	Ti Grade 16	4 52	4464	27 49	0 0294	4 64	28-1B	90°C water line SCW
FWE 111	Ti Grade 16	4 52	4464	28 21	0 0292	4 49	28-1A	90°C vapor SCW
FWE 112	Ti Grade 16	4 52	4464	27 85	0 0192	2 99	28-1A	90°C vapor SCW
FWE 113	Ti Grade 16	4 52	4464	28 11	0 0289	4 46	28-1A	90°C vapor SCW
FWE 114	Ti Grade 16	4 52	4464	28 03	0 0326	5 05	28-1B	90°C aqueous SCW
FWE 115	Ti Grade 16	4 52	4464	27 74	0 0831	13 01	28-1B	90°C aqueous SCW
FWE 116	Ti Grade 16	4 52	4464	28 00	0 0362	5 61	28-1B	90°C aqueous SCW
FWE 141	Ti Grade 16	4 52	4464	27 67	0 0158	2 48	29-1A	60°C vapor SDW
FWE 142	Ti Grade 16	4 52	4464	27 57	0 0267	4 20	29-1B	60°C aqueous SDW
FWE 151	Ti Grade 16	4 52	4464	27 87	0 0271	4 22	29-1B	60°C water line SDW
FWE 164	Ti Grade 16	4 52	4392	27 38	0 0253	4 08	30-1B	90°C water line SDW
FWE 168	Ti Grade 16	4 52	4392	27 60	0 0177	2 83	30-1A	90°C vapor SDW
FWE 169	Ti Grade 16	4 52	4392	27 57	0 0472	7 55	30-1B	90°C aqueous SDW
GWA 001	Monel 400	8 80	4536	28 49	0 0061	0 47	19-1A	60°C vapor SAW
GWA 002	Monel 400	8 80	4536	28 20	0 0117	0 91	19-1A	60°C vapor SAW
GWA 003	Monel 400	8 80	4536	28 39	0 0153	1 18	19-1A	60°C vapor SAW
GWA 004	Monel 400	8 80	4536	28 40	1 4796	114 33	19-1B	60°C aqueous SAW
GWA 005	Monel 400	8 80	4536	27 93	1 4297	112 33	19-1B	60°C aqueous SAW
GWA 006	Monel 400	8 80	4536	28 38	1 5462	119 57	19-1B	60°C aqueous SAW
GWA 007	Monel 400	8 80	8760	28 04	0 0110	0 45	19-2A	60°C vapor SAW
GWA 008	Monel 400	8 80	8760	27 98	0 0119	0 48	19-2A	60°C vapor SAW
GWA 009	Monel 400	8 80	8760	28 43	0 0108	0 43	19-2A	60°C vapor SAW
GWA 010	Monel 400	8 80	8760	28 53	1 6761	66 76	19-2B	60°C aqueous SAW
GWA 011	Monel 400	8 80	8760	28 51	1 6655	66 39	19-2B	60°C aqueous SAW
GWA 012	Monel 400	8 80	8760	27 99	1 6915	68 68	19-2B	60°C aqueous SAW
GWA 031	Monel 400	8 80	4536	27 71	1 0818	85 69	19-1A	60°C water line SAW

Sample identification	Alloy	Density (g/cc)	Exposure time (hours)	Surface area (sq cm)	Weight loss (g)	Corrosion rate (μm/y)	Vessel number-rack number	Test environment
GWA 032	Monel 400	8 80	8760	27 75	1 3017	53 30	19-2A	60°C water line SAW
GWA 036	Monel 400	8 80	4392	28 02	0 7423	60 05	18-1A	90°C water line SAW
GWA 037	Monel 400	8 80	8760	27 93	0 8876	36 11	18-2A	90°C water line SAW
GWA 041	Monel 400	8 80	4392	28 75	0 0487	3 84	18-1A	90°C vapor SAW
GWA 042	Monel 400	8 80	4392	28 73	0 0568	4 48	18-1A	90°C vapor SAW
GWA 043	Monel 400	8 80	4392	27 94	0 0522	4 23	18-1A	90°C vapor SAW
GWA 044	Monel 400	8 80	4392	28 67	0 9861	77 96	18-1B	90°C aqueous SAW
GWA 045	Monel 400	8 80	4392	27 60	1 0208	83 84	18-1B	90°C aqueous SAW
GWA 046	Monel 400	8 80	4392	28 37	1 0802	86 29	18-1B	90°C aqueous SAW
GWA 047	Monel 400	8 80	8760	28 42	0 0491	1 96	18-2A	90°C vapor SAW
GWA 048	Monel 400	8 80	8760	28 26	0 0504	2 03	18-2A	90°C vapor SAW
GWA 049	Monel 400	8 80	8760	27 91	0 0580	2 36	18-2A	90°C vapor SAW
GWA 050	Monel 400	8 80	8760	28 61	1 1329	45 00	18-2B	90°C aqueous SAW
GWA 051	Monel 400	8 80	8760	27 84	1 1457	46 76	18-2B	90°C aqueous SAW
GWA 052	Monel 400	8 80	8760	28 66	1 1759	46 63	18-2B	90°C aqueous SAW
GWF 001	Monel 400	8 80	4536	27 17	0 0107	0 86	19-1A	60°C vapor SAW
GWF 002	Monel 400	8 80	4536	27 77	0 0143	1 13	19-1A	60°C vapor SAW
GWF 003	Monel 400	8 80	4536	27 77	0 0129	1 02	19-1A	60°C vapor SAW
GWF 004	Monel 400	8 80	4536	27 53	1 4721	117 34	19-1B	60°C aqueous SAW
GWF 005	Monel 400	8 80	4536	27 49	1 5264	121 87	19-1B	60°C aqueous SAW
GWF 006	Monel 400	8 80	4536	27 18	1 5832	127 84	19-1B	60°C aqueous SAW
GWF 007	Monel 400	8 80	8760	27 29	0 0185	0 77	19-2A	60°C vapor SAW
GWF 008	Monel 400	8 80	8760	27 80	0 0337	1 38	19-2A	60°C vapor SAW
GWF 009	Monel 400	8 80	8760	27 76	0 0319	1 31	19-2A	60°C vapor SAW
GWF 010	Monel 400	8 80	8760	27 85	1 5732	64 19	19-2B	60°C aqueous SAW
GWF 011	Monel 400	8 80	8760	27 38	1 5294	63 47	19-2B	60°C aqueous SAW
GWF 012	Monel 400	8 80	8760	27 16	1 5600	65 26	19-2B	60°C aqueous SAW
GWF 031	Monel 400	8 80	4536	27 12	1 0996	88 97	19-1A	60°C water line SAW
GWF 032	Monel 400	8 80	8760	27 97	1 3393	54 42	19-2A	60°C water line SAW
GWF 036	Monel 400	8 80	4392	26 95	0 6858	57 68	18-1A	90°C water line SAW
GWF 037	Monel 400	8 80	8760	27 38	0 9459	39 26	18-2A	90°C water line SAW
GWF 041	Monel 400	8 80	4392	27 64	0 0480	3 94	18-1A	90°C vapor SAW
GWF 042	Monel 400	8 80	4392	27 49	0 0518	4 27	18-1A	90°C vapor SAW
GWF 043	Monel 400	8 80	4392	27.69	0 0424	3 47	18-1A	90°C vapor SAW
GWF 044	Monel 400	8 80	4392	26 87	1 0116	85 33	18-1B	90°C aqueous SAW
GWF 045	Monel 400	8 80	4392	27 40	1 0926	90 38	18-1B	90°C aqueous SAW
GWF 046	Monel 400	8 80	4392	27 27	1 1571	96 15	18-1B	90°C aqueous SAW
GWF 047	Monel 400	8 80	8760	27 29	0 0560	2 33	18-2A	90°C vapor SAW
GWF 048	Monel 400	8 80	8760	26 90	0 0460	1 94	18-2A	90°C vapor SAW
GWF 049	Monel 400	8 80	8760	27 30	0 0526	2 19	18-2A	90°C vapor SAW

Sample identification	Alloy	Density (g/cc)	Exposure time (hours)	Surface area (sq cm)	Weight loss (g)	Corrosion rate (μm/y)	Vessel number-rack number	Test environment
GWF 050	Monel 400	8 80	8760	27 65	1 1954	49 14	18-2B	90°C aqueous SAW
GWF 051	Monel 400	8 80	8760	27 66	1 2342	50 70	18-2B	90°C aqueous SAW
GWF 052	Monel 400	8 80	8760	27 27	1 2562	52 35	18-2B	90°C aqueous SAW
HWA 001	CDA 715	8 94	4536	27 51	0 0402	3 16	19-1A	60°C vapor SAW
HWA 002	CDA 715	8 94	4536	27 58	0 0543	4 25	19-1A	60°C vapor SAW
HWA 003	CDA 715	8 94	4536	28 22	0 0618	4 73	19-1A	60°C vapor SAW
HWA 004	CDA 715	8 94	4536	27 84	3 2743	254 02	19-1B	60°C aqueous SAW
HWA 005	CDA 715	8 94	4536	27 87	3 4426	266 83	19-1B	60°C aqueous SAW
HWA 006	CDA 715	8 94	4536	27 91	3 7590	290 90	19-1B	60°C aqueous SAW
HWA 007	CDA 715	8 94	8760	27 71	0 0814	3 29	19-2A	60°C vapor SAW
HWA 008	CDA 715	8 94	8760	27 80	0 0895	3 60	19-2A	60°C vapor SAW
HWA 009	CDA 715	8 94	8760	27 77	0 0993	4 00	19-2A	60°C vapor SAW
HWA 010	CDA 715	8 94	8760	27 99	3 3825	135 18	19-2B	60°C aqueous SAW
HWA 011	CDA 715	8 94	8760	27 33	3 3421	136 77	19-2B	60°C aqueous SAW
HWA 012	CDA 715	8 94	8760	27 57	3 5737	144 97	19-2B	60°C aqueous SAW
HWA 031	CDA 715	8 94	4536	27 48	4 7230	371 32	19-1A	60°C water line SAW
HWA 032	CDA 715	8 94	8760	27 65	5 4566	220 73	19-2A	60°C water line SAW
HWA 036	CDA 715	8 94	4392	27 79	3 5809	287 50	18-1A	90°C water line SAW
HWA 037	CDA 715	8 94	8760	27 95	6 1186	244 87	18-2A	90°C water line SAW
HWA 041	CDA 715	8 94	4392	27 79	0 2227	17 88	18-1A	90°C vapor SAW
HWA 042	CDA 715	8 94	4392	27 64	0 1531	12 36	18-1A	90°C vapor SAW
HWA 043	CDA 715	8 94	4392	27 72	0 1116	8 98	18-1A	90°C vapor SAW
HWA 044	CDA 715	8 94	4392	28 26	3 2813	259 03	18-1B	90°C aqueous SAW
HWA 045	CDA 715	8 94	4392	27 98	3 2059	255 62	18-1B	90°C aqueous SAW
HWA 046	CDA 715	8 94	4392	27 48	3 6026	292 46	18-1B	90°C aqueous SAW
HWA 047	CDA 715	8 94	8760	27 86	0 3061	12 29	18-2A	90°C vapor SAW
HWA 048	CDA 715	8 94	8760	27 94	0 2586	10 35	18-2A	90°C vapor SAW
HWA 049	CDA 715	8 94	8760	28 22	0 1936	7 67	18-2A	90°C vapor SAW
HWA 050	CDA 715	8 94	8760	28 12	4 2182	167 79	18-2B	90°C aqueous SAW
HWA 051	CDA 715	8 94	8760	27 78	6 0110	242 05	18-2B	90°C aqueous SAW
HWA 052	CDA 715	8 94	8760	27 54	3 8218	155 24	18-2B	90°C aqueous SAW
HWG 001	CDA 715	8 94	4536	26 81	0 0435	3 50	19-1A	60°C vapor SAW
HWG 002	CDA 715	8 94	4536	26 89	0 0484	3 89	19-1A	60°C vapor SAW
HWG 003	CDA 715	8 94	4536	26 88	0 0660	5 30	19-1A	60°C vapor SAW
HWG 004	CDA 715	8 94	4536	26 74	2 5337	204 66	19-1B	60°C aqueous SAW
HWG 005	CDA 715	8 94	4536	26 66	2 7715	224 56	19-1B	60°C aqueous SAW
HWG 006	CDA 715	8 94	4536	26 53	3 1442	255 99	19-1B	60°C aqueous SAW
HWG 007	CDA 715	8 94	8760	26 72	0 0562	2 35	19-2A	60°C vapor SAW
HWG 008	CDA 715	8 94	8760	26 74	0 0939	3 93	19-2A	60°C vapor SAW
HWG 009	CDA 715	8 94	8760	26 81	0 1004	4 19	19-2A	60°C vapor SAW

Sample Identification	Alloy	Density (g/cc)	Exposure time (hours)	Surface area (sq cm)	Weight loss (g)	Corrosion rate (μm/y)	Vessel number-rack number	Test environment
HWG 010	CDA 715	8 94	8760	26 56	2 6060	109 74	19-2B	60°C aqueous SAW
HWG 011	CDA 715	8.94	8760	26 83	2 7953	116 54	19-2B	60°C aqueous SAW
HWG 012	CDA 715	8 94	8760	26 73	3 0622	128 13	19-2B	60°C aqueous SAW
HWG 031	CDA 715	8 94	4536	26 83	5 3929	434 28	19-1A	60°C water line SAW
HWG 032	CDA 715	8 94	8760	26 89	5 0582	210 41	19-2A	60°C water line SAW
HWG 036	CDA 715	8 94	4392	26 83	3 3935	282 14	18-1A	90°C water line SAW
HWG 037	CDA 715	8 94	8760	26 77	4 7066	196 68	18-2A	90°C water line SAW
HWG 041	CDA 715	8 94	4392	26 82	0 1346	11 20	18-1A	90°C vapor SAW
HWG 042	CDA 715	8 94	4392	26 92	0 1047	8 68	18-1A	90°C vapor SAW
HWG 043	CDA 715	8 94	4392	26 82	0 0953	7 93	18-1A	90°C vapor SAW
HWG 044	CDA 715	8 94	4392	26 75	3 4887	290 97	18-1B	90°C aqueous SAW
HWG 045	CDA 715	8 94	4392	26 91	3 6809	305 21	18-1B	90°C aqueous SAW
HWG 046	CDA 715	8 94	4392	26 84	3 7686	313 24	18-1B	90°C aqueous SAW
HWG 047	CDA 715	8 94	8760	26 89	0 2696	11 21	18-2A	90°C vapor SAW
HWG 048	CDA 715	8 94	8760	26 61	0 2005	8 43	18-2A	90°C vapor SAW
HWG 049	CDA 715	8 94	8760	26 35	0 1964	8 34	18-2A	90°C vapor SAW
HWG 050	CDA 715	8 94	8760	26 78	5 2821	220 62	18-2B	90°C aqueous SAW
HWG 051	CDA 715	8 94	8760	26 84	5 4112	225 50	18-2B	90°C aqueous SAW
HWG 052	CDA 715	8 94	8760	26 79	5 4941	229 43	18-2B	90°C aqueous SAW
IWA 001	A387 Grade 22	7 86	4536	28 68	0 2073	17 76	23-1A	60°C vapor SDW
IWA 002	A387 Grade 22	7 86	4536	28 86	0 2647	22 54	23-1A	60°C vapor SDW
IWA 003	A387 Grade 22	7 86	4536	29 18	0 5066	42 65	23-1A	60°C vapor SDW
IWA 004	A387 Grade 22	7 86	4536	28 43	0 5857	50 62	23-1B	60°C aqueous SDW
IWA 005	A387 Grade 22	7 86	4536	29 02	0 2817	23 85	23-1B	60°C aqueous SDW
IWA 006	A387 Grade 22	7 86	4536	29 03	1 4452	122 30	23-1B	60°C aqueous SDW
IWA 007	A387 Grade 22	7 86	8760	29 05	0 2910	12 74	23-2A	60°C vapor SDW
IWA 008	A387 Grade 22	7 86	8760	28 52	0 3327	14 84	23-2A	60°C vapor SDW
IWA 009	A387 Grade 22	7 86	8760	28 95	0 6259	27 51	23-2A	60°C vapor SDW
IWA 010	A387 Grade 22	7 86	8760	28 54	2 0178	89 95	23-2B	60°C aqueous SDW
IWA 011	A387 Grade 22	7 86	8760	28 30	2 2737	102 23	23-2B	60°C aqueous SDW
IWA 012	A387 Grade 22	7 86	8760	28 95	2 7486	120 79	23-2B	60°C aqueous SDW
IWA 031	A387 Grade 22	7 86	4536	29 01	1 6293	138 02	23-1A	60°C water line SDW
IWA 032	A387 Grade 22	7 86	8760	28 97	3 6390	159 84	23-2A	60°C water line SDW
IWA 036	A387 Grade 22	7 86	4632	28 87	2 4882	207 41	22-1A	90°C water line SDW
IWA 037	A387 Grade 22	7 86	8832	28 97	3 8451	167 51	22-2A	90°C water line SDW
IWA 041	A387 Grade 22	7 86	4632	28 86	0 5304	44 22	22-1A	90°C vapor SDW
IWA 042	A387 Grade 22	7 86	4632	28 88	0 5403	45 02	22-1A	90°C vapor SDW
IWA 043	A387 Grade 22	7 86	4632	28 94	0 4968	41 31	22-1A	90°C vapor SDW
IWA 044	A387 Grade 22	7 86	4632	28 80	1 3652	114 06	22-1B	90°C aqueous SDW
IWA 045	A387 Grade 22	7 86	4632	28 69	1 2959	108 68	22-1B	90°C aqueous SDW

Sample identification	Alloy	Density (g/cc)	Exposure time (hours)	Surface area (sq cm)	Weight loss (g)	Corrosion rate (μm/y)	Vessel number-rack number	Test environment
IWA 046	A387 Grade 22	7 86	4632	28 79	0 9445	78 94	22-1B	90°C aqueous SDW
IWA 047	A387 Grade 22	7 86	8832	28 81	0 8075	35 36	22-2A	90°C vapor SDW
IWA 048	A387 Grade 22	7 86	8832	28 96	0 8414	36 67	22-2A	90°C vapor SDW
IWA 049	A387 Grade 22	7 86	8832	29 08	0 9785	42 46	22-2A	90°C vapor SDW
IWA 050	A387 Grade 22	7 86	8832	28 92	1 7311	75 54	22-2B	90°C aqueous SDW
IWA 051	A387 Grade 22	7 86	8832	28 96	1 8040	78 59	22-2B	90°C aqueous SDW
IWA 052	A387 Grade 22	7 86	8832	28 87	1 8432	80 56	22-2B	90°C aqueous SDW
IWA 071	A387 Grade 22	7 86	4392	27 26	0 9572	89 10	21-1A	60°C vapor SCW
IWA 072	A387 Grade 22	7 86	4392	28 96	1 5336	134 36	21-1A	60°C vapor SCW
IWA 073	A387 Grade 22	7 86	4392	29 05	1 9986	174 56	21-1A	60°C vapor SCW
IWA 074	A387 Grade 22	7 86	4392	29 07	0 2220	19 38	21-1B	60°C aqueous SCW
IWA 075	A387 Grade 22	7 86	4392	28 77	0 1779	15 69	21-1B	60°C aqueous SCW
IWA 076	A387 Grade 22	7 86	4392	28 91	0 2982	26 17	21-1B	60°C aqueous SCW
IWA 077	A387 Grade 22	7 86	8760	29 06	1 5731	68 87	21-2A	60°C vapor SCW
IWA 078	A387 Grade 22	7 86	8760	28 96	3 1742	139 42	21-2A	60°C vapor SCW
IWA 079	A387 Grade 22	7 86	8760	28 77	4 0826	180 52	21-2A	60°C vapor SCW
IWA 080	A387 Grade 22	7 86	8760	28 75	0 1690	7 48	21-2B	60°C aqueous SCW
IWA 081	A387 Grade 22	7 86	8760	28 55	0 1672	7 45	21-2B	60°C aqueous SCW
IWA 082	A387 Grade 22	7 86	8760	27 30	0 1270	5 92	21-2B	60°C aqueous SCW
IWA 101	A387 Grade 22	7 86	4392	28 80	1 8391	162 02	21-1A	60°C water line SCW
IWA 102	A387 Grade 22	7 86	8760	28 71	3 3904	150 23	21-2A	60°C water line SCW
IWA 106	A387 Grade 22	7 86	4344	29 08	0 6845	60 39	20-1A	90°C water line SCW
IWA 107	A387 Grade 22	7 86	8736	28 84	2 6919	119 08	20-2A	90°C water line SCW
IWA 111	A387 Grade 22	7 86	4344	28 71	1 0126	90 49	20-1A	90°C vapor SCW
IWA 112	A387 Grade 22	7 86	4344	29 01	1 3432	118 80	20-1A	90°C vapor SCW
IWA 113	A387 Grade 22	7 86	4344	29 10	2 0452	180 31	20-1A	90°C vapor SCW
IWA 114	A387 Grade 22	7 86	4344	28 95	0 1481	13 12	20-1B	90°C aqueous SCW
IWA 115	A387 Grade 22	7 86	4344	28 84	0 1323	11 77	20-1B	90°C aqueous SCW
IWA 116	A387 Grade 22	7 86	4344	28 75	0 1594	14 23	20-1B	90°C aqueous SCW
IWA 117	A387 Grade 22	7 86	8736	28 82	5 6546	250 33	20-2A	90°C vapor SCW
IWA 118	A387 Grade 22	7 86	8736	28 74	8 2820	367 59	20-2A	90°C vapor SCW
IWA 119	A387 Grade 22	7 86	8736	28 88	6 9939	308 92	20-2A	90°C vapor SCW
IWA 120	A387 Grade 22	7.86	8736	28 81	0 1424	6 31	20-2B	90°C aqueous SCW
IWA 121	A387 Grade 22	7 86	8736	27 46	0 1594	7 41	20-2B	90°C aqueous SCW
IWA 122	A387 Grade 22	7 86	8736	28 84	0 1769	7 83	20-2B	90°C aqueous SCW
IWH 001	A387 Grade 22	7 86	4536	29 12	0 2385	20 12	23-1A	60°C vapor SDW
IWH 002	A387 Grade 22	7 86	4536	27 94	0 3676	32 33	23-1A	60°C vapor SDW
IWH 003	A387 Grade 22	7 86	4536	29 37	0 6853	57 34	23-1A	60°C vapor SDW
IWH 004	A387 Grade 22	7 86	4536	29 10	0 4067	34 34	23-1B	60°C aqueous SDW
IWH 005	A387 Grade 22	7 86	4536	29 05	0 3622	30 64	23-1B	60°C aqueous SDW

Sample identification	Alloy	Density (g/cc)	Exposure time (hours)	Surface area (sq cm)	Weight loss (g)	Corrosion rate (μm/y)	Vessel number-rack number	Test environment
IWH 006	A387 Grade 22	7 86	4536	29 18	0 4538	38 21	23-1B	60°C aqueous SDW
IWH 007	A387 Grade 22	7 86	8760	29 24	0 4200	18 27	23-2A	60°C vapor SDW
IWH 008	A387 Grade 22	7 86	8760	29 15	0 5590	24 40	23-2A	60°C vapor SDW
IWH 009	A387 Grade 22	7 86	8760	28 94	0 8521	37 46	23-2A	60°C vapor SDW
IWH 010	A387 Grade 22	7 86	8760	29 11	2 6131	114 20	23-2B	60°C aqueous SDW
IWH 011	A387 Grade 22	7 86	8760	28 78	2 4676	109 08	23-2B	60°C aqueous SDW
IWH 012	A387 Grade 22	7 86	8760	29 17	0 4248	18 53	23-2B	60°C aqueous SDW
IWH 031	A387 Grade 22	7 86	4536	28 99	1 6319	138 31	23-1A	60°C water line SDW
IWH 032	A387 Grade 22	7 86	8760	29 28	3 5821	155 67	23-2A	60°C water line SDW
IWH 036	A387 Grade 22	7 86	4632	28 04	2 5592	219 58	22-1A	90°C water line SDW
IWH 037	A387 Grade 22	7 86	8832	28 86	3 7071	162 12	22-2A	90°C water line SDW
IWH 041	A387 Grade 22	7 86	4632	29 11	0 6336	52 37	22-1A	90°C vapor SDW
IWH 042	A387 Grade 22	7 86	4632	29 23	0 6235	51 33	22-1A	90°C vapor SDW
IWH 043	A387 Grade 22	7 86	4632	29 16	0 6283	51 85	22-1A	90°C vapor SDW
IWH 044	A387 Grade 22	7 86	4632	29 21	1 3804	113 72	22-1B	90°C aqueous SDW
IWH 045	A387 Grade 22	7 86	4632	29 18	1 2912	106 46	22-1B	90°C aqueous SDW
IWH 046	A387 Grade 22	7 86	4632	29 06	1 5030	124 44	22-1B	90°C aqueous SDW
IWH 047	A387 Grade 22	7 86	8832	29 00	1 1770	51 21	22-2A	90°C vapor SDW
IWH 048	A387 Grade 22	7 86	8832	29 04	0 9553	41 51	22-2A	90°C vapor SDW
IWH 049	A387 Grade 22	7 86	8832	28 43	0 9245	41 04	22-2A	90°C vapor SDW
IWH 050	A387 Grade 22	7 86	8832	28 96	1 7169	74 80	22-2B	90°C aqueous SDW
IWH 051	A387 Grade 22	7 86	8832	29 07	2 0195	87 66	22-2B	90°C aqueous SDW
IWH 052	A387 Grade 22	7 86	8832	29 17	1 6894	73 07	22-2B	90°C aqueous SDW
IWH 071	A387 Grade 22	7 86	4392	29 21	1 2434	108 02	21-1A	60°C vapor SCW
IWH 072	A387 Grade 22	7 86	4392	29 18	1 3570	118 02	21-1A	60°C vapor SCW
IWH 073	A387 Grade 22	7 86	4392	29 19	1 9149	166 45	21-1A	60°C vapor SCW
IWH 074	A387 Grade 22	7 86	4392	29 12	0 3411	29 72	21-1B	60°C aqueous SCW
IWH 075	A387 Grade 22	7 86	4392	29 26	0 3521	30 54	21-1B	60°C aqueous SCW
IWH 076	A387 Grade 22	7 86	4392	29 17	0 3025	26 31	21-1B	60°C aqueous SCW
IWH 077	A387 Grade 22	7 86	8760	29 13	2 8172	123 03	21-2A	60°C vapor SCW
IWH 078	A387 Grade 22	7 86	8760	29 33	3 6720	159 31	21-2A	60°C vapor SCW
IWH 079	A387 Grade 22	7 86	8760	29 12	3 5753	156 21	21-2A	60°C vapor SCW
IWH 080	A387 Grade 22	7 86	8760	27 94	0 1572	7 16	21-2B	60°C aqueous SCW
IWH 081	A387 Grade 22	7 86	8760	29 46	0 1446	6 25	21-2B	60°C aqueous SCW
IWH 082	A387 Grade 22	7 86	8760	29 05	0 1588	6 95	21-2B	60°C aqueous SCW
IWH 101	A387 Grade 22	7 86	4392	29 14	2 0023	174 36	21-1A	60°C water line SCW
IWH 102	A387 Grade 22	7 86	8760	28 84	2 7097	119 53	21-2A	60°C water line SCW
IWH 106	A387 Grade 22	7 86	4344	29 03	1 2430	109 85	20-1A	90°C water line SCW
IWH 107	A387 Grade 22	7 86	8736	28 91	1 7789	78 50	20-2A	90°C water line SCW
IWH 111	A387 Grade 22	7 86	4344	29 12	2 5059	220 76	20-1A	90°C vapor SCW

Sample identification	Alloy	Density (g/cc)	Exposure time (hours)	Surface area (sq cm)	Weight loss (g)	Corrosion rate (μm/y)	Vessel number-rack number	Test environment
IWH 112	A387 Grade 22	7 86	4344	29 00	5 0985	451 11	20-1A	90°C vapor SCW
IWH 113	A387 Grade 22	7 86	4344	29 14	0 5900	51 94	20-1A	90°C vapor SCW
IWH 114	A387 Grade 22	7 86	4344	29 29	0 1525	13 36	20-1B	90°C aqueous SCW
IWH 115	A387 Grade 22	7 86	4344	29 12	0 1673	14 74	20-1B	90°C aqueous SCW
IWH 116	A387 Grade 22	7 86	4344	29 04	0 1841	16 27	20-1B	90°C aqueous SCW
IWH 117	A387 Grade 22	7 86	8736	28 96	5 3066	233 79	20-2A	90°C vapor SCW
IWH 118	A387 Grade 22	7 86	8736	29 16	9 3263	407 97	20-2A	90°C vapor SCW
IWH 119	A387 Grade 22	7 86	8736	29 31	13 9834	608 57	20-2A	90°C vapor SCW
IWH 120	A387 Grade 22	7 86	8736	29 04	0 0718	3 15	20-2B	90°C aqueous SCW
IWH 121	A387 Grade 22	7 86	8736	29 17	0 0735	3 21	20-2B	90°C aqueous SCW
IWH 122	A387 Grade 22	7 86	8736	29 04	0 0672	2 95	20-2B	90°C aqueous SCW
JWA 001	A516 Grade 55	7 86	4536	28 70	0 3233	27 68	23-1A	60°C vapor SDW
JWA 002	A516 Grade 55	7 86	4536	28 86	0 2539	21 62	23-1A	60°C vapor SDW
JWA 003	A516 Grade 55	7 86	4536	28 66	0 4892	41 94	23-1A	60°C vapor SDW
JWA 004	A516 Grade 55	7 86	4536	28 40	1 1677	101 01	23-1B	60°C aqueous SDW
JWA 005	A516 Grade 55	7 86	4536	28 32	1 2497	108 43	23-1B	60°C aqueous SDW
JWA 006	A516 Grade 55	7 86	4536	28 81	1 2349	105 33	23-1B	60°C aqueous SDW
JWA 007	A516 Grade 55	7 86	8760	28 70	0 4950	21 94	23-2A	60°C vapor SDW
JWA 008	A516 Grade 55	7 86	8760	28 49	0 5526	24 67	23-2A	60°C vapor SDW
JWA 009	A516 Grade 55	7 86	8760	28 13	0 8404	38 00	23-2A	60°C vapor SDW
JWA 010	A516 Grade 55	7 86	8760	28 79	1 8102	80 00	23-2B	60°C aqueous SDW
JWA 011	A516 Grade 55	7 86	8760	28 66	1 5038	66 75	23-2B	60°C aqueous SDW
JWA 012	A516 Grade 55	7 86	8760	28 61	1 7383	77 31	23-2B	60°C aqueous SDW
JWA 031	A516 Grade 55	7 86	4536	29 19	2 6075	219 46	23-1A	60°C water line SDW
JWA 032	A516 Grade 55	7 86	8760	28 39	3 7620	168 61	23-2A	60°C water line SDW
JWA 036	A516 Grade 55	7 86	4632	27 77	2 4751	214 42	22-1A	90°C water line SDW
JWA 037	A516 Grade 55	7 86	8832	28 50	1 9016	84 19	22-2A	90°C water line SDW
JWA 041	A516 Grade 55	7 86	4632	28 84	0 8489	70 83	22-1A	90°C vapor SDW
JWA 042	A516 Grade 55	7 86	4632	28 57	0 7100	59 79	22-1A	90°C vapor SDW
JWA 043	A516 Grade 55	7 86	4632	28 36	0 7533	63 91	22-1A	90°C vapor SDW
JWA 044	A516 Grade 55	7 86	4632	29 06	1 0797	89 41	22-1B	90°C aqueous SDW
JWA 045	A516 Grade 55	7 86	4632	28 40	0 8133	68 90	22-1B	90°C aqueous SDW
JWA 046	A516 Grade 55	7 86	4632	29 48	1 0294	84 02	22-1B	90°C aqueous SDW
JWA 047	A516 Grade 55	7 86	8832	27 71	1 0232	46 59	22-2A	90°C vapor SDW
JWA 048	A516 Grade 55	7 86	8832	29 19	1 0397	44 95	22-2A	90°C vapor SDW
JWA 049	A516 Grade 55	7 86	8832	29 06	1 0305	44 75	22-2A	90°C vapor SDW
JWA 050	A516 Grade 55	7 86	8832	28 86	0 9982	43 65	22-2B	90°C aqueous SDW
JWA 051	A516 Grade 55	7 86	8832	28 72	1 0286	45 19	22-2B	90°C aqueous SDW
JWA 052	A516 Grade 55	7 86	8832	28 31	1 0836	48 30	22-2B	90°C aqueous SDW
JWA 071	A516 Grade 55	7 86	4392	28 56	2 2380	198 86	21-1A	60°C vapor SCW

Sample identification	Alloy	Density (g/cc)	Exposure time (hours)	Surface area (sq cm)	Weight loss (g)	Corrosion rate (μm/y)	Vessel number-rack number	Test environment
JWA 072	A516 Grade 55	7 86	4392	27 26	2 8459	264 87	21-1A	60°C vapor SCW
JWA 073	A516 Grade 55	7 86	4392	27 46	3 1926	295 00	21-1A	60°C vapor SCW
JWA 074	A516 Grade 55	7 86	4392	28 59	0 6150	54 59	21-1B	60°C aqueous SCW
JWA 075	A516 Grade 55	7 86	4392	28 71	0 6219	54 97	21-1B	60°C aqueous SCW
JWA 076	A516 Grade 55	7 86	4392	28 42	0 5627	50 25	21-1B	60°C aqueous SCW
JWA 077	A516 Grade 55	7 86	8760	29 30	3 6173	157 05	21-2A	60°C vapor SCW
JWA 078	A516 Grade 55	7 86	8760	28 52	4 6929	209 38	21-2A	60°C vapor SCW
JWA 079	A516 Grade 55	7 86	8760	28 72	4 8081	213 02	21-2A	60°C vapor SCW
JWA 080	A516 Grade 55	7 86	8760	29 55	0 1842	7 93	21-2B	60°C aqueous SCW
JWA 081	A516 Grade 55	7 86	8760	28 55	0 2510	11 19	21-2B	60°C aqueous SCW
JWA 082	A516 Grade 55	7 86	8760	29 15	0 1841	8 03	21-2B	60°C aqueous SCW
JWA 101	A516 Grade 55	7 86	4392	29 65	2 3122	197 90	21-1A	60°C water line SCW
JWA 102	A516 Grade 55	7 86	8760	28 90	2 9941	131 80	21-2A	60°C water line SCW
JWA 106	A516 Grade 55	7 86	4344	28 74	0 2115	18 88	20-1A	90°C water line SCW
JWA 107	A516 Grade 55	7 86	8736	28 65	1 5234	67 85	20-2A	90°C water line SCW
JWA 111	A516 Grade 55	7 86	4344	29 28	2 7599	241 82	20-1A	90°C vapor SCW
JWA 112	A516 Grade 55	7 86	4344	28 25	3 5412	321 66	20-1A	90°C vapor SCW
JWA 113	A516 Grade 55	7 86	4344	29 19	2 9348	257 97	20-1A	90°C vapor SCW
JWA 114	A516 Grade 55	7 86	4344	29 37	0 1467	12 81	20-1B	90°C aqueous SCW
JWA 115	A516 Grade 55	7 86	4344	29 54	0 1598	13 88	20-1B	90°C aqueous SCW
JWA 116	A516 Grade 55	7 86	4344	28 64	0 1219	10 92	20-1B	90°C aqueous SCW
JWA 117	A516 Grade 55	7 86	8736	29 59	7 9562	342 99	20-2A	90°C vapor SCW
JWA 118	A516 Grade 55	7 86	8736	28 80	8 2022	363 36	20-2A	90°C vapor SCW
JWA 120	A516 Grade 55	7 86	8736	28 62	0 1562	6 96	20-2B	90°C aqueous SCW
JWA 121	A516 Grade 55	7 86	8736	28 77	0 1297	5 75	20-2B	90°C aqueous SCW
JWA 122	A516 Grade 55	7 86	8736	27 78	0 0803	3 69	20-2B	90°C aqueous SCW
JWI 001	A516 Grade 55	7 86	4536	27 50	0 4384	39 16	23-1A	60°C vapor SDW
JWI 002	A516 Grade 55	7 86	4536	27 76	0 4193	37 11	23-1A	60°C vapor SDW
JWI 003	A516 Grade 55	7 86	4536	27 42	0 6981	62 56	23-1A	60°C vapor SDW
JWI 004	A516 Grade 55	7 86	4536	28 09	1 0079	88 15	23-1B	60°C aqueous SDW
JWI 005	A516 Grade 55	7 86	4536	27 49	1 1405	101 95	23-1B	60°C aqueous SDW
JWI 006	A516 Grade 55	7 86	4536	27.89	1 3384	117 92	23-1B	60°C aqueous SDW
JWI 007	A516 Grade 55	7 86	8760	27 84	0 4071	18 60	23-2A	60°C vapor SDW
JWI 008	A516 Grade 55	7 86	8760	27.64	0 4418	20 34	23-2A	60°C vapor SDW
JWI 009	A516 Grade 55	7 86	8760	27 52	0 8367	38 69	23-2A	60°C vapor SDW
JWI 010	A516 Grade 55	7 86	8760	27 84	1 5283	69 84	23-2B	60°C aqueous SDW
JWI 011	A516 Grade 55	7 86	8760	27 68	1 8222	83 74	23-2B	60°C aqueous SDW
JWI 012	A516 Grade 55	7 86	8760	27 47	1 7121	79 29	23-2B	60°C aqueous SDW
JWI 031	A516 Grade 55	7 86	4536	27 85	2 5852	228 06	23-1A	60°C water line SDW
JWI 032	A516 Grade 55	7 86	8760	28 02	4 8260	219 11	23-2A	60°C water line SDW

Sample identification	Alloy	Density (g/cc)	Exposure time (hours)	Surface area (sq cm)	Weight loss (g)	Corrosion rate (μm/y)	Vessel number-rack number	Test environment
JWI 036	A516 Grade 55	7 86	4632	28 05	3 1770	272 52	22-1A	90°C water line SDW
JWI 037	A516 Grade 55	7 86	8832	27 80	3 0561	138 74	22-2A	90°C water line SDW
JWI 041	A516 Grade 55	7 86	4632	27 90	0 8859	76 41	22-1A	90°C vapor SDW
JWI 042	A516 Grade 55	7 86	4632	27 94	1 0990	94 64	22-1A	90°C vapor SDW
JWI 043	A516 Grade 55	7 86	4632	28 12	1 2261	104 93	22-1A	90°C vapor SDW
JWI 044	A516 Grade 55	7 86	4632	28 12	1 0243	87 65	22-1B	90°C aqueous SDW
JWI 045	A516 Grade 55	7 86	4632	27 66	1 2352	107 46	22-1B	90°C aqueous SDW
JWI 046	A516 Grade 55	7 86	4632	28 40	1 5348	130 02	22-1B	90°C aqueous SDW
JWI 047	A516 Grade 55	7 86	8832	28 09	1 1352	51 00	22-2A	90°C vapor SDW
JWI 048	A516 Grade 55	7 86	8832	28 26	1 3274	59 26	22-2A	90°C vapor SDW
JWI 049	A516 Grade 55	7 86	8832	28 02	1 3047	58 76	22-2A	90°C vapor SDW
JWI 050	A516 Grade 55	7 86	8832	28 12	1 2473	55 97	22-2B	90°C aqueous SDW
JWI 051	A516 Grade 55	7 86	8832	28 25	1 4235	63 58	22-2B	90°C aqueous SDW
JWI 052	A516 Grade 55	7 86	8832	28 29	1 1245	50 17	22-2B	90°C aqueous SDW
JWI 071	A516 Grade 55	7 86	4392	28 00	1 7925	162 43	21-1A	60°C vapor SCW
JWI 072	A516 Grade 55	7 86	4392	28 02	1 7055	154 47	21-1A	60°C vapor SCW
JWI 073	A516 Grade 55	7 86	4392	28 02	2 1305	192 96	21-1A	60°C vapor SCW
JWI 074	A516 Grade 55	7 86	4392	27 74	0 7498	68 58	21-1B	60°C aqueous SCW
JWI 075	A516 Grade 55	7 86	4392	27 90	0 9368	85 21	21-1B	60°C aqueous SCW
JWI 076	A516 Grade 55	7 86	4392	28 10	1 0138	91 55	21-1B	60°C aqueous SCW
JWI 077	A516 Grade 55	7 86	8760	28 24	4 4491	200 47	21-2A	60°C vapor SCW
JWI 078	A516 Grade 55	7 86	8760	28 04	5 8348	264 75	21-2A	60°C vapor SCW
JWI 079	A516 Grade 55	7 86	8760	28 12	5 7048	258 15	21-2A	60°C vapor SCW
JWI 080	A516 Grade 55	7 86	8760	27 94	0 2074	9 45	21-2B	60°C aqueous SCW
JWI 081	A516 Grade 55	7 86	8760	28 06	0 2438	11 05	21-2B	60°C aqueous SCW
JWI 082	A516 Grade 55	7 86	8760	27 75	0 1986	9 10	21-2B	60°C aqueous SCW
JWI 101	A516 Grade 55	7 86	4392	27 86	2 5297	230 40	21-1A	60°C water line SCW
JWI 102	A516 Grade 55	7 86	8760	27 85	2 9865	136 42	21-2A	60°C water line SCW
JWI 106	A516 Grade 55	7 86	4344	27 93	0 1359	12 48	20-1A	90°C water line SCW
JWI 107	A516 Grade 55	7 86	8736	28 07	1 0687	48 57	20-2A	90°C water line SCW
JWI 111	A516 Grade 55	7 86	4344	28 53	2 6476	238 11	20-1A	90°C vapor SCW
JWI 112	A516 Grade 55	7 86	4344	27 73	2 1105	195 23	20-1A	90°C vapor SCW
JWI 113	A516 Grade 55	7 86	4344	27 90	2 0883	192 02	20-1A	90°C vapor SCW
JWI 114	A516 Grade 55	7 86	4344	28 25	0 2101	19 08	20-1B	90°C aqueous SCW
JWI 115	A516 Grade 55	7 86	4344	27 95	0 1526	14 01	20-1B	90°C aqueous SCW
JWI 116	A516 Grade 55	7 86	4344	27 86	0 1759	16 20	20-1B	90°C aqueous SCW
JWI 117	A516 Grade 55	7.86	8736	28 04	7 8826	358 68	20-2A	90°C vapor SCW
JWI 118	A516 Grade 55	7 86	8736	28 25	9 3670	423 06	20-2A	90°C vapor SCW
JWI 119	A516 Grade 55	7 86	8736	27 51	4 1127	190 72	20-2A	90°C vapor SCW
JWI 120	A516 Grade 55	7 86	8736	27 91	0 2045	9 35	20-2B	90°C aqueous SCW

Sample identification	Alloy	Density (g/cc)	Exposure time (hours)	Surface area (sq cm)	Weight loss (g)	Corrosion rate (μm/y)	Vessel number-rack number	Test environment
JWI 121	A516 Grade 55	7 86	8736	27 76	0 1405	6 46	20-2B	90°C aqueous SCW
JWI 122	A516 Grade 55	7 86	8736	27 98	0 1502	6 85	20-2B	90°C aqueous SCW
KWA 001	A27 Grade 70-40	7 82	4536	28 34	0 4362	38 01	23-1A	60°C vapor SDW
KWA 002	A27 Grade 70-40	7.82	4536	28 17	0 2313	20 28	23-1A	60°C vapor SDW
KWA 003	A27 Grade 70-40	7 82	4536	28 23	0 4351	38 06	23-1A	60°C vapor SDW
KWA 004	A27 Grade 70-40	7 82	4536	28 06	1 3262	116 72	23-1B	60°C aqueous SDW
KWA 005	A27 Grade 70-40	7 82	4536	28 09	0 4700	41 31	23-1B	60°C aqueous SDW
KWA 006	A27 Grade 70-40	7 82	4536	28 15	1 0919	95 78	23-1B	60°C aqueous SDW
KWA 007	A27 Grade 70-40	7 82	8760	28 17	0 7855	35 66	23-2A	60°C vapor SDW
KWA 008	A27 Grade 70-40	7 82	8760	28 16	0 5552	25 21	23-2A	60°C vapor SDW
KWA 009	A27 Grade 70-40	7 82	8760	28 15	0 7363	33 45	23-2A	60°C vapor SDW
KWA 010	A27 Grade 70-40	7 82	8760	28 00	1 9919	90 97	23-2B	60°C aqueous SDW
KWA 011	A27 Grade 70-40	7 82	8760	28 12	1 8306	83 26	23-2B	60°C aqueous SDW
KWA 012	A27 Grade 70-40	7 82	8760	28 21	1 6387	74 29	23-2B	60°C aqueous SDW
KWA 031	A27 Grade 70-40	7 82	4536	28 22	2 3064	201 84	23-1A	60°C water line SDW
KWA 032	A27 Grade 70-40	7 82	8760	28 26	5 1990	235 24	23-2A	60°C water line SDW
KWA 036	A27 Grade 70-40	7 82	4632	28 15	3 1445	270 15	22-1A	90°C water line SDW
KWA 037	A27 Grade 70-40	7 82	8832	28 14	2 3383	105 38	22-2A	90°C water line SDW
KWA 041	A27 Grade 70-40	7 82	4632	28 16	1 0636	91 35	22-1A	90°C vapor SDW
KWA 042	A27 Grade 70-40	7 82	4632	28 28	0 5573	47 65	22-1A	90°C vapor SDW
KWA 043	A27 Grade 70-40	7 82	4632	27 84	0 7197	62 53	22-1A	90°C vapor SDW
KWA 044	A27 Grade 70-40	7 82	4632	28 30	0 8423	71 97	22-1B	90°C aqueous SDW
KWA 045	A27 Grade 70-40	7 82	4632	28 19	0 9280	79 61	22-1B	90°C aqueous SDW
KWA 046	A27 Grade 70-40	7 82	4632	28 02	1 1289	97 43	22-1B	90°C aqueous SDW
KWA 047	A27 Grade 70-40	7 82	8832	28 03	0 9801	44 36	22-2A	90°C vapor SDW
KWA 048	A27 Grade 70-40	7 82	8832	28 12	0 6153	27 75	22-2A	90°C vapor SDW
KWA 049	A27 Grade 70-40	7 82	8832	28 21	0 5048	22 69	22-2A	90°C vapor SDW
KWA 050	A27 Grade 70-40	7 82	8832	28 18	1 0395	46 79	22-2B	90°C aqueous SDW
KWA 051	A27 Grade 70-40	7 82	8832	28 00	1 5213	68 91	22-2B	90°C aqueous SDW
KWA 052	A27 Grade 70-40	7 82	8832	27 89	1 0273	46 72	22-2B	90°C aqueous SDW
KWA 071	A27 Grade 70-40	7 82	4392	28 13	1 9195	174 02	21-1A	60°C vapor SCW
KWA 072	A27 Grade 70-40	7 82	4392	28 06	2 4878	226 13	21-1A	60°C vapor SCW
KWA 073	A27 Grade 70-40	7 82	4392	28 18	3 9854	360 78	21-1A	60°C vapor SCW
KWA 074	A27 Grade 70-40	7 82	4392	28 40	0 8134	73 05	21-1B	60°C aqueous SCW
KWA 075	A27 Grade 70-40	7 82	4392	28.36	0 8716	78 39	21-1B	60°C aqueous SCW
KWA 076	A27 Grade 70-40	7 82	4392	27 83	0 7729	70 84	21-1B	60°C aqueous SCW
KWA 077	A27 Grade 70-40	7 82	8760	27 87	1 6645	76 38	21-2A	60°C vapor SCW
KWA 078	A27 Grade 70-40	7 82	8760	28 01	1 9880	90 77	21-2A	60°C vapor SCW
KWA 079	A27 Grade 70-40	7 82	8760	28 27	2 8218	127 64	21-2A	60°C vapor SCW
KWA 080	A27 Grade 70-40	7 82	8760	28 30	0 2362	10 67	21-2B	60°C aqueous SCW

Sample identification	Alloy	Density (g/cc)	Exposure time (hours)	Surface area (sq cm)	Weight loss (g)	Corrosion rate (μm/y)	Vessel number-rack number	Test environment
KWA 081	A27 Grade 70-40	7 82	8760	27 88	0 2180	10 00	21-2B	60°C aqueous SCW
KWA 082	A27 Grade 70-40	7 82	8760	27 93	0 1620	7 42	21-2B	60°C aqueous SCW
KWA 101	A27 Grade 70-40	7 82	4392	28 22	2 0872	188 62	21-1A	60°C water line SCW
KWA 102	A27 Grade 70-40	7 82	8760	28 20	3 9143	177 53	21-2A	60°C water line SCW
KWA 106	A27 Grade 70-40	7 82	4344	28 37	1 4599	132 71	20-1A	90°C water line SCW
KWA 107	A27 Grade 70-40	7 82	8736	28 16	2 6998	122 94	20-2A	90°C water line SCW
KWA 111	A27 Grade 70-40	7 82	4344	28 16	1 8152	166 22	20-1A	90°C vapor SCW
KWA 112	A27 Grade 70-40	7 82	4344	28 29	2 8697	261 61	20-1A	90°C vapor SCW
KWA 113	A27 Grade 70-40	7 82	4344	28 21	2 2235	203 28	20-1A	90°C vapor SCW
KWA 114	A27 Grade 70-40	7 82	4344	28 11	0 1252	11 48	20-1B	90°C aqueous SCW
KWA 115	A27 Grade 70-40	7 82	4344	28 04	0 1487	13 67	20-1B	90°C aqueous SCW
KWA 116	A27 Grade 70-40	7 82	4344	27 88	0 0976	9 03	20-1B	90°C aqueous SCW
KWA 117	A27 Grade 70-40	7 82	8736	28 35	4 7050	212 81	20-2A	90°C vapor SCW
KWA 118	A27 Grade 70-40	7 82	8736	28 32	4 2686	193 28	20-2A	90°C vapor SCW
KWA 119	A27 Grade 70-40	7 82	8736	27 93	5 9267	272 06	20-2A	90°C vapor SCW
KWA 120	A27 Grade 70-40	7 82	8736	28 27	0 1435	6 51	20-2B	90°C aqueous SCW
KWA 121	A27 Grade 70-40	7 82	8736	28 44	0 1582	7 13	20-2B	90°C aqueous SCW
KWA 122	A27 Grade 70-40	7 82	8736	28 24	0 1171	5 32	20-2B	90°C aqueous SCW
KWI 001	A27 Grade 70-40	7 82	4536	28 54	0 7067	61 16	23-1A	60°C vapor SDW
KWI 002	A27 Grade 70-40	7 82	4536	28 45	0 5307	46 07	23-1A	60°C vapor SDW
KWI 003	A27 Grade 70-40	7 82	4536	28 09	0 8026	70 57	23-1A	60°C vapor SDW
KWI 004	A27 Grade 70-40	7 82	4536	28 26	1 1524	100 69	23-1B	60°C aqueous SDW
KWI 005	A27 Grade 70-40	7 82	4536	27 89	1 0008	88 62	23-1B	60°C aqueous SDW
KWI 006	A27 Grade 70-40	7 82	4536	28 53	1 2701	109 93	23-1B	60°C aqueous SDW
KWI 007	A27 Grade 70-40	7 82	8760	27 81	0 7467	34 34	23-2A	60°C vapor SDW
KWI 008	A27 Grade 70-40	7 82	8760	28 04	0 8135	37 10	23-2A	60°C vapor SDW
KWI 009	A27 Grade 70-40	7 82	8760	28 06	0 9692	44 17	23-2A	60°C vapor SDW
KWI 010	A27 Grade 70-40	7 82	8760	28 52	1 6251	72 87	23-2B	60°C aqueous SDW
KWI 011	A27 Grade 70-40	7 82	8760	28 39	1 6309	73 47	23-2B	60°C aqueous SDW
KWI 012	A27 Grade 70-40	7 82	8760	27 95	1 8289	83 66	23-2B	60°C aqueous SDW
KWI 031	A27 Grade 70-40	7 82	4536	27 37	2 2139	199 75	23-1A	60°C water line SDW
KWI 032	A27 Grade 70-40	7 82	8760	28 04	3 9510	180 21	23-2A	60°C water line SDW
KWI 036	A27 Grade 70-40	7 82	4632	28 26	2 4648	210 93	22-1A	90°C water line SDW
KWI 037	A27 Grade 70-40	7 82	8832	27 28	2 8428	132 17	22-2A	90°C water line SDW
KWI 041	A27 Grade 70-40	7 82	4632	27 66	1 1642	101 81	22-1A	90°C vapor SDW
KWI 042	A27 Grade 70-40	7 82	4632	28 21	0 7152	61 30	22-1A	90°C vapor SDW
KWI 043	A27 Grade 70-40	7 82	4632	27 71	0 8577	74 85	22-1A	90°C vapor SDW
KWI 044	A27 Grade 70-40	7 82	4632	28 02	0 8749	75.50	22-1B	90°C aqueous SDW
KWI 045	A27 Grade 70-40	7 82	4632	28 16	0 7917	67 99	22-1B	90°C aqueous SDW
KWI 046	A27 Grade 70-40	7 82	4632	28 14	1 0459	89 88	22-1B	90°C aqueous SDW

Sample identification	Alloy	Density (g/cc)	Exposure time (hours)	Surface area (sq cm)	Weight loss (g)	Corrosion rate (μm/y)	Vessel number-rack number	Test environment
KWI 047	A27 Grade 70-40	7 82	8832	28 16	0 8939	40 26	22-2A	90°C vapor SDW
KWI 048	A27 Grade 70-40	7 82	8832	28 08	0 6022	27 20	22-2A	90°C vapor SDW
KWI 049	A27 Grade 70-40	7 82	8832	28 39	0 6925	30 94	22-2A	90°C vapor SDW
KWI 050	A27 Grade 70-40	7 82	8832	28 16	1 0281	46 31	22-2B	90°C aqueous SDW
KWI 051	A27 Grade 70-40	7 82	8832	28 40	0 8144	36 38	22-2B	90°C aqueous SDW
KWI 052	A27 Grade 70-40	7 82	8832	27 93	1 4508	65 88	22-2B	90°C aqueous SDW
KWI 071	A27 Grade 70-40	7 82	4392	28 30	1 9898	179 32	21-1A	60°C vapor SCW
KWI 072	A27 Grade 70-40	7 82	4392	27 66	2 2157	204 34	21-1A	60°C vapor SCW
KWI 073	A27 Grade 70-40	7 82	4392	28 16	2 7674	250 65	21-1A	60°C vapor SCW
KWI 074	A27 Grade 70-40	7 82	4392	28 37	0 5969	53 66	21-1B	60°C aqueous SCW
KWI 075	A27 Grade 70-40	7 82	4392	27 71	0 6270	57 72	21-1B	60°C aqueous SCW
KWI 076	A27 Grade 70-40	7 82	4392	28 10	0 6101	55 38	21-1B	60°C aqueous SCW
KWI 077	A27 Grade 70-40	7 82	8760	28 53	1 7246	77 30	21-2A	60°C vapor SCW
KWI 078	A27 Grade 70-40	7 82	8760	28 33	1 7060	77 01	21-2A	60°C vapor SCW
KWI 079	A27 Grade 70-40	7 82	8760	28 20	2 1671	98 26	21-2A	60°C vapor SCW
KWI 080	A27 Grade 70-40	7 82	8760	28 47	0 1801	8 09	21-2B	60°C aqueous SCW
KWI 081	A27 Grade 70-40	7 82	8760	28 08	0 2266	10 32	21-2B	60°C aqueous SCW
KWI 082	A27 Grade 70-40	7 82	8760	28 61	0 2424	10 83	21-2B	60°C aqueous SCW
KWI 101	A27 Grade 70-40	7 82	4392	27 43	2 5415	236 28	21-1A	60°C water line SCW
KWI 102	A27 Grade 70-40	7 82	8760	28 07	4 4400	202 28	21-2A	60°C water line SCW
KWI 106	A27 Grade 70-40	7 82	4344	27 97	0 6114	56 36	20-1A	90°C water line SCW
KWI 107	A27 Grade 70-40	7 82	8736	28 27	1 2315	55 86	20-2A	90°C water line SCW
KWI 111	A27 Grade 70-40	7 82	4344	27 75	1 6176	150 33	20-1A	90°C vapor SCW
KWI 112	A27 Grade 70-40	7 82	4344	28 57	2 3328	210 60	20-1A	90°C vapor SCW
KWI 113	A27 Grade 70-40	7 82	4344	27 30	3 3143	313 05	20-1A	90°C vapor SCW
KWI 114	A27 Grade 70-40	7 82	4344	27 19	0 1775	16 84	20-1B	90°C aqueous SCW
KWI 115	A27 Grade 70-40	7 82	4344	27 35	0 2339	22 06	20-1B	90°C aqueous SCW
KWI 116	A27 Grade 70-40	7 82	4344	27 60	0 1933	18 06	20-1B	90°C aqueous SCW
KWI 117	A27 Grade 70-40	7 82	8736	28 23	1 7647	80 15	20-2A	90°C vapor SCW
KWI 118	A27 Grade 70-40	7 82	8736	27 79	2 6178	120 81	20-2A	90°C vapor SCW
KWI 119	A27 Grade 70-40	7 82	8736	28 02	3 6868	168 75	20-2A	90°C vapor SCW
KWI 120	A27 Grade 70-40	7 82	8736	27 82	0 1330	6 13	20-2B	90°C aqueous SCW
KWI 121	A27 Grade 70-40	7 82	8736	28 32	0 1305	5 91	20-2B	90°C aqueous SCW
KWI 122	A27 Grade 70-40	7 82	8736	27 48	0 1756	8 20	20-2B	90°C aqueous SCW
LWA 001	Inconel 625	8 44	4296	28 22	–0 0004	–0 03	25-1A	60°C vapor SAW
LWA 002	Inconel 625	8 44	4296	28 26	–0 0002	–0 02	25-1A	60°C vapor SAW
LWA 003	Inconel 625	8 44	4296	28 14	–0 0005	–0 04	25-1A	60°C vapor SAW
LWA 004	Inconel 625	8 44	4296	28.29	–0 0016	–0 14	25-1B	60°C aqueous SAW
LWA 005	Inconel 625	8 44	4296	28 23	–0 0017	–0 15	25-1B	60°C aqueous SAW
LWA 006	Inconel 625	8 44	4296	28 18	–0 0018	–0 15	25-1B	60°C aqueous SAW

Sample identification	Alloy	Density (g/cc)	Exposure time (hours)	Surface area (sq cm)	Weight loss (g)	Corrosion rate (μm/y)	Vessel number-rack number	Test environment
LWA 007	Inconel 625	8 44	8376	28 25	0 0000	0 00	25-2A	60°C vapor SAW
LWA 008	Inconel 625	8 44	8376	28 27	–0 0004	–0 02	25-2A	60°C vapor SAW
LWA 009	Inconel 625	8 44	8376	28 27	–0 0002	–0 01	25-2A	60°C vapor SAW
LWA 010	Inconel 625	8 44	8376	28 17	–0 0004	–0 02	25-2B	60°C aqueous SAW
LWA 011	Inconel 625	8 44	8376	28 21	–0 0004	–0 02	25-2B	60°C aqueous SAW
LWA 012	Inconel 625	8 44	8376	28 20	–0 0006	–0 03	25-2B	60°C aqueous SAW
LWA 031	Inconel 625	8 44	4296	28 32	–0 0005	–0 04	25-1A	60°C water line SAW
LWA 032	Inconel 625	8 44	8376	28 37	–0 0001	0 00	25-2A	60°C water line SAW
LWA 036	Inconel 625	8 44	4344	27 81	0 0004	0 03	26-1A	90°C water line SAW
LWA 037	Inconel 625	8 44	8784	28 29	0 0000	0 00	26-2A	90°C water line SAW
LWA 041	Inconel 625	8 44	4344	28 32	0 0002	0 02	26-1A	90°C vapor SAW
LWA 042	Inconel 625	8 44	4344	28 43	0 0001	0 01	26-1A	90°C vapor SAW
LWA 043	Inconel 625	8 44	4344	28 37	0 0005	0 04	26-1A	90°C vapor SAW
LWA 044	Inconel 625	8 44	4344	28 30	–0 0004	–0 03	26-1B	90°C aqueous SAW
LWA 045	Inconel 625	8 44	4344	28 24	–0 0010	–0 08	26-1B	90°C aqueous SAW
LWA 046	Inconel 625	8 44	4344	28 20	–0 0006	–0 05	26-1B	90°C aqueous SAW
LWA 047	Inconel 625	8 44	8784	28 18	0 0002	0 01	26-2A	90°C vapor SAW
LWA 048	Inconel 625	8 44	8784	28 14	0 0004	0 02	26-2A	90°C vapor SAW
LWA 049	Inconel 625	8 44	8784	28 08	0 0004	0 02	26-2A	90°C vapor SAW
LWA 050	Inconel 625	8 44	8784	28 23	–0 0003	–0 01	26-2B	90°C aqueous SAW
LWA 051	Inconel 625	8 44	8784	28 24	0 0000	0 00	26-2B	90°C aqueous SAW
LWA 052	Inconel 625	8 44	8784	28 23	0 0005	0 02	26-2B	90°C aqueous SAW
LWA 071	Inconel 625	8 44	4392	28 27	0 0011	0 09	27-1A	60°C vapor SCW
LWA 072	Inconel 625	8 44	4392	28 24	0 0008	0 07	27-1A	60°C vapor SCW
LWA 073	Inconel 625	8 44	4392	28 25	0 0010	0 08	27-1A	60°C vapor SCW
LWA 074	Inconel 625	8 44	4392	28 26	0 0009	0 08	27-1B	60°C aqueous SCW
LWA 075	Inconel 625	8 44	4392	28 27	0 0006	0 05	27-1B	60°C aqueous SCW
LWA 076	Inconel 625	8 44	4392	28 45	0 0012	0 10	27-1B	60°C aqueous SCW
LWA 101	Inconel 625	8 44	4392	28 25	0 0013	0 11	27-1A	60°C water line SCW
LWA 106	Inconel 625	8 44	4464	28 33	0 0005	0 04	28-1A	90°C water line SCW
LWA 111	Inconel 625	8 44	4464	28 10	0 0004	0 03	28-1A	90°C vapor SCW
LWA 112	Inconel 625	8 44	4464	28 27	0 0004	0 03	28-1A	90°C vapor SCW
LWA 113	Inconel 625	8 44	4464	28 25	0 0004	0.03	28-1A	90°C vapor SCW
LWA 114	Inconel 625	8 44	4464	28 17	0 0006	0 05	28-1B	90°C aqueous SCW
LWA 115	Inconel 625	8 44	4464	28 21	0 0009	0 07	28-1B	90°C aqueous SCW
LWA 116	Inconel 625	8 44	4464	28 12	0 0005	0 04	28-1B	90°C aqueous SCW
LWA 141	Inconel 625	8 44	4464	28 31	0 0009	0 07	29-1A	60°C vapor SDW
LWA 142	Inconel 625	8 44	4464	28 34	0 0006	0 05	29-1B	60°C aqueous SDW
LWA 151	Inconel 625	8 44	4464	28 25	0 0002	0 02	29-1A	60°C water line SDW
LWA 164	Inconel 625	8 44	4392	28 25	0 0007	0 06	30-1A	90°C water line SDW

Sample identification	Alloy	Density (g/cc)	Exposure time (hours)	Surface area (sq cm)	Weight loss (g)	Corrosion rate (μm/y)	Vessel number-rack number	Test environment
LWA 168	Inconel 625	8 44	4392	28 20	0 0005	0 04	30-1A	90°C vapor SDW
LWA 169	Inconel 625	8 44	4392	28 11	0 0012	0 10	30-1B	90°C aqueous SDW
LWJ 001	Inconel 625	8 44	4296	27 60	–0 0004	–0 04	25-1A	60°C vapor SAW
LWJ 002	Inconel 625	8 44	4296	27 71	–0 0012	–0 10	25-1A	60°C vapor SAW
LWJ 003	Inconel 625	8 44	4296	27 72	0 0000	0 00	25-1A	60°C vapor SAW
LWJ 004	Inconel 625	8 44	4296	27 74	–0 0001	–0 01	25-1B	60°C aqueous SAW
LWJ 005	Inconel 625	8 44	4296	27 68	0 0004	0 03	25-1B	60°C aqueous SAW
LWJ 006	Inconel 625	8 44	4296	27 71	–0 0004	–0 03	25-1B	60°C aqueous SAW
LWJ 007	Inconel 625	8 44	8376	27.79	0 0000	0 00	25-2A	60°C vapor SAW
LWJ 008	Inconel 625	8 44	8376	27 70	0 0000	0 00	25-2A	60°C vapor SAW
LWJ 009	Inconel 625	8 44	8376	27 77	–0 0001	0 00	25-2A	60°C vapor SAW
LWJ 010	Inconel 625	8 44	8376	27 62	0 0001	0 00	25-2B	60°C aqueous SAW
LWJ 011	Inconel 625	8 44	8376	27 76	0 0002	0 01	25-2B	60°C aqueous SAW
LWJ 012	Inconel 625	8 44	8376	27 74	–0 0002	–0 01	25-2B	60°C aqueous SAW
LWJ 031	Inconel 625	8 44	4296	27 62	–0 0004	–0 03	25-1B	60°C water line SAW
LWJ 032	Inconel 625	8 44	8376	27 54	–0 0002	–0 01	25-2B	60°C water line SAW
LWJ 036	Inconel 625	8 44	4344	27 58	0 0002	0 02	26-1B	90°C water line SAW
LWJ 037	Inconel 625	8 44	8784	27 63	–0 0001	0 00	26-2B	90°C water line SAW
LWJ 041	Inconel 625	8 44	4344	27 47	0 0001	0 01	26-1A	90°C vapor SAW
LWJ 042	Inconel 625	8 44	4344	27 66	0 0001	0 01	26-1A	90°C vapor SAW
LWJ 043	Inconel 625	8 44	4344	27 77	0 0012	0 10	26-1A	90°C vapor SAW
LWJ 044	Inconel 625	8 44	4344	27 68	0 0011	0 09	26-1B	90°C aqueous SAW
LWJ 045	Inconel 625	8 44	4344	27 79	–0 0005	–0 04	26-1B	90°C aqueous SAW
LWJ 046	Inconel 625	8 44	4344	27 67	0 0001	0 01	26-1B	90°C aqueous SAW
LWJ 047	Inconel 625	8 44	8784	27 67	0 0005	0 02	26-2A	90°C vapor SAW
LWJ 048	Inconel 625	8 44	8784	27 71	0 0004	0 02	26-2A	90°C vapor SAW
LWJ 049	Inconel 625	8 44	8784	27 84	0 0004	0 02	26-2A	90°C vapor SAW
LWJ 050	Inconel 625	8 44	8784	27 75	–0 0003	–0 01	26-2B	90°C aqueous SAW
LWJ 051	Inconel 625	8 44	8784	27.77	–0 0003	–0 01	26-2B	90°C aqueous SAW
LWJ 052	Inconel 625	8 44	8784	27 69	0 0000	0 00	26-2B	90°C aqueous SAW
LWJ 071	Inconel 625	8 44	4392	27 89	0 0004	0 03	27-1A	60°C vapor SCW
LWJ 072	Inconel 625	8 44	4392	27 50	0 0009	0 08	27-1A	60°C vapor SCW
LWJ 073	Inconel 625	8 44	4392	27 67	0 0006	0 05	27-1A	60°C vapor SCW
LWJ 074	Inconel 625	8 44	4392	27 85	0 0012	0 10	27-1B	60°C aqueous SCW
LWJ 075	Inconel 625	8 44	4392	27 50	0 0010	0 09	27-1B	60°C aqueous SCW
LWJ 076	Inconel 625	8 44	4392	27 64	0 0007	0 06	27-1B	60°C aqueous SCW
LWJ 101	Inconel 625	8 44	4392	27 75	0 0006	0 05	27-1B	60°C water line SCW
LWJ 106	Inconel 625	8 44	4464	27 73	0 0003	0 03	28-1B	90°C water line SCW
LWJ 111	Inconel 625	8 44	4464	27 65	0 0003	0 03	28-1A	90°C vapor SCW
LWJ 112	Inconel 625	8 44	4464	27 56	–0 0002	–0 02	28-1A	90°C vapor SCW

Sample identification	Alloy	Density (g/cc)	Exposure time (hours)	Surface area (sq cm)	Weight loss (g)	Corrosion rate (μm/y)	Vessel number-rack number	Test environment
LWJ 113	Inconel 625	8 44	4464	27 78	0 0002	0 02	28-1A	90°C vapor SCW
LWJ 114	Inconel 625	8 44	4464	27 63	0 0005	0 04	28-1B	90°C aqueous SCW
LWJ 115	Inconel 625	8 44	4464	27 59	0 0005	0 04	28-1B	90°C aqueous SCW
LWJ 116	Inconel 625	8 44	4464	27.81	0 0003	0 03	28-1B	90°C aqueous SCW
LWJ 141	Inconel 625	8 44	4464	27 76	0 0002	0 02	29-1A	60°C vapor SDW
LWJ 142	Inconel 625	8 44	4464	27 77	0 0002	0 02	29-1B	60°C aqueous SDW
LWJ 151	Inconel 625	8 44	4464	27 86	0 0000	0 00	29-1B	60°C water line SDW
LWJ 164	Inconel 625	8 44	4392	27 77	0 0002	0 02	30-1B	90°C water line SDW
LWJ 168	Inconel 625	8 44	4392	27 75	0 0008	0 07	30-1A	90°C vapor SDW
LWJ 169	Inconel 625	8 44	4392	27 75	0 0004	0 03	30-1B	90°C aqueous SDW

EMCR Section 2.2.6 Supplement 2: Crevice-corrosion results.

Sample identification	Alloy	Density (g/cc)	Exposure time (hours)	Surface area (sq cm)	Weight loss (g)	Corrosion rate (μm/y)	Vessel number-rack number	Test environment
ACA 001	I825	8 14	4296	52 00	–0 0003	–0 01	25-1B	60°C vapor SAW
ACA 002	I825	8 14	4296	52 19	0 0009	0 04	25-1B	60°C vapor SAW
ACA 003	I825	8 14	4296	52 18	0 0015	0 07	25-1B	60°C vapor SAW
ACA 004	I825	8 14	4296	52 25	0 0526	2 52	25-1A	60°C aqueous SAW
ACA 005	I825	8 14	4296	52 32	0 0275	1 32	25-1A	60°C aqueous SAW
ACA 006	I825	8 14	4296	52 22	0 0091	0 44	25-1A	60°C aqueous SAW
ACA 007	I825	8 14	8376	52 10	0 0017	0 04	25-2B	60°C vapor SAW
ACA 008	I825	8 14	8376	52 13	0 0010	0 02	25-2B	60°C vapor SAW
ACA 009	I825	8 14	8376	52 42	0 0012	0 03	25-2B	60°C vapor SAW
ACA 010	I825	8 14	8376	52 39	0 1213	2 97	25-2A	60°C aqueous SAW
ACA 011	I825	8 14	8376	51 82	0 0876	2 17	25-2A	60°C aqueous SAW
ACA 012	I825	8 14	8376	52 41	0 1265	3 10	25-2A	60°C aqueous SAW
ACA 031	I825	8 14	4344	52 45	0 0029	0 14	26-1B	90°C vapor SAW
ACA 032	I825	8 14	4344	51 81	0 0017	0 08	26-1B	90°C vapor SAW
ACA 033	I825	8 14	4344	52 52	0 0015	0 07	26-1B	90°C vapor SAW
ACA 034	I825	8 14	4344	52 80	0 0634	2 97	26-1A	90°C aqueous SAW
ACA 035	I825	8 14	4344	51 90	0 0571	2 73	26-1A	90°C aqueous SAW
ACA 036	I825	8 14	4344	51 83	0 0670	3 20	26-1A	90°C aqueous SAW
ACA 037	I825	8 14	8784	51 81	0 0013	0 03	26-2B	90°C vapor SAW
ACA 038	I825	8 14	8784	52 25	0 0011	0 03	26-2B	90°C vapor SAW
ACA 039	I825	8 14	8784	52 68	0 0008	0 02	26-2B	90°C vapor SAW
ACA 040	I825	8 14	8784	52 33	0 1266	2 96	26-2A	90°C aqueous SAW
ACA 041	I825	8 14	8784	52 38	0 0996	2 33	26-2A	90°C aqueous SAW
ACA 042	I825	8 14	8784	52 66	0 1381	3 21	26-2A	90°C aqueous SAW
ACA 061	I825	8 14	4392	52 76	0 0013	0 06	27-1B	60°C vapor SCW
ACA 062	I825	8 14	4392	51 58	0 0014	0 07	27-1B	60°C vapor SCW
ACA 063	I825	8 14	4392	52 65	0 0015	0 07	27-1B	60°C vapor SCW
ACA 064	I825	8 14	4392	51 90	0 0012	0 06	27-1A	60°C aqueous SCW
ACA 065	I825	8 14	4392	52 66	0 0023	0 11	27-1A	60°C aqueous SCW
ACA 066	I825	8 14	4392	52 41	0 0018	0 08	27-1A	60°C aqueous SCW
ACA 091	I825	8 14	4464	52 43	0 0017	0 08	28-1B	90°C vapor SCW
ACA 092	I825	8 14	4464	51 84	0 0015	0 07	28-1B	90°C vapor SCW
ACA 093	I825	8 14	4464	51 98	0 0017	0 08	28-1B	90°C vapor SCW
ACA 094	I825	8 14	4464	52 00	0 0026	0 12	28-1A	90°C aqueous SCW
ACA 095	I825	8 14	4464	52 63	0 0023	0 11	28-1A	90°C aqueous SCW
ACA 096	I825	8 14	4464	51 78	0 0015	0 07	28-1A	90°C aqueous SCW
ACA 121	I825	8 14	4464	51 93	0 0021	0 10	29-1B	60°C vapor SDW
ACA 122	I825	8 14	4464	52 44	0 0023	0 11	29-1B	60°C vapor SDW

Sample identification	Alloy	Density (g/cc)	Exposure time (hours)	Surface area (sq cm)	Weight loss (g)	Corrosion rate (μm/y)	Vessel number-rack number	Test environment
ACA 123	I825	8 14	4464	52 46	0 0014	0 06	29-1B	60°C vapor SDW
ACA 124	I825	8 14	4464	52 50	0 0016	0 07	29-1A	60°C aqueous SDW
ACA 125	I825	8 14	4464	52 21	0 0022	0 10	29-1A	60°C aqueous SDW
ACA 126	I825	8 14	4464	52 54	0 0019	0 09	29-1A	60°C aqueous SDW
ACA 157	I825	8 14	4392	52 32	0 0011	0 05	30-1B	90°C vapor SDW
ACA 158	I825	8 14	4392	52 40	0 0012	0 06	30-1B	90°C vapor SDW
ACA 159	I825	8 14	4392	52 64	0 0018	0 08	30-1B	90°C vapor SDW
ACA 160	I825	8 14	4392	52 39	0 0010	0 05	30-1A	90°C aqueous SDW
ACA 161	I825	8 14	4392	52 36	0 0018	0 08	30-1A	90°C aqueous SDW
ACA 162	I825	8 14	4392	52 78	0 0028	0 13	30-1A	90°C aqueous SDW
ACB 001	I825	8 14	4296	52 10	0 0013	0 06	25-1B	60°C vapor SAW
ACB 002	I825	8 14	4296	51 90	0 0019	0 09	25-1B	60°C vapor SAW
ACB 003	I825	8 14	4296	51 07	0 0012	0 06	25-1B	60°C vapor SAW
ACB 004	I825	8 14	4296	51 88	0 0497	2 40	25-1A	60°C aqueous SAW
ACB 005	I825	8 14	4296	51 09	0 0035	0 17	25-1A	60°C aqueous SAW
ACB 006	I825	8 14	4296	51 70	0 0017	0 08	25-1A	60°C aqueous SAW
ACB 007	I825	8 14	8376	51 98	0 0002	0 00	25-2B	60°C vapor SAW
ACB 008	I825	8 14	8376	52 33	0 0000	0 00	25-2B	60°C vapor SAW
ACB 009	I825	8 14	8376	52 17	0 0001	0 00	25-2B	60°C vapor SAW
ACB 010	I825	8 14	8376	52 08	0 0872	2 15	25-2A	60°C aqueous SAW
ACB 011	I825	8 14	8376	52 70	0 0778	1 90	25-2A	60°C aqueous SAW
ACB 012	I825	8 14	8376	52 10	0 0485	1 20	25-2A	60°C aqueous SAW
ACB 031	I825	8 14	4344	51 85	0 0010	0 05	26-1B	90°C vapor SAW
ACB 032	I825	8 14	4344	52 08	0 0019	0 09	26-1B	90°C vapor SAW
ACB 033	I825	8 14	4344	51 29	0 0015	0 07	26-1B	90°C vapor SAW
ACB 034	I825	8 14	4344	51 15	0 0427	2 07	26-1A	90°C aqueous SAW
ACB 035	I825	8 14	4344	51 90	0 0281	1 34	26-1A	90°C aqueous SAW
ACB 036	I825	8 14	4344	52 67	0 0476	2 24	26-1A	90°C aqueous SAW
ACB 037	I825	8 14	8784	51 08	0 0003	0 01	26-2B	90°C vapor SAW
ACB 038	I825	8 14	8784	51 55	–0 0001	0 00	26-2B	90°C vapor SAW
ACB 039	I825	8 14	8784	52 82	0 0008	0 02	26-2B	90°C vapor SAW
ACB 040	I825	8 14	8784	52 32	0 1200	2.81	26-2A	90°C aqueous SAW
ACB 041	I825	8 14	8784	51 92	0 1536	3 62	26-2A	90°C aqueous SAW
ACB 042	I825	8 14	8784	52 19	0 1422	3 34	26-2A	90°C aqueous SAW
ACB 061	I825	8 14	4392	52 25	0 0010	0 05	27-1B	60°C vapor SCW
ACB 062	I825	8 14	4392	51 99	0 0014	0 07	27-1B	60°C vapor SCW
ACB 063	I825	8 14	4392	51.62	0 0015	0 07	27-1B	60°C vapor SCW
ACB 064	I825	8 14	4392	51 75	0 0020	0 09	27-1A	60°C aqueous SCW
ACB 065	I825	8 14	4392	51 93	0 0033	0 16	27-1A	60°C aqueous SCW
ACB 066	I825	8 14	4392	51 97	0 0016	0 08	27-1A	60°C aqueous SCW

Sample Identification	Alloy	Density (g/cc)	Exposure time (hours)	Surface area (sq cm)	Weight loss (g)	Corrosion rate (μm/y)	Vessel number-rack number	Test environment
ACB 091	I825	8 14	4464	51 61	0 0014	0 07	28-1B	90°C vapor SCW
ACB 092	I825	8 14	4464	52 17	0 0013	0 06	28-1B	90°C vapor SCW
ACB 093	I825	8 14	4464	51 60	0 0017	0 08	28-1B	90°C vapor SCW
ACB 094	I825	8 14	4464	52 29	0 0020	0 09	28-1A	90°C aqueous SCW
ACB 095	I825	8 14	4464	52 15	0 0025	0 12	28-1A	90°C aqueous SCW
ACB 096	I825	8 14	4464	52 18	0 0022	0 10	28-1A	90°C aqueous SCW
ACB 121	I825	8 14	4464	52 06	0 0014	0 06	29-1B	60°C vapor SDW
ACB 122	I825	8 14	4464	51 58	0 0015	0 07	29-1B	60°C vapor SDW
ACB 123	I825	8 14	4464	51 58	0 0020	0 09	29-1B	60°C vapor SDW
ACB 124	I825	8 14	4464	51 36	0 0018	0 08	29-1A	60°C aqueous SDW
ACB 125	I825	8 14	4464	51 73	0 0014	0 07	29-1A	60°C aqueous SDW
ACB 126	I825	8 14	4464	51 72	0 0015	0 07	29-1A	60°C aqueous SDW
ACB 157	I825	8 14	4392	52 37	0 0010	0 05	30-1B	90°C vapor SDW
ACB 158	I825	8 14	4392	51 70	0 0010	0 05	30-1B	90°C vapor SDW
ACB 159	I825	8 14	4392	50 70	0 0011	0 05	30-1B	90°C vapor SDW
ACB 160	I825	8 14	4392	51 19	0 0012	0 06	30-1A	90°C aqueous SDW
ACB 161	I825	8 14	4392	52 81	0 0012	0 06	30-1A	90°C aqueous SDW
ACB 162	I825	8 14	4392	52 63	0 0007	0 03	30-1A	90°C aqueous SDW
BCA 001	G3	8 27	4296	52 44	0 0017	0 08	25-1B	60°C vapor SAW
BCA 002	G3	8 27	4296	52 27	0 0016	0 08	25-1B	60°C vapor SAW
BCA 003	G3	8 27	4296	52 51	0 0026	0 12	25-1B	60°C vapor SAW
BCA 004	G3	8 27	4296	52 44	0 0016	0 08	25-1A	60°C aqueous SAW
BCA 005	G3	8 27	4296	51 65	0 0014	0 07	25-1A	60°C aqueous SAW
BCA 006	G3	8 27	4296	52 42	0 0016	0 08	25-1A	60°C aqueous SAW
BCA 007	G3	8 27	8376	51 97	0 0010	0 02	25-2B	60°C vapor SAW
BCA 008	G3	8 27	8376	51 75	0 0012	0 03	25-2B	60°C vapor SAW
BCA 009	G3	8 27	8376	52 41	0 0012	0 03	25-2B	60°C vapor SAW
BCA 010	G3	8 27	8376	52 74	0 0033	0 08	25-2A	60°C aqueous SAW
BCA 011	G3	8 27	8376	52 14	0 0025	0 06	25-2A	60°C aqueous SAW
BCA 012	G3	8 27	8376	52 13	0 0020	0 05	25-2A	60°C aqueous SAW
BCA 031	G3	8 27	4344	52 70	0 0020	0 09	26-1B	90°C vapor SAW
BCA 032	G3	8 27	4344	51 76	0 0008	0 04	26-1B	90°C vapor SAW
BCA 033	G3	8 27	4344	52.62	0 0018	0 08	26-1B	90°C vapor SAW
BCA 034	G3	8 27	4344	51 68	0 0031	0 15	26-1A	90°C aqueous SAW
BCA 035	G3	8 27	4344	51 87	0 0022	0 10	26-1A	90°C aqueous SAW
BCA 036	G3	8 27	4344	52 55	0 0016	0 07	26-1A	90°C aqueous SAW
BCA 037	G3	8 27	8784	51 90	0 0015	0 03	26-2B	90°C vapor SAW
BCA 038	G3	8 27	8784	52 66	0 0046	0 11	26-2B	90°C vapor SAW
BCA 039	G3	8 27	8784	52 55	0 0006	0 01	26-2B	90°C vapor SAW
BCA 040	G3	8 27	8784	52 19	0 0006	0 01	26-2A	90°C aqueous SAW

Sample identification	Alloy	Density (g/cc)	Exposure time (hours)	Surface area (sq cm)	Weight loss (g)	Corrosion rate (μm/y)	Vessel number-rack number	Test environment
BCA 041	G3	8 27	8784	52 31	0 0010	0 02	26-2A	90°C aqueous SAW
BCA 042	G3	8 27	8784	52 12	0 0013	0 03	26-2A	90°C aqueous SAW
BCA 061	G3	8 27	4392	52 23	0 0018	0 08	27-1B	60°C vapor SCW
BCA 062	G3	8 27	4392	52 64	0 0017	0 08	27-1B	60°C vapor SCW
BCA 063	G3	8 27	4392	51 98	0 0012	0 06	27-1B	60°C vapor SCW
BCA 064	G3	8 27	4392	52 86	0 0042	0 19	27-1A	60°C aqueous SCW
BCA 065	G3	8 27	4392	52 67	0 0037	0 17	27-1A	60°C aqueous SCW
BCA 066	G3	8 27	4392	51 43	0 0031	0 15	27-1A	60°C aqueous SCW
BCA 091	G3	8 27	4464	52 21	0 0006	0 03	28-1B	90°C vapor SCW
BCA 092	G3	8 27	4464	52 13	0 0010	0 05	28-1B	90°C vapor SCW
BCA 093	G3	8 27	4464	52 36	0 0004	0 02	28-1B	90°C vapor SCW
BCA 094	G3	8 27	4464	52 29	0 0019	0 09	28-1A	90°C aqueous SCW
BCA 095	G3	8 27	4464	52 56	0 0027	0 12	28-1A	90°C aqueous SCW
BCA 096	G3	8 27	4464	52 51	0 0016	0 07	28-1A	90°C aqueous SCW
BCA 121	G3	8 27	4464	51 88	0 0015	0 07	29-1B	60°C vapor SDW
BCA 122	G3	8 27	4464	52 56	0 0025	0 11	29-1B	60°C vapor SDW
BCA 123	G3	8 27	4464	51 85	0 0016	0 07	29-1B	60°C vapor SDW
BCA 124	G3	8 27	4464	52 41	0 0010	0 05	29-1A	60°C aqueous SDW
BCA 125	G3	8 27	4464	52 00	0 0016	0 07	29-1A	60°C aqueous SDW
BCA 126	G3	8 27	4464	52 45	0 0017	0 08	29-1A	60°C aqueous SDW
BCA 157	G3	8 27	4392	51 95	0 0012	0 06	30-1B	90°C vapor SDW
BCA 158	G3	8 27	4392	51 87	0 0021	0 10	30-1B	90°C vapor SDW
BCA 159	G3	8 27	4392	52 12	0 0018	0 08	30-1B	90°C vapor SDW
BCA 160	G3	8 27	4392	52 29	0 0019	0 09	30-1A	90°C aqueous SDW
BCA 161	G3	8 27	4392	52 20	0 0020	0 09	30-1A	90°C aqueous SDW
BCA 162	G3	8 27	4392	52 32	0 0022	0 10	30-1A	90°C aqueous SDW
BCC 001	G3	8 27	4296	52 27	0 0013	0 06	25-1B	60°C vapor SAW
BCC 002	G3	8 27	4296	52 26	0 0012	0 06	25-1B	60°C vapor SAW
BCC 003	G3	8 27	4296	52 33	0 0010	0 05	25-1B	60°C vapor SAW
BCC 004	G3	8 27	4296	51 94	0 0020	0 09	25-1A	60°C aqueous SAW
BCC 005	G3	8 27	4296	52 61	0 0014	0 07	25-1A	60°C aqueous SAW
BCC 006	G3	8 27	4296	52 43	0 0009	0 04	25-1A	60°C aqueous SAW
BCC 007	G3	8 27	8376	52 23	0 0015	0 04	25-2B	60°C vapor SAW
BCC 008	G3	8 27	8376	52 72	0 0012	0 03	25-2B	60°C vapor SAW
BCC 009	G3	8 27	8376	53 00	0 0005	0 01	25-2B	60°C vapor SAW
BCC 010	G3	8 27	8376	52 02	0 0019	0 05	25-2A	60°C aqueous SAW
BCC 011	G3	8 27	8376	52 22	0 0021	0 05	25-2A	60°C aqueous SAW
BCC 012	G3	8 27	8376	52 33	0 0021	0 05	25-2A	60°C aqueous SAW
BCC 031	G3	8 27	4344	52 54	0 0006	0 03	26-1B	90°C vapor SAW
BCC 032	G3	8 27	4344	52 74	0 0012	0 06	26-1B	90°C vapor SAW

Sample identification	Alloy	Density (g/cc)	Exposure time (hours)	Surface area (sq cm)	Weight loss (g)	Corrosion rate (μm/y)	Vessel number-rack number	Test environment
BCC 033	G3	8 27	4344	52 36	0 0013	0 06	26-1B	90°C vapor SAW
BCC 034	G3	8 27	4344	52 84	0 0013	0 06	26-1A	90°C aqueous SAW
BCC 035	G3	8 27	4344	52 38	0 0011	0 05	26-1A	90°C aqueous SAW
BCC 036	G3	8 27	4344	52 61	0 0223	1 03	26-1A	90°C aqueous SAW
BCC 037	G3	8 27	8784	52 38	0 0001	0 00	26-2B	90°C vapor SAW
BCC 038	G3	8 27	8784	52 54	0 0004	0 01	26-2B	90°C vapor SAW
BCC 039	G3	8 27	8784	52 08	0 0003	0 01	26-2B	90°C vapor SAW
BCC 040	G3	8 27	8784	52 48	0 0081	0 19	26-2A	90°C aqueous SAW
BCC 041	G3	8 27	8784	52 58	0 0003	0 01	26-2A	90°C aqueous SAW
BCC 042	G3	8 27	8784	52 11	0 0008	0 02	26-2A	90°C aqueous SAW
BCC 061	G3	8 27	4392	52 33	0 0019	0 09	27-1B	60°C vapor SCW
BCC 062	G3	8 27	4392	52 31	0 0016	0 07	27-1B	60°C vapor SCW
BCC 063	G3	8 27	4392	52 10	0 0013	0 06	27-1B	60°C vapor SCW
BCC 064	G3	8 27	4392	52 66	0 0022	0 10	27-1A	60°C aqueous SCW
BCC 065	G3	8 27	4392	51 88	0 0020	0 09	27-1A	60°C aqueous SCW
BCC 066	G3	8 27	4392	52 02	0 0026	0 12	27-1A	60°C aqueous SCW
BCC 091	G3	8 27	4464	52 04	0 0010	0 05	28-1B	90°C vapor SCW
BCC 092	G3	8 27	4464	53 37	0 0007	0 03	28-1B	90°C vapor SCW
BCC 093	G3	8 27	4464	52 56	0 0008	0 04	28-1B	90°C vapor SCW
BCC 094	G3	8 27	4464	52 02	0 0029	0 13	28-1A	90°C aqueous SCW
BCC 095	G3	8 27	4464	52 80	0 0028	0 13	28-1A	90°C aqueous SCW
BCC 096	G3	8 27	4464	50 97	0 0036	0 17	28-1A	90°C aqueous SCW
BCC 121	G3	8 27	4464	52 44	0 0013	0 06	29-1B	60°C vapor SDW
BCC 122	G3	8 27	4464	51 84	0 0009	0 04	29-1B	60°C vapor SDW
BCC 123	G3	8 27	4464	52 32	0 0017	0 08	29-1B	60°C vapor SDW
BCC 124	G3	8 27	4464	52 21	0 0012	0 05	29-1A	60°C aqueous SDW
BCC 125	G3	8 27	4464	52 19	0 0017	0 08	29-1A	60°C aqueous SDW
BCC 126	G3	8 27	4464	52 59	0 0013	0 06	29-1A	60°C aqueous SDW
BCC 157	G3	8 27	4392	52 34	0 0019	0 09	30-1B	90°C vapor SDW
BCC 158	G3	8 27	4392	52 18	0 0007	0 03	30-1B	90°C vapor SDW
BCC 159	G3	8 27	4392	52 55	0 0012	0 06	30-1B	90°C vapor SDW
BCC 160	G3	8 27	4392	52 60	0 0015	0 07	30-1A	90°C aqueous SDW
BCC 161	G3	8 27	4392	52 38	0 0009	0 04	30-1A	90°C aqueous SDW
BCC 162	G3	8 27	4392	52 30	0 0014	0 06	30-1A	90°C aqueous SDW
CCA 001	C4	8 60	4296	52 02	0 0035	0 16	25-1B	60°C vapor SAW
CCA 002	C4	8 60	4296	51 91	0 0015	0 07	25-1B	60°C vapor SAW
CCA 003	C4	8 60	4296	52 03	0 0024	0 11	25-1B	60°C vapor SAW
CCA 004	C4	8 60	4296	51 99	0 0028	0 13	25-1A	60°C aqueous SAW
CCA 005	C4	8 60	4296	51 95	0 0022	0 10	25-1A	60°C aqueous SAW
CCA 006	C4	8 60	4296	52 07	0 0024	0 11	25-1A	60°C aqueous SAW

Sample Identification	Alloy	Density (g/cc)	Exposure time (hours)	Surface area (sq cm)	Weight loss (g)	Corrosion rate (μm/y)	Vessel number-rack number	Test environment
CCA 007	C4	8 60	8376	51 95	0 0013	0 03	25-2B	60°C vapor SAW
CCA 008	C4	8 60	8376	51 98	0 0011	0 03	25-2B	60°C vapor SAW
CCA 009	C4	8 60	8376	51 96	0 0010	0 02	25-2B	60°C vapor SAW
CCA 010	C4	8 60	8376	51 95	0 0025	0 06	25-2A	60°C aqueous SAW
CCA 011	C4	8 60	8376	52 08	0 0029	0 07	25-2A	60°C aqueous SAW
CCA 012	C4	8 60	8376	51 87	0 0033	0 08	25-2A	60°C aqueous SAW
CCA 031	C4	8 60	4344	52 30	0 0009	0 04	26-1B	90°C vapor SAW
CCA 032	C4	8 60	4344	50 78	0 0008	0 04	26-1B	90°C vapor SAW
CCA 033	C4	8 60	4344	51 46	0 0005	0 02	26-1B	90°C vapor SAW
CCA 034	C4	8 60	4344	51 39	0 0058	0 26	26-1A	90°C aqueous SAW
CCA 035	C4	8 60	4344	51 43	0 0048	0 22	26-1A	90°C aqueous SAW
CCA 036	C4	8 60	4344	51 33	0 0057	0 26	26-1A	90°C aqueous SAW
CCA 037	C4	8 60	8784	52 50	0 0024	0 05	26-2B	90°C vapor SAW
CCA 038	C4	8 60	8784	51 51	0 0025	0 06	26-2B	90°C vapor SAW
CCA 039	C4	8 60	8784	50 70	0 0021	0 05	26-2B	90°C vapor SAW
CCA 040	C4	8 60	8784	51 52	0 0066	0 15	26-2A	90°C aqueous SAW
CCA 041	C4	8 60	8784	51 35	0 0061	0 14	26-2A	90°C aqueous SAW
CCA 042	C4	8 60	8784	50 77	0 0060	0 14	26-2A	90°C aqueous SAW
CCA 061	C4	8 60	4392	51 46	0 0022	0 10	27-1B	60°C vapor SCW
CCA 062	C4	8 60	4392	52 08	0 0017	0 08	27-1B	60°C vapor SCW
CCA 063	C4	8 60	4392	52 17	0 0019	0 08	27-1B	60°C vapor SCW
CCA 064	C4	8 60	4392	51 89	0 0025	0 11	27-1A	60°C aqueous SCW
CCA 065	C4	8 60	4392	51 72	0 0024	0 11	27-1A	60°C aqueous SCW
CCA 066	C4	8 60	4392	51 68	0 0038	0 17	27-1A	60°C aqueous SCW
CCA 091	C4	8 60	4464	52 43	0 0007	0 03	28-1B	90°C vapor SCW
CCA 092	C4	8 60	4464	52 22	0 0004	0 02	28-1B	90°C vapor SCW
CCA 093	C4	8 60	4464	52 32	0 0010	0 04	28-1B	90°C vapor SCW
CCA 094	C4	8 60	4464	52 31	0 0026	0 11	28-1A	90°C aqueous SCW
CCA 095	C4	8 60	4464	52 43	0 0031	0 13	28-1A	90°C aqueous SCW
CCA 096	C4	8 60	4464	52 41	0 0028	0 12	28-1A	90°C aqueous SCW
CCA 121	C4	8 60	4464	52 45	0 0011	0 05	29-1B	60°C vapor SDW
CCA 122	C4	8 60	4464	51 97	0 0007	0 03	29-1B	60°C vapor SDW
CCA 123	C4	8 60	4464	52 18	0 0017	0 07	29-1B	60°C vapor SDW
CCA 124	C4	8 60	4464	52 14	0 0009	0 04	29-1A	60°C aqueous SDW
CCA 125	C4	8 60	4464	52 35	0 0014	0 06	29-1A	60°C aqueous SDW
CCA 126	C4	8 60	4464	52 20	0 0008	0 03	29-1A	60°C aqueous SDW
CCA 157	C4	8 60	4392	52 16	0 0011	0 05	30-1B	90°C vapor SDW
CCA 158	C4	8 60	4392	52 32	0 0020	0 09	30-1B	90°C vapor SDW
CCA 159	C4	8 60	4392	52 24	0 0025	0 11	30-1B	90°C vapor SDW
CCA 160	C4	8 60	4392	52 24	0 0004	0 02	30-1A	90°C aqueous SDW

Sample identification	Alloy	Density (g/cc)	Exposure time (hours)	Surface area (sq cm)	Weight loss (g)	Corrosion rate (μm/y)	Vessel number-rack number	Test environment
CCA 161	C4	8 60	4392	51 67	0 0013	0 06	30-1A	90°C aqueous SDW
CCA 162	C4	8 60	4392	51 12	0 0018	0 08	30-1A	90°C aqueous SDW
CCB 001	C4	8 60	4296	51 27	0 0025	0 12	25-1B	60°C vapor SAW
CCB 002	C4	8 60	4296	51 26	0 0020	0 09	25-1B	60°C vapor SAW
CCB 003	C4	8 60	4296	50 70	0 0024	0 11	25-1B	60°C vapor SAW
CCB 004	C4	8 60	4296	51 04	0 0043	0 20	25-1A	60°C aqueous SAW
CCB 005	C4	8 60	4296	50 66	0 0030	0 14	25-1A	60°C aqueous SAW
CCB 006	C4	8 60	4296	51 00	0 0027	0 13	25-1A	60°C aqueous SAW
CCB 007	C4	8 60	8376	50 70	0 0019	0 05	25-2B	60°C vapor SAW
CCB 008	C4	8 60	8376	51 63	0 0022	0 05	25-2B	60°C vapor SAW
CCB 009	C4	8 60	8376	51.55	0 0018	0 04	25-2B	60°C vapor SAW
CCB 010	C4	8 60	8376	51 30	0 0038	0 09	25-2A	60°C aqueous SAW
CCB 011	C4	8 60	8376	51 79	0 0040	0 09	25-2A	60°C aqueous SAW
CCB 012	C4	8 60	8376	50 86	0 0033	0 08	25-2A	60°C aqueous SAW
CCB 031	C4	8 60	4344	51 95	0 0042	0 19	26-1B	90°C vapor SAW
CCB 032	C4	8 60	4344	51.19	0 0018	0 08	26-1B	90°C vapor SAW
CCB 033	C4	8 60	4344	50 55	0 0012	0 06	26-1B	90°C vapor SAW
CCB 034	C4	8 60	4344	51 30	0 0036	0 16	26-1A	90°C aqueous SAW
CCB 035	C4	8 60	4344	50 86	0 0035	0 16	26-1A	90°C aqueous SAW
CCB 036	C4	8 60	4344	52 05	0 0047	0 21	26-1A	90°C aqueous SAW
CCB 037	C4	8 60	8784	51 14	0 0021	0 05	26-2B	90°C vapor SAW
CCB 038	C4	8 60	8784	51 30	0 0020	0 05	26-2B	90°C vapor SAW
CCB 039	C4	8 60	8784	51 08	0 0021	0 05	26-2B	90°C vapor SAW
CCB 040	C4	8 60	8784	51 72	0 0044	0 10	26-2A	90°C aqueous SAW
CCB 041	C4	8 60	8784	51 66	0 0049	0 11	26-2A	90°C aqueous SAW
CCB 042	C4	8 60	8784	50 86	0 0042	0 10	26-2A	90°C aqueous SAW
CCB 061	C4	8 60	4392	51 75	0 0008	0 04	27-1B	60°C vapor SCW
CCB 062	C4	8 60	4392	51 63	0 0011	0 05	27-1B	60°C vapor SCW
CCB 063	C4	8 60	4392	51 39	0 0009	0 04	27-1B	60°C vapor SCW
CCB 064	C4	8 60	4392	51 47	0 0026	0 12	27-1A	60°C aqueous SCW
CCB 065	C4	8 60	4392	51 14	0 0026	0 12	27-1A	60°C aqueous SCW
CCB 066	C4	8 60	4392	51 63	0 0030	0 13	27-1A	60°C aqueous SCW
CCB 091	C4	8 60	4464	51 25	0 0005	0 02	28-1B	90°C vapor SCW
CCB 092	C4	8 60	4464	51.44	0 0002	0 01	28-1B	90°C vapor SCW
CCB 093	C4	8 60	4464	51 55	0 0009	0 04	28-1B	90°C vapor SCW
CCB 094	C4	8 60	4464	51 59	0 0024	0 11	28-1A	90°C aqueous SCW
CCB 095	C4	8 60	4464	51 75	0 0032	0 14	28-1A	90°C aqueous SCW
CCB 096	C4	8 60	4464	51 37	0 0038	0 17	28-1A	90°C aqueous SCW
CCB 121	C4	8 60	4464	51 66	0 0012	0 05	29-1B	60°C vapor SDW
CCB 122	C4	8 60	4464	50 70	0 0009	0 04	29-1B	60°C vapor SDW

Sample identification	Alloy	Density (g/cc)	Exposure time (hours)	Surface area (sq cm)	Weight loss (g)	Corrosion rate (μm/y)	Vessel number-rack number	Test environment
CCB 123	C4	8 60	4464	51 24	0 0014	0 06	29-1B	60°C vapor SDW
CCB 124	C4	8 60	4464	51 73	0 0016	0 07	29-1A	60°C aqueous SDW
CCB 125	C4	8 60	4464	51 46	0 0013	0 06	29-1A	60°C aqueous SDW
CCB 126	C4	8 60	4464	51 54	0 0010	0 04	29-1A	60°C aqueous SDW
CCB 157	C4	8 60	4392	51 43	0 0009	0 04	30-1B	90°C vapor SDW
CCB 158	C4	8 60	4392	51 08	0 0020	0 09	30-1B	90°C vapor SDW
CCB 159	C4	8 60	4392	51 06	0 0015	0 07	30-1B	90°C vapor SDW
CCB 160	C4	8 60	4392	51 29	0 0011	0 05	30-1A	90°C aqueous SDW
CCB 161	C4	8 60	4392	50 94	0 0014	0 06	30-1A	90°C aqueous SDW
CCB 162	C4	8 60	4392	51 01	0 0010	0 05	30-1A	90°C aqueous SDW
DCA 001	C22	8 60	4296	52 52	0 0019	0 09	25-1B	60°C vapor SAW
DCA 002	C22	8 60	4296	52 64	0 0025	0 11	25-1B	60°C vapor SAW
DCA 003	C22	8 60	4296	52 36	0 0017	0 08	25-1B	60°C vapor SAW
DCA 004	C22	8 60	4296	52 57	0 0023	0 10	25-1A	60°C aqueous SAW
DCA 005	C22	8 60	4296	52 64	0 0018	0 08	25-1A	60°C aqueous SAW
DCA 006	C22	8 60	4296	52 88	0 0026	0 12	25-1A	60°C aqueous SAW
DCA 007	C22	8 60	8376	51 99	0 0018	0 04	25-2B	60°C vapor SAW
DCA 008	C22	8 60	8376	52 69	0 0022	0 05	25-2B	60°C vapor SAW
DCA 009	C22	8 60	8376	52 40	0 0038	0 09	25-2B	60°C vapor SAW
DCA 010	C22	8 60	8376	52 87	0 0022	0 05	25-2A	60°C aqueous SAW
DCA 011	C22	8 60	8376	52 76	0 0018	0 04	25-2A	60°C aqueous SAW
DCA 012	C22	8 60	8376	52 50	0 0021	0 05	25-2A	60°C aqueous SAW
DCA 031	C22	8 60	4344	52 64	0 0017	0 08	26-1B	90°C vapor SAW
DCA 032	C22	8 60	4344	51 56	0 0012	0 05	26-1B	90°C vapor SAW
DCA 033	C22	8 60	4344	52 83	0 0022	0 10	26-1B	90°C vapor SAW
DCA 034	C22	8 60	4344	52 65	0 0055	0 24	26-1A	90°C aqueous SAW
DCA 035	C22	8 60	4344	52 62	0 0164	0 73	26-1A	90°C aqueous SAW
DCA 036	C22	8 60	4344	52 03	0 0039	0 18	26-1A	90°C aqueous SAW
DCA 037	C22	8 60	8784	52 78	0 0014	0 03	26-2B	90°C vapor SAW
DCA 038	C22	8 60	8784	51 69	0 0022	0 05	26-2B	90°C vapor SAW
DCA 039	C22	8 60	8784	52 85	0 0012	0 03	26-2B	90°C vapor SAW
DCA 040	C22	8 60	8784	51 72	0 0019	0 04	26-2A	90°C aqueous SAW
DCA 041	C22	8 60	8784	52 57	0 0018	0 04	26-2A	90°C aqueous SAW
DCA 042	C22	8 60	8784	51 66	0 0010	0 02	26-2A	90°C aqueous SAW
DCA 061	C22	8 60	4392	52 39	0 0018	0 08	27-1B	60°C vapor SCW
DCA 062	C22	8 60	4392	52 48	0 0022	0 10	27-1B	60°C vapor SCW
DCA 063	C22	8 60	4392	52 37	0 0023	0 10	27-1B	60°C vapor SCW
DCA 064	C22	8 60	4392	52 07	0 0022	0 10	27-1A	60°C aqueous SCW
DCA 065	C22	8 60	4392	51 54	0 0024	0 11	27-1A	60°C aqueous SCW
DCA 066	C22	8 60	4392	52 61	0 0024	0 11	27-1A	60°C aqueous SCW

Sample identification	Alloy	Density (g/cc)	Exposure time (hours)	Surface area (sq cm)	Weight loss (g)	Corrosion rate (μm/y)	Vessel number-rack number	Test environment
DCA 091	C22	8 60	4464	52 85	0 0016	0 07	28-1B	90°C vapor SCW
DCA 092	C22	8 60	4464	51 95	0 0011	0 05	28-1B	90°C vapor SCW
DCA 093	C22	8 60	4464	52 74	0 0108	0 47	28-1B	90°C vapor SCW
DCA 094	C22	8 60	4464	52 41	0 0023	0 10	28-1A	90°C aqueous SCW
DCA 095	C22	8 60	4464	52 40	0 0015	0 07	28-1A	90°C aqueous SCW
DCA 096	C22	8 60	4464	52 63	0 0033	0 14	28-1A	90°C aqueous SCW
DCA 121	C22	8 60	4464	52 49	0 0022	0 10	29-1B	60°C vapor SDW
DCA 122	C22	8 60	4464	52 55	0 0017	0 07	29-1B	60°C vapor SDW
DCA 123	C22	8 60	4464	52 64	0 0020	0 09	29-1B	60°C vapor SDW
DCA 124	C22	8 60	4464	52 69	0 0020	0 09	29-1A	60°C aqueous SDW
DCA 125	C22	8 60	4464	52 56	0 0015	0 07	29-1A	60°C aqueous SDW
DCA 126	C22	8 60	4464	52 65	0 0013	0 06	29-1A	60°C aqueous SDW
DCA 157	C22	8 60	4392	51 97	0 0013	0 06	30-1B	90°C vapor SDW
DCA 158	C22	8 60	4392	52 26	0 0014	0 06	30-1B	90°C vapor SDW
DCA 159	C22	8 60	4392	52 00	0 0013	0 06	30-1B	90°C vapor SDW
DCA 160	C22	8 60	4392	51 94	0 0023	0 10	30-1A	90°C aqueous SDW
DCA 161	C22	8 60	4392	51 83	0 0027	0 12	30-1A	90°C aqueous SDW
DCA 162	C22	8 60	4392	51 71	0 0011	0 05	30-1A	90°C aqueous SDW
DCB 001	C22	8 60	4296	50 71	0 0006	0 03	25-1B	60°C vapor SAW
DCB 002	C22	8 60	4296	50 63	0 0004	0 02	25-1B	60°C vapor SAW
DCB 003	C22	8 60	4296	50 95	0 0002	0 01	25-1B	60°C vapor SAW
DCB 004	C22	8 60	4296	50 62	0 0014	0 07	25-1A	60°C aqueous SAW
DCB 005	C22	8 60	4296	50 21	0 0014	0 07	25-1A	60°C aqueous SAW
DCB 006	C22	8 60	4296	50 38	0 0010	0 05	25-1A	60°C aqueous SAW
DCB 007	C22	8 60	8376	50 79	0 0010	0 02	25-2B	60°C vapor SAW
DCB 008	C22	8 60	8376	50 08	0 0011	0 03	25-2B	60°C vapor SAW
DCB 009	C22	8 60	8376	50 25	0 0012	0 03	25-2B	60°C vapor SAW
DCB 010	C22	8 60	8376	51 33	0 0041	0 10	25-2A	60°C aqueous SAW
DCB 011	C22	8 60	8376	50 65	0 0015	0 04	25-2A	60°C aqueous SAW
DCB 012	C22	8 60	8376	50 33	0 0019	0 05	25-2A	60°C aqueous SAW
DCB 031	C22	8 60	4344	50 40	0 0011	0 05	26-1B	90°C vapor SAW
DCB 032	C22	8 60	4344	50 21	0 0010	0 05	26-1B	90°C vapor SAW
DCB 033	C22	8 60	4344	50 45	0 0015	0 07	26-1B	90°C vapor SAW
DCB 034	C22	8 60	4344	50 25	0 0000	0 00	26-1A	90°C aqueous SAW
DCB 035	C22	8 60	4344	50 70	0 0009	0 04	26-1A	90°C aqueous SAW
DCB 036	C22	8 60	4344	50 29	0 0023	0 11	26-1A	90°C aqueous SAW
DCB 037	C22	8 60	8784	50 44	0.0007	0 02	26-2B	90°C vapor SAW
DCB 038	C22	8 60	8784	50 04	0 0008	0 02	26-2B	90°C vapor SAW
DCB 039	C22	8 60	8784	50 55	0 0007	0 02	26-2B	90°C vapor SAW
DCB 040	C22	8 60	8784	51 32	0 0025	0 06	26-2A	90°C aqueous SAW

Sample identification	Alloy	Density (g/cc)	Exposure time (hours)	Surface area (sq cm)	Weight loss (g)	Corrosion rate (μm/y)	Vessel number-rack number	Test environment
DCB 041	C22	8 60	8784	50 37	0 0012	0 03	26-2A	90°C aqueous SAW
DCB 042	C22	8 60	8784	51 57	0 0045	0 10	26-2A	90°C aqueous SAW
DCB 061	C22	8 60	4392	50 41	0 0012	0 06	27-1B	60°C vapor SCW
DCB 062	C22	8 60	4392	51 69	0 0023	0 10	27-1B	60°C vapor SCW
DCB 063	C22	8 60	4392	51 62	0 0025	0 11	27-1B	60°C vapor SCW
DCB 064	C22	8 60	4392	50 13	0 0028	0 13	27-1A	60°C aqueous SCW
DCB 065	C22	8 60	4392	50 34	0 0020	0 09	27-1A	60°C aqueous SCW
DCB 066	C22	8 60	4392	50 41	0 0019	0 09	27-1A	60°C aqueous SCW
DCB 091	C22	8 60	4464	51 48	0 0000	0 00	28-1B	90°C vapor SCW
DCB 092	C22	8 60	4464	51 39	0 0006	0 03	28-1B	90°C vapor SCW
DCB 093	C22	8 60	4464	51 21	0 0009	0 04	28-1B	90°C vapor SCW
DCB 094	C22	8 60	4464	51 11	0 0015	0 07	28-1A	90°C aqueous SCW
DCB 095	C22	8 60	4464	51 91	0 0057	0 25	28-1A	90°C aqueous SCW
DCB 096	C22	8 60	4464	51 53	0 0023	0 10	28-1A	90°C aqueous SCW
DCB 121	C22	8 60	4464	50 84	0 0016	0 07	29-1B	60°C vapor SDW
DCB 122	C22	8 60	4464	50 83	0 0019	0 09	29-1B	60°C vapor SDW
DCB 123	C22	8 60	4464	50 97	0 0020	0 09	29-1B	60°C vapor SDW
DCB 124	C22	8 60	4464	50 81	0 0022	0 10	29-1A	60°C aqueous SDW
DCB 125	C22	8 60	4464	50 01	0 0016	0 07	29-1A	60°C aqueous SDW
DCB 126	C22	8 60	4464	51 73	0 0023	0 10	29-1A	60°C aqueous SDW
DCB 157	C22	8 60	4392	50 49	0 0016	0 07	30-1B	90°C vapor SDW
DCB 158	C22	8 60	4392	50 80	0 0017	0 08	30-1B	90°C vapor SDW
DCB 159	C22	8 60	4392	51 75	0 0011	0 05	30-1B	90°C vapor SDW
DCB 160	C22	8 60	4392	50 89	0 0014	0 06	30-1A	90°C aqueous SDW
DCB 161	C22	8 60	4392	51 69	0 0018	0 08	30-1A	90°C aqueous SDW
DCB 162	C22	8 60	4392	50 76	0 0009	0 04	30-1A	90°C aqueous SDW
ECA 001	Ti Grade 12	4 43	4296	52 24	0 0567	5 00	25-1B	60°C vapor SAW
ECA 002	Ti Grade 12	4 43	4296	53 56	0 0555	4 77	25-1B	60°C vapor SAW
ECA 003	Ti Grade 12	4 43	4296	50 30	0 0936	8 56	25-1B	60°C vapor SAW
ECA 004	Ti Grade 12	4 43	4296	51 92	0 0855	7 58	25-1A	60°C aqueous SAW
ECA 005	Ti Grade 12	4 43	4296	52 94	0 0649	5 64	25-1A	60°C aqueous SAW
ECA 006	Ti Grade 12	4 43	4296	49 19	0 0812	7 60	25-1A	60°C aqueous SAW
ECA 007	Ti Grade 12	4 43	8376	51 01	-0 0005	–0 02	25-2B	60°C vapor SAW
ECA 008	Ti Grade 12	4 43	8376	50 33	0 0002	0 01	25-2B	60°C vapor SAW
ECA 009	Ti Grade 12	4 43	8376	52 67	–0 0006	–0 03	25-2B	60°C vapor SAW
ECA 010	Ti Grade 12	4 43	8376	51 11	0 0010	0 05	25-2A	60°C aqueous SAW
ECA 011	Ti Grade 12	4.43	8376	51 44	0 0015	0 07	25-2A	60°C aqueous SAW
ECA 012	Ti Grade 12	4.43	8376	50 99	0 0009	0 04	25-2A	60°C aqueous SAW
ECA 031	Ti Grade 12	4.43	4344	53 01	0 1173	10 07	26-1B	90°C vapor SAW
ECA 032	Ti Grade 12	4 43	4344	53 15	0 0934	8 00	26-1B	90°C vapor SAW

Sample identification	Alloy	Density (g/cc)	Exposure time (hours)	Surface area (sq cm)	Weight loss (g)	Corrosion rate (μm/y)	Vessel number-rack number	Test environment
ECA 033	Ti Grade 12	4 43	4344	53 69	0 0477	4 04	26-1B	90°C vapor SAW
ECA 034	Ti Grade 12	4 43	4344	53 74	0 0063	0 53	26-1A	90°C aqueous SAW
ECA 035	Ti Grade 12	4 43	4344	50 80	0 0501	4 49	26-1A	90°C aqueous SAW
ECA 036	Ti Grade 12	4 43	4344	50 38	0 0583	5 27	26-1A	90°C aqueous SAW
ECA 037	Ti Grade 12	4 43	8784	51 01	–0 0010	–0 04	26-2B	90°C vapor SAW
ECA 038	Ti Grade 12	4 43	8784	51 57	–0 0020	–0 09	26-2B	90°C vapor SAW
ECA 039	Ti Grade 12	4 43	8784	51 32	–0 0015	–0 07	26-2B	90°C vapor SAW
ECA 040	Ti Grade 12	4 43	8784	51 06	–0 0097	–0 43	26-2A	90°C aqueous SAW
ECA 041	Ti Grade 12	4 43	8784	50 73	–0 0061	–0 27	26-2A	90°C aqueous SAW
ECA 042	Ti Grade 12	4 43	8784	50 53	–0 0056	–0 25	26-2A	90°C aqueous SAW
ECA 061	Ti Grade 12	4 43	4392	52 67	0 0948	8 10	27-1B	60°C vapor SCW
ECA 062	Ti Grade 12	4 43	4392	52 56	0 1051	9 00	27-1B	60°C vapor SCW
ECA 063	Ti Grade 12	4 43	4392	52 49	0 0789	6 77	27-1B	60°C vapor SCW
ECA 064	Ti Grade 12	4 43	4392	51 72	0 0861	7 49	27-1A	60°C aqueous SCW
ECA 065	Ti Grade 12	4 43	4392	52 62	0 0897	7 68	27-1A	60°C aqueous SCW
ECA 066	Ti Grade 12	4 43	4392	51 50	0 0821	7 18	27-1A	60°C aqueous SCW
ECA 091	Ti Grade 12	4 43	4464	52 76	0 1209	10 15	28-1B	90°C vapor SCW
ECA 092	Ti Grade 12	4 43	4464	52 77	0 0921	7 73	28-1B	90°C vapor SCW
ECA 093	Ti Grade 12	4 43	4464	52 76	0 0739	6 20	28-1B	90°C vapor SCW
ECA 094	Ti Grade 12	4 43	4464	52 28	0 4216	35 72	28-1A	90°C aqueous SCW
ECA 095	Ti Grade 12	4 43	4464	51 13	0 0804	6 96	28-1A	90°C aqueous SCW
ECA 096	Ti Grade 12	4 43	4464	51 86	0 0901	7 70	28-1A	90°C aqueous SCW
ECA 121	Ti Grade 12	4 43	4464	53 60	0 0721	5 96	29-1B	60°C vapor SDW
ECA 122	Ti Grade 12	4 43	4464	53 87	0 0551	4 53	29-1B	60°C vapor SDW
ECA 123	Ti Grade 12	4 43	4464	53 58	0 0493	4 08	29-1B	60°C vapor SDW
ECA 124	Ti Grade 12	4 43	4464	53 09	0 0677	5 65	29-1A	60°C aqueous SDW
ECA 125	Ti Grade 12	4 43	4464	53 49	0 0538	4 46	29-1A	60°C aqueous SDW
ECA 126	Ti Grade 12	4 43	4464	53 66	0 0686	5 66	29-1A	60°C aqueous SDW
ECA 157	Ti Grade 12	4 43	4392	52 18	0 0899	7 76	30-1B	90°C vapor SDW
ECA 158	Ti Grade 12	4 43	4392	52 57	0 0911	7 80	30-1B	90°C vapor SDW
ECA 159	Ti Grade 12	4 43	4392	52 42	0 1056	9 07	30-1B	90°C vapor SDW
ECA 160	Ti Grade 12	4 43	4392	52 16	0 0784	6 77	30-1A	90°C aqueous SDW
ECA 161	Ti Grade 12	4 43	4392	52 58	0 0804	6 88	30-1A	90°C aqueous SDW
ECA 162	Ti Grade 12	4 43	4392	51 54	0 0851	7 43	30-1A	90°C aqueous SDW
ECD 001	Ti Grade 12	4 43	4296	53 59	0 0567	4 87	25-1B	60°C vapor SAW
ECD 002	Ti Grade 12	4 43	4296	53 69	0 0445	3 81	25-1B	60°C vapor SAW
ECD 003	Ti Grade 12	4 43	4296	53 93	0 0880	7 51	25-1B	60°C vapor SAW
ECD 004	Ti Grade 12	4 43	4296	53 74	0 0278	2 38	25-1A	60°C aqueous SAW
ECD 005	Ti Grade 12	4 43	4296	53 57	0 0297	2 55	25-1A	60°C aqueous SAW
ECD 006	Ti Grade 12	4 43	4296	53 76	0 0312	2 67	25-1A	60°C aqueous SAW

Sample identification	Alloy	Density (g/cc)	Exposure time (hours)	Surface area (sq cm)	Weight loss (g)	Corrosion rate (μm/y)	Vessel number-rack number	Test environment
ECD 007	Ti Grade 12	4 43	8376	53 72	–0 0010	–0 04	25-2B	60°C vapor SAW
ECD 008	Ti Grade 12	4 43	8376	53 91	–0 0007	–0 03	25-2B	60°C vapor SAW
ECD 009	Ti Grade 12	4 43	8376	53 43	–0 0002	–0 01	25-2B	60°C vapor SAW
ECD 010	Ti Grade 12	4 43	8376	53 49	0 0008	0 04	25-2A	60°C aqueous SAW
ECD 011	Ti Grade 12	4 43	8376	53 89	0 0006	0 03	25-2A	60°C aqueous SAW
ECD 012	Ti Grade 12	4 43	8376	53 88	0 0000	0 00	25-2A	60°C aqueous SAW
ECD 031	Ti Grade 12	4 43	4344	53 62	0 1265	10 74	26-1B	90°C vapor SAW
ECD 032	Ti Grade 12	4 43	4344	53 45	0 0797	6 79	26-1B	90°C vapor SAW
ECD 033	Ti Grade 12	4 43	4344	53 93	0 1362	11 50	26-1B	90°C vapor SAW
ECD 034	Ti Grade 12	4 43	4344	53 96	0 0804	6 78	26-1A	90°C aqueous SAW
ECD 035	Ti Grade 12	4 43	4344	53 61	0 0468	3 97	26-1A	90°C aqueous SAW
ECD 036	Ti Grade 12	4 43	4344	53 92	0 0478	4 04	26-1A	90°C aqueous SAW
ECD 037	Ti Grade 12	4 43	8784	53 67	–0 0011	–0 05	26-2B	90°C vapor SAW
ECD 038	Ti Grade 12	4 43	8784	53 75	–0 0016	–0 07	26-2B	90°C vapor SAW
ECD 039	Ti Grade 12	4 43	8784	53 65	–0 0015	–0 06	26-2B	90°C vapor SAW
ECD 040	Ti Grade 12	4 43	8784	53 66	–0 0054	–0 23	26-2A	90°C aqueous SAW
ECD 041	Ti Grade 12	4 43	8784	53 83	–0 0060	–0 25	26-2A	90°C aqueous SAW
ECD 042	Ti Grade 12	4 43	8784	53 29	–0 0058	–0 25	26-2A	90°C aqueous SAW
ECD 061	Ti Grade 12	4 43	4392	53 83	0 0884	7 39	27-1B	60°C vapor SCW
ECD 062	Ti Grade 12	4 43	4392	53 74	0 1104	9 25	27-1B	60°C vapor SCW
ECD 063	Ti Grade 12	4 43	4392	53 68	0 0684	5 74	27-1B	60°C vapor SCW
ECD 064	Ti Grade 12	4 43	4392	53 59	0 0937	7 87	27-1A	60°C aqueous SCW
ECD 065	Ti Grade 12	4 43	4392	53 87	0 0790	6 60	27-1A	60°C aqueous SCW
ECD 066	Ti Grade 12	4 43	4392	53 69	0 0815	6 83	27-1A	60°C aqueous SCW
ECD 091	Ti Grade 12	4 43	4464	52 79	0 0696	5 84	28-1B	90°C vapor SCW
ECD 092	Ti Grade 12	4 43	4464	53 93	0 0682	5 60	28-1B	90°C vapor SCW
ECD 093	Ti Grade 12	4 43	4464	53 93	0 0962	7 90	28-1B	90°C vapor SCW
ECD 094	Ti Grade 12	4 43	4464	54 04	0 0842	6 90	28-1A	90°C aqueous SCW
ECD 095	Ti Grade 12	4 43	4464	53 49	0 0995	8 24	28-1A	90°C aqueous SCW
ECD 096	Ti Grade 12	4 43	4464	53 71	0 0939	7 74	28-1A	90°C aqueous SCW
ECD 121	Ti Grade 12	4 43	4464	53 70	0 0619	5 11	29-1B	60°C vapor SDW
ECD 122	Ti Grade 12	4 43	4464	54 16	0 0685	5 60	29-1B	60°C vapor SDW
ECD 123	Ti Grade 12	4 43	4464	53 96	0 0966	7 93	29-1B	60°C vapor SDW
ECD 124	Ti Grade 12	4 43	4464	53 36	0 0796	6 61	29-1A	60°C aqueous SDW
ECD 125	Ti Grade 12	4 43	4464	53 98	0 0642	5 27	29-1A	60°C aqueous SDW
ECD 126	Ti Grade 12	4 43	4464	53 84	0 0567	4 67	29-1A	60°C aqueous SDW
ECD 157	Ti Grade 12	4 43	4392	53.75	0 1051	8 80	30-1B	90°C vapor SDW
ECD 158	Ti Grade 12	4 43	4392	53 95	0 1011	8 44	30-1B	90°C vapor SDW
ECD 159	Ti Grade 12	4 43	4392	53 77	0 0747	6 25	30-1B	90°C vapor SDW
ECD 160	Ti Grade 12	4 43	4392	53 86	0 0683	5 71	30-1A	90°C aqueous SDW

Sample identification	Alloy	Density (g/cc)	Exposure time (hours)	Surface area (sq cm)	Weight loss (g)	Corrosion rate (μm/y)	Vessel number-rack number	Test environment
ECD 161	Ti Grade 12	4 43	4392	53 70	0 0746	6 26	30-1A	90°C aqueous SDW
ECD 162	Ti Grade 12	4 43	4392	53 83	0 0793	6 63	30-1A	90°C aqueous SDW
FCA 001	Ti Grade 16	4 52	4296	52 53	0 1175	10 09	25-1B	60°C vapor SAW
FCA 002	Ti Grade 16	4 52	4296	52 02	0 0450	3 90	25-1B	60°C vapor SAW
FCA 003	Ti Grade 16	4 52	4296	52 47	0 0449	3 86	25-1B	60°C vapor SAW
FCA 004	Ti Grade 16	4 52	4296	52 78	0 0415	3 55	25-1A	60°C aqueous SAW
FCA 005	Ti Grade 16	4 52	4296	52 54	0 0563	4 83	25-1A	60°C aqueous SAW
FCA 006	Ti Grade 16	4 52	4296	52 39	0 0417	3 59	25-1A	60°C aqueous SAW
FCA 007	Ti Grade 16	4 52	8376	52 39	–0 0002	–0 01	25-2B	60°C vapor SAW
FCA 008	Ti Grade 16	4 52	8376	52 84	–0 0008	–0 04	25-2B	60°C vapor SAW
FCA 009	Ti Grade 16	4 52	8376	52 60	–0 0006	–0 03	25-2B	60°C vapor SAW
FCA 010	Ti Grade 16	4 52	8376	52 72	0 0001	0 00	25-2A	60°C aqueous SAW
FCA 011	Ti Grade 16	4 52	8376	52 67	–0 0001	0 00	25-2A	60°C aqueous SAW
FCA 012	Ti Grade 16	4 52	8376	52 53	0 0001	0 00	25-2A	60°C aqueous SAW
FCA 031	Ti Grade 16	4 52	4344	52 25	0 0541	4 62	26-1B	90°C vapor SAW
FCA 032	Ti Grade 16	4 52	4344	52 42	0 0575	4 89	26-1B	90°C vapor SAW
FCA 033	Ti Grade 16	4 52	4344	52 13	0 0793	6 79	26-1B	90°C vapor SAW
FCA 034	Ti Grade 16	4 52	4344	51 98	0 0216	1 85	26-1A	90°C aqueous SAW
FCA 035	Ti Grade 16	4 52	4344	52 38	0 0186	1 58	26-1A	90°C aqueous SAW
FCA 036	Ti Grade 16	4 52	4344	52 29	0 0322	2 75	26-1A	90°C aqueous SAW
FCA 037	Ti Grade 16	4 52	8784	52 42	–0 0012	–0 05	26-2B	90°C vapor SAW
FCA 038	Ti Grade 16	4 52	8784	52 71	–0 0014	–0 06	26-2B	90°C vapor SAW
FCA 039	Ti Grade 16	4 52	8784	52 35	–0 0012	–0 05	26-2B	90°C vapor SAW
FCA 040	Ti Grade 16	4 52	8784	52 94	–0 0050	–0 21	26-2A	90°C aqueous SAW
FCA 041	Ti Grade 16	4 52	8784	52 91	–0 0059	–0 25	26-2A	90°C aqueous SAW
FCA 042	Ti Grade 16	4 52	8784	52 45	–0 0056	–0 24	26-2A	90°C aqueous SAW
FCA 061	Ti Grade 16	4 52	4392	52 38	0 0674	5 68	27-1B	60°C vapor SCW
FCA 062	Ti Grade 16	4 52	4392	52 38	0 0582	4 90	27-1B	60°C vapor SCW
FCA 063	Ti Grade 16	4 52	4392	52 32	0 0563	4 75	27-1B	60°C vapor SCW
FCA 064	Ti Grade 16	4 52	4392	52 41	0 0589	4 96	27-1A	60°C aqueous SCW
FCA 065	Ti Grade 16	4 52	4392	52 90	0 0442	3 69	27-1A	60°C aqueous SCW
FCA 066	Ti Grade 16	4 52	4392	52 27	0 0559	4 72	27-1A	60°C aqueous SCW
FCA 091	Ti Grade 16	4 52	4464	52 64	0 0902	7 44	28-1B	90°C vapor SCW
FCA 092	Ti Grade 16	4 52	4464	52 87	0 1321	10 85	28-1B	90°C vapor SCW
FCA 093	Ti Grade 16	4 52	4464	52 59	0 1158	9 56	28-1B	90°C vapor SCW
FCA 094	Ti Grade 16	4 52	4464	52 89	0 0800	6 57	28-1A	90°C aqueous SCW
FCA 095	Ti Grade 16	4 52	4464	52 43	0 0811	6 72	28-1A	90°C aqueous SCW
FCA 096	Ti Grade 16	4 52	4464	52 49	0 1044	8 63	28-1A	90°C aqueous SCW
FCA 121	Ti Grade 16	4 52	4464	52 82	0 0567	4 66	29-1B	60°C vapor SDW
FCA 122	Ti Grade 16	4 52	4464	52 52	0 0535	4 42	29-1B	60°C vapor SDW

Sample identification	Alloy	Density (g/cc)	Exposure time (hours)	Surface area (sq cm)	Weight loss (g)	Corrosion rate (μm/y)	Vessel number-rack number	Test environment
FCA 123	Ti Grade 16	4 52	4464	52 82	0 0725	5 96	29-1B	60°C vapor SDW
FCA 124	Ti Grade 16	4.52	4464	52 66	0 0572	4 72	29-1A	60°C aqueous SDW
FCA 125	Ti Grade 16	4 52	4464	53 16	0 0634	5 18	29-1A	60°C aqueous SDW
FCA 126	Ti Grade 16	4 52	4464	52 81	0 0628	5 16	29-1A	60°C aqueous SDW
FCA 157	Ti Grade 16	4 52	4392	52 92	0 1595	13 30	30-1B	90°C vapor SDW
FCA 158	Ti Grade 16	4 52	4392	52 23	0 0832	7 03	30-1B	90°C vapor SDW
FCA 159	Ti Grade 16	4 52	4392	52 68	0 0816	6 83	30-1B	90°C vapor SDW
FCA 160	Ti Grade 16	4 52	4392	53 03	0 0569	4 73	30-1A	90°C aqueous SDW
FCA 161	Ti Grade 16	4 52	4392	52 83	0 0632	5 28	30-1A	90°C aqueous SDW
FCA 162	Ti Grade 16	4 52	4392	52 88	0 0684	5 71	30-1A	90°C aqueous SDW
FCE 001	Ti Grade 16	4 52	4296	51 86	0 0679	5 91	25-1B	60°C vapor SAW
FCE 002	Ti Grade 16	4 52	4296	51 57	0 0897	7 85	25-1B	60°C vapor SAW
FCE 003	Ti Grade 16	4 52	4296	51 84	0 0588	5 12	25-1B	60°C vapor SAW
FCE 004	Ti Grade 16	4 52	4296	51 34	0 0397	3 49	25-1A	60°C aqueous SAW
FCE 005	Ti Grade 16	4 52	4296	51 83	0 0182	1 58	25-1A	60°C aqueous SAW
FCE 006	Ti Grade 16	4 52	4296	51 84	0 0249	2 17	25-1A	60°C aqueous SAW
FCE 007	Ti Grade 16	4 52	8376	51 79	–0 0003	–0 01	25-2B	60°C vapor SAW
FCE 008	Ti Grade 16	4 52	8376	51 74	–0 0004	–0 02	25-2B	60°C vapor SAW
FCE 009	Ti Grade 16	4 52	8376	51 82	–0 0006	–0 03	25-2B	60°C vapor SAW
FCE 010	Ti Grade 16	4 52	8376	51 79	0 0007	0 03	25-2A	60°C aqueous SAW
FCE 011	Ti Grade 16	4 52	8376	51 54	0 0014	0 06	25-2A	60°C aqueous SAW
FCE 012	Ti Grade 16	4 52	8376	52 04	0 0009	0 04	25-2A	60°C aqueous SAW
FCE 031	Ti Grade 16	4 52	4344	51 89	0 0580	4 99	26-1B	90°C vapor SAW
FCE 032	Ti Grade 16	4 52	4344	51 74	0 0649	5 60	26-1B	90°C vapor SAW
FCE 033	Ti Grade 16	4 52	4344	50 80	0 0508	4 46	26-1B	90°C vapor SAW
FCE 034	Ti Grade 16	4 52	4344	50 92	0 0322	2 82	26-1A	90°C aqueous SAW
FCE 035	Ti Grade 16	4 52	4344	51 81	0 0409	3 52	26-1A	90°C aqueous SAW
FCE 036	Ti Grade 16	4 52	4344	51 17	0 0289	2 52	26-1A	90°C aqueous SAW
FCE 037	Ti Grade 16	4 52	8784	52 30	–0 0005	–0 02	26-2B	90°C vapor SAW
FCE 038	Ti Grade 16	4 52	8784	51 84	–0 0017	–0 07	26-2B	90°C vapor SAW
FCE 039	Ti Grade 16	4 52	8784	51 34	–0 0018	–0 08	26-2B	90°C vapor SAW
FCE 040	Ti Grade 16	4 52	8784	51 69	–0 0052	–0 22	26-2A	90°C aqueous SAW
FCE 041	Ti Grade 16	4 52	8784	51 79	–0 0054	–0 23	26-2A	90°C aqueous SAW
FCE 042	Ti Grade 16	4 52	8784	51 42	–0 0038	–0 16	26-2A	90°C aqueous SAW
FCE 061	Ti Grade 16	4 52	4392	51 54	0 2982	25 53	27-1B	60°C vapor SCW
FCE 062	Ti Grade 16	4 52	4392	51 45	–0 1295	–11 11	27-1B	60°C vapor SCW
FCE 063	Ti Grade 16	4 52	4392	51 06	0 0429	3 71	27-1B	60°C vapor SCW
FCE 064	Ti Grade 16	4 52	4392	51 27	0 0398	3 43	27-1A	60°C aqueous SCW
FCE 065	Ti Grade 16	4 52	4392	51 17	0 0411	3 54	27-1A	60°C aqueous SCW
FCE 066	Ti Grade 16	4 52	4392	51 10	0 0513	4 43	27-1A	60°C aqueous SCW

Sample identification	Alloy	Density (g/cc)	Exposure time (hours)	Surface area (sq cm)	Weight loss (g)	Corrosion rate (μm/y)	Vessel number-rack number	Test environment
FCE 091	Ti Grade 16	4 52	4464	50 65	0 0812	6 96	28-1B	90°C vapor SCW
FCE 092	Ti Grade 16	4 52	4464	50 94	0 0874	7 45	28-1B	90°C vapor SCW
FCE 093	Ti Grade 16	4 52	4464	51 62	0 0791	6 65	28-1B	90°C vapor SCW
FCE 094	Ti Grade 16	4 52	4464	51 39	0 0742	6 27	28-1A	90°C aqueous SCW
FCE 095	Ti Grade 16	4 52	4464	51 13	0 0625	5 31	28-1A	90°C aqueous SCW
FCE 096	Ti Grade 16	4 52	4464	51 56	0 0706	5 94	28-1A	90°C aqueous SCW
FCE 121	Ti Grade 16	4 52	4464	51 42	0 0686	5 79	29-1B	60°C vapor SDW
FCE 122	Ti Grade 16	4 52	4464	51 51	0 0677	5 71	29-1B	60°C vapor SDW
FCE 123	Ti Grade 16	4 52	4464	51 90	0 0663	5 55	29-1B	60°C vapor SDW
FCE 124	Ti Grade 16	4 52	4464	51 25	0 0692	5 86	29-1A	60°C aqueous SDW
FCE 125	Ti Grade 16	4 52	4464	51 21	0 0457	3 87	29-1A	60°C aqueous SDW
FCE 126	Ti Grade 16	4 52	4464	51 44	0 0508	4 29	29-1A	60°C aqueous SDW
FCE 157	Ti Grade 16	4 52	4392	51 45	0 1385	11 88	30-1B	90°C vapor SDW
FCE 158	Ti Grade 16	4 52	4392	51 20	0 0987	8 51	30-1B	90°C vapor SDW
FCE 159	Ti Grade 16	4 52	4392	51 35	0 0595	5 11	30-1B	90°C vapor SDW
FCE 160	Ti Grade 16	4 52	4392	51 54	0 0724	6 20	30-1A	90°C aqueous SDW
FCE 161	Ti Grade 16	4 52	4392	51 85	0 0608	5 17	30-1A	90°C aqueous SDW
FCE 162	Ti Grade 16	4 52	4392	51 81	0 0704	6 00	30-1A	90°C aqueous SDW
GCA 001	Monel 400	8 80	4536	51 91	0 0110	0 47	19-1B	60°C vapor SAW
GCA 002	Monel 400	8 80	4536	52 37	0 0160	0 67	19-1B	60°C vapor SAW
GCA 003	Monel 400	8 80	4536	51 32	0 0180	0 77	19-1B	60°C vapor SAW
GCA 004	Monel 400	8 80	4536	52 41	2 3345	97 75	19-1A	60°C aqueous SAW
GCA 005	Monel 400	8 80	4536	52 15	2 2476	94 57	19-1A	60°C aqueous SAW
GCA 006	Monel 400	8 80	4536	51 61	2 2643	96 28	19-1A	60°C aqueous SAW
GCA 007	Monel 400	8 80	8760	52 28	0 0201	0 44	19-2B	60°C vapor SAW
GCA 008	Monel 400	8 80	8760	51.79	0 0262	0 57	19-2B	60°C vapor SAW
GCA 009	Monel 400	8 80	8760	52 26	0 0376	0 82	19-2B	60°C vapor SAW
GCA 010	Monel 400	8 80	8760	51 71	2 0265	44 53	19-2A	60°C aqueous SAW
GCA 011	Monel 400	8 80	8760	52 21	2 0635	44 91	19-2A	60°C aqueous SAW
GCA 012	Monel 400	8 80	8760	52 47	2 1587	46 75	19-2A	60°C aqueous SAW
GCA 031	Monel 400	8 80	4392	52 29	0 0583	2 53	18-1B	90°C vapor SAW
GCA 032	Monel 400	8 80	4392	52 12	0 0714	3 11	18-1B	90°C vapor SAW
GCA 033	Monel 400	8 80	4392	52 19	0 0689	2 99	18-1B	90°C vapor SAW
GCA 034	Monel 400	8 80	4392	52 21	1 3834	60 05	18-1A	90°C aqueous SAW
GCA 035	Monel 400	8 80	4392	52 15	1 4217	61 79	18-1A	90°C aqueous SAW
GCA 036	Monel 400	8 80	4392	52 44	1 4913	64 46	18-1A	90°C aqueous SAW
GCA 037	Monel 400	8 80	8760	52 29	0 1080	2 35	18-2B	90°C vapor SAW
GCA 038	Monel 400	8 80	8760	52 25	0 1132	2 46	18-2B	90°C vapor SAW
GCA 039	Monel 400	8 80	8760	52 27	0 1074	2 33	18-2B	90°C vapor SAW
GCA 040	Monel 400	8 80	8760	52.16	1 4891	32 44	18-2A	90°C aqueous SAW

Sample identification	Alloy	Density (g/cc)	Exposure time (hours)	Surface area (sq cm)	Weight loss (g)	Corrosion rate (μm/y)	Vessel number-rack number	Test environment
GCA 041	Monel 400	8 80	8760	51 96	1.5235	33 32	18-2A	90°C aqueous SAW
GCA 042	Monel 400	8 80	8760	52 11	1 5811	34 48	18-2A	90°C aqueous SAW
GCF 001	Monel 400	8 80	4536	51 70	0 0162	0 69	19-1B	60°C vapor SAW
GCF 002	Monel 400	8 80	4536	50 65	0 0247	1 07	19-1B	60°C vapor SAW
GCF 003	Monel 400	8 80	4536	51 09	0 0272	1 17	19-1B	60°C vapor SAW
GCF 004	Monel 400	8 80	4536	51 05	3 0196	129 82	19-1A	60°C aqueous SAW
GCF 005	Monel 400	8 80	4536	50 93	2 9966	129 13	19-1A	60°C aqueous SAW
GCF 006	Monel 400	8 80	4536	51 01	3 5070	150 88	19-1A	60°C aqueous SAW
GCF 007	Monel 400	8 80	8760	51 35	0 0502	1 11	19-2B	60°C vapor SAW
GCF 008	Monel 400	8 80	8760	50 81	0 0509	1 14	19-2B	60°C vapor SAW
GCF 009	Monel 400	8 80	8760	51 20	0 0945	2 10	19-2B	60°C vapor SAW
GCF 010	Monel 400	8 80	8760	51 08	2 9694	66 06	19-2A	60°C aqueous SAW
GCF 011	Monel 400	8 80	8760	51 35	3 0303	67 06	19-2A	60°C aqueous SAW
GCF 012	Monel 400	8 80	8760	51 11	3 2255	71 72	19-2A	60°C aqueous SAW
GCF 031	Monel 400	8 80	4392	50 45	0 0879	3 95	18-1B	90°C vapor SAW
GCF 032	Monel 400	8 80	4392	50 60	0 0936	4 19	18-1B	90°C vapor SAW
GCF 033	Monel 400	8 80	4392	50 08	0 0808	3 66	18-1B	90°C vapor SAW
GCF 034	Monel 400	8 80	4392	50 46	2 8835	129 51	18-1A	90°C aqueous SAW
GCF 035	Monel 400	8 80	4392	50 80	2 8827	128 63	18-1A	90°C aqueous SAW
GCF 036	Monel 400	8 80	4392	51 06	3 1031	137 75	18-1A	90°C aqueous SAW
GCF 037	Monel 400	8 80	8760	50 92	0 1333	2 97	18-2B	90°C vapor SAW
GCF 038	Monel 400	8 80	8760	50 89	0 1323	2 95	18-2B	90°C vapor SAW
GCF 039	Monel 400	8 80	8760	51 23	0 1263	2 80	18-2B	90°C vapor SAW
GCF 040	Monel 400	8 80	8760	50 79	3 1933	71 44	18-2A	90°C aqueous SAW
GCF 041	Monel 400	8 80	8760	51 27	3 4558	76 59	18-2A	90°C aqueous SAW
GCF 042	Monel 400	8 80	8760	51 46	3 7458	82 72	18-2A	90°C aqueous SAW
HCA 001	CDA 715	8 94	4536	53 29	0 0408	1 65	19-1B	60°C vapor SAW
HCA 002	CDA 715	8 94	4536	53 32	0 0480	1 94	19-1B	60°C vapor SAW
HCA 003	CDA 715	8 94	4536	53 04	0 0673	2 74	19-1B	60°C vapor SAW
HCA 004	CDA 715	8 94	4536	53 14	4 2705	173 61	19-1A	60°C aqueous SAW
HCA 005	CDA 715	8 94	4536	52 73	4 4611	182 76	19-1A	60°C aqueous SAW
HCA 006	CDA 715	8 94	4536	52 28	4 4947	185 71	19-1A	60°C aqueous SAW
HCA 007	CDA 715	8 94	8760	53 18	0 0967	2 03	19-2B	60°C vapor SAW
HCA 008	CDA 715	8 94	8760	53 29	0 1159	2 43	19-2B	60°C vapor SAW
HCA 009	CDA 715	8 94	8760	53 14	0 1316	2 77	19-2B	60°C vapor SAW
HCA 010	CDA 715	8 94	8760	53 18	5 2422	110 27	19-2A	60°C aqueous SAW
HCA 011	CDA 715	8 94	8760	53 32	4 8345	101 43	19-2A	60°C aqueous SAW
HCA 012	CDA 715	8 94	8760	53 22	4 9012	103 01	19-2A	60°C aqueous SAW
HCA 031	CDA 715	8 94	4392	52 78	0 2102	8 89	18-1B	90°C vapor SAW
HCA 032	CDA 715	8 94	4392	53 16	0 2388	10 02	18-1B	90°C vapor SAW

Sample Identification	Alloy	Density (g/cc)	Exposure time (hours)	Surface area (sq cm)	Weight loss (g)	Corrosion rate (μm/y)	Vessel number-rack number	Test environment
HCA 033	CDA 715	8 94	4392	53 27	0 2724	11 41	18-1B	90°C vapor SAW
HCA 034	CDA 715	8 94	4392	53 48	5 6175	234 32	18-1A	90°C aqueous SAW
HCA 035	CDA 715	8 94	4392	53 28	5 6138	235 06	18-1A	90°C aqueous SAW
HCA 036	CDA 715	8 94	4392	53 27	6 0580	253 73	18-1A	90°C aqueous SAW
HCA 037	CDA 715	8 94	8760	53 40	0 4103	8 59	18-2B	90°C vapor SAW
HCA 038	CDA 715	8 94	8760	53 44	0 3852	8 06	18-2B	90°C vapor SAW
HCA 039	CDA 715	8 94	8760	52 88	0 4099	8 67	18-2B	90°C vapor SAW
HCA 040	CDA 715	8 94	8760	51 84	7 8630	169 67	18-2A	90°C aqueous SAW
HCA 041	CDA 715	8 94	8760	53 07	11 3696	239 65	18-2A	90°C aqueous SAW
HCA 042	CDA 715	8 94	8760	52 74	10 5725	224 23	18-2A	90°C aqueous SAW
HCG 001	CDA 715	8 94	4536	51 60	0 0692	2 90	19-1B	60°C vapor SAW
HCG 002	CDA 715	8 94	4536	51 49	0 0965	4 05	19-1B	60°C vapor SAW
HCG 003	CDA 715	8 94	4536	51 24	0 1240	5 23	19-1B	60°C vapor SAW
HCG 004	CDA 715	8 94	4536	51 48	4 4934	188 56	19-1A	60°C aqueous SAW
HCG 005	CDA 715	8 94	4536	51 52	4 5945	192 64	19-1A	60°C aqueous SAW
HCG 006	CDA 715	8 94	4536	51 88	5 0990	212 32	19-1A	60°C aqueous SAW
HCG 007	CDA 715	8 94	8760	51 45	0 1521	3 31	19-2B	60°C vapor SAW
HCG 008	CDA 715	8 94	8760	51 71	0 1816	3 93	19-2B	60°C vapor SAW
HCG 009	CDA 715	8 94	8760	51 60	0 2094	4 54	19-2B	60°C vapor SAW
HCG 010	CDA 715	8 94	8760	51 35	4 6992	102 37	19-2A	60°C aqueous SAW
HCG 011	CDA 715	8 94	8760	51 59	4 8497	105 16	19-2A	60°C aqueous SAW
HCG 012	CDA 715	8 94	8760	51 61	5 1464	111 53	19-2A	60°C aqueous SAW
HCG 031	CDA 715	8 94	4392	51 65	0 2843	12 28	18-1B	90°C vapor SAW
HCG 032	CDA 715	8 94	4392	51 41	0 2661	11 55	18-1B	90°C vapor SAW
HCG 033	CDA 715	8 94	4392	51 63	0 2507	10 83	18-1B	90°C vapor SAW
HCG 034	CDA 715	8 94	4392	51 06	7 0815	309 42	18-1A	90°C aqueous SAW
HCG 035	CDA 715	8 94	4392	51 94	7 0810	304 18	18-1A	90°C aqueous SAW
HCG 036	CDA 715	8 94	4392	51 83	7 5893	326 71	18-1A	90°C aqueous SAW
HCG 037	CDA 715	8 94	8760	51 84	0 4667	10 07	18-2B	90°C vapor SAW
HCG 038	CDA 715	8 94	8760	51 79	0 3938	8 50	18-2B	90°C vapor SAW
HCG 039	CDA 715	8 94	8760	51 56	0 2787	6 05	18-2B	90°C vapor SAW
HCG 040	CDA 715	8 94	8760	51 78	10 4589	225 92	18-2A	90°C aqueous SAW
HCG 041	CDA 715	8 94	8760	51.52	11 1313	241 66	18-2A	90°C aqueous SAW
HCG 042	CDA 715	8 94	8760	51 64	10 9110	236 36	18-2A	90°C aqueous SAW
ICA 001	A387 Grade 22	7.86	4536	53 03	0 2703	12 52	23-1B	60°C vapor SDW
ICA 002	A387 Grade 22	7.86	4536	53 08	0 2546	11 79	23-1B	60°C vapor SDW
ICA 003	A387 Grade 22	7.86	4536	53 26	0 2455	11 33	23-1B	60°C vapor SDW
ICA 004	A387 Grade 22	7 86	4536	52 95	2 1500	99 76	23-1A	60°C aqueous SDW
ICA 005	A387 Grade 22	7 86	4536	53 03	2 2049	102 16	23-1A	60°C aqueous SDW
ICA 006	A387 Grade 22	7 86	4536	52 74	2 1720	101 20	23-1A	60°C aqueous SDW

Sample identification	Alloy	Density (g/cc)	Exposure time (hours)	Surface area (sq cm)	Weight loss (g)	Corrosion rate (μm/y)	Vessel number-rack number	Test environment
ICA 007	A387 Grade 22	7 86	8760	53 06	0 4225	10 13	23-2B	60°C vapor SDW
ICA 008	A387 Grade 22	7 86	8760	52 91	0 3357	8 07	23-2B	60°C vapor SDW
ICA 009	A387 Grade 22	7 86	8760	52 90	0 4473	10 76	23-2B	60°C vapor SDW
ICA 010	A387 Grade 22	7 86	8760	52 77	3 5142	84 73	23-2A	60°C aqueous SDW
ICA 011	A387 Grade 22	7 86	8760	53 02	4 7819	114 75	23-2A	60°C aqueous SDW
ICA 012	A387 Grade 22	7 86	8760	53 13	3 9595	94 82	23-2A	60°C aqueous SDW
ICA 031	A387 Grade 22	7 86	4632	53 19	0 6025	27 26	22-1B	90°C vapor SDW
ICA 032	A387 Grade 22	7 86	4632	52 95	0 4919	22 35	22-1B	90°C vapor SDW
ICA 033	A387 Grade 22	7 86	4632	53 06	0 3954	17 93	22-1B	90°C vapor SDW
ICA 034	A387 Grade 22	7 86	4632	52 46	1 9657	90 16	22-1A	90°C aqueous SDW
ICA 035	A387 Grade 22	7 86	4632	53 17	1 9743	89 34	22-1A	90°C aqueous SDW
ICA 036	A387 Grade 22	7 86	4632	53 17	2 1206	95 96	22-1A	90°C aqueous SDW
ICA 037	A387 Grade 22	7 86	8832	53 13	1 0401	24 70	22-2B	90°C vapor SDW
ICA 038	A387 Grade 22	7 86	8832	53 12	0 6884	16 35	22-2B	90°C vapor SDW
ICA 039	A387 Grade 22	7 86	8832	53 28	0 7931	18 78	22-2B	90°C vapor SDW
ICA 040	A387 Grade 22	7 86	8832	53 24	2 6970	63 93	22-2A	90°C aqueous SDW
ICA 041	A387 Grade 22	7 86	8832	53 02	2 1697	51 64	22-2A	90°C aqueous SDW
ICA 042	A387 Grade 22	7 86	8832	53 17	3 0014	71 23	22-2A	90°C aqueous SDW
ICA 061	A387 Grade 22	7 86	4392	53 34	1 1379	54 13	21-1B	60°C vapor SCW
ICA 062	A387 Grade 22	7 86	4392	52 91	1 2126	58 15	21-1B	60°C vapor SCW
ICA 063	A387 Grade 22	7 86	4392	53 43	1 2510	59 41	21-1B	60°C vapor SCW
ICA 064	A387 Grade 22	7 86	4392	53 05	0 4566	21 84	21-1A	60°C aqueous SCW
ICA 065	A387 Grade 22	7 86	4392	52 61	0 4204	20 28	21-1A	60°C aqueous SCW
ICA 066	A387 Grade 22	7 86	4392	53 30	0 4010	19 09	21-1A	60°C aqueous SCW
ICA 067	A387 Grade 22	7 86	8760	53 00	2 0071	48 18	21-2B	60°C vapor SCW
ICA 068	A387 Grade 22	7 86	8760	53 15	2 6897	64 39	21-2B	60°C vapor SCW
ICA 069	A387 Grade 22	7 86	8760	53 15	4 8859	116 96	21-2B	60°C vapor SCW
ICA 070	A387 Grade 22	7 86	8760	52 52	0 2117	5 13	21-2A	60°C aqueous SCW
ICA 071	A387 Grade 22	7 86	8760	53 27	0 1924	4 60	21-2A	60°C aqueous SCW
ICA 072	A387 Grade 22	7 86	8760	52 62	0 3660	8 85	21-2A	60°C aqueous SCW
ICA 091	A387 Grade 22	7 86	4344	52 89	1 7901	86 83	20-1B	90°C vapor SCW
ICA 092	A387 Grade 22	7 86	4344	53 19	2 7451	132 40	20-1B	90°C vapor SCW
ICA 093	A387 Grade 22	7 86	4344	53 15	4 0261	194 33	20-1B	90°C vapor SCW
ICA 094	A387 Grade 22	7 86	4344	53 15	0 1791	8 65	20-1A	90°C aqueous SCW
ICA 095	A387 Grade 22	7 86	4344	53 43	0 1997	9 59	20-1A	90°C aqueous SCW
ICA 096	A387 Grade 22	7 86	4344	53 19	0 2301	11 10	20-1A	90°C aqueous SCW
ICA 097	A387 Grade 22	7 86	8736	53 01	3 3840	81 44	20-2B	90°C vapor SCW
ICA 098	A387 Grade 22	7 86	8736	53 09	5 8262	140 01	20-2B	90°C vapor SCW
ICA 099	A387 Grade 22	7 86	8736	52 70	8 2831	200 53	20-2B	90°C vapor SCW
ICA 100	A387 Grade 22	7 86	8736	52 90	0 1382	3 33	20-2A	90°C aqueous SCW

Sample identification	Alloy	Density (g/cc)	Exposure time (hours)	Surface area (sq cm)	Weight loss (g)	Corrosion rate (μm/y)	Vessel number-rack number	Test environment
ICA 101	A387 Grade 22	7 86	8736	52 82	0 1401	3 38	20-2A	90°C aqueous SCW
ICA 102	A387 Grade 22	7 86	8736	52 15	0 1386	3 39	20-2A	90°C aqueous SCW
ICH 001	A387 Grade 22	7 86	4536	53 00	0 3047	14 12	23-1B	60°C vapor SDW
ICH 002	A387 Grade 22	7 86	4536	53 05	0 3523	16 32	23-1B	60°C vapor SDW
ICH 003	A387 Grade 22	7 86	4536	52 88	0 6660	30 94	23-1B	60°C vapor SDW
ICH 004	A387 Grade 22	7 86	4536	52 99	2 4095	111 73	23-1A	60°C aqueous SDW
ICH 005	A387 Grade 22	7 86	4536	53 00	1 7030	78 95	23-1A	60°C aqueous SDW
ICH 006	A387 Grade 22	7 86	4536	53 07	1 8889	87 45	23-1A	60°C aqueous SDW
ICH 007	A387 Grade 22	7 86	8760	53 15	0 5510	13 19	23-2B	60°C vapor SDW
ICH 008	A387 Grade 22	7 86	8760	53 17	0 6223	14 89	23-2B	60°C vapor SDW
ICH 009	A387 Grade 22	7 86	8760	53 32	0 9945	23 73	23-2B	60°C vapor SDW
ICH 010	A387 Grade 22	7 86	8760	52 93	4 7824	114 95	23-2A	60°C aqueous SDW
ICH 011	A387 Grade 22	7 86	8760	52 52	3 6757	89 05	23-2A	60°C aqueous SDW
ICH 012	A387 Grade 22	7 86	8760	52 71	1 4627	35 30	23-2A	60°C aqueous SDW
ICH 031	A387 Grade 22	7 86	4632	53 03	0 4093	18 57	22-1B	90°C vapor SDW
ICH 032	A387 Grade 22	7 86	4632	52 97	0 3557	16 16	22-1B	90°C vapor SDW
ICH 033	A387 Grade 22	7 86	4632	52 55	0 8031	36 77	22-1B	90°C vapor SDW
ICH 034	A387 Grade 22	7 86	4632	52 31	2 1534	99 05	22-1A	90°C aqueous SDW
ICH 035	A387 Grade 22	7 86	4632	52 01	1 2662	58 57	22-1A	90°C aqueous SDW
ICH 036	A387 Grade 22	7 86	4632	52 32	3 1047	142 77	22-1A	90°C aqueous SDW
ICH 037	A387 Grade 22	7 86	8832	52 20	1 0520	25 43	22-2B	90°C vapor SDW
ICH 038	A387 Grade 22	7 86	8832	52 33	1 4243	34 35	22-2B	90°C vapor SDW
ICH 039	A387 Grade 22	7 86	8832	52 83	2 4344	58 14	22-2B	90°C vapor SDW
ICH 040	A387 Grade 22	7 86	8832	52 66	2 4830	59 50	22-2A	90°C aqueous SDW
ICH 041	A387 Grade 22	7 86	8832	52 65	3 5803	85 81	22-2A	90°C aqueous SDW
ICH 042	A387 Grade 22	7 86	8832	53 14	2 9301	69 58	22-2A	90°C aqueous SDW
ICH 061	A387 Grade 22	7 86	4392	52 96	1 5668	75 08	21-1B	60°C vapor SCW
ICH 062	A387 Grade 22	7 86	4392	52 97	2 0224	96 88	21-1B	60°C vapor SCW
ICH 063	A387 Grade 22	7 86	4392	53 07	3 7594	179 74	21-1B	60°C vapor SCW
ICH 064	A387 Grade 22	7 86	4392	52 88	0 5769	27 68	21-1A	60°C aqueous SCW
ICH 065	A387 Grade 22	7 86	4392	52 12	0 5883	28 64	21-1A	60°C aqueous SCW
ICH 066	A387 Grade 22	7 86	4392	52 44	0 6079	29 42	21-1A	60°C aqueous SCW
ICH 067	A387 Grade 22	7 86	8760	52 06	5 9884	146 36	21-2B	60°C vapor SCW
ICH 068	A387 Grade 22	7 86	8760	52 50	7 3001	176 91	21-2B	60°C vapor SCW
ICH 069	A387 Grade 22	7 86	8760	52 37	8 3929	203 89	21-2B	60°C vapor SCW
ICH 070	A387 Grade 22	7 86	8760	52 50	0 3598	8 72	21-2A	60°C aqueous SCW
ICH 071	A387 Grade 22	7 86	8760	52 76	0 3466	8 36	21-2A	60°C aqueous SCW
ICH 072	A387 Grade 22	7 86	8760	52 87	0 3402	8 19	21-2A	60°C aqueous SCW
ICH 091	A387 Grade 22	7 86	4344	52 96	5 2295	253 33	20-1B	90°C vapor SCW
ICH 092	A387 Grade 22	7 86	4344	52 99	6 6431	321 66	20-1B	90°C vapor SCW

Sample identification	Alloy	Density (g/cc)	Exposure time (hours)	Surface area (sq cm)	Weight loss (g)	Corrosion rate (μm/y)	Vessel number-rack number	Test environment
ICH 093	A387 Grade 22	7 86	4344	52 41	9 2181	451 26	20-1B	90°C vapor SCW
ICH 094	A387 Grade 22	7 86	4344	52 76	0 1791	8 71	20-1A	90°C aqueous SCW
ICH 095	A387 Grade 22	7 86	4344	52 74	0 1718	8 36	20-1A	90°C aqueous SCW
ICH 096	A387 Grade 22	7 86	4344	52 62	0 1764	8 60	20-1A	90°C aqueous SCW
ICH 097	A387 Grade 22	7 86	8736	52 99	11 4118	274 76	20-2B	90°C vapor SCW
ICH 098	A387 Grade 22	7 86	8736	52 74	11 5974	280 53	20-2B	90°C vapor SCW
ICH 100	A387 Grade 22	7 86	8736	52 65	0 1297	3 14	20-2A	90°C aqueous SCW
ICH 101	A387 Grade 22	7 86	8736	52 48	0 1347	3 27	20-2A	90°C aqueous SCW
ICH 102	A387 Grade 22	7 86	8736	52 59	0 1303	3 16	20-2A	90°C aqueous SCW
JCA 001	A516 Grade 55	7 86	4536	52 87	1 3607	63 23	23-1B	60°C vapor SDW
JCA 002	A516 Grade 55	7 86	4536	52 57	1 1356	53 07	23-1B	60°C vapor SDW
JCA 003	A516 Grade 55	7 86	4536	53 49	1 0760	49 42	23-1B	60°C vapor SDW
JCA 004	A516 Grade 55	7 86	4536	52 72	1 8839	87 80	23-1A	60°C aqueous SDW
JCA 005	A516 Grade 55	7 86	4536	52 90	1 9011	88 29	23-1A	60°C aqueous SDW
JCA 006	A516 Grade 55	7 86	4536	53 48	1 7132	78 71	23-1A	60°C aqueous SDW
JCA 007	A516 Grade 55	7 86	8760	53 33	1 1052	26 37	23-2B	60°C vapor SDW
JCA 008	A516 Grade 55	7 86	8760	53 03	0 8082	19 39	23-2B	60°C vapor SDW
JCA 009	A516 Grade 55	7 86	8760	52 97	0 8234	19 78	23-2B	60°C vapor SDW
JCA 010	A516 Grade 55	7 86	8760	52 56	2 9437	71 25	23-2A	60°C aqueous SDW
JCA 011	A516 Grade 55	7 86	8760	52 29	2 7033	65 77	23-2A	60°C aqueous SDW
JCA 012	A516 Grade 55	7 86	8760	52 68	2 8983	70 00	23-2A	60°C aqueous SDW
JCA 031	A516 Grade 55	7 86	4632	53 13	2 9867	135 26	22-1B	90°C vapor SDW
JCA 032	A516 Grade 55	7 86	4632	53 34	2 8839	130 09	22-1B	90°C vapor SDW
JCA 033	A516 Grade 55	7 86	4632	53 67	2 0111	90 15	22-1B	90°C vapor SDW
JCA 034	A516 Grade 55	7 86	4632	53 65	1 7160	76 96	22-1A	90°C aqueous SDW
JCA 035	A516 Grade 55	7 86	4632	52 81	1 5462	70 45	22-1A	90°C aqueous SDW
JCA 036	A516 Grade 55	7 86	4632	53 01	1 6367	74 29	22-1A	90°C aqueous SDW
JCA 037	A516 Grade 55	7 86	8832	52 73	2 6810	64 16	22-2B	90°C vapor SDW
JCA 038	A516 Grade 55	7 86	8832	52 76	2 4686	59 04	22-2B	90°C vapor SDW
JCA 039	A516 Grade 55	7 86	8832	53 16	2 1727	51 58	22-2B	90°C vapor SDW
JCA 040	A516 Grade 55	7 86	8832	52 76	1 7739	42 42	22-2A	90°C aqueous SDW
JCA 041	A516 Grade 55	7 86	8832	52 78	1 9203	45 91	22-2A	90°C aqueous SDW
JCA 042	A516 Grade 55	7 86	8832	53 25	1 2460	29 53	22-2A	90°C aqueous SDW
JCA 061	A516 Grade 55	7 86	4392	53 40	2 5857	122 87	21-1B	60°C vapor SCW
JCA 062	A516 Grade 55	7 86	4392	53 49	3 4959	165 83	21-1B	60°C vapor SCW
JCA 063	A516 Grade 55	7 86	4392	53 36	4 4477	211 50	21-1B	60°C vapor SCW
JCA 064	A516 Grade 55	7 86	4392	53 22	1 3672	65 19	21-1A	60°C aqueous SCW
JCA 065	A516 Grade 55	7 86	4392	52 51	1 3518	65 32	21-1A	60°C aqueous SCW
JCA 066	A516 Grade 55	7 86	4392	53 05	1 3174	63 02	21-1A	60°C aqueous SCW
JCA 067	A516 Grade 55	7 86	8760	53 17	4 5428	108 70	21-2B	60°C vapor SCW

Sample identification	Alloy	Density (g/cc)	Exposure time (hours)	Surface area (sq cm)	Weight loss (g)	Corrosion rate (μm/y)	Vessel number-rack number	Test environment
JCA 068	A516 Grade 55	7 86	8760	52 56	5 3039	128 38	21-2B	60°C vapor SCW
JCA 069	A516 Grade 55	7 86	8760	53 11	6 1912	148 32	21-2B	60°C vapor SCW
JCA 070	A516 Grade 55	7 86	8760	52 71	0 2804	6 77	21-2A	60°C aqueous SCW
JCA 071	A516 Grade 55	7 86	8760	53 06	0 4198	10 07	21-2A	60°C aqueous SCW
JCA 072	A516 Grade 55	7 86	8760	53 86	0 4961	11 72	21-2A	60°C aqueous SCW
JCA 091	A516 Grade 55	7 86	4344	52 88	3 8224	185 47	20-1B	90°C vapor SCW
JCA 092	A516 Grade 55	7 86	4344	53 68	4 7766	228 28	20-1B	90°C vapor SCW
JCA 093	A516 Grade 55	7 86	4344	53 67	4 7703	228 04	20-1B	90°C vapor SCW
JCA 094	A516 Grade 55	7 86	4344	53 11	0 2533	12 24	20-1A	90°C aqueous SCW
JCA 095	A516 Grade 55	7 86	4344	53 09	0 1665	8 05	20-1A	90°C aqueous SCW
JCA 096	A516 Grade 55	7 86	4344	52 73	0 1780	8 66	20-1A	90°C aqueous SCW
JCA 097	A516 Grade 55	7 86	8736	52 79	5 7757	139 58	20-2B	90°C vapor SCW
JCA 098	A516 Grade 55	7 86	8736	53 63	5 6287	133 91	20-2B	90°C vapor SCW
JCA 099	A516 Grade 55	7 86	8736	53 62	5 0981	121 31	20-2B	90°C vapor SCW
JCA 100	A516 Grade 55	7 86	8736	53 08	0 3199	7 69	20-2A	90°C aqueous SCW
JCA 101	A516 Grade 55	7 86	8736	53 31	0 2728	6 53	20-2A	90°C aqueous SCW
JCA 102	A516 Grade 55	7 86	8736	52 93	0 2141	5 16	20-2A	90°C aqueous SCW
JCI 001	A516 Grade 55	7 86	4536	51 69	1 1230	53 38	23-1B	60°C vapor SDW
JCI 002	A516 Grade 55	7 86	4536	53 65	1 3672	62 62	23-1B	60°C vapor SDW
JCI 003	A516 Grade 55	7 86	4536	51 80	1 5169	71 95	23-1B	60°C vapor SDW
JCI 004	A516 Grade 55	7 86	4536	51 63	2 3630	112 46	23-1A	60°C aqueous SDW
JCI 005	A516 Grade 55	7 86	4536	52 04	2 1855	103 18	23-1A	60°C aqueous SDW
JCI 006	A516 Grade 55	7 86	4536	52 45	2 1291	99 73	23-1A	60°C aqueous SDW
JCI 007	A516 Grade 55	7 86	8760	51 94	1 1230	27 51	23-2B	60°C vapor SDW
JCI 008	A516 Grade 55	7 86	8760	51 64	1 1154	27 48	23-2B	60°C vapor SDW
JCI 009	A516 Grade 55	7 86	8760	51 56	1 5948	39 35	23-2B	60°C vapor SDW
JCI 010	A516 Grade 55	7 86	8760	51 41	2 9353	72 64	23-2A	60°C aqueous SDW
JCI 011	A516 Grade 55	7 86	8760	51 61	2 9572	72 89	23-2A	60°C aqueous SDW
JCI 012	A516 Grade 55	7 86	8760	52 62	4 4224	106 93	23-2A	60°C aqueous SDW
JCI 031	A516 Grade 55	7 86	4632	52 57	1 3978	63 98	22-1B	90°C vapor SDW
JCI 032	A516 Grade 55	7 86	4632	51 67	1 3903	64 74	22-1B	90°C vapor SDW
JCI 033	A516 Grade 55	7 86	4632	52 45	2 0873	95 75	22-1B	90°C vapor SDW
JCI 034	A516 Grade 55	7 86	4632	51 70	3 8763	180 42	22-1A	90°C aqueous SDW
JCI 035	A516 Grade 55	7 86	4632	51 93	1 2534	58 08	22-1A	90°C aqueous SDW
JCI 036	A516 Grade 55	7 86	4632	52 56	1 4476	66 27	22-1A	90°C aqueous SDW
JCI 037	A516 Grade 55	7 86	8832	52 69	2 3028	55 15	22-2B	90°C vapor SDW
JCI 038	A516 Grade 55	7 86	8832	51 87	2 7491	66 88	22-2B	90°C vapor SDW
JCI 039	A516 Grade 55	7 86	8832	51 75	3 0260	73 79	22-2B	90°C vapor SDW
JCI 040	A516 Grade 55	7 86	8832	52 13	2 6870	65 04	22-2A	90°C aqueous SDW
JCI 041	A516 Grade 55	7 86	8832	51 72	2 6943	65 73	22-2A	90°C aqueous SDW

Sample identification	Alloy	Density (g/cc)	Exposure time (hours)	Surface area (sq cm)	Weight loss (g)	Corrosion rate (μm/y)	Vessel number-rack number	Test environment
JCI 042	A516 Grade 55	7 86	8832	51 74	3 6357	88 68	22-2A	90°C aqueous SDW
JCI 061	A516 Grade 55	7 86	4392	51 66	4 2432	208 44	21-1B	60°C vapor SCW
JCI 062	A516 Grade 55	7 86	4392	51 79	4 7602	233 23	21-1B	60°C vapor SCW
JCI 063	A516 Grade 55	7 86	4392	51 78	5 2537	257 47	21-1B	60°C vapor SCW
JCI 064	A516 Grade 55	7 86	4392	51 81	1 1847	58 03	21-1A	60°C aqueous SCW
JCI 065	A516 Grade 55	7 86	4392	51 57	1 2228	60 17	21-1A	60°C aqueous SCW
JCI 066	A516 Grade 55	7 86	4392	52 47	1 2927	62 52	21-1A	60°C aqueous SCW
JCI 067	A516 Grade 55	7 86	8760	52 42	7 1119	172 62	21-2B	60°C vapor SCW
JCI 068	A516 Grade 55	7 86	8760	51 79	8 3212	204 41	21-2B	60°C vapor SCW
JCI 069	A516 Grade 55	7 86	8760	51 72	10 8980	268 07	21-2B	60°C vapor SCW
JCI 070	A516 Grade 55	7 86	8760	51 62	0 4949	12 20	21-2A	60°C aqueous SCW
JCI 071	A516 Grade 55	7 86	8760	51 55	0 5228	12 90	21-2A	60°C aqueous SCW
JCI 072	A516 Grade 55	7 86	8760	52 81	0 5393	12 99	21-2A	60°C aqueous SCW
JCI 091	A516 Grade 55	7 86	4344	51 75	5 5776	276 51	20-1B	90°C vapor SCW
JCI 092	A516 Grade 55	7 86	4344	51 85	3 5537	175 85	20-1B	90°C vapor SCW
JCI 093	A516 Grade 55	7 86	4344	52 75	5 5332	269 12	20-1B	90°C vapor SCW
JCI 094	A516 Grade 55	7 86	4344	52 63	0 1516	7 39	20-1A	90°C aqueous SCW
JCI 095	A516 Grade 55	7 86	4344	51 55	0 1832	9 12	20-1A	90°C aqueous SCW
JCI 096	A516 Grade 55	7 86	4344	51 51	0 1811	9 02	20-1A	90°C aqueous SCW
JCI 097	A516 Grade 55	7 86	8736	51 72	5 8566	144 45	20-2B	90°C vapor SCW
JCI 098	A516 Grade 55	7 86	8736	52 30	5 4115	132 00	20-2B	90°C vapor SCW
JCI 099	A516 Grade 55	7 86	8736	51 82	5 9495	146 48	20-2B	90°C vapor SCW
JCI 100	A516 Grade 55	7 86	8736	51 72	0 2693	6 64	20-2A	90°C aqueous SCW
JCI 101	A516 Grade 55	7 86	8736	52 91	0 2492	6 01	20-2A	90°C aqueous SCW
JCI 102	A516 Grade 55	7 86	8736	52 73	0 2585	6 25	20-2A	90°C aqueous SCW
KCA 001	A27 Grade 70-40	7 82	4536	51 85	1 5080	71 83	23-1B	60°C vapor SDW
KCA 002	A27 Grade 70-40	7 82	4536	51 82	1 2345	58 83	23-1B	60°C vapor SDW
KCA 003	A27 Grade 70-40	7 82	4536	51 88	1 3747	65 43	23-1B	60°C vapor SDW
KCA 004	A27 Grade 70-40	7 82	4536	51 96	2 1528	102 33	23-1A	60°C aqueous SDW
KCA 005	A27 Grade 70-40	7 82	4536	51 27	2 1123	101 74	23-1A	60°C aqueous SDW
KCA 006	A27 Grade 70-40	7 82	4536	52 14	2 7595	130 70	23-1A	60°C aqueous SDW
KCA 007	A27 Grade 70-40	7 82	8760	51 84	1 5936	39 31	23-2B	60°C vapor SDW
KCA 008	A27 Grade 70-40	7 82	8760	51 67	1 4780	36 58	23-2B	60°C vapor SDW
KCA 009	A27 Grade 70-40	7 82	8760	51 61	1 5809	39 17	23-2B	60°C vapor SDW
KCA 010	A27 Grade 70-40	7 82	8760	51 97	3 0283	74 51	23-2A	60°C aqueous SDW
KCA 011	A27 Grade 70-40	7 82	8760	51 72	3 0173	74 60	23-2A	60°C aqueous SDW
KCA 012	A27 Grade 70-40	7 82	8760	51 84	3 0572	75 41	23-2A	60°C aqueous SDW
KCA 031	A27 Grade 70-40	7 82	4632	52 31	2 1361	98 76	22-1B	90°C vapor SDW
KCA 032	A27 Grade 70-40	7 82	4632	51 94	1 9102	88 93	22-1B	90°C vapor SDW
KCA 033	A27 Grade 70-40	7 82	4632	51 68	1 3464	63 00	22-1B	90°C vapor SDW

Sample identification	Alloy	Density (g/cc)	Exposure time (hours)	Surface area (sq cm)	Weight loss (g)	Corrosion rate (μm/y)	Vessel number-rack number	Test environment
KCA 034	A27 Grade 70-40	7 82	4632	51 91	1 6924	78 85	22-1A	90°C aqueous SDW
KCA 035	A27 Grade 70-40	7 82	4632	51 96	1 8275	85 06	22-1A	90°C aqueous SDW
KCA 036	A27 Grade 70-40	7 82	4632	51 94	1 7086	79 56	22-1A	90°C aqueous SDW
KCA 037	A27 Grade 70-40	7 82	8832	51 35	1 8885	46 65	22-2B	90°C vapor SDW
KCA 038	A27 Grade 70-40	7 82	8832	52 11	2 1384	52 05	22-2B	90°C vapor SDW
KCA 039	A27 Grade 70-40	7 82	8832	51 80	1 8046	44 19	22-2B	90°C vapor SDW
KCA 040	A27 Grade 70-40	7 82	8832	51 98	2 3967	58 48	22-2A	90°C aqueous SDW
KCA 041	A27 Grade 70-40	7 82	8832	51 92	1 4684	35 87	22-2A	90°C aqueous SDW
KCA 042	A27 Grade 70-40	7 82	8832	51 88	2 0512	50 14	22-2A	90°C aqueous SDW
KCA 061	A27 Grade 70-40	7 82	4392	51 79	2 2727	111 93	21-1B	60°C vapor SCW
KCA 062	A27 Grade 70-40	7 82	4392	51 65	2 2598	111 59	21-1B	60°C vapor SCW
KCA 063	A27 Grade 70-40	7 82	4392	51 65	2 3443	115 77	21-1B	60°C vapor SCW
KCA 064	A27 Grade 70-40	7 82	4392	51 88	1 2545	61 67	21-1A	60°C aqueous SCW
KCA 065	A27 Grade 70-40	7 82	4392	51 77	1 2354	60 87	21-1A	60°C aqueous SCW
KCA 066	A27 Grade 70-40	7 82	4392	51 63	1 2578	62 14	21-1A	60°C aqueous SCW
KCA 067	A27 Grade 70-40	7 82	8760	50 80	3 1889	80 27	21-2B	60°C vapor SCW
KCA 068	A27 Grade 70-40	7 82	8760	51 54	4 2533	105 54	21-2B	60°C vapor SCW
KCA 069	A27 Grade 70-40	7 82	8760	51 63	4 9141	121 72	21-2B	60°C vapor SCW
KCA 071	A27 Grade 70-40	7 82	8760	51 83	0 4899	12 09	21-2A	60°C aqueous SCW
KCA 072	A27 Grade 70-40	7 82	8760	49 81	0 5594	14 36	21-2A	60°C aqueous SCW
KCA 091	A27 Grade 70-40	7 82	4344	52 07	1 5204	75 29	20-1B	90°C vapor SCW
KCA 092	A27 Grade 70-40	7 82	4344	51 66	1 8697	93 33	20-1B	90°C vapor SCW
KCA 093	A27 Grade 70-40	7 82	4344	51 67	2 0501	102 31	20-1B	90°C vapor SCW
KCA 094	A27 Grade 70-40	7 82	4344	51 32	0 2941	14 78	20-1A	90°C aqueous SCW
KCA 095	A27 Grade 70-40	7 82	4344	51 41	0 2997	15 03	20-1A	90°C aqueous SCW
KCA 096	A27 Grade 70-40	7 82	4344	52 00	0 2541	12 60	20-1A	90°C aqueous SCW
KCA 097	A27 Grade 70-40	7 82	8736	52 09	2 9636	72 96	20-2B	90°C vapor SCW
KCA 098	A27 Grade 70-40	7 82	8736	51 84	3 4384	85 05	20-2B	90°C vapor SCW
KCA 099	A27 Grade 70-40	7.82	8736	52 10	3 5607	87 64	20-2B	90°C vapor SCW
KCA 100	A27 Grade 70-40	7 82	8736	52 26	0 3425	8 40	20-2A	90°C aqueous SCW
KCA 101	A27 Grade 70-40	7 82	8736	51 62	0 3156	7 84	20-2A	90°C aqueous SCW
KCA 102	A27 Grade 70-40	7 82	8736	51 92	0 3336	8 24	20-2A	90°C aqueous SCW
KCl 001	A27 Grade 70-40	7 82	4536	52 20	1 2639	59 80	23-1B	60°C vapor SDW
KCl 002	A27 Grade 70-40	7 82	4536	51 92	1 3488	64 16	23-1B	60°C vapor SDW
KCl 003	A27 Grade 70-40	7 82	4536	52 10	1 5664	74 25	23-1B	60°C vapor SDW
KCl 004	A27 Grade 70-40	7 82	4536	52 38	2 3001	108 44	23-1A	60°C aqueous SDW
KCl 005	A27 Grade 70-40	7 82	4536	52 15	1 9619	92 90	23-1A	60°C aqueous SDW
KCl 006	A27 Grade 70-40	7 82	4536	51 43	2 5326	121 60	23-1A	60°C aqueous SDW
KCl 007	A27 Grade 70-40	7 82	8760	50 55	1 5673	39 65	23-2B	60°C vapor SDW
KCl 008	A27 Grade 70-40	7 82	8760	52 44	1 6007	39 04	23-2B	60°C vapor SDW

Sample identification	Alloy	Density (g/cc)	Exposure time (hours)	Surface area (sq cm)	Weight loss (g)	Corrosion rate (μm/y)	Vessel number-rack number	Test environment
KCl 009	A27 Grade 70-40	7 82	8760	51 30	1 4713	36 68	23-2B	60°C vapor SDW
KCl 010	A27 Grade 70-40	7 82	8760	51.49	2 9077	72 21	23-2A	60°C aqueous SDW
KCl 011	A27 Grade 70-40	7 82	8760	52 05	3 2916	80 87	23-2A	60°C aqueous SDW
KCl 012	A27 Grade 70-40	7 82	8760	51 78	3 4692	85 68	23-2A	60°C aqueous SDW
KCl 031	A27 Grade 70-40	7 82	4632	52 26	1 5021	69 51	22-1B	90°C vapor SDW
KCl 032	A27 Grade 70-40	7 82	4632	50 37	1 0963	52 63	22-1B	90°C vapor SDW
KCl 033	A27 Grade 70-40	7 82	4632	52 51	0 9677	44 57	22-1B	90°C vapor SDW
KCl 034	A27 Grade 70-40	7 82	4632	51 63	1 5919	74 56	22-1A	90°C aqueous SDW
KCl 035	A27 Grade 70-40	7 82	4632	52 10	1 6205	75 23	22-1A	90°C aqueous SDW
KCl 036	A27 Grade 70-40	7 82	4632	52 30	1 6664	77 05	22-1A	90°C aqueous SDW
KCl 037	A27 Grade 70-40	7 82	8832	53 19	1 9821	47 27	22-2B	90°C vapor SDW
KCl 038	A27 Grade 70-40	7 82	8832	51 52	1 8171	44 74	22-2B	90°C vapor SDW
KCl 039	A27 Grade 70-40	7 82	8832	52 62	1 7186	41 43	22-2B	90°C vapor SDW
KCl 040	A27 Grade 70-40	7 82	8832	52 47	2 0312	49 10	22-2A	90°C aqueous SDW
KCl 041	A27 Grade 70-40	7 82	8832	52 22	2 2224	53 98	22-2A	90°C aqueous SDW
KCl 042	A27 Grade 70-40	7 82	8832	52 29	1 6682	40 46	22-2A	90°C aqueous SDW
KCl 061	A27 Grade 70-40	7 82	4392	52 41	3 5040	170 54	21-1B	60°C vapor SCW
KCl 062	A27 Grade 70-40	7 82	4392	51 64	3 6310	179 34	21-1B	60°C vapor SCW
KCl 063	A27 Grade 70-40	7 82	4392	52 36	5 1544	251 10	21-1B	60°C vapor SCW
KCl 064	A27 Grade 70-40	7 82	4392	52 12	1 7984	88 01	21-1A	60°C aqueous SCW
KCl 065	A27 Grade 70-40	7 82	4392	52 15	2 1304	104 20	21-1A	60°C aqueous SCW
KCl 066	A27 Grade 70-40	7 82	4392	51 83	1 7999	88 57	21-1A	60°C aqueous SCW
KCl 067	A27 Grade 70-40	7 82	8760	51 65	6 9146	171 18	21-2B	60°C vapor SCW
KCl 068	A27 Grade 70-40	7 82	8760	52 72	6 6746	161 90	21-2B	60°C vapor SCW
KCl 069	A27 Grade 70-40	7 82	8760	52 65	7 3699	179 01	21-2B	60°C vapor SCW
KCl 070	A27 Grade 70-40	7 82	8760	51 70	0 4937	12 21	21-2A	60°C aqueous SCW
KCl 071	A27 Grade 70-40	7 82	8760	52 36	0 4889	11 94	21-2A	60°C aqueous SCW
KCl 072	A27 Grade 70-40	7 82	8760	52 20	0 5152	12 62	21-2A	60°C aqueous SCW
KCl 091	A27 Grade 70-40	7 82	4344	52 64	2 6357	129 12	20-1B	90°C vapor SCW
KCl 092	A27 Grade 70-40	7 82	4344	51 87	3 6374	180 84	20-1B	90°C vapor SCW
KCl 093	A27 Grade 70-40	7 82	4344	52 32	4 4346	218 57	20-1B	90°C vapor SCW
KCl 094	A27 Grade 70-40	7 82	4344	52 66	0 1988	9 74	20-1A	90°C aqueous SCW
KCl 095	A27 Grade 70-40	7 82	4344	51 20	0 2076	10 46	20-1A	90°C aqueous SCW
KCl 096	A27 Grade 70-40	7 82	4344	51 99	0 2312	11 47	20-1A	90°C aqueous SCW
KCl 097	A27 Grade 70-40	7 82	8736	52 82	4 6898	113 86	20-2B	90°C vapor SCW
KCl 098	A27 Grade 70-40	7 82	8736	52 38	5 9939	146 72	20-2B	90°C vapor SCW
KCl 099	A27 Grade 70-40	7.82	8736	52 16	8 9523	220 08	20-2B	90°C vapor SCW
KCl 100	A27 Grade 70-40	7 82	8736	52 20	0 3202	7 87	20-2A	90°C aqueous SCW
KCl 101	A27 Grade 70-40	7 82	8736	52 06	0.3264	8 04	20-2A	90°C aqueous SCW
KCl 102	A27 Grade 70-40	7.82	8736	52 31	0 2984	7 32	20-2A	90°C aqueous SCW

Sample identification	Alloy	Density (g/cc)	Exposure time (hours)	Surface area (sq cm)	Weight loss (g)	Corrosion rate (μm/y)	Vessel number-rack number	Test environment
LCA 001	Inconel 625	8 44	4296	52 18	–0 0001	0 00	25-1B	60°C vapor SAW
LCA 002	Inconel 625	8 44	4296	51 52	0 0001	0 00	25-1B	60°C vapor SAW
LCA 003	Inconel 625	8 44	4296	52 37	0 0183	0 84	25-1B	60°C vapor SAW
LCA 004	Inconel 625	8 44	4296	51 66	0 0018	0 08	25-1A	60°C aqueous SAW
LCA 005	Inconel 625	8 44	4296	52 04	0 0007	0 03	25-1A	60°C aqueous SAW
LCA 006	Inconel 625	8 44	4296	52 13	0 0007	0 03	25-1A	60°C aqueous SAW
LCA 007	Inconel 625	8 44	8376	51 59	0 0011	0 03	25-2B	60°C vapor SAW
LCA 008	Inconel 625	8 44	8376	51 44	0 0002	0 00	25-2B	60°C vapor SAW
LCA 009	Inconel 625	8 44	8376	52 40	0 0007	0 02	25-2B	60°C vapor SAW
LCA 010	Inconel 625	8 44	8376	50 91	0 0014	0 03	25-2A	60°C aqueous SAW
LCA 011	Inconel 625	8 44	8376	52 28	0 0012	0 03	25-2A	60°C aqueous SAW
LCA 012	Inconel 625	8 44	8376	52 53	0 0008	0 02	25-2A	60°C aqueous SAW
LCA 031	Inconel 625	8 44	4344	52 87	–0 0001	0 00	26-1B	90°C vapor SAW
LCA 032	Inconel 625	8 44	4344	52 17	0 0013	0 06	26-1B	90°C vapor SAW
LCA 033	Inconel 625	8 44	4344	52 21	–0 0001	0 00	26-1B	90°C vapor SAW
LCA 034	Inconel 625	8 44	4344	52 44	0 0002	0 01	26-1A	90°C aqueous SAW
LCA 035	Inconel 625	8 44	4344	52 48	0 0005	0 02	26-1A	90°C aqueous SAW
LCA 036	Inconel 625	8 44	4344	52 36	0 0000	0 00	26-1A	90°C aqueous SAW
LCA 037	Inconel 625	8 44	8784	52 02	0 0006	0 01	26-2B	90°C vapor SAW
LCA 038	Inconel 625	8 44	8784	52 07	0 0007	0 02	26-2B	90°C vapor SAW
LCA 039	Inconel 625	8 44	8784	52 50	0 0004	0 01	26-2B	90°C vapor SAW
LCA 040	Inconel 625	8 44	8784	52 12	–0 0049	-0 11	26-2A	90°C aqueous SAW
LCA 041	Inconel 625	8 44	8784	52 30	–0 0008	–0 02	26-2A	90°C aqueous SAW
LCA 042	Inconel 625	8 44	8784	52 28	–0 0006	–0 01	26-2A	90°C aqueous SAW
LCA 061	Inconel 625	8 44	4392	52 23	0 0012	0 05	27-1B	60°C vapor SCW
LCA 062	Inconel 625	8 44	4392	51 79	0 0007	0 03	27-1B	60°C vapor SCW
LCA 063	Inconel 625	8 44	4392	51 77	0 0013	0 06	27-1B	60°C vapor SCW
LCA 064	Inconel 625	8 44	4392	52 21	0 0015	0 07	27-1A	60°C aqueous SCW
LCA 065	Inconel 625	8 44	4392	52 22	0 0011	0 05	27-1A	60°C aqueous SCW
LCA 066	Inconel 625	8 44	4392	52 44	0 0018	0 08	27-1A	60°C aqueous SCW
LCA 091	Inconel 625	8 44	4464	51 11	0 0004	0 02	28-1B	90°C vapor SCW
LCA 092	Inconel 625	8 44	4464	52 11	0 0002	0 01	28-1B	90°C vapor SCW
LCA 093	Inconel 625	8 44	4464	52 37	0 0011	0 05	28-1B	90°C vapor SCW
LCA 094	Inconel 625	8 44	4464	52 71	0 0025	0 11	28-1A	90°C aqueous SCW
LCA 095	Inconel 625	8 44	4464	52 49	0 0022	0 10	28-1A	90°C aqueous SCW
LCA 096	Inconel 625	8 44	4464	52 41	0 0055	0 24	28-1A	90°C aqueous SCW
LCA 121	Inconel 625	8 44	4464	51 79	0 0004	0 02	29-1B	60°C vapor SDW
LCA 122	Inconel 625	8 44	4464	52 05	0 0001	0 00	29-1B	60°C vapor SDW
LCA 123	Inconel 625	8 44	4464	52 12	0 0004	0 02	29-1B	60°C vapor SDW
LCA 124	Inconel 625	8 44	4464	52 12	0 0003	0 01	29-1A	60°C aqueous SDW

Sample identification	Alloy	Density (g/cc)	Exposure time (hours)	Surface area (sq cm)	Weight loss (g)	Corrosion rate (μm/y)	Vessel number-rack number	Test environment
LCA 125	Inconel 625	8 44	4464	51 25	0 0006	0 03	29-1A	60°C aqueous SDW
LCA 126	Inconel 625	8 44	4464	51 78	0 0008	0 04	29-1A	60°C aqueous SDW
LCA 157	Inconel 625	8 44	4392	52 13	0 0004	0 02	30-1B	90°C vapor SDW
LCA 158	Inconel 625	8 44	4392	52 47	0 0003	0 01	30-1B	90°C vapor SDW
LCA 159	Inconel 625	8 44	4392	52 39	0 0000	0 00	30-1B	90°C vapor SDW
LCA 160	Inconel 625	8 44	4392	52 33	0 0003	0 01	30-1A	90°C aqueous SDW
LCA 161	Inconel 625	8 44	4392	52 19	0 0014	0 06	30-1A	90°C aqueous SDW
LCA 162	Inconel 625	8 44	4392	52 25	0 0007	0 03	30-1A	90°C aqueous SDW
LCJ 001	Inconel 625	8 44	4296	51 21	–0 0004	–0 02	25-1B	60°C vapor SAW
LCJ 002	Inconel 625	8 44	4296	50 52	–0 0003	–0 01	25-1B	60°C vapor SAW
LCJ 003	Inconel 625	8 44	4296	51 45	–0 0003	–0 01	25-1B	60°C vapor SAW
LCJ 004	Inconel 625	8 44	4296	51 59	0 0007	0 03	25-1A	60°C aqueous SAW
LCJ 005	Inconel 625	8 44	4296	51 44	0 0011	0 05	25-1A	60°C aqueous SAW
LCJ 006	Inconel 625	8 44	4296	51 12	0 0016	0 08	25-1A	60°C aqueous SAW
LCJ 007	Inconel 625	8 44	8376	51 42	0 0004	0 01	25-2B	60°C vapor SAW
LCJ 008	Inconel 625	8 44	8376	51 61	0 0007	0 02	25-2B	60°C vapor SAW
LCJ 009	Inconel 625	8 44	8376	51 36	0 0009	0 02	25-2B	60°C vapor SAW
LCJ 010	Inconel 625	8 44	8376	51 17	0 0015	0 04	25-2A	60°C aqueous SAW
LCJ 011	Inconel 625	8 44	8376	51 34	0 0024	0 06	25-2A	60°C aqueous SAW
LCJ 012	Inconel 625	8 44	8376	51 27	0 0019	0 05	25-2A	60°C aqueous SAW
LCJ 031	Inconel 625	8 44	4344	51 57	0 0001	0 00	26-1B	90°C vapor SAW
LCJ 032	Inconel 625	8 44	4344	51 53	0 0007	0 03	26-1B	90°C vapor SAW
LCJ 033	Inconel 625	8 44	4344	51 67	0 0004	0 02	26-1B	90°C vapor SAW
LCJ 034	Inconel 625	8 44	4344	51 47	0 0007	0 03	26-1A	90°C aqueous SAW
LCJ 035	Inconel 625	8 44	4344	51 42	0 0000	0 00	26-1A	90°C aqueous SAW
LCJ 036	Inconel 625	8 44	4344	50 41	–0 0006	–0 03	26-1A	90°C aqueous SAW
LCJ 037	Inconel 625	8 44	8784	51 55	0 0003	0 01	26-2B	90°C vapor SAW
LCJ 038	Inconel 625	8 44	8784	51 70	0 0006	0 01	26-2B	90°C vapor SAW
LCJ 039	Inconel 625	8 44	8784	50 38	–0 0004	–0 01	26-2B	90°C vapor SAW
LCJ 040	Inconel 625	8 44	8784	51 68	–0 0006	–0 01	26-2A	90°C aqueous SAW
LCJ 041	Inconel 625	8 44	8784	50 49	–0 0013	–0 03	26-2A	90°C aqueous SAW
LCJ 042	Inconel 625	8 44	8784	51 40	–0 0005	–0 01	26-2A	90°C aqueous SAW
LCJ 061	Inconel 625	8 44	4392	51 34	0 0006	0 03	27-1B	60°C vapor SCW
LCJ 062	Inconel 625	8 44	4392	50 85	0 0021	0 10	27-1B	60°C vapor SCW
LCJ 063	Inconel 625	8 44	4392	51 14	0 0005	0 02	27-1B	60°C vapor SCW
LCJ 064	Inconel 625	8 44	4392	51 10	0 0017	0 08	27-1A	60°C aqueous SCW
LCJ 065	Inconel 625	8 44	4392	51 35	0 0014	0 06	27-1A	60°C aqueous SCW
LCJ 066	Inconel 625	8 44	4392	51 27	0 0022	0 10	27-1A	60°C aqueous SCW
LCJ 091	Inconel 625	8 44	4464	51 38	0 0002	0 01	28-1B	90°C vapor SCW
LCJ 092	Inconel 625	8 44	4464	51 50	0 0006	0 03	28-1B	90°C vapor SCW

Sample identification	Alloy	Density (g/cc)	Exposure time (hours)	Surface area (sq cm)	Weight loss (g)	Corrosion rate (μm/y)	Vessel number-rack number	Test environment
LCJ 093	Inconel 625	8 44	4464	51 34	0 0004	0 02	28-1B	90°C vapor SCW
LCJ 094	Inconel 625	8 44	4464	51 47	0 0013	0 06	28-1A	90°C aqueous SCW
LCJ 095	Inconel 625	8 44	4464	51 47	0 0015	0 07	28-1A	90°C aqueous SCW
LCJ 096	Inconel 625	8 44	4464	51 21	0 0026	0 12	28-1A	90°C aqueous SCW
LCJ 121	Inconel 625	8 44	4464	51 16	0 0002	0 01	29-1B	60°C vapor SDW
LCJ 122	Inconel 625	8 44	4464	50 83	0 0007	0 03	29-1B	60°C vapor SDW
LCJ 123	Inconel 625	8 44	4464	50 64	–0 0003	–0 01	29-1B	60°C vapor SDW
LCJ 124	Inconel 625	8 44	4464	51 06	0 0008	0 04	29-1A	60°C aqueous SDW
LCJ 125	Inconel 625	8 44	4464	51 29	0 0003	0 01	29-1A	60°C aqueous SDW
LCJ 126	Inconel 625	8 44	4464	50 66	0 0000	0 00	29-1A	60°C aqueous SDW
LCJ 157	Inconel 625	8 44	4392	51 62	0 0004	0 02	30-1B	90°C vapor SDW
LCJ 158	Inconel 625	8 44	4392	51 42	0 0018	0 08	30-1B	90°C vapor SDW
LCJ 159	Inconel 625	8 44	4392	51 43	0 0004	0 02	30-1B	90°C vapor SDW
LCJ 160	Inconel 625	8 44	4392	50 07	0 0001	0 00	30-1A	90°C aqueous SDW
LCJ 161	Inconel 625	8 44	4392	50 45	0 0005	0 02	30-1A	90°C aqueous SDW
LCJ 162	Inconel 625	8 44	4392	52 06	0 0016	0 07	30-1A	90°C aqueous SDW

2.3 Electrochemical Corrosion Testing

by Ajit Roy

2.3.1 Potentiodynamic and Potentiostatic Polarization

Electrochemical cyclic potentiodynamic polarization (CPP) experiments have been performed on several candidate waste-package container materials The purpose of the CPP experiments is to evaluate the materials' susceptibility to localized attack, such as pitting and crevice corrosion, in deaerated acidic, neutral, and alkaline brines containing 1, 5, and 10 weight percent (wt%) NaCl at room temperature, 50°, 60°, 70°, and 90°C. The materials tested include

- Austenitic Types 304 and 316L stainless steels
- Iron–nickel–chromium–molybdenum (Fe-Ni-Cr-Mo) Alloys 825, G-3, and G-30.
- Nickel-base Alloys C-4, 625, and C-22
- Titanium-base Alloy Ti Gr-12
- Nickel-copper Alloy 400
- 70/30 Cupronickel

All test solutions were prepared with distilled water and reagent-grade chemicals Whereas acidification was done by adding sulfuric acid to the brine, calcium hydroxide was added to prepare the alkaline salt solution. The pH of the solutions ranged between 2 and 3, 6 and 7, and 10 and 11, respectively Current CPP experiments are being performed on a few, selected, candidate inner container materials, such as Alloys 625, C-22, and Ti Gr-12 in acidic brines containing NaCl and $FeCl_3$ at different temperatures

A three-electrode technique is being used to conduct the CPP and potentiostatic polarization experiments in Pyrex corrosion cells that contained a test specimen as a working electrode, two graphite counter electrodes, and a Luggin capillary connected to a reference electrode Initially, a saturated calomel reference electrode was used at ambient temperature and 60°C Later, Ag/AgCl was used as the reference electrode at all test temperatures Cylindrical specimens were used in the CPP tests Specimens for the potentiostatic polarization experiments were both cylindrical and disc-shaped The test specimens were polished with 600-grit paper and cleaned with distilled water and ethanol before their exposure to the test solutions

Before conducting the polarization experiments, a few confirmatory tests (ASTM, 1995) were performed on Type 430 stainless steel in deaerated 1 0 N sulfuric acid solution at 30°C The purpose of these tests was to obtain standard polarization plots and to verify the reproducibility of the instrumentation Electrochemical potential was applied to the test specimens using EG&G Models 273 and 283 potentiostats controlled by an IBM-compatible PC with EG&G Model 252/352 Softcorr II software A controlled-temperature water bath maintained the test temperature at the desired value within ±0 1°C For tests at elevated temperatures, a Pyrex condenser was fitted to one port of the cell to capture evaporated water and return it to the test cell. Dynamic potential scans were carried out in CPP experiments in the noble direction at various rates, including the ASTM-specified rate (ASTM, 1995) of 0 17 mV/s, and at rates of 0.043, 0 085 and 0.34 mV/s. These scans commenced at the stable corrosion potential E_{corr}, and continued to a potential sufficiently noble to cause pitting or exhibit pit-like behavior before reversing the scan at the same rate.

In electrochemical terms, the initiation of pitting occurs at a critical potential E_{pit} (Baboian and Haynes, 1981), which is used as a measure of resistance to pitting corrosion At E_{pit}, the anodic polarization curve changes its slope abruptly, showing a dramatic increase in current density The more noble E_{pit} is, the more resistant the material is to pitting attack. For susceptible metals and alloys, as the direction of polarization is reversed after some degree of anodic polarization greater than E_{pit}, a hysteresis is observed in which the return polarization curve follows an active (higher-current) path, compared to the initial anodic one The crossover at the passive current density defines a repassivation or protection potential E_{prot} (Baboian and Haynes, 1981), below which established pits are presumed not to continue to grow In contrast, new pits can initiate only at potentials greater than E_{pit} Between E_{prot} and E_{pit}, new pits cannot initiate, but old ones can still grow

Values of E_{pit} measured by CPP experiments were used in selecting the controlled potential to be applied (E_{app}) in potentiostatic polarization tests involving Alloys 825, G-3, G-30, C-4, 625, C-22,and Ti Gr-12 These tests were performed only in an acidic brine containing 5 wt% NaCl at temperatures of 30°, 60°, and 90°C. The purpose was to evaluate the initiation and growth of localized attack at various controlled potentials, which were located either above or below the measured E_{pit} values

The pH of the test solution was measured at room temperature before and after each experiment At the conclusion of each test, each specimen was cleaned with distilled water and ethanol The cleaned specimen was visually examined, followed by an optical microscopic evaluation to detect the presence or absence of pitting The specimen underwent further metallographic examination if pits were detected by optical microscopy

2.3.2 Cyclic Potentiodynamic Polarization Test Results

As expected, results indicate that Types 304 and 316L stainless steels were susceptible to severe pitting corrosion in all three tested environments at 60° and 90°C, showing discernible E_{pit} values (Roy et al , 1995a, Roy and McCright, 1995b, Roy et al , 1996) Alloy 400 and 70/30 Cupronickel showed a propensity to dissolution in all environments both at ambient and elevated temperatures Thick, orange-colored corrosion products were seen floating in the solutions, suggesting that elemental nickel, relatively electronegative compared to copper (i e , –250 mV versus +337 mV, SHE), might have undergone preferential dissolution in response to the application of potential during the CPP experiments As with austenitic stainless steels, the maximum current density attained just prior to the potential scan reversal was quite high

Results indicate that Alloys 825, G-3, and G-30 underwent pitting and crevice corrosion in all tested environments, with Alloy 825 showing the maximum susceptibility (Roy et al , 1997a, Roy et al., 1998) Alloy C-4 suffered from pitting and crevice corrosion in 90°C acidic, neutral, and alkaline brines. However, the extent of damage was less severe compared to that of Fe-Ni-Cr-Mo alloys Alloy C-22 and Ti Grade-12 were immune to localized attack under all test conditions used, indicating their suitability for application as nuclear waste-package container materials The specimen surface appearance of Fe-Ni-Cr-Mo alloys, Ni-Cr-Mo alloys, and Ti Gr-12 tested in 90°C acidic brine containing 10 wt% NaCl is shown in Figure 2 3-1 A comparison of specimen surface appearance of Alloys C-22 and 625 (Roy et al , 1997b) revealed that the latter alloy was susceptible to degradation, including crevice corrosion, pitting corrosion, and intergranular attack (Figure 2 3-2), once again demonstrating the superior corrosion resistance of Alloy C-22

Figure 2.3-1. Surface appearance (horizontal mode) of materials tested in acidic brines containing 10 wt% NaCl at 90°C.

Figure 2.3-2. Surface appearance (vertical mode) of alloys C-22 and 625 in acidic brines containing 10 wt% NaCl at 90°C.

For alloys susceptible to pitting, the critical pitting potential E_{pit} was shifted to more active values with increasing chloride ion (Cl^-) concentration (Figure 2 3-3), confirming results of other investigators The mechanism of transition from passivity to pitting in these alloys may be based on reversible competitive adsorption of Cl^- into the double layer (oxide/liquid interface) with oxygen for sites on the alloy surface. For Alloy C-22 and Ti Grade-12, which did not suffer from localized attack, the critical potential became sufficiently noble to overlap the transpassive region Formation of protective oxides on the alloy surface resulting from oxygen evolution due to electrolysis of test solutions may possibly account for enhanced pitting corrosion resistance of these two alloys.

Figure 2.3-3. Critical pitting potential versus chloride concentration in acidic brines at 90°C.

The E_{pit} for susceptible alloys was shifted to more noble values due to a change in pH from acidic to neutral, as shown in Figure 2 3-4 At alkaline pH, Alloys G-3, G-30, and C-4 showed somewhat lower E_{pit} values compared to those in neutral brines For Alloy 825, E_{pit} was shifted to a slightly more noble value in alkaline brine. The more active E_{pit} value for susceptible alloys in acidic brines may be the result of acceleration of cathodic reaction due to high concentration of hydrogen ions The inhibitive effect of hydroxyl ions may possibly account for the noble E_{pit} value at alkaline pH

Figure 2.3-4. Pitting potential versus pH in brines containing 10 wt% NaCl at 90°C.

In general, E_{pit} became more active with increasing temperature (Figure 2 3-5 and Figure 2 3-6), confirming the results of other studies These results may suggest the possibility of a temperature-induced change in the protective properties of passive film, resulting in a reduction in resistance to localized breakdown as temperature is increased

Figure 2.3-5. Pitting potential versus temperature for alloy G-3 in acidic brines.

Figure 2.3-6. Pitting potential versus temperature for alloy G-30 in neutral brines.

In terms of the effect of potential scan rate on E_{pit}, a general trend was not observed that would be valid for all the alloy and environment combinations studied. However, two basic types of E_{pit} response to increasing scan rate were observed The first response is an initial shift in E_{pit} to more noble values with increasing scan rate, followed by a shift in the active direction (Figure 2 3-7). The second type of response may consist of an initial shift of E_{pit} in the noble direction in response to a faster scan rate, followed by subsequent shifts in the active and noble directions, respectively, as shown in Figure 2 3-8. The E_{pit} response to scan rate appears to be a function of the kinetics of passive film formation at applied potentials

No consistent pattern was observed for the effect of Cl^- concentration, temperature, pH, and potential scan rate on E_{corr} and E_{prot}

Figure 2.3-7. **Pitting potential versus scan rate in alkaline brines containing 10 wt% NaCl at 90°C.**

Figure 2.3-8. **Pitting potential versus scan rate in acidic brines containing 10 wt% NaCl at 90°C.**

2.3.3 Potentiostatic Polarization Test Results

2.3.3.1 Tests at $E_{app} > E_{pit}$

Controlled potentials (E_{app}) of 150, 160, 170, and 180 mV (versus Ag/AgCl) were selected for tests involving Alloy 825 in view of its measured E_{pit} value of 130 mV in an acidic brine of 5 wt% NaCl at 90°C Results (Roy et al , 1997c) indicate that pitting was initiated at all E_{app} values, and the extent of pitting was more pronounced at higher applied potentials, as shown in Figure 2 3-9. Except at 150 mV, fairly deep, round pits were observed in specimens tested at the other three E_{app} values These three specimens were also characterized by deep crevice corrosion, which possibly resulted from solution trapped under the gasket used in the specimen holder Most of the pits were located away from the crevice region.

For Alloy G-3, tests were performed in a similar environment at E_{app} values of 355, 390, 420, and 440 mV because an E_{pit} value of 326 mV (Ag/AgCl) was obtained from the CPP diagram Pitting was observed at all four E_{app} values However, their shapes were different from those seen on Alloy 825 specimens In contrast to round pits observed with Alloy 825, pits observed in Alloy G-3 specimens were elongated and deeper, with some pits located along the crevice boundary As observed with Alloy 825, the maximum pitting of Alloy G-3 was experienced at the highest applied potential

Figure 2.3-9. **Microscopic view of potentiostatically polarized Alloy 825 specimens in 90°C acidic brines at various controlled electrochemical potentials (E_{app}).**

2.3.3.2 Tests at $E_{app} > E_{corr}$

The measured E_{corr} value for Alloy 825 in 30°C brine ranged between –164 and –285 mV Potentials of 250, 275, 300, and 350 mV with respect to E_{corr} value were used under potentiostatic control to initiate localized attack in this alloy. Results (Roy et al , 1997c) indicate that this material was immune to pitting and crevice corrosion at E_{cont} values of 250 and 275 mV at 30°C for exposure times of 125 and 90 hours, respectively Severe crevice corrosion was observed with this alloy at the higher E_{app} values even after exposure for only 20 hours at a similar temperature For Alloy G-30, no localized attack was observed in a similar environment at E_{app} values of 200 to 300 mV, but it became susceptible to crevice corrosion at 350 and 400 mV after 20 hours of testing at 30°C Similarly, Alloy C-4 did not show any attack at E_{app} values of 200 and 300 mV at 30°C However, crevice corrosion was observed in this alloy at an applied potential of 350 mV at this temperature

As to the localized corrosion behavior of Alloys 625 and C-22, the former alloy exhibited a tendency to crevice corrosion in a 30°C brine at E_{app} values of 650, 750, and 800 mV after testing for 167 hours. Furthermore, surface cracks were observed with this material in the crevice region On the other hand, Alloy C-22 was immune to localized attack in the same environment at potentiostatic potentials of 500, 600, and 700 mV for a similar test duration However, this alloy experienced a crevice corrosion tendency at 60°C under an E_{app} value of 700 mV, suggesting that the critical crevice corrosion temperature for Alloy C-22 may be higher than that for Alloy 625 when tested in an acidic brine under potentiostatic control No

pitting was observed with any high-nickel alloys tested at 30 ° and 60°C Finally, Ti Grade-12 was immune to localized corrosion at E_{app} values of 500 to 750 mV, even up to a test temperature of 90°C.

2.3.3.3 Combined Potentiodynamic and Potentiostatic Tests

For Alloy C-22, the results of a room-temperature potentiodynamic polarization experiment performed at a potential scan rate of 10^{-6} mV/s indicated a slope change in the E versus I curve at an approximate electrochemical potential of 810 mV (Roy et al., 1997c). The test specimen was then potentiostatically polarized for almost 96 hours at an E_{app} value of 820 mV. The specimen did not exhibit any localized attack, only slight discoloration of the specimen was noticed

A second potentiodynamic test was performed in a similar environment using an Alloy C-22 specimen at a potential scan rate of 0 17 mV/s. A slope change was observed in the polarization diagram at approximately 864 mV. An examination of the same specimen, which was subsequently polarized under potentiostatic control at 870 mV for almost 94 hours, revealed more discoloration of the test specimen, yet no localized corrosion. The potentiostatic polarization diagram (Figure 2 3-10) showed a gradual increase in current density up to 33 hours of testing, followed by a sharp drop between 33 and 50 hours, and eventual stabilization beyond this period

Figure 2.3-10. Potentiostatic polarization curve for Alloy C-22 in a 30°C acidic brine (pH ≈ 2.69) at an E_{cont} value of 870 mV (Ag/AgCl).

Figure 2 3-11 shows the results (Roy et al , 1997c) of an ambient-temperature potentiostatic polarization experiment involving Alloy 625 in a similar environment at an E_{cont} value of 854 mV A drop in current density was observed in the E versus I curve up to the initial 9 hours of testing, followed by a gradual shift in the upward direction until reaching a stable value after 50 hours of testing Examination of the polarized specimen by optical microscopy showed both crevice corrosion and surface attack in and around the crevice region, but no pits Additional potentiostatic testing for a much longer duration is in progress using both Alloy C-22 and Ti Gr-12

Figure 2.3-11. Potentiostatic polarization curve for Alloy 625 in a 30°C acidic brine (pH ≈ 2.69) at an E_{cont} value of 854 mV (Ag/AgCl).

2.3.4 Galvanic Corrosion Testing

The precise method of fabricating the nuclear waste packages is yet to be finalized Two alternative approaches are currently being considered One approach is to fabricate the two barriers separately, and then to shrink-fit the inner barrier inside the outer barrier by slipping the inner container into the outer one that will be expanded by heating prior to insertion of the inner container. Although this method may provide sufficient bonding between the two barriers, it is likely that gaps will occur at some locations where breached liquid may be trapped, thus causing galvanic interaction between the two barriers Under this scenario, the more electronegative outer container material may undergo increased corrosion attack while protecting the more noble inner container material.

The second approach is to fabricate the waste packages from clad or weld-overlay materials. In this case, the outer corrosion-allowance metallic barrier will have a thin layer of

corrosion-resistant clad material inside, thus eliminating the gap between the two barriers while still providing galvanic protection to the more noble material. In view of these considerations for waste package design, we evaluated the corrosion behavior of galvanically coupled candidate inner and outer container materials

The materials tested include Fe-Ni-Cr-Mo Alloys 825, G-3, and G-30, Ni-Cr-Mo Alloys C-4 and C-22, a titanium-base alloy Ti Grade-12; and a carbon steel (A 516) Test specimens consisting of 2- x 2-in squares were fabricated from heat-treated materials by a qualified vendor. Additional thermal treatments were not given to these specimens before their exposure to the test environments Because the precise environment surrounding the waste packages is unknown, tests were performed in a deaerated acidic brine containing 5 wt% NaCl at 30°, 60°, and 80°C Acidification was done by adding sulfuric acid to the brine The pH of the salt solution was approximately 2 70 The rationale for selecting an acidic brine as a test environment has been provided elsewhere (Roy et al , 1996)

Galvanic contact between A 516 steel and a corrosion-resistant alloy was established by short circuiting them through use of a computer-controlled EG&G Model 283 potentiostat, which acted as a zero-resistance ammeter. Cell connections were made using A 516 steel as an anode, and a corrosion-resistant alloy as a cathode A modified EG&G Pyrex cell was used to contain the two working electrodes and an Ag/AgCl reference electrode Equal exposed areas (1 cm^2 each) of anodic and cathodic materials were tested with a separating distance of 12 cm between them. A controlled-temperature, liquid (water and ethylene glycol mixture) bath maintained the desired test temperature Tests were performed for periods ranging between seven and eight days Both measured galvanic current and galvanic potential were monitored as a function of time

The specimens were cleaned with distilled water, acetone, and ethanol before exposure to the test solution The pH of the test solution was measured at room temperature both before and after each experiment At the conclusion of each test, the specimen was cleaned with distilled water, acetone, and ethanol. The cleaned specimen was visually examined, followed by an optical microscopic examination to evaluate the extent of damage in both electrodes resulting from galvanic interaction

2.3.5 Galvanic Corrosion Test Results

Optical microscopic examination revealed that A 516 steel individually coupled to corrosion-resistant alloys suffered from general corrosion and crevice corrosion at all three test temperatures, and the extent of damage was more pronounced at higher temperatures (Roy et al , 1997d) Formation of shallow pits was also observed on the exposed surface of a few specimens Some of the A 516 steel specimens were covered with thick, brownish corrosion products, which were not analyzed In terms of the surface characteristics of corrosion-resistant alloys due to galvanic interaction with A 516 steel, it appears that Alloys 825, G-3, and G-30 suffered from moderate crevice corrosion at 60° and 80°C A slight crevice corrosion tendency was also observed with Alloys C-4 and C-22, and Ti Grade-12 at 60° and 80°C All three alloys were covered with black surface films at these temperatures, and the maximum amount of film was formed on Ti Grade-12 (Roy et al., 1997c).

At 30°C, the equilibrium or steady-state galvanic current for A 516 steel coupled to Alloys 825, G-3, G-30, C-4, and C-22 ranged between 17 and 30 μA (Roy et al., 1997d). However, the galvanic current for the A 516 steel/Ti Grade-12 couple was substantially higher (86 μA) at the same temperature. At higher temperatures (60° and 80°C), the value of the steady-state galvanic current in all couples ranged between 20 and 56 μA, with a value of

34 μA for the A 516 steel/Ti Grade-12 couple. The value of the equilibrium galvanic potential of these couples at 30°C was in the vicinity of –670 to –682 mV, however, a higher galvanic potential of –785 mV was observed for the A 516 steel/Ti Grade-12 couple. Except for the A 516 steel/Alloy C-4, A 516 steel/Alloy C-22, and A 516 steel/Ti Grade-12 couples, the magnitude of the galvanic potential value did not change significantly at 60° and 80°C The galvanic potential for these three couples became more noble at higher temperatures. For the A 516 steel/C-4 couple, the galvanic potential was –240 and –390 mV, respectively, at 60° and 90°C. Similarly, a positive shift in galvanic potential (from –680 to –530 mV) was observed for the A 516 steel/Alloy C-22 couple at higher temperatures Noble galvanic potentials of –215 and –303 mV, respectively, were observed for the A 516 steel/Ti Grade-12 couple at these temperatures Comparisons of galvanic current and galvanic potential as a function of test duration for all six couples at the three temperatures are shown in Figure 2 3-12 through Figure 2 3-17

Figure 2.3-12. Galvanic current density versus time for all six couples at 30°C.

Figure 2.3-13. Galvanic current density versus time for all six couples at 60°C.

Figure 2.3-14. Galvanic current density versus time for all six couples at 80°C.

Figure 2.3-15. Galvanic potential versus time for all six couples at 30°C.

Figure 2.3-16. Galvanic potential versus time for all six couples at 60°C.

Figure 2.3-17. Galvanic potential versus time for all six couples at 80°C.

The excellent corrosion resistance of titanium alloys, which are known to exhibit active–passive transition behavior, is primarily due to the inert, tightly adherent protective oxide films that cover their surfaces Although the passive oxide film covering the titanium alloy surface is effective in avoiding or limiting hydrogen uptake, under certain conditions, hydrogen may be evolved on the alloy surface causing hydrogen embrittlement of the alloy Three conditions must be met for hydrogen attack to occur The conditions are the generation of critical concentration of atomic hydrogen on the titanium alloy surface resulting from galvanic coupling, exposure of the alloy surface at temperatures at which the hydrogen diffusion rate is significant, and maintenance of solution pH at or below 3 A natural result of galvanic coupling is the evolution of hydrogen gas and absorption of atomic hydrogen at the surface of the cathodic member while the anodic material undergoes dissolution. A temperature of 80°C has been cited as the critical temperature above which hydrogen diffusion through the titanium-surface oxide film may be significant. As mentioned earlier, Ti grade-12 coupled to A 516 steel showed an adherent black surface film at 60° and 80°C along with a slight crevice corrosion tendency, even though its surface was shiny and unattacked at 30°C It is possible that hydrogen evolution and absorption at 30°C was quite insignificant, and that hydrogen gases formed at 60° and 80°C were precipitated on the alloy surface as black hydride films that were not detrimental from a corrosion viewpoint

The iron content in the corrosion product resulting from dissolution of A 516 steel in the acidic brine is most frequently in the form of ferric ions It has been suggested that ferric ions may act as cathodic depolarizers and shift the corrosion potential of titanium alloys in the

positive direction, a phenomenon that was also observed in this study As mentioned earlier, the galvanic potential of the A 516 steel/Ti Grade-12 couple was shifted to more noble values (–785 mV versus –215 and –303 mV) at higher temperatures that resulted in more dissolution product and, thus, might have produced more ferric ions It is possible that a similar mechanism of ennoblement of steady-state galvanic potential may be applicable to A 516/Alloy C-4 and A-516/Alloy C-22 couples at higher temperatures, because adherent black films were also formed on the exposed surfaces of Alloys C-4 and C-22 while galvanically coupled to A 516 steel

Galvanic corrosion testing using zero-resistance ammeter method is ongoing Current tests are being performed on Alloy C-22, Ti Gr-12, and A 516 steel in both neutral and acidic brines at different temperatures using three different anode-to-cathode area ratios and electrode distances

2.3.6 References for 2.3

ASTM (1995) *Standard Reference Test Method for Making Potentiostatic and Potentiodynamic Anodic Polarization Measurements* (ASTM Designation G5-94) Philadelphia, PA American Society for Testing and Materials. (Book of Standards, Vol 3 01) [231902]

Baboian, R , and G S Haynes (1981) "Cyclic Polarization Measurements—Experimental Procedure and Evaluation of Test Data " F. Mansfeld and U Bertocci, eds. *Electrochemical Corrosion Testing* pp 274-282 Philadelphia American Society for Testing and Materials [231903]

Roy, A K , D L Fleming, and B Y Lum (1997a). *Effect of Environmental Variables on Localized Corrosion of High-Performance Container Materials* In proceedings from the *5th International Conference on Nuclear Engineering*, Paper No ICONE5-2093, May 1997, Nice, France (Also UCRL-JC-125329, Livermore, CA Lawrence Livermore National Laboratory) [MOL 19971217 0031]

Roy, A K , D L Fleming, and B Y Lum (1997b) *Electrochemical and Metallographic Evaluation of Alloys C-22 and 625*. (UCRL-ID-127355) Livermore, CA Lawrence Livermore National Laboratory [MOL 19980211 0560]

Roy, A K , D L. Fleming, and B Y Lum (1997c) *Initiation and Growth of Localized Attack in Nuclear Waste Package Materials* In proceedings from the *6th International Conference on Nuclear Engineering*, Paper No ICONE-6014, May 10–14, 1998, San Diego, CA. (Also UCRL-JC-129068, Livermore, CA Lawrence Livermore National Laboratory) [MOL 19980421 0093]

Roy, A K , D L Fleming, and B Y Lum (1997d) *Galvanic Corrosion Study of Container Materials Using Zero Resistance Ammeter* In proceedings from *Corrosion/98*, Paper No 98156, March 1998, San Diego, CA (Also UCRL-JC-128475, Livermore, CA: Lawrence Livermore National Laboratory) [MOL 19980121.0137]

Roy, A K , D L. Fleming, and B. Y. Lum (1998). "Localized Corrosion Behavior of Candidate Nuclear Waste Package Container Materials." *Mater Perform* 37(3) 54–58

Roy, A K , D L Fleming, and S. R Gordon (1996) *Localized Corrosion of Container Materials in Anticipated Repository Environments*. In proceedings from the *189th Meeting of The Electrochemical Society, Inc* , Los Angeles, CA, May 5–10, 1996 (Meeting

Abstracts Vol 96-1, Abstract No 85, 112–113) (Also UCRL-JC-122861, Livermore, CA. Lawrence Livermore National Laboratory) [MOL 19960708 0433]

Roy, A K , G A Henshall, and R D. McCright (1995) *Electrochemical Corrosion Studies of Container Materials in Repository-Relevant Environments* (UCRL-ID-122860) Livermore, CA Lawrence Livermore National Laboratory [MOL 19960626.0174]

Roy, A K , and R.D McCright (1996). "Pitting Corrosion of Container Materials in Anticipated Repository Environments " *Proceedings of the Seventh International Conference on High-Level Radioactive Waste Management* La Grange Park, IL American Nuclear Society (Also UCRL-JC-122572, Livermore, CA Lawrence Livermore National Laboratory) [MOL.19960409 0153]

2.4 Stress Corrosion Cracking Tests

by Ajit Roy

The precise method of fabricating the currently designed multi-barrier nuclear waste packages has not yet been finalized. Regardless of the fabrication technique, some form of welding of container metallic materials will be involved in producing cylindrical packages of large diameters The process may generate enough residual stresses to make the waste package materials susceptible to stress corrosion cracking (SCC) as they come in contact with the repository environment Accordingly, our testing was initiated to evaluate the SCC behavior of candidate inner container materials using different techniques

The SCC is an environment-assisted cracking phenomenon resulting from the combined and synergistic interactions of tensile stress and a specific corrosive environment Environments causing SCC are usually aqueous, and they can be either condensed layers of moisture or bulk solutions. Hydrogen embrittlement (HE) is also a form of environment-induced failure that results most often from the combined action of hydrogen and residual or applied tensile stress Even though several mechanisms for SCC and HE have been proposed on the basis of numerous parametric studies, no single, unique mechanism has been widely accepted All proposed mechanisms contain elements of speculation, and none has been demonstrated unequivocally

The approach of linear elastic fracture mechanics (LEFM) recognizes the presence, or early initiation, of cracks in a structural component, and that structural failure results from the growth of such cracks by SCC. With the advent of LEFM, there has been a trend towards quantitatively relating crack growth rates to the mechanical driving force under various environmental conditions The mechanical driving force for crack growth is considered to be given by the crack-tip stress intensity factor K_I defined by linear elasticity

A notched specimen is generally used to evaluate the crack growth rate of engineering materials resulting from SCC (ASTM, 1996) The specimen size must meet two distinct and separate requirements, one pertaining to the applicability of LEFM, and the other to the condition of constraint at the crack tip (i e , plane strain versus plane stress) The first requirement concerns the minimum size of the crack and other planar dimensions of the specimens that are needed to satisfy the assumptions of limited plasticity The second requirement concerns the degree of relief of constraint in the thickness direction by localized plastic deformation (yielding) at the crack tip Both requirements relate to the size of the crack-tip plastic zone. It has become convenient (ASTM, 1996) to use the parameter $(K_I/\sigma_{YS})^2$ as a measure of the size of the plastic zone at the crack-tip, where σ_{YS} is the uniaxial tensile yield strength To satisfy the assumption of limited plasticity, fracture toughness data suggest that the minimum crack length a and specimen thickness B should be equal to or greater than $2\,5\,(K_I/\sigma_{YS})^2$.

The double-cantilever beam (DCB) test is a crack-arrest type of fracture mechanics test for measuring the resistance of metallic materials to propagation of SCC, expressed in terms of critical stress intensity for SCC, K_{ISCC} A detailed discussion on this technique is provided in the activity plan E-20-56 (Roy, 1996) However, no attempt has yet been made to monitor the corrosion or open circuit potential (E_{corr}) of the wedge-loaded DCB specimen while exposed to the test solution. Future tests proposed in activity plan E-20-45 will attempt to periodically measure the E_{corr} value over the entire test duration by placing a reference electrode close to the DCB specimen (Roy, 1997) The resultant crack extension in an individual specimen will then be correlated to the measured E_{corr} value

Activity plan E-20-45 is also aimed at evaluating the SCC behavior of susceptible container materials under measured and/or controlled electrochemical potential in repository-relevant environments using slow-strain-rate (SSR) test specimens The selected magnitude of the controlled potential will be based on the measured "critical potentials" obtained from the cyclic potentiodynamic polarization (CPP) experiment performed earlier in a similar environment The resultant data will enable the mechanistic understanding of the cracking process in materials of interest under the synergistic influence of applied stress and a corrosive medium Results will be used in developing and validating the SCC models for long-term performance assessment

2.4.1 Self-Loaded Stress Corrosion Cracking Tests

The materials we tested include iron–nickel–chromium–molybdenum (Fe-Ni-Cr-Mo) Alloys 825, G-3, and G-30, Ni-Cr-Mo Alloys C-4, C-22, and 625, and a titanium-base alloy Ti Grade-12 The rectangular DCB specimens were 4 in long, 1 in wide, and 0 375 in thick One end was slotted for wedge-loading, and V-shaped side grooves extending from the slot to the opposite end were fabricated by a qualified vendor from mill-annealed plate materials Additional thermal treatments were not given to these specimens before their exposure to the test environment The DCB specimens were machined such that the crack plane was perpendicular to the short transverse direction, and so that crack propagation would occur in the longitudinal rolling direction Test specimens were fatigue-precracked under load control (load ratio of 0 10) at a frequency of 20 Hz using an Instron Servohydraulic testing machine with a 55-kip load cell A clip gauge was attached to the specimen to determine the precrack length from the compliance measured during the fatigue cycle The precracked DCB specimen was then loaded by inserting a double taper wedge made of a similar material into the specimen slot using the same Instron testing machine The wedge thickness ranged between 0 110 and 0 115 in to provide specimen arm displacement of about 0 016 to 0 020 in

A total of eight specimens per candidate alloy were tested Duplicate specimens of each alloy were totally immersed in a vertical position into the test solution contained in a glass vessel that was heated to the desired test temperature by means of a hot water bath The environment was a 90°C deaerated acidic brine (pH ≈ 2 70) containing 5 wt% NaCl Selection of the acidic brine as the test environment was based on the results of a recent electrochemical localized corrosion study, which revealed the most severe pitting and crevice corrosion tendency of susceptible container materials in a similar environment (Roy et al , 1996) The pH of the test solution was measured before, during, and after each test Tests were performed for periods ranging between one and eight months At the conclusion of each test, the specimens were visually examined, followed by an optical microscopic evaluation of cracking along the side grooves. The final or equilibrium wedge load was then measured by applying a separating force to the specimen arms in the Instron testing machine The final crack length was measured by both compliance and metallographic techniques For metallographic measurement, the test specimen was pulled apart, and the crack length was measured on the broken faces Values for K_I and K_{ISCC} were obtained using the following equation (Heady, 1997):

$$K = \frac{Pa\left(2\sqrt{3} + 2.38\,h/a\right)\left(B/B_n\right)^{1/\sqrt{3}}}{Bh^{3/2}} \qquad (2.7\text{-}1)$$

where.

P = Wedge load (before or after exposure) measured in the loading plane

a = Initial or final crack length measured from the load line

h = Height of each arm

B = Specimen thickness.

B_n = Web thickness (NACE, 1990)

At the time this report was prepared, the 8-month tests were ongoing for all six alloys Therefore, results of testing conducted for periods ranging between 1 and 5 months are presented

2.4.2 DCB Test Results

Results (Roy et al., 1997) indicate that for Alloy 825, which had shown the maximum susceptibility to localized corrosion in a previous study (Roy et al , 1997a), the stress intensity factor value was significantly reduced upon exposure to the test solution (**Table 2.4-1**) Data indicate that, compared to the K_I value, the final stress intensity K_{ISCC} was at least 8 to 21 ksi•in.$^{1/2}$ less after testing for one, two, and four months The average crack growth during these test periods was 0 036, 0 065, and 0 046 in , respectively Compared to Alloy 825, the average crack growth for Alloy G-30 was 0 011 in following exposure for one month. The crack extension in this alloy was approximately 0 031 in for both two- and four-month exposure periods, suggesting that the crack growth might have stopped after two months The reduction in the stress intensity factor ($\Delta K = K_I - K_{ISCC}$) value for this material upon completion of testing was much smaller (approximately 2 to 7 ksi•in $^{1/2}$) compared to that for Alloy 825

Table 2.4-1 Results of SCC tests

Material	$K_I\left(ksi\sqrt{in}\right)$*		$K_{ISCC}\left(ksi\sqrt{in}\right)$*		$\Delta K\left(ksi\sqrt{in}\right)$*		Avg. crack growth (in)	Test duration (hr)
Alloy 825	35 57	38 43	27 26	18 45	8 31	19 98	0 036	738
	25 84	39 68	13 41	18 43	12 43	21 25	0 065	1484
	38 48	35 30	25 43	21 66	13 05	13 64	0 046	2898
Alloy G-30	41 07	40 19	37 79	38 35	3 28	1 84	0 011	811 50
	36 56	37 35	33 77	33 53	2 79	3 82	0 031	1415 50
	38 04	37 95	31 10	31 42	6 94	6 53	0 031	2879 50
Alloy C-4	38 14	42 48	30 33	41 21	7 81	1 27	0 036	716
	36 72	42 28	29 31	26 23	7 41	16 05	0 037	1458
	43 89	37 72	38 70	32 77	5 19	4 95	0 036	2880
Alloy C-22	38 78	32 44	28 73	28 78	10 05	3 66	None	698
	35 12	36 33	27 96	30 94	7 16	5 39	0 036	1414 50
	36 59	36 35	29 58	32 39	7 01	3 96	0 065	3598
Alloy 625	40 01	37 20	37 84	35 97	2 17	1.23	None	1467 50
	45 02	38 11	41 20	33 00	3 82	5 11	0 042	2180 50
Ti Grade-12	23 82	23 49	19 51	20 67	4 31	2 82	0 033	2927.50

*Measured on duplicate specimens

A comparison (Roy et al , 1997b) of crack-growth behavior of Alloys C-4 and C-22 indicates that the later alloy did not show any crack extension after one month of testing even though the average applied K_I value for both materials was within a very narrow range (36 to 40 ksi•in $^{1/2}$) The extent of crack growth in both alloys was similar (0 036 to 0 037 in) when tested for two months. Data (Roy et al , 1997b) also indicate that Alloy C-4 showed an average crack extension of 0 036 in. after four months of testing, suggesting that no appreciable crack growth occurred between two and four months of testing However, the average crack growth for Alloy C-22 was almost doubled (0 036 versus 0 065 in) as the test duration was increased from two to five months

No measurable crack extension was observed in Alloy 625 after two months of testing An average crack extension of 0 042 in was observed in this alloy when tested for three months For Ti Grade-12, only the four-month testing has been completed. Results show an average crack growth of 0.033 in., which is similar to the results for Alloys G-30 and C-4, tested for almost an identical duration The value of ΔK for Alloy 625 and Ti Grade-12 was very low, ranging between 2 and 5 ksi•in$^{1/2}$. The relation between average crack growth and exposure time for all six alloys is shown in Figure 2 4-1

Figure 2.4-1. Crack growth versus exposure time for specimens in a 90°C, pH ≈ 2.70 environment containing 5 wt% NaCl.

A comparison of pH of the test solution measured before, during, and after SCC testing indicates that for Alloy 825, the pH was shifted to more neutral values (up to 6 55) with increased exposure time. At the completion of testing, the test solution showed some light, orange-colored corrosion product at the bottom of the cell, which was not analyzed It is possible that the higher pH values may be the result of dissolution of elements, such as iron, copper, and nickel An examination of an Alloy 825 DCB specimen revealed significant crevice corrosion at the slotted end where the wedge was inserted A shift in pH from 2 66 to 5 51 was also observed with Alloy C-4 after four months of testing The amount of corrosion product in this case was negligible No attempt has been made to evaluate the morphology of cracking observed in materials tested so far. Future studies will be made of the mode of cracking (intergranular versus transgranular) in selected materials

2.4.3 Slow-Strain-Rate SCC Testing

During SSR testing, a smooth tensile specimen will be continuously strained in tension until fracture, in contrast to the more conventional SCC testing conducted under a sustained load The application of slow dynamic straining (10^{-6} to 10^{-8} in. per in /s) to the tensile specimen will facilitate cracking in materials that may not exhibit cracking under constant load, or that may take a prohibitively long time for crack initiation. Thus, the tensile specimen in SSR testing can undergo fast failure in a ductile manner if SCC does not occur, or prematurely in a brittle manner if SCC occurs

As mentioned earlier, electrochemistry may play a significant role in characterizing the SCC behavior of materials of interest Accordingly, the E_{corr} value of the test specimen will be measured with respect to a Ag/AgCl reference electrode contained inside an autoclave made of a suitable corrosion-resistant alloy, and capable of maintaining test temperatures of at least up to 100°C. The tensile specimen immersed into the test solution will be pulled in tension using an Instron testing machine By knowing the E_{corr} value and the measured critical potentials from previous CPP experiments, the magnitude of the applied electrochemical

potential E_{app} will be selected This potential will be applied to the tensile specimen under potentiostatic control during the entire straining period A graphite rod will be used as a cathode during potentiostatic polarization

In conventional, static SCC tests, the cracking susceptibility is commonly expressed in terms of either a threshold stress below which cracking does not occur in an arbitrary period of time, or the time to failure at a given applied stress With SSR tests, however, similar approaches cannot be made because the test specimen is subjected to a continuously changing stress during straining The cracking tendency at a given strain rate can be characterized by several readily measurable and quantifiable parameters obtained from the load-deflection curve and examination of the broken specimen

Because SCC is usually associated with relatively little macroscopic plastic deformation during crack propagation, ductility parameters, such as percent elongation (*El%*) and reduction in area (*RA%*) are useful in expressing the cracking propensity In addition, the true fracture stress σ_f obtained from the load-deflection curve can characterize the extent of cracking tendency

Attempts will be made to determine an average crack growth rate from broken test specimens The deepest secondary crack along the surface of the gage section will be measured from the polished metallographic mount of two broken halves of a specimen The morphology of cracking (intergranular versus transgranular) will also be established from the metallographic evaluation By knowing the deepest secondary crack (a) and the total time-to-failure (TTF = t), the average crack growth rate (da/dt) will be determined Both da/dt and σ_f will be correlated to the measured or applied electrochemical potential Similarly, *El%* and *RA%* will be correlated to the electrochemical parameters The following parameters will be available from SSR testing

- E_{corr} and E_{app}
- Maximum load (P_{max})
- Failure load (P_f)
- σ_f
- TTF
- *El%*
- *RA%*
- *da/dt*
- Metallurgical microstructure
- Fracture characteristics

The Instron testing machine, which will be used to pull the tensile specimens at different strain rates, has recently been calibrated Other ancillary parts have also been assembled Calibration of the extensometer is in progress SSR testing will be initiated soon, upon successful performance verification of the test equipment.

2.4.4 References for 2.4

ASTM (1996). Designation· E 399-90 "Standard Test Method for Plane-Strain Fracture Toughness of Metallic Materials " *1996 Book of Standards* Vol 03 01, 407–437 Philadelphia, PA: American Society for Testing and Materials.

Heady, R. B. (1997). "Evaluation of Sulfide Corrosion Cracking Resistance in Low Alloy Steels " *Corros* 33(7) 98–107.

NACE (1990). Standard TM0177-90. "Standard Test Method—Method D (Double-Cantilever-Beam Test) "Item No. 53040 Houston, TX. National Association of Corrosion Engineers.

Roy, A K. (1996) *Yucca Mountain Project Activity Plan, Stress Corrosion Cracking Tests Using Double Cantilever Beam Specimen, Metallic Barriers* (MB SIP Activity E-20-56) Livermore, CA Lawrence Livermore National Laboratory [MOL 19970108 0028]

Roy, A K (1997). *Yucca Mountain Project Activity Plan, Environment-Assisted Cracking under Measured and/or Controlled Electrochemical Potential* (MB SIP Activity E-20-45) Livermore, CA. Lawrence Livermore National Laboratory

Roy, A K, D L Fleming, and B Y Lum (1997a) *Effect of Environmental Variables on Localized Corrosion of High-Performance Container Materials.* In proceedings from the *5th International Conference on Nuclear Engineering*, Paper No ICONE5-2093, May 1997, Nice, France. (Also UCRL-JC-125329, Livermore, CA Lawrence Livermore National Laboratory) [MOL 19971217 0031]

Roy, A K, D L Fleming, and B Y Lum (1997b) *Stress Corrosion Cracking of Fe-Ni-Cr-Mo, Ni-Cr-Mo, and Ti Alloys in 90°C Acidic Brine* In proceedings from *Corrosion 98*, Paper No 98157, March 1998, San Diego, CA (Also UCRL-JC-128477, Livermore, CA Lawrence Livermore National Laboratory)

Roy, A K, D L Fleming, and S R Gordon (1996) *Localized Corrosion of Container Materials in Anticipated Repository Environments* In proceedings from the *189th Meeting of The Electrochemical Society, Inc*, Los Angeles, CA, May 5–10, 1996 (Meeting Abstracts Vol 96-1, Abstract No 85, 112–113) (Also UCRL-JC-122861, Livermore, CA Lawrence Livermore National Laboratory) [MOL 19960708.0433]

2.5 Microbiologically Influenced Corrosion

by Joanne Horn

2.5.1 Approach

The impact of microbiologically influenced corrosion (MIC) on nuclear-waste containment can only be predicted by determining the range of probabilities, rates, and required conditions for MIC of candidate container materials Therefore, a program has been established to determine

- Whether microorganisms contained within the post-construction Yucca Mountain (YM) environment have activities that have been associated with metal corrosion
- Boundary conditions and rates of MIC reactions under varying conditions including required conditions and rates of growth and colonization on candidate waste-package (WP) materials.
- The overall rate of MIC of candidate WP container materials under accelerated testing conditions

The potential for MIC within the repository will depend on the presence of microorganisms capable of performing corrosion-related activities, the conditions under which these organisms can grow, and rates of any resulting MIC-associated reactions A survey of YM microorganisms for corrosion activities (McCright, 1997) established the potential for MIC in the repository by showing that some YM organisms are able to carry out biochemical activities associated with MIC. Quantification of the rates of microbial growth and MIC activities under varying conditions makes possible accurate prediction of MIC over the long term anticipated to be necessary for adequate waste containment, and such quantification helps to identify those periods over the evolution of the repository when MIC can occur Finally, accelerated testing provides an estimate of the overall degree to which corrosion rates increase due to microbial activities, and determines the resistance of various candidate materials to microbial corrosion

Complementary approaches to determine MIC rates include field testing of candidate WP materials under simulated but concerted repository conditions, analyses of nonbacterial YM microorganisms for corrosive activities, and monitoring alternate corrosion studies for the presence of microorganisms. In pursuit of these goals, MIC studies have been deployed in the Drift-Scale Test (DST) to test the effect of YM organisms on candidate WP materials under representational repository conditions Fungi have been isolated from YM and tested for their respective MIC-associated activities, and Long-Term Corrosion Test Facility (LTCTF), discussed in Section 2, has been analyzed for the presence of microorganisms. The work reported in this section follows from Metallic Barrier SIP Activity E-20-60 An activity plan has been prepared.

2.5.2 Quantification of Microbial Biomass

Phospholipids are components of intact bacterial cell membranes The quantity of intact phospholipid fatty acids (PLFA) is a direct indicator of viable or potentially viable cells in an environmental sample (Tunlid and White, 1992) PLFA analysis permits the direct quantification of bacterial biomass in environmental samples without culturing microorganisms, a method that is limited because any given bacterial growth medium allows the proliferation of only a small fraction of a microbial community (Atlas, 1982, Roznak and Colwell, 1987)

The number of bacteria present in a rock sample aseptically collected from the Exploratory Studies Facility (ESF) was quantified using PLFA analysis A single rock core was collected and split into the region facing the tunnel (proximal to the drift), and the region reaching into the tunnel wall (distal to the drift) Phospholipids were directly extracted, analyzed, and quantified using gas chromatography/mass spectrometry according to established protocols Cell equivalents were calculated from standards of known numbers of bacteria isolated from soils. Using this measure, we deduced that the shallow ESF rock samples facing the drift (proximal), contained 6 9 × 10^4 cells/g dry rock, whereas the deeper-dwelling samples (distal, contained within the tunnel wall) had 4 0 × 10^4 cells/g dry rock (Figure 2 5-1) Only a single rock sample was analyzed, however, the observation that twice as many organisms were present on the drift-facing wall as in the wall itself may show that either exposure of rock by drift construction allowed colonization by invading bacteria, or that excavation changed conditions to favor the growth of endogenous cells

Figure 2.5-1. PLFA analyses of drift samples.

2.5.3 Growth-Limiting Nutrients under in situ YM Conditions

The impact of microorganisms on WP-material corrosion will depend on the abilities of deleterious bacteria to grow and multiply in the repository environment Previous studies had demonstrated that YM microbial communities shown significant growth in low-nutrient media at incubation temperatures up to 50°C (McCright, 1997) Therefore, experiments were undertaken to define nutrient conditions conducive or inhibitory to growth of ESF bacterial communities in modified YM pore water Specifically, we sought to define nutrients that limit bacterial growth in YM and to determine growth rates under aerobic, saturated conditions

Growth media formulations were generated using The Geochemist's Workbench, a geochemical modeling code (Bethke, 1994) The media formulations were based on M9 defined bacterial medium and a ten-fold concentration (10×) of J-13 well water (Table 2 5-1, Miller, 1972), which is the pore water in the vicinity of the YM site (Delaney, 1985) The concentrations of chloride and bicarbonate ions in the "YM Complete" medium were fixed at 10× J-13 levels, because these ions can affect corrosion rates and pH The levels of organic carbon (as added glucose), phosphate, sodium, potassium, nitrogen (as nitrate and ammonium), and magnesium ions in YM Complete medium approached those found in M9 Sulfate concentration was increased to maintain electrical neutrality Other media used in these studies were variations of YM Complete medium The "Dilute Complete" medium was 0 1× YM Complete medium. The "Carbon Deficient" and "Phosphate Deficient" media contained no organic carbon or phosphate, respectively, approximating the levels of these species found in J-13 well water (Delaney, 1985) The concentrations of the other macronutrients, sulfate and nitrogen, were likewise adjusted in "J-13-SO_4" and "J-13-NO_3," respectively, by decreasing them to match those found in 1× J-13 Finally, all experimental media were predicted to have a pH of 7 2

Table 2.5-1. Compositions of 10× J-13 well water, M9 medium, and experimental media.

	Concentration (mM)							
Component	10× J-13	M9	YM complete	Dilute complete	Carbon deficient	J-13 + NO_3	J-13 + SO_4	Phosphate deficient
Na	19 10	93 12	130 65	13 07	130 65	130 00	130 50	93 00
K	1 31	22 00	18 28	1 83	18 28	22 01	22 12	22 00
Mg	0 79	1 00	0 87	0 09	0 87	1 01	1 12	1 01
Ca	3 12							0 10
Cl	1 95	27 50	1 88	0 19	1 88	1 88	1 89	1 89
NH		18 70	3 75	0 38	3 75			19 02
NO_3	1 55		14 95	1 50	14 95	0 10	19 60	1 00
SO_4	1 95	1 00	9 74	0 97	9 74	9 98	0 17	57 92
PO_4		64 30	57 05	5 71	57 05	64 00	64 00	
HCO_3	20 50		18 90	1 89	18 90	19 00	19 00	19 00
Glucose		11 10	5 55	0 56		5 55	5 55	5 55
F	1 16							
Si	9 61							

Growth rates of YM bacteria were determined by periodically measuring cell densities in batch flask cultures and continuously fed microcosms, both contained YM tuff as bacterial inoculum. YM tuff was aseptically collected from YM ESF alcoves 5, 6, and 7, and was then aseptically crushed (1 68–2 38 mm) and homogenized Batch cultures were contained in 125-ml flasks with 5 g of crushed tuff and 20 ml of indicated media Cultures were incubated at 30°C with continuous agitation (150 rpm), and media were not replenished in these systems Microcosms, however, initially contained 50 g of crushed YM tuff and 200 ml of indicated media and were continuously supplied with fresh media (5 ml/hr). All microcosms were incubated at 22°C and were contained within the microcosm vessel through the use of filters (0.2 mm) fitted on outlets (Figure 2 5-2) Sterile control batch and microcosm systems contained crushed YM tuff that was gamma-irradiated (3 Mrads) by exposure to a ^{60}Co source, these were incubated in YM Complete medium

Figure 2.5-2. Configuration of microcosms for growth studies.

Cell densities were determined by live plating (Brock and Madigan, 1991, pp. 310–311). The aqueous phases of microcosms and batch cultures were periodically sampled, serially diluted, and plated on R2 agar (Difco, 1996) Plates were incubated at 30°C until colonies, which arise from single cells, could be counted (24–36 hr) Colonies per plate were counted, and the density of the original suspension (cells/ml) was calculated by multiplying the number of cells/plate by the total dilution factor.

Despite decreased levels of macronutrients in all but the YM Complete-fed cultures, bacterial growth from YM tuff was detected in all batch and microcosm systems tested except those containing sterilized tuff (Figure 2.5-3). Microcosm-grown cultures demonstrated similar growth rates, despite the absence of organic carbon and phosphate or the reduction of nitrogen and sulfate from their respective media (Figure 2.5-3a). Excepting the Phosphate Deficient-grown culture and the sterile control, these cultures produced near-equivalent lag periods (of approximately 2 days) and similar doubling times (averaging 2 hr) Maximum cell

densities achieved in these cultures did differ, however, from approximately 10^6 cells/ml (Carbon Deficient media) to 10^8–10^9 cells/ml (Dilute Complete medium, J-13-NO_3, and J-13-SO_4) during the incubation period of 6 days In contrast, the culture incubated with Phosphate Deficient medium demonstrated a longer lag period of approximately 3 5 days and a doubling time of 4.8 hr, generating 10^7 cells/ml after 7 days of incubation (Figure 2 5-3a)

Figure 2.5-3. Growth rates of YM bacterial communities as a function of macronutrient concentration.

Batch cultures, which were aerated and grown without media replenishment, showed similar growth trends when compared with microcosm cultures, however, community doubling times in batch cultures were slightly longer, averaging 2 3 hr in all media except Phosphate Deficient and the sterile control Again, variation in the maximal cell densities depended on media formulation, varying from 10^6 cells/ml (Phosphate Deficient media) to greater than 10^9 cells/ml (J-13-SO_4 media). In addition, the initial lag periods of J-13-NO_3 and Phosphate Deficient media averaged 4–5 days, compared with lag periods of 1–2 days in the other media

Whole bacterial communities found in YM tuff demonstrated significant growth in media that approximated the composition of M9 medium but contained 10× J-13 levels of chloride and carbonate Nutrients that are used in the greatest quantities for bacterial metabolism ("macronutrients") were individually reduced to levels found in YM pore water, and significant growth was still observed These findings strongly suggest that bacterial growth within YM is not limited by a lack of organic carbon, phosphate, nitrogen, or sulfate, at least under saturated, aerobic conditions Sterilized YM tuff produced no growth, indicating that the observed bacterial growth in nonsterilized cultures originated from YM tuff

The growth of microorganisms in the absence of added organic carbon (YM tuff contains no organic sources of carbon) suggests that bacterial carbon dioxide fixation accounted for growth under these conditions Nitrogen and sulfate concentrations in YM pore water are also apparently sufficient to support microbial growth, as growth was observed when the concentrations of these species were reduced to J-13 levels

J-13 well water reportedly contains no phosphate (Delany, 1985), which microbes normally use in large quantities for metabolism, however, bacterial growth was also observed in both batch and microcosm cultures when phosphate was eliminated from growth media Because YM tuff contains traces of phosphate (200 ppm, Broxton et al , 1987), dissolution due to microbial activities may account for the observed growth in Phosphate Deficient medium

These results strongly suggest that in situ YM nutrient levels are sufficient to support growth of endogenous bacteria, so we undertook follow-on studies to assess the growth of ESF bacterial communities in simulated 10× J-13

2.5.4 Bacterial Growth Rates and Limiting Nutrients in Simulated J-13 Water

Growth media formulations were again compiled using The Geochemist's Workbench (Bethke, 1994) Formulations were based on 10× J-13 well water (Delaney, 1985) Differences between the composition of measured in situ J-13 (increased 10× in concentration) and "10× J-13 Synthetic" medium included decreased levels of sodium to preserve charge balance, decreased levels of calcium and carbonate to preclude precipitation of media components, exclusion of silica to control pH, and elimination of trace elements, 0.1% glucose was added

to all media formulations (Table 2.5-2) The predicted pH of 10× J-13 Synthetic medium was 8 0, actual pH was 7.8. Other media formulations used in this study were variations of 10× J-13 Synthetic "10× Syn J-13 + SO_4" contained an almost 5-fold higher concentration of sulfate "10× Syn J-13 + NO_3" contained more than a 10-fold increased concentration of nitrate "10× Syn J-13 + SN" contained higher levels of both nitrate and sulfate, with a higher sodium concentration to preserve the ionic balance. Fluoride was added to 10× J-13 Synthetic, but not to other media used in these experiments (Table 2 5-2)

Table 2.5-2. Compositions of 10× J-13 well water and altered macronutrient formulas.

	Concentration (mM)				
Component	10× J-13 natural	10× J-13 synthetic pH8	syn 10× J-13 + SO_4 pH8	syn 10× J-13 + NO_3 pH8	syn 10× J-13 + SN pH8
Na	19 1	6 143	20 6	22 13	37 73
K	1 31	1 306	1 306	1 306	1 306
Ca	3 12	0 02505	0 03505	0 0290	0 03505
Mg	0 79	0 79	0 79	0 79	0 79
NO_3	1 55	1 553	1 553	18 67	18 66
Cl	1 95	1 951	1 949	1 95	1 949
CO_3	20 5	0 527	0 566	0 562	0 589
SO_4	1 95	1 949	9 743	1 949	9 743
Li	0 0605	0	0	0	0
Sr	0 00399	0	0	0	0
Al	0 00445	0	0	0	0
Fe	0 00107	0	0	0	0
Si	9 61	0	0	0	0
F	1 16	1 16	0	0	0
Glucose	0	5 55	5 55	5 55	5 55

Growth rates of YM bacteria were determined by periodic live plating on R2 agar (Difco) of planktonic cells in continuously fed microcosms (as in the in situ experiment previously described), configured as shown in Figure 2 5-2 YM tuff aseptically collected from ESF, alcove 5 (in the post-construction repository horizon), and crushed (1–4 mm), was used as a source of bacterial inoculum and to account for tuff-generated chemical factors in growth determinations Microcosms initially contained 50 g of crushed YM tuff and 250 ml of indicated media and were continuously supplied with fresh media (2 ml/hr). All microcosms were incubated at 22°C Sterile control microcosm systems contained crushed YM tuff that was gamma-irradiated (3 Mrads) by exposure to a ^{60}Co source, these were incubated in 10× Syn J-13 + SN.

Observed growth rates, as judged by the increase in planktonic cell concentrations, showed growth in 10× J-13 Synthetic medium alone or with an added nitrogen and/or sulfur source Cell concentrations increased from nondetectable to 10^5–10^6 cells/ml of media within 2 days or less (Figure 2.5-4). Doubling times were on the order of 0.66 hr No significant difference in final cell concentrations or growth rates was apparent between cultures incubated with added nitrate or sulfate (or both) and those lacking any nutrient amendment,

proving that neither the supply of nitrate or sulfate were limiting bacterial growth under these experimental conditions, which closely mimic that of natural J-13 well water

Figure 2.5-4. Growth rates of YM bacterial communities in modified YM pore water.

To discern which nutrient was limiting bacterial growth in simulated 10× J-13 well water, 10 mM phosphate was added when cells had achieved their greatest densities After the addition of phosphate, cell concentrations increased dramatically—by at least one order of magnitude—within 1–2 days' incubation, reaching more than 10^9 cells/ml of media in the instance of 10× Syn J-13 + SO_4 After reaching peak cell densities (and presumably exhausting the added phosphate supply), cell concentrations dropped (Figure 2 5-4) This sequence shows that phosphate is the limiting nutrient for growth in YM pore waters under the saturated conditions described here

Defining growth rates of bacteria under simulated conditions is central to predicting MIC in the proposed repository, because the total number of MIC-causing bacteria at any given time will partially determine the magnitude of their effect on corrosion The described findings demonstrate that YM bacteria grow to high cell densities under conditions that are similar to those present in the ESF now However, analyses of the number of bacteria in YM rock do not match those indicated by these growth studies the measured number of bacteria present in the rock is on the order of 50,000/g (see Section 2 5 2), but our studies with simulated pore water show that bacterial numbers should be greater than 50,000/g if YM bacteria can indeed grow in pore water

Then what is preventing in situ growth of YM bacteria? Answers may be revealed by analyzing the differences between the simulated 10× J-13 used for growth studies and 1× J-13 found in situ

- Concentration may be a factor in the observed stimulation of growth in laboratory studies Sulfate and nitrate concentrations appear to be sufficient at 10× concentration, but may be insufficient to support growth at the 1× concentration found in situ presently. However, concentrations of pore water ions are predicted to increase during water reflux during the evolution of the repository (Hardin et al , 1998)
- Simulated 10× J-13 used for growth studies contains 0 1% glucose, both to mimic introduced organic carbon into the repository environment and to facilitate accelerated downstream testing of repository materials (see Section 2 5 7) In situ YM pore water reportedly contains no organic carbon (Delaney, 1985) Thus, the added glucose might be the factor that produces growth exceeding that found in situ However, the preliminary studies using modified M9 media (described previously) showed that deleting organic carbon from growth media still resulted in significant growth of YM bacteria In addition, organic materials are being introduced into the repository
- The degree of saturation could be a factor in the increased bacterial growth in laboratory studies The most recent estimates of in situ saturation of YM tuff is 92% (Hardin et al ,1998), but growth studies were conducted at 100% saturation. However, it is predicted that dripping, concentrated pore water will eventually contact waste packages (Hardin et al , 1998)

Taken together, most of the relevant differences between laboratory and in situ conditions will be eliminated during the evolution of the repository Repository evolution will mimic many of the conditions that produced high rates of bacterial growth Further studies need to be conducted to provide full confidence in these conclusions We plan to test growth in 1×

Simulated J-13 waters and in the absence of organic carbon Further experiments addressing the minimum saturation required to achieve biofilm growth will also be conducted (see Section 2 5.11) Finally, those organisms that dominate the community after growth in 10× J-13 with and without nutrient supplements are being isolated and characterized to indicate their possible impacts on MIC

We have defined the nutrient factor that limits growth at YM. Because lack of added nitrogen or sulfate did not affect increases in cell growth, but added phosphate did, lack of phosphate in pore waters and YM tuff is shown to limit bacterial growth in native YM rock No phosphate was added to synthetic 10× J-13 media, therefore, required phosphate, which is used in significant amounts for both membrane and DNA synthesis, was mobilized by cells to support growth Yet because phosphate limitation prevents growth beyond the observed maximum level, cell-mobilized phosphate from rock is apparently not sufficient to support unlimited growth

The finding that phosphate limits bacterial growth at YM has implications for repository design, the composition of introduced materials, and predictions of the periods of active MIC If bacterial activities are shown to significantly increase rates of WP corrosion, then those nutrients that limit bacterial growth should not be introduced into the repository Should these materials be introduced, the period during which they become available for bacterial uptake would constitute a factor in predicting MIC activity

2.5.5 Effects of Bacterial Growth on Alteration of pH

Earlier studies focused on the ability of individual YM bacterial isolates to affect alterations of pH in various types of media When various, individual YM bacteria were tested in the presence of either added glucose or protein, some bacteria required these supplemental nutrients to cause a decrease in pH, but others were more independent of nutrient requirements with respect to acid production (McCright, 1997) Because the repository environment does not contain a single type of bacterium, but rather harbors an entire community or admixture of bacterial types, a preliminary experiment to assess the effects of the entire microbial community on pH was undertaken

We used 25-g samples of aseptically collected and crushed tuff (1 0 mm) from ESF alcoves 5, 6, and 7, and inoculated these samples into 100 ml of various dilutions of sterile modified M9 media (Miller, 1972), or sterile Artificial Pore Water (APW, a formulation similar to the composition of J-13, Amy et al., 1992) M9 was modified from the original formulation (Miller, 1972) by substituting sodium phosphate with monobasic potassium phosphate to minimize the buffering effects of the media Dilutions of modified M9 were the original concentration (1×), 1:10 (0.1×), or 1·100 (0 01×), and APW was used at its original concentration (1×), and diluted 1·10 (0.1×). All dilutions were made in deionized water All types of media were amended with 0 5% glucose, and the pH was adjusted to 7.0 before the addition of crushed tuff Incubations were carried out in Ehrlenmeyer flasks, aerobically, with agitation (150 rpm), at both 22° and 60°C Parallel flasks containing sterile media with no added rock were also incubated to account for media-induced pH changes The pH was assessed by periodic withdrawal of an aliquot of media and probing with a standard pH meter

Results showed that pH was not altered significantly in any type of media after 2 5 or 8 days of incubation. Control cultures containing only sterilized media showed pH alteration from 0 01–0.3 pH units, whereas those containing rock and endogenous microorganisms displayed alterations in pH ranging from 0 01 to 1 28 pH units Those pH changes that were

greater than 0.5 pH units were actually pH increases, making the bulk solution slightly alkaline, however all incubations remained in the approximately neutral pH range. Given that individual strains showed much greater abilities to produce acid and decrease pH in R2 media (McCright, 1997), the reason the same effects were not observed here probably relates to the buffering capacity of the M9 and APW formulations. APW contains silicate and carbonate, with the capacity to buffer the bulk phase even in the presence of bacterial acid production Although efforts were made to decrease the pH buffering capacity of M9, any source of phosphate (including the potassium phosphate used) would provide buffering capacity Because both APW and M9 are poor representatives of J-13, these experiments will be repeated using flow-through systems (similar to that shown in Figure 2.5-2 but described in Section 2 5 10) fed with 10× J-13 Synthetic media, which is much more similar to the in situ J-13 formulation and has correspondingly lower buffering capacity. This medium will provide a better assessment of the impact of YM bacteria on the pH of bulk pore waters

2.5.6 Isolation of YM Fungi and the Impact of Fungal Growth on pH

Fungi are higher organisms possessing a cellular structure similar to that of mammals ("eukaryotic") Bacteria, on the other hand, have a far simpler cellular organization ("prokaryotic") The differences between these two basic forms of life are so fundamental that they define two biological Kingdoms Although most studies of MIC have focused on bacterial activities, fungi have also been shown to cause corrosion of metal surfaces The prolific production of organic acids by fungi has been shown to corrode aluminum alloys (Videla et al , 1993) as well as portlandite cement (Perfettini et al , 1991) Fungi also contribute to metal corrosion by consuming nitrate, which is an inhibitor of the corrosive effects of chlorine (Parberry, 1968). The production of phospholipids and fatty acids, which act as surfactants to break down passive film/metal adhesion, also contributes to the corrosive effects of fungi (Videla, 1996) Because fungi can be aggressive agents of corrosion, and because their growth is favored by the low-humidity and acidic environmental conditions anticipated during the evolution of the proposed repository, efforts were made to isolate and preliminarily characterize these organisms from YM rock

Historically, fungal growth media with an acidic pH have been used to discourage the growth of bacteria More recently, it was found that many fungi grow at neutral or slightly alkaline pH, so dyes, salts, and antibiotics have been used instead to select for fungi under neutral conditions (Difco, 1996) Because YM pore waters are neutral pH (Delany, 1985), we reasoned that use of fungal-selective media in the neutral pH range (with the addition of antibiotics) might best detect YM fungi. For this purpose, a series of neutral-pH fungal media (all obtained from Difco Laboratories, Inc., Detroit, MI) were tested for their abilities to grow fungi from crushed YM tuff Tuff was aseptically collected from alcoves 5, 6, and 7, of the ESF and aseptically crushed (1 0 mm) Littman Oxgall medium, Cooke Rose Bengal medium (which use crystal violet and rose bengal, respectively, to discourage bacterial growth), Yeast and Mold medium, Mycological medium, and Malt Extract medium were prepared with agar (according to the manufacturer's suggestions) for subsequent solidification in petri dishes Before final solidification, 40 μg/ml of streptomycin was added to each type of media to discourage bacterial growth. Approximately 1–2 g of crushed tuff was dispersed over the surface of each type of solidified agar. In separate parallel trials, each media type was also incubated uninoculated with tuff to serve as a means of assessing media contamination during preparation or incubation. All petri plates containing media were incubated at room temperature

After five to seven days of incubation, the Mycological agar showed the best results in obtaining fungal growth from YM tuff, although both Littman Oxgall and Cooke Rose Bengal media supported satisfactory growth. No bacterial growth was observed in any of the types of media tested Sterile control incubations of media showed no growth, demonstrating that observed growth rose from added YM tuff Figure 2 5-5 shows some of the various types of fungal growth observed on these different media types.

Figure 2.5-5. Isolation of fungi from YM tuff.

Because fungal production of acids is a well-documented MIC mechanism, we determined rates of acid production by YM fungi grown in Mycological media (as liquid broth, without the addition of agar). We added 25 g of crushed YM tuff (1.0 mm) to 125 ml of Mycological broth media containing 40 mg/ml streptomycin in a 250 ml flask, and agitated the mixture (125 rpm) at 22°C. Mycological medium with 40 μg/ml streptomycin was also incubated without addition of YM tuff to account for any spontaneous changes in the pH of the media during incubation, and to serve as a control for the maintenance of uncontaminated conditions. Periodically, 5–10 ml samples of media and fungi were withdrawn and pH was determined with a standard pH meter Three separate trials were conducted, two trials lasted for 5 5 days each, and the third lasted for 13 5 days (results of the longest trial are depicted in Figure 2 5-6) Results showed that during 10 days of incubation, fungal growth from unsterilized tuff caused a decrease in pH of the medium to pH 3 During the same period, uninoculated medium retained a pH of 6 3 Thus, given adequate nutrients, growth arising from fungi contained in YM tuff can cause significant decreases in pH and thereby contribute to WP corrosion Environmental limiting factors to fungal growth (including nutrients, temperature, humidity, and radiation) have yet to be determined, but discovering these would allow the prediction of those periods during which fungal-induced corrosion would be important to overall corrosion rates of WP materials

Figure 2.5-6. Effect of YM fungal growth on pH.

2.5.7 Overall MIC Rates on Candidate Materials

Bacterial isolates from YM geologic material possess biochemical activities associated with MIC. Various microbial isolates demonstrated abilities to oxidize iron, produce sulfide, generate acids, and produce exopolysaccharides, or "slime" layers, establishing some potential for MIC in the potential repository environment (Horn et al , 1996, McCright, 1997)

One focus of the MIC research program has been to determine the contribution of YM bacteria to corrosion by testing candidate WP materials under accelerated conditions employing sterile versus nonsterile conditions Using this approach, results from tests employing sterile conditions can be subtracted from those under nonsterile conditions, resulting in measurements of bacterial contributions Coupled with well-accepted electrochemical polarization techniques, this approach has been used to measure overall corrosion rates in the presence of characterized, YM MIC-causing microbes, or in their absence The determinations were carried out in collaboration with the University of Nevada, Reno (Denny Jones, Tiangan Lian).

2.5.7.1 Methods

Two types of corrosion cells were used to gather electrochemical polarization data The Type 1 cell (Jones et al , 1997) consisted of a glass flat-bottom vessel filled with 100 ml R2

bacterial growth media (Reasoner and Geldrich, 1985) supplemented with 0 5% glucose and 0 75% proteose peptone #3 (from Difco) in 100× simulated J-13 well water Addition of 0 5% agar produced a semi-solid electrolyte that retained inoculated bacteria near the specimen surfaces The cell contained a working electrode (5 × 0.5 × 0.032 in., 21.4 cm^2 surface area) and a platinum-wire counter electrode, as well as a Luggin capillary solution bridge filled with 1% KCl in 1 5% agar The Luggin bridge was connected to another glass vessel containing 1% KCl and a reference saturated calomel electrode (SCE) A schematic diagram of the Type 1 corrosion cell is shown in Figure 2 5-7. All elements that came into contact with the growth media had been previously sterilized

Figure 2.5-7. Type 1 corrosion cell configuration.

The Type 2 cell (Figure 2 5-8) was devised to improve the signal-to-noise ratio and provide more consistent results for corrosion-resistant alloys It consisted of a cylindrical glass flange with an O-ring seal The working-electrode sheet specimen was clamped to the flange seal, forming the bottom of the cell with an exposed area of 28 3 cm^2 Cell volume was increased to 450 ml but remained fluid without agar addition, to better facilitate nutrient diffusion to the coupon surface Composition remained as noted above The SCE reference was directly immersed in the cell, along with the platinum counter electrode.

Figure 2.5-8. Type 2 corrosion cell configuration.

Working electrodes of C1020 carbon steel (similar in composition to the candidate material A516), Alloy 400 (Monel 400, M400, UNS N04400), Hastelloy C22 (C22), Incolloy 625 (I625), and stainless steel 304 (SS304) were wet-polished with abrasive paper progressively to 600-grit, cleaned with acetone and distilled water, and then sterilized by autoclaving, before being inoculated with a mixture of 12 strains of YM bacteria, including acid, slime, and sulfide producers, as well as iron-oxidizing bacteria (McCright, 1997). Cell densities were established before aseptically combining and spreading a defined number (at least 10^8 bacterial cells of each strain) of all isolates on specimens, which were air dried before they were exposed to growth media in corrosion cells Sterile control cells contained uninoculated working electrodes to assess abiotic corrosion effects

The dc linear polarization technique was used to conduct polarization resistance (R_p) measurements in both Type 1 and Type 2 cells A potentiostat (EG&G Model 283) performed potential scans from 20 mV less than the corrosion potential (E_{corr}) to 20 mV greater than E_{corr} at a scan rate of 0.04 mV/sec The R_p value was calculated by the EG&G Model 252/352 Softcorr II software

Corrosion rates as current density (i_{corr}) were calculated (Stern and Geary, 1957) from the measured R_p as $\mu A/cm^2$: $i_{corr} = B/R_p$, where $B = \beta_a\beta_c/[2\ 303\ \ (\beta_a+\beta_c)]$

Polarization measurements gave $\beta_a = \beta_c = 0\ 15$ V/decade for the sterile carbon steel C1020, and $\beta_a = 0\ 035$V/decade and $\beta_c = 0.315$V/decade for C1020 inoculated cells The i_{corr} was converted to corrosion rate r in $\mu m/yr$ $r = 3.277\ i_{corr}\ a/(nD)$, where atomic weight $a = 56$ g, equivalent number $n = 2$, and density $D = 7\ 84\ g/cm^3$ for carbon steel, and $a = 60$, $n = 2$, and $D = 8.84\ g/cm^3$ for Alloy 400. For Alloy 400, the corrosion-rate calculations were made with $\beta_a = \beta_c = 0\ 1$ V/decade, because a Tafel range polarization had not been determined.

2.5.7.2 Results

2 5 7 2.1 Carbon Steel. Type 1 Cell

Replicate tests on carbon steel C1020 in separate cells showed evidence of corrosion in less than 24 hours following inoculation with YM bacteria MIC was evidenced by accumulation of corrosion products at the medium–headspace interface, dark coloration of the coupon within the solidified media, and consistently low corrosion potentials Sterile cells, on the other hand, did not show accumulation of corrosion products and maintained significantly higher corrosion potentials Figure 2 5-9 shows the changes in corrosion potentials on inoculated and sterile C1020 coupons over 62 days MIC in inoculated cells demonstrated an active E_{corr} of approximately –670 mV versus SCE After five days of incubation, inoculated cells had visible microbial colonies scattered through the agar medium, and voids were observed to form within the media, which may have been caused by gaseous end-products of microbial metabolism

Figure 2.5-9. Corrosion potentials of carbon steel C1020.

The corrosion rate of C1020 was significantly increased by exposure to inoculated bacteria (Figure 2 5-10) By the fourth day following inoculation, the MIC rate was 42 42 μm/yr, 20 times greater than corrosion rates in parallel sterile cells (2 03 μm/yr) MIC rates in inoculated cells decreased, reaching a steady state rate of 34 29 μm/yr after two weeks. Sterile cells showed an increase in corrosion rate during the same period, reaching 6 11 μm/yr after three weeks of incubation Thus, the difference between corrosion rates on sterile and inoculated C1020 coupons was reduced to between five- and sixfold after a steady state had been achieved These observations reaffirm those reported in an earlier EMCR (McCright, 1997) and in the literature (Jones et al , 1997)

Figure 2.5-10. Corrosion rates of carbon steel C1020.

C1020 was not only observed to have a higher corrosion rate in the biotic environment, but also developed corrosion-characteristic electrochemical properties (Figure 2 5-11) The anodic polarization behavior of C1020 in inoculated cells was quite active in anodic dissolution and demonstrated a low β_a value (approximately 0.035 V/decade). Activation of the anodic reaction on inoculated coupons could be due to acid production or other localized effects caused by the bacteria In contrast, sterile cells showed low corrosion rates at relatively high corrosion potentials Thus, C1020 apparently has a relatively low corrosion rate in sterile test conditions, but corrosion rates significantly increased when C1020 was exposed to the mixture of YM bacteria selected for these experiments

Figure 2.5-11. Anodic polarization behavior of C1020.

Figure 2.5-12 shows the comparison of cathodic polarization behavior in inoculated and sterile cells. The cathodic reaction displays similar properties between sterile and biotic cells, and it appears that both the biotic and abiotic systems display largely diffusion-controlled cathodic polarization in the inoculated cell

Figure 2.5-12. Cathodic polarization behavior of C1020.

2 5.7 2 2 Carbon Steel C1020 and Monel 400· Type 2 Cell

Polarization-resistance measurements using larger C1020 and M400 coupons in the Type 2 cell design (Figure 2 5-8) improved signal quality significantly Even where corrosion rates were low for M400 coupons, R_p measurements did not display noise or unstable potential effects

Results from duplicate and triplicate tests in Type 2 cells containing C1020 and M400 inoculated with YM bacteria are presented in Figure 2 5-13 The observed corrosion rate of M400, as expected, was lower than that observed for C1020 However, the corrosion rate of M400 increased nearly threefold during the first two weeks of incubation, whereas that of C1020 decreased Thus, even though there was an initial 80-fold difference in corrosion rate (0.31 μm/yr for M400 and 24 89 μm/yr for C1020), this decreased to between seven- and eightfold after steady state was achieved (approximately 1.02 μm/yr for M400 and 7.62 μm/yr for C1020)

Figure 2.5-13. Corrosion rates of Monel 400 and carbon steel C1020.

The decrease in corrosion rate of the C1020 was much more marked than that observed in the Type 1 cells using smaller coupons (compare Figure 2 5-10 and Figure 2 5-13) Because the coupon in these experiments was submerged in liquid rather than agar-solidified media, a uniform electrochemical condition was created in these cells rather than a local condition at the medium–headspace interface This difference almost certainly contributed to the difference in observed corrosion rates from one corrosion cell type to another

At the start of the incubation period, redox potentials (as measured by a bare platinum electrode) of solution in M400 cells were more noble, at about –180 mV versus the reference electrode, compared to about –400 mV in C1020 cells Because all other conditions were equivalent, except the type of metal coupon, the increased Fe^{2+} in the C1020 cells could have caused a greater consumption of oxygen by iron-oxidizing bacteria, or C1020 may be more favorable to microbial growth generally, causing a greater degree of oxygen uptake by aerobic organisms Alternatively, reduction of dissolved oxygen by anodic oxidation of Fe to Fe^{2+} or subsequent chemical oxidation of soluble Fe^{2+} would de-aerate the solution in C1020 cells, and thereby lower redox potential These results correlate well with observed corrosion potentials The E_{corr} of C1020 was on the order of –660 mV versus the reference electrode, whereas that of M400 increased from –380 mV to –300 mV during continuous incubation

2 5 7 2 3 Corrosion-Resistant Alloys Type 2 Cell

Corrosion rates for Alloys C22, I625, and Type 304 stainless steel inoculated with YM bacteria were all measured at less than 0.04 μm/yr, as shown in Figure 2.5-14. All are passive and resistant to corrosion, although Type 304 is susceptible to MIC pitting Alteration of the test environment is needed to simulate localized pitting conditions for these corrosion-resistant alloys As in the C1020/M400 test, the Type 2 cell was successful in measuring these very low corrosion rates, but these results may not be representative of likely repository corrosion Conditions in these cells were probably not conducive to encouraging corrosion because conditions in the bottom of the cell, where the coupon resides (Figure 2 5-8), most likely becomes anaerobic after a short period of incubation. Because there is no mixing or replenishment of media, nutrients available to bacteria residing on the coupons depended entirely on diffusion

Figure 2.5-14. Corrosion rates of Hastelloy C22, Incolloy I625, and stainless steel SS304.

The next iteration of this type of experiment will include:

- Continual gassing of the media to maintain aerobic conditions and to better simulate expected repository conditions
- Addition of YM tuff (sterile or nonsterile) to include the entire complement of YM organisms
- Replenishment of media to mimic dripping water onto WPs
- Replacement of microbial growth media with Synthetic 10× J-13 media (Table 2 5-2), to better represent repository conditions

Alteration of these factors will both provide for a more accelerated test and produce conditions more representative of those expected within the potential repository.

2 5 7 2 4 Alterations in Bulk Chemistry Shows De-alloying of Test Materials

Corrosion of candidate materials can also be revealed by analyzing chemical changes in the bulk solution (or in this case, growth media) surrounding the test coupon Specifically, primary and alloying elements dissolved from metal into the aqueous phase may be detectable After five months of incubation with inoculated bacteria, bulk phases from several cells containing different alloys were sampled and analyzed by inductively coupled plasma atomic emission spectroscopy (ICP)

The results of ICP, on bulk solutions from various cells, are listed in Table 2 5-3 The ICP analysis may underrepresent the actual corrosion rate, but it can help determine if there has been significant preferential dissolution from the test alloys There was an almost 20-fold greater dissolution of nickel than copper from Monel 400, indicating a de-alloying of the metal under conditions where bacteria were present Chromium dissolution was observed in Alloy C22, Alloy I625, and Type 304 stainless steel, even though their overall corrosion rates, as determined by linear polarization resistance, were low Chromium dissolution may be even greater for these alloys in an environment that is more conducive to corrosion than the test cells used here (such as the environment planned for future tests, described in Section 2 5.7 2 3)

Table 2.5-3. Endpoint ICP analysis of spent media from Type 2 cells after 5 months' incubation with test coupons inoculated with YM bacteria.

Material exposed in the medium	Cu (mg/l)	Fe (mg/l)	Cr (mg/l)	Ni (mg/l)
Unincubated growth medium	n d	0 25	n d	n d
C1020	n d	16 50	N/A	n d
M400	1 00	0 40	N/A	18 50
SS304	n d	0 57	1 03	0 04
I625	n d	0 33	1 07	0 12
C22	n d	0 32	1 05	0 10

2 5 7 2 5 Surfacial Observations of Test Coupons Inoculated with YM Bacteria

In the cells containing C1020 and M400, considerable progressive accumulation of biofilm or bioproducts was observed on coupon surfaces as incubation progressed. However, little biofilm or bioproducts were observed to accrue on C22, I625, and SS304 coupons These

observations correlate with the observed corrosion rates rates were greater on C1020 and M400, and less on the other alloys Whether MIC-specific effects are also much less on the more resistant alloys has yet to be determined (this must necessarily await the analyses of sterile control cells) However, assuming MIC has less effect on the more resistant alloys, our observations may indicate that the more resistant alloys provide a less hospitable environment for the establishment of bacterial colonization, and thus are less susceptible to MIC. Current experiments being undertaken in collaboration with Montana State University (MSU), Bozeman, Montana (Gill Geesey), will establish colonization rates on C1020 and C22 by YM bacteria (see Section 2 5 10)

All candidate materials tested showed no pitting corrosion during the 5-month exposure in the test environment General corrosion was evident uniformly on the exposed surfaces of C1020 coupons, but de-alloying was observed in M400 coupons The de-alloying was supported by the discoloration of incubated M400 coupons in the presence of YM bacteria, where the preferential dissolution of Ni left behind a brown, copper-like appearance Scanning electron microscopy/energy dispersive x-ray analysis (SEM/EDAX) of incubated M400 revealed that the surface layer under the biofilm was indeed Cu-enriched, even though the initial Ni–Cu ratio was about 7.3 in M400 SEM examination of incubated M400 coupon surfaces also showed some degree of deterioration Therefore, the corrosion rate measured using polarization resistance of M400 apparently did not completely represent the actual penetration by corrosion, the de-alloying or degraded layer was thicker than the number indicated by the polarization resistance corrosion rates in μm/yr on this material. These observations support the need for endpoint surfacial analyses in addition to electrochemical testing to achieve accurate corrosion-rate predictions

Tested C22, I625, and SS304 coupons have been preserved for SEM/EDAX at a later time, though these coupons did not visibly show any gross corrosion morphology However, ICP analysis indicated preferential dissolution of Cr It remains to be seen whether SEM/EDAX can provide evidence of de-alloying damage on C22 and I625 similar to that observed in M400

After 5 months of incubation with YM bacteria, an anodic polarization measurement was performed, Figure 2 5-15 shows these polarizations. Except for the difference in corrosion potential, C1020 and M400 had similar polarization behaviors, and both demonstrated active corrosion (low passivity) Therefore, metal dissolution during the course of corrosion occurred on a wide range of surfaces, and localized pitting corrosion appeared unlikely.

Figure 2.5-15. Anodic polarization behavior of several candidate waste-container materials.

The anodic polarization behaviors of C22 and I625 were almost identical and similar to that of SS304, except that the latter showed even higher transpassive potential No pitting was generated by anodic polarization in any of these three materials Therefore, the given microbial environment is not aggressive enough to cause pitting of these corrosion-resistant materials (CRMs) However, a more aggressive (and representative) microbial environment may accelerate the preferential dissolution of Cr in C22 and other Ni-based alloys The de-alloying of Ni-based alloys not only degrades the materials, it can also alter the local bulk chemistry because released Cr^{2+} may cause a significant pH decrease of the surrounding solution

2.5.7.3 Discussion

The goals of these studies were to design and implement a system that could quantify the contribution of YM bacteria to overall corrosion rates of candidate WP alloys Furthermore, we aimed to generate a system in which environmental factors could be altered, candidate alloys could be tested for their relative susceptibilities to MIC, and some mechanisms of MIC attack might also be discerned Although our initial attempts (Figure 2.5-7) were sufficient to measure MIC on the more susceptible carbon-steel coupons, background noise and resistance prevented sufficient signal resolution to determine MIC of more corrosion-resistant alloys The signal-to-noise ratio was greatly improved by enlarging the coupon and by integrating the reference electrode directly into the same cell containing the working electrode (Figure 2 5-8) Development of this new cell type has permitted us to evaluate the MIC of more corrosion-resistant WP candidate alloys

However, because the coupon is entirely submerged in the improved cell, and because the media remained unaerated throughout the incubation period, electrochemical conditions at the coupon surface were more uniform and more anoxic than in the original system. We presume oxygen was progressively consumed by aerobic microbial activities in the improved system The enhancement of differential oxygen concentrations by microbial activities (causing water-line corrosion observed in the original cell design) was not observed in the new system, and corrosion rates were correspondingly lower Future modifications to this system will therefore include periodic or continual aeration of the media to better mimic prospective YM repository conditions, and to obtain better estimates of MIC rates

Measured rates of corrosion on both inoculated and sterile coupons changed during the incubation period until they reached a steady-state value Initial elevated rates on inoculated coupons may reflect the ready availability of nutrients Lower rates observed later in the incubation period could indicate exhaustion of the media immediately surrounding the alloy coupon or buildup of toxic endproducts Because diffusion of nutrients and end products, especially in the agar-solidified system, would be minimal, we expect that the observed steady state may not reflect conditions that would occur in a continuously fed system Because water (and accompanying solutes) are expected to eventually invade the repository continuously, a continuously fed test system may better reflect actual repository conditions and provide a better measure of MIC over the long term. Media replacement will be performed in subsequent iterations of this test system

Despite these caveats, it was possible using this system to discern a 5- to 6-fold increase in corrosion caused by inoculated bacteria to carbon steel coupons, and detect a 7- to 8-fold difference in MIC between carbon steel and Monel 400 Corrosion rates on CRMs were on the order of hundredths of μm/year, but because SS304 is well known to be susceptible to microbially induced pitting (and this was not observed in this system), it is clear that conditions were not conducive to observe MIC of these materials. Planned alterations in this system, which will also be more representative of repository conditions, should permit observation of MIC effects on CRMs.

Bulk chemical and surfacial endpoint analyses of spent media and coupon surfaces showed preferential dissolution of nickel from Monel 400 coupons, this observation was supported by surfacial EDAX of the coupons after incubation with YM bacteria SEM also showed greater damage to the M400 surface than that indicated by electrochemcial detection methods Furthermore, chromium was detected in bulk solutions incubated with inoculated CRM coupons. Thus, although electrochemical testing did not indicate a high degree of

corrosion during these incubations, similar to the case with M400, SEM may show a greater degree of damage of CRMs than can be detected electrochemically

2.5.8 Determining the Presence of Bacteria in Long-Term Corrosion Testing

Long-term testing of candidate WP materials under anticipated repository conditions is being undertaken in large tanks, where, at six-month or yearly intervals, replicate candidate coupons are withdrawn and analyzed Variables for testing include temperature (60° and 90°C), ionic strength of simulated J-13 (10× and 1000×), and pH (for more details refer to Section 2 2) The tank systems deployed for containing these tests are not completely isolated from the surrounding environment, there is some gaseous exchange with the ambient air In addition, solutions in the tanks were not introduced in a sterile state, nor were the tanks initially sterilized before use Thus, there is the possibility that microorganisms could be present in these long-term corrosion test (LTCT) tanks. If deleterious microorganisms were present in large enough numbers (due to introduction or growth), and conditions were favorable to carry out corrosion-inducing reactions, these microorganisms could effect overall corrosion rates. Therefore, techniques were developed to assess the presence and concentrations of bacteria contained in the LTCT tanks, to preliminarily determine if MIC might be a factor in observed corrosion rates of tested materials. By extension, possible MIC of candidate materials in LTCT tanks could indicate corrosion of WP materials in the proposed repository Organisms that are present under LTCT conditions could also be present in the repository environment

After testing several protocols, the following was developed to successfully observe and distinguish collected bacteria from suspended corrosion products, precipitates, and associated background fluorescence We removed 250-ml samples of solution aseptically from certain LTCT tanks using a peristaltic pump, and filtered these samples aseptically (0 2 μm) to retain microorganisms on the filter. Retained particles were resuspended in 20 ml of sterilized deionized water by vortexing Resuspended cells were fluorescently stained using 3 μl of dye stock per 1 ml of suspended cells (Live/Dead BacLight, Molecular Probes Inc., Eugene, OR) The stained cell suspension was refiltered through a sterile black polycarbonate filter (0.2 μm, Nucleopore) to reduce background fluorescence and concentrate cells Cells were counted using a fluorescence microscope (1000×) equipped with a calibrated ocular grid, using excitation at a wavelength of 470 nm and observing emission at 500–650 nm Under these conditions live cells emit green (500–550 nm light), but dead cells emit red (625–650 nm light)

After developing this protocol, LTCT Tanks 21, 22, and 23 were assessed for the presence of bacteria Tank 21 had many bacteria evident, whereas Tank 23 had low concentrations, and it was questionable whether Tank 22 had any bacteria Bacterial cells, when evident, could be identified by their distinguishing fluorescence emission and characteristic shape (either rod-like or spherical), even when large quantities of corrosion products were evident on the filter The same tanks were also swiped on the sides of the tank with sterile filters to assess whether bacteria were accumulating on tank surfaces (bacteria readily adhere to surfaces) Filters that were swiped were treated by resuspending cells and staining them fluorescently Swiped surfaces from Tank 21 clearly showed bacteria, but it was not clear that surfaces from Tanks 22 and 23 had any adhering cells Thus, at least in Tanks 21 and 23 bacteria are present and discernible, but their presence is questionable in Tank 22 All of these tanks are pH 9–10, and Tanks 21 and 23 are at 60°C containing 1000× and 10× simulated pore water, respectively. Given that bacteria were present in these, but absent in Tank 22, which contains 10× J-13 at 90°C, the elevated temperature may well preclude growth in Tank 22 Temperature was the

distinguishing determinant between tanks that could preclude growth. Although certain microorganisms are known to survive and even grow at these elevated temperatures (in hot springs, for example), it does not appear that they are present in Tank 22 or in the general LLNL environment. Whether such organisms persist at the YM site still needs to be determined However, as discussed below, higher temperatures during repository evolution will be accompanied by drying, which would definitely prevent bacterial activity (and corrosion) MIC would only be of concern after water returned to the drifts, coincident with the decrease in the ambient temperature

Whether observed bacteria are causing MIC still remains to be determined, bacteria that are present should be isolated, counted, and characterized to establish whether they are contributing to corrosion of WP materials The remaining tanks need to be evaluated for the presence and type of possible extant bacteria, as conditions in these tanks are different from those in Tanks 21 and 23, and these alternative conditions may not support either bacterial growth or MIC activities. Similarly, corrosion products on withdrawn WP coupons might be examined for biofilm formation and, if bacteria are present, for bacterial types and activities, to further establish whether bacteria in the LTCT are contributing to corrosion of test materials

2.5.9 In situ Field Trials: the Drift-Scale Test

The Drift-Scale Test (DST) was designed primarily to study hydrological and geochemical parameters in the repository horizon at elevated temperatures, by placing large heaters in an experimental drift near Alcove 5 in the ESF. To gain a better understanding of WP material behaviors under conditions of the test, replicate coupons of carbon steel 516 and Alloys 625, Monel 400, and C22 were placed at different locations near heaters in the test drift We expect that many types of bacteria present at YM after construction will be unable to survive the elevated temperatures expected upon waste emplacement, and likewise many will not survive the conditions in the immediate region of the DST (heaters will reach 200°C) Therefore, bacteria that survive the heat pulse (primarily through sporulating), and those that recolonize the repository (with pore water migration) after temperatures decrease and relative humidity increases, are of greater concern with respect to their effects on WP corrosion However, the DST provides an opportunity to observe how bacteria contained on WP materials and in tuff contained in the repository drifts would survive and possibly affect corrosion immediately following the heat pulse, in the absence of the re-entry of pore water

Replicate coupons of the four candidate WP materials were placed in the test drift under four different conditions Samples of 100 g of either sterile (gamma-irradiated) or nonsterile crushed YM tuff (1–4 mm) were placed in ceramic dishes covering metal coupons, this was intended to provide both the chemical environment of the rock with or without the total complement of bacteria contained in the rock Other coupons were inoculated with a mixture of characterized YM bacteria, including acid producers, slime generators, iron oxidizers, and sulfide producers (all of these activities are associated with MIC, see McCright, 1997), 10^8–10^9 cells of each strain of bacteria were spread on each coupon Finally, a set of coupons was emplaced without exposure to either rock or bacteria. All coupons were cleaned, weighed, and sterilized before either emplacement or inoculation

Heaters were turned on, commencing the Test, in November, 1997 At the conclusion of the test, coupons will be withdrawn, analyzed for corrosion product chemistry, weight loss, surface topography, presence of biofilm, and surviving bacteria

2.5.10 Biochemical Contributions to Pore Water and Metal Corrosion Chemistry

Prediction of the rates of MIC on WP materials requires establishing rate constants of individual MIC reactions. Quantitative assessment of the chemical contribution of YM microbial communities to overall corrosion rates, including reaction-rate determinations, is being undertaken in continual-flow systems fed with synthetic 10× J-13 pore water and containing crushed YM rock (with endogenous bacteria) and candidate WP materials Abiotic chemical-corrosion reaction rates are also being determined in identical systems containing sterilized YM rock The overall approach has been to measure the accumulation of corrosion products over time in sterile and nonsterile systems and, given the known chemistry of the reactants, deduce relevant rate constants, calculate mass balances, and finally establish corrosion rates When rates and levels of abiotic corrosion are subtracted from those calculated from nonsterile systems, biotic contributions can be determined

These experiments are being carried out in microcosms configured as shown in Figure 2 5-2, except that planktonic organisms contained in the bulk phase are drained in the outflow Thus, instead of an in-line filter on the outflow tube, media break-tubes have been inserted to allow outflow of free-floating organisms but to prevent back-contamination into the microcosm vessel We have added 100 g of sterile or nonsterile crushed YM tuff to the microcosm vessels along with carbon steel C1020 coupons, or Alloy C22 coupons, or 50 g synthesized waste-form glass Microcosms are fed at a constant flow rate (2 ml/hr, residence time 5 days) with 10× J-13 Synthetic medium (containing 0 1% glucose), pH 8 (Table 2 5-2) Similar experiments are being undertaken at the Center for Biofilm Engineering at MSU, at a pH of 4 and 10 MSU collaborators (Gill Geesey and coworkers) will also determine the colonization rates and types of bacteria that colonize coupons throughout the incubation period All initial experiments are being conducted at room temperature, later iterations will include elevated temperatures

Bulk-phase and solid-phase (on coupons) chemistry will be periodically determined throughout the incubation period. Results from nonsterile tuff will be compared to those with sterilized tuff to account for abiotic corrosion effects Periodically, bulk outflow solutions are assayed for pH, metals, and ions using ICP and ion chromatography (IC) Coupons are periodically removed and chemically analyzed using SEM/EDAX and XRD Collaborators at MSU will also analyze surfacial corrosion products with x-ray photoelectron spectroscopy (XPS) Corrosion products and biofilm are also removed, homogenized, and examined using XRD, ICP, and IC. Finally, incubated and cleaned coupons are analyzed for weight loss, and for surface topography by microscopy or atomic force microscopy (AFM)

These experiments have been initiated and are currently in progress, because sampling points are at two-month intervals, no significant trends in the data have been detected thus far Future plans include incorporating titanium alloys and ceramic materials, as well as increased temperatures and ionic strengths.

2.5.11 Minimum *RH* Requirements for Biofilm Formation on Candidate WP Materials

All biological activities depend on the presence of water. During the early evolution of the potential repository, it is estimated that the WP will remain dry However, starting 100 years after waste emplacement the relative humidity (*RH*) of the WP is expected to gradually increase, approaching 100% around year 1000 (Hardin et al , 1998). MIC of the waste package will largely depend on the ability of microorganisms to colonize surfaces, grow, and form biofilms (or accretions of bacterial growth on surfaces). The definitive factor in biofilm development is expected to be the presence of sufficient water, because other

required factors (nutrients, temperature, and radiation fields) may well be within ranges that permit at least some organisms to survive and maintain activity. Therefore, experiments are being undertaken at both Lawrence Livermore National Laboratory (LLNL) and the University of Nevada, Las Vegas (UNLV, Penny Amy and coworkers), to determine the critical *RH* at which biofilm development can initiate on candidate WP materials to predict when MIC may be a factor in WP corrosion

At LLNL, constant-humidity chambers at 80°–85°C will be used to test biofilm formation at 98, 78, and 50% *RH* Sterile glass petri dishes containing aseptically collected and crushed YM tuff and candidate material coupons (Alloys C22, Monel 400, titanium grade 16, or carbon steel C1020) will be incubated at each *RH*. Petri dishes containing sterilized YM tuff will serve as a negative control to ensure that biofilm development in nonsterilized tuff arises from the rock, and coupons inoculated with a mixture of cultivated YM bacteria (described in McCright, 1997) will serve as a control to indicate whether bacteria contained in tuff can colonize test coupons Periodically, coupons will be withdrawn and analyzed for biofilm development by SEM and culturing of colonized bacteria. Corrosion products will be analyzed by XRD, IC, and ICP. Microscopic and AFM analyses of cleaned coupon surfaces will provide an indicator of alterations in surface topography, and weight-loss determinations will provide an overall measure of corrosion. These experiments are just being initiated at LLNL

Studies to be undertaken at UNLV are still in the planning stages, but will employ saturated salt solutions to achieve various *RH*s (Acheson, 1965) under a greater range of temperature regimens We estimate that *RH*s of 97, 69, and 38% will be employed at 30°, 60°, and 80°C Test materials will include C22 and titanium, these will be contained in both sterile and nonsterile tuff Analyses of withdrawn coupons will at least include an assessment of the types of bacteria that grow on the coupon and may also help determine the types of bacteria that colonize at various *RH*s and temperatures

Acknowledgments

The author gratefully acknowledges the expert technical assistance of Michael Davis, Sue Martin, Brett Masterson, and Annabelle Miranda in generating the results presented in Section 2 5 Tiangan Lian designed electrochemical experiments, carried out these determinations, assembled data, and assisted in readying results for publication Finally, the author wishes to thank Denny Jones for his helpful guidance throughout the course of this work

2.5.12 References

Amy, P S , D. L Halderman, D H Ringelberg, and C Russell (1992) "Comparison of Identification Systems for Classification of Bacteria Isolated from Water and Endolithic Habitats within the Deep Subsurface " *Appl Environ Microbiol* 58·3367–3373

Atlas, R M. (1982) "Enumeration and Estimation of Biomass of Microbial Components in the Biosphere." R. G. Burns and J H. Slater, eds *Experimental Microbial Ecology*. p. 84 Oxford, England: Blackwell Scientific Publishers

Bethke, C M (1994) *The Geochemist's Workbench™, Version 2 0 A User's Guide to Rxn, Act2, Tact, React, and Gtplot* Champaign, IL: Hydrology Program, University of Illinois

Brock, T D , and M T Madigan (1991) *Biology of Microorganisms.* Englewood Cliffs, NJ. Prentice-Hall

Broxton, D E., D L Bish, and R G Warren (1987) "Distribution and Chemistry of Diagentic Minerals at Yucca Mountain, Nye County, Nevada." *Clays and Clay Min* 35(2) 89–110. [NNA 890327 0036]

Delany, J M (1985) *Reaction of Topopah Spring Tuff with J-13 Water A Geochemical Modeling Approach Using the EQ3/6 Reaction Path Modeling Code* (UCRL-53631) Livermore, CA: Lawrence Livermore National Laboratory [NNA 871111 0114, HQS 19880517 2419]

Difco Inc (1996) *Dehydrated Culture Meida and Reagents for Microbiology* Tenth edition Detroit, MI Difco Laboratories, Inc

Hardin, E L , S C. Blair, T. A Buscheck, D. A Chesnut, L D DeLoach, W. E Glassley, J W Johnson, R. B Knapp, K Lee, A Meike, K Myers, J J Nitao, C E Palmer, L L Rogers, N. D. Rosenberg, B E Viani, H F Wang , C Wittwer, and T J Wolery (1998) *Near-Field/Altered-Zone Models Report* Milestone report for the CRWMS Management and Operating Contractor, U S Department of Energy (SP3100M3) Livermore, CA· Lawrence Livermore National Laboratory (UCRL-ID-129179 DR)

Horn, J M , B Economides, A Meike, and R D McCright (1996). *Initial Studies to Assess Microbial Impacts on Nuclear Waste Disposal* (UCRL-JC-122587) Livermore, CA Lawrence Livermore National Laboratory [MOL 19960409 0170]

Jones, D A , B Pitonzo, and P S Amy (1997) "Electrochemical Characteristics of Anticipated MIC in Deep Geologic Nuclear Waste Storage Environments at Yucca Mountain, Nevada, USA " J. Wolfram, R D. Rogers, and L D Gazso, eds Microbial Degradation Processes in Radioactive Waste Repository and Nuclear Fuel Storage Areas (Boston, MA Kluwer)

McCright, R D. (1997). *Engineered Materials Characterization Report.* Milestone report for the CRWMS Management and Operating Contractor, U S. Department of Energy (TR251F89, Rev 1) Livermore, CA Lawrence Livermore National Laboratory (Also UCRL-ID-119564, Rev 1) [MOL 19980105 0616]

Miller, J H (1972) *Experiments in Molecular Genetics* Cold Spring Harbor, N Y . Cold Spring Harbor Laboratory Press.

Parberry, D. G (1968) "The Role of Cladosporium Resinae in the Corrosion of Aluminium Alloys " *Intl Biodeterioration Bull* 4.79

Perfettini, J V , E Revertegat, and N. Langomazino (1991) "Evaluation of Cement Degradation Induced by the Metabolic Products of Two Fungal Strains." *Experientia* 47·527-533

Reasoner, D J , and E. E. Geldreich (1985). "A New Medium for the Enumeration and Subculture of Bacteria from Potable Water." *Appl. Environ Microbiol* 49 1-7

Roznak, D. B , and R. R. Colwell (1987), "Survival Strategies of Bacteria in the Natural environment." *Microbiol Rev* 51·365-379

Stern, M , and A. L. Geary (1957) "Electrochemical Polarization I A Theoretical Analysis of the Shape of Polarization Curves." *J Electrochem Soc* **104**:56

Tunlid, A , and D C. White (1992) "Biochemical Analysis of Biomass, Community, Structure, Nutritional Status, and Metabolic Activity of the Microbial Communities in Soil." Bollag and Stotzky, eds. *Soil Biochemistry* Vol. 7, p. 229 New York, NY: Dekker.

Videla, H A (1996) "Fundamentals of Electrochemistry." *Manual of Biocorrosion* pp 96–97 Boca Raton, FL: CRC Press

Videla, H. A , P S. Guiamet, S DoValle, and E H Reinoso (1993) "Effects of Fungal and Bacterial Contaminants of Kerosene Fuels on the Corrosion of Storage and Distribution Systems " G Kobrain, ed *A Practical Manual on Microbiologically Influenced Corrosion* p 125 Houston, TX· NACE International

2.6 Physical Metallurgy and Fracture Mechanics

by Donald W. Stevens, with a contribution from Tammy Summers on microstructural characterization

2.6.1 Introduction

The information contained in this section of the EMCR represents the initial entry for this task, although some of the subjects were mentioned briefly in the previous *Engineered Materials Characterization Report* (McCright, 1997, pp 1-2, 2 2-1, and 2 2-2)

The selection of alloys for the canister is based primarily on corrosion requirements The selected alloys are A516 carbon steel for the corrosion-allowance material (CAM) and Ni–Cr–Mo alloys (first 625, then Alloy C-22) for the corrosion resistant material (CRM) We have begun a major effort to provide for the physical metallurgical soundness and fracture stability of the selected alloys The objective is to enhance canister survival upon manufacturing and during lengthy (10,000-yr) repository service at 100° to 400°C.

The physical metallurgy of canisters involves relations among their manufacturing processes, repository aging, microstructures, and properties Such relations, shown in Figure 2 6-1, must be understood and controlled to obtain canisters suitable for 10,000 years of service

Figure 2.6-1. Relations between waste-package container manufacturing process and repository aging on resulting microstructure properties.

To describe the relations shown in Figure 2 6-1 in more detail, we use Alloy C-22 as an example The same metallurgical principles would apply to steel and other canister alloys that might arise Only the process methods and details vary

Manufacturing processes include

- Melt refining of the alloy, hot forging, hot and cold rolling, pickling, and heat treating to produce thick plates, followed by
- Canister fabrication and welding, including hot and cold rolling, end bending, roll forming, cutting, grinding, machining, heat treating and welding by multiple methods

Repository aging is simply the thermal profile of 100°–400°C over a period of 10,000 years

The manufacturing processes establish a particular metallurgical microstructure, and subsequent repository aging will alter this microstructure Microstructure consists of one or more major phases and secondary phases, such as intermetallic precipitates, ordered domains, and impurity inclusions Each of the phases has its grains of various sizes, shapes and orientations, twins, crystalline defects such as dislocations and stacking faults, chemical segregation, and more. The ensemble of these microstructural features establishes the engineering properties and performance of the alloys, such as corrosion resistance, strength, toughness, and so forth. Some of the relations are illustrated for Alloy C-22 by the following examples

Example 1 Classical sensitization (see Figure 2 6-2) can occur upon slow cooling from welding, which allows Cr immediately adjacent to the grain boundaries (gb) to diffuse to the boundaries and form carbides with carbon that tends to segregate there. This depletes Cr

from the matrix on either side of the gb, leaving the narrow regions vulnerable to localized corrosion The situation worsens if the $Cr_{23}C_6$ carbides are continuous, or nearly so, along the gb because residual stresses from welding could cause intergranular fracture along the carbide trail

Figure 2.6-2. Possible effect of welding on corrosion and fracture.

Example 2 Molybdenum is depleted from the matrix adjacent to the gb (see Figure 2 6-3) when it forms an intermetallic compound while in repository service Unlike continuous carbides, the $MoNi_3$ intermetallic is not continuous along the gb, but worse, is the sharp-tipped sigma phase Residual welding stresses could form cracks at the sharp tips, then propagate them across the grains to cause transgranular fracture

Figure 2.6-3. Possible effect of repository aging on corrosion and fracture.

As is expected from the foregoing examples, the phase stability of Alloy C-22 is a major concern Thus, the topic of phase stability is discussed in more detail below

2.6.2 Phase Stability of C-22

Our work on the phase stability of Alloy C-22 refers to activity E-20-67 of the Scientific Investigation Plan (SIP), Phase Stability Studies, in Metal Barrier Selection and Testing We wish to determine the effects of manufacturing processes and repository aging on the metallurgical phase stability of C-22 for both parent and welded metals because phase instabilities can degrade corrosion and mechanical properties Of prime concern are the causes (composition shifts, stress, deformation, temperature, time, and the like) and kinetics of detrimental phase changes The following describes why and how such phase and property changes occur

Alloy C-22 is a Ni–Cr–Mo alloy consisting of about 57Ni–23Cr–13Mo–3W–3Fe–0 01C with 0.5 Nb, Ta, V, Mn, and Al + Ti (wt%) In its mill-annealed and most corrosion-resistant condition, Alloy C-22 is solution treated at about 1200°C, then rapidly quenched in water The process retains nearly all of the alloying elements in solid solution in the Ni matrix However, this is a thermodynamically unstable condition, with a considerable chemical driving force to form metastable or stable compounds from the dissolved elements The problem is that upon subsequent heating, such as during welding, stress relieving, and service life, some of the alloying elements (particularly Cr and Mo) precipitate from the Ni matrix into carbides and intermetallic compounds (such as mu, P, or sigma), or they form short- or long-range ordered structures, particularly type-A_2B long-range ordering of ostensibly Ni_2Cr The new phases can degrade corrosion resistance and mechanical properties, such as impact resistance and ductility. A literature survey by Gdowski (1991) has elucidated such events.

Such phase instabilities are troublesome enough in the parent metal However, they are usually worse in weldments where high residual stresses, chemical segregation, and nonequilibrium structures abound.

2.6.2.1 Workshops on Phase Stability in C-22

2 6 2 1 1 Nickel Development Institute Workshop in San Diego, California, March 19 and 20, 1998

Because of our considerable concern for the phase stability in C-22, we enlisted the aid of the Nickel Development Institute (NiDI) to sponsor a one-and-one-half-day workshop in San Diego, California, in March 1998, just prior to the National Association of Corrosion Engineers (NACE) meeting The 25 participants represented the leading producers of Alloy C-22 (Haynes, Inco, and Krupp-VDM, producers of a like alloy, 59), three national laboratories [Lawrence Livermore National Laboratory (LLNL), Idaho National Engineering and Environmental Laboratory (INEEL), and Atomic Energy of Canada, Limited (AECL)], the Nuclear Regulatory Commission (NRC), and TRW Environmental Safety Systems, Inc , Management and Operating (M&O) Contractor from Las Vegas, Nevada Others from the private sector included EIS, representing SYSWELD (the leading software provider for analysis of welding stresses), and AEA Technology, representing its Thermo-Calc chemical thermodynamic software, related databases, and kinetic models to predict time–temperature–transformation (TTT) diagrams

Figure 2 6-4 is a schematic of a hypothetical TTT diagram The diagram uses fictitious data to show a curve that is intended merely to help describe a planned aging experiment

Figure 2.6-4. Schematic of a C-22 TTT diagram showing the planned aging experiment to produce data (filled circles) that will extend the curve and verify a model yet to be developed. This hypothetical figure is for illustrative purposes only and contains no actual data.

Bounding exercises were highly recommended to help identify critical variables and their extreme values, without which the metallurgist faces a confoundingly large number of variables This approach has been employed in our recent design of a 300-yr aging experiment for Alloy C-22 (see Section 2 6 2 1 3), for example, where the hottest (SAW) and coolest (GTAW) welds will be analyzed to bracket the effect of welding heat on phase stability

M Fahrman of Inco (Fuhrman, 1998) reported TTT aging results for alloys 625LCF and C-276 Experimental results were compared to thermodynamic predictions obtained from the AEA Thermo-Calc program Some phases were predicted, others were not Fahrman believes much more improvement in the calculation is required before accurate predictions will be realized When extrapolating to lower temperatures to obtain a particular drop in impact strength, Fahrman employed activation energies half that of bulk diffusion to account (correctly, it is thought) for grain-boundary-diffusion control at the lower temperatures

Both Inco and Haynes reported aging acceleration by cold working (Rebak and Koon, 1998) This process will be employed in the 300-yr aging experiment at LLNL.

G. Hodge and R Rebak of Haynes (Rebak and Koon, 1998) reported their nearly 5-yr-long aging data of Alloy C-22, C-4, and C-276 down to 427°C, the lowest temperature and longest time known to exist that approaches the 100° to 400°C storage temperatures at the potential Yucca Mountain repository. Analytical transmission electron microscopy (TEM) showed that W-free C-4 was, as expected, free of all secondary phases, whereas Alloy C-22 contained primary carbides and long-range ordering (LRO). These, however, had little effect on corrosion and mechanical behavior. An extrapolation of the TTT curve to 300°C

(representative of potential Yucca Mountain storage conditions) predicted that only single-phase gamma (no secondary phases) would prevail after 1000 yr However, such extrapolations are risky at best because they assume the same rate-controlling reactions at both high and low temperatures.

Although corrosion and mechanical test samples from Haynes included welded regions, no weldments had been examined by analytical TEM to establish the TTT curve. In retrospect, this proved to be a dramatic omission because, throughout the workshop, concern was frequently raised about the unpredictable, potentially troublesome microstructural perturbations generated during welding [e g , chemical segregation, mixed grain structures, heat-affected zones (HAZ), high stresses, and unpredictable phases]. It is believed that phase instabilities would very likely reside in the weldments and HAZs rather than in the relatively homogenous, well-controlled parent metal To determine the location of phase stabilities, Haynes provided some of its aged samples to LLNL for microstructural characterization by analytical TEM and other methods The two parties then met at LLNL to review early results and conceptually design a 300-yr aging experiment.

2 6 2 1 2 LLNL and Haynes Workshop in Livermore, California, May 27, 1998

Microstructural characterization of aged Hastelloy Alloy C-22 samples was conducted at LLNL by Tammy Summers Two samples from Haynes were aged for 16,000 hr, one at 760°C and the other at 593°C, and then examined after Charpy impact testing The fracture surface of the sample aged at 760°C is shown in Figure 2 6-5 and, in profile, in Figure 2 6-6 At 760°C, an as-yet-unidentified phase formed at the grain boundaries and throughout the bulk of the specimen This phase appears to be brittle, causing failure to occur at the grain boundaries Preliminary TEM results suggest that this is the mu phase The sample aged at 593°C also broke intergranularly However, as shown in Figure 2 6-7, the fracture surface appears quite different from that for the sample aged at 760°C. Ordering is known to occur in similar Ni–Cr–Mo alloys (Tawancy et al , 1983, Tawancy, 1980) at lower temperatures, and such ordering causes the alloy to deform by twinning (Tawancy et al , 1983) The unique appearance of the fracture surface in Figure 2 6-7b may be due to twinning This sample is currently being studied by TEM to determine whether any long-range ordering has occurred.

Figure 2.6-5. Scanning electron microscope (SEM) image of a Charpy impact specimen from Alloy C-22 aged 16,000 hr at 760°C.

Figure 2.6-6. SEM backscattered electron image of a profile view of the fracture surface shown in Figure 2.6-5.

Figure 2.6-7. SEM images of a Charpy impact specimen from Alloy C-22 aged 16,000 hr at 593°C.

A welded Alloy C-22 sample aged at 427°C for 40,000 hr is also being studied As shown in Figure 2 6-9 and Figure 2 6-10, A_2B-type ordering was seen in both the weld and the base metal An intermetallic phase was also present in the weld filler metal but, as shown in Figure 2.6-11, it was not uniformly distributed throughout the weld. Several intermetallics are known to form in the as-welded condition (Cieslak et al , 1986). TEM work aimed at identifying these intermetallics is currently in progress. No intermetallics have been observed to date in the base metal. Figure 2.6-8 shows an optical micrograph of an Alloy C-22 sample welded by GTAW with matching filler aged 40,000 hr at 427°C

Figure2.6-8. Optical low-magnification micrograph of aged Alloy C-22 weld.

Figure2.6-9. (a) TEM dark field image from a (1/3)<220> reflection showing ordered domains (white spots) in Alloy C-22 base metal aged 40,000 hr at 427°C. (b) Selected area diffraction pattern showing (1/3)<220> reflection used for the image shown in (a).

Figure 2.6-10. (a) TEM bright field image and (b) dark field image from a (1/3)<220> reflection showing ordered domains in Alloy C-22 weld metal aged for 40,000 hr at 427°C.

Figure 2.6-11. SEM micrograph showing nonuniform distribution of intermetallics in Alloy C-22 weld metal aged 40,000 hr at 427°C.

2 6.2 1 3 Design of a 300-yr Aging Experiment for Alloy C-22

A 300-yr aging experiment to be conducted at LLNL was conceptually designed in the workshop to extend the TTT diagram for Alloy C-22 at 427° and 350°C Both temperatures are well below one-third of the melting point and would thus encompass the low-temperature regime-of-diffusion control that includes the 100° to 400°C potential repository temperature The primary samples will contain welds and HAZs Cold working will be employed to accelerate the transformation kinetics Corrosion tests, mechanical tests, and microstructural analysis will be performed on samples pulled periodically from the aging furnaces

The objective of this approach is shown conceptually in Figure 2 6-4, which is merely a schematic of the TTT aging experiment, but not actual data The higher-temperature curve (solid line in Figure 2 6-4) is extended into the lower-temperature regime with a model (dotted line) yet to be developed Data to verify the model are shown as solid black circles Samples would be pulled from the aging furnaces and microstructurally characterized for periods up to 300 years to predict whether the canisters will last If it appears that the canisters will fail, they can be extricated to correct the problem Because backfilling is planned at year 300 to safeguard against falling rocks crushing the canisters, it will not be feasible to extricate the canisters after that

2.6.2.2 Current Work on Phase Stability of Alloy C-22

2 6.2 2 1 Collaboration with Haynes and other Alloy C-22 Producers

The collaborative study on aging with Haynes emanated from their having invaluable samples aged for 5 years at 427°C and LLNL having advanced analytical TEM with which to analyze the aged samples. The other C-22 producers, Allegheny–Ludlum and Inco, are cognizant of this collaboration, and informal talks have been initiated on possible collaborations

LLNL will continue to analyze the microstructure of aged samples (particularly weld metal) from Haynes by analytical TEM, SEM, and metallography, as described above The microstructural results will be correlated with Haynes' mechanical and corrosion test results to develop relations among processes, microstructure, and properties. A report will be issued on the results by February 1999 for inclusion in the Yucca Mountain License Application in mid-1999

2 6 2 2 2 300-Yr Aging Experiment

This experiment was described in Section 2 6 2 1 3.

2.6.2 2.3 Kinetic Model to Extend TTT Curves

Aging data to generate TTT curves exist downward to only 5 yr at 427°C Our goal is to have a model developed to extend the curves to lower temperatures (100° to 400°C) and much longer times (10,000 yr) to portray the potential repository conditions, as shown in Figure 2 6-4

Simple extrapolation downward from the higher temperatures and shorter times suffers from the assumption that the mechanisms and rate-controlling processes of phase transformations are the same at high and low temperatures We know that such an assumption fails for diffusion control because grain boundary diffusion at low temperatures is more rapid than that predicted from high-temperature extrapolation, where lattice diffusion dominates The assumption would also fail if the lower-temperature phases are somehow different from their higher-temperature counterparts (for example, bainite at lower temperatures, and pearlite at higher temperatures in steel). Because of such uncertainties with extrapolation, it seems necessary to establish kinetic models of TTT curves to predict phase transformations during the extraordinarily long times and low temperatures that are predicted for the repository. AEA Technology has such a model based on Thermo-Calc, and the model was used at Inco, as reported previously This model is potentially powerful, but it requires refinement for our alloys and conditions

2 6.2 2 4 Bounding Predictions from Thermochemical and Electronic Modeling

This is not a Yucca Mountain Site Characterization Project (YMSCP)-funded task, rather, it is financed by LLNL under its Laboratory Directed Research and Development Program The principal investigators will be Wilhelm Wolfer and Patrice Turchi, both of whom will be working closely with us to better focus their activity on YMSCP concerns These researchers will attempt to purchase the Thermo-Calc software to make thermochemical predictions of phases that might be present under YMSCP conditions of 100° to 400°C up to 10,000 yr In addition, electronic calculations will be used to predict metastable and stable phases as well as phases not yet in the thermochemical database upon which Thermo-Calc relies to make a prediction These methods are capable of providing invaluable bounding conditions of phase space (i.e., what phases might exist under the service times and temperatures of the canister) One year or more will probably be required to obtain the first results from this endeavor

2 6 2 2 5 Melt-Refining Effects on Phase Stability

A melt refiner, Allegheny-Ludlum, was visited as the first effort to identify possible causes of phase instability in the 1-in.-thick plates that serve as starting material for the canisters. Allegheny-Ludlum prepares basic chemistry melts in a vacuum-induction melt (VIM) furnace and, after deslagging, transfers its liquid metal to a 32T argon–oxygen decarb (AOD) furnace Chemical segregation, which appears to be the most likely cause of concern for our purposes, would occur within and between the two ingots obtained from each tap of the AOD furnace We would likely want these ingots to be remelted by electroslag remelt (ESR) to obtain the cleanest metal

2.6.3 Fracture Mechanics

2.6.3.1 Stress Analysis

A first step in considering fracture of the metal canisters is to perform a stress analysis of welding The other stress sources—namely, shrink fitting, fabrication, and content loading—are much smaller than welding stresses. The welding stresses encountered during fabrication of the first model cylinder exceeded the yield stress of the steel, as noted by its gross plastic deformation suffered upon welding We intend to calculate and measure residual stresses from welding The initial calculations will use two different software applications The first employs LLNL's TOPAZ3D on an electron-beam-welded plate of steel This analysis is underway. The second will involve SYSWELD, a commercial product we are attempting to purchase It will be applied to the YMSCP canister

2.6.3.2 Fracture Processes

2 6 3 2 1 Thermal Embrittlement of Carbon Steel (A516)

Jai-Song Huang of LLNL calculated that phosphorus (P) embrittlement in carbon steel would not occur by P diffusion to the grain boundaries (Huang, 1998) Details of this calculation are presented in Section 2 8 Since then, the temperature profile expected within the repository has increased from about 200° to 400°C to reflect backfilling The increased temperature may increase the diffusion of P—and, perhaps, S—to critically high values If backfilling has a reasonably high probability of occurring, the 400°C consequence must be calculated At the NACE 98 conference in San Diego, Gustavo Cragnolino of NRC reported his analysis of P embrittlement for the same material and conditions (Cragnolino et al, 1996) Those results appeared to be consistent with the results of Huang These two analyses are compared in detail in the following subsection to see if they are in full agreement

2.6 3 2 2 Stress Corrosion Cracking

Huang (1998) employed linear-elastic fracture mechanics to calculate stress corrosion cracking (SCC) for both carbon steel (A516) and Alloy C-22 of the canister Huang used data from the open literature for the carbon steel, and K_{ISCC} data for Alloy C-22 from Ajit Roy, who employed precracked double-cantilever beam (DCB) tests (Roy, 1997) Huang assumed that cracks would initiate at corrosion pits Huang's results indicate that SCC would not likely occur for either alloy in the base or weld metal, even without relief of residual weld stresses. However, the uncertainty in his analysis led to the suggestion that the Alloy C-22 analysis be repeated using elastic-plastic (versus linear-elastic) fracture analysis. In the meantime, the residual welding stresses should be relieved to 75% of their initial levels This suggests a cautionary position on the occurrence of SCC in Alloy C-22. Haynes reported in the workshops cited previously that, in numerous different U-bend corrosion tests, no SCC occurred. However, this notch-free test is less severe than DCB. Work continues on Alloy C-22 SCC. Ajit Roy is repeating his DCB tests, Gustavo Cragnolina of NRC is experimentally validating Roy's results using the same Haynes material lot, and Jai-Song Huang is planning compact-tension-reverse DCB tests

2.6.4 Fabrication and Welding Support

We are providing physical metallurgical support to the TRW engineering group responsible for designing and specifying the manufacture of the canisters Such support requires working closely with the engineers to see that metallurgical principles and sound

metallurgical practices are followed in the design, fabrication, and welding of the canister Otherwise, poor metallurgical structures could be produced with correspondingly poor mechanical and corrosion properties. For example, during shrink fitting of model cylinder No. 1, gray paint markings were abundant on the outer surface of the nickel-alloy inner cylinder During its heatup upon shrink fitting, elemental contaminants (such as C or S) in the paint could damage the nickel alloy The C could sensitize the grain boundaries to corrosion attack The S could form a brittle network of NiS_2 precipitates along the grain boundaries, leading to premature fracture This problem was rectified in making model cylinder No. 2 by machine cleaning all of the shrink-fit matching surfaces of the steel and nickel-alloy cylinders

Figure 2.6-12 and Figure 2.6-13 show the shrink-fitting operation for cylinder No 2 The C-22 Ni-alloy inner cylinder in the foreground of Figure 2 6-12 awaits flame heating to reach 700°F for the A516 carbon-steel outer cylinder in the background When the steel cylinder reached this temperature, the Alloy C-22 cylinder was lowered by chainfall into it and is shown at rest in Figure 2 6-13. The inner steel surface shown in Figure 2.6-13 was clean, bright, and blue tinged after the operation, indicating a very thin, tight oxide

Figure 2.6-12. C-22 Ni alloy (foreground) awaits 700°F heating of A516 carbon steel (background) for shrink fitting.

Figure 2.6-13. Cold Ni alloy at rest inside the hot carbon steel.

We also provided metallurgical support when a novel canister design was proposed by design engineers The idea was to substitute thinner nickel-alloy lids for thicker steel lids to reduce welding time and thus decrease costs A metallurgical review, however, revealed that the design introduced a nickel-alloy/steel interface that would lead to rapid galvanic corrosion

Another purpose of our metallurgical support is to analyze the metallurgical structure of canisters and relate the structures to the properties and behavior of the canisters For example, oxide on the steel facing the nickel alloy after shrink fitting was found by analysis to consistent of a contiguous, tight iron oxide layer about 8 μm thick This oxide layer would retard crevice corrosion and would interfere with the electrical coupling required for galvanic protection of Alloy C-22 by the carbon steel If no changes are made or planned for canister materials and processes, Alloy C-22 in model cylinder No 2, particularly its weldments, will be tested for mechanical and corrosion properties

2.6.5 References

Cieslak, M J , T. J Headley, and A D Romig, Jr. (1986). "The Welding Metallurgy of Hastelloy Alloy C-4, Alloy C-22, and Alloy C-276." *Met Trans A*, 17(11).2035-2047. [NNA 19910419.0011]

Cragnolino, G. A , H. K Manaktala, and Y.-M Pan (1996) *Thermal Stability and Mechanical Properties of High-Level Radioactive Waste Container Materials Assessment of Carbon and Low-Alloy Steels* CNWRA 96-004, San Antonio, TX.

Fuhrmann, M. (1998). "Effect of Long-Term Exposures on the Phase Constitution and Selected Properties of INCONEL™ Alloy 625LCF™ and INCO™ Alloy C-276 " In *Workshop on Phase Stability in Nickel Alloys for Radioactive Waste Containers* Toronto, Ontario: Nickel Development Institute. [MOL.19980618.0080]

Gdowski, G. E (1991) *Survey of Degradation Modes of Four Nickel-Chromium-Molybdenum Alloys*. (UCRL-ID-108330) Livermore, CA Lawrence Livermore National Laboratory. [NNA.19910521 0010]

Huang, Jia-Song (1998) *Thermal Embrittlement of Carbon Steels in Canistered Waste Disposal Containers* (UCRL-ID-130062) Livermore, CA. Lawrence Livermore National Laboratory [MOL 19980114 0092]

Huang, Jia-Song (1998) *Stress Corrosion Cracking in Canistered Waste Package Containers Welds and Base Metals* (UCRL-ID-130063) Livermore, CA· Lawrence Livermore National Laboratory [MOL 19980126 0559]

McCright, R D. (1997) *Engineered Materials Characterization Report*, Vol. 3 Milestone report for the CRWMS Management and Operating Contractor, U S Department of Energy (UCRL-ID-119564 Rev. 1) Livermore, CA Lawrence Livermore National Laboratory [MOL 19971218 0927; MOL 19980105 0616]

Rebak, R B , and N E Koon (1998) "Localized Corrosion Effect of Alloy and Weldment Aging at 427°C for Up to 40,000 h " *Workshop on Phase Stability in Nickel Alloys for Radioactive Waste Containers* Toronto, Ontario Nickel Development Institute [MOL.19980618 0080]

Roy, A K , D L Fleming, and B. Y Lum (1997) *Stress Corrosion Cracking of Fe-Ni-Cr-Mo, Ni-Cr-Mo, and Ti Alloys in 90°C Acidic Brine* (UCRL-JC-128477) Livermore, CA Lawrence Livermore National Laboratory

Tawancy, H M (1980). "Order-Strengthening in a Nickel-Base Superalloy (Hastelloy Alloy S) " *Met Trans A*, **11**:1764–1765

Tawancy, H M., R. B Herchenroeder, and A I Asphahani (1983) "High-Performance Ni-Cr-Mo-W Alloys " *J Metals* **35**(6) 37–43 [NNA 19910419 0026]

2.7 Development of Surface Analytical Techniques for Engineered Barrier Systems

Peter J. Bedrossian, Joseph C. Farmer, and Gregory E. Gdowski,

2.7.1 Introduction

This section describes the progress to date on a new, experimental component of the Engineered Barrier System (EBS) of the Fissile Materials Disposition Program We have applied several thin-film analytical techniques, including Raman spectroscopy, photoemission, x-ray diffraction (XRD), and the electron microprobe, to detect corrosion products on representative coupons extracted from various, ongoing corrosion test facilities To assess the feasibility of applying Raman spectroscopy to characterize corrosion products, we have applied Raman methods to both corrosion coupons and bulk samples representing various corrosion products fabricated at LLNL We find that stable, nonintrusive Raman measurements for corrosion products under consideration depend critically on the wavelength and the power level of the excitation used

Specimens examined in this study included.

- Four samples of C-22, of which one was a control and three were extracted from controllec aqueous environments in the Long-Term Corrosion Test Facility (LTCTF) at LLNL
- One coupon of 1020 carbon steel from a field test at Yucca Mountain
- One coupon of A516 carbon steel from a humidity test at LLNL
- Pressed-powder oxides of iron
- One sample of naturally occurring magnetite

The various analytical techniques used in this study employ excitations of different kinds and different energies, and they probe different scales of depth and surface area Thus, they provide complimentary information when taken as an ensemble In general, none of the techniques is sufficient by itself to characterize the composition of a corrosion film

In our Raman spectroscopy, a solid or liquid specimen is exposed to a focused beam of monochromatic light while the inelastically scattered light is collected and detected Spectral shifts arising from phonon emission and absorption for specific materials can then be observed. The technique is ideally suited for our planned corrosion studies because it can be performed either in liquid solution or ambient air and in real time, without surface treatment, which might alter corrosion products. Raman spectroscopy is therefore compatible with existing corrosion test facilities as well as prototype, bench-top, electrochemical-cell experiments

The electron microprobe in a scanning electron microscope (SEM) uses an electron beam to excite characteristic x rays from the various constituent elements in a specimen. The width and depth of the region sampled are on the order of 1 μm, so the variations in the elemental composition across a film can be correlated with structural features observable in electron micrographs, such as the presence of a scale

X-ray photoelectron spectroscopy (XPS) uses a monoenergetic x-ray source to induce electronic transitions in a specimen and can result in the ejection of electrons of various kinetic energies, which are detected and analyzed. It is a straightforward, useful technique for the identification of atomic species at a solid surface. The depth of material sampled by XPS is the mean escape depth for electrons at the kinetic energy of ejection, which is typically

10 to 20Å, far less than that sampled with SEM Because the excitation source in XPS is much broader than the electron-beam source used in the SEM, XPS does not offer the spatial resolution available with SEM Because electron-binding energies for a given element are altered by the chemical environment of the element, the bonding environments of elements detected by XPS are reflected in shifts of the observed binding energies. Unlike SEM, XPS therefore offers sensitivity to chemical binding and oxidation states of the elements under study

Finally, analysis of the composition of thin films is aided by XRD, which can identify crystalline phases near a solid surface The diffraction signal from a film is enhanced with respect to the signal that arises from the substrate by using a glancing-angle geometry Feldman and Mayer (1986) provide a review of techniques useful in thin-film and surface analysis

2.7.2 Methods

Raman spectra of various corrosion products have been collected with a Dilor LABRAM system at Surface Science Laboratories in Mountain View, CA A helium–neon laser operating at 632 8 nm was used as the excitation source Unless otherwise noted, the spectra presented in this report were acquired with an excitation power level reduced 100 μW by a neutral-density filter The scattered light passes through a holographic notch filter to remove Rayleigh scattering, then through an 1800 gr/mm grating, and is detected by a charge-coupled device (CCD) array The sample is mounted on an Olympus BX40 confocal microscope

Raman spectra of chloride salts were collected with a SPEX Model 1488 dispersive spectrometer at LLNL, now controlled with a SPEX SPECTRAQ controller and the DM3000B software package for DOS The excitation is provided by a Cytonics 15-mW, 488-nm, argon-ion laser, which passes directly into the Model 1439A Macro chamber, in which the laser light is focused onto a specimen The scattered light is collected and focused onto the monochrometer's entrance slit with a Nikkor 50-mm, f/1 2 lens The system employs a SPEX Model 1680B double-monochrometer system, with 1800 gr/mm gratings Finally, the scattered light is detected with a photomultiplier The double-monochrometer system routinely affords resolution of ≤0 3 wave numbers

The SEM, XPS, and XRD analyses all make use of commercial instruments The SEM is a Hitachi Model S-4500 with a field emission source and an Oxford/Link, energy-dispersive, x-ray microprobe with a high-purity germanium detector for elemental analysis XPS analysis is performed with a PHI 5400 system, using Mg Ka (15-kV, 400-W) radiation for the excitation XRD is performed with a Rigaku Model RU-300 rotating-Cu anode, operated at 40 kV and 200 mA The scan rate was one degree per minute, in steps of 0 02 degrees

The following samples were analyzed Coupons of Alloy C-22 were held at 90°C for one year in an aqueous solution of pH = 2 7 in the LTCTF at LLNL The solution included the following constituents

- Ca^{2+} 58 ppm
- Mg^{2+} 53 ppm
- K^{+} 4,300 ppm
- Na^{+} 43,000 ppm
- Si 50 ppm
- SO_4^{2-} 40,000 ppm

- Cl^- 27,000 ppm
- NO_3^- 24,000 ppm
- F^- 0 ppm
- HCO_3^- 0 ppm

The samples were rinsed in distilled water before the analysis

One coupon of 1020 carbon steel was exposed during a Single Heater Test at Yucca Mountain in unsaturated rock, above the water table The coupon was exposed to elevated temperatures (30° to 80°C), to high relative humidities, and possibly to episodic dripping of liquid water Its location was Borehole 18, Cavity 2

We have also tested one coupon of A516 Gr55 carbon steel, which was stored in an environment of 77°C and 83% relative humidity, on which salts were deposited using an aerosol The salt contained Na, K, Mg, Ca, Si, SO_4, Cl, NO_3, F, and HCO_3.

2.7.3 Results

We have found close agreement between our measured Raman spectra and previously published Raman spectra for $NiCl_2$•6H2O in solid form (Sridhar and Dunn, 1997) (see Figure 2 7-1), $FeCl_3$•6H2O in solid form (see Figure 2 7-2), and $FeCl_3$ in solution (Bouchert et al , 1991) (see Figure 2 7-3), using the SPEX 1488 dispersive spectrometer.

Figure 2.7-1. Raman spectrum of a solid chunk of NiCl2•6H2O collected on the SPEX 1488 spectrometer. The slit opening was 0.2 mm, the sweep rate was 0.33 s/pt, the resolution was 1 cm^{-1}/pt, and six sweeps were averaged.

Figure 2.7-2 Raman spectrum of a solid chunk of $FeCl_3$•6H_2O collected on the SPEX 1488 spectrometer. The slit opening was 0.2 mm, the sweep rate was 0.33 s/pt, the resolution was 1 cm^{-1}/pt, and three sweeps were averaged.

Figure 2.7-3. Raman spectrum of $FeCl_3$ in solution, collected on the SPEX 1488 spectrometer. The slit opening was 0.2 mm, the sweep rate was 0.5 s/pt., the resolution was 2 cm^{-1}/pt, and 25 sweeps were averaged.

Using the Dilor LABRAM Raman system, we have also found close agreement with previously published spectra for pressed samples of Fe_2O_3 (Figure 2 7-4) and Fe_3O_4 (Figure 2.7-5) powders, and for the mineral form of magnetite (Fe_3O_4) (Figure 2.7-6) (Oblonsky and Devine, 1997, Thierry et al , 1991, Hugot-LeGoff et al., 1986, Gardiner et al , 1987) The high sensitivity of the LABRAM system permits the use of a low-power (100-μW) excitation, which is needed to avoid heating the specimen and altering the oxidation states of the constituents present. When the magnetite was exposed instead to a 10-mW excitation power level, the resulting spectrum was characteristic of hematite (Fe_2O_3), and a micron-scale lesion appeared on the sample at the irradiated position The higher laser power altered the oxidation state of the iron in the sample

Figure 2.7-4. Raman spectrum of Fe_2O_3 pressed-powder disk, collected on a Dilor LABRAM spectrometer. The collection time was 120 s.

Figure 2.7-5. Raman spectrum of Fe_3O_4 pressed-powder disk, collected on a Dilor LABRAM spectrometer. The collection time was 120 s.

Figure 2.7-6. Raman spectrum of the mineral form of magnetite (Fe_3O_4) collected on a Dilor LABRAM spectrometer. The collection time was 120 s.

Using the same spectrometer, we have acquired Raman spectra from several of the corrosion test coupons The 1020 carbon-steel coupon from the Single Heater Test at Yucca Mountain had visible rust spots The Raman spectrum acquired above one of those spots (Figure 2 7-7) corresponds closely with previously reported Raman spectra for goethite (α–FeOOH) No such Raman spectrum is obtained from the same sample away from a rust spot (Figure 2 7-8)

Figure 2.7-7. Raman spectrum from a rust spot on the 1020 carbon-steel coupon described in the text. The spectrum is characteristic of α-FeOOH (goethite). The collection time was 120 s.

Figure 2.7-8. Raman spectrum away from any rust spots on the 1020 carbon-steel coupon described in the text. No spectrum was detected. The collection time was 120 s.

The presence of goethite on both of the carbon steel specimens was confirmed by XRD (Figure 2 7-9) In addition, the coupon of 1020 carbon steel from the field test showed peaks arising from magnetite and possibly maghemite (Figure 2 7-10). Furthermore, supporting evidence of the presence of goethite in the rust on that sample is found in the splitting of the oxygen 1s peak in XPS (Figure 2 7-11), which is specific to goethite among the various iron oxides (Brundle et al , 1977)

Figure 2.7-9. Theta/two-theta x-ray scan of the rust accumulation on the A516 sample from the humidity test described in the text. The spectrum indicates the presence of α - FeOOH (goethite).

Figure 2.7-10. Theta/two-theta x-ray scan of the rust accumulation on the 1020 carbon steel coupon from the field test, as described in the text. The spectrum indicates the presence of goethite, magnetite, and possibly maghemite.

Figure 2.7-11. Oxygen 1s photoemission spectrum acquired from a rust spot on the 1020 carbon steel coupon from the field test described in the text.

The C-22 specimens that had been submerged in the aqueous solution showed only traces of the C/Na/Cl deposit, instead, more than 80% of their surface areas were covered with an oxide film The oxide itself consisted of at least two distinct morphologies An interfacial layer was composed of round particles of diameter less than 50 nm, whereas the top surface was composed of a dense arrangement of blade-like particles, approximately 50 nm thick (Figures 2.7-12 and 2 7-13). X-ray chemical spectra of the oxide film indicate that that material is composed primarily of O, Fe, and W, with some Ni and Mo present, and the presence of W is reduced in the surrounding material (Figure 2.7-14)

Figure 2.7-12. SEM image at 15,000× showing the oxide formation on a coupon of C22 submerged in an acidic, aqueous solution, as described in the text.

Figure 2.7-13. SEM image at 60,000× showing the oxide formation on a coupon of C22 submerged in an acidic, aqueous solution, as described in the text.

Figure 2.7-14. (a) X-ray microanalysis of the bare metal surface exposed in Figure 2.7-13. (b) X-ray microanalysis of the bladed oxide in Figure 2.7-13.

Of the C-22 samples examined from the LTCTF, those that had been placed above the water line had at least half of their surfaces covered by a noncontinuous thin film, which, according to the x-ray microprobe measurement, consisted of C, Na, and Cl (Figures 2 7-15 and 2 7-17a) The film was found to exceed 5 microns in thickness The remainder of the surface was coated with a material suggestive of a thin oxide film (Figure 2 7-16) For reference, Figure 2 7-18 shows an x-ray microanalysis of a control coupon of C-22 that had not been exposed to the aqueous bath

Figure 2.7-15. SEM image at 500× showing the noncontinuous film formed on a coupon of C-22 above the water line in a bath containing an acidic, aqueous solution, as described in the text.

Figure 2.7-16. SEM image at 50,000× suggesting a thin oxide film formed on a coupon of C-22 above the water line in a bath containing an acidic, aqueous solution, as described in the text.

Figure 2.7-17. (a) X-ray microanalysis of the deposit shown in Figure 2.7-15. (b) X-ray microanalysis of the bare metal surface exposed in Figure 2.7-16.

Figure 2.7-18. X-ray microanalysis of a control coupon of C-22, which was not exposed to an aqueous bath.

The immense variety of possible corrosion products on the C-22 surfaces made it impractical to identify individual constituent species definitively with either XPS or XRD Preliminary experiments using Raman spectroscopy of submerged coupons yielded distinct spectra characteristic of either scale-covered or nonscale-covered regions. Spectra acquired over scale-free regions showed peaks at 241 and 302 cm^{-1}, whereas those acquired over the scale regions showed additional broad features at 706 and 880 cm^{-1}. Definitive identification of those peaks is complicated by the strongly anisotropic, blade-like structure of the scales Previous studies of the oxides of Mo and W have identified sharply distinct Raman spectra according to the alignment of similarly anisotropic crystallites with respect to the orientation of the electric field vector of the excitation Further work will be necessary to identify the corrosion products on this material definitively

2.7.4 Conclusions

Raman spectroscopy, with supporting data from XPS and XRD, have proven effective in identifying corrosion products produced in a variety of environments. Distinct iron oxides, which would yield similar XPS spectra, yield strongly distinct Raman spectra The presence

of goethite on carbon-steel test coupons from both the field test and the humidity test has been established with a combination of Raman spectroscopy, XPS, and XRD In addition, XRD suggests the presence of some magnetite on the coupon from the field test C-22 coupons submerged for a year in an aqueous solution with pH = 2.7 exhibited a delicate, blade-like oxide scale, with enhanced tungsten concentration with respect to the substrate Those coupons held above the water line in a bath containing the same aqueous solution exhibited a thicker, but heavily pitted and discontinuous, coating composed of C, Na, and Cl

2.7.5 Acknowledgments

The authors are grateful to C. Evans for XPS measurements, to J. Ferreira for SEM measurements, and to D Del Guidice for x-ray measurements

2.7.6 References

ASTM (1995) *Standard Reference Test Method for Making Potentiostatic and Potentiodynamic Anodic Polarization Measurements.* (ASTM Designation G5-94) Philadelphia, PA American Society for Testing and Materials (Book of Standards, Vol 3 01) [231902]

Baboian, R , and G S Haynes (1981) "Cyclic Polarization Measurements—Experimental Procedure and Evaluation of Test Data " F Mansfeld and U Bertocci, eds. *Electrochemical Corrosion Testing* pp. 274-282 Philadelphia American Society for Testing and Materials [231903]

Roy, A K , and R D McCright (1996) "Pitting Corrosion of Container Materials in Anticipated Repository Environments " *Proceedings of the Seventh International Conference on High-Level Radioactive Waste Management* La Grange Park, IL American Nuclear Society (Also UCRL-JC-122572, Livermore, CA Lawrence Livermore National Laboratory) [MOL 19960409 0153]

Roy, A K , D L Fleming, and S. R Gordon (1996) *Localized Corrosion of Container Materials in Anticipated Repository Environments* In proceedings from the *189th Meeting of The Electrochemical Society, Inc* , Los Angeles, CA, May 5–10, 1996 (Meeting Abstracts Vol 96-1, Abstract No 85, 112–113) (Also UCRL-JC-122861, Livermore, CA Lawrence Livermore National Laboratory) [MOL 19960708 0433]

Roy, A K , D L Fleming, and B Y Lum (1997a) *Effect of Environmental Variables on Localized Corrosion of High-Performance Container Materials.* In proceedings from the *5th International Conference on Nuclear Engineering,* Paper No ICONE5-2093, May 1997, Nice, France (Also UCRL-JC-125329, Livermore, CA. Lawrence Livermore National Laboratory) [MOL 19971217.0031]

Roy, A K., D L. Fleming, and B Y Lum (1997b). *Electrochemical and Metallographic Evaluation of Alloys C-22 and 625* (UCRL-ID-127355) Livermore, CA. Lawrence Livermore National Laboratory [MOL 19980211.0560]

Roy, A K., D. L. Fleming, and B. Y. Lum (1997c) *Initiation and Growth of Localized Attack in Nuclear Waste Package Materials.* In proceedings from the *6th International Conference on Nuclear Engineering,* Paper No. ICONE-6014, May 10–14, 1998, San Diego, CA (Also UCRL-JC-129068, Livermore, CA: Lawrence Livermore National Laboratory) [MOL 19980421.0093]

Roy, A K., D L Fleming, and B Y Lum (1997d). *Galvanic Corrosion Study of Container Materials Using Zero Resistance Ammeter* In proceedings from *Corrosion/98*, Paper No 98156, March 1998, San Diego, CA (Also UCRL-JC-128475, Livermore, CA Lawrence Livermore National Laboratory) [MOL 19980121 0137]

Roy, A K., D L Fleming, and B Y. Lum (1998) "Localized Corrosion Behavior of Candidate Nuclear Waste Package Container Materials " *Mater Perform* 37(3) 54–58

Roy, A K , G A Henshall, and R D. McCright (1995). *Electrochemical Corrosion Studies of Container Materials in Repository-Relevant Environments* (UCRL-ID-122860) Livermore, CA: Lawrence Livermore National Laboratory [MOL 19960626 0174]

2.8 Corrosion Model Development

Input for corrosion model development was compiled and written by Joseph Farmer.

2.8.1 Introduction

A key component of the Engineered Barrier System (EBS) being designed for containment of spent-fuel and high-level waste at the proposed geological repository at Yucca Mountain, Nevada is a two-layer canister In this particular design, candidate inner-barrier corrosion resistant materials (CRMs) are Alloy 825, 625, or C-22, candidate outer-barrier corrosion-allowance materials (CAMs), are A516 Gr 55 or Alloy 400 Alloy C-22 and A516 Gr 55 are the principal materials for the Viability Assessment (VA) design This section presents integrated, mechanistically based degradation models This work constitutes activities E-20-75 through E-20-86 in the metallic barriers Scientific Investigation Plan (SIP)

2.8.1.1 Environment and Modes of Degradation

Initially, the containers will be hot and dry because of the heat generated by radioactive decay However, the temperature will eventually drop to levels where both humid-air and aqueous-phase corrosion will be possible As the outer barrier is penetrated, corrosion of the underlying CRM will initiate, as shown in Figure 2 8-1 For Alloys 825, 625, and C-22, it is believed that a crevice will have to form before significant penetration of the CRM could occur The crevice creates a localized environment with suppressed pH and elevated chloride Jones and Wilde have prepared solutions of $FeCl_2$, $NiCl_2$, and $CrCl_3$ to simulate such localized environments and measured substantial pH suppression (Jones and Wilde, 1978) Wang has made similar measurements with $FeCl_3$ solutions, which are reported here As pointed out by McCoy, the measured pH in active, artificial crevices is 3 3 to 4 7 if the crevice is formed with carbon steel, 2 4 to 4 0 if the crevice is formed with a Fe-Cr alloy, and $\leq$ 2 3 if the crevice is formed with a stainless steel (Szjkarsja-Smialowska, 1986, pp 311–312) It must be noted that crevice corrosion of candidate CRMs has been well documented For example, Lillard and Scully have induced crevice corrosion in Alloy 625 during exposure to artificial sea water (Lillard and Scully, 1994), though others have observed no significant localized attack in less severe environments (Hack, 1983) Haynes International has published corrosion rates of Alloys 625 and C-22 in artificial crevice solutions (5–10 wt% $FeCl_3$) at various temperatures (25, 50, and 75°C) (Haynes International, Inc , 1987, Asphahani, 1980) In this case, the observed rates for Alloy C-22 appear to be due to passive dissolution It appears that Alloy C-22 must be at an electrochemical potential above the repassivation potential to initiate localized corrosion (LC)

Figure 2.8-1. Conceptual representation of corrosive attack of horizontal high-level waste container with outer barrier made of corrosion-allowance material (CAM) and inner wall made of corrosion resistant material (CRM).

2.8.1.2 Selection of Materials for Inner and Outer Barriers (CAM and CRM)

From the standpoint of corrosion engineering, the current container design has several desirable attributes. For example, the thick outer barrier (10 cm of A516 Gr 55) enables construction of a relatively low-cost, robust container that will provide substantial mechanical integrity during emplacement Furthermore, it will provide shielding, thereby reducing the effect of radiolysis products, such as H_2O_2, on the electrochemical corrosion

potential (E_{corr}) (Glass et al , 1986). After penetration of the CAM, it will suppress the electrochemical potential of the CRM at the point of penetration (crevice mouth). The relatively thin inner barrier (2 cm of Alloy C-22) then provides superior corrosion resistance Note that Ti-based alloys were considered for the inner barrier, but they are much more susceptible to hydrogen embrittlement (HE) Others have expressed concern that galvanic coupling of the inner barrier (CRM) to a less-noble outer barrier (CAM) could result in cathodic hydrogen charging of the CRM Alloys 825 and 625 are more prone to localized corrosion (LC) than Alloy C-22 (Haynes International, Inc , 1987, Asphahani, 1980) The unusual LC resistance of Alloy C-22 is believed to be due to the additions of both Mo and W, which stabilize the passive film at very low pH (Farmer, 1998b, Table 13). Consequently, this material exhibits a very high repassivation potential (E_{pass}), approaching the potential required for O_2 evolution (Gruss et al , 1998) Note that E_{pass} is accepted by most corrosion scientists as the threshold for LC initiation Furthermore, preliminary predictions made with a modified pit-stifling criterion predict that the maximum pit depth, Δx, is less than the wall thickness (2 cm) over the range of pH extending from –1 to 10 In experiments with simulated crevice solutions (10 wt% $FeCl_3$), very low (passive) corrosion rates are observed Finally, no attack of Alloy C-22 was observed in CAM–CRM crevices exposed to simulated acidified water (SAW) for one year These tests were conducted in the Long-Term Corrosion Test Facility (LTCTF) at Lawrence Livermore National Laboratory (LLNL)

2.8.1.3 Ceramic Coating for Outer Barrier

The CAM may be protected with a thermally sprayed, ceramic coating (Hopper, Farmer, and Wilfinger, 1998). Unlike metallic alloys, the ceramic coating is an oxidized material, thermodynamically stable against further oxidation Such materials exhibit very slow rates of dissolution, which was a primary consideration in the recent selection of a ceramic for immobilization of plutonium Porosities of less than 2% have been achieved with the high-velocity oxygenated fuel (HVOF) process Samples coated with Al_2O_3-TiO_2 have shown no corrosion at the ceramic–CAM interface after exposure to concentrated J-13 water at elevated temperature for six months It is assumed that the inhibition of corrosion is primarily due to the impedance of O_2 transport through the pores Liquid-filled pores provide greater impedance to O_2 transport than gas-filled pores. It may be possible to completely eliminate transport through the use of inorganic sealants These coatings have also proven to be mechanically robust Additional work on development of ceramic coatings is discussed in Section 3 of this report

2.8.1.4 Model Development

A variety of research at LLNL is being directed towards degradation of the CAM and CRM. Corrosion modeling for Total System Performance Assessment (TSPA) is a key component of this work Models include simple correlations of experimental data (Farmer, 1998a), as well as detailed mechanistic models necessary for believable long-term predictions (Farmer, 1997, Farmer and McCright, 1998). Several interactive modes of corrosion are shown by Figure 2.8-2 This publication describes (a) a corrosion-inhibition and spallation model to account for the effects of the ceramic coating on CAM life, (b) a crevice corrosion model based on mass transport and solution equilibria for prediction of pH suppression and Cl^- elevation in the crevice, (c) deterministic and probabilistic models for pit initiation, (d) deterministic models for pit growth and stifling, (e) a criterion for the initiation of stress corrosion cracking (SCC) at a pre-existing flaw such as a pit, and (f) a deterministic model for thermal embrittlement of the CAM based on the diffusion of phosphorous to grain boundaries

Confirmatory testing to support these mechanistic models, such as the development of in situ chemical sensors (pH microprobes), is also discussed

Figure 2.8-2. Conceptual representation of interactive modes of corrosion and degradation in CAM-CRM crevice.

2.8.1.5 Testing Program

Models are also supported by a variety of other corrosion tests For example, atmospheric corrosion is being investigated with humidity chambers, a thermogravimetric analyzer (TGA, quartz microbalance), and a variety of surface analytical probes Electrochemical testing includes both potentiostatic and cyclic polarization, as well as ac impedance spectroscopy Mechanical testing involves double-cantilever beam (DCB) experiments, slow-strain-rate testing (SSRT), and other techniques

The LTCTF appears to be the most complete source of corrosion data for Alloy C-22 in environments relevant to the proposed high-level waste repository at Yucca Mountain This facility is equipped with an array of cubic fiberglass tanks (4 × 4 × 4 ft) Each tank has a total volume of ~2000 L and is filled with ~1000 L of aqueous test solution The solution in a particular tank is controlled at either 60° or 90°C, purged with air flowing at approximately 150 cm^3/min, and agitated The test environments used in the LTCTF are referred to as simulated dilute well (SDW) water, simulated concentrated well (SCW) water, simulated acidified well (SAW) water, and simulated cement-modified water (SCMW) The descriptions and compositions of these solutions are summarized in Table 2 8-1 Four generic types of samples, U-bends, crevices, weight loss samples, and galvanic couples, are mounted on insulating racks and placed in tanks. Approximately half of the samples are submersed, half are in the saturated vapor above the aqueous phase, and a limited number at the water line It is important to note that condensed water can form on specimens located in the saturated vapor In regard to Alloys 516 Gr 55 [UNS K01800, 0 2C-0 5Mn-Fe(bal)] and C-22 [UNS N06022, 21Cr-13Mo-4Fe-3W-2Co-Ni(bal)], the rates of penetration observed in the LTCTF during the first six months of testing are included in the analyses presented here The loss in weight and change in dimension were measured with electronic instruments calibrated to traceable standards Because all data were digitally transferred to computer, the possibility of human key-punch error was minimized Thus far, more than 16,000 samples have been incorporated into tests Additional discussion of the LTCTF is found in Section 2 2 of this report

Table 2.8-1. Conditions in the long-term corrosion test facility at LLNL

Media	Temp. (°C)	pH	Ca^{2+} (ppm)	Mg^{2+} (ppm)	K^{+} (ppm)	Na^{+} (ppm)	Si (ppm)	SO_4^{2-} (ppm)	Cl^{-} (ppm)	NO_3^{-} (ppm)	F^{-} (ppm)	HCO_3^{-} (ppm)	Equiv. NaCl (ppm)
SDW	60	9 5	3 5	1 2	36	430	17	170	68	62	14	720	112
SDW	90	9 9	3 4	ND	38	460	16	180	74	64	15	700	122
SCW	60	9 2	16	29	4600	36000	18	13000	7400	7000	330	44000	12199
SCW	90	9 2	15	3 4	4500	44000	58	13000	7500	7200	1400	51000	12363
SAW	60	2 7	58	52	4300	43000	30	41000	28000	23000	0	0	46157
SAW	90	2 7	58	53	4300	43000	50	40000	27000	24000	0	0	44508
SCMW	60	7 8	400	4	85	10	10	1200	11	10	< 0 1	< 1	18

SDW: Simulated dilute well water (10 × J-13)
SCW Simulated concentrated well water (1000 × J-13)
SAW: Simulated acidified well water
SCMW Simulated cement-modified water

2.8.2 General Corrosion

2.8.2.1 Dry Oxidation of the Outer Barrier (CAM)

Degradation of the CAM is assumed to occur by abiotic processes that can be categorized as (a) dry oxidation, (b) humid-air corrosion, (c) aqueous-phase corrosion, (d) stress corrosion cracking, or (e) thermal embrittlement In the case of aqueous-phase corrosion, attack can be general or localized It is now assumed that general corrosion will occur below pH 10, whereas pitting is assumed to occur under more alkaline conditions Correlations of data from the LTCTF and TGA are being developed to predict rates of generalized corrosion in the simulated NFE (SDW, SCW, SAW, and SCMW) CAM corrosion is impeded by the presence of a thermally sprayed ceramic coating Ultimately, the impact of microbial influenced corrosion will also be quantified

The model favored for dry oxidation of the CAM (A516 Gr 55) was developed by Henshall (Henshall, 1996b) This model is represented by

$$x_{ox}(t)^2 = x_{ox}(t_0)^2 + 2k_p \int_{t_0}^{t} \exp[-Q/RT(t)]dt \quad , \qquad \text{(Eq. 2 8-1a)}$$

where

$$k_p = 4\,3 \times 10^{-5} \frac{cm^2}{s} \quad , \qquad \text{(Eq 2 8-1b)}$$

$$Q = 104 \frac{kJ}{mol} \quad , \qquad \text{(Eq 2.8-1c)}$$

and

$$R = 8\,314 \frac{\mathrm{J}}{\mathrm{mol}} \qquad \text{(Eq 2 8-1d)}$$

where x_{ox} is the oxide thickness, k_p is a rate constant, Q is the apparent activation energy, R is the universal gas constant, T is the absolute temperature, and t is time This expression predicts an oxide thickness of only 6 24 μm after 1000 years of dry oxidation at a fixed temperature of 150°C Refer to EMCR, Vol 3, Rev 1, Section 2 10 for a more complete discussion of the oxidation model

2.8.2.2 Corrosion of the Outer Barrier (CAM) in Aqueous and Vapor Phases

Data from the LTCTF is being used as the basis of empirical corrosion models for the aqueous and vapor phases The following linear equation has been used to correlate the penetration rate data for Alloy 516

$$\ln\left(\frac{\Delta p}{\Delta t}\right) = b_0 + b_1\left(\frac{1000}{T+273}\right) + b_2(\mathrm{pH}) + b_3(C_{\mathrm{NaCl}}) \quad , \qquad \text{(Eq 2 8-2a)}$$

where $\Delta p / \Delta t$ is the apparent penetration rate (μm/yr), T is the temperature (°C), and C_{NaCl} is the equivalent concentration of NaCl (wt%) (Farmer, 1998a) Note that the "equivalent NaCl concentration" is used as an independent variable in correlations This parameter is defined in terms of the concentration of free chloride, as follows

$$C_{\mathrm{NaCl}} = C_{\mathrm{Cl}^-}\left(1 + \frac{22\,98977}{35\,453}\right) \quad . \qquad \text{(Eq 2 8-2b)}$$

Alternatively, the concentration of free chloride can be used, adjusting the coefficient b_3 accordingly Within the bounds of experimental observations for Alloy 516, the coefficients are defined as given in Table 2 8-2 Six regression analyses were performed

- Case 1: all data correlated together
- Case 2 vapor phase, general corrosion from weight loss samples
- Case 3 aqueous phase, weight loss samples
- Case 4 vapor phase, crevice samples
- Case 5 aqueous phase, crevice samples
- Case 6 water line, general corrosion from weight loss samples

These data are illustrated graphically in Figure 2 8-3 The specific data used for Cases 2 through 6 are given in Tables 2 8-3 through 2 8-7, respectively. In Cases 1, 3, 5, and 6, which all pertain to aqueous phase exposures, the positive values of b_1 indicate that the penetration rates decrease with increasing temperature. This surprising result may be due to either salt deposition or decreased oxygen solubility. As will be seen in the subsequent section, the correlation for Alloy C-22 indicates that rates increase with temperature, as would normally be expected

Figure 2.8-3. General corrosion (penetration) rates of A516 Gr 55 after 6 months of exposure in the Long Term Corrosion Test Facility at LLNL. Data are for tests with simulated dilute well water (SDW), simulated concentrated well water (SCW), and simulated acidified well water. Samples were placed in the aqueous phase (AQ), the vapor phase (VP), and at the water line (WL). The maximum observed rate was about 300 μm/yr.

Table 2.8-2. Summary of regression analysis of data for Alloy 516.

Coefs.	Case 1 All data	Case 2 VP–WLS	Case 3 AP-WLS	Case 4 VP-CS	Case 5 AP-CS	Case 6 WL-WLS
b_0	290 25	–10 035	–47 709	–2 4360	–58 993	–91 805
b_1	3 7598	–0 46570	6 1826	–0 49354	7.8535	10 720
b_2	2 8092	1 5795	3 5555	0 83926	4 2052	6 8424
b_3	1 0682	1 8258	0 50585	1 2022	0 69899	1 6603
b_4	–324 34					
b_5	–323 50					
$s_{y/123...k}$	0 62425	0 071465	0 039343	0 057914	0 55798	0 031678
$r_{y/123...k}$	0 31931	0 90761	0 95062	0 86171	0 94379	0 98847

VP = vapor phase, AP = aquous phase, WL = water line
WLS = weight loss sample; CS = crevice sample

Table 2.8-3. Alloy 516, vapor phase, general corrosion (Case 2).

j	*y* predicted ln(*dp/dt*) ln(μm/yr)	*y* measured ln(*dp/dt*) ln(μm/yr)	x_1 1000/T $K^{-1} \times 10^3$	x_2 pH	x_3 C_{NaCl} wt%
1	3 5918	3 3206	3 0030	9 5	0 01122
2	3 5918	3 0735	3 0030	9 5	0 01122
3	3 5918	3 7363	3 0030	9 5	0 01122
4	3 5918	3 6678	3 0030	9 5	0 01122
5	3 5918	3 6138	3 0030	9 5	0 01122
6	3 5918	4 1361	3 0030	9 5	0 01122
7	4 3409	4 2603	2 7548	9 9	0 01220
8	4 3409	4 0908	2 7548	9 9	0 01220
9	4 3409	4 1575	2 7548	9 9	0 01220
10	4 3409	4 3361	2 7548	9 9	0 01220
11	4 3409	4 5501	2 7548	9 9	0 01220
12	4 3409	4 6533	2 7548	9 9	0 01220
13	5 3247	5 2926	3 0030	9 2	1 2199
14	5 3247	5 5792	3 0030	9 2	1 2199
15	5 3247	5 6870	3 0030	9 2	1 2199
16	5 3247	5 0902	3 0030	9 2	1 2199
17	5 3247	5 0400	3 0030	9 2	1 2199
18	5 3247	5 2625	3 0030	9.2	1 2199
19	5 4704	5 4882	2 7548	9 2	1 2363
20	5 4704	5 7735	2 7548	9 2	1 2363
21	5 4704	5 5528	2 7548	9 2	1 2363
22	5 4704	5 4728	2 7548	9 2	1 2363
23	5 4704	5 2742	2 7548	9 2	1 2363
24	5 4704	5 2576	2 7548	9 2	1 2363

Table 2.8-4. Alloy 516, aqueous phase, general corrosion (Case 3).

j	*y* predicted ln(*dp/dt*) ln(μm/yr)	*y* measured ln(*dp/dt*) ln(μm/yr)	x_1 1000/T $K^{-1} \times 10^3$	x_2 pH	x_3 C_{NaCl} wt%
1	4 6398	4 6152	3 0030	9 5	0 01122
2	4 6398	4 6861	3 0030	9 5	0 01122
3	4 6398	4 6571	3 0030	9 5	0 01122
4	4 6398	4 4790	3 0030	9 5	0 01122
5	4 6398	4 6245	3 0030	9 5	0 01122
6	4 6398	4 7700	3 0030	9 5	0 01122
7	4 5281	4 4932	2 7548	9 9	0 01220
8	4 5281	4 2327	2 7548	9 9	0 01220
9	4 5281	4 4310	2 7548	9 9	0 01220
10	4 5281	4 4733	2 7548	9 9	0 01220
11	4 5281	4 6771	2 7548	9 9	0 01220
12	4 5281	4 8677	2 7548	9 9	0 01220
13	4 1845	3 9999	3 0030	9 2	1 2199
14	4 1845	4 0067	3 0030	9 2	1 2199
15	4 1845	3 9170	3 0030	9 2	1 2199
16	4 1845	4 2281	3 0030	9 2	1 2199
17	4 1845	4 4451	3 0030	9 2	1 2199
18	4 1845	4 5169	3 0030	9 2	1 2199
19	2 6585	2 5505	2 7548	9 2	1 2363
20	2 6585	2 6304	2 7548	9 2	1 2363
21	2 6585	2 3905	2 7548	9 2	1 2363
22	2 6585	2 9485	2 7548	9 2	1 2363
23	2 6585	2 6396	2 7548	9 2	1 2363
24	2 6585	2 7850	2 7548	9 2	1 2363

Table 2.8-5. Alloy 516, vapor phase, crevice corrosion (Case 4).

j	*y* predicted ln(*dp/dt*) ln(μm/yr)	*y* measured ln(*dp/dt*) ln(μm/yr)	x_1 1000/T $K^{-1} \times 10^3$	x_2 pH	x_3 C_{NaCl} wt%
1	4 0684	4 1469	3 0030	9 5	0 01122
2	4 0684	3 9717	3 0030	9 5	0 01122
3	4 0684	3 9004	3 0030	9 5	0 01122
4	4 0684	3 9774	3 0030	9 5	0 01122
5	4 0684	4 1371	3 0030	9 5	0 01122
6	4 0684	4 2759	3 0030	9 5	0 01122
7	4 5278	4 9072	2 7548	9 9	0 01220
8	4 5278	4 8682	2 7548	9 9	0 01220
9	4 5278	4 5015	2 7548	9 9	0 01220
10	4 5278	4 1585	2 7548	9 9	0 01220
11	4 5278	4 1705	2 7548	9 9	0 01220
12	4 5278	4 5618	2 7548	9 9	0 01220
13	5 2696	4 8111	3 0030	9 2	1 2199
14	5 2696	5 1110	3 0030	9 2	1 2199
15	5 2696	5 3542	3 0030	9 2	1 2199
16	5 2696	5 3397	3 0030	9 2	1 2199
17	5 2696	5 4520	3 0030	9 2	1 2199
18	5 2696	5 5509	3 0030	9 2	1 2199
19	5 4119	5 2229	2 7548	9 2	1 2363
20	5 4119	5 4306	2 7548	9 2	1 2363
21	5 4119	5 4295	2 7548	9 2	1 2363
22	5 4119	5 6223	2 7548	9 2	1 2363
23	5 4119	5 1697	2 7548	9 2	1 2363
24	5 4119	5 5952	2 7548	9 2	1 2363

Table 2.8-6. Alloy 516, aqueous phase, crevice corrosion (Case 5).

j	*y* predicted ln(*dp/dt*) ln(μm/yr)	*y* measured ln(*dp/dt*) ln(μm/yr)	x_1 1000/T $K^{-1} \times 10^3$	x_2 pH	x_3 C_{NaCl} wt%
1	4 5482	4 4751	3 0030	9 5	0 01122
2	4 5482	4 4806	3 0030	9 5	0 01122
3	4 5482	4 3657	3 0030	9 5	0 01122
4	4 5482	4 7226	3 0030	9 5	0 01122
5	4 5482	4 6365	3 0030	9 5	0 01122
6	4 5482	4 6025	3 0030	9 5	0 01122
7	4 2818	4 3433	2 7548	9 9	0 01220
8	4 2818	4 2549	2 7548	9 9	0 01220
9	4 2818	4 3080	2 7548	9 9	0 01220
10	4 2818	5 1953	2 7548	9 9	0 01220
11	4 2818	4 0618	2 7548	9 9	0 01220
12	4 2818	4 0618	2 7548	9 9	0 01220
13	4 2818	4 0618	2 7548	9 9	0 01220
14	4 2818	4 0618	2 7548	9 9	0 01220
15	4 2818	4 1937	2 7548	9 9	0 01220
16	4 1314	4 1773	3 0030	9 2	1 2199
17	4 1314	4 1793	3 0030	9 2	1 2199
18	4 1314	4 1434	3 0030	9 2	1 2199
19	4 1314	4 0610	3 0030	9 2	1 2199
20	4 1314	4 0971	3 0030	9 2	1 2199
21	4 1314	4 1354	3 0030	9 2	1 2199
22	2 1938	2 5044	2 7548	9 2	1 2363
23	2 1938	2 0852	2 7548	9 2	1 2363
24	2 1938	2 1587	2 7548	9 2	1 2363
25	2 1938	2 0001	2 7548	9 2	1 2363
26	2 1938	2 2103	2 7548	9 2	1 2363
27	2 1938	2 1995	2 7548	9 2	1 2363

Table 2.8-7. Alloy 516, water line, general corrosion (Case 6).

j	*y* predicted ln(*dp/dt*) ln(μm/yr)	*y* measured ln(*dp/dt*) ln(μm/yr)	x_1 1000/T $K^{-1} \times 10^3$	x_2 pH	x_3 C_{NaCl} wt%
1	5 4101	5 3912	3 0030	9 5	0 01122
2	5 4101	5 4296	3 0030	9 5	0 01122
3	5 4881	5 3679	2 7548	9 9	0 01220
4	5 4881	5 6077	2 7548	9 9	0 01220
5	5 3642	5 2877	3 0030	9 2	1 2199
6	5 3642	5 4398	3 0030	9 2	1 2199
7	2 7309	2 9382	2 7548	9 2	1 2363
8	2 7309	2 5243	2 7548	9 2	1 2363

2.8.2.3 Delay Mechanisms for Corrosion of the Outer Barrier (CAM)

Engineers are exploring several mechanisms to delay corrosive attack of the CAM by dripping water, including drip shields and ceramic coatings Ceramic coatings deposited with HVOF have exhibited a porosity of only 2% at a thickness of 0 15 cm A model has been developed to account for the inhibition of corrosion by these coatings It is assumed that the overall mass-transfer resistance governing the corrosion rate is due to the combined resistances of ceramic coating and interfacial corrosion products Two porosity models (simple cylinder and cylinder–sphere chain) are considered in estimation of the mass-transfer resistance of the ceramic coating It is evident that a substantial impedance to O_2 transport is encountered if pores are filled with liquid water It may be possible to use sealants to eliminate porosity Spallation (rupture) of the ceramic coating is assumed to occur if the strain introduced by corrosion products at the ceramic–CAM interface exceeds fracture strain of the coating (Hopper, Farmer, and Wilfinger, 1998)

During the initial period of dry oxidation, any porosity in the ceramic coating is assumed to be filled with gas If the porosity is interconnected, the impedance to O_2 transport and oxidation is believed to be relatively insignificant In such a case, a good approximation is to simply apply the dry oxidation rate provided by Henshall (Henshall, 1996b) The impact of dry oxidation underneath the porous ceramic is believed to be relatively insignficant based on preliminary calculations

During the period of humid-air corrosion (HAC), pores may be filled with either gas or liquid If porosity is interconnected and gas-filled, the ceramic coating may not significantly impede the rate of HAC. However, the Kelvin effect can lead to condensation in very small pores For example, at 100°C and 99% *RH*, 0 07-μm pores would be expected to be liquid filled. In such a case, the impedance to O_2 transport and corrosion should be similar to that for aqueous-phase corrosion (APC) Additional work on HAC studies is described in Section 2 1 of this report

During the APC regime (RH ≥ 80% and dripping conditions), pores are expected to be completely filled with water It is assumed that typical aqueous-phase corrosion rates apply at the ceramic–CAM interface (Hopper, Farmer, and Wilfinger, 1998) Development of an appropriate model begins with consideration of the flux of oxygen N_A through multiple diffusion barriers, represented by subscripts P and Q (phases P and Q)

$$N_A = k_p(a_{PB} - a_{Pi}) = k_Q(a_{Qi} - a_{QB}) = K_A(a_{PB} - a_{QB}) \qquad \text{(Eq 2 8-3)}$$

The overall mass-transfer coefficient (mass-transfer resistance) can be expressed in terms of the individual mass-transfer coefficients for phases P and Q (Sherwood, Pigford, and Wilke, 1975, pp 117–182)

$$\frac{1}{K_A} = \frac{1}{k_p} + \frac{1}{k_Q} \quad . \qquad \text{(Eq 2 8-4)}$$

Pores are treated as long cylinders of length δ.

$$N_A = \frac{D_A}{\delta}(a_{PB} - a_{Pi}) \quad . \qquad \text{(Eq 2 8-5a)}$$

The average flux of oxygen per unit area of waste package is then

$$\overline{N_A} = \frac{\theta}{\delta} D_A(a_{PB} - a_{Pi}) \quad , \qquad \text{(Eq 2 8-5b)}$$

where θ is the fraction of the CAM exposed to the aqueous phase at the ceramic–CAM interface This can be interpreted as porosity Values of 0 02–0 03 have been routinely achieved with HVOF The overall mass-transfer coefficient is then

$$\frac{1}{K} = \frac{1}{k_0} + \frac{1}{k_I} = \frac{1}{k_0} + \frac{\delta}{\theta D_A} \quad , \qquad \text{(Eq 2 8-6a)}$$

where

$$K = \frac{1}{\frac{1}{k_0} + \frac{\delta}{\theta D_A}} \qquad \text{(Eq 2 8-6b)}$$

The factor used to correct the oxygen-limited corrosion rate for the presence of a porous ceramic barrier is then

$$g = \frac{\overline{N_A}}{\overline{N_{A,0}}} = \frac{\frac{1}{k_0}}{\frac{1}{k_0} + \frac{\delta}{\theta D_A}} = \frac{1}{1 + \frac{k_0 \delta}{\theta D_A}} \qquad \text{(Eq. 2 8-7a)}$$

This correction factor assumes simple cylindrical pores, which may be unrealistic It is believed that the pores in ceramic coatings can be better represented by an array of chains, each link composed of a hollow sphere and a relatively narrow hollow cylinder connected in series In such a case, the analysis of porosity described by Hopper should be used (R. Hopper, Ceramic Barrier Performance Model, Version 1.0, Description of Initial PA Input, Memorandum, Lawrence Livermore National Laboratory, Livermore, CA, March 30, 1998) Specifically, the mass-transfer coefficient for the ceramic coating, k_t, should be reduced by a factor $f(\varepsilon,\lambda)$

$$k_{I,corrected} = f(\varepsilon,\lambda) \times k_I \quad , \qquad \text{(Eq 2 8-9a)}$$

where f(ε,λ) is defined as

$$f(\varepsilon,\lambda) = \frac{3}{2}\frac{(1+\lambda)^2}{\lambda}\varepsilon^2 \qquad \text{(Eq 2 8-9b)}$$

Here, the dimensionless parameters ε and λ represent the geometry of the sphere–cylinder chain

$$\varepsilon = \frac{\text{diameter of cylinder in chain}}{\text{diameter of sphere in chain}} \quad , \qquad \text{(Eq 2 8-9c)}$$

and

$$\lambda = \frac{\text{length of cylinder in chain}}{\text{diameter of sphere in chain}} \qquad \text{(Eq 2 8-9d)}$$

Hopper has concluded that reasonable estimates for ε range from 0 01 to 0 05, depending on the actual microstructure. Similarly, he has concluded that reasonable estimates of λ range from 5 to 10 Therefore, the $f(\varepsilon,\lambda)$ is estimated to be somwhere between 0 016 and 0 045 As an average for now, we estimate $f(\varepsilon,\lambda)$ to be approximately 0 03, which is mid-range Given this model for the interconnected porosity in a ceramic coating, the modified factor used to correct the oxygen-limited corrosion rate for the presence of a porous ceramic barrier is then

$$g_{corrected} = \frac{1}{1+\left(\frac{k_0\delta}{\theta D_A}\right)\left(\frac{1}{f(\varepsilon,\lambda)}\right)} \qquad \text{(Eq. 2 8-9e)}$$

The following stoichiometry is assumed to exist between iron and oxygen

$$4Fe + 3O_2 \longrightarrow 2Fe_2O_3 \qquad \text{(Eq 2 8-10)}$$

The relation between the oxygen flux in a single pore, N_A, and the corrosion rate dp/dt can be written as

$$3N_{A,0} = 3k_0\left(C_{oxygen}\right) = 4\frac{\rho}{w}\frac{dp}{dt} \quad , \qquad \text{(Eq 2 8-11a)}$$

where the atomic weight (w) is 55 847 g/mol and the density of iron (ρ) is 7.86 g/cm^3. A conservative value of the aqueous-phase corrosion rate is assumed as a basis for calculating the apparent mass-transfer coefficient representing corrosion in the absence of a porous ceramic barrier

$$\frac{dp}{dt} \approx 300\frac{\mu m}{y} = 9\,513 \times 10^{-10}\frac{cm}{s} \qquad \text{(Eq. 2 8-11b)}$$

This corrosion rate is a conservative estimate based on 6-month data from the LTCTF, which is illustrated in Figure 2 8-3 (Farmer, 1998a) The concentration of oxygen dissolved in water (equilibrium with ambient air) at the air–ceramic interface is

$$C_{oxygen} = 2\,56 \times 10^{-7}\ \frac{mol}{cm^3} \qquad \text{(Eq. 2 8-11c)}$$

This solubility value was provided by Andresen and can be found in Farmer's input to the Expert Elicitation Panel (Farmer, 1998b, Table 13) The solubility of oxygen is diminished by the addition of salt

The flux of oxygen associated with this mass-transfer coefficient is

$$N_{A,0} = \left(\frac{4}{3}\right)\frac{7\,86 \times 9\,513 \times 10^{-10}}{55\,847}\ \frac{mol}{cm^2 s} = 1\,790 \times 10^{-10}\ \frac{mol}{cm^2 s} \qquad \text{(Eq. 2 8-11d)}$$

The mass-transfer coefficient in the absence of a ceramic barrier is then estimated as

$$k_0 = \frac{1}{C_{oxygen}}\left(\frac{4}{3}\right)\frac{\rho}{w}\frac{dp}{dt}\ , \qquad \text{(Eq 2 8-11e)}$$

or

$$k_0 = \frac{1\,785 \times 10^{-10}\ \frac{mol}{cm^2 s}}{2\,56 \times 10^{-7}\ \frac{mol}{cm^3}} = 6\,973 \times 10^{-4}\ \frac{cm}{s} \qquad \text{(Eq 2 8-11f)}$$

The factor needed for correction of the corrosion rate for the presence of a porous ceramic coating is then

$$g_{corrected} = \frac{0.02 \times 0.03 \times 10^{-5}\ \frac{cm^2}{s}}{\left(0\,02 \times 0\,03 \times 10^{-5}\ \frac{cm^2}{s}\right) + \left(0.15\ cm \times 6\,973 \times 10^{-14}\ \frac{cm^2}{s}\right)} = 5\,736 \times 10^{-5} \qquad \text{(Eq 2 8-12a)}$$

Therefore, the porous ceramic coating would lower the aqueous-phase corrosion rate from approximately 300 μm/yr to only 1.721×10^{-2} μm/yr

$$\frac{dp}{dt} = g_{corrected}\left(\frac{dp}{dt}\right)_0 = 1.721 \times 10^{-2}\ \frac{\mu m}{yr}\ . \qquad \text{(Eq 2 8-12b)}$$

An estimate of the time to fracture due to the formation of corrosion products at the ceramic–CAM interface can be estimated, provided that the mechanical properties of the ceramic are known Estimated properties for the ceramic coating are taken from a text on engineering materials and are summarized in Table 2 8-8 (Thornton and Colangelo, 1985) The range of fracture toughness values given for typical ceramics is given as

$$K_{IC} = 3.3 \text{ to } 5.8 \text{ MPa}\sqrt{\text{m}} = 3\,0 \text{ to } 5\,3 \text{ ksi}\sqrt{\text{in}} \qquad \text{(Eq 2 8-13)}$$

Table 2.8-8. Mechanical properties of ceramic coatings.

Property Units	Elastic modulus (E) MPa	Elastic modulus (E) Mpsi	Fracture strength (σ^*) Mpa	Fracture strength (σ^*) ksi
Al_2O_3	365,000	53	172	25
ZrO_2	144,900	21	55	8

Whereas these properties serve as a good starting place for TSPA-VA, handbook values for mechanical properties of ceramics will probably need to be revised to better reflect those of actual coatings Direct measurement of the elastic modulus is required

The rate of expansion of the inner radius of the ceramic barrier coating is estimated from the penetration rate, accounting for the expansion at the interface due to the density difference between Fe_2O_3 and Fe

$$\frac{dR}{dt} = 2\frac{dp}{dt} = 2 \times 1\,721 \times 10^{-2}\,\frac{\mu\text{m}}{\text{yr}} = 3\,442 \times 10^{-8}\,\frac{\text{m}}{\text{yr}} \qquad \text{(Eq 2 8-14a)}$$

If the inner radius of the ceramic coating (outer radius of the CAM) is assumed to be approximately 1 meter ($R \approx 1$ m), the strain rate in the coating can be estimated with

$$\frac{de}{dt} = \frac{1}{2\pi R} 2\pi \frac{dR}{dt} = 3\,442 \times 10^{-8}\,\frac{1}{\text{yr}} \qquad \text{(Eq 2 8-14b)}$$

The stress and strain are related through the elastic modulus

$$\sigma = E \times e \qquad \text{(Eq 2 8-14c)}$$

The fracture strain can then be estimated from the elastic modulus and the fracture stress

$$e^* = \frac{\sigma^*}{E} = \frac{172 \text{ MPa}}{356{,}000 \text{ MPa}} = 4\,831 \times 10^{-4} \qquad \text{(Eq 2 8-14d)}$$

The time required for the strain to reach the fracture strain determines the time to fracture This is the time required for formation of the first crack in the ceramic coating, but does not necessarily imply failure of the coating

$$\tau^* = \frac{e^*}{de/dt} = \frac{4\,831 \times 10^{-4}}{3.442 \times 10^{-8}} \text{ y} = 14{,}037 \text{ yr} \qquad \text{(Eq. 2 8-15)}$$

The critical flaw size for crack initiation in the ceramic coating is estimated with

$$a^* \approx \left(\frac{K_{IC}}{\sigma^*}\right)^2 \frac{1}{\pi} = \left(\frac{3\,3 \text{ MPa}\sqrt{m}}{172 \text{ MPa}}\right)^2 \frac{1}{\pi} = 1\,172 \times 10^{-4} \text{m} = 117\,2\,\mu\text{m} \quad , \qquad \text{(Eq. 2 8-16a)}$$

where the fracture toughness is defined by

$$K_{IC} = \sigma\sqrt{\pi a} f(a,W) \qquad \text{(Eq 2 8-16b)}$$

In addition to the contiguous coating assumed in the previous paragraphs, a variation of the model has been developed for TSPA-VA This variation assumes that the ceramic coating spalls due to the formation of blisters, as shown in Figure 2 8-4 Each blister is assumed to have a radius that is equivalent to the patch size assumed in the WAPDEG TSPA code The volume of corrosion product (Fe_2O_3) in the blister is defined as

$$V_{\text{blister}} = \frac{4}{3}\pi a^2 b \quad , \qquad \text{(Eq 2 8-17)}$$

where a and b define the dimensions of the oblate spheriod After significant growth of the blister, the surface area of the blister is

$$A_{\text{blister}} = \frac{1}{2}\left[2\pi a^2 + \frac{\pi b^2}{\gamma}\ln\left(\frac{1+\gamma}{1-\gamma}\right)\right] \quad t > 0 \quad , \qquad \text{(Eq 2 8-18a)}$$

where the parameter g is defined as

$$\gamma = \frac{\sqrt{a^2 - b^2}}{a} \qquad \text{(Eq 2 8-18b)}$$

Figure 2.8-4. Conceptual representation of degradation-mode model for ceramic coating.

In contrast, the area of the blister is essentially that of a flat disk at time zero

$$A_{\text{blister}} = \pi a^2 \quad t = 0 \qquad \text{(Eq 2 8-18c)}$$

The strain in the ceramic coating covering the blister is then defined in terms of the exposed area of the blister after interfacial corrosion ($t > 0$) relative to the initial area ($t = 0$)

$$e = \frac{A_{\text{blister}}(t>0)}{A_{\text{blister}}(t=0)} - 1 \qquad \text{(Eq 2 8-19a)}$$

The strain can be rewritten in terms of the blister dimensions

$$e = \left(\frac{b}{a}\right)^2\left(\frac{1}{2\gamma}\right)\ln\left(\frac{1+\gamma}{1-\gamma}\right) \qquad \text{(Eq 2 8-19b)}$$

The criterion for fracture (spallation) of the blister is then

$$e > e^* \approx 4\,831\times10^{-4} \quad , \qquad \text{(Eq. 2 8-19c)}$$

where e^* is the fracture strain of the ceramic The relation between the volume of corrosion product (blister) and the volume of oxidized iron is

$$V_{\text{blister}} = 3\,6055 \times V_{\text{iron}} \qquad \text{(Eq 2 8-20a)}$$

This equation can be used to express the height of the blister in terms of the volume of oxidized CAM, which is assumed to be essentially iron

$$b = \frac{3}{4}\left(\frac{3\,6055 \times V_{\text{iron}}}{\pi a^2}\right) \qquad \text{(Eq 2 8-20b)}$$

The volume of oxidized CAM is time dependent and calculated from the corrosion rate at the ceramic–CAM interface during three successive phases of corrosion dry oxidation, humid-air corrosion, and aqueous-phase corrosion This is an approximation, assuming growth of a cylindrical volume of oxide beneath a flat, circular disk The flux of oxygen driving the formation of corrosion product is assumed to be through the circular-shaped disk of oxide

$$V_{\text{iron}} \approx \pi a^2 \left[\int_0^{c_{\text{dry}}} g_{\text{dry}} \left(\frac{dp}{dt}\right)_{\text{dry}} dt + \int_{c_{\text{dry}}}^{c_{\text{HAC}}} g_{\text{HAC}} \left(\frac{dp}{dt}\right)_{\text{HAC}} dt + \int_{c_{\text{HAC}}}^{c_{\text{APC}}} g_{\text{APC}} \left(\frac{dp}{dt}\right)_{\text{APC}} dt \right] \qquad \text{(Eq 2 8-20c)}$$

Given these assumptions and the above equation, the time-dependent height of the blister can be calculated with

$$b \approx 2\,7041 \left[\int_0^{c_{\text{dry}}} g_{\text{dry}} \left(\frac{dp}{dt}\right)_{\text{dry}} dt + \int_{c_{\text{dry}}}^{c_{\text{HAC}}} g_{\text{HAC}} \left(\frac{dp}{dt}\right)_{\text{HAC}} dt + \int_{c_{\text{HAC}}}^{c_{\text{APC}}} g_{\text{APC}} \left(\frac{dp}{dt}\right)_{\text{APC}} dt \right] \qquad \text{(Eq 2 8-20d)}$$

This alternative model for impedance and spallation has been used to provide what appears to be reasonable estimates

From preliminary calculations based upon Eqs (2 8-3) through (2 8-16), it is believed that the existence of a slightly porous ceramic coating on the surface could significantly lengthen the life of the container, adding an estimated 14,037 years to the life of the waste package (Table 2 8-9) It should be possible to further increase life by taking steps to close interconnected porosity in the coating For example, Zn or Al could be deposited on the outer surface of the ceramic, as well as inside near-surface pores These deposits would oxidize in air, thereby sealing porosity with the corresponding metal oxides Both Zn and Al are attractive candidates for sealing porosity because unoxidized metal would be sacrificial to the A516 Gr 55 in galvanic couples. Other possible sealants have also been identified The modified *g*-factor presented here can be used as a practical means to adjust CAM corrosion rates to account for the ceramic coating.

Table 2.8-9. Extension of WP life with ceramic coating.

	Life with ceramic coating (*y*)	Life without ceramic coating (*y*)
Thermal pulse	~ 1000	~ 1000
Ceramic barrier	> 14,037	~ 0
CAM after exfoliation	> 333	> 333

Work is in progress at LLNL to verify the corrected g-factor through application of ac impedance spectroscopy A PAR Model 273 with a PAR Model 5610 dual-channel, lock-in amplifier is now being used to determine the complex impedance of the electrolyte-filled ceramic barrier over the frequency range extending from 0 001 to 100,000 Hz Preliminary data indicate that a ceramic coating with 1 to 2% porosity can increase the interfacial electrical impedance by approximately eight orders of magnitude (10^8) With a well planned experiment and proper interpretation of the data, insight into transport in the pores should be possible It should also be possible to develop some understanding of the layer of corrosion products at the base of the pores Note that dc measurements have also been done

2.8.2.4 Passive Corrosion of the Inner Barrier (CRM)

The modes of corrosion that are believed to be relevant to the ultimate failure of the CRM include passive corrosion, crevice corrosion, pitting, and stress corrosion cracking Passive corrosion of the CRM is expected to occur on surfaces where the CAM has exfoliated, as well as on surfaces that lie inside the CAM–CRM crevice, provided that environmental conditions (pH, chloride, potential, and temperature) are below the thresholds for localized attack A correlation of Alloy C-22 passive corrosion rates with temperature, pH, equivalent NaCl concentration, and $FeCl_3$ concentration has been developed (Farmer, 1998a) The rates used as a basis of this correlation are from the LTCTF, Roy's electrochemical measurements (Roy, Fleming, and Lum, 1997b, 1996, 1997a), and Haynes International (Haynes International, Inc , 1987, Asphahani, 1980) These data are summarized in Tables 2 8-10 and 2 8-11, and illustrated in Figure 2 8-5 The following linear equation was found to be adequate for the correlation

$$\ln\left(\frac{\Delta p}{\Delta t}\right) = b_0 + b_1\left(\frac{1000}{T+273}\right) + b_2(\mathrm{pH}) + b_3\left(C_{\mathrm{NaCl}}\right) + b_4\left(C_{\mathrm{FeCl_3}}\right) \quad , \qquad \text{(Eq 2 8-21a)}$$

where $\Delta p/\Delta t$ is the apparent penetration rate (μm/yr), T is the temperature (°C), C_{NaCl} is the equivalent concentration of NaCl (wt%), and C_{FeCl3} is the concentration of $FeCl_3$ (wt%) Within the bounds of 38 experimental observations for Alloy C-22, the coefficients were determined to be

$$\begin{aligned} b_0 &= +13\,409\,, \\ b_1 &= -5\,5587\,, \\ b_2 &= -0\,87409\,, \\ b_3 &= +0\,56965\,, \\ &\text{and} \\ b_4 &= +0.60801\quad . \end{aligned} \qquad \text{(Eq 2 8-21b-f)}$$

Figure 2.8-5. Passive corrosion (penetration) rates of Alloy C-22 after 6 months of exposure in the Long Term Corrosion Test Facility at LLNL. These data are for simulated acidified well water (SAW). Samples were placed in the aqueous phase (AQ), the vapor phase (VP), and at the water line (WL). Rates were less than 1 μm/yr.

Table 2.8-10. Passive corrosion rate data for Alloy C-22: basis of regression, LTCTF.

	Comments	Exposure (hours)	*dp/dt* (μm/yr)	Temp (°C)	pH (none)	NaCl (wt%)	$FeCl_3$ (wt%)	Air Sat.
1	Long-term test SAW	4296	2.53×10^{-2}	60	2.7	4.616	0	1
2	Long-term test SAW	4296	5.07×10^{-2}	60	2.7	4.616	0	1
3	Long-term test SAW	4296	1.13×10^{-1}	60	2.7	4.616	0	1
4	Long-term test SAW	4296	1.64×10^{-1}	60	2.7	4.616	0	1
5	Long-term test SAW	4296	6.03×10^{-2}	60	2.7	4.616	0	1
6	Long-term test SAW	4296	3.45×10^{-2}	60	2.7	4.616	0	1
7	Long-term test SAW	4296	3.47×10^{-2}	60	2.7	4.616	0	1
15	Long-term test SAW	4296	8.58×10^{-2}	60	2.7	4.616	0	1
16	Long-term test SAW	4296	1.13×10^{-1}	60	2.7	4.616	0	1
17	Long-term test SAW	4296	7.70×10^{-2}	60	2.7	4.616	0	1
18	Long-term test SAW	4296	2.81×10^{-2}	60	2.7	4.616	0	1
19	Long-term test SAW	4296	1.87×10^{-2}	60	2.7	4.616	0	1
20	Long-term test SAW	4296	9.31×10^{-3}	60	2.7	4.616	0	1
21	Long-term test SAW	4296	1.04×10^{-1}	60	2.7	4.616	0	1
22	Long-term test SAW	4296	8.11×10^{-2}	60	2.7	4.616	0	1
23	Long-term test SAW	4296	1.17×10^{-1}	60	2.7	4.616	0	1
24	Long-term test SAW	4296	6.56×10^{-2}	60	2.7	4.616	0	1
25	Long-term test SAW	4296	6.61×10^{-2}	60	2.7	4.616	0	1
26	Long-term test SAW	4296	4.71×10^{-2}	60	2.7	4.616	0	1
27	Long-term test SAW	4344	2.45×10^{-1}	90	2.7	4.616	0	1
28	Long-term test SAW	4344	7.31×10^{-1}	90	2.7	4.616	0	1
29	Long-term test SAW	4344	1.76×10^{-1}	90	2.7	4.616	0	1
30	Long-term test SAW	4344	4.16×10^{-2}	90	2.7	4.616	0	1
31	Long-term test SAW	4344	1.07×10^{-1}	90	2.7	4.616	0	1

Table 2.8-11. Passive corrosion rate data for Alloy C-22: basis of regression, LTCTF.

	Comments	Exposure (hours)	*dp/dt* (μm/yr)	Temp. (°C)	pH (none)	NaCl (wt%)	$FeCl_3$ (wt%)	Air Sat.
8	Cyclic polarization - NaCl	~1	$3\,00 \times 10^{-4}$	60	2 69	1	0	1
9	Cyclic polarization - NaCl	~1	$3\,00 \times 10^{-3}$	60	6 53	5	0	1
10	Cyclic polarization - NaCl	~1	$2\,01 \times 10^{-2}$	90	6 53	5	0	1
11	Cyclic polarization - NaCl	~1	$3\,02 \times 10^{-2}$	90	6 83	10	0	1
12	Cyclic polarization - NaCl	~1	$2\,01 \times 10^{-1}$	90	2 69	1	0	0
13	Cyclic polarization - NaCl	~1	$2\,01 \times 10^{-1}$	90	2 67	1	0	0
14	Cyclic polarization - NaCl	~1	$2\,01 \times 10^{-1}$	90	2 69	5	0	0
32	Cyclic polarization - $FeCl_3$	~1	$3\,00 \times 10^{-3}$	90	2 14	0	0 61	0
33	Cyclic polarization - $FeCl_3$	~1	$6\,00 \times 10^{-3}$	90	2 16	0	0 61	0
34	Cyclic polarization - $FeCl_3$	~1	$2\,01 \times 10^{-1}$	90	1 72	0	3 05	0
35	Cyclic polarization - $FeCl_3$	~1	2 01	90	1 72	0	3 05	0
36	Haynes - $FeCl_3$	100	2 50	25	0 7	0	10	1
37	Haynes - $FeCl_3$	100	2 50	50	0 7	0	10	1
38	Haynes - $FeCl_3$	100	12 7	75	0 7	0	10	1

More specifically, the correlation for Alloy C-22 is

$$\ln\left(\frac{\Delta p}{\Delta t}\right) = 13\,409 - \left(\frac{5558\,7}{T+273}\right) - 0\,87409(\mathrm{pH}) + 0\,56965(C_{\mathrm{NaCl}}) + 0\,60801(C_{\mathrm{FeCl_3}}) \qquad \text{(Eq 2 8-21g)}$$

Based on this correlation, it is concluded that the apparent activation energy is approximately 12 kcal/mol, which is quite reasonable The "standard error of estimate" ($s_{y/1234}$) and the "sample multiple variable regression coefficient" ($r_{y/1234}$) are defined by Crow, Davis and Maxfield (Crow, Davis, and Maxfield, 1960, pp 147–149). The standard error of estimate is a measure of the scatter of the observed penetration rates about the regression plane About 95% of the points in a large sample are expected to lie within $\pm 2s_{y/123\ k}$ of the plane, measured in the y direction Values for the above correlation are

$$s_{y/1234} = 1\,5092\,,$$

and (Eq 2.8-23a-b)

$$r_{y/1234} = 0\,65628$$

The multiple variable regression coefficient indicates a reasonably good fit to the data set, given the large number of independent variables As discussed in the literature, uncertainty in a given model parameter, β_j, can be determined from the standard error of estimate, as shown by Eqs (23a) and (23b) (Crow, Davis, and Maxfield, 1960, pp. 147–149)

$$s_{b_j} = s_{y/123\ \ k}\sqrt{ne_{jj}} \qquad \text{(Eq. 2 8-23a)}$$

$$\beta_j = b_j \pm \left(t_{a/2,n-k-1}\right) \times s_{b_j} \qquad \text{(Eq 2 8-23b)}$$

This simple correlation has been tested within the bounds of anticipated conditions The predictions appear to be reasonable for combinations of input parameters representative of the NFE, simulated dilute well (SDW), simulated concentrated well (SCW), and simulated acidified well (SAW) waters, simulated cement-modified water (SCMW), the unusually harsh, simulated crevice corrosion test of Haynes International (10 wt% $FeCl_3$) (Haynes International, Inc , 1987, Asphahani, 1980), and the conditions predicted during preliminary tests of the LLNL crevice transport model (Farmer, 1997, Farmer and McCright, 1998) The worst case within the bounds of the regression analysis is the simulated crevice condition used by Haynes International (10 wt% $FeCl_3$) In the repository, the concentration of $FeCl_3$ is expected to be limited to much lower values by the presence of carbonate, which precipitates iron It must be noted that combinations of input parameters that are clearly beyond the range of the data included in the correlation cannot be used to generate reasonable predictions Therefore, this correlation should not be used for saturated solutions of J-13 and/or $FeCl_3$ Within the limits of the experimental data, predictions are believed to be good representations of the observations

The estimation of passive corrosion rates from Roy's cyclic polarization measurements is now explained (Farmer, 1998a, Roy, Fleming, and Lum, 1997b, 1996, 1997a) It is well known that the corrosion (or penetration) rate of an alloy, dp/dt, can be calculated from the corrosion current density, i_{corr}, as follows

$$\frac{dp}{dt} = \frac{i_{corr}}{\rho_{alloy} n_{alloy} F} \quad , \qquad \text{(Eq 2 8-24a)}$$

where ρ_{alloy} is the density of the alloy, assumed to be approximately 8 4 g/cm^3, and F is Faraday's constant The number of gram equivalents per gram of alloy, n_{alloy}, is calculated with the following equation

$$n_{alloy} = \sum_j \left(\frac{f_j n_j}{a_j} \right) \quad , \qquad \text{(Eq 2 8-24b)}$$

where f_j is the mass fraction of the jth alloying element in the material, n_j are the number of electrons involved in the anodic dissolution process, which is assumed to be congruent, and a_j is the atomic weight of the jth alloying element These equations have been used to calculate penetration rates for Alloy C-22 from apparent corrosion currents determined during cyclic polarization measurements In principle, such electrochemically determined rates should be consistent with those observed in the LTCTF, although experience indicates that such electrochemically determined rates are conservative (higher than those actually observed)

TSPA codes require that corrosion rates be represented by appropriate cummulative probability distribution functions (CDFs) In the case of passive corrosion of Alloy C-22 in 1000X J-13, CDFs can be based on the above correlation, because the chloride concentration is within the range of data included in the correlation (Farmer, 1998a). In the case of saturated J-13, estimates can be based on the article by Smailos, Schwarzkopf, and Koster (Smailos, Schwarzkopf, and Koster, 1986), as interpreted by Shoesmith The data quoted by Shoesmith is for Q-brine and Z-brine electrolytes, as shown in Table 2 8-12

Table 2.8-12. Data for passive corrosion of Alloy C-4 in saturated brines (Smailos et al. 1986; Shoesmith, 1998).

Brine	pH	NaCl (wt%)	KCl (wt%)	$MgCl_2$ (wt%)	$MgSO_4$ (wt%)	H_2O (wt%)	90°C rate (μm/yr)	170°C rate (μm/yr)	pH (Shoesmith)
Q	4 9	1 4	4 7	26 8	1 4	65 7	0 02	0 15–0 66	~5
Z	3 6	0 2	0 66	36 4	0 87	61 9	10–14		~2

Construction of CDFs for Alloy C-22 passive corrosion rates in 1000X and saturated J-13 waters requires estimation of the means, as well as the width of the distributions at those means It is assumed that logarithimic rates are normally distributed To establish a CDF for 1000X J-13, the correlation (Eq 21g) is first used to estimate the logarithimic rate (Eq 25a) at the 50th percentile·

$$y = \ln\left[\frac{\Delta p}{\Delta t}\right] \qquad \text{(Eq 2 8-25a)}$$

Equations 25b through 25g are then used to estimate the logarithmic rates at the 5th, 95th, 1st, and 99th percentiles

$$y_{5\%} \approx y_{\text{predicted}} - \delta y_{a=0\,05} \approx y_{\text{predicted}} - t_{a=0\,05} s_{y/123\ \ k}\ , \qquad \text{(Eq 2 8-25b)}$$

$$y_{95\%} \approx y_{\text{predicted}} + \delta y_{a=0\,05} \approx y_{\text{predicted}} + t_{a=0\,05} s_{y/123\ \ k}\ , \qquad \text{(Eq 2 8-25c)}$$

$$t_{a=0\,05} \approx 1\,70\ , \qquad \text{(Eq 2 8-25d)}$$

$$y_{1\%} \approx y_{\text{predicted}} - \delta y_{a=0\,01} \approx y_{\text{predicted}} - t_{a=0\,01} s_{y/123\ \ k}\ , \qquad \text{(Eq 2 8-25e)}$$

$$y_{99\%} \approx y_{\text{predicted}} + \delta y_{a=0\,01} \approx y_{\text{predicted}} + t_{a=0\,01} s_{y/123\ \ k}\ , \qquad \text{(Eq 2 8-25f)}$$

$$t_{a=0\,01} \approx 2\,46\ . \qquad \text{(Eq 2 8-25g)}$$

Equations 25h through 25k are used to construct CDFs in terms of actual rates

$$r_{5\%} = \left[\frac{\Delta p}{\Delta t}\right]_{5\%} \approx \exp\left[y_{\text{predicted}} - 1\,70 \times s_{y/123\ \ k}\right]\ , \qquad \text{(Eq. 2 8-25h)}$$

$$r_{95\%} = \left[\frac{\Delta p}{\Delta t}\right]_{95\%} \approx \exp\left[y_{\text{predicted}} + 1\,70 \times s_{y/123\ \ k}\right]\ , \qquad \text{(Eq 2 8-25i)}$$

$$r_{1\%} = \left[\frac{\Delta p}{\Delta t}\right]_{1\%} \approx \exp\left[y_{\text{predicted}} - 2\,46 \times s_{y/123\ \ k}\right]\ , \qquad \text{(Eq 2 8-25j)}$$

$$r_{99\%} = \left[\frac{\Delta p}{\Delta t}\right]_{99\%} \approx \exp\left[y_{\text{predicted}} + 2\,46 \times s_{y/123\quad k}\right] \qquad \text{(Eq 2 8-25k)}$$

Because no data for brines have been generated in the LTCTF, the CDFs for saturated J-13 are based on the measurements of Smailos et al , which are summarized in Table 2 8-12 (Smailos, Schwarzkopf, and Koster, 1986) The rate of 0.02 μm/yr for Alloy C-4 in Q-brine at 90°C (pH ≈ 5) is interpreted as a "typical" value (taken here as the rate at the 50th percentile) The rate of 10–14 μm/yr for Alloy C-4 in Z-brine at 90°C (pH ~ 2) is interpreted as the "maximum possible" value by Shoesmith (taken here as the rate at 99th percentile) According to Smailos et al , "After three years of exposure until now Hastelloy C-4 has remained resistant to pitting corrosion, and to stress corrosion cracking At 90°C local crevice corrosion attacks occurred at single points at the metal/PTFE and metal/metal contact surfaces, with maxiumum depths of 250 μm (metal/PTFE) and 20–70 μm (metal/metal), respectively " This translates into a maximum rate of 15–51 μm/yr It must be noted that the rates from the Smailos et al had to be scaled for pH and temperature so that all conditions of interest in this elicitation could be covered While the base rate used was taken from the Z-brine data, the activation energy used to scale the rate for temperature had to be inferred from the Q-brine data A reasonable value of the activation energy E_a was determined to be approximately 12 kcal/mol from the correlation (Eq 21g). The estimate was made with the following equation, which is based on an Arrhenius-type rate expression

$$\frac{r_1}{r_2} = \exp\left[\frac{E_a}{R}\left(\frac{1}{T_2} - \frac{1}{T_1}\right)\right] \qquad \text{(Eq 2 8-26a)}$$

At 170°C (T_1), the observed penetration rates were given as 0 66 and 0 15 μm/yr, which were averaged to give a single value of 0 4 μm/yr (r_1) At a lower temperature of 90°C (T_2), the observed rate was given as 0 02 μm/yr (r_2) Rates were scaled with the pH as implied by the correlation (Eq 21g), since no better means of estimating the response is available Therefore, the rates were assumed to obey the following empirical law

$$\frac{r_1}{r_2} = \exp\left[0\,87409(\text{pH}_2 - \text{pH}_1)\right] \qquad \text{(Eq. 2 8-26b)}$$

In this case, the standard deviation was estimated to be about 1 6228, the value of $u_{\alpha=0.05}$ was assumed to be 1 645 and the value of $u_{\alpha=0.01}$ was assumed to be 2 326 (Farmer, 1998b, Table 13). These CDF constructions are given in Table 2 8-13

Table 2.8-13. Estimates of CDFs for passive corrosion rates of Alloy C-22 with dripping.

Data source		Regression (Farmer)	Regression (Farmer)	Regression (Farmer)	Smailos[a] (Shoesmith[b])	Smailos (Shoesmith)	Smailos (Shoesmith)	Smailos (Shoesmith)
Environment		1000X J-13	1000X J-13	1000X J-13	Z-Brine	Z-Brine	Z-Brine	Z-Brine
NaCl (wt%)		1 2	1 2	1 2	Saturated	Saturated	Saturated	Saturated
T (°C)		25	50	100	90	25	50	100
Percentile (%)	pH	μm/yr	μm/yr	μm/yr	μm/yr	μm/yr	μm/yr	μm/yr
50	1	4.36×10^{-3}	1.85×10^{-2}	1.86×10^{-1}	6.60×10^{-1}	1.71×10^{-2}	8.29×10^{-2}	1.03
50	2	1.82×10^{-3}	7.71×10^{-3}	7.74×10^{-2}	2.75×10^{-1}	7.13×10^{-3}	3.46×10^{-2}	4.31×10^{-1}
50	3	7.59×10^{-4}	3.22×10^{-3}	3.23×10^{-2}	1.15×10^{-1}	2.98×10^{-3}	1.44×10^{-2}	1.80×10^{-1}
50	5	1.32×10^{-4}	5.60×10^{-4}	5.62×10^{-3}	2.00×10^{-2}	5.18×10^{-4}	2.51×10^{-3}	3.13×10^{-2}
50	7	2.30×10^{-5}	9.75×10^{-5}	9.79×10^{-4}	3.48×10^{-3}	9.02×10^{-5}	4.38×10^{-4}	5.46×10^{-3}
50	10	1.67×10^{-6}	7.08×10^{-6}	7.11×10^{-5}	2.53×10^{-4}	6.55×10^{-6}	3.18×10^{-5}	3.96×10^{-4}
5	1	3.35×10^{-4}	1.42×10^{-3}	1.43×10^{-2}	4.57×10^{-2}	1.18×10^{-3}	5.75×10^{-3}	7.16×10^{-2}
5	2	1.40×10^{-4}	5.93×10^{-4}	5.95×10^{-3}	1.91×10^{-2}	4.94×10^{-4}	2.40×10^{-3}	2.99×10^{-2}
5	3	5.84×10^{-5}	2.47×10^{-4}	2.48×10^{-3}	7.96×10^{-3}	2.06×10^{-4}	1.00×10^{-3}	1.25×10^{-2}
5	5	1.02×10^{-5}	4.31×10^{-5}	4.32×10^{-4}	1.39×10^{-3}	3.59×10^{-5}	1.74×10^{-4}	2.17×10^{-3}
5	7	1.77×10^{-6}	7.49×10^{-6}	7.53×10^{-5}	2.41×10^{-4}	6.25×10^{-6}	3.03×10^{-5}	3.78×10^{-4}
5	10	1.29×10^{-7}	5.44×10^{-7}	5.47×10^{-6}	1.75×10^{-5}	4.54×10^{-7}	2.20×10^{-6}	2.75×10^{-5}
95	1	5.67×10^{-2}	2.40×10^{-1}	2.41	9.52	2.47×10^{-1}	1.20	14.9
95	2	2.37×10^{-2}	1.00×10^{-1}	1.01	3.97	1.03×10^{-1}	4.99×10^{-1}	6.23
95	3	9.88×10^{-3}	4.19×10^{-2}	4.20×10^{-1}	1.66	4.30×10^{-2}	2.08×10^{-1}	2.60
95	5	1.72×10^{-3}	7.29×10^{-3}	7.32×10^{-2}	2.89×10^{-1}	7.48×10^{-3}	3.63×10^{-2}	4.52×10^{-1}
95	7	2.99×10^{-4}	1.27×10^{-3}	1.27×10^{-2}	5.03×10^{-2}	1.30×10^{-3}	6.31×10^{-3}	7.87×10^{-2}
95	10	2.17×10^{-5}	9.21×10^{-5}	9.25×10^{-4}	3.65×10^{-3}	9.46×10^{-5}	4.59×10^{-4}	5.72×10^{-3}
1	1	1.06×10^{-4}	4.51×10^{-4}	4.53×10^{-3}	1.51×10^{-2}	3.92×10^{-4}	1.90×10^{-3}	2.37×10^{-2}
1	2	4.44×10^{-5}	1.88×10^{-4}	1.89×10^{-3}	6.32×10^{-3}	1.64×10^{-4}	7.94×10^{-4}	9.90×10^{-3}
1	3	1.85×10^{-5}	7.85×10^{-5}	7.89×10^{-4}	2.64×10^{-3}	6.83×10^{-5}	3.31×10^{-4}	4.13×10^{-3}
1	5	3.23×10^{-6}	1.37×10^{-5}	1.37×10^{-4}	4.59×10^{-4}	1.19×10^{-5}	5.77×10^{-5}	7.19×10^{-4}
1	7	5.62×10^{-7}	2.38×10^{-6}	2.39×10^{-5}	7.99×10^{-5}	2.07×10^{-6}	1.00×10^{-5}	1.25×10^{-4}
1	10	4.08×10^{-8}	1.73×10^{-7}	1.74×10^{-6}	5.80×10^{-6}	1.50×10^{-7}	7.29×10^{-7}	9.09×10^{-6}
99	1	1.79×10^{-1}	7.57×10^{-1}	7.60	28.8	7.45×10^{-1}	3.61	45.1
99	2	7.45×10^{-2}	3.16×10^{-1}	3.17	12.0	3.11×10^{-1}	1.51	18.8
99	3	3.11×10^{-2}	1.32×10^{-1}	1.32	5.01	1.30×10^{-1}	6.29×10^{-1}	7.84
99	5	5.41×10^{-3}	2.29×10^{-2}	2.30×10^{-1}	8.72×10^{-1}	2.26×10^{-2}	1.10×10^{-1}	1.37
99	7	9.43×10^{-4}	3.99×10^{-3}	4.01×10^{-2}	1.52×10^{-1}	3.93×10^{-3}	1.91×10^{-2}	2.38×10^{-1}
99	10	6.85×10^{-5}	2.90×10^{-4}	2.91×10^{-3}	1.10×10^{-2}	2.86×10^{-4}	1.39×10^{-3}	1.73×10^{-2}

a Smailos, Schwarzkopf, and Koster, 1986

b Shoesmith, 1998

2.8.2.5 Data Published by Haynes International

Data published by Haynes International (Haynes International, Inc , 1987, Asphahani, 1980) and compiled by Gdowski (Gdowski, 1991) have also been used as the basis of the following correlations for Alloys 825, 625, C-4, C-22, and C-276, respectively

$$\text{Alloy 825} \quad \ln(\Psi) = \ln\left(2\ 1164 \times 10^{1}\right) - 5\ 9141 \times 10^{-6}(T - T_0)^2 - 1\ 1235 \times 10^{-3}(T - T_0), \qquad \text{(Eq 2 8-27a)}$$

$$\text{Alloy 625} \quad \ln(\Psi) = \ln\left(4\ 3493 \times 10^{-2}\right) - 2\ 4010 \times 10^{-3}(T - T_0)^2 - 2\ 3662 \times 10^{-1}(T - T_0), \qquad \text{(Eq 2 8-27b)}$$

$$\text{Alloy C-4} \quad \ln(\Psi) = \ln\left(8.6758 \times 10^{-3}\right) - 2\ 5403 \times 10^{-3}(T - T_0)^2 - 4\ 2970 \times 10^{-2}(T - T_0), \qquad \text{(Eq 2 8-27c)}$$

$$\text{Alloy C-22} \quad \ln(\Psi) = \ln\left(2\ 8539 \times 10^{-3}\right) + 1\ 2375 \times 10^{-3}(T - T_0)^2 - 2\ 9369 \times 10^{-2}(T - T_0), \qquad \text{(Eq 2 8-27d)}$$

and

$$\text{Alloy C-276.} \quad \ln(\Psi) = \ln\left(5\ 8219 \times 10^{-3}\right) - 1\ 5234 \times 10^{-3}(T - T_0)^2 - 3\ 7309 \times 10^{-2}(T - T_0) \qquad \text{(Eq 2 8-27e)}$$

where T is the absolute temperature of the CRM, and T_0 is the reference temperature of 298K The parameter Ψ is defined as follows

$$\Psi = \frac{d}{\sqrt{t}} \quad , \qquad \text{(Eq 2 8-27f)}$$

where d is the penetration in microns (μm) and t is the time in hours (h) Figure 2 8-6a shows actual data published by Haynes International, Figure 2 8-6b is a graphical representation of the above correlations (Eqs. 27a through 27f) Figure 2 8-7a shows penetrations of the candidate CRMs in a simulated crevice solution with 10 wt% $FeCl_3$ at 80°C, predicted with the correlations Predicted penetrations for Alloy C-22 at several temperature levels between 20 and 100°C are shown in Figure 2 8-7b Such empirical models can be used as a basis of materials selection, but they may not be adequate for predictions over extremely long periods of time

Figure 2.8-6. **Corrosion data published by Haynes International (Asphahani, 1980) for exposure of candidate CRMs to simulated crevice solutions (10 wt% $FeCl_3$).**

Figure 2.8-7. **Extrapolations of corrosion data published by Haynes International (Asphahani, 1980) based on the analysis shown in Figure 2.8-6. (which assumes that $d = \Psi_t^{-1/2}$).**

2.8.3 Crevice Corrosion Model

2.8.3.1 Introduction to Crevice Corrosion

Crevices will be formed between waste package and supports, beneath mineral precipitates, corrosion products, dust, rocks, cement and biofilms, and between CAM and CRM. It is well known that the crevice environment will be more severe than the NFE The hydrolysis of dissolved metal will lead to the accumulation of H^+ and the corresponding suppresion of pH As previously discussed, Jones and Wilde have prepared solutions of $FeCl_2$, $NiCl_2$, and $CrCl_3$ to simulate such localized environments and measured substantial pH suppression (Jones and Wilde, 1978) Wang has made similar measurements with $FeCl_3$ solutions, which are reported here As pointed out by McCoy, the measured pH in active, artificial crevices is 3 3 to 4 7 if the crevice is formed with carbon steel, 2 4 to 4 0 if the crevice is formed with a Fe-Cr alloy, and ≤ 2 3 if the crevice is formed with a stainless steel (Szjkarsja-Smialowska, 1986, pp 311–312) These data and measurements are summarized in Tables 2 8-14, 2 8-15, and 2 8-16. Field-driven electromigration of Cl^- (and other anions) into crevice must occur to balance cationic charge associated with H^+ ions. The exacerbated conditions inside the crevice set the stage for subsequent attack of the CRM by passive corrosion, pitting (initiation and propagation), stress corrosion cracking (initiation and propagation), or other mechanisms Clearly, the development of an adequate crevice corrosion model for determination of the exact nature of the local environment is prudent

Table 2.8-14. **Measured pH of metal salt solutions at 25°C (Jones, 1996, p. 102).**

Salt	1 N	3 N	Saturated
$FeCl_2$	2 1	0 8	0 2
$NiCl_2$	3 0	2 7	2 7
$CrCl_3$	1 1	–0 3	–1 4

Table 2.8-15. **Measured pH of $FeCl_3$ solutions at 25°C**

Conc. (wt%)	pH
1	1 92
2	1 83
3	1 71
4	1 63
10	0 70

Table 2.8-16. Transport-limited pH in crevice.

Source of information	pH
EEP (expected for WP)	2 5
Transport model (Alloy 625)	2 8 to 3 2
Artificial crevices (carbon steel)	3 3 to 4 7
Artificial crevices (Fe-Cr alloys)	2 4 to 4 0
Artificial crevices (stainless steels)	≤ 2 3

A detailed deterministic model has been developed to calculate the spatial distributions of electrochemical potential and current density in the CAM–CRM crevice, as well as transient concentration profiles of dissolved metals and ions (Farmer, 1997, Farmer and McCright, 1998) The local concentration of hydrogen cation is assumed to be limited by either anion transport into the crevice or hydrogen ion production and transport out of the crevice If the limitation is assumed to be due to anion transport, all hydrolysis reactions at each point inside the crevice are assumed to instantaneously reach equilibrium Furthermore, it is assumed that electroneutrality is maintained at each point In contrast, if the limitation is assumed to be hydrogen ion production and transport, the local generation rate of hydrogen ion must be known and is assumed to be proportional to the dissolution rates of dissolved metals, with proportionality constants being calculable from hydrolysis equilibrium constants Rate constants for the hydrolysis reactions are unknown, with experimental determination being impractical In this case, anion concentrations are calculated at each point based on electroneutrality This model can be used to estimate the extent of pH suppression in the CAM–CRM crevice due to the simultaneous hydrolysis and transport of dissolved Fe, Ni, Cr, Mo, and W It is assumed that crevice corrosion passes through two phases Dissolution of the CAM at a relatively low electrochemical potential is assumed to occur during Phase 1 After anodic oxidation (consumption) of the accessible CAM, the electrochemical potential of the CRM will increase to high levels Dissolution of the CRM is assumed to predominate during Phase 2 Lower pH values can be reached during Phase 2 crevice corrosion than during Phase 1 crevice corrosion, due primarily to the hydrolysis of dissolved chromium In the case of crevice corrosion of Alloy 625, the predicted pH inside the crevice was 2 8 to 3 2, with a corresponding increase in chloride concentration This calculation assumed a temperature of 25°C, an electrochemical potential at the crevice mouth that is 100 mV above the critical pitting potential, and a uniform crevice width (CAM–CRM separation) of 0 075 mm Tighter crevices should lead to lower pH and higher chloride It is also predicted that the electrochemical potential E will decrease with increasing depth Therefore, the potential should never be more severe (closer to the threshold for LC) than at the crevice mouth

Fluxes of ions in the crevice are calculated with the Nernst–Planck equation, which governs electromigration, diffusion, and convective transport (Newman, 1991) The current density is then defined in terms of these fluxes In cases with strong supporting electrolyte, the electromigration term can be ignored Transient concentrations can be determined from the gradient of the flux. The concentration of dissolved iron is assumed to include Fe^{2+}, Fe^{3+}, $Fe(OH)^{+}$, and $Fe(OH)^{2+}$. Similar assumptions are made for other dissolved metals. The partial differential equations (PDEs) that describe the transport of such reactive species in the crevice can be solved numerically. Both the Crank–Nicholson and the explicit methods have been used (Jenson and Jeffreys, 1963, pp 410–422, McCracken and Dorn, 1964, pp 377–385). The assumed boundary conditions (BCs) imply that the concentrations of dissolved metals are

zero at the crevice mouth (NFE), and that crevices are symmetric about a mirror plane where the flux is zero The BCs for H^+ and dissolved O_2 are slightly different in that nonzero concentrations are assigned at the crevice mouth The PDEs that define transient concentrations in the crevice require determination of the potential gradient, as well as the (apparent) homogeneous rates First, the axial current density along the length of the crevice is calculated by integrating the wall current density The electrode potential along the length of the crevice can then be calculated from the axial current density. This technique is similar to that employed in other models (Gartland, 1997, Xu and Pickering, 1993, Nystrom et al , 1994)

2.8.3.2 Crevice Chemistry

Dissolution of the CAM wall will produce iron ions, whereas dissolution of the CRM wall will produce iron, nickel, chromium, molybdenum, and tungsten ions As discussed by Oldfield and Sutton, metal ions produced by anodic dissolution are assumed to undergo the following hydrolysis reactions (Oldfield and Sutton, 1978)

$$Fe^{2+} + H_2O \underset{K_{3,1}}{\longleftrightarrow} Fe(OH)^+ + H^+ \quad , \qquad \text{(Eq 2 8-28a)}$$

$$Fe^{3+} + H_2O \underset{K_{4,1}}{\longleftrightarrow} Fe(OH)^{2+} + H^+ \quad , \qquad \text{(Eq 2 8-28b)}$$

$$Ni^{2+} + H_2O \underset{K_{5,1}}{\longleftrightarrow} Ni(OH)^+ + H^+ \quad , \qquad \text{(Eq 2 8-28c)}$$

$$Cr^{3+} + H_2O \underset{K_{1,1}}{\longleftrightarrow} Cr(OH)^{2+} + H^+ \quad , \qquad \text{(Eq. 2 8-28d)}$$

and

$$Cr(OH)^{2+} + H_2O \underset{K_{1,2}}{\longleftrightarrow} Cr(OH)_2^+ + H^+ \qquad \text{(Eq 2 8-28e)}$$

Relevant equilibrium constants are defined as follows (Oldfield and Sutton, 1978)

$$K_{3,1} = \frac{\left[Fe(OH)^+\right]\left[H^+\right]}{\left[Fe^{2+}\right]} \quad , \qquad \text{(Eq 2 8-29a)}$$

$$K_{4,1} = \frac{\left[Fe(OH)^{2+}\right]\left[H^+\right]}{\left[Fe^{3+}\right]} \quad , \qquad \text{(Eq 2 8-29b)}$$

$$K_{5,1} = \frac{\left[Ni(OH)^+\right]\left[H^+\right]}{\left[Ni^{2+}\right]} \quad , \qquad \text{(Eq 2 8-29c)}$$

$$K_{1,1} = \frac{\left[Cr(OH)^{2+}\right]\left[H^{+}\right]}{\left[Cr^{3+}\right]} \quad , \qquad \text{(Eq 2 8-29d)}$$

and

$$K_{1,2} = \frac{\left[Cr(OH)_2^{+}\right]\left[H^{+}\right]}{\left[Cr(OH)^{2+}\right]} \qquad \text{(Eq 2 8-29e)}$$

If the dissolved metals exceed the solubility limits, precipitation will occur

$$Fe(OH)_2(s) \xleftrightarrow[K_{3\,3}]{} Fe^{2+} + 2OH^{-} \quad , \qquad \text{(Eq 2 8-30a)}$$

$$Ni(OH)_2(s) \xleftrightarrow[K_{5\,3}]{} Ni^{2+} + 2OH^{-} \quad , \qquad \text{(Eq 2 8-30b)}$$

and

$$Cr(OH)_3(s) \xleftrightarrow[K_{1\,3}]{} Cr^{3+} + 3OH^{-} \qquad \text{(Eq 2 8-30c)}$$

The corresponding solubility products are

$$K_{3,3} = \left[Fe^{2+}\right]\left[OH^{-}\right]^2 \quad , \qquad \text{(Eq 2 8-31a)}$$

$$K_{5,3} = \left[Ni^{2+}\right]\left[OH^{-}\right]^2 \quad , \qquad \text{(Eq 2 8-31b)}$$

and

$$K_{1,3} = \left[Cr^{3+}\right]\left[OH^{-}\right]^3 \qquad \text{(Eq 2 8-31c)}$$

The effects of hexavalent chromium, molybdenum, and tungsten hydrolysis on pH have been ignored in this preliminary version of the model, but they will be accounted for in the future If solubility limits are exceeded, $Fe(OH)_2$, $Ni(OH)_2$, $Cr(OH)_3$, and $Mo(OH)_3$ precipitates are assumed to form. The hydrolysis equilibrium constants were found in the literature and are summarized in Table 2 8-17 (Oldfield and Sutton, 1978, Cotton and Wilkinson, 1988, pp 679–755, Saleh, 1996) Better equilibrium data from the EQ3/6 code will be used in the future, as has recently been done by others (Walton, Cragnolino, and Kalandros, 1996). The EQ3/6 code was also developed by LLNL

Table 2.8-17. $K_{i,j}$ for *i*th species and *j*th reaction at 25°C.

Species	*i*	Ref.	$K_{i,1}$	$K_{i,2}$	$K_{i,3}$	$K_{i,4}$	$K_{i,5}$	$K_{i,5}$
Cr(III)	1	15,21	1.58×10^{-4}	6.31×10^{-7}	4.0×10^{-38}	2.00×10^{3}	3.16×10^{4}	3.16×10^{3}
Cr(VI)	2	21	6.92×10^{-11}					
Fe(II)	3	15	5.0×10^{-9}		7.9×10^{-16}			
Fe(III)	4	13	1.84×10^{-3}	unknown	unknown			
Ni(II)	5	15	3.16×10^{-4}		1.35×10^{-15}			

2.8.3.3 Option 1 - Limitiation Due to Anion Transport

In this case, it is assumed that acidification of the crevice solution is limited by the transport of Cl^- into the crevice, instead of being limited by H^+ production and transport out of the crevice As discussed by Xu and Pickering (Xu and Pickering, 1993), Cl^- will be driven into the crevice by the potential gradient The corresponding concentration in the crevice is

$$\left[Cl^-\right] = \left[Cl^-\right]_0 \exp\left[-\frac{F}{RT}\Phi(x)\right] \quad , \qquad \text{(Eq 2.8-32)}$$

where $[Cl^-]_0$ is the concentration at the crevice mouth, $\Phi(x)$ is the potential in the crevice relative to that at the mouth, and (x) is the distance from the crevice mouth After the Cl^- concentration is established, the H^+ concentration can be determined with the equation for electroneutrality The general expression is

$$\sum_{j=1}^{m_a} n_j^- z_j^- = \sum_{j=1}^{m_c} n_j^+ z_j^+ \quad , \qquad \text{(Eq 2.8-33a)}$$

where n_j^- is the molar concentration of the *j*th anion, z_j^- is the charge of that anion, m_a is the total number of anionic species, n_j^+ is the molar concentration of the *j*th cation, z_j^+ is the charge of that cation, and m_c is the total number of cationic species This can be written more specifically in terms of anticipated species·

$$\begin{aligned}\left[OH^-\right]+\left[Cl^-\right]+\left[F^-\right]+\left[NO_3^-\right]+\left[HCO_3^-\right]+2\left[SO_4^{2-}\right]+2\left[S^{2-}\right]+2\left[Cr_2O_7^{2-}\right] = \\ \left[H^+\right]+\left[Na^+\right]+\left[K^+\right]+2\left[Mg^{2+}\right]+2\left[Ca^{2+}\right]+2\left[Mn^{2+}\right]+2\left[Ni^{2+}\right]+\left[Ni(OH)^+\right]+ \\ 2\left[Fe^{2+}\right]+\left[Fe(OH)^+\right]+3\left[Fe^{3+}\right]+2\left[Fe(OH)^{2+}\right]+\left[Fe(OH)_2^+\right]+ \\ 3\left[Cr^{3+}\right]+2\left[Cr(OH)^{2+}\right]+\left[Cr(OH)_2^+\right]\end{aligned} \qquad \text{(Eq 2.8-33b)}$$

Here too, the concentrations of dissolved species are expressed in terms of the hydrogen ion concentration, equilibrium constants for the hydrolysis reactions, solubilities of corrosion products, and the dissociation constant for water. The resulting equation is a polynomial in $[H^+]$ whose roots can be used determine the pH (Farmer, 1997; Farmer and McCright, 1998)

2.8.3.4 Option 2 - Limitiation Based On Transport of Hydrogen Ion

An alternative strategy assumes that the accumulation of H^+ ions (pH suppression) in the crevice is limited by the overall production rate of H^+ due to the hydrolysis of dissolved metals, and the loss rate of H^+ due to leakage from the crevice mouth To quantify this effect, the net mass balance for H^+ ions must first be established

$$\left[H^+\right]=\left[H^+\right]_{Fe(II)}+\left[H^+\right]_{Fe(III)}+\left[H^+\right]_{Ni(II)}+\left[H^+\right]_{Cr(III)}-\left[H^+\right]_{H_2}-\left[H^+\right]_{O_2} \qquad \text{(Eq 2 8-34a)}$$

In the present model, the effects of hexavalent chromium, molybdenum, and tungsten on pH are assumed to be insignificant The quantity of hydrogen ions generated by the hydrolysis of divalent iron ions produced during the dissolution of either the CAM or CRM is

$$\left[H^+\right]_{Fe(II)}=2\left[Fe(OH)_2\right](s)+\left[Fe(OH)^+\right] \qquad \text{(Eq 2 8-34b)}$$

The dissolved Fe^{2+} can be converted to Fe^{3+} by microbial action, oxidation by naturally occurring MnO_2 or other oxidants, or anodic oxidation Once formed, it is assumed that Fe^{3+} can also undergo hydrolysis The quantity of hydrogen ions produced by this reaction is

$$\left[H^+\right]_{Fe(III)}\approx\left[Fe(OH)^{2+}\right] \qquad \text{(Eq 2 8-34c)}$$

Dissolution of the CRM will produce divalent nickel and trivalent chromium ions, in addition to divalent iron ions The equations for the divalent nickel are analogous to those for the divalent iron

$$\left[H^+\right]_{Ni(II)}=2\left[Ni(OH)_2\right](s)+\left[Ni(OH)^+\right] \qquad \text{(Eq 2 8-34d)}$$

The equations for the trivalent chromium are similar to those for the trivalent iron

$$\left[H^+\right]_{Cr(III)}=3\left[Cr(OH)_3\right](s)+2\left[Cr(OH)_2^+\right]+\left[Cr(OH)^{2+}\right] \qquad \text{(Eq 2 8-34e)}$$

Hydrogen ions lost due to hydrogen evolution and the cathodic reduction of oxygen are represented by

$$\left[H^+\right]_{H_2}=2\left[H_2\right] \quad , \qquad \text{(Eq 2 8-34f)}$$

and

$$\left[H^+\right]_{O_2}=4\left[O_2\right] \qquad \text{(Eq 2 8-34g)}$$

Equations (34b) through (34g) are substituted into Eq. (34a) The concentrations of soluble hydrolysis products are then expressed in terms of $[H^+]$ and the concentrations of unhydrolyzed metal ions. The result is then differentiated with respect to time to yield the following H^+ generation rate

$$\frac{d[H^+]}{dt} = \frac{\left\{\frac{K_{3,1}}{[H^+]}\frac{d[Fe^{2+}]}{dt} + \frac{K_{4,1}}{[H^+]}\frac{d[Fe^{3+}]}{dt} + \frac{K_{5,1}}{[H^+]}\frac{d[Ni^{2+}]}{dt} + \frac{K_{1,1}}{[H^+]}\frac{d[Cr^{3+}]}{dt} + \frac{2K_{1,1}K_{1,2}}{[H^+]dt}\frac{d[Cr^{3+}]}{dt} - 2\frac{d[H_2]}{dt} - 4\frac{d[O_2]}{dt}\right\}}{\left\{1 + \frac{K_{3,1}[Fe^{2+}]}{[H^+]^2} + \frac{K_{4,1}[Fe^{3+}]}{[H^+]^2} + \frac{K_{5,1}[Ni^{2+}]}{[H^+]^2} + \frac{K_{1,1}[Cr^{3+}]}{[H^+]^2} + \frac{4K_{1,1}K_{1,2}[Cr^{3+}]}{[H^+]^3}\right\}} \quad \text{(Eq. 2 8-34h)}$$

The consumption of H^+ by hydrogen evolution and cathodic oxygen reduction is accounted for Because the H^+ generation rate approaches zero as [H+] and the concentrations of unhydrolyzed metal ions approach infinity (large values), the extent of pH suppression in the crevice is limited If solubility limits are exceeded, $Fe(OH)_2$, $Ni(OH)_2$, and $Cr(OH)_3$ precipitates are assumed to form Under these conditions, the H^+ generation rate is proportional to the rates of precipitation, which are directly related to the rates of dissolution As previously discussed, the hydrolysis equilibrium constants can be found in the literature (Oldfield and Sutton, 1978, Cotton and Wilkinson, 1988, pp. 679–755, Saleh, 1996).

2.8.3.5 Ion Transport in Crevice

Attention is now directed to the specific issue of ion transport in the crevice separating the CAM and CRM As discussed by Newman, fluxes of ions are estimated with the Nernst–Planck equation, which governs electromigration, diffusion, and convective transport (Newman, 1991)·

$$\overline{N}_i = -z_i u_i F c_i \overline{\nabla}\Phi - D_i \overline{\nabla} c_i + \overline{v} c_i \quad , \qquad \text{(Eq 2 8-35)}$$

where N_i is the flux, z_i is the charge, u_i is the mobility, c_i is the concentration, and D_i is the diffusivity of the ith ion, Φ is the potential in the electrolyte, and v is the convective velocity of the electrolyte The current density is then defined in terms of the flux

$$\overline{i} = -F^2 \overline{\nabla}\Phi \sum_i z_i^2 u_i c_i - F \sum_i z_i D_i \overline{\nabla} c_i \qquad \text{(Eq 2 8-36)}$$

In cases with strong supporting electrolyte, the electromigration term can be ignored Transients in concentration can be dealt with through application of Eq (37)

$$\frac{\partial c_i}{\partial t} = -\overline{\nabla}\ \overline{N}_i + R_i \quad , \qquad \text{(Eq 2 8-37)}$$

where R_i is the apparent local homogeneous rate (ALHR) In the simple one-dimensional (1D) problem, the ALHR for each dissolved metal is assumed to be proportional to the local dissolution (corrosion) rate The ALHR for H^+ production is also assumed to be proportional to the local dissolution rates, as illustrated by Eq. (34h) The concentration of dissolved iron is assumed to include all dissolved species, including Fe^{2+}, Fe^{3+}, $Fe(OH)^+$, and $Fe(OH)^{2+}$. Similar assumptions are made for other dissolved metals The hyperbolic partial differential equations (PDEs) that describe the transport of such reactive species in the crevice can be solved numerically. Both the Crank–Nicholson and the explicit methods have been used (Jenson and Jeffreys, 1963, pp. 410–422, McCracken and Dorn, 1964, pp. 377–385). The assumed BCs imply that the concentrations are zero at the crevice mouth (NFE), and that crevices are symmetric about a mirror plane where the flux is zero The BCs for H^+ and

dissolved O_2 are slightly different in that nonzero concentrations are assigned at the crevice mouth

2.8.3.6 Current and Potential

The PDEs that define transient concentrations in the crevice require determination of the potential gradient, as well as the (apparent) homogeneous rates. First, the axial current density along the length of the crevice, $i_x(x)$, is calculated by integrating the wall current density, $i_y(x)$

$$i_x(x) = \frac{\int_x^L i_y(x)dx}{h(x)} \quad , \qquad \text{(Eq 2 8-38)}$$

where L is the maximum crevice depth, and $h(x)$ is the separation between the two crevice walls at position (x) The electrode potential along the length of the crevice, $E(x)$, can then be calculated from $i_x(x)$

$$E(x) = \int_0^x \rho(x) i_x(x) d\lambda \quad , \qquad \text{(Eq 2 8-39)}$$

where $\rho(x)$ is the resistivity of the crevice solution at position (x) This technique is similar to that employed in other published models (Gartland, 1997, Xu and Pickering, 1993, Nystrom et al , 1994)

2.8.3.7 Simultaneous Numerical Solution of Transport Equations

Actual calculation of the transient concentrations is described here First, the terms for electromigration in the Nernst–Planck equation are assumed to be insignificant, which is valid in cases involving a strong supporting electrolyte (Newman, 1991) A single, lumped-sum concentration is then used to represent each dissolved metal For example, the lumped-sum concentration of dissolved iron includes contributions of Fe^{2+}, Fe^{3+}, $Fe(OH)^+$, and $Fe(OH)^{2+}$ It is necessary to employ this concept of the concentration because rates of reaction (apparent homogeneous rates) for individual species are unknown An overall generation rate for each dissolved metal can be calculated from the wall current density Individual species must be assumed to reach instantaneous equilibrium Equilibrium constants for hydrolysis reactions are available, kinetic rate constants are not The hyperbolic PDEs that describe the transport of reactive species in the crevice are solved numerically with either the explicit method, or the Crank–Nicholson method (Jenson and Jeffreys, 1963, pp. 410–422, McCracken and Dorn, 1964, pp 377–385). The explicit method for solution of these PDEs is represented by the following algorithm.

$$C_{m,n+1} = A\left(C_{m+1,n} + C_{m-1,n}\right) + (1-2A)C_{m,n} + (\Delta t)R_{m,n} \quad , \qquad \text{(Eq 2 8-40a)}$$

where $C_{m,n}$ is the lumped-sum concentration at position m and time n, $R_{m,n}$ is the corresponding rate of generation or loss, A is the modulus of the equation, and Δt is the time step The truncation error for the explicit method is

$$T_{m,n} \le \frac{A(6A-1)}{12} Mh^4 \qquad \text{(Eq 2 8-40b)}$$

The Crank–Nicholson method is represented by

$$C_{m,n+1} = \frac{A}{2(1+A)}\left(C_{m+1,n+1} + C_{m-1,n+1}\right) + \frac{(1-A)}{(1+A)}C_{m,n} + \frac{A}{2(1+A)}\left(C_{m+1,n} + C_{m-1,n}\right) + \frac{(\Delta t)}{(1+A)}R_{m,n} \quad , \qquad \text{(Eq 2 8-41a)}$$

where the truncation error is

$$T_{m,n} \le \frac{A}{12}Mh^4 \qquad \text{(Eq 2 8-41b)}$$

The modulae for both algorithms are identical and equivalent to

$$A = \frac{D(\Delta t)}{(\Delta x)^2} \qquad \text{(Eq 2 8-42)}$$

In cases involving dissolved metals, the following BCs apply

$$C_{1,n} = 0 \quad , \qquad \text{(Eq 2 8-43a)}$$

and

$$C_{m+1,n} = C_{m-1,n} \qquad \text{(Eq 2 8-43b)}$$

These BCs imply that the concentrations are zero at the crevice mouth (NFE), and that crevices are symmetric about a mirror plane where the flux is zero The BCs for H^+ and dissolved O_2 are slightly different in that nonzero concentrations are assigned at the crevice mouth Similar numerical techniques can be used for calculation of the current and potential

2.8.3.8 Predicted Environment in Crevice

The Crank–Nicholson method was used to calculate concentration and pH profiles during Phase 1 crevice corrosion, as shown in Figures 2 8-8a and 2 8-8b, respectively Soluble iron species included in the calculation were Fe^{2+}, Fe^{3+}, $Fe(OH)^{2+}$, and $Fe(OH)^+$ All precipitated iron is assumed to be $Fe(OH)_2$. Furthermore, it is assumed that (a) the temperature is 90°C or 363 K, the potential at the mouth of the crevice is at +10 mV relative to the corrosion potential of Alloy 516, the assumed CAM, the solution conductivity is 50,000 μS cm^{-1}; and the diffusion coefficient of all dissolved species is approximately 1 $0x10^{-5}$ cm^2 sec^{-1} Roy et al have measured relevant corrosion, pitting and repassivation potentials for Alloys 516, 825, 625, and C-22 (Roy, Fleming, and Lum, 1997b, 1996, 1997a). Results at 0, 600, 1200, 1800, 2400, and 3000 seconds are presented, though calculations were done at intervals of 1 second. The peak in the iron concentration near the crevice mouth is due to the combined effects of a potential that decays with increasing crevice depth (x), and the assumed BC of zero concentration at the crevice mouth. Results obtained with the explicit method are identical

Figure 2.8-8. Transient concentrations of dissolved iron and hydrogen ion (pH) as functions of crevice depth during phase 1 crevice corrosion, which assumes preferential attack of the CAM wall.

Calculations for Phase 2 crevice corrosion of Alloy 625 are shown in Figures 2 8-9 through 2 8-11. Transients in the total concentration of dissolved iron are shown at 0, 600, 1200, 1800, 2400, 3000, and 3600 s Dissolved metal species included in the calculation are Fe^{2+}, $Fe(OH)^{+}$, Fe^{3+}, $Fe(OH)^{2+}$, Ni^{2+}, $Ni(OH)^{+}$, Cr^{3+}, $Cr(OH)^{2+}$, $Cr(OH)_2^{+}$, and Mo^{3+}. Precipitates are assumed to be $Fe(OH)_2$, $Ni(OH)_2$, $Cr(OH)_3$, and $Mo(OH)_3$. It is further assumed that the temperature is 90°C, or 363K, the potential at the mouth of the crevice is at +100 mV relative to the pitting potential of Alloy 625, the assumed CRM, the solution conductivity is 1000 μS/cm, and the diffusion coefficient of all dissolved species is approximately $1\,9 \times 10^{-5}$ cm^2/s Based on the work of Roy et al. (Roy, Fleming, and Lum, 1997b, 1996, 1997a), the pitting potential is assumed to be +689 mV versus SCE As shown in Figure 2 8-9, the concentrations of dissolved metals rise sharply from zero at the crevice mouth to peak values inside the crevice (~0 3 cm) Recall that the concentrations are assumed to be zero at the crevice mouth At large distances into the crevice (~0 9 cm), the concentrations fall from the peak values to plateaus Because H^+ is generated by the hydrolysis of iron, nickel, and chromium, and because it is transported in a similar fashion, its transient concentration profiles (not shown) track those of the dissolved metals Figure 2 8-10a shows the pH profiles that correspond to Figure 2 8-9 In this particular case, it is concluded that reasonable pH values for the crevice solution lie between 2 8 and 3 2 during Phase 2 The concentrations of dissolved metal ions and H^+ are used to calculate Cl^- concentration, as shown in Figure 2 8-10b Alternatively, the Cl^- concentration could be calculated directly from the potential, as suggested by Pickering and Frankenthal (Pickering and Frankenthal, 1972), as well as Galvele (Galvele, 1976) As shown in Figure 2 8-11a, the potential drops to more cathodic values as the distance into the crevice increases The applied potential at the crevice mouth is assumed to be +1,030 mV versus NHE (+789 mV versus SCE) At a depth of 1 cm, the predicted potential is somewhere between +870 and +910 mV versus NHE (+630 and +670 mV versus SCE) The oscillations in the potential profiles are due to the antagonistic effects of chloride and potential on the anodic current density at the crevice wall More specifically, the anodic current due to localized attack is driven by the difference between the electrode potential E and the pitting potential E_{crit} The pitting potential is assumed to obey the expression given by Galvele (Galvele, 1976)

$$E_{crit} = A - B\ln\left[Cl^-\right] \quad , \qquad \text{(Eq 2 8-44)}$$

where A and B are constants Note that B is given as ~88 mV for Fe-18Cr-8Ni in NaCl solutions As the potential in the crevice decreases, the chloride concentration increases, thereby driving the pitting potential to more cathodic levels (less stability) Thus, the anodic current is simultaneously driven by two opposed forces, increasing chloride and decreasing potential The axial and wall current densities also exhibit oscillations, as shown in Figure 2 8-11b. In the future, the data collected by Roy et al. should be used to establish the dependence of E_{crit} on Cl^- concentration (Roy, Fleming, and Lum, 1997b, 1996, 1997a) Measurements of critical potentials are found in Section 2 3 of this report.

Figure 2.8-9. Transient concentrations of dissolved iron and nickel as functions of crevice depth during phase 2 crevice corrosion (attack of CRM). It is assumed that the CRM is Alloy 625 and that electrochemical potential at the mouth of the crevice is maintained 100 mV above the critical pitting potential. Results for other metals not shown.

Figure 2.8-10. **Transient pH and chloride anion concentration as functions of crevice depth during phase 2 crevice corrosion (attack of CRM). It is assumed that the CRM is Alloy 625 and that electrochemical potential at the mouth of the crevice is maintained 100 mV above the critical pitting potential.**

Figure 2.8-11. **Transient potential and current density as functions of crevice depth during phase 2 crevice corrosion (attack of CRM). In this case it is assumed that the CRM is Alloy 625 and that electrochemical potential at the mouth of the crevice is maintained 100 mV above the critical pitting potential.**

2.8.3.9 Validation Experiments for the Crevice Corrosion Model

Microsensors are being developed and used to map conditions in crevice Ultimately, fiber optic microprobes should enable in situ determination of pH, Fe(II)/Fe(III), Ni(II), Cr(III)/Cr(VI), and other species Figure 2 8-12 shows preliminary data obtained with a new pH microprobe specifically developed by LLNL for validation of the crevice corrosion model The 488-nm line from an argon ion laser is used to induce pH-dependent fluorescence in a dy adsorbed at the tip of a fiber optic The small peak at 514 5 nm is residual output from the laser; the broad band at 535 nm is the florescence It should also be possible to use microelectrodes to determine local electrochemical potential, O_2, Cl^-, NO_3^- and SO_4^{2-}, as well as Fe(II)/Fe(III), Ni(II) Cr(III)/Cr(VI), and other species It may be possible to determine pH, Cl^-, NO_3^-, SO_4^{2-} by other techniques such as minature ion-selective electrodes (ISEs) Other techniques such as Raman spectroscopy could provide valuable insight into processes occuring inside the crevice Post-test examination of crevice walls with scanning confocal and electron microscopes should provide detailed understanding of the distribution of penetration depth inside the crevice region This work is further described in Section 2 7 of this report

Figure 2.8-12. **Results from new pH microprobe developed by LLNL for validation of the crevice corrosion model. The 488-nm line from an argon ion laser is used to induce pH-dependent fluorescence in a dye adsorbed at the tip of a fiber optic. The small peak at 514.5 nm is residual output from the laser; the broadband centered at 535 nm is the fluorescence.**

2.8.4 Pitting Models

2.8.4.1 Published Models

Crevice corrosion will result in acidification of the electrolyte and a corresponding elevation in Cl^- concentration This harsh localized environment may cause pitting, as well as intergranular corrosion. Several pitting models have been reviewed in detail by Farmer (Farmer, 1991). Those for pit initiation include the halide nuclei theory by Okada (Okada, 1984b, 1984a); the point-defect model by Chao, Lin, and McDonald (Chao, Lin, and McDonald, 1981), the electrostriction model by Sato (Sato, 1971), and the stochastic probability model by Shibata (Shibata and Takeyama, 1977, Shibata, 1996) Models for pit propagation include the Pickering–Frankenthal model (Pickering and Frankenthal, 1972), which assumes passive walls and an active base, the Galvele modification of the Pickering–Frankenthal model (Galvele, 1976), which accounts for the effects of metal ion hydrolysis on pH suppression, and the Beck–Alkire model, which deals with a hemispherical pit covered by a thin, resistive halide film (Beck and Alkire, 1979) Henshall was the first to apply

probabilistic pitting models to the performance assessment of high-level waste containers (Henshall, 1992, 1994, 1996a)

2.8.4.2 Probabilistic Pitting Model

A probabilistic model has been developed for pitting of the CRM in the harsh crevice environment (Farmer, 1997, Farmer and McCright, 1998) This model divides the container surface into a two-dimensional (2D) array of hypothetical cells, where probabilities for the transition from one pitting state to another can be assigned As described by Shibata (Shibata and Takeyama, 1977, Shibata, 1996), nucleation or death of a pit embryo is determined by comparing random numbers to an environment-dependent birth or death probability, respectively Random numbers are generated by a power residue method After a pit embryo reaches a critical age, it is assumed to become a stable pit This approach has already been explored for modeling pit initiation and growth on high-level waste containers by Henshall (Henshall, 1992, 1994, 1996a). However, the approach employed by Henshall required additional work to enable it to deal with important environmental parameters, such as pH Furthermore, that approach used functions for calculating the birth and death probabilities could have values much greater than unity (>>1), though the code limited the values to one (≤1) It is better to use probability expressions where all calculated values lie between zero and one, as done by Shibata. This feature has now been incorporated into the probabilistic pitting model described here (Farmer, 1997, Farmer and McCright, 1998)

From empirical observations regarding the roles of Cl^- and $E-E_{crit}$ on pit initiation (birth), as well as empirical observations regarding the roles of OH^- and $E-E_{pass}$ on repassivation (death), the following equations are assumed for the rates of embryo birth and death

$$\lambda_1 = \lambda_0\left[Cl^-\right]\exp\left(\frac{a_\lambda F}{RT}\left(E-E_{crit}\right)\right) \quad , \qquad \text{(Eq 2 8-45)}$$

and

$$\mu_1 = \mu_0\left[OH^-\right]\exp\left(-\frac{a_\mu F}{RT}\left(E-E_{pass}\right)\right) \quad , \qquad \text{(Eq 2 8-46)}$$

where $[Cl^-]$ is the concentration of the chloride anion, $[OH^-]$ is the concentration of the hydroxyl anion, F is Faraday's constant, R is the universal gas constant, T is the absolute temperature, E is the electrochemical potential applied to the surface, E_{crit} is the critical pitting potential, E_{pass} is the repassivation potential, α_λ and α_μ are constants; and λ_0 and μ_0 are intrinsic rate constants for the birth and death of embryos, respectively It is evident that the proposed model involves competitive adsorption of Cl^- and OH^-, which is consistent with the discussion by Strehblow and others (Strehblow, 1995, pp 201–237). This approach introduces the needed dependence on pH The rate of converting an embryo into a stable pit is defined here as the transition rate γ_1. This conversion process is assumed to be thermally activated and governed by the Arrhenius rate law

$$\gamma_1 = \gamma_0 \exp\left(-\frac{A_\gamma}{RT}\right) \quad , \qquad \text{(Eq. 2 8-47)}$$

where A_γ is the apparent activation energy, and γ_0 is the intrinsic rate constant. In lieu of a transition rate, an induction or incubation time can be used The induction time τ_1 is the age

that an embryo must reach before it can become a stable pit. This quantity is also assumed to obey an Arrhenius-like expression

$$\tau_1 = \tau_0 \exp\left(-\frac{A_r}{RT}\right) \quad , \qquad \text{(Eq 2 8-48)}$$

where A_r is the apparent activation energy, and τ_0 is the intrinsic induction time. As described by Shibata [Eqns 63 & 64, (Shibata, 1996)], the birth probability in a single cell ($0 < \lambda < 1$) is calculated from the rate as follows

$$\lambda = 1 - e^{-\lambda_1 \delta t} \qquad \text{(Eq 2 8-49)}$$

The death and transition probabilities are calculated in a similar manner

$$\mu = 1 - e^{-\mu_1 \delta t} \quad , \qquad \text{(Eq 2 8-50)}$$

and

$$\gamma = 1 - e^{-\gamma_1 \delta t} \qquad \text{(Eq 2 8-51)}$$

At a given time step, an embryo will be born in a vacant cell if the following criteria are met.

$$RND \le \lambda \quad , \qquad \text{(Eq 2 8-52)}$$

where *RND* is a random number. The random number embodies the stochastic nature of pitting events on the surface Similarly, an existing embryo will die if

$$RND \le \mu \qquad \text{(Eq 2 8-53)}$$

An embryo will become a stable pit if one of the following criteria are met

$$RND \le \gamma \quad , \qquad \text{(Eq 2 8-54)}$$

or

$$\tau_{age} \ge \tau_1 \quad , \qquad \text{(Eq 2 8-55)}$$

where τ_{age} is the age of the embryo under consideration It was recognized by Henshall that it is necessary to let the birth probability decay with time to obtain a symmetric distribution of pits centered at the mean pit depth (Henshall, 1996a) However, model parameters, such as the birth probability, should be time invariant An expression for the birth probability is proposed that accomplishes the same end as Henshall's formulation, and avoids explicit use of time as an independent variable

$$\lambda = \lambda\left(A\theta_p^n \exp\left[-B\theta_p\right]\right) \quad , \qquad \text{(Eq. 2 8-56)}$$

where A and B are constants, θ_P is the fractional coverage of the surface by stable pits, and n is the exponent of θ_P The ability of such "shape factors" to mimic observed pit distributions may be related to implicit memory effects recognized by Scully and others (Scully, 1997) More desirable alternatives to Eq (56) should be explored in the future

2.8.4.3 Simulations Based On Probabilistic Model of Pit Initiation

Figure 2 8-13a shows the calculated pit distribution, which is typical of those obtained with the stochastic pitting model with time-invariant probabilities Distinguishing characteristics include a peak near the maximum pit depth and a long tail Figure 2 8-13b shows the corresponding pit density (cells or number per 100 cm^2) as a function of time, based on the probabilistic model As expected, the number of vacancies (unpitted area) decreases with time, whereas the number of stable pits increases. Initially, the number of pit embryos increases rapidly with time However, the embryo density reaches a maximum and begins to fall at the point where the rate of embryo conversion to stable pits exceeds the rate of embryo births The overall pit-generation rate is proportional to the embryo density, and also passes through a maximum Calculations were performed with parametric values shown in Table 2 8-18 These values enabled the model to mimic the experimental pit distribution data for Alloy 825 that was collected by Roy and published by Henshall (Henshall, 1996a) In Roy's experiment, samples were exposed to 5 wt% NaCl solution at a pH of 2 57 and a temperature of 90°C for 240 minutes A total of 68 pits were observed in an area of approximately 1 cm^2 The mean depth was 0 345 mm, with a maximum pit depth of 0 505 mm These data are used as a benchmark for model development

Figure 2.8-13. **Use of probabilistic pit-initiation model to simulate the distributions of pit depth observed during experiments with Alloy 825 (data of Ajit Roy). Parameters in the model were adjusted so that the fractional coverage of the surface by stable pits, the average pit depth, and the maximum pit depth could be accurately predicted.**

Table 2.8-18. **Parameter values used in probabilistic pitting model.**

Parameter	Units	Assumed value
λ_0	min^{-1}	$6\ 7572 \times 10^{-2}$
α_λ	none	0 5
E_{crit}	mV versus SCE	+86
μ_0	min^{-1}	$2\ 2137 \times 10^{12}$
α_μ	none	0 5
E_{pass}	mV versus SCE	+1
γ_0	min^{-1}	$5\ 0 \times 10^2$
A_γ	J $mole^{-1}$	$3\ 0 \times 10^4$
τ_0	min	1.0
A_τ	J $mole^{-1}$	$3\ 0 \times 10^4$
A	none	9 0
B	none	3 0
N	none	1 0
K_0	cm^2 L $mole^{-1}$ sec^{-1} V^{-1}	$4\ 4106\ 540 \times 10^{-4}$

The effect of pH suppression on pitting of the CRM was investigated with the probabilistic model. These calculations were also performed with the parametric values given in Table 2.8-18 Figure 2.8-14 shows transients in the vacancy, embryo, and stable-pit densities (cells) that were predicted for two cases, direct exposure to the NFE, and exposure to the low-pH crevice solution In the NFE case, the assumed environment is a 1100 ppm NaCl solution at pH ~7 and 60°C. The CRM is assumed to be polarized at a level slightly above the pitting potential, approximately +90 mV versus SCE In the crevice case, the assumed environment is a 2000 ppm NaCl solution at pH ~3 and 60°C Here too the potential is assumed to be approximately +90 mV versus SCE The number of vacancies (cells without embryos or stable pits) decreases with time in both cases, whereas the number of stable pits increases Initially, the number of pit embryos increases rapidly with time A maximum is reached at the point where the rate of embryo conversion to stable pits (loss) exceeds the rate of embryo births (generation) The overall pit-generation rate is proportional to the embryo density and passes through a maximum Clearly, suppressed pH increases the rate of pit generation, which is consistent with experience. The effect of polarization on the pitting of the inner barrier is shown in Figure 2 8-15. Case A assumes a 1000 ppm TDS NaCl solution at pH ~7, a temperature of 60°C, and an applied potential of –712 mV versus SCE, which corresponds roughly to the corrosion potential of the CAM Case B assumes a 2000 ppm TDS NaCl solution at pH ~3, a temperature of 60°C, and a potential of +90 mV versus SCE, which corresponds roughly to the pitting potential of the CRM Whereas rapid pitting of the CRM is predicted for Case B, no pitting is predicted in Case A. The model predicts that the corrosion potential of the CAM provides some protection for the inner barrier

Figure 2.8-14 **Application of the probabilistic pit-initiation model to predict transients in the density of vacancies, embryos, and stable pits during the polarization of Alloy 825 near the critical pitting potential. Predictions for two assumed cases are compared: 1100 ppm TDS and pH 7, assumed NFE; 2000 ppm TDS and pH 3, assumed crevice condition.**

Figure 2.8-15. **Application of the probabilistic pit-initiation model to predict transients in the density of vacancies, embryos, and stable pits at 60°C. Predictions for two assumed cases are compared. Case A: 1000 ppm TDS, pH 7, and –712 mV SCE (the corrosion potential of CAM). Case B: 2000 ppm TDS, pH 3, and +90 mV versus SCE (pitting potential of CRM).**

2.8.4.4 Deterministic Model of Pit Initiation

A deterministic model has been formulated by Farmer, and can also be used to predict the transients in vacancy, embryo, and stable pit density (Farmer, 1997, Farmer and McCright, 1998) This model gives results comparable to the stochastic pitting model proposed by Shibata (Shibata and Takeyama, 1977, Shibata, 1996), but promises to be more computationally efficient. It was motivated by the similarity between adsorption kinetics and the transition probabilities for birth and death presented by Shibata (Shibata, 1996). The fractions of the surface covered by vacancies, embryos, and stable pits must sum to one

$$\theta_E + \theta_V + \theta_P = 1 \quad , \qquad \text{(Eq. 2.8-57)}$$

where θ_E is the fraction of the surface covered by embryos, θ_V is the fraction of the surface that remains vacant, and θ_P is the fraction of the surface covered by stable pits The

accumulation rate of pit embryos on the surface is determined by the difference in birth and death rates

$$\frac{d\theta_E}{dt} = k_{\text{birth}}\left[\text{Cl}^-\right]^a\left(1-\theta_E-\theta_p\right) - k_{\text{death}}\left[\text{OH}^-\right]^b\theta_E - k_{\text{pit}}\theta_E \quad , \qquad \text{(Eq 2.8-58)}$$

where k_{birth} is analogous to λ_1, k_{death} is analogous to μ_1, and k_{pit} is analogous to γ_1 Consistent with experience, Cl^- is assumed to promote formation of pit embryos, whereas OH^- is assumed to promote repassivation and embryo death It is evident that this proposed model involves competitive adsorption of Cl^- and OH^-, which is also consistent with the discussion by Strehblow and others (Strehblow, 1995, pp 201–237) There is no induction time per se The accumulation rate of stable pits on the surface is then proportional to the fractional coverage of the surface by embryos

$$\frac{d\theta_p}{dt} = k_{\text{pit}}\theta_E \qquad \text{(Eq 2 8-59)}$$

This rate expression assumes that a stable pit evolves from a single embryo In reality, several embryos may coalesce to form a pit Thus, the dependence of the pit generation rate on θ_E may not be first order Coalescence of n embryos would give rise to an nth order rate expression These two first-order, ordinary differential equations can be solved simultaneously by numeric integration with a fourth-order Runge–Kutta algorithm

2.8.4.5 Dependence of the Pit Generation Rate on Electrochemical Potential

The probability of initiating localized corrosion is based on the stochastic probability theory of pit initiation, as discussed by Baroux (Baroux, 1995, pp 265–309) First, the expression for the survival probability is

$$\delta P_s = 1 - \overline{\omega} \times \delta S \quad , \qquad \text{(Eq 2 8-60)}$$

where δP is the survival probability (probability of no pitting) of an infinitesimal area δS on a sample of area S The survival probability of the entire surface S is then

$$P_s = \left[1 - \overline{\omega} \times \delta S\right]^{\frac{S}{\delta S}} \qquad \text{(Eq 2 8-61)}$$

The *pit*-generation rate PGR is then defined in terms of the time derivative of the elementary pitting probability

$$\frac{d\overline{\omega}}{dt} = g = PGR \quad , \qquad \text{(Eq 2 8-62)}$$

where

$$\overline{\omega} = \int_0^t (PGR)dt \qquad \text{(Eq 2 8-63)}$$

We then make the following simplification by assuming that PGR is independent of time and that $\delta S \sim S$ Although it would be better to avoid such gross over simplification, it does provide some degree of insight into the expected dependence of the survival probability, and

the probability of pit initiation, on electrochemical potential This insight is needed to address the question regarding probability of pitting

$$P_s \approx 1 - PGR \times t \times S \qquad \text{(Eq. 2 8-64)}$$

The probability of pitting (localized corrosion, LC) is then assumed to be

$$P_{LC} \approx PGR \times t \times S \qquad \text{(Eq 2 8-65)}$$

It is observed empirically that

$$\ln(PGR) \approx \beta\left(E - E_{pit}\right) \qquad \text{(Eq 2 8-66a)}$$

Therefore,

$$\ln\left(\frac{P_{LC,1}}{P_{LC,2}}\right) \approx \ln\left(\frac{PGR_1}{PGR_2}\right) \approx \beta\left(E_1 - E_2\right) \qquad \text{(Eq. 2 8-66b)}$$

We can estimate the empirical constant β as

$$\beta = \frac{\ln\left(P_{LC,1}/P_{LC,2}\right)}{\left(E_1 - E_2\right)} \qquad \text{(Eq 2 8-66c)}$$

For the purpose of illustration, consider a hypothetical case where the repassivation potential is assumed to be the point at which there is a 5% chance of initiating localized corrosion Furthermore, assume that the average repassivation potential is 800 mV versus SHE, and that the observed scatter around the averate ± 50 mV The probability of initiating localized corrosion at 800 mV versus SHE is assumed to be 5%, and the probability of initiating localized corrosion at 800-50 mV versus SHE is assumed to be 1% In this hypothetical case,

$$\beta = \frac{\ln(5/1)}{(800\ \text{mV} - 750\ \text{mV})} \approx 0\ 032\ \text{mV}^{-1} \qquad \text{(Eq 2 8-66d)}$$

Based on these assumptions, the maximum probability of pitting is calculated to be less than 15% at the 99th percentile, with typical values of 0 01 to 2 12% at the 50th percentile

2.8.4.6 Electrochemical Potential

It is believed that the electrochemical potential at the mouth of the crevice will be somewhere between the mixed potential of A516 Gr 55 and Alloy C-22, in either concentrated J-13 or a representative crevice solution (10 wt% $FeCl_3$) In the absence of $FeCl_3$, the greatest mixed potential at 90°C is expected to be somewhere between –520 and –24 mV versus SHE With 10 wt% $FeCl_3$, potentials as high as +714 mV versus SHE have been observed (Table 2 8-19). Since the observed mixed potential has never exceeded the pitting or repassivation potentials, localized attack is not expected. Several candidate CRMs were anodically polarized in 5 wt% NaCl at pH 2 7, as illustrated by Figure 2.8-16. Severe pitting was observed in Alloy 825 at 600 mV versus Ag/AgCl ($E > E_{pass}$) In contrast, no pitting was

observed in Alloy C-22 at the same potential ($E < E_{pass}$) Data summarized in Table 2 8-20 also indicates no localized attack of Alloy C-22 at potentials below the repassivation potential ($E < E_{pass}$)

Figure 2.8-16. Photographs of candidate CRM materials subjected to severe polarization in acid chloride solutions (LLNL data collected by Ajit Roy). Alloy 825 is much more prone to pitting than Alloy C-22. It is believed that no pitting of Alloy C-22 has been observed below the repassivation potential, which is assumed to be the threshold for localized corrosion.

Table 2.8-19. Expected electrochemical potentials in repository, based on measurements of A516 Gr 12 (CAM) and Alloy C-22 (CRM).

Case	A	B	C	D	E
T (°C)	90	90	90	90	90
NaCl (wt%)	10	1	0	0	5
$FeCl_3$ (wt%)	0	0	0 6	3 1	0
PH	6 8	2 7	2 14	1 72	2 7
Radiolysis	No	No	No	No	No
Deaerated	No	Yes	Yes	Yes	No
E_{corr} (mV versus SHE) A516 Gr 55					-520
E_{corr} (mV versus SHE) C-22	–24	–29	+661	+714	
E_{pit} (mV versus SHE) C-22	+442	+758	+905	+889	> +730
E_{pass} (mV versus SHE) C-22	+550	+793	+857	+896	> +730
Above threshold potential	No	No	No	No	No

Table 2.8-20. Potentiostatic polarization of Alloy C-22 in acidic salt solutions at LLNL (Roy).

T (°C)	NaCl (wt%)	$FeCl_3$ (wt%)	pH	E_{corr} (mV versus Ag/AgCl)	E_{corr} (mV versus E_{corr})	Duration (hours)	Observation	ID #
30	5	0	2 6–2 7	–31	681	167	No attack	062797C1 PS
30	5	0	2 6–2 7	177	423	167	No attack	041497C1 PS
30	5	0	2 6–2 7	155	545	167	No attack	041497C2 PS
60	5	0	2 6–2 7	–147	847	167	Slight crevice	042197C2 PS
90	5	0	2 6–2 7	247	600	26 5	No attack	112097C1 PS
90	0	3 05	1 68	447	880	167	Slight crevice	110697C1 PS

From transport modeling of corrosion in the CAM–CRM crevice, it is known that the electrochemical potential inside the crevice is less anodic (less severe) than the potential established or applied at the mouth of the crevice (Farmer, 1997, Farmer and McCright, 1998) This is due to ohmic drop along the length of the crevice Consequently, any estimate of corrosion rate based on the electrochemical potential at the crevice mouth, coupled with the assumption of suppressed pH and elevated chloride inside the crevice, should be conservative.

Smailos, Schwarzkopf, and Koster state (Smailos, Schwarzkopf, and Koster, 1986) "Hastelloy C-4 has also resisted pitting corrosion and stress corrosion cracking, in the absence of irradiation, and its corrosion rate has been low at all testing temperatures (< 1 μm/yr), but it has been attacked by crevice corrosion " However, they go on to state that when it is exposed to gamma irradiation at ~10^5 rad/hr, pitting corrosion was observed This pitting corrosion is believed by several investigators in the field to be due to the formation of oxidants such as H_2O_2, which shift the corrosion potential in the anodic direction, closer to the pitting and repassivation potential Glass performed definitive radiolysis experiments at LLNL showing that the corrosion potential of 316L stainless steel in 0 018 M NaCl at 30°C shifted from approximately –100 mV versus SCE to approximately +100 mV versus SCE when exposed to gamma irradiation (3 3 × 10^6 rad/hr) from a Co-60 source (Glass et al., 1986). The level of radiation expected at the outer surface of the CRM at the instant of CAM penetration is estimated to be several orders of magnitude less than these exposures (10^5–10^6 rad/hr). Note that radiolysis could also form other oxidants However, such effects are not expected to be great at low levels of radiation

2.8.4.7 Growth and Stifling of Stable Pits

Propagation of a stable pit requires that the local electrochemical potential remain above a threshold ($E > E_{pass}$). If this condition is met, propagation occurs at a rate that is depth-dependent. The depth can be calculated from the age of the pit As the pit becomes deeper, the rate becomes slower due to mass-transport limitations. The maximum possible depth can then be estimated with an appropriate stifling criterion, which is based on a limiting mass flux

Determination of the distribution of pit depths requires calculation of the pit penetration d, which is a function of pit age T_{age} The corresponding penetration rate can be assumed to be limited by either diffusion or electromigration Both cases yield a square-root dependence of the pit depth on time Diffusion-limited penetration will be discussed briefly in the following section Here, for the sake of illustration, the penetration is assumed to obey the following empirical expression·

$$d = \sqrt{2KT_{age}} \quad , \qquad \text{(Eq 2 8-67a)}$$

where the rate constant K is defined as

$$K = K_0\left[H^+\right](E - E_{crit}) \quad , \qquad \text{(Eq 2 8-67b)}$$

where K_0 is a constant, $[H^+]$ is the hydrogen ion concentration, E is the applied voltage, and E_{crit} is the critical pitting potential It should be noted that this expression implies growth driven by the electric field Future pitting calculations should use assumptions that are more consistent with those implicit in the crevice model, such as the assumption of a strong supporting electrolyte

In principle, a pit will cease to grow (die) if the depth becomes so great that the current density at the base of the pit falls below the passive current density The importance of "stifling" has also been pointed out by Marsh (Marsh, Taylor, and Sooi, 1988). In the case of pit propagation in carbon steel, Marsh gives the following criterion based on the passive current density and the diffusive flux of dissolved oxygen.

$$\frac{i_{pass}}{4F} \le -D\frac{\partial C(x,t)}{\partial x}\bigg|_{x=0} , \qquad \text{(Eq 2.8-68)}$$

where i_{pass} is the passive current density at the base of the pit, F is Faraday's constant, D and C are the diffusivity and concentration of dissolved oxygen, respectively, x is the distance into the pit from the mouth of the pit, and t is time It was noted that careful measurements of i_{pass} are required for any theoretical analysis The critical concentration gradient across the pit is estimated to be

$$-\frac{\Delta C}{\Delta x}\bigg|_{critical} \ge \frac{i_{pass}}{4FD} \qquad \text{(Eq 2 8-69)}$$

Alternatively, given a maximum possible differential concentration of dissolved oxygen, the maximum possible pit depth at stifling (death) can be calculated

$$\Delta x \le -\frac{4FD\Delta C}{i_{pass}} \qquad \text{(Eq 2 8-70a)}$$

The largest critical pit depth occurs when the dissolved oxygen is saturated at the mouth of the pit, and entirely depleted at the base of the pit ($\Delta C \approx 0 - C_{sat}$)

$$\Delta x \le \frac{4FDC_{sat}}{i_{pass}} \qquad \text{(Eq 2 8-70b)}$$

Estimates of the critical pit depth, based on the diffusion-limited current density associated with oxygen reduction are summarized in Table 2 8-21 The following assumptions were made. $F = 9\ 64846 \times 10^4$ C equiv^{-1}, $D \approx 10^{-5}$ cm^2/s, and $i_{pass} = 4 \times 10^{-6}$ A/cm^2 The oxygen solubilites were given by Andresen (Andresen, 1998, p 12)

Table 2.8-21. Pit-stifling criterion based on flux of dissolved oxygen at 25°C.

NaCl (wt%)	O_2 (ppm)	O_2 (mol/cm^3)	Δx (cm)
0	8 2	$2\ 56 \times 10^{-7}$	0 25
3 5	6 8	$2\ 13 \times 10^{-7}$	0 20
5	6 0	$1\ 88 \times 10^{-7}$	0 18
16	2 9	$9\ 06 \times 10^{-8}$	0 09
Satd	< 2 0	$<6\ 25 \times 10^{-8}$	<0 06

An alternative criterion for pit stifling can be formulated based on the diffusion-limited flux of dissolved metal inside the pit In the case of a multicomponent material, such as Alloy C-22, the modified stifling criterion can be expressed in terms of the total concentration gradient of the ith dissolved metal (Fe, Ni, Cr, Mo, or W)

$$\frac{\Delta C_i}{\Delta x}\bigg|_{critical} \ge \frac{f_i}{n_i}\frac{i_{pass}}{FD_i} , \qquad \text{(Eq 2 8-71a)}$$

where C_i is the total concentration of the ith dissolved metal, x is the distance from the mouth of the pit, f_i is the mole fraction of the passive current producing the ith dissolved metal, i_{pass} is the passive current density at the base of the pit, n_i is the the number of electrons involved in the anodic dissolution of the ith dissolved metal, F is Faraday's constant, and D_i is the apparent or overall diffusivity of the ith dissolved metal. To transport dissolved metal out of the pit without accumulation, precipitation, passivation, and stifling, this critical concentration gradient must be maintained If one assumes $f_i = 0\ 01$, $i_{pass} = 4 \times 10^{-6}$ A/cm^2, $n_i = 6$, $F = 9\ 64846 \times 10^4$ C/equiv, $D_i \sim 10^{-5}$ cm^2/s and $\Delta x = 2$ cm, the critical differential concentration, ΔC_i, is estimated to be 1.38×10^{-8} mol/g ($1\ 38 \times 10^{-5}$ mol/kg). Values of the mole fraction f_i are given in Table 2 8-22 Note that the solubility of WO_3 is only ~10^{-10} mol/kg at pH ~ 2. If any dissolved species at the base of the pit has a solubility less than this limiting value, the pit will die before wall penetration is achieved Alternatively, given a maximum possible differential concentration, the maximum possible pit depth at stifling (death) can be calculated

$$\Delta x \le \frac{n_i F D_i \Delta C_i}{f_i i_{pass}} \qquad \text{(Eq 2 8-71b)}$$

The largest differential concentration and the largest critical pit depth occur when the solution at the base of the pit is saturated and when the concentration at the mouth of the pit is zero

$$\Delta x \le \frac{n_i F D_i C_{sat,i}}{f_i i_{pass}} \qquad \text{(Eq 2 8-71c)}$$

Table 2.8-22. Alloy composition assumed for congruent dissolution of Alloy C-22, required by modified pit-stifling criterion.

Component	Wt. fract	MW	mol/gram	mol fract. (f_i)
Fe	0 04	55 847	0 000716243	0 043879444
Co	0 02	58 9332	0 000339367	0 020790788
Cr	0 21	51 996	0 004038772	0 24742885
W	0 03	183 85	0 000163177	0 009996745
Mo	0 13	95 94	0 001355014	0 083012714
Ni	0 57	58 7	0 009710392	0 594891456
Total	1			1

The solubilities of various oxides and hydroxides believed to be formed during dissolution of Alloy C-22 are given by Pourbaix (Pourbaix, 1966). From the solubility versus pH curves given by Pourbaix, it appears that the following empirical relation is obeyed over limited ranges of pH

$$\log\left[C_{sat,i}\right] = m_i \times \left[\mathrm{pH}\right] + b_i \quad , \qquad \text{(Eq 2 8-72)}$$

where $C_{sat,i}$ is the concentration of the ith dissolved metal at saturation (mol/kg), m_i is the slope, and b_i is the intercept. Values of the slope and intercept were estimated from the curves

of Pourbaix and are also given in Table 2 8-23 This abstracted model for solubility was used to estimate the logarithims of solubilities given in Table 2 8-24

Table 2.8-23. Solubilities given by Pourbaix for various compounds responsible for passivation of Alloy C-22.

Film species	$\log(C_{i,1})$	pH_1	$\log(C_{i,2})$	pH_2	m_i	b_i	Ref.
$Fe(OH)_2$	–2 5	8	–6 5	10	–2	13 5	Pourbaix p 311
$Fe(OH)_3$	–1	2	–3	3	–2 00	3 00	Pourbaix p 311
Fe_2O_3	–1	0	–8	2 5	–2 80	–1 00	Pourbaix p 311
$Ni(OH)_2$	–1	6 5	–8	10	–2 00	12 00	Pourbaix p 336
$Cr(OH)_3$	–3	2 5	–12	5 7	–2 81	4 03	Pourbaix p 268
Cr_2O_3	–3	3 7	–9 5	6	–2 83	7 46	Pourbaix p 268
$Cr(OH)_3$–nH_2O	0	4	–4	6	–2 00	8 00	Pourbaix p 268
MoO_3	–3 7	0	1	4 7	1 00	–3 70	Pourbaix p 276
WO_3	–8	3	0	7	2 00	–14 00	Pourbaix p 283

Table 2.8-24. Predicted logarithims of solubilities at various pH values based on slopes and intercepts in Table 2.8-23.

pH	$Fe(OH)_2$	$Fe(OH)_3$	Fe_2O_3	$Ni(OH)_2$	$Cr(OH)_3$	Cr_2O_3	$Cr(OH)_3$–nH_2O	MoO_3	WO_3
–1	15 50	5 00	1 80	14 00	6 84	10 29	10 00	–4 70	–16 00
0	13 50	3 00	–1 00	12 00	4 03	7 46	8 00	–3 70	–14 00
1	11 50	1 00	–3 80	10 00	1 22	4 63	6 00	–2 70	–12 00
2	9 50	–1 00	–6 60	8 00	–1 59	1 80	4 00	–1 70	–10 00
3	7 50	–3 00	–9 40	6 00	–4 40	–1 03	2 00	–0 70	–8 00
4	5 50	–5 00	–12 20	4 00	–7 21	–3 86	0 00	0 30	–6 00
5	3 50	–7 00	–15 00	2 00	–10 02	–6 69	–2 00	1 30	–4 00
6	1 50	–9 00	–17 80	0 00	–12 83	–9 52	–4 00	2 30	–2 00
7	–0 50	–11 00	–20.60	–2 00	–15 64	–12 35	–6 00	3 30	0 00
8	–2 50	–13 00	–23 40	–4 00	–18 45	–15 18	–8 00	4 30	2 00
9	–4 50	–15 00	–26 20	–6 00	–21 26	–18 01	–10 00	5 30	4 00
10	–6 50	–17 00	–29 00	–8 00	–24 07	–20 84	–12 00	6 30	6 00

Based on the estimated solubilites given in Table 2 8-24, the critical pit depths were calculated and are given in Table 2 8-25 Ranges of pH where localized corrosion is stiffled by a particular film-forming compound are in boldface type The pit depth is limited to a different extent by each oxide or hydroxide At low pH, MoO_3 and WO_3 appear to be primarily responsible for the superior corrosion performance of Alloy C-22. Based on this calculation, one would expect the localized corrosion of Alloy C-22 to be stifled over the entire range of pH, extending from –1 to 10 This is consistent with observations in acidic media of interest (simulated crevice solution of 10 wt% $FeCl_3$) There are unusual acidic environments where corrosion is known to occur. Both experience and calculation appear to indicate that pits should not propagate in Alloy C-22 during exposure to crevice conditions

Soluble oxychlorides have not been considered in the initial calculation, but should be included in future calculations.

Table 2.8-25. Maximum possible pit depths (Δx/cm) in Alloy C-22 predicted with modified stifling criterion, assuming $\Delta C \sim 100\%$, C_{sat}, and $i_{pass} \sim 4\ \mu A/cm^2$.

pH	$Fe(OH)_2$	$Fe(OH)_3$	Fe_2O_3	$Ni(OH)_2$	$Cr(OH)_3$	Cr_2O_3	$Cr(OH)_3$–nH_2O	MoO_3	WO_3
–1	$3\ 48 \times 10^{19}$	$1\ 65 \times 10^{9}$	$1\ 04 \times 10^{6}$	$8\ 11 \times 10^{16}$	$2\ 02 \times 10^{10}$	$5\ 70 \times 10^{13}$	$2\ 92 \times 10^{13}$	$3\ 48 \times 10^{-1}$	$1\ 45 \times 10^{-11}$
0	$3\ 48 \times 10^{17}$	$1\ 65 \times 10^{7}$	1.65×10^{3}	$8\ 11 \times 10^{14}$	$3\ 13 \times 10^{7}$	$8\ 43 \times 10^{10}$	$2\ 92 \times 10^{11}$	3 48	$1\ 45 \times 10^{-9}$
1	$3\ 48 \times 10^{15}$	$1\ 65 \times 10^{5}$	2 61	$8\ 11 \times 10^{12}$	$4\ 85 \times 10^{4}$	$1\ 25 \times 10^{8}$	$2\ 92 \times 10^{9}$	$3\ 48 \times 10^{1}$	$1\ 45 \times 10^{-7}$
2	$3\ 48 \times 10^{13}$	$1\ 65 \times 10^{3}$	$4\ 14 \times 10^{-3}$	$8\ 11 \times 10^{10}$	$7\ 52 \times 10^{1}$	$1\ 85 \times 10^{6}$	$2\ 92 \times 10^{7}$	$3\ 48 \times 10^{2}$	$1\ 45 \times 10^{-5}$
3	$3\ 48 \times 10^{11}$	$1\ 65 \times 10^{1}$	$6\ 57 \times 10^{-6}$	$8\ 11 \times 10^{8}$	1.16×10^{-1}	$2\ 73 \times 10^{2}$	$2\ 92 \times 10^{5}$	$3\ 48 \times 10^{3}$	1.45×10^{-3}
4	$3\ 48 \times 10^{9}$	$1\ 65 \times 10^{-1}$	$1\ 04 \times 10^{-8}$	$8\ 11 \times 10^{6}$	1.80×10^{-4}	$4\ 04 \times 10^{-1}$	$2\ 92 \times 10^{3}$	$3\ 48 \times 10^{4}$	$1\ 45 \times 10^{-1}$
5	$3\ 48 \times 10^{7}$	$1\ 65 \times 10^{-3}$	$1\ 65 \times 10^{-11}$	$8\ 11 \times 10^{4}$	$2\ 79 \times 10^{-7}$	5.97×10^{-4}	$2\ 92 \times 10^{1}$	$3\ 48 \times 10^{5}$	$1\ 45 \times 10^{1}$
6	$3\ 48 \times 10^{5}$	$1\ 65 \times 10^{5}$	$2\ 61 \times 10^{-14}$	$8\ 11 \times 10^{2}$	$4\ 33 \times 10^{-10}$	$8\ 83 \times 10^{-7}$	$2\ 92 \times 10^{-1}$	$3\ 48 \times 10^{6}$	$1\ 45 \times 10^{3}$
7	$3\ 48 \times 10^{3}$	$1\ 65 \times 10^{-7}$	4.14×10^{-17}	8 11	$6\ 70 \times 10^{-13}$	$1\ 31 \times 10^{-9}$	$2\ 92 \times 10^{-3}$	$3\ 48 \times 10^{7}$	$1\ 45 \times 10^{5}$
8	$3\ 48 \times 10^{1}$	$1\ 65 \times 10^{-9}$	$6\ 57 \times 10^{-20}$	$8\ 11 \times 10^{-2}$	$1\ 04 \times 10^{-15}$	1.93×10^{-12}	$2\ 92 \times 10^{-5}$	$3\ 48 \times 10^{8}$	$1\ 45 \times 10^{7}$
9	$3\ 48 \times 10^{-1}$	$1\ 65 \times 10^{-11}$	$1\ 04 \times 10^{-22}$	8.11×10^{-4}	$1\ 61 \times 10^{-18}$	$2\ 86 \times 10^{-15}$	2.92×10^{-7}	$3\ 48 \times 10^{9}$	$1\ 45 \times 10^{9}$
10	$3\ 48 \times 10^{-3}$	1.65×10^{-13}	$1\ 65 \times 10^{-25}$	$8\ 11 \times 10^{-6}$	$2\ 49 \times 10^{-21}$	$4\ 23 \times 10^{-18}$	$2\ 92 \times 10^{-9}$	$3\ 48 \times 10^{10}$	$1\ 45 \times 10^{11}$

Notes
1 Ranges of pH where localized corrosion is stiffled by a particular film-forming compound are in boldface type
2 At low pH, MoO_3 and WO_3 appear to be primarily responsible for the superior corrosion performance of Alloy C-22
3 Localized corrosion should be stiffled over the entire range of pH, extending from –1 to 10
4 This is consistent with observations in relevant (anticipated) acidic media
5 Soluble oxychlorides have not been included in initial calculation, but will be included in the future

2.8.5 Stress Corrosion Cracking

2.8.5.1 Criterion for SCC

For stress corrosion cracking (SCC) to occur, three factors have to exist stress, a flaw (crack-initation site), and a material-specific corrosive environment Flaws can either pre-exist due to poor manufacturing practices or be initiated at locations where high stress concentration exists, such as grooves and corrosion pits Stress can exist due to welding residual stress, shrink-fit stress, or weight stress. These contributions to stress are illustrated in Figure 2.8-17 and are summarized in Table 2.8-26 Fracture mechanics is, by far, the best approach to assess the tendency for SCC to occur Once a crack is initiated, the crack will grow by SCC when the applied stress intensity factor K is equal to or larger than SCC resistance parameter K_{ISCC}, as follows

$$K \geq K_{ISCC} \quad . \qquad \text{(Eq 2 8-73)}$$

Figure 2.8-17. There appear to be three contributions to the overall stress in an unperturbed, horizontally placed high-level waste container that could promote stress corrosion cracking (SCC). These are the weight stress, the weld stress, and the shrink-fit stress. Note that r_o is the outer radius of the outer barrier (CAM), r_i is the outer radius of the inner barrier, R is the inner radius of the outer barrier, L is the length of the container between supports, and E is the modulus (CAM or CRM).

Table 2.8-26. Three contributions to stress in unperturbed waste package.

Quantity	Weight stress (MPa)	Shrink-fit stress (MPa)	Maximum residual weld stress (MPa)	Maximum total stress (MPa)
A516 Gr 55	0 46	40	205	245
Alloy C-22	2 6	0	407	409 6
Alloy 625	2 6	0	483	485 6

K_{ISCC} is a material- and environment-dependent property that can be obtained through fracture mechanics testing of the materials in the specified environment The stress intensity factor can be calculated with the following fracture mechanics formula

$$K = \beta\sigma(\pi a)^{1/2} \quad , \qquad \text{(Eq 2 8-74)}$$

where β is a geometry factor dependent on the shape of the crack For a surface elliptical crack with depth (a) and length ($2c$) under tensile loading, β depends upon the aspect ratio (a/2c) The solutions for β are readily available in typical fracture mechanics textbooks such as the one written by Anderson (Anderson, 1995), and will not be duplicated here Equation 74 applies only to an ideal crack For a corrosion pit, a small crack must be initiated at the base of the pit before it can grow by SCC A crack can be initiated in several ways such as over-load induced tearing, grain boundary sensitization, or breakage of a near-by inclusion To determine exactly when a small crack will be initiated is a difficult task In our analysis, we assume that a crack fissure with the length of δa is readily developed along the base of the pit on the plane normal to the applied stress direction. It is further assumed that δa is determined by the size of one grain, which is estimated to be approximately 40 μm (0 0015 inches) An idealized crack initiation site is illustrated in Figure 2 8-18 Under this situation, the criteria for this crack to continue to grow by SCC can be expressed by the following formula

$$K = a\beta\sigma\left[\pi\left(a_{\text{pit}} + \delta a\right)\right]^{1/2} \quad , \qquad \text{(Eq 2 8-75)}$$

where a_{pit} is the depth of the pit, β is a geometry factor dependent on the depth and aspect ratio of the pit (as described in Eq 74), and α is another geometry factor that accounts for the fact that the pit and crack fissure do not constitute an ideal crack The solution for α has been derived by Newman in graphical form (Newman, Year?). It should be noted that for the asymptotic situation, where the crack fissure size is much less than the depth of the corrosion pit ($\delta a << a_{pit}$), the applied stress intensity factor can be expressed as

$$K = \beta K_t \sigma(\delta a)^{1/2} \quad , \qquad \text{(Eq. 2.8-76)}$$

where K_t is the elastic stress concentration factor at the tip of the pit and is calculated as

$$K_t = 1 + \frac{2a}{c} \quad . \qquad \text{(Eq. 2 8-77a)}$$

Figure 2.8-18. Conceptual representation of the ideal flaw (pit or other imperfection) that was used as the basis for calculating the critical flaw size for initiation of stress corrosion cracking (SCC).

2.8.5.2 Stress Analysis

SCC of A516 Gr 55, Alloy 625, or Alloy C-22 can initiate at a pre-existing flaw or pit of critical size, provided that there is adequate stress It is assumed that there are three contributions to the stress of an unperturbed high-level waste container· weight stress, shrink-fit stress, and weld stress In the base metals of containers, the only stresses that exist are the weight stress and shrink-fit stress

2.8.5.3 Weight Stress

The weight stress can be calculated by the elasticity theory of a beam, which is given as

$$\sigma = \frac{Mr}{I} \qquad \text{(Eq 2 8-77b)}$$

where the the stress along the longitudinal direction of the container is σ, and the distance of any location of interest away from the center-axis of the container is r The moment of inertia of the cross section of the container is I

$$I = \frac{\pi\left(r_o^4 - r_i^4\right)}{4} \quad , \qquad \text{(Eq 2 8-77c)}$$

where r_o and r_i are the outer and inner radius of the cylinder container. For the analysis of the outer barrier, r_o is taken as 0 825 m (32 48 in), and r_i is taken as 0 725 m (28 54 inches) For the analysis of the inner barrier, r_o is taken as 0 725 m (28 54 inches), and r_i is taken as 0 705 m (27 75 inches) Eq 2 8-77d is used to calculate M in Eq 2 8-73b.

$$M = \frac{1}{8pL^2} \quad , \qquad \text{(Eq 2.8-77d)}$$

where L is the length of the container between base supports of the container, and p is the uniformly distributed weight along the length of the container In our analysis, L is taken as half of the total container length (L = 2.67 m). The weight of the package W is estimated to be 50,423 kg. Then p can be calculated as

$$p = \frac{W}{2L} \qquad \text{(Eq. 2 8-77e)}$$

Based on the above equations, the maximum weight stresses calculated for the container system are 0 46 MPa in the CAM (A516 Gr 55) and 2 6 MPa in the CRM (Alloy 625 or C-22)

2.8.5.4 Shrink-fit Stress

The stresses due to the shrink fitting of two cylinders are treated by Shigley and Mischke (Shigley and Mischke, 1989, pp 62–63) At the outer surface of the CAM, the tangential shrink-fit stress can be calculated as

$$\sigma_o = 2p\left[\frac{R^2}{\left(r_o^2 - R^2\right)}\right] \quad . \qquad \text{(Eq 2 8-77f)}$$

At the CAM–CRM interface, the maximum tangential stress in the inner cylinder (CRM) can be calculated as

$$\sigma_i = p\left[\frac{\left(R^2 + r_i^2\right)}{\left(R^2 - r_i^2\right)}\right] \quad , \qquad \text{(Eq 2 8-78)}$$

where r_o is the outer radius of the DAM, taken as 0 825 m (32 48 in), R is the inner radius of the outer container, taken as 0 725 m (28 54 inches), and r_i is the inner radius of the inner container, taken as 0.705 m (27.75 inches) The contact pressure on the CAM–CRM interface due to the slight over-size of the outer radius of the CRM relative to the inner radius of the CAM is

$$p + \frac{E\delta}{R}\left[\frac{\left(r_o^2 - R^2\right)\left(R^2 - r_i^2\right)}{2R^2\left(r_o^2 - r_i^2\right)}\right] \quad , \qquad \text{(Eq 2 8-79)}$$

where the oversize is quantified through the radial interference δ, which is assumed to be 0 89 mm (0 035 inches) The elastic modulus E of both the CAM and CRM was assumed to be approximately 207,000 MPa (30,000 ksi) in this preliminary analysis Based on the above equations, the contact pressure is calculated as 5 85 MPa (847.5 psi), the shrink-fit stress at the outer surface of the CAM is calculated as 40 MPa (5,742 psi), and the maximum shrink-fit stress for the CRM is calculated as –207 Mpa (30,199 psi), which is a compressive stress It is noted that the maximum shrink-fit stress of the CRM will approach zero as the CAM undergoes corrosive dissolution Therefore, the shrink-fit stress in the CRM is assumed to be zero

2.8.5.5 Weld Stress

In the welds, the welding residual stress has to be considered In the fabrication of the waste package containers, the welds will be mostly stress relieved except the final closure weld, which has not been specified to be relieved In this case, the welding residual stress can be as high as the yield strength of the material The yield strength is 205 MPa for A516 Gr 55, 407 MPa for Alloy C-22, and 483 MPa for Alloy 625 (Huang, 1998)

2.8.5.6 SCC Resistance

Fracture mechanics SCC testing has been performed on Alloys 625 and C-22 by Roy (Roy, Fleming, and Lum, 1998). Preliminary measured values of K_{ISCC} are 30 MPa $m^{1/2}$ for Alloy C-22 and 33 MPa $m^{1/2}$ for Alloy 625 These values are summarized in Table 2 8-27 and were used in this preliminary analysis to determine whether or not SCC will occur in flaws or corrosion pits developed in these alloys Also refer to Section 2 4 of this report for more information on SCC measurements.

For carbon steel, a correlation between K_{ISCC} and Vicker hardness has been reported for aqueous solutions of NaCl (3 5 wt%) (Davis, 1996, p 349) Because the Vicker hardness for

A516 Gr 55 carbon steel is typically 120, the K_{ISCC} of this material is estimated to be approximately 71 MPa $m^{1/2}$.

Table 2.8-27. Measured values of K_{ISCC} (Roy).

Material	K_{ISCC} (MPa $m^{1/2}$)
A516 Gr 55	~71
Alloy 625	~33
Alloy C-22	~30

2.8.5.7 Results of SCC Analysis

Corrosion pits can be developed at welds and base metals of waste package containers after long exposure to the environment These act as stress risers to initiate crack fissures at the bases of the pits SCC can be initiated at these pits when the applied stress intensity factors are equal to or larger than K_{ISCC} Using the expression for K given as Eq (75) and the K_{ISCC} data from the previous section, the critical flaw size for initiation can be defined ($K = K_{ISCC}$) These critical flaw sizes have been calculated and are given in Table 2 8-28 as a function of aspect ratio ($a/2c$) at various stress levels Note that the critical flaw sizes for SCC initiation is always larger than the thickness of the respective barriers, except at extremely high aspect ratio ($a/2c$~5) At this very high aspect ratio ($a/2c$~5), the critical flaw sizes for SCC initiation in unannealed welds of Alloys 625 and C-22 are 1 2 cm and 1 4 cm, respectively Because these values are somewhat less than the wall thickness (2 cm), SCC may be possible in the unannealed closure weld Because stresses in the base metals are expected to be much lower than that in the corresponding, unannealed welds, it is concluded that SCC should not occur in the base metals Even though the weld residual stress can be very high, it has been observed by Henshall and Roy that the aspect ratio of corrosion pits in Alloy 825 seldom exceeds one ($a/2c$<1) (Henshall, 1996a) Such pits are shown in Figure 2 8-16 The results in Table 2 8-28 suggest that SCC will not occur at corrosion pits at welds, even if the welds are not stress relieved

The current analysis is based on linear elastic fracture mechanics When the stress applied on a crack or corrosion pit is close to or beyond yield stress, there is a possibility that the linear elastic fracture overestimates the critical flaw size for initiation of SCC Under this situation, elastic–plastic fracture mechanics based on the J-integral approach should be used To use this elastic–plastic fracture mechanics approach, accurate stress–strain curves for each material are needed to characterize its strain-hardening behavior We will pursue such data and conduct elastic–plastic fracture mechanics analysis in the future In the interim stage, we recommend that the maximum stress on the welds be relieved to less than 75% of the yield strength of the material

Table 2.8-28. Critical flaw size required to initiate stress corrosion cracking.

	a/2c = 0 25	a/2c = 0 5	a/2c = 1	a/2c = 2	a/2c = 5
A516 Gr 55 (t = 100 mm)					
245 MPa	> t	> t	> t	> t	> t
153 8 MPa	> t	> t	> t	> t	> t
102 5 MPa	> t	> t	> t	> t	> t
Alloy 625 (t = 20 mm)					
485 6 MPa	> t	> t	> t	> t	12 mm
362 3 MPa	> t	> t	> t	> t	> t
241 5 MPa	> t	> t	> t	> t	> t
Alloy C-22 (t = 20 mm)					
409 6 MPa	> t	> t	> t	> t	14 mm
305 3 MPa	> t	> t	> t	> t	> t
203 5 MPa	> t	> t	> t	> t	> t

Values greater than the wall thickness t will not lead to SCC

2.8.6 Thermal Embrittlement

2.8.6.1 Background on Thermal Embrittlement

In the current repository design, the temperature of high-level waste containers loaded with 10-year spent nuclear fuel (SNF) is expected to reach a peak temperature of 200°C after 10 years of emplacement The waste package will require approximately 1000 years to cool to 100°C This extended period at elevated temperature has lead to concern regarding the possibility of thermal embrittlement (TE), which is also known as temper embrittlement It is well known that fracture toughness in steels, especially in low-alloy steels, is severly reduced by isothermal aging or slow cooling in the 350° to 575°C range It is also recognized that the segregation of impurities, such as Sb, P, Sn, and As at grain boundaries, is the main cause of TE The most potent embrittling elements, in order of decreasing potency, are As, Sn, P, and As However, Sb, Sn, and As are not generally present in steels Thus, phosphorous poses the greatest threat of TE in materials such as A516 McMahon has concluded in his review that plain carbon steels containing less than 0 5 wt% Mn are not susceptible to TE (McMahon, 1968, pp. 127–167) However, higher levels of Mn may enhance P-induced TE It is apparent that not enough data exist on the long-term aging of carbon steels to completely disregard the possibility of TE, especially in the case of high-Mn steels

2.8.6.2 TE Predictive Model

To address this issue, we have analyzed the segregation of P in steels after both a typical thermal embrittlement cycle at 350 to 575°C, and a typical temperature cycle expected in a high-level waste container These two profiles are shown in Table 2 8-29

Table 2.8-29. Predicted segregation of phosphorous at grain boundaries of carbon steel.

Temperature (°C)	Time (days)	Segregation of P
Typical thermal embrittlement cycle in steels		
575	0 04	0 84
538	0 08	0 88
524	0 5	0 89
496	2	0 91
468	3	0 93
350	5	0 97
Expected waste-package temperature cycle		
200	1,825	0 005
180	36,500	0 011
140	365,000	0 012
80	3,650,000	0 012

Estimates of the extent of TE rely on both thermodynamics, kinetics, and transport phenomena McLean developed a theory of grain-boundary segregation using statistical thermodynamics (McLean, 1957) His expression [Eq (80)] is used to calculate the segregation of P at grain boundaries after thermodynamic equilibrium is reached

$$\frac{X_b}{(1-X_b)} = \left[\frac{X_c}{(1-X_c)}\right]\exp\left(-\frac{\delta G}{RT}\right) \quad , \qquad \text{(Eq 2 8-80)}$$

where X_b is the equilibrium fraction of grain boundary being covered with a monolayer of the impurity of concern, X_c is the solubility of the impurity in the matrix, and δG is the Gibbs free energy of segregation For phosporous segregation in steel, Bruce and his coworkers have derived δG as a function of temperature T based on experimental data (Druce, Gage, and Jordan, 1986) This is represented by

$$\delta G(\text{J/mol}) = -63000 + 21\,0 \times T(K) \qquad \text{(Eq 2 8-81)}$$

The solubility of P in steels, X_c, can be estimated by inspection of the Fe-P phase diagram (Massalski, 1986) Two data points, one at 400°C and another at 443°C, were obtained and fit to an the Arrhenius expression

$$X_c = 0.19 \times \exp\left[-\frac{2598}{T}\right] \quad , \qquad \text{(Eq 2 8-82)}$$

where T is in Kelvin. McClean also developed a theory for the kinetics of grain-boundary segregation. The fraction of grain boundary coverage ($X_b(t)$) at a given time t and temperature T is given as

$$\frac{[X_b(t) - X_b(0)]}{[X_b - X_b(0)]} = 1 - \exp\left[\frac{4Dt}{\beta^2 f^2}\right] erfc\left[\frac{4Dt}{\beta^2 f^2}\right]^{0\,5} \quad , \qquad \text{(Eq 2.8-83)}$$

where D is the diffusion coefficient of the solute (phosphorous), and β is the grain-boundary enrichment ratio (X_b/X_c) The remaining parameter f is defined as

$$f = \frac{a^3}{b^2} \quad , \qquad \text{(Eq 2.8-84)}$$

where a and b are the atomic sizes of the matrix and impurity elements, respectively For phosphorous in steels, it is assumed that a and b are 1 24 and 1 0 Å, respectively Bruce developed the following expressing for the diffusion coefficient

$$D = 0\ 25 \exp\left[-\frac{20000(\mathrm{J/mol})}{RT}\right] \qquad \text{(Eq 2 8-85)}$$

2.8.6.3 TE Analysis

Equations (80) through (85) were used to calculate segregation in steel (the fraction of grain boundary being covered with a monolayer of P) after the typical TE cycle in steels and the expected waste package temperature cycle. The results are shown in Table 2 8-29 and indicate that the total grain-boundary segregation of P after the typical TE cycle is 0 97, whereas that for the expected waste package temperature cycle is only 0 012 The segregation expected for the waste package is only about 1 2% of that for the typical TE cycle in steels Therefore, we conclude that TE in the CAM is very unlikely

2.8.7 Microbial Influenced Corrosion (MIC)

The possible acceleration of abiotic corrosion processes by microbial growth has also been a concern Bacteria and fungi alter local environment in biofilm For example, H^+ is known to be generated by bacterial isolates from Yucca Mountain (Horn et al , 1998) Furthermore, thiobaccilus ferrooxidans oxidize Fe^{2+}, while geobacter metallireducens reduce Fe^{3+} Other microbes can reduce SO_4^{2-} and produce S^{2-}. In the future, we hope to calculate concentration transients in biofilms with a relatively simple bioreactor model Also refer to Section 2 5 of this report for additional work or MIC evaluation in Yucca Mountain

2.8.8 Summary

Concentration profiles inside the CAM–CRM crevice have been calculated, first during corrosive attack of the CAM wall, then during corrosive attack of the CRM wall A peak is predicted in the iron concentration near the crevice mouth due to the combined effects of a potential that decays with increasing crevice depth, and the assumed BC of zero concentration at the crevice mouth Calculations for corrosive attack of the CRM wall have also been performed The predicted concentrations of dissolved metals rise sharply from zero at the crevice mouth to peak values inside the crevice At large distances into the crevice, the predicted concentrations fall from the peak values to plateaus. Because H^+ is generated by the hydrolysis of dissolved metals, and it is transported in a similar fashion, its predicted concentration profiles track those of the dissolved metals In general, the pH is found to approach an asymptotic value (pH ≈ 3) Such representative values can be used as input for predictive pitting models.

In simulations, the number of vacancies (unpitted area) decreases with time, whereas the number of stable pits increases. Initially, the number of pit embryos increases rapidly. The

embryo density evenutally reaches a maximum and begins to fall at the point where the rate of embryo conversion to stable pits exceeds the rate of embryo births The overall pit-generation rate is proportional to the embryo density and passes through a maximum. The effect of pH suppression and imposed potential on pitting of the CRM has also been simulated The predicted rate of pit generation is enhanced by pH suppression, which is consistent with experimental observation. These models predict that the corrosion potential of the CAM provides some protection for the CRM within the crevice

Propagation of a stable pit requires that the local electrochemical potential remain above a threshold ($E > E_{pass}$) If this condition is met, propagation occurs at a rate that is depth-dependent. The depth can be calculated from the age of the pit As the pit becomes deeper, the rate becomes slower due to mass-transport limitations The maximum possible depth can then be estimated with an appropriate stifling criterion, which is based on a limiting mass flux.

Corrosion pits can be developed at welds and base metals of waste package containers after long exposure to the environment. These act as stress risers to initiate crack fissures at the bases of the pits SCC can be initiated at these pits when the applied stress intensity factors are equal to or larger than K_{ISCC}. The critical flaw size for initiation of SCC can be defined by equating K and K_{ISCC} These critical flaw sizes have been calculated as a function of aspect ratio ($a/2c$) at various stress levels The critical flaw sizes for SCC initiation is always larger than the thickness of the respective barriers, except at extremely high aspect ratio ($a/2c$~5) At this very high aspect ratio ($a/2c$~5), the critical flaw sizes for SCC initiation in unannealed welds of Alloys 625 and C-22 are 1 2 cm and 1 4 cm, respectively. Because these values are somewhat less than the wall thickness (2 cm), SCC may be possible in the weld Because stresses in the base metals are expected to be much lower than that in the corresponding, unannealed welds, it is concluded that SCC should not occur in the base metals Even though the weld residual stress can be very high, it has been observed by Henshall and Roy that the aspect ratio of corrosion pits in Alloy 825 seldom exceeds one ($a/2c$<1) Preliminary results suggest that SCC will not occur at corrosion pits at welds, even if the welds are not stress relieved

The current analysis is based on linear elastic fracture mechanics When the stress applied on a crack or corrosion pit is close to or beyond yield stress, there is a possibility that the linear elastic fracture overestimates the critical flaw size for initiation of SCC Under this situation, elastic–plastic fracture mechanics based on the J-integral approach should be used [Anderson, 1995] To use this elastic–plastic fracture mechanics approach, accurate stress-strain curves for each material are needed to characterize its strain-hardening behavior. We will pursue such such data and conduct elastic–plastic fracture mechanics analysis in the future In the interim stage, we recommend that the maximum stress on the welds be relieved to less than 75% of the yield strength of the material

Estimates of the extent of TE rely on thermodynamics, kinetics, and transport phenomena Such models have been used to calculate segregation in steel (the fraction of grain boundary being covered with a monolayer of P) after the typical TE cycle in steels and the expected waste package temperature cycle. Preliminary results indicate that the total grain-boundary segregation of P after the typical TE cycle is 0.97, whereas that for the expected waste package temperature cycle is only 0 012 The segregation expected for the waste package is only about 1.2% of that for the typical TE cycle in steels. Therefore, we conclude that TE in the CAM is very unlikely.

2.8.9 Future Work

The stability of the passive film formed on Alloy C-22 should be determined with the scanning tunneling microscope (STM) and the atomic force microscope (AFM) These techniques provide means of generating in situ high-resolution images of the alloy surface In the case of STM, atomic resolution may be possible, provided that the passive film is sufficiently conductive (Bedrossian, 1994, 1995a, 1995b, Golovchenko, 1986)

Microsensors and in situ optical techniques should be employed to actually measure the localized environment inside the CAM–CRM crevice Fiber optic microprobes (fluorescence, absorption, and inelastic Raman scattering) should be used to determine pH, as well as the concentrations of dissolved metals and anions Microelectrodes should be used to establish potential profiles within the crevice Such measurements will eliminate much of the need for speculation about the crevice environment Such sensors have already been demonstrated at LLNL and will be applied to this important problem in the future, provided that funding is maintained In specific regard to Alloy C-22, it may be possible to use interferometry and other reflection techniques (ellipsometry) to quantify the very small penetration rates anticipated in crevices For example, an artificial crevice could be formed beneath a quartz optical window, with $FeCl_3$ additions to simulate the dissolved CAM

Thin-film corrosion sensors should be fabricated and deployed in the drifts at Yucca Mountain (ESF) to continuously monitor corrosion rates of A516 Gr 12, Alloy C-22, and other metallic alloys of interest Such films can be deposited on piezoelectric crystals so that mass change due to corrosion can be measured Alternatively, the resistance through a sputtered thin film of the material can also be monitored Such atmospheric corrosion studies are now being conducted at LLNL to study the impact of various gas-phase impurities on the tarnish rate of unprotected metallic mirrors in the National Ignition Facility Phase stability could be studied with sputtered multilayers (well-defined, calibrated microstructure)

Process-level (mechanistic) models for pitting and crevice corrosion should be further developed and improved so that experimental data can be used for reliable predictions on the repository time frame The CAM–CRM crevice transport model should be enhanced to include

- Localized concentration- and temperature-dependent solution conductivity
- Terms to account for electromigration at low ionic strengths
- Equations to account for sulfate, nitrate, carbonate, and other anions
- An appropriate activity coefficient model
- Improved computationally efficient model of solution equilibria, including proper hydrolysis equilibrium constants
- Ability to deal with variable width crevice
- Ability to account for localized breakdown of the passive film within the crevice
- A rigorous criterion for cessation of localized attack

Improvements are also needed in the stochastic pitting model, as previously discussed.

The correlations presented here are viewed as a starting point, and they require continuous improvement and updating More appropriate, nonlinear functional forms should be explored. Such functional forms will enable TSPA to interpret coefficients as activation energies, orders of reaction, and related kinetic parameters. Modification of the existing test matrix should be considered By adding additional test conditions as needed (tanks), it may be possible to achieve the advantages of a factorial design

All cyclic polarization measurements should be accompanied by microscopic photographs, and perhaps even images generated by a scanning electron microscope (SEM), to substantiate the absence of localized corrosion below threshold potentials (repassivation potential, etc). This approach has been successfully employed with great success by others (Gruss et al., 1998), and should be emulated by LLNL.

It is believed that uncertainty regarding the waste package environment is the largest source of uncertainty on corrosion modeling Significant effort must be expended by the entire program to reduce the uncertainty and to provide those involved in TSPA and materials testing with well-specified anticipated environments

Acknowledgements

Contributions to Section 2.8 of this report were provided by Jia-Song Huang for stress corrosion modeling and stress analysis, Keith Wilfinger and Bob Hopper for ceramic coating modeling, Ajit Roy for critical potential measurements and K_{ISCC} measurements, Francis Wang for $FeCl_3$ pH measurements, Peter Bedrossian for information on crevice corrosion validation experiments, John Estill for long-term corrosion data for Ni-hose alloys, Joanne Horn for microbial growth information, Kevin McCoy for estimates of transport-limited pH, Dave Shoesmith for passive corrosion rates on Ni-hose alloys, Greg Gdowski for capillary pore estimates

2.8.10 References

Anderson, T. L (1995) *Fracture Mechanics* (Second Edition) Boca Raton, FL CRC Press, Inc

Andresen, P L (1998) *Assessment of Corrosion Rate Properties for the Hastelloy C-22 Inner Barrier, An Environment for Waste Packages, Background Information for Consideration* General Electric Research Center

Asphahani, A I. (1980). "Corrosion Resistance of High Performance Alloys " *Mat Perf* **19**(12)·33–43 [NNA 19910419 0028]

Baroux, B. (1995) "Further Insights on the Pitting Corrosion of Stainless Steels," Chapter 9 of *Corrosion Mechanisms in Theory and Practice* P. Marcus and J Oudar (Eds) New York, NY. Marcel Dekker, Inc

Beck, T R., and R C. Alkire (1979). "Occurrence of Salt Films During Initiation and Growth of Corrosion Pits " *J Electrochem Soc* **123**(4):464–474 [NNA.19891109 0056]

Bedrossian, P (1994) "One-Dimensional Ordering at the Mo/Si Interface " *Surface Sci* **320**:247.

Bedrossian, P. (1995a) "Nucleation and Ordering of $MoSi_2$ on Si(100)" *Surface Sci* **322** 73

Bedrossian, P J. (1995b) "Scanning Tunneling Microscopy: Opening a New Era of Materials Engineering " pp 4–11. *Science & Technology Review* Livermore, CA Lawrence Livermore National Laboratory.

Chao, C. Y , L F Lin, and D D. McDonald (1981). "A Point Defect Model for Anodic Passive Films, II. Chemical Breakdown and Pit Initiation " *J Electrochem Soc* **128**(6):1194–1198. [NNA.19891005 0093]

Cotton, F A., and G. Wilkinson (1988) *Advanced Inorganic Chemistry* (5th Edition) New York, NY· John Wiley & Sons [236867]

Crow, E. L , F A Davis, and M W Maxfield (1960). *Statistics Manual* New York, NY Dover Publications, Inc [MOL 19980506 0047]

Davis, J R (Ed) (1996) *ASM Specialty Handbook Carbon and Alloy Steel* Materials Park, OH ASM International

Druce, S G , G Gage, and G. Jordan. (1986) "Effects of Aging on Properties of Pressure-Vessel Steels " *Acta Metallurgica* **34**(4) 641–652

Farmer, J C (1997) *Crevice Corrosion and Pitting of High-Level Waste Containers A First Step Towards the Integration of Deterministic and Probabilistic Models* (UCRL-ID-128381) Livermore, CA Lawrence Livermore National Laboratory [MOL 19980130 0592]

Farmer, J C (1998a) "Development of Corrosion Models for High-Level Waste Containers" In proceedings from *Sixth International Conference on Nuclear Engineering (ICONE-6)* San Francisco, CA May 10–15, 1998. American Society of Mechanical Engineers.

Farmer, J C (1998b). "Input on the Corrosion of CRM Alloy C-22"(Rev 7, Table 13) In proceedings from *Waste Package Degradation Expert Elicitation Panel* San Francisco, CA Geomatrix

Farmer, J C G E Gdowski, R. D McCright, and H S Ahluwahlia (1991) "Corrosion Models for Performance Assessment of High-Level Radioactive-Waste Containers " *Nucl Eng Design* **129** 57–88 [NNA 1191002 0070]

Farmer, J C , and R D McCright (1998). *Crevice Corrosion and Pitting of High-Level Waste Containers Integration of Deterministic and Probabilistic Models* (UCRL-ID-127980) Also Paper No 98160, Symposium 98-T-2A in proceedings from *Corrosion 98* San Diego, CA March 22-27, 1998 Houston, TX National Association of Corrosion Engineers [MOL 19980113 0389]

Galvele, J R (1976) "Transport Processes and the Mechanism of Pitting of Metals," *J Electrochem Soc* **123**(4) 464–474 [NNA 19891026 0018]

Gartland, P O. (1997) "A Simple Model of Crevice Corrosion Propagation for Stainless Steels in Sea Water " In proceedings from *Corrosion 97* (Paper No 417) Houston, TX. National Association of Corrosion Engineers

Gdowski, G E (1991). *Survey of Degradation Modes of Four Nickel-Chromium-Molybdenum Alloys* (UCRL-ID-108330) Livermore, CA Lawrence Livermore National Laboratory, University of California [NNA 19910521 0010]

Glass , R S , G E Overturf, R A Van Konynenburg, and R D McCright (1986) "Gamma-Radiation Effects on Corrosion· I Electrochemical Mechanisms for the Aqueous Corrosion Processes of Austenitic Stainless Steels Relevant to Nuclear Waste-Disposal in Tuff." *Corros Sci.* **26**(8) 577–590 [NNA 19900405 0461]

Golovchenko, J. (1986). "The Tunneling Microscope: A New Look at the Atomic World " *Science* **232** 48.

Gruss, K. A , D. S Dunn, G. A Cragnolino, and N Sridar (1998) "Repassivation Potential for Localized Corrosion of Alloys 625 and C-22 in Simulated Repository Environments." Paper No 98149, Symposium 98-T-2A *Corrosion 98* San

Diego, CA. March 22–27. Houston, TX National Association of Corrosion Engineers (NACE)

Hack, H P (1983). "Crevice Corrosion Behavior of Molybdenum-Containing Stainless Steel in Seawater " *Mat Perf* **22**(6):24–30 [NNA 19910419.0037]

Haynes International, Inc (1987) *Hastelloy Alloy C-276* Haynes Product Brochure H-2002B Haynes International, Inc

Henshall, G A (1992)."Modeling Pitting Corrosion Damage of High-Level Radioactive-Waste Containers Using a Stochastic Approach " *J Nucl Mat* **195** 109–125 [NNA 19921222 0001]

Henshall, G A (1994) "Stochastic Modeling of the Influence of Environment on Pitting Corrosion Damage of Radioactive-Waste Containers " In proceedings from *Mat Res Soc Symposium* **353**:679–686 [MOL 19940802 0078]

Henshall, G A (1996a) *Modeling Pitting Degradation of Corrosion Resistant Alloys* (UCRL-ID-125300) Livermore, CA. Lawrence Livermore National Laboratory [MOL 19970122 0131]

Henshall, G A. (1996b) *Numerical Predictions of Dry Oxidation of Iron and Low-Carbon Steel at Moderately Elevated Temperatures* (UCRL-JC-124639) Livermore, CA Lawrence Livermore National Laboratory [MOL 19970122 0120]

Hopper, R , J C Farmer, and K Wilfinger (1998) *Summary of Model to Account for Inhibition of CAM Corrosion by Porous Ceramic Coating* (UCRL-IF-130502) Livermore, CA Lawrence Livermore National Laboratory

Horn, J , A Rivera, T Lian, and D A Jones (1998) "MIC Evaluation and Testing for the Yucca Mountain Repository " (UCRL-JC-129198) In proceedings from *Corrosion NACEEXPO 98* San Diego, CA March 22–27, 1998 Houston, TX National Association of Corrosion Engineers (NACE) [222145]

Huang, J. S. (1998). *Stress Corrosion Cracking in Canistered Waste Package Containers Welds and Bare Metals* (UCRL-IDD-120063) Livermore, CA. Lawrence Livermore National Laboratory. [MOL.19980126.0559, 234846]

Jenson, V. G , and G. V. Jeffreys (1963). *Mathematical Methods in Chemical Engineering* New York, NY Academic Press

Jones, D A (1996) *Principles and Prevention of Corrosion* (2nd Edition) Upper Saddle River, NJ Prentice Hall.

Jones, D A , and B E Wilde (1978)"Galvanic Reactions During Localized Corrosion on Stainless Steel " *Corrosion Science*. **18**:631–643

Lillard, R. S , and J. R Scully (1994). "Modeling of the Factors Contributing to the Initiation and Propagation of the Crevice Corrosion of Alloy 625." *J Electrochem Soc* **141**(11):3006–3015 [MOL 19980429 0502]

Marsh, G P , K J Taylor, and Z Sooi (1988). *The Kinetics of Pitting Corrosion of Carbon Steel* (SKB Technical Report 88-09) Stockholm. Swedish Nuclear Fuel and Waste Management Company (SKB). [NNA 19891026.0015, 206501]

Massalski, T B (Ed) (1986). *Binary Alloy Phase Diagrams*, Vol 1 American Society for Metals

McCracken, D D , and W. S. Dorn (1964) *Numerical Methods and Fortran Programming with Applications in Science and Engineering* New York, NY· John Wiley and Sons

McLean, D (1957) *Grain Boundaries in Metals.* London, UK· Oxford University Press

McMahon, C J , Jr. (1968) "Temper Brittleness—An Interpretive Review " *Temper Embrittlement in Steel.* (ASTM STP 407) Philadelphia, PA American Society for Testing and Materials [MOL 19980505 0196, 236535]

Newman, J S (1991) *Electrochemical Systems* (2nd Edition) Englewood Cliffs, NJ Prentice Hall

Nystrom, E A , J B. Lee, A A Sagues, and H W Pickering (1994) "An Approach for Estimating Anodic Current Distributions in Crevice Corrosion from Potential Measurements " *J Electrochem Soc* **141**(2) 358–361 [MOL 19980429 0503, 236472]

Okada, T (1984a) "A Theory of Perturbation-Initiated Pitting " In Proceedings from International Symposium Honoring Professor Marcel Pourbaix on his Eightieth Birthday: *Equilibrium Diagrams and Localized Corrosion.* R. P. Frankenthal, and J Kruger (Eds) Pennington, NJ· *Electrochem Soc* 84(9) 402–431 [NNA 19891005.0088]

Okada, T (1984b) "Halide Nuclei Theory of Pit Initiation in Passive Metals " *J Electrochem Soc* **131**(2) 241–247 [NNA 19891005 0087]

Oldfield, J W , and W H Sutton (1978). "Crevice Corrosion of Stainless Steels· I A Mathematical Model " *Brit Corros J* **13**(1) 13–22 [NNA 19891215 0067]

Pickering, H W , and R P Frankenthal (1972) "On the Mechanism of Localized Corrosion of Iron and Stainless Steel I Electrochemical Studies " *J Electrochem, Soc* 119(10)·1297–1304 [NNA 19891005 0089]

Pourbaix, M (1966) *Atlas of Electrochemical Equilibria in Aqueous Solutions* (English Translation by J A Franklin) New York, NY Pergamon Press, Cebelcor [NNA 19891005 0098]

Rooke, D P , and D J Cartwright, eds (1976) *Stress Intensity Factors* London, UK Her Majesty's Stationary Office

Roy, A K , D L. Fleming, and B Y Lum (1996) *Localized Corrosion of Container Materials in Anticipated Repository Environments* (UCRL-JC-122861) Livermore, CA Lawrence Livermore National Laboratory [MOL 19960708 0433]

Roy, A K , D. L. Fleming, and B Y Lum (1997a). *Electrochemical and Metallographic Evaluation of Alloy C-22 and 625* (UCRL-ID-127355) Livermore, CA Lawrence Livermore National Laboratory [MOL 19980114 0137]

Roy, A K ,D L. Fleming, and B Y. Lum (1997b) *Effect of Environmental Variables on Localized Corrosion of High-Performance Container Materials* (UCRL-JC-125329) Livermore, CA. Lawrence Livermore National Laboratory [MOL 19971217 0031]

Roy, A. K , D L Fleming, and B Y. Lum (1998) "Stress Corrosion Cracking of Fe-Ni-Cr-Mo, Ni-Cr-Mo, and Ti Alloys in Acidic Brine." In proceedings from *Corrosion 98* (Paper 157, Symposium 98-T-2A) San Diego, CA· March 22–27, 1998 National Association of Corrosion Engineers (NACE).

Saleh, F. Y , G. E. Mbamalu, Q. H. Jaradat, and C. E Brungardt (1996) "Ion Chromatography Photodiode Array UV-Visible Detection of Cr(III) Hydrolytic Polymerization Products in Pure and Natural Waters " *Analyt Chem* 68(5) 740–745 [MOL 19980423.0003, 236426]

Sato, N. (1971) *Electrochim Acta* 19.1683

Scully, J R (1997) "Appendix D, Elicitation Interview Summaries " *Waste Package Degradation Expert Elicitation Project* K. J Coppersmith, R C Perman, M Pendleton, J L. Younker Final report for the Civilian Radioactive Waste Management System Management and Operating Contractor. San Francisco, CA Geomatrix Consultants [MOL.19980218 0231]

Sherwood, T K , P L Pigford, and C R Wilke (1975) *Mass Transfer* San Francisco, CA McGraw-Hill [NNZ 19870406 0367]

Shibata, T (1996) "Statistical and Stochastic Approaches to Localized Corrosion " *Corros* 52(11)·813 [MOL.19980514 0049]

Shibata, T , and T Takeyama (1977) "Stochastic Theory of Pitting Corrosion " *Corros* 33(7) 243–251 [NNA.19891005.0090]

Shigley, J E , and C R Mischke (1989). *Mechanical Engineering Design* (Fifth Edition) New York, NY: McGraw-Hill

Smailos, E , W Schwarzkopf, and R Koster (1986) *Corrosion Behaviour of Container Materials for the Disposal of High-Level Wastes in Rock Salt Formations* (DUR 10400 Nuclear Science and Technology, Commission of the European Communities

Strehblow, H -H (1995) "Mechanisms of Pitting Corrosion, " Chapter 7 in *Corrosion Mechanisms in Theory and Practice* P Marcus and J. Oudar (Eds) New York, NY Marcel Decker [104415, TA462 C65575(1995)]

Szjkarsja-Smialowska, Z (1986) *Pitting Corrosion of Metals* Houston, TX. NACE

Thornton, P A , and V J. Colangelo (1985) *Fundamentals of Engineering Materials* Englewood Cliffs, NJ Prentice Hall

Walton, J. C., G. Cragnolino, and S K Kalandros (1996) "A Numerical Model of Crevice Corrosion for Passive and Active Metals,." *Corros Sci* 38(1) 1–18 [233439]

Xu, Y , and H W. Pickering (1993). "The Initial Potential and Current Distributions of the Crevice Corrosion Process" *J Electrochem Soc* 140(3) 658–668 [233645]

3. Ceramic Materials Testing and Modeling

by Keith R. Wilfinger and Joseph C. Farmer

3.1 Introduction

Certain refractory ceramics, notably oxides, have properties suitable for the construction of ceramic waste containers for long-term use in nuclear waste disposal applications. In particular, oxide ceramics are far less prone to environmental corrosion than metals under realistic repository conditions The aqueous corrosion rates of oxides, such as magnesium aluminate spinel ($MgAl_2O_4$) and alumina (Al_2O_3), fall in the range of a few millimeters per million years Oxide ceramics are also unlikely to be subject to microbiologically influenced corrosion, which apparently can attack most, if not all, of the available engineering metals.

Ceramics have a reputation for poor mechanical performance, and large, impermeable objects are not easily fabricated by most current fabrication methods. As a result, the most promising approach for incorporating ceramics in large waste packages (WPs) appears to be the application of a high-density ceramic coating to a supporting metallic structure Ceramic coatings applied by a thermal-spray technique can be made effectively seamless and provide a method for final closure of the WP while maintaining low average temperatures for the entire assembly The corrosion resistance of the ceramic should prevent or delay water penetration to the underlying metal, which will, in turn, provide most of the mechanical strength and toughness required by the application In this way, the major concerns regarding a ceramic coating are centered on three issues. ensuring that the coating is impervious to moisture, that it adheres to underlying metal, and that it remains resistant to mechanical stresses during handling or from rock fall in the repository Without water, electrochemical corrosion and microbiologically influenced corrosion processes are considered to be impossible, so a complete coating should protect the metal vessels for far longer than the current design requirements. Even an imperfect coating should extend the life of the package, delaying the onset and reducing the severity of corrosion by limiting the transport of water and oxygen to the ceramic–metal interface

3.1.1 Thermal-Spray Processes

Thermal-spray techniques for ceramic coating of metallic structures are currently being explored The mechanics of thermal spray resembles spray painting in many respects, allowing large surfaces and contours to be covered smoothly. All of the relevant thermal-spray processes use a high-energy input to melt or partially melt a powdered oxide material, along with a high-velocity gas to impinge the molten droplets onto a substrate where they conform, quench, solidify, and adhere mechanically The energy input can be an arc-generated plasma, an oxygen-fuel flame, or an explosion The appropriate feed material and resulting coating morphologies vary with technique and with application parameters To date, several versions of arc-plasma systems, a detonation coating system, and two variations of high-velocity oxygenated-fuel (HVOF)–fired processes have been investigated using several different ceramic materials.

For any given material, the choice of process, initial particle size, and process parameters is largely a heat-transfer issue. Particle size is important because particles that are too coarse may not melt in the short time available for heat transfer, whereas particles that are too fine may bounce off the spray plume and not reach their melting temperatures Either type can

still become entrained in the coating, leading to defects and porosity Semi-molten particles can quench without fully conforming to the site of impact. Shadowing effects arising from uneven coating build rates, uneven gas streams, and so forth, can also contribute defects

Thermal spray of ceramics requires that a balance be maintained between droplets that are too hot and those that are too cold. Droplets that remain significantly above the melting temperature may rebound upon impact prior to solidification or simply vaporize, those that are too cold are not molten The various spray techniques are simply different methods for getting more particles to the correct state to deposit high-density coatings with maximum efficiency and minimum defects. Detonation spraying uses explosive gas velocity for great impact energies but (relatively) low particle temperatures, counting on mechanical deformation to help achieve high coating density. High-power plasmas heat the particles at very high currents under the premise that the higher the local energy density, the more particles will be heated to the correct temperature. Axial-injection plasma systems introduce particulates to the center of the flame, preventing them from bouncing off the plume and increasing dwell time in the flame. HVOF systems use high flame temperatures and high velocities to achieve performance Each spray technique has an optimum particle size for each material being sprayed Available powders are not necessarily identical, and unfortunately not all materials are readily available in appropriate particle sizes Some control of spray conditions is possible to allow for variations in particle size and composition, but good coatings do not generally result from a random pairing of powder and process

3.1.2 Coating Modeling

A model was developed to account for corrosion protection of steel by a thermal-sprayed ceramic This model accounts for increased impedance to oxygen transport due to a porous ceramic coating and a consequent reduction in corrosion rate As part of this model, a quantity g is defined to account for pore geometries and pore fractions The model also accounts for expansion (strain) of the coating due to the accumulation of corrosion products at the ceramic–metal interface to predict the onset of cracking required for spallation It does not predict the ultimate degree of the potential spallation or its specific location The model has been documented (Hopper, 1998) and is discussed in Section 3 5

Important considerations in this model are as follows

- The substrate corrosion mechanisms are not changed by the presence of the coating, only slowed by reduced transport rates. If a substantial portion of a coating simply disappeared, the situation would be no worse than it would have been without a coating The metallic corrosion modeling presently being done would apply, but over a limited region that can be treated statistically
- In the calculation presented in Section 3.5, aqueous corrosion rates at the substrate are reduced from 300 μm/yr to $8\,6 \times 10^{-2}$ μm/yr. The model treats the ceramic coating as an isotropic continuum and treats the WP in its entirety to predict the onset of the first crack in the coating. Such an approach allows a conservative estimate of an additional 14,000 years of life for the corrosion-allowance material (CAM) in a saturated environment The formation of a single crack would not constitute total failure and removal of the coating, although it would tend to relieve stresses that might lead to further cracking.
- The uncorrected g-factor is an estimate applied to compensate for the effect of a porous coating on the transport of oxygen to the metallic substrate If the oxygen transport is impeded, the corrosion rate will decrease The uncorrected g-factor is

based on the presumption of a simple, cylindrical-pore geometry. The corrected *g*-factor accounts for the influence of more realistic pores An idealized version of a real pore geometry consists of a series of spheres, which dominates the total pore fraction, and a series of smaller interconnecting cylinders, which dominates the impedance to oxygen transport In describing the pores mathematically, regular forms are a convenient fiction, just as they are in particle-size measurement Particle-size distributions are reported in terms of "equivalent spherical diameter" because it is mathematically intractable to describe each of the billions of particles exactly, nor is it necessary when describing an average behavior The same applies to pores and channels that are uniformly distributed throughout a coating The model calculation is highly sensitive to the values assigned to the pore parameters, especially the cylinder diameters The example pore dimensions used to illustrate the model were not rigorously determined, so the explicit results cannot yet be trusted for accuracy Likewise, the value of elastic modulus used in the failure calculation was taken from the literature. Each of these quantities will need to be determined experimentally

- The impedance to oxygen transport imposed by a porous coating depends on whether the pores are filled with liquid, gas, or an appropriate sealant To be conservative, the *g*-factor for dry oxidation was assumed to be unity due to unsealed, gas-filled porosity Effectively, the ceramic was ignored for purposes of calculating dry oxidation, even though about 98% of the substrate surface is covered and the remainder is exposed only through long, convoluted, and narrow channels The *g*-factor for aqueous-phase corrosion will necessarily be much smaller than this, due to reduced diffusion rates of oxygen through liquid-filled pores The *g*-factor for the humid-air corrosion regime is the largest source of uncertainty and is simply assumed to lie somewhere between the *g*-factor for dry oxidation and that for aqueous-phase corrosion In the absence of conclusive experimental data, the uncertainty in the *g*-factor for this regime could easily be several orders of magnitude

3.2 Test Design

3.2.1 Materials Under Test

After a prior literature and vendor study (Wilfinger, 1995), the coating materials initially selected for experimental tests were magnesium aluminate spinel ($MgAl_2O_4$), aluminum oxide (Al_2O_3), titanium dioxide (TiO_2), and a few combinations of these materials Combinations of materials are reported to result in improved toughness when the materials are cosprayed, otherwise, their chemical and structural properties resemble those of the pure oxides Each ceramic being considered is a chemically stable oxide with good corrosion resistance, naturally occurring analogs, and no glassy component. Each melts at about 2150°C or less Alumina and titania were chosen because of solubility studies performed in Sweden during the late 1970s, which suggested that either material is likely to survive more or less indefinitely in contact with water underground (Swedish Corrosion Institute, 1980) Their dissolution rates in aqueous corrosion are on the order of a few millimeters per million years The spinel was originally chosen because of its extreme radiation tolerance, chemical resistance, and similarity to alumina in working properties Stabilized zirconia (ZrO_2) is another ceramic that has been considered as an additional option, although it is not actively being pursued in the current work because of the increased difficulty of producing dense coatings with such a refractory material (melting point >2700°C)

Of the materials being tested, alumina is the most common commercially and is somewhat stronger than the others, but its thermal-sprayed form is subject to a phase transition that could possibly cause cracking over time As part of the initial experimental work at LLNL, the tendency for this transformation to take place over long times at moderately elevated temperatures was verified during a year-long thermal treatment study As a result, we eventually concluded that spinel offers the best combination of physical properties, because it does not have a metastable form that might transform after spraying

3.2.2 Test Methods

The major analytical methods used in this assessment are

- Metallography to evaluate coating structures, total porosity and corrosion behavior
- Adhesive/cohesive bond-strength measurements
- Impact testing to simulate rock fall
- Alternating-current (ac) impedance spectroscopy to estimate the resistance to oxygen transport through a porous ceramic coating.

Additional analytical techniques were x-ray diffraction (XRD), scanning electron microscopy (SEM), and die-penetrant examinations

3.2.3 Sample Types

Three general configurations of ceramic-coated, carbon-steel samples have been used in the work done to date Flat-plate samples (various sizes) are examined using die penetrants and sectioned to evaluate the structures of the ceramic coatings Larger versions are used for impact studies Smaller versions are used for XRD and heat-treatment studies Flat-ended, bond-strength coupons (1 in diameter) conforming to American Society for Testing and Materials (ASTM) C633-79 are used to measure the adhesive/cohesive strength of the coatings on their substrates Corrosion test coupons (6 in long by 1 in diameter) are cross-sectioned following exposure to various environmental conditions to locate and measure corrosion products at the ceramic–metal interface Some of these samples are deliberately damaged by slicing with a diamond saw prior to corrosion testing to expose a portion of the substrate The same sample type is sectioned for ac impedance measurements and allows a modified version of the adhesive/cohesive bond-strength test to be conducted following corrosion testing

3.2.4 Process Evaluation and Characterization

For this study, samples of conventional arc-plasma-generated alumina coatings on steel were produced in-house at LLNL Other samples of various materials were supplied by Vartec Inc , a commercial coating service More recently, samples of spinel were provided by the Idaho National Engineering and Environmental Laboratory (INEEL). The work at INEEL was contracted directly by the M&O. Samples of HVOF alumina-titania and spinel coatings produced using hydrogen as a fuel were purchased from Vartec Detonation-sprayed samples of alumina, titania, and spinel were purchased from Demeton America Inc., an equipment manufacturer. Samples of various materials produced using an axial-injection, plasma-spray technique have been ordered from Northwest Mettech, another equipment manufacturer. The Center for Thermal Spray Research at Stony Brook declined to provide samples coated using a water-stabilized plasma system on the grounds that coatings produced by that technique can be manufactured quickly but are not particularly high in density

3.2.5 Status of Ordered Samples

All samples ordered from Vartec and Demeton, as of April 30, 1998, have been delivered and are being tested. These orders did not include ASTM-style test coupons One full set of plasma-sprayed spinel samples with no bond coat was delivered by INEEL, out of six different sets originally requested. The corrosion-style coupons they delivered were uncoated at the ends. As part of a subcontract with INEEL, subcontractor TAFA has delivered two full sets of cylindrical specimens (with and without bond coat) produced using a high-power plasma ("Plazjet") system. These samples also have uncoated ends TAFA has not yet delivered any flat-plate or mechanical test specimens Because they used propylene as a fuel, TAFA tried but was unable to coat any specimens with spinel using their HVOF system, also as part of work subcontracted by INEEL. INEEL issued a final report (Wright, 1998) based on their own development work and the work at TAFA All remaining undelivered samples are approximately one month past due

3.2.6 Bond Coats

Some coating samples were applied over a bond coat of a nickel-based alloy resembling C-22 This was done to determine whether improved adhesion might result and possibly to limit an expansion-upon-rusting failure issue that was raised regarding the corrosion products generated by oxidation of steel. A counterargument has been suggested that an inadvertent mechanical penetration of the coating and the thin nickel-alloy bond coat could lead to the formation of an undesirable electrochemical potential, possibly accelerating local corrosion of the carbon-steel CAM

The presence of a bond coat also complicates the issues of package closure and rework following any mechanical damage. If the patch is improperly prepared or executed, a situation could arise where a new portion of the bond coat would be applied over a portion of the undamaged ceramic Such an overlap might or might not be dangerous, but is undesirable because it represents an unpredictable physical discontinuity Similar objections can be raised regarding graded coatings because it is always difficult to blend the old with the new perfectly If the limiting factor is the cohesive strength of the ceramic rather than the adhesive strength of the bond, bond coats and graded coatings may be superfluous

3.3 Test Types

3.3.1 Metallography

Optical and SEM metallography of sample cross sections demonstrate the morphology of the various coating types received. Image analysis was used to estimate the total fraction of porosity Polishing reveals overlapping splat patterns quite well There is usually a contrast difference between adjacent grains, which may be due to variations in polishing along different crystallographic axes. There is also some tendency for relief polishing to occur at the boundaries between grains. A few representative micrographs are included in this section Figure 3 3-1 shows an optical micrograph of a low-density (~19% porous) coating made via conventional plasma spray The coating shown has been corrosion tested, but the microstructure is unchanged

Figure 3.3-1. Porous plasma-sprayed alumina coating after 6 months in 10× concentrated, simulated J-13 water at 90°C.

Figure 3 3-2 is an example SEM micrograph showing the pore structure of a conventional plasma coating For low-density coatings in particular, large numbers of circular and elongated (sausage-like) pores are visible between the flattened plates making up the coating As would be expected, these elongated pores run more or less parallel to the substrate surface along the grain edges. Many of the apparently circular pores might be the elongated type revealed in cross section The lines of grains appear to undulate, probably due to each splat falling only partially over the others, and to varying grain size In places, there are radial separations (microcracks or pores), which appear to be submicron in thickness and a few microns long (as long as the grains are thick), running between layers. Other interesting features include rounded inclusions (particles that apparently had melted but resolidified before striking the surface) and sharp-edged inclusions (particles that apparently had never melted but were merely trapped in the coating)

Figure 3.3-2. SEM micrograph showing the structure of a plasma-sprayed coating.

In high-density coatings (i e , HVOF), the splats are less obvious but still visible at high magnification due to contrast differences. An optical cross section of an HVOF-type coating is shown in Figure 3.3-3 Figure 3 3-4 is an SEM image showing the finer grain and pore structures in an HVOF coating There are still pores in evidence but far fewer and with less obvious links between them Many of the pores appear to be equiaxed (sphere-like) There is still some evidence of inclusions but far more of the rounded variety than the sharp ones

Figure 3.3-3. Dense HVOF-sprayed alumina-titania coating after 6 months in 10× concentrated, simulated J-13 water at 90°C.

Figure 3.3-4. SEM micrograph showing the structure of an HVOF-sprayed coating.

Figure 3 3-5 shows an optical micrograph provided by INEEL representing the structure of a conventionally plasma-sprayed spinel coating produced at their facility. Figure 3.3-3 is an optical micrograph also provided by INEEL showing a high-density coating produced at TAFA using their Plazjet high-power coating system In both cases, INEEL reports porosities (measured optically) of less than 1% These results are comparable to the 2% porosity estimated for Vartec HVOF coatings and, in the case of the conventional plasma, are quite unexpected. Porosity estimates made on the INEEL and TAFA samples at LLNL are slightly higher (about 2%). Regardless of the exact number, this work has demonstrated that very high-density ceramic coatings can be fabricated by several different thermal-spray methods, without recourse to unconventional methods or diagnostic devices

Figure 3.3-5. Optical micrograph of spinel coating deposited using Metco 9MB torch (INEEL).

Figure 3.3-6. Optical micrograph of spinel coating deposited using TAFA Plazjet (INEEL).

3.3.2 Corrosion Testing

Corrosion testing of ceramic-coated coupons is being carried out under various conditions but especially in the LLNL Long-Term Corrosion Test Facility (LTCTF). Initially, sets of six coupons coated with plasma-sprayed alumina and an HVOF-sprayed alumina-titania composite were placed in one of the tanks containing 10× concentrated, simulated J-13 well water at 90°C (total dissolved solids ~1500 ppm, pH between 10.0 and 10 2). The samples

straddled the water line, exposing them to water, oxygen, and deposited salts due to evaporation, which should be the most corrosive conditions likely to occur Six of each type of sample were put in whole, and six of each were deliberately slotted in two places (above and below the water line) to induce corrosion damage underneath the coatings Figure 3.3-1 and Figure 3.3-3 show samples that have undergone testing for six months in this environment

At various intervals and as they become available, additional sample materials applied via the various thermal-spray techniques have been placed in the corrosion tank described above as well as in a tank containing water acidified to pH 2 7 using organic acids The later samples have primarily been coated with spinel, although given the long lead times involved in ordering large numbers of small coated parts, some samples that have yet to arrive will still be coated with other materials Humid-air corrosion (HAC) tests are planned in humidity chambers currently being used to evaluate HAC of uncoated metals Samples of several different types are available for this purpose As of April 30, 1998, the racks ordered to support the samples have not been delivered

Samples have been withdrawn from the corrosion baths at intervals for examination. Prior to sectioning, the slotted regions are filled with epoxy to trap any corrosion products that might be present They are then sectioned across the slot and polished The substrates are etched with Nitol to reveal the grain structure Metallography of 10 ceramic coated samples, tested for periods of 3 and 6 months in 10× concentrated, simulated J-13 water, was completed on April 28, 1998. Cross sections of several of these samples are shown in Figure 3 3-1, Figure 3 3-3, Figure 3 3-7, and Figure 3.3-8

Figure 3.3-7. Optical micrographs showing 19% porous plasma-sprayed alumina and 2% porous HVOF-sprayed alumina-titania after 6 months in 10× concentrated, simulated J-13 water at 90°C (slotted samples).

Figure 3.3-8. Detonation-sprayed alumina coatings with and without Ni bond coat. Tested for 3 months in 10× concentrated, simulated J-13 water at 90°C.

As might be expected, highly porous coatings (~19% porosity) afforded incomplete corrosion protection. As shown in Figure 3 3-7a, these coatings were subject to spallation near the slot In some places away from the slot, it appeared that the substrate was not corroded at all, although there were also places in unslotted samples where the corrosion was relatively thick (>0.1 mm), as shown in Figure 3 3-1. This corrosion is comparable to the thickness of the corrosion actually observed inside the slot, which was unprotected. The corrosion adjacent to one side of the slot was thick enough to cause spallation and appeared to penetrate quite deeply along the interface (>1 cm) On the other side of the slot, the corrosion layer was thinner (~0 05 mm) and did not penetrate as far along the interface (~0 3 mm) This corrosion outcome suggests that the coating properties were highly variable or that the coating was stressed and partly separated from the substrate by the slotting operation before corrosion testing

Dense HVOF (~2% porous) and detonation (~6% porous) coatings are shown in Figure 3 3-7b and Figure 3.3-8. One of the detonation coatings has a nickel-based bond coat All three of these coatings gave significant corrosion protection, with no apparent corrosion of the substrates detected, except where they had been deliberately exposed by slotting. There was significantly more corrosion apparent in the sample with the bond coat than without, possibly resulting from an electrochemical interaction There was no apparent undercutting

of any of the dense coatings by corrosion, suggesting that penetration of oxygen beneath a properly applied, dense coating is very slow.

Corrosion products seemed to accumulate in the slots (~0 3 mm wide) on several samples, apparently causing a plugging effect Such an effect suggests that minor defects in otherwise high-quality coatings might be self-limiting to some degree, as long as no mechanism is available to remove the corrosion products.

3.3.3 Contact Conductivity and AC Impedance Spectroscopy

Using a millivolt source, simple contact conductivity (DC resistance) measurements were made on high-porosity plasma (~19% porous) and low-porosity HVOF (~2% porous) coated samples immersed in distilled water When the electrodes were applied to a dry coating, the DC resistance was effectively infinite in both cases Upon the addition of water, the more porous coating achieved a minimum resistance of several tens of ohms, which increased within minutes to a few hundred thousand ohms The denser coating offered a minimum resistance of a few hundred thousand ohms, which increased over a slightly longer time to several megaohms The behavior was the same regardless of polarity. There was considerable difference in the time of response and the low and high resistance values achieved, but it was clear that a conductive pathway to the substrate was established quickly in each case It was not clear from this simplistic test whether the increase in apparent resistance was the result of polarization, nor how much of the substrate surface was actually exposed

AC impedance spectroscopy was then carried out using a potentiostat on several variations of thermal-sprayed samples, following a technique described by Farmer (1985) Measurements were made on samples with no coating, ~2% porous coatings, ~6% porous coatings, and ~19% porous coatings. All were immersed in concentrated, simulated J-13 water (~130,000 ppm dissolved solids) Some variability in the exposed sample size for these initial tests made it difficult to distinguish quantitatively between the two high-density coated samples, but a standard preparation method has now been selected to eliminate such experimental variability from future tests. A graph of the experimental results is shown in Figure 3 3-9

Figure 3.3-9. AC impedance measurements of ceramic coatings made by various thermal-spray techniques

The impedance of the denser coatings was approximately 8 orders of magnitude greater than that of the bare substrate at low frequencies and 4 orders of magnitude greater at high frequencies The highly porous coating behaved much like the bare substrate, which was not surprising because metallography of this type coating clearly shows large-scale interconnected porosity. A 6% porosity is the normally accepted division point between interconnected and fully isolated porosity This is a rule of thumb regarding isotropic sintered materials rather than highly oriented materials produced by other methods, but the rule is accurate enough for use with most ceramics.

Because electrical conductivity through liquid-filled channels is directly related to the ease with which various species (including dissolved oxygen) can pass through the channels, the electrical impedance measured at low frequencies should correspond directly to the impedance of oxygen transport from the outside to the substrate. An increase in impedance of 8 orders of magnitude corresponds to a reduction in oxygen-transport rate by 8 orders of magnitude, and therefore represents a similar reduction in corrosion rate compared to the uncoated condition. These results are in agreement with the physical observations of the lack

of corrosion detected beneath dense coatings in the long-term test At high ac frequencies, there is still electrical conductivity due to charge transfer, but one can picture the ions themselves merely oscillating in place, so that there would still be reduced net transport of oxygen to the substrate.

3.3.4 Impact Studies

Because of the possibility of point loads during handling and as a result of rock falls, the robustness of coatings on waste containers was evaluated qualitatively using drop tests on alumina-coated steel substrates Various 4-in.-thick steel blocks, which were plasma-coated with 0 02 in or more of alumina, were struck from a height of up to 2.5 m using a 100-kg load. This would be equivalent to a rock slightly larger than 1 ft^3 in size falling from a similar distance Rounded and pointed impactors were used to simulate the most likely extremes of shapes to be encountered during a rock fall Metallic impactors were deemed unsuitable because their elastic and fracture response would be quite different from those of the natural rock Instead, porcelain-tipped impactors that closely match the average chemistry and physical behavior of the Yucca Mountain welded tuff were used

Surrogates were needed because of the wide variability in the physical properties of the natural material, combined with the expense of producing specific shapes by machining of rock The impactors were cylinders 2 in in diameter by 4 5 in long, with shaped ends Whereas the chemical composition is relatively easy to reproduce using a porcelain body (clay, flint, and feldspar), obtaining a matching load-unload pulse during impact is more difficult A reasonable match to the pressure pulse caused by impact of the natural material was achieved by varying firing conditions to control the total porosity of the porcelain impactors

The nose configuration of the impactor plays a major role in determining whether the coating will maintain its integrity under impact As might be expected, a pointed nose appears to be the worst case, causing chipping of the coating under relatively low kinetic energies Any impact that permanently deformed the underlying substrate caused the coating to fracture over the deformed area Most fractures penetrated only part way into the coating, leaving some protection, although a few actually exposed bare metal No extended cracking or collateral damage of the coating outside the impact zone was observed and there did not seem to be any difference in behavior when impacts were repeated on adjacent areas of samples previously tested

3.3.5 Mechanical Test

ASTM test procedure C633-79 measures the adhesive/cohesive strength of the coatings This procedure is being used to establish a baseline for the bond strength of coatings prior to corrosion testing A modified pull test, using pins with somewhat smaller dimensions than those called for in the standard, is being used on corrosion-style coupons to determine the bond strength after exposure This test is being calibrated against the ASTM configuration To date, only HVOF samples from Vartec and plasma coatings generated at LLNL have been mechanically tested As of April 30, 1998, one set of ASTM-style samples with no bond coat had been delivered by INEEL, although that organization reported a bond strength of approximately 1900 psi with and without a bond coat during their internal testing This result has not yet been confirmed by LLNL because comparable samples with a bond coat have not been shipped—neither have additional samples that INEEL subcontracted to TAFA nor others being fabricated by Northwest Mettech.

The open literature reports that, for spinel, a nickel-based bond improves the overall strength measured on steel substrates In reality, failure occurs at the weakest link in the chain being tested This link can be the metal-to-metal bond (where a bond coat is used), the ceramic-to-metal bond, the adhesive bond used to attach the test fixture, or within one of the layers. To date, the samples tested in this study have almost all failed at the glue bond (up to about 5000 psi), leaving the coating intact The only exception was a case where the pull pin was inadvertently bent sideways as it was pulled, in which case a portion of the coating adhered to the pull pin and separated from the sample in shear Only a few layers of particles adhered to the pin, the coating did not fail down to bare metal There was no separate bond coat in this case.

A possible implication of the lone discrepancy (although not proven) is that the bond between either metal phase and the ceramic will be stronger than the interparticle bonds within the ceramic coating If this is true in all cases, then for thick coatings in particular, the measured strength will always be limited by the ceramic cohesion rather than the adhesion (if not by the adhesive used in the test). This is a logical assumption because, unlike ceramics, metals are able to deform plastically even when spray conditions are not ideal, producing more complete conformance to previous layers It may not be necessary to worry about the strength of the ceramic to metal bond, as long as it is stronger than the strength of the coating itself

The adhesive used in most of the testing done to date is not one of the specific filled epoxy products listed in ASTM test procedure C633-79 None of the listed products was available The manufacturers of the nearest equivalents list their average tensile strength at 2300 psi, which is only about half of what the standard suggests they should be This seems to be an inconsistency in the standard, although it is possible that fresh batches of the filled adhesive actually match the performance cited by the ASTM A pure resin system based on Epon 815 was substituted, resulting in stronger adhesion, but there is some concern that the unfilled adhesive could penetrate porous coatings and skew the results Newer filled epoxy adhesives with a reported adhesive strength of about 12 to 15 kpsi are on order from Masterbond Adhesives

3.3.6 Thermal Cycling

Coated corrosion-style coupons were rapidly cycled five times between ambient temperature and 400°C at a rate of about 100°C/hr with no apparent effect on the coatings This is a higher temperature and far more rapid cycling than could take place in the repository, which is expected to heat and cool over a span of years Samples were thermal-shock tested by heating to temperatures as high as 600°C and quenching into either room temperature or boiling water, again with no discernible effect. This result is consistent with (and far more severe than) thermal-stress modeling results (Plinski, 1997), which suggest that residual stresses in ceramic coatings due to heating by emplaced waste should be insufficient to materially affect the bond strength, even at the large sizes projected for the WPs

3.4 Test Analysis

3.4.1 Interim Conclusions

HVOF using hydrogen as the fuel source has provided the most successful thermal-sprayed ceramic coatings tested to date Metallography of INEEL plasma and TAFA Plazjet samples shows that these techniques are also capable of producing high-density coatings.

Detonation-coated samples are slightly lower in density, but offer similar impedance to oxygen transport

A model has been developed to account for reduced corrosion of metallic substrates by porous ceramic coatings Predictions of significantly increased corrosion lifetimes are supported by preliminary corrosion test results and by ac impedance spectroscopy, which demonstrates an increase in impedance by 8 orders of magnitude, corresponding to an 8-order-of-magnitude decrease in oxygen transport through low-porosity coatings.

Nickel-based bond coats may actually degrade corrosion protection of steel substrates due to electrochemical effects if the coating and bond coat are inadvertently damaged

3.4.2 Future Work

Immediate future goals of this project are to complete the planned evaluations on the various purchased samples as they arrive More extensive ac impedance measurements will be made, including measurements of materials that have been sealed using various inorganic and metallic sealant materials If the corrosion work continues to be as promising as early results indicate, we will shift toward use of larger samples to demonstrate that high-density coatings can be applied to larger surfaces more closely resembling the proposed WP designs An attempt will be made to apply nondestructive evaluation techniques to larger coated surfaces and determine the size and severity of flaws that may be buried in the coatings Various methods will be used to artificially implant flaws of various sizes in known locations Possible artificial flaws include

- Overcoating materials glued onto the substrate or onto a partially complete coating
- Rubbing solder onto a partially complete coating with a hot iron
- Striking the coating with a center punch prior to spraying over with a final coat
- Deliberately forming a heavy rust scale on a portion of the substrate
- Rubbing areas with a refractory cement prior to coating
- Drilling holes in the substrate parallel to the coating.

3.5 Model of Inhibition of CAM Corrosion by Porous Ceramic Coating

Corrosion occurs during five characteristic periods or regimes

3.5.1 Regime I: Initial Period of Dry Oxidation

The impedance to gas-phase mass transport is relatively insignificant A good approximation is to simply apply the dry oxidation rate provided by Henshall (1996)

$$x_{ox}(t)^2 = x_{ox}(t_0)^2 + 2k_p \int_{t_0}^{t} \exp[-Q/RT(t)]dt, \qquad (3\,5\text{-}1)$$

where $k_p = 4\,3 \times 10^{-5}$ cm^2/s, $Q = 104$ kJ/mol, and $R = 8\,314$ J/mol The ratio of metal penetration to oxide thickness, β, is 0.48. Note that Eq 3 1-1 predicts an oxide thickness of approximately 6 24 μm after 1000 years of dry oxidation at a fixed temperature of 150°C

3.5.2 Regime IIa: Pores Partially Filled with Moisture

During this period, the corrosion rate is assumed to be limited solely by oxygen transport through gas-filled pores. Impedance of the corrosion rate by the oxide formed at the air–CAM interface during Regime I is ignored In this specific case, the estimated corrosion rate is

unrealistically high. Although this hypothetical scenario (regime) was considered, we do not believe that it is relevant to actual WP performance and Total System Performance Assessment–Viability Assessment (TSPA-VA)

3.5.3 Regime IIb: Pores Partially Filled with Moisture

The corrosion rate is assumed to be limited by the corrosion layer formed at the air-CAM interface (located at the base of pores) Typical HAC rates apply (60% < *RH* < 80% and no dripping condition) The gas-filled pores do not significantly impede the rate of HAC Assuming a penetration rate of only 10 μm/yr, it will take several thousand years to reach the fracture strain. The system should transition to Regime III–IV (80% < *RH* and dripping condition) long before fracture occurs

3.5.4 Regime III–IV: Pores Completely Filled with Moisture

Typical aqueous-phase corrosion rates apply at the ceramic–CAM interface (80% < *RH* and dripping condition) In this case, development of an appropriate model begins with consideration of the flux of oxygen N_A through multiple diffusion barriers, represented by subscripts P and Q (phases P and Q)

$$N_A = k_P\left(a_{PB} - a_{Pi}\right) = k_Q\left(a_{Qi} - a_{QB}\right) = k_a\left(a_{PB} - a_{QB}\right) \qquad (3\ 5\text{-}2)$$

The overall mass-transfer coefficient (mass-transfer resistance) can be expressed in terms of the individual mass-transfer coefficients for phases P and Q (Sherwood, 1975, pp. 178-182):

$$\frac{1}{K_A} = \frac{1}{k_P} + \frac{1}{k_Q} \qquad (3\ 5\text{-}3)$$

Pores are treated as long cylinders of length δ, where

$$N_A = \frac{D_A}{\delta}\left(a_{PB} - a_{Pi}\right) \qquad (3\ 5\text{-}4)$$

The average flux of oxygen per unit area of WP is then

$$\overline{N_A} = \frac{\theta}{\delta} D_A\left(a_{PB} - a_{Pi}\right), \qquad (3\ 5\text{-}5)$$

where θ is the fraction of the CAM exposed to the aqueous phase at the ceramic–CAM interface. This fraction θ can be interpreted as porosity. Values of 0 02–0 03 have been achieved with HVOF The overall mass-transfer coefficient is then

$$\frac{1}{K} = \frac{1}{k_0} + \frac{1}{k_I} = \frac{1}{k_0} + \frac{\delta}{\theta D_A}, \qquad (3.5\text{-}6)$$

or

$$K = \frac{1}{\frac{1}{k_0} + \frac{\delta}{\theta D_A}} \qquad (3\ 5\text{-}7)$$

The factor used to correct the oxygen-limited corrosion rate for the presence of a porous ceramic barrier is then

$$g = \frac{\overline{N_A}}{\overline{N_{A,0}}} = \frac{\dfrac{1}{k_0}}{\dfrac{1}{k_0} = \dfrac{\delta}{\theta D_A}} = \frac{1}{1 + \dfrac{k_0 \delta}{\theta D_A}}. \qquad (3\,5\text{-}8)$$

This correction factor assumes simple cylindrical pores, which is unrealistic. The pores in ceramic coatings can be better represented by an array of chains, each link being composed of a hollow sphere and a relatively narrow hollow cylinder, connected in series In such a case, a more detailed analysis of porosity should be used Specifically, the mass-transfer coefficient for the ceramic coating, k_t, should be reduced by a factor $f(\varepsilon,\lambda)$, thus $k_{t,\text{corrected}} = f(\varepsilon,\lambda) \times k_t$, Here $f(\varepsilon,\lambda)$ is defined as

$$f(\varepsilon,\lambda) = \frac{3}{2}\frac{(1+\lambda)^2}{\lambda}\varepsilon^2 \qquad (3\,5\text{-}9)$$

Here the dimensionless parameters ε and λ represent the geometry of the sphere–cylinder chain

$$\varepsilon = \frac{\text{diameter of cylinder in chain}}{\text{diameter of sphere in chain}}, \qquad (3\,5\text{-}10a)$$

$$\lambda = \frac{\text{length of cylinder in chain}}{\text{diameter of sphere in chain}} \qquad (3\,5\text{-}10b)$$

Reasonable estimates for ε based on actual microstructures vary from a low of 0 01 or 0 03 (a good guess) to a high of 0 05 (the upper limit or worst case). Reasonable estimates for λ based on actual microstructures range from a minimum of 5 to a maximum of 30, with 10 considered the best guess A range of $f(0\,03,10) = 0\,016$ to $f(0\,05,10) = 0\,045$ is therefore considered reasonable.

As an average for now, we estimate $f(\varepsilon,\lambda)$ to be approximately 0 03, which is mid-range Given this model for the interconnected porosity in the ceramic coating, the modified factor used to correct the oxygen-limited corrosion rate for the presence of a porous ceramic barrier is then

$$g_{\text{corrected}} = \frac{1}{1 + \left(\dfrac{k_0 \delta}{\theta D_A}\right)\left(\dfrac{1}{f(\varepsilon,\lambda)}\right)} \qquad (3\,5\text{-}11)$$

The following stoichiometry is assumed to exist between iron and oxygen

$$4Fe + 3O_2 \longrightarrow 2Fe_2O_3 \qquad (3\,5\text{-}12)$$

The relation between the oxygen flux in a single pore, N_A, and the corrosion rate dp/dt can be written as

$$3N_{A,0} = 3k_0\left(C_{oxygen}\right) = 4\frac{\rho}{w}\frac{dp}{dt}, \tag{3.5-13}$$

where w is the atomic weight of iron (w = 55.847 g mol^{-1}) and ρ is the density of iron (ρ = 7 86 g cm^{-3})

A very conservative value of the aqueous-phase corrosion rate is assumed as a basis for calculating the apparent mass-transfer coefficient representing corrosion in the absence of a porous ceramic barrier·

$$\frac{dp}{dt} \approx 300\frac{\mu m}{yr} = \frac{300\times10^{-4}}{365\times24\times3600}\frac{cm}{s} = 9\,513\times10^{-10}\frac{cm}{s} \tag{3 5-14}$$

This corrosion rate is six-month data from the LTCTF at LLNL and is documented by Farmer (1998) The concentration of oxygen dissolved in water (equilibrium with ambient air) at the air–ceramic interface is C_{oxygen} = 2.56 × 10^{-7} mol/cm^3. This solubility is lowered with the addition of salt This value can be found in Farmer's input to the Expert Elicitation Panel (1998, Table 13)

The flux of oxygen associated with this mass-transfer coefficient is then

$$N_{A,0} = \left(\frac{4}{3}\right)\frac{7.86\times9\,513\times10^{-10}}{55\,847}\frac{mol}{cm^2s} = \left(\frac{4}{3}\right)1\,339\times10^{-10}\frac{mol}{cm^2s} = 1\,785\times10^{-10}\frac{mol}{cm^2s} \tag{3 5-15}$$

The mass-transfer coefficient in the absence of a ceramic barrier is then estimated as

$$k_0 = \frac{1}{C_{oxygen}}\left(\frac{4}{3}\right)\frac{\rho}{w}\frac{dp}{dt}, \tag{3 5-16}$$

or

$$k_0 = \frac{1.785\times10^{-10}}{2\,56\times10^{-7}}\frac{\frac{mol}{cm^2s}}{\frac{mol}{cm^3}} = 6\,973\times10^{-4}\frac{cm}{s} \tag{3 5-17}$$

The factor needed to correct the corrosion rate for the presence of a porous ceramic coating is then

$$g_{corrected} = \frac{1}{1+\dfrac{(0\,15cm)\left(6.973\times10^{-4}\dfrac{cm}{s}\right)}{(0.02)\left(10^{-5}\dfrac{cm^2}{s}\right)(0\,03)}} = 5\,736\times10^{-5}. \tag{3 5-18}$$

Therefore, the porous ceramic coating would lower the aqueous-phase corrosion rate from approximately 300 μm/yr to only 8.602 × 10^{-2} μm/yr:

$$\frac{dp}{dt} = g_{\text{corrected}}\left(\frac{dp}{dt}\right)_0 = 1.721 \times 10^{-2}\ \frac{\mu\text{m}}{\text{yr}}. \qquad (3\ 5\text{-}19)$$

An estimate of the time to fracture due to the formation of corrosion products at the ceramic–CAM interface can be estimated, provided that the mechanical properties of the ceramic are known Estimated properties for the ceramic coating are taken from a text on engineering materials (Thornton, 1985) and are summarized in Table 3 5-1

Table 3.5-1 Mechanical properties of ceramic coatings.

Property	Elastic modulus (E)	Elastic modulus (E)	Fracture strength (σ)	Fracture strength (σ)
Units	MPa	Mpsi	MPa	kpsi
Al_2O_3	365,000	53	172	25
ZrO_2	144,900	21	55	8

The range of fracture toughness values observed for typical ceramics is given as K_{IC} = 3 3 to 5 8 MPa · $m^{1/2}$ = 3 0 to 5 3 kpsi · $in^{1/2}$

Although these properties serve as a good starting place for TSPA-VA, handbook values for mechanical properties of ceramics will probably need to be revised to better reflect those of actual coatings Direct measurement of the elastic modulus is required

The rate of expansion of the inner radius of the ceramic barrier coating is estimated from the penetration rate, accounting for the expansion at the interface due to the density difference between Fe_2O_3 and Fe

$$\frac{dR}{dt} = 2\frac{dp}{dt} = 2 \times 1\ 721 \times 10^{-2}\ \frac{\mu\text{m}}{\text{yr}} = 3\ 442 \times 10^{-2}\ \frac{\mu\text{m}}{\text{yr}} = 3\ 442 \times 10^{-8}\ \frac{\text{m}}{\text{yr}} \qquad (3\ 5\text{-}20)$$

Given the inner radius, R = 1 m, the strain rate in the ceramic coating can be estimated as

$$\frac{de}{dt} = \frac{1}{2\pi R} 2\pi \frac{dR}{dt} = 3.442 \times 10^{-8}\ \frac{1}{\text{yr}} \qquad (3\ 5\text{-}21)$$

The relation between the stress and strain must be noted $\sigma = E \times e$. The fracture strain can then be estimated from the elastic modulus and the fracture stress·

$$e^* = \frac{\sigma^*}{E} = \frac{172\ \text{MPa}}{356{,}000\ \text{MPa}} = 4\ 831 \times 10^{-4} \qquad (3\ 5\text{-}22)$$

The time required for the strain to reach the fracture strain determines the time to fracture

$$\tau^* = \frac{e^*}{de/dt} = \frac{4.831 \times 10^{-4}}{3\ 442 \times 10^{-8}}\ \text{yr} = 14{,}037\ \text{yr} \qquad (3\ 5\text{-}23)$$

This is the time required for formation of the first crack in the ceramic coating, but it does not necessarily imply failure of the coating

The critical flaw size for crack initiation is estimated as

$$a^* \approx \left(\frac{K_{IC}}{\sigma^*}\right)^2 \frac{1}{\pi} = \left(\frac{3\,3\ \text{MPa}\sqrt{m}}{172\ \text{MPa}}\right)^2 \frac{1}{\pi} = 1.172 \times 10^{-4}\,\text{m} = 117\,2\ \mu\text{m}, \qquad (3\,5\text{-}24)$$

where the fracture toughness is defined as $K_{IC} = \sigma \cdot (\pi a)^{1/2}\ f(a,W)$

3.5.5 Regime V: Corrosion Due to Excessive Carbon Dioxide in Gas Phase

This type of corrosion is considered unlikely

3.5.6 Summary: Regimes I–V

The existence of a slightly porous ceramic coating on the surface will significantly lengthen the life of the container, adding an estimated minimum of 14,037 years to the life of the WP (Table 3.5-2) It is more likely that considerably more time would be added Additional life can be added by taking steps to close interconnected porosity in the porous ceramic coating For example, the surface could be impregnated with silicate based coatings, with or without fine metal particles, which would oxidize, thereby filling the pores Both Zn and Al are possible candidates for closing porosity because they would be sacrificial to the A516 Gr 55 in possible galvanic couples. The modified *g*-factor presented here can be used as a practical means to adjust CAM corrosion rates to account for the ceramic coating.

Table 3.5-2 Extension of WP life with ceramic coating.

	Life with ceramic coating (yr)	Life without ceramic coating (yr)
Thermal pulse	~ 1,000	~ 1,000
Ceramic barrier	> 14,037	0
CAM after exfoliation	> 333	> 333

Work is in progress at LLNL to verify the corrected *g*-factor through application of ac impedance spectroscopy This technique has been applied to a variety of other practical problems over the past 15 years by one of the authors (Farmer, 1985) A PAR Model 273 with either a Solaritron frequency-response analyzer or a dual-channel lock-in amplifier will be used to determine the complex impedance of the electrolyte-filled ceramic barrier over the frequency range extending from 0.001 Hz to 500 kHz With a well-planned experiment and proper interpretation of the data, insight into transport in the pores should be possible It should also be possible to develop some understanding of the layer of corrosion products at the base of the pores

3.6 References

Farmer, J C (1985) "Underpotential Deposition of Copper on Gold and the Effects of Thiourea Studied by AC Impedance " *J. Electrochem Soc* **132**(11)·2640–2648.

Farmer, J C (1998a). "Development of corrosion models for high-level waste containers " In proceedings from *Sixth International Conference on Nuclear Engineering (ICONE-6)* San Francisco May 10–15, 1998 American Society of Mechanical Engineers 13 p

Farmer, J. C (1998b) "Input on the Corrosion of CRM Alloy C-22 " In proceedings from *Waste Package Degradation Expert Elicitation Panel* San Francisco March 14, 1998 Geomatrix. 30 p. (Rev. 7) [MOL.19980507.0376]

Henshall, G A (1996). *Numerical Predictons of Dry Oxidation of Iron and Low-Carbon Steel at Moderately Elevated Temperatures* (UCRL-JC-124639) Livermore, CA Lawrence Livermore National Laboratory [MOL.19970122 0120]

Hopper, R , J C Farmer, and K Wilfinger (1998) *Summary of Model to Account for Inhibition of CAM Corrosion by Porous Ceramic Coating* (UCRL-ID-130502) Livermore, CA· Lawrence Livermore National Laboratory.

Plinski, M J (1997) *Thermal Stress Analysis of Thermally Sprayed Coatings on a Spent Nuclear Fuel Waste Package* Las Vegas, NV University of Nevada, Department of Mechanical Engineering M S thesis

Sherwood, T K , P L Pigford, and C R. Wilke (1975) *Mass Transfer* San Francisco, CA McGraw-Hillp [NNZ 19870406 0367]

Swedish Corrosion Institute (1980) *Aluminum Oxide as an Encapsulation Material for Unreprocessed Nuclear Fuel Waste—Evaluation from the Viewpoint of Corrosion* (Final Report 1980-03-19) Stockholm. Swedish Corrosion Institute

Thornton, P A , and V. J. Colangelo (1985) *Fundamentals of Engineering Materials* Englewood Cliffs, NJ· Prentice Hall

Wilfinger, K (1995) *Ceramic Package Fabrication for YMP Nuclear Waste Disposal* (UCRL-ID-118660) Livermore, CA Lawrence Livermore National Laboratory [MOL 19941108 0106]

Wright, R N , W D Swank, R H. Averill, and J R Fincke (1998) *Feasibility of Impermeable MgAl2O4 Thermal Spray Ceramic Coatings* Lockheed Martin Idaho Technologies Company, ID 83415-2218 Idaho National Engineering and Environmental Laboratory (INEEL)

4. Basket Materials Testing and Modeling

by R. Daniel McCright

The Viability Assessment (VA) designs for spent-nuclear-fuel waste packages (WPs), which were described in Section 1.0, consist of several internal elements that offer structural support to the fuel-rod assemblies, allow heat conduction from the fuel to the container, and provide nuclear criticality control Criticality control becomes important after the double-barrier container wall has been breached and water is allowed entry and contact with the spent fuel, so studies are being made of the performance of structural materials with neutron-absorbing additions

These designs incorporate a "basket" assembly into which the spent-fuel assemblies are to be inserted (see Figures 1-1 and 1-2 in the Introduction section) Because these basket assemblies will be required to contribute to nuclear criticality control over an extended period of time, they will need to successfully withstand corrosion and dissolution in the operating environment inside the eventually breached WPs

A scoping study of possible candidate basket materials was discussed previously (McCright, 1997). Additional materials have since been tested under the same conditions

4.1 Completion of Basket Material Survey Test

The additional materials tested in the scoping studies were specimens of anodized Boral, furnished by AAR Advanced Structures Boral is a trademarked aluminum–boron carbide composite material The anodized material was reportedly developed for improved corrosion resistance. Because the anodized layer could potentially become scratched, both unscratched and intentionally scratched anodized Boral samples were tested to determine whether surface defects have a significant effect on corrosion performance The test environment was.

0 01 M formic acid (HCOOH),
0 01 M sodium formate (NaCOOH),
0.02 M sodium oxalate ($Na_2C_2O_4$),
0.01 M nitric acid (HNO_3),
0.01 M sodium chloride (NaCl),
0.01 M hydrogen peroxide (H_2O_2),
in distilled water

The environment simulates a highly radiolyzed aqueous solution that might develop inside the WP The carboxylic acids would be formed from radiolysis of CO_2 and water, nitric acid, from radiolysis of N_2 and water, and hydrogen peroxide, from radiolysis of water The initial pH of the test environment was 3 89 The tests were conducted at 90°C for 96 hr. Specimens were weighed before and after test, and the weight loss was converted into an annualized corrosion rate.

Table 4.1-1. Selected corrosion and pH results from the candidate basket material scoping test.

Sample Number	Sample	Mass Loss (g)	Corrosion Rate (mm/yr)[a]	Final pH
3	Boral	0 061	1 8	7 32
29	Anodized Boral	0 010	0 26	6 52
30[b]	Anodized Boral	0 118	3 0	6 57
31	Anodized Boral	0 084	2 2	6 65
33[b]	Anodized Boral	0 545	16 6	6 35
34	Anodized Boral	0 133	3 5	6 52
36[b]	Anodized Boral	0 229	6 2	6 52
32	Control	–	–	3 89

[a] Pitting was observed Rates do not represent uniform corrosion
[b] Intentionally scratched specimens

The anodized Boral did not perform better than as-processed Boral Pitting was not observed on the anodized specimens, but, for most anodized samples, corrosion rates were higher There is some scatter in the corrosion rates in Table 4.1-1, we believe this scatter is due to the enamel applied to the edges of the anodized Boral specimens In some cases, the enamel was difficult to remove, leading to errors in the final weight of the corroded specimens However, scratching the surface apparently did increase the corrosion rate A recent report (Van Konynenburg et al , 1998) includes the results from the anodized Boral specimens and all of the previous candidate materials

4.2 Corrosion Testing of Boron Stainless Steels

Interest in criticality-control materials has largely focused on 300-series types of austenitic stainless steels containing boron as the neutron absorber Results from the scoping testing on these materials in the simulated radiolysis environments (Van Konynenburg et al , 1998) indicated that these materials should perform adequately Stainless steel has other attributes favorable for construction of the basket partitions The basket would be formed from interlocking plates of the boron stainless steel and would not be welded. Previous results from the survey test showed intense corrosion in the welded areas, and the welded area would be expected to be brittle because of the high boron content

Boron stainless steels have been introduced into the Long-Term Corrosion Test Facility The content analyses, provided by the material suppliers, of the five materials presently under test is presented in Table 4.2-1

Table 4.2-1. Chemical analysis (wt%) of stainless steels under long-term corrosion test.

Material	Neutronit A978, heat #N156129	Neutronit A978, heat #E084295	Neutrosorb PLUS	Austenitic Type 304	Austenitic Type 304
Supplier	Böhler-Bleche of Austria	Böhler-Bleche of Austria	Carpenter Technology	Metal Samples, Inc.	Metal Samples, Inc.
Type	wrought alloy boron-containing	wrought alloy boron-containing	powder metallurgy boron-containing	standard stainless steel	standard stainless steel
C	0 02	0 05	0 08 max	0 07	0 04
Si	0 5	0 83	0 75 max	0 49	0 57
Mn	1 08	1 44	2 0 max	1 85	1 78
P	0 022	0 017	0 045 max	0 028	0 025
S	0 004	0 015	0 03 max	0 001	0 0004
Cr	17 26	16 21	18–20	18 26	16 13
Mo	2 08	2 1		0 15	2 1
Ni	13 07	12 31	12–15	8 16	10 42
Co	0 051	0 039			
B	1 62	1 38	1 75		
N			0 1 max	0 07	
Cu				0 4	0 2

Two standard stainless steels were included to provide material for comparison Previous electrochemical testing, in which specimens were subjected to a range of anodically polarized potentials, indicated that there was preferential dissolution of the austenitic matrix, leaving behind the boride phase Preferential dissolution of one of the phases may or may not occur in the long-term corrosion test environment, because these specimens are maintained at the open-circuit corrosion potential The pattern of corrosion attack on the boron-containing specimens will be noted

Available for testing were 27 specimens of each of the five materials In March, 1998, they were emplaced in three vessels, all maintained at 90°C Vessel 26, containing high ionic strength water (~1000× J-13 well water), Vessel 28, containing acidified high ionic strength water (pH ~2 7), and Vessel 32, containing concrete-conditioned water Specimens will be withdrawn for examination after six months, details about the vessels, test solutions, and test procedures can be found in Section 2 2 Additional analytical results on the composition of these materials and documentation of their microstructures are being acquired.

4.3 References for Section 4

McCright, R.D. (1997) *Engineered Materials Characterization Report* Milestone report for the CRWMS Management and Operating Contractor, U.S. Department of Energy (TR251FB9, Rev. 1) Livermore, CA: Lawrence Livermore National Laboratory (Also UCRL-ID-119564, Rev. 1) [MOL.19980105.0616]

Van Konynenburg, R A., P.G Curtis, and T S E Summers (1998) *Scoping Corrosion Tests on Candidate Waste Package Basket Materials for the Yucca Mountain Project* (UCRL-ID-130386) March, 1998. Livermore, CA Lawrence Livermore National Laboratory.

5. Engineered Barrier System Materials

by Annemarie Meike

5.1 Introduction

The chemical composition of high-level radioactive-waste emplacement drifts at the proposed Yucca Mountain (YM) site is expected to be extremely heterogeneous and significantly different than the surrounding rock The presence of a large volume of construction materials introduces chemistry and even some processes that are outside of those normally considered in geological arena However, much of the characterization work can be accomplished using well-developed geological concepts and principles In fact, we are describing the low-grade metamorphism of construction materials The purpose of this work has been to interact with design effort to identify materials and design options that might jeopardize the long-term robustness of a high-level radioactive-waste repository and to develop the basis for the selection of alternatives We examine the chemical and physical evolution of construction materials, the interaction of these materials with water, and ways in which these materials may be explicitly engineered to obtain chemistry and physical properties that are desirable for the waste-package (WP) environment

This section reviews the main categories of relevant materials and processes We then focus on the Engineered Barrier System (EBS) materials that presently represent the largest volume of introduced material and the mechanical support for the drift and vehicles Material options presently under consideration for mechanical support of the drift are steel sets, precast concrete liners and cast-in-place concrete Invert materials under consideration are concrete, crushed material (tuff), or other material, possibly including an agent to engineer a chemical or physical conditioning effect Currently, the preferred option is to construct 95–98% of the drifts in precast concrete and the remaining 2–5%, which require geological mapping, in steel sets Calculations of bulk volumes and compositions per meter of repository tunnel are presented in this section

5.2 Construction Materials of Interest

Ten years ago, a report by West (1988) pointed out that a wide range of materials is normally introduced into an underground-tunnel construction site A point that was less clear was that materials in an underground high-level radioactive-waste repository may be present in combinations, exposed to conditions (e g., temperature), and required to be tracked over periods of time that are not heretofore within the common experience of the engineers designing it Therefore, the construction of a high-level radioactive-waste repository may require design restrictions and construction methods that are beyond the normal construction practice Since the inception of the Introduced Materials effort, our goal has been to predict and quantify materials usage, to predict the evolution of those materials over time as a function of repository conditions, and to determine whether their presence affects repository processes

Our preliminary attempts to estimate materials usage are outlined in Meike (1996) Introduced materials include those used for excavation, mechanical support and stabilization, transportation, mucking, and dust control In the absence of much specific compositional information on the repository design itself, we relied heavily on the construction of the Exploratory Studies Facility (ESF) as an analog for standard quality-assured construction

practices. Those observations have led us to useful conclusions regarding normal construction activities—the necessary deviations from and inherent flexibility in a construction design, auxiliary and implicit materials, and accidental spills, all resulting in the use of materials that may not be included in design drawings. These observations will be used to develop more realistic estimates of material usage than can be obtained from the design drawings

Since the publication of the synthesis report, additional information (Tang, 1997) has allowed us to estimate bulk volumes and chemical compositions of the basic elements of the base-case repository design However, in some cases we have relied on detailed construction drawings from the ESF as representative of standard modern construction practice, in the absence of equivalent detail on the repository design. This information is presented below Recent information from repository design (Appendix A) appears to validate our first estimates as conservative but reasonable

The chemical composition and design of two standard types of mechanical ground support presently under consideration, steel sets and concrete liners, were obtained from Tang (1997) Using this and other relevant information we have calculated bulk oxide compositions per meter of tunnel. We will incorporate relevant modifications from later revisions of the Tang report into our work as they appear

5.2.1 Metal Alloys

Metals that are introduced into a repository environment as a result of construction are used for many different functions and are composed of almost as many different alloys Thus, the concerns of the introduced-materials studies are far different from those of studies to select a material for the WP Many of the high-tech alloys considered for waste-packaging materials are not used widely in construction Conversely, the alloys that are used in construction are the more common and cheaper metals that may not make the best WP. Fortunately, most of the metals used in construction have been used for many years and provide a foundation of knowledge in this area In addition, the corrosion of carbon steel is receiving attention in other activities (see Section 2) For that reason, we restrict our discussion to calculations of volumes and chemical compositions of the EBS materials

Steel Set Calculations

We have used the following statements from the Tang (1997) report to guide our calculations.

- "The outer barrier material of the waste packages is carbon steel, which is very similar to the material for the steel sets." (p. 15)
- Grade and specification of carbon steel has not yet been determined (p. 64)
- Use steel conforming to American Society for Testing and Materials (ASTM) standard A36 (p. 63)
- Keep carbon content low. Steel with 0.11% carbon is six times tougher than steel with 0 88% carbon (p 63).
- There will be no protective coatings on the steel sets (p. 65)

We have used the following assumptions and baseline data

- Quantities of items per meter were based on as-built usage in the ESF. The total numbers of the items were obtained from reports by the engineering firm Kiewitt The most complete information we have is for the section of ESF between 58 and 800 m

into the tunnel. We have arrived at a per-meter usage by dividing by the total number of meters (742 m).

- The diameter of the ESF is 7.62 m (the diameter of the tunnel-boring machine) and the diameter of the emplacement drift is 5.5 m (Tang, 1997), so the radius of the emplacement drift will be 72 2% of the radius of the ESF
- Calculations of quantity of steel did not include quantities of rock bolts and wire mesh.
- Bolts are the same composition as the carbon steel used for steel sets
- Final volume and mass of the steel in the emplacement drift was obtained by summing the volume and mass of steel in a linear meter of ESF tunnel and calculating 72.2% of those amounts In reality, different scaling considerations will apply.
- Schedule 40 steel-pipe dimensions are from Lawrence Livermore National Laboratory (LLNL) Engineering Standard Reference FSC No. 47, "Pipe and Tube."
- Drawings show that one shim pack is available for each steel set. A shim pack contains 7 shims: two 0 125-in , two 0 25-in , two 0 5-in., and one 1.0-in. The width of the total shim pack is 2 75 in. We do not have data on which size was used and assumed that the 0.5-in size was used.
- Bolt length for 0.5-in.- and 1.0-in.-diameter bolts is 3.0 in.
- Nuts and washers were not included in these calculations. Bolt volumes are calculated as cylinders
- We did not calculate a volume or mass for steel wedges Their use is optional, and the quantity of steel is insignificant compared to other steel set components.
- Steel mass was calculated by multiplying the volume of steel by 7.86 g/cm^3, the density of carbon steel.
- Insert length is variable (Heiner, 1994, note 4) We assumed that the average length is 7.0 in (maximum inside length is ~7.75 in)
- When correlating Kiewitt reports to drawings, we assume the following nomenclature translations·
  - Top component = crown segment
  - Side component = wall segment
  - Dutchman = insert
  - Bottom component = foot plate

Where possible, actual usage was calculated. Quantities of the various components used per meter of ESF are tabulated in Table 5.2-1. Quantities of items not shown in Table 5 2-1 are based on estimates. Estimates were made from engineering drawings. For example, a drawing indicates that there are four bolts between each top component and side component. Quantities were calculated as a ratio of number of the items per steel set, multiplied by the number of steel sets, divided by 742 m

Table 5.2-1. Quantities of steel set components used in the ESF.

Steel set component	Distance into ESF tunnel (m)					Quantity per m
	58–200	200–400	400–600	600–800	Total	
Top component	116	83	132	135	466	0 63
Bottom component	232	166	264	270	932	1 26
Shims and dutchmen	232	166	264	270	932	1 26
Side components	232	166	264	270	932	1 26
Shims	486	835	1879	1325	4525	6 1
Lagging	3521	3567	6017	6973	20,078	27 1
Tie rods	1276	891	1430	1485	5082	6 85

In the absence of more specific information, our calculations used the composition of carbon steel (density = 7.86 g/cm^3) (see Table 5.2-2) that is being tested for use in the outermost layer of the WP (McCright, 1996, Van Konynenburg et al , 1997) The alloy composition, provided by the mill that fabricated the product, apparently conforms to ASTM A516 for grade 55 carbon steel. These values can now be compared to our present compositional information provided by repository design reports (Prater and Bhattacharyya, 1998) For the calculation of chemical composition, see Table 5 2-3.

Table 5.2-2. Comparison of the composition of experimental carbon steel (A516) used for these preliminary calculations, compared to steel set (A36) and Swellex Rock Bolt compositions.[a]

Element	Waste package (A516) wt%	Steel sets (A36) wt%	Swellex bolts[a] (F32-95) wt%
C	0 14	0 26	0 79
Mn	0 72	–	–
Si	0 25	0 40	–
Cr	0 04	–	–
Mo	0 01	–	–
N	0 047	–	–
P	0 01	0 04	0 058
Cu	0 04	–	–
Ni	0 02	–	–
Al	–	–	–
Cd	0.0001	–	–
S	0 021	0 05	0 13
V	0 02	–	–
Fe	98 68	99.25	99 02

[a] Composition of washer, plate, and shell not included in this table

Table 5.2-3. Mass calculation for emplacement drift steel sets.

Steel set component	Avg. # per m	Max. # per m	Vol. of steel (cm^3/item)	Vol. of steel (cm^3/m ESF)	Max. vol. steel (cm^3/m ESF)	Mass of steel (kg/item)	Mass of steel (kg/m ESF)	Max. mass steel (kg/m ESF)	Vol. in empl. drift (cm^3/m ESF)	Max. vol. (cm^3/m ESF)	Mass in empl. (kg/m ESF)	Max. mass (kg/m ESF)
Top component (1)	0.63		34,980	21,969		274	172		15,861	15,861	124	124
Bottom component (2)	1.26		6,978	8,765		54.8	68.9		6,328	6,328	49.7	49.7
Dutchmen (2)	1.26		2,499	3,138		19.6	24.7		2,265	2,265	17.8	17.8
Side components (2)	1.26		34,980	43,937		274	345		31,722	31,722	249	248
Shims	6.10		396	2,417		3.12	19.0		1,745	1,745	13.7	13.7
Lagging (×1 m lengths)	27.06	79	2,181	59,016	172299	17 1	463	1354	42,609	124,399	334	977
Tie rods (×1 m lengths)	6.85	22	285	1,952	6270	2.24	15.3	49.3	1,409	4,526	11 1	35.6
Steel pipe (x 1 m lengths)	6.85	22	516	3,533	11347	4.05	27.8	89.2	2,550	8,192	20.0	64.4
End plates (6)	3.77		726	2,736		5.71	21.5		1,975	1,975	15.5	15.5
Bolts 1 in. dia. × 3 in.	15.07		38.6	582		0.3	4.57		420	420	3.30	3.30
Bolts 0.5 in. dia. × 3 in.	54.12	99	9.65	522	957	0.08	4.11	7.53	377	691	2.96	5.44
Bolts 0.75 in. dia. × 2.25 in.	2.51		4.07	10.2		0.03	0.08		7.39	7.39	0.058	0.06
Lagging plates	54.12	99	96.8	5,239	9605	0.76	41.2	75.5	3,782	6,935	29.7	54.5
Lagging plates	54.12	99	145	7,842	14378	1 14	61.6	113	5,661	10,381	44.5	81.6
Steel wedges	?											
Total				161,658			1,270		116,717	215,454	917	1,692

Calculation check: total volume per linear meter of emplacement drift multiplied by density of carbon steel = 917.40.

5.2.2 Concrete and Cement

The standard concrete utilized in underground construction is manufactured using Ordinary Portland Cement (OPC) A number of formulations are available, depending on the engineering needs. The variations in the formulations are aimed primarily toward controlling the amount of silicon, aluminum, and sulfur (see Table 5 2-4), but are found to represent a range of compositions not fully realized from Table 5.2-4 A number of additives are used to obtain desired emplacement or cure characteristics These additives are organic and inorganic compounds and can be present in extremely variable percentages of the whole material In addition, concrete contains aggregate, which is often specified primarily by size, not chemical composition Thus, while a number of general expectations can be stated for the long-term impact of concrete such as the potential for increasing the pH of water, the inherent uncertainty of this calculation is quite large due to the potential variability of the formulation An explicit prediction of the long-term degradation of concrete and its impacts on aqueous, mechanical, and biotic processes depends to some extent on the original formulation Further comments regarding the impact of the original formulation are in Section 5 8.4 Conversely, if the potential long-term impacts of various aspects of concrete are made clear, it is possible that formulations can be modified somewhat to control or avert some negative impacts

Table 5.2-4. Typical compositions of portland cements (Kosmatka and Panarese, 1994).

Types of portland cement (OPC)[b]	General chemical composition (oxide wt%)[a]					
	CaO	SiO_2	Al_2O_3	Fe_2O_3	SO_3	MgO
I	64 4	20 9	5 2	2 3	2 9	2 8
II	63 6	21 7	4 7	3 6	2 4	2 9
III	64 9	21 3	5 1	2 3	3 1	3 0
IV	62 3	24 3	4 3	4 1	1 9	1 8
V	64 4	25 0	3 4	2 8	1 6	1 9

[a] Note that these are modal compositions and do not represent the mineral phases present

[b] OPC types are developed for specific purposes and that the latitude in chemical composition can vary from the general composition listed in this table In addition, the amount of control over any particular component may vary, even within one grout type

It is clear from our examination of the use of cementitious materials in the ESF (e g , Meike, 1996) that grout, shotcrete, and precast concrete are all standard materials of considerable utility, from rock bolt emplacement to invert material to cast-in-place mechanical support All of these materials are under consideration in the latest repository design documents as of this report.

Concrete Liner Calculations

Considerations regarding the concrete formulation for an emplacement-drift environment are discussed on pp. 16–53 of Tang (1997) The estimates of quantities of concrete components per linear meter of lining were calculated using the estimated weights of material per linear meter taken from p 30 of Tang (1997) and the following assumptions and caveats

- Silica fume wt% used corresponds to the silicon metal variety (Tang, 1997, p. 39)
- No wt% information for other concrete components. water-reducing admixture, superplasticizer, steel fiber.

- Wt% for aggregate has been calculated water-free, as shown in Table 5 2 5, using the following assumptions·
  - Fine aggregate· 3% moisture content. 0.03 × 2990 kg = 89 7 kg (90 kg), so dry weight ≈ 2900 kg.
  - Coarse aggregate: 1% moisture content. 0 01 × 3864 kg = 38.64 kg (39 kg), so dry weight ≈ 3825 kg
- Steel fiber composition is similar to that used in Fibercrete™ emplaced in the ESF Composition is from Meike (1996)

The coarse and fine aggregate are given the composition of dry tuff Because of the volume and mass contribution of aggregate to the concrete liner, variations or modifications in the aggregate will significantly affect the chemical signature of the concrete liner Also, aggregate sources vary in composition. It cannot be assumed, without explicit specification, for example, that fine aggregate consists of quartz sand Aggregate compositions are also expected to vary with time

Table 5.2-5. Estimate of quantities of concrete components per meter of lining.

	Cement type V		Coarse aggregate		Fine aggregate		H_2O		Silica fume		Steel f
	wt%	Wt. (kg)	wt%	Wt. (kg)	wt%	Wt. (kg)	wt%	Wt. (kg)	wt%	Wt. (kg)	wt%[a]
SiO_2	25	382	78.7	2,994	78.7	2,270			95	215	
Al_2O_4	3.4	52.0	12.2	465	12.2	352			0.7	1.59	
Fe_2O_3 (Fe)[a]	2.8	42.8	0.996	38.1	1.0	28.9			0.3	0.68	99.8
CaO	64.4	985	0.474	18.1	0.47	13.7			0.3	0.68	
MgO	1.9	29.1	0.123	4.70	0.12	3.57			0.2	0.45	
TiO_2		0	0.101	3.86	0.10	2.93				0	
Na_2O		0	4.08	156	4.08	118			0.3	0.68	
K_2O		0	3.28	125	3.28	95.1			0.3	0.68	
P_2O_5 (P)[a]		0	0.02	0.77	0.02	0.58				0	0.04
MnO (Mn)[a]		0	0.052	2.0	0.05	1.51				0	0.075
SO_3 (S)[a]	1.6	24.5							0.8	1.82	0.05
C (inorganic)		0							1.3	2.95	0.02
Organic[b]											
H_2O		0					100	617			
Total	99.1	1516	99.6	3809	99.6	2888	100	617	99.2	225	

r.a. = reduc. admix; superplas = superplasticizer.

[a] Cation only (not oxide) calculated in alloy composition.

[b] Undetermined organic compounds and water

5.2.3 Backfill

Interest in backfill material comes from a number of areas. First and primary interest has been for mechanical support. However, engineered backfill has been proposed in a number of plans to improve or stabilize certain desired hydrological or chemical conditioning effects. Glassley and Meike (1997) conducted a simulation study of a backfill composed of quart sand, lime and an iron phase

A review was conducted of a range of solid phases that may act as potential pH and redox buffers in backfill material (Glassley and Meike, 1997) The approach taken was to consider only metals, oxides, hydroxides, carbonates, sulfides and sulfates These compounds were chosen for consideration because their chemistries are relatively simple, their reaction rates are often well established, and their thermodynamic properties are usually better known than those of more complex compounds.

5.2.4 Microbes

Native microorganisms reside within the potential repository environment Microbial communities have been characterized from a variety of deep subsurface environments, and ongoing work has already identified some of the native microbiota in the YM region (Russell et al , 1994). In addition, microbes will be introduced during the construction and monitoring period of the potential repository. Native and introduced bacteria can alter chemical, radionuclide transport, and hydrological properties of the surrounding engineered and rock barriers Studies to assess potential impacts of microbial activity on the YM repository are focused on determining the significant microbial processes, to provide bounds for both the effects of microbial activity (rates, biomass, material substrates, and products) and for the conditions under which microbial activities will occur Our laboratory studies are intended to determine bounding conditions for various microbially mediated reactions. We focus on the chemical and hydrological impacts of entire microbial communities rather than the microbes themselves, and this sometimes leads us in directions that are outside the scope of traditional microbiology These studies are conducted primarily using YM–derived microbial isolates (representative of both native and introduced populations), although carefully chosen analog studies also supplement characterization of in situ reaction rates to best predict long-term microbial effects.

Biomass can act as colloidal particles or can modify fracture characteristics and thus hydrological flow paths. Even the prediction of the chemical impacts of microbes is predicated on the ability to predict biomass. Preliminary determination of growth rates of whole YM microbial communities under varying conditions has been undertaken to support modeling efforts. Our preliminary findings demonstrate that microbes present at the YM site are capable of survival and growth under conditions approaching those anticipated after waste deposition (see, e.g., Meike, 1996; Horn and Meike, 1995). Single bacterial strains were isolated both aerobically and anaerobically from whole and aseptically crushed (1.7–2.4 mm) rock samples at room temperature. Identified and preserved YM bacterial isolates included representatives of the following genera: *Bacillus, Arthrobacter, Cellulomonas, Corynebacterium, Pseudomonas, Staphylococcus, Xanthomonas,* and *Flavobacterium.* These bacterial classes collectively contain members that are capable of forming spores, producing acids, degrading a wide variety of organic compounds, and remaining active under both aerobic and anaerobic conditions. Some examined microbes can grow in the absence of oxygen and at temperatures of at least 50°C. Growth rates are measurable at ambient and elevated temperatures, and probable spore-forming organisms are even capable of surviving repeated

exposure to 120°C. Further in vitro determinations will aid in determining in situ rates of growth, which can then be correlated with hydrologic flow rates Depleted nutrient conditions favor the growth of only a select group of microbes, but these are capable of reaching high cell densities under aerobic conditions, even at 50°C.

5.2.5 Water

Introduced water comes from a number of construction sources, including dust-control and mucking operations The preferred rheology of the cement at the time of emplacement dictates the quantity of water added to the dry cement mix and usually exceeds that required for complete hydration. Therefore, extra water is expected anywhere that wet grout is emplaced During the construction of the ESF, much of the introduced water was labeled with a LiBr tracer. The water "bleeding" from cast-in-place grout and shotcrete, however, was not labeled, because LiBr accelerated curing, so it has been difficult to determine the significance of water from cast-in-place cementitious material in the ESF

5.2.6 Organic Materials

Our examination of potential chemical effects of organic materials has been conducted with two very different goals. The first goal is to assess the potential contamination of studies conducted in the ESF by introduced materials The second goal is to examine organic materials in the context of a radioactive-waste repository, whether they may react with the surrounding rocks, causing changes in repository porosity, and whether they may react with the WP or waste form and enhance the mobility of radionuclide species

5.2.6.1 Polymers

Organic compounds take many forms, but perhaps the one class of compounds that is pervasive and deserves the most detailed scrutiny is polymers Polymers are pervasive in the construction industry. For many polymers, temperatures within the range of potential repository conditions produce significant degradation, sometimes within hours rather than the thousands of years for which the repository must contain the waste Because of a number of potential thermal degradation effects, epoxy resins should not be included in the permanent structure, without detailed long-term tests. The chemical significance and usage requirements of polymer resins need to be assessed and established on a case-by-case basis. Even then, some care will need to be taken because the very-long-term effects (e.g., thousands of years) are outside our ability to observe between now and the time that a repository is needed. Therefore, it may be important to include the effects of polymer degradation in some modeling scenarios. For polymers that degrade over short periods of time, much of the chemical modeling of long-term chemical effects on the near-field environment (NFE) may be conducted with the final products of the polymer degradation as reactants. The final products of most polymers are known; the majority are monomer hydrocarbons and some volatile products such as toluene, xylene, and cresol. For further discussion of polymers, see Meike (1996).

5.2.6.2 Organic Content of Concrete.

Formulations for concrete and grout sometimes contain additives that improve the workability, curing time, or other characteristics of the concrete. Some of these additives (e.g., superplasticizers) are organic.

5.2.6.3 Diesel Fuel and Exhaust

Two studies have been conducted on different aspects of diesel fuel contamination The first was conducted primarily to assess the potential impact of diesel operation on geochemical studies conducted in the ESF. The other study was oriented toward understanding the significant long-term degradation processes at elevated temperature Chemical isotope studies of selected introduced materials were conducted in the ESF in support of geochemical tests to determine what the potential effect of contamination would be to those geochemical studies (Meike, 1996). One effect is the potential contamination of ^{14}C from a number of sources A preliminary interpretation of these results is that any possible contamination of geologic samples taken from ESF by diesel fuels would result in apparent ^{14}C ages older than their real ages. The extent of mixing of carbon indigenous to ESF geologic samples with fuel-derived carbon can be assessed, however, this task is beyond the scope of this preliminary report It is significant that apparently young ^{14}C ages from ESF materials could not have been produced by contamination with fuel or exhaust from diesel fuel

The second study, an investigation of long-term diesel exhaust effects was conducted using N-Tunnel (Nevada Test Site) as a historical analog (Meike et al , 1995) The study represents a broad approach to material degradation that aimed first to assess the rate-determining processes before embarking on the detailed experiments. Biotic and abiotic processes were considered, and organic and inorganic materials were analyzed

5.2.6.4 Miscellaneous Organics

Our observation of construction in the ESF makes it clear that certain stabilization and other needs may be met by the use of cellulose materials These include excelsior (wood shavings) and rags

5.3 Phase and Chemical Stability: Material and Fluid Evolution with Time and Environment

5.3.1 Range of Processes

The product phases of material evolution, disintegration, biodegradation, and corrosion may include oxides of metals, sulfides, chlorides, carbonates, and silicates, as well as organic compounds, alkali metals, and halogen elements. These materials have the potential to alter the pH, ionic strength and composition of water that may be present at some time in the lifetime of the repository. In addition to aging, gamma-radiation effects must be considered in the WP environment, as discussed in Van Konynenburg (1984). The chemical effects of gamma radiation on man-made materials remain largely uninvestigated, even though aggressive substances, such as nitric acid, can be a product of such processes

We distinguish between those chemical processes that are biotic, or mediated by living organisms, from those that are abiotic, or independent of living organisms. As will be discussed, most of our predictive chemical-modeling capabilities are abiotic. Thus, to use that modeling capability without explicit recognition of biotic chemical processes implicitly assumes that they are insignificant compared to abiotic processes. Clearly, this is untrue for some materials, such as some organic compounds, over long periods of time in natural environments. In addition, given the potential confusion in terminology, we define at the outset "organic chemistry"—those processes that involve organic compounds—as distinct from "biotic chemistry," which involves a living intermediary, such as a colony of microbes. Microbially mediated (biotic) processes do not necessarily depend on the presence of organic

compounds (e.g., hydrocarbons) and can significantly affect inorganic chemistry (see discussions in Hardin et al , 1998; Meike, 1996; and Horn and Meike, 1995).

5.3.2 Evolution of Materials at Elevated Temperature

A unique aspect of the Yucca Mountain (YM) strategy relative to other high-level radioactive-waste strategies around the world is that water will probably contact the repository materials only after it has been exposed to elevated temperatures (>100°C) for an extended period of time (>150 years) Thus, the mineralogical composition of many of these materials is expected to evolve, and the subsequent material–water interaction may be quite different than with the original material.

5.3.2.1 Evolution of Metals

Metals that may be introduced into the WP environment for construction purposes will be primarily iron and iron alloys, which can degrade through several mechanisms Oxidation is one common degradation process. Such processes depend strongly upon the Eh and pH of the environment within which oxidation occurs. According to corrosion test results (see Section 2) there will be a mixture of oxides that form from carbon steel. If conditions are very oxidizing, primarily hematite is expected. If the conditions are less extremely oxidizing then the various FeOOH phases are expected. Under even less oxidizing conditions, magnetite is expected According to abiotic corrosion studies (see Section 2), hydrated oxide, $Fe_2O_3 \cdot xH_2O$, is also to be expected Although $Fe_2O_3\ xH_2O$ may account for only a small fraction of the total oxide weight percent, the hydrated oxide has a much lower density, and thus may be significant with respect to volume changes during corrosion At present, this aspect of corrosion and its relation to relative humidity are being pursued (see Section 2). However, even a simple calculation, assuming that all of the iron (917 401 kg/m, calculated in Table 5 2-3) is converted to hematite (Fe_2O_3), indicates that a major increase in volume is associated with the oxidation, thus

(917 kg/m alloy)(0 9868 wt%) = 905,291 g Fe per linear meter of drift

= 16,210 2 moles/m Fe (55.85 gram-molecular wt)

= 8,105.1 moles/m Fe_2O_3 (2 moles Fe/mole Fe_2O_3)

= 1,294.3 kg/m Fe_2O_3 (159.69 gram-molecular wt)

= 0.245 m^3/m (density of Fe_2O_3 is 5.28209 g/cm^3).

This represents an increase in volume of 0.12 m^3 per linear meter of tunnel, or 109%. Iron, if present in large volumes, has the potential to consume large quantities of oxygen during its oxidation and to influence the atmospheric chemistry around WPs if the environment is sealed or semi-permeable to gas. Another simple calculation, using the assumption that all iron is converted to hematite, indicates that at 25°C,

8,105 1 moles/m Fe_2O_3 requires 24,315.3 moles of oxygen

= 12,157.65 moles O_2

= (105 V)/(298.15)(8.314510) (ideal gas equation)

and V = 301.4 m^3 of oxygen gas per meter of drift will be consumed during the complete oxidation of this iron.

Experimental studies of copper corrosion in sea water and in the presence of sulfide ions (Mor and Beccaria, 1975) indicate that a variety of copper sulfides can form that also depend on pH. The specific conductivity and resistance to corrosion of the metal depend on the corrosion product, which is pH-dependent. In general, the rate at which metal ions are added to the water, and thus contribute to the water chemistry, depends on the corrosion products

5.3.2.2 Evolution of Cementitious Materials

5 3 2.2.1 Previous Studies

Reactions known to occur in cementitious materials, over time and at room temperature, are expected to contribute to alterations in the mineral assemblage and to their degradation and reduction of mechanical strength These reactions are chloride attack, the alkali–silica reaction, and delayed ettringite formation (DEF) Chloride attack works by the ingress of chloride-bearing water through permeable grout or cracks to contact and corrode the metal reinforcement (rebar). Expansion of the rebar due to corrosion causes the cementitious materials to crack and spall. One source of chloride attack for the present application is the use of aggregate, from desert climates, that may contain evaporated salts (Taylor, 1990) Alkali silica reaction occurs when silica-bearing aggregate reacts with alkali impurities in the cement paste. As with chloride attack, expansion occurs due to formation of the product phases, causing cracking (Taylor, 1990). DEF is also a cracking process due to the late formation of sulfate-bearing phases (Taylor, 1990). There is still much debate about the causes of DEF However, some significant DEF has been related to the heat-curing of sulfate-bearing cements. A phenomenon similar to DEF may also occur through the formation of thaumasite, a sulfate–carbonate mineral

Roy and Langton (1983, 1989) have studied ancient concretes to ascertain mineral stabilities and instabilities that may be applicable to modern portland cements The ancient concretes, which were made from lime formulations, are not completely analogous to modern concretes, which are formed from more reactive alite and belite phases that require higher temperatures for manufacture. Although made with unknown processes as well as varying starting materials, and mixed using unknown water–cement ratios, ancient Roman concretes often incorporated pyroclastics, including tuffaceous material. A main conclusion that Roy and Langton draw from examination of ancient materials is that low-permeability cements, and particularly pozzolanic cements, have the greatest durability A study of mortars from the Byzantine basilica of Hagia Sophia, Istanbul, suggests that a calcium–silicate–hydrate phase is present. The degree of crystallinity is not well constrained, however, and the mortar appears to be dominated by a calcium carbonate phase (Livingston et al., 1992). A cursory examination of a portland cement that had been submerged in water for 63 years at near room temperature (Rhoderick, 1981) suggested no "significant effect" on either composition or microstructure. The relevant experimental literature has been summarized in a synthesis report (Meike, 1996).

Portlandite and many of the Ca-Si-H_2O phases are unstable when in contact with CO_2 gas. Over time, excess portlandite in concrete converts to $CaCO_3$, usually in the form of calcite. Crystalline Ca-Si-H_2O phases, e.g., tobermorite (see discussion in Hardin et al., 1998), also react with CO_2 gas, forming $CaCO_3$ and SiO_2. Unknown, however, are the relations between temperature, CO_2 fugacity, relative humidity and phase stability that would allow us to predict, for a given environmental scenario, the identity of the mineral assemblages making up the evolving material and the composition of water in contact with that material.

Notably scarce are detailed studies of cementitious materials that have been exposed to elevated temperatures for the extended periods of time required to obtain even the relations between temperature and phase stability. Elevated temperatures will cause changes in composition, phase and microstructure, which would ultimately affect the chemistry of the water in contact with the material, as well as its structural integrity. It is likely that the cementitious materials will dehydrate and transform to a more crystalline mineral assemblage Many phases in the crystalline Ca-Si H_2O system can develop in cement exposed over long periods of time to temperatures above 25°C. The phases themselves are found both naturally and in synthetic systems

5 3 2 2 2 Hydrothermal Alteration of Concrete· Pressure Vessel Experiments

Experiments were designed to provide data for a quick engineering assessment of the microstructural, mineralogical, and (to a lesser extent) mechanical changes in hydrothermally altered concrete and changes in associated water chemistry (Meike et al., 1997b, Myers and Meike, 1997). In emplacement drifts, concrete will be subjected to elevated temperatures of at least 150°–200°C, and perhaps even greater temperature if backfill is used.

In our experiments, we used two types of cementitious material—invert concrete and shotcrete—both from the Exploratory Studies Facility (ESF). Our analyses reveal that the invert concrete is composed primarily of carbonate aggregate, especially within the larger size fraction. The shotcrete aggregate is composed primarily of quartz and other silicate minerals

Three experimental suites of progressively longer duration were performed and analyzed. Each suite consisted of a vapor (invert and shotcrete) and an aqueous (invert only) 1 M NaCl treatment and 1 M $NaHCO_3$ treatment, and a dry treatment in which an aqueous solution (deionized water) was added only for the last 2 weeks of the longest (8-month) experiment In the future, we intend to compare the aqueous and the mineralogical results from these experiments with chemical-modeling simulations to assess the adequacy of our thermodynamic and kinetic data (Clodic and Meike, 1997).

The results demonstrate that concrete alteration in an aqueous environment can be very different from alteration taking place in a vapor-phase environment We expect, based on these and other studies, that alteration in the vapor phase can depend on the composition of the gas phase. In the vapor-phase oxygen-rich alteration case, hydrous minerals are formed, which can shrink and swell as a function of humidity, affecting the strength. In contrast, vapor-phase alteration in a CO_2-rich environment will favor the formation of carbonates

We expected the chemistry of the original aqueous solutions to be modified by the sample coupon (invert material) that was inserted in the aqueous solution. The samples exposed to the vapor phase on top of the platform were not expected to affect the solution chemistry The pH of the $NaHCO_3$ solution increased with time to a value of 9.50 at the end of 8 months. The solution had achieved a steady state with respect to the concrete sample, at the conditions of the experiment, within 6 weeks (the duration of Batch 1). The pH of the NaCl solution increased to a value of nearly 11.5. This solution achieved a steady state with the concrete sample, at the conditions of the experiment, within 4 months (the duration of CN-3, which represents Batch 2). We suspect that the Batch 1 aqueous solution achieved a pH of nearly 11.5 rather rapidly, consistent with the $NaHCO_3$ solution results and with the high pH of dry Batch 3 (8-month) samples. In the latter experiment, deionized water was added before the last 2 weeks of thermal treatment (90°C) and was measured at a value of 11.84 pH units.

Thin-section and SEM evidence indicates that secondary calcite is precipitated in many of these experiments The relative magnitude of secondary-calcite formation is not straightforward and will require further work to determine. However, preliminary work suggests that secondary calcite formation is more predominant in the vapor-phase samples of the $NaHCO_3$ solution than in the vapor-phase samples of the NaCl solution or in the dry samples. This suggests some influence of a higher partial pressure of CO_3 gas in the $NaHCO_3$ pressure vessel Secondary calcite is found in all of the aqueous-phase samples, which are all of invert composition, containing a large quantity of carbonate aggregate (calcite and dolomite). Clearly, the presence of carbonate minerals in the original aggregate affects the character of secondary mineralization in the aqueous phase

An abundance of secondary crystalline Ca-Si–hydrate phases was observed in the vapor-phase samples. The secondary mineralization on the vapor-phase samples was extremely heterogeneously distributed, due to the localized nature of the vapor-phase reactions The signal of these phases is so weak as to be overcome by the signal of other minerals in x-ray diffraction. Thus, some of these minerals have not yet been uniquely identified. Much of the reaction was located at the boundary between the aggregate and the grout, suggesting possible mechanical consequences. The aqueous-phase samples exhibit far less heterogeneous distribution of secondary phases, and far fewer total phases Scawtite, a Ca-Si–carbonate–hydrate, and kilalite, a Ca-Si–hydrate, were observed consistently in the long-term NaCl experiments Neither of these phases is represented in our thermodynamic data bases, therefore, it will not be possible to incorporate them into simulations that are attempted in the near future

We are able to link the formation of analcime directly to the aqueous $NaHCO_3$ treatment, demonstrating the chemical truth that the formation of a particular phase is a complex combination depending not only on the concentration of the constituent ions in solution, but also the solution's pH We will be particularly interested in our ability to simulate the precipitation of analcime from solution using our models and the new cement data (Clodic and Meike, 1997).

The results of the mechanical tests exhibit extreme variability, and interpretation is deferred until the magnitude of the error has been firmly established. The trend, however, appears to be toward increased mechanical strength in the samples that have experienced secondary-carbonate formation, especially those samples subjected to $NaHCO_3$ treatment. This interpretation is at least consistent with industry practice, in which precast concrete is carbonated for increased strength (Rubin et al., 1997). All treatments may involve more than atmospheric CO_2 because of the presence of large amounts of limestone in the aggregate. The sensitivity of tobermorite and other crystalline Ca-Si–hydrates that may exist in ordinary portland cement to the partial pressure of CO_2 suggests that, in a repository environment, much of the cementitious material could evolve into $CaCO_3$ phases, such as calcite and vaterite and other carbonates (e.g., scawtite).

The consequences to the pH are significant. Whereas a young cement–water system could register pH values of 11 or 12, a system dominated by calcite–water would have a significantly lower pH. We have found that alteration in an aqueous environment leads to a far more homogeneous secondary mineral assemblage than alteration in the vapor phase. This observation is consistent with expectations, because aqueous-phase alteration is expected to be in equilibrium with the aqueous solution. These observations, however, have provided the grounds for a more explicit description of solids as the repository evolves. Specific representative mineral assemblages are calculated below.

Mechanically samples exposed to the bicarbonate treatments appear to be the strongest overall. The dry samples appear to increase markedly in strength over time. The relation between these experiments, conducted at vapor pressure at 200°C, and the atmospheric-pressure thermal treatment expected in a high-level nuclear-waste repository, will be discussed in the final report for the hydrothermal alteration of concrete experiments (see also Myers and Meike, 1997) Further comparisons will be drawn to ESF concrete emplaced in the Large-Block Test (LBT), the Single-Heater Test (SHT), and the Drift-Scale Test (DST)

5.3.2.3 Evolution of Organics

5 3 2 3 1 Diesel Fuel and Other Hydrocarbons

If abiotic degradation were the only mechanism then the hydrocarbons would remain indefinitely (see discussion in Meike, 1996). However, microbial activity can significantly alter that rate of degradation (see discussions in Meike et al , 1995, and Horn and Meike, 1995).

5.3 2.3.2 Polymers

At present our data base for modeling aqueous chemistry includes some possible degradation products, but our modeling capabilities are limited, as is our capability to predict the thermal evolution of the solids over long periods of time The primary modes of degradation for synthetic polymers are thermal degradation, oxidation, and photodegradation and biodegradation The degradation of a polymer cannot be followed by observing the behavior of a similar but simpler molecule. Models have been developed to predict specific degradation processes over times significant to a radioactive-waste repository (Burnay, 1990), however, most models are for normal lifetimes and under normal service conditions (Kenny et al , 1993) An activation energy, which can be derived from thermal analysis, must be reached before degradation begins (Ravanetti and Zini, 1992). The Arrhenius equation is often used to predict the half-lives of materials (Barr-Kumarakulasighe, 1994) It has been found that thermal-degradation rates are increased by higher temperatures, the presence of a radiation flux, oxidative agents, some chemical contaminants, and light. In addition, many polymers can exhibit dose-rate effects or synergism between radiation and temperature or chemical contamination (Burnay, 1990).

There are two types of thermal degradation. The first, depolymerization, involves the breaking of the main polymer-chain backbone so that at any intermediate stage, the monomer units can be recognized (Grassie and Scott, 1985). This is common for polymers that have high values of chain scission at ambient temperature (Garrett et al., 1990). The second, substitution reaction, involves a change in the chemical nature of the substituents attached to the backbone of the polymer molecules, even though the chain structure may remain intact In this case, volatile products will differ from the monomer (Grassie and Scott, 1985).

Specific materials of interest to construction include epoxy resins. Leedy and Watters (1994) found that rock bolt epoxy degrades at temperatures as low as 50°C and should thus not be used for long-term mechanical support in areas that will be exposed to elevated temperature. However, a variation in degradation behavior exists that probably depends on the epoxy. At 125°C, the primary degradation mechanism for epoxy resins is initiated by oxygen attacks rather than by a free-radical mechanism. Many epoxy-resin systems manifest significant oxidative degradation in air at temperatures as low as 100°C (Burton, 1993). A change in mass begins just below 250°C.

5.3.3 Radiation Effects on Polymers

The effect of radiation on polymeric materials has been studied since the construction of the first nuclear power plants in the 1950s When exposed to high-energy radiation, polymeric materials undergo chemical changes. The energy from the radiation excites the polymer molecules, leading to chemical change Most energy is deposited in the substrate by Compton scattering, whereby the ejection of a valence electron is accompanied by deflection of the incident photon by the electron cloud around the atom. At lower energies, the incident photon is completely absorbed by the substrate atom to produce ionization. Radiation degradation can be measured from changes in the molecular weight, from which the degree of cross-linking and scission can be determined. After irradiation, polymers continue to undergo changes For example, irradiation in air leads to the formation of peroxides, and these compounds have characteristic rate-versus-temperature relations for decomposition, usually with significant rates in the range 50°–150°C (O'Donnell, 1990)

Radiation enhances degradation, especially thermal effects, which often occur in parallel with radiation exposure. As energy is added to a system, the temperature is raised The reaction rates are often quite different in a glass and rubber of a given polymer and undergo changes at the transition temperatures. The deterioration in the properties of polymers may be markedly increased by relatively small rises in temperature (Garrett et al., 1990) This tends to be the case with most chemical reactions due to the energy provided by an increase in temperature. An increase in temperature, when combined with radiation, leads to an increase in chain scission. Radical reaction kinetics depend on the polymer morphology, crystallinity, molecular weight distribution, and the main chain stability as well as its higher structure (morphology) (Kaplan, 1991). Time–temperature–dose-rate models have been developed to predict the long-term aging of polymers exposed to radiation (Gillen and Clough, 1989)

The surface effects of radiation tend to be much greater than the effects to the core of a sample, due to greater exposure of the surface As a result of energy transfer, molecular components that are present in only small amounts may be the main sites of chemical change (O'Donnell, 1990) In addition, hydrogen atoms are often yielded due to radiation, which can lead to cross-linking The penetration of low-molecular-weight liquids into polymers leads many to a decrease in the radiation yield of cross-linking (Smirnov and Dubova, 1992) Some correlations can be made between photodegradation and gamma radiation Because absorption of radiation is an essential first step to photodegradation, strongly absorbed radiation will be attenuated as it passes through the polymer and reaction will be concentrated in the surface layers. Thus, photolysis is often identified by the evolution of hydrogen, the development of insolubility, and discoloration. In addition, ultraviolet radiation often initiates oxidation. Photodegradation cannot readily be predicted from the chemical structure due to small impurities and abnormalities often present in polymer chains. It must be tested experimentally.

Thermosets have much more stability to irradiation than thermoplastics. Counterintuitively, perhaps, thermosets exposed to radiation in air degrade more the *lower* the dose rate, because of the oxygen concentration in the interior of samples. The dissolved oxygen reacts with the radiation-induced radicals and builds peroxides. Thus, the thermoset becomes unstable and slowly decays by chain scission. The longer the irradiation time, the more complete is the breakdown of the peroxides and the damage to the material (Wilski, 1990).

5.3.4 Solid-State Response as a Function of *RH*

As part of an experimental and modeling program to characterize the effect that cement will have on the water budget at the potential YM repository, water sorption studies of crystalline calcium–silicate–hydrate phases are being performed These experiments (Martin et al , 1996) demonstrate that many of the crystalline phases expected to form in concrete at elevated temperature are sensitive to changes in relative humidity, *RH*. That is, they shrink and swell, sometimes within an hour in response to a *RH* change of 10%. This characteristic has potential significance for the mechanical stability of concrete after the thermal pulse

5.3.5 Water Stored in Solids

The potential for concrete to act as a reservoir for large amounts of water has not previously been adequately discussed. The identity of the concrete constituents has implications for water retention in repository materials and water availability as a function of temperature, *T*, in the repository.

Water will be conserved in a number of ways within concrete as a function of thermal evolution and of age. Water can be present in liquid form within concrete pores It can be present in solid minerals with varying levels of binding energy—that is, different amounts of energy are required to release that water. For example, if we consider the two sulfate-bearing phases used in these calculations, ettringite begins to lose water rapidly at around 50°C (Taylor, 1990), and thaumasite begins rapid weight loss at 110°C (Taylor, 1990) Other phases also hold water in a different manner. C-S-H is an amorphous structure and holds its water loosely, unlike the higher-temperature crystalline Ca-Si-hydrate phases (such as tobermorite). According to Lea (1971), tobermorite is stable between approximately 100°C and 180°C, beyond that, xonotlite is stable. For our purpose, we allow tobermorite to experience slow, linear dehydration between 100° and 180°C. Tobermorite will lose water reversibly to a certain extent with increasing *T* and decreasing *RH*. Based on this information we have constructed five cumulative water-loss scenarios (see discussion in Meike, 1996) as a function of *T* for concretes with the idealized mineral assemblages.

5.3.6 Water–Material Interaction

It is clear that the addition of man-made materials to the NFE may modify the chemical environment and influence the geochemical reactions that may occur. The most significant of these interactions, based on pure volume of material used, appear to be the effects of cements and metals.

5.3.6.1 Metals

Much of our understanding of the long-term chemical processes involving metals that may be used in a radioactive-waste repository will be based on a firm understanding of historical analogs. Studies of metal artifacts from a variety of ages demonstrate that some phases that form cannot be predicted from our present knowledge of material degradation. Some products of these man-made materials rarely occur naturally and are therefore not necessarily predictable from a geochemical data base. Botallackite, a rare hydroxide of copper chloride, for example, has been observed associated with the corrosion of a copper object exposed to chloride ion (Pollard et al., 1989). Stability fields and reactive sequences of the basic copper (II) chlorides have only recently been proposed (Pollard et al., 1989), extrapolated from this and other historical data as a complement to experimental data, where experimental data alone has previously failed. That diffusion-controlled phenomena should

be expected over time periods of at least 2,000 years is apparent from investigations of corrosion phenomena in ancient bronzes (Scott, 1985). Development of some phases appears to be mediated by the activity of microorganisms (McNeil et al., 1990). In addition, some information on the long-term corrosion of materials has been assembled from the New Zealand analog site (Bruton et al., 1995, Meike, 1996). In the respect that these data represent materials and methods that are more similar to present construction, and more is known about the current environment, some of these data may be more useful to chemical model assessment than much older archaeological artifacts

5.3.6.2 Cementitious Materials

According to the present repository design, concrete may be one of the most prevalent introduced materials in the proposed YM repository, as a liner providing mechanical support in most of the emplacement drifts and as invert under the WPs providing support for the transportation system The present discussion of aqueous chemistry is focused on concrete, which, given its large volume in the present repository design and its ability to modify pH (depending on formulation and age), could be the single most significant material conditioning aqueous chemistry in the repository. Concrete is certainly a major source of uncertainty in the aqueous chemistry, due to the variability in its impact as a function of the original engineered formulation and its evolution through the lifetime of the repository Our ability to predict the chemistry of water in contact with concrete has made progress in both the creation of a more precise conceptual statement of the model and in the expansion of the thermodynamic data base to include phases that must be represented to adequately simulate interactions between water and phases found in concrete. Both of these aspects of our work are described in more detail in Hardin et al (1998).

Concrete is a major source of calcium and silicate chemical species and, depending on the formulation, sulfate and chloride. Organic components, used to condition the wet concrete paste before it is cured, are usually present in very small quantities At low temperatures, they may be a minor source of nutrients for microbes, which may convert these components to other organic compounds or to water and carbon dioxide (Haveman et al , 1996). During a thermal pulse, however, it is possible that the organic components will volatilize and redistribute or even diffuse away from the emplacement drift

The presence of cementitious material may greatly alter the chemistry of water in the proposed repository, and adds a major uncertainty in the prediction of the aqueous chemistry. These materials provide a large reservoir of unstable Ca–silicate phases, which will dissolve and reprecipitate at the rock–water interface Chemical interactions between water and non-thermally-treated grout at 20°–60°C may be dominated by the dissolution kinetics of the unstable amorphous and crystalline phases and precipitation kinetics of the metastable or stable phases (see, e.g., Atkins et al., 1991). Tobermorite (14-Å) forms in water at temperatures below 80°C, but begins to lose interlayer water at 70°C in dry CO_2-free air to yield 11-Å-tobermorite. This type of low-temperature interaction has received much attention internationally and can be found in the radioactive-waste-disposal literature (see the discussion in Meike, 1996).

The pH of water in contact with relatively young cement can be relatively high (10–12). Disintegration and dissolution of cementitious materials may change the pH of water to values as high as 11.5, even at 100°–200°C (e.g., Myers and Meike, 1997). Ca(OH) (portlandite) and alkali hydroxides are responsible for this chemical phenomenon.

Tests in which concretes were leached at 100°–200°C with either distilled water or Standard Canadian Shield Saline Solution in contact with a sodium-bentonite, a waste-glass, or a silica-fume additive, have indicated that the identity and concentration of species in solution is time-dependent (Khomarneni and Roy, 1983, Burnett et al., 1985, Heimann and Hooton 1986, Heimann, 1988a and b) The fate of C-S-H and the cement minerals, and their interaction with the aggregate, are a function of time, temperature, solid and aqueous solution compositions, and the availability of water. Of particular concern to the degradation of concrete is whether the concrete is exposed to air, CO_2, or water, the aluminate and ferrite content of the cement, and the activities of carbonate and sulfate content of the water.

To some extent, physical properties that can regulate the rate of, and the long-term susceptibility to, chemical attack are determined by the initial formulation. One such property, interconnected porosity, is affected by initial water–cement ratios and thus potentially by the method of emplacement Leaching will preferentially dissolve some minerals, such as portlandite, from the set material and thus can increase permeability, which will influence the rate of degradation. Sufficiently high activities of sulfate or CO_2 can react with concrete At elevated temperatures, residual portlandite reacts with carbonates to form calcite (Milestone et al , 1987)

With regard to the potential survival of concrete, we recognize an important distinction between performance lifetime, which is linked to the mechanical stability of the structure, and chemical lifetime, which represents the duration of the chemical effects of the material long after the material has ceased to perform its function. It will be important to explicitly specify the mechanical performance lifetime required of the cements by the design, because it may be possible to obtain modern high-performance formulations that will perform a mechanical function throughout the retrieval period, and perhaps stretching into some of the period after closure However, it may not be necessary (or even possible) to engineer (or prove the stability of) a cement with a performance lifetime of thousands of years

It is highly likely that long after the mechanical "performance lifetime" of the cementitious materials has ended, these materials could perform chemical functions such as sorbing radionuclides, especially if the cement formulation were to contain zeolites as aggregate or pozzolana. In fact, at the point in the evolution of the repository where sorption is required, an invert that has disintegrated, and thus increased surface area, may be an asset, because large surface areas predominantly determine the effectiveness of a sorbent Thus, a cementitious material that becomes greatly fractured or disaggregated increases the effectiveness of the constituent sorbant materials.

5.3.6.3 Backfill

The results of EQ3/6 and OS3D/GIMRT simulations (Glassley and Meike, 1997) demonstrated that quartz and magnetite are not significantly affected for the duration of the simulation and that changes in porosity depend on lime consumption and on calcite and portlandite generation. This is true of both ventilated and unventilated cases The movement of a reaction front through the system as a function of time is clear from the longitudinal profiles of pH, mineral assemblage and aqueous speciation.

These simulations demonstrate that a backfill composed of quartz sand, magnetite and lime will not control oxygen fugacity or pH unless the drifts are completely sealed. Even then, the chemical-conditioning effects would be minor and would probably not achieve the engineering goals. A candidate backfill should be further tested over prolonged periods of time and various temperature gradients. However, the simulations conducted here are

sufficient to demonstrate that this backfill option does not sufficiently improve the robustness of the repository concept to warrant further consideration. All of the chemical evolution shown here, including the desired chemical conditioning, takes place within a matter of decades, a time frame which is insignificant with respect to the lifetime of the repository. Given the other potential effects of backfill in general and material-specific coupled effects in this case, it is possible that addition of the iron–lime–sand backfill may not add any beneficial effects but may, by adding complexity to the system, increase uncertainty

Similar to the case of the pH conditioning, the desired Eh-conditioning effect (reducing environment) is achieved only in the case of the closed system In the open system, the Eh remains positive Although at the end of the OS3D/GIMRT simulations (2–3 years) the amount of magnetite in the system appears unaffected because only a small amount of reactant phase (hematite) is generated, it is clear from the EQ3/6 simulations that the Eh-conditioning effect is transient Given that the effect is only achieved in a closed system and that it would be very difficult to achieve or prove the existence of a pneumatically sealed environment over the time period in question, the extended simulations that would be required to determine the duration of the conditioning effects (Eh or pH) were not carried out

A few engineering considerations become clear from these results. First, fundamental to engineering design is the observation that, in the open system, pH is maximized during the transient period, that is, while the system is evolving but has not achieved equilibrium In the closed system, pH is maximized during the transient state but remains elevated during the steady-state condition in which lime is present. Once lime is consumed, the pH decreases The iron phase only affects oxygen availability in the (airtight) closed system, and even then the effect is transient Given the hydrological scenario associated with the backfill case, in which water will be driven away from the WPs as a result of elevated temperatures, we suggest that the system will probably have evolved to a hematite + portlandite + quartz assemblage before significant water infiltration occurs.

Other considerations that are not explicitly evaluated in these simulations bear examination It is clear from reaction processes that alteration will first occur along grain surfaces, resulting in the formation of a secondary mineral precipitation on and between the original backfill grains. Given the movement of fluids as a reaction front, it is possible that a solidified crust could form at the point of water entry into the backfill or at depth. This type of process is well known and is responsible for the formation of lateritic and bauxitic crusts in tropical climates In an extreme case, the result could profoundly modify assumed hydrological properties of the backfill, including the possible development of fast flow paths to a container surface, and needs careful evaluation. In addition, reaction rate is a function of grain size and water availability, which remained constant for these simulations. Completeness of the reaction may be a function of grain size (passivation may occur in larger grains). Our simulations are conducted assuming that the reaction is complete.

5.3.6.4 Organics: Hydrous Pyrolysis of Diesel Fuel

Although diesel fuel spills, if present, will be located below the WP and are therefore of limited interest to prediction the lifetime of the WP, the application of the general conclusion of this work to hydrocarbons that may be used above the WP may be useful. The potential thermal degradation of diesel fuel in the presence of water was studied at elevated temperatures (Meike, 1996). These experiments were carried out at 200° and 315°C, to directly determine the rate and products of diesel fuel degradation within a 2- to 3-month laboratory experiment. They thus provide an upper limit for the rate of abiotic degradation within the

chemical system studied. It was found that thermal degradation of diesel fuel is not enhanced in the presence of cementitious material or at alkaline pH. Given the very slow nature of the abiotic reaction, microbial metabolism of these materials may be the most significant rate-determining processes to incorporate into a long-term chemical model for repository performance.

5.3.6.5 Microbial Processes

5 3 6.5.1 Microbially Mediated Chemistry

Microbes vary widely in their types of metabolic activities, and the consequent alterations to the surrounding environment that they can facilitate (Horn and Meike, 1995). Historically, bacteria (and *Archea*, which are closely related) have been classified according to their individual metabolic types. The potential reactions actually performed by bacteria are dictated both by innate metabolic ability and by the conditions to which they are exposed. The types of metabolic activities that are possible are governed by the availability of substrates The demands of establishing boundary conditions for microbial activity in the context of a radioactive-waste repository extend beyond the information that is presently available in the literature

We have conducted traditional biochemical-assay techniques that can be supplemented with more advanced molecular techniques to better predict the impact of microbial affects on geochemistry and repository components

Organisms collected from the ESF have been cultured and assembled into a Yucca Mountain Project (YMP) library These microbes were grown in low-nutrient media with various amendments and screened for various activities of significance to the long-term chemical and hydrological properties of the NFE Corrosion-specific bacteria, acid-producing bacteria, sulfide-producing bacteria, and slime-producing bacteria have all been isolated (see discussion in Section 2 5 as well as in Horn and Meike, 1995), and thus those processes may be identified as significant processes to model

5 3 6 5 2 Biodegradation of Polymers

While natural polymers are readily broken down by microbes, synthetic polymers are more resistant. One reason for this is that a main source of energy for microorganisms is the breaking of the carbon–hydrogen bonds, which releases energy. Another reason is that the enzymes required to break down these synthetic polymers are not found in nature The biodegradation of polymers also depends on the intrinsic viscosity and the product structure; for example, a flexible foam will degrade faster than a rigid foam, which in turn will degrade faster than a solid product. A last reason is that the most important type of enzymatic polymer-cleavage reaction is hydrolysis, which occurs exclusively inside microbial cells. Thus, high-molecular-mass polymers would need to enter the cytoplasm before depolymerization. It would seem that by copolymerizing a synthetic polymer with a natural polymer, degradation could be achieved. However, studies in which starch is incorporated into the polymer structure have shown that, although the starch components degrade, the synthetic polymer structure only collapses into smaller pieces that still resist degradation. However, many degradation products of polymers are biodegradable (see discussion in Meike, 1996).

5 3.6.5.3 Limiting Factors: Water and Nutrients

It is clear from the discussion above that microbial biota are integral to environmental mass transfer Thus, microbial contributions to overall environmental chemistry cannot and should not be ignored in prediction of the long-term aqueous processes. A review of the microbiological literature makes it clear that the impact and the character, even the very processes, of microbial activity depend on nutrient conditions (see, e g , Horn and Meike, 1995, and Meike, 1996). Microbes are capable of utilizing a wide range of organic compounds to serve as sources of carbon. Autotrophic organisms are capable of carbon-dioxide fixation to satisfy carbon requirements for synthesis of cellular materials Energy can be derived from either reduced organic or inorganic compounds. Hydrogen gas, nitrogen, ammonia, nitrite, ferrous iron, and reduced-sulfur compounds, for example, can all be used as energy sources by various microbial groups Similarly, oxygen or a wide array of inorganic compounds may be utilized as a terminal electron sink. Nutrient supply, rate of nutrient transport, and the composition of the repository community will govern the specific types of metabolic activities that occur. Because little literature is available on the variability of chemical impact as a function of microbial activity, we are performing experiments to provide the needed modeling information.

In these flow-through experiments a basic growth medium is modified so that the macronutrient (C, N, P, S) concentrations are varied to represent all possible combinations of a maximum, midrange, and minimum value of each These trials are conducted at room temperature and at 50°C. The bioreactor is inoculated with YM tuff that contains native microbes and microbes introduced by construction activities. Samples of efflux solution are collected on a regular basis and analyzed chemically until a steady state has been achieved. The results of these experiments are being used in modeling efforts described in Hardin et al (1998).

5.4 Implications for Modeling

Our ability to predict the chemistry of water in contact with materials introduced into a high-level radioactive-waste repository at YM is beset by the same environmental uncertainties as our ability to predict the geochemistry of water in contact with rock That is, chemistry depends on temperature and gas-composition evolution, which are uncertain In addition, there is variability in the uncertainty of our predictions, and even the type of prediction that can be made (e.g., uncertainty envelope, sensitivity analysis, or process-level scenario simulation) depending on the material and the type of process that is considered. The reason for this variability is discussed in greater detail in Hardin et al. (1998).

Currently we cannot integrate the prediction of water chemistry based on biotic processes with that of abiotic processes because our understanding and our ability to describe these processes are not at the same conceptual level. Whereas the ability to simulate abiotic chemistry, which is firmly rooted in a framework of constitutive equations, is limited by the availability of energetic data (e.g., free energies of formation, heat capacities and solubilities), the ability to simulate microbially mediated chemistry, for which appropriate constitutive equations have not been developed, is in a far more infantile stage. We are merely able to provide the broadest of bounding conditions for the potential effects of microbial activity and, therefore, the inclusion of these processes greatly increases the uncertainty of any prediction. Eventually we expect to be able to reduce that uncertainty as we are able to simulate integrated abiotic and biotic processes.

The water-conditioning effect of concrete in normal construction environments is known, and simulations have been attempted at 25°C and slightly elevated temperatures. The major impact is a significant increase in pH. We have examples of microbial activity reducing pH through the neutral range and even into the acidic range, but at present our ability to incorporate these processes into a simulation is just beginning to show progress In the balance of this section we will discuss strictly abiotic simulations, keeping in mind that microbial activity within any of these scenarios will extend a range of uncertainty toward the acidic end of the pH scale, resulting in consequent changes to the fluid chemistry. In other words, we do not expect that the result of microbial activity will result in an increase in pH, and thus the abiotic simulation represents an upper bound to the pH for any given simulation

5.5 Predictive Capabilities and Modeling Resources

Successful prediction of the evolution of the proposed Yucca Mountain (YM) repository will require the development and integration of models and simulations at a number of different scales and with a number of different purposes Where possible, and where the appropriate constitutive laws are understood, we are gathering fundamental data and constructing the data bases that are required to simulate process level scenarios of interest to the YMP. On a larger scale, we are demonstrating feasibility of models that will be required to integrate concepts from more than one process. Where constitutive laws are not understood, we are conducting the experiments, literature searches, and analog studies that will allow sensitivity analyses to be produced Also, for topics in which great progress is possible through a transition from sensitivity analysis to a process-level model, we are conducting optimization studies to understand and demonstrate the most significant processes

5.5.1 Drift-Scale Thermochemical Models

Our intent is to integrate drift-scale chemistry into repository-scale, and ultimately mountain-scale, models, by progressively establishing those spatial and temporal characteristics that need to be transferred to the next larger scale Thus, we have not chosen a software program that provides easy initial rendering of the engineered features Rather, we have worked closely with a software company (Dynamic Graphics, Inc.) to push the limits of a geological modeling program (EarthVision™) in its ability to render engineering details

The purpose of this work was to determine whether it would be possible to represent repository design features at an appropriate level of detail within the EarthVision™ software modeling framework. The various features that are shown in these models were produced by routines that were originally formulated to produce geological features Therefore, all of the physical features were produced by combinations of faulting, deposition, erosion, and drilling wells, which would not be worthwhile if they were only intended as graphic representations. However, once built, the potential ultimate benefits are great because they are directly integrable with the mountain-scale geological model.

Our goal is to use these representations for drift-, repository-, and mountain-scale hydrological and chemical modeling that include modifications due to construction. The advantage of this software is that physical attributes can be assigned to the various forms, these attributes can be used to visualize the evolution of complex chemical, hydrological and coupled chemical-hydrological models. An additional intention is to locate materials, calculate volumes with ease, and locate the interfaces between materials of interest. Various

aspects of spatial heterogeneity and interfaces between materials that are fundamental to understanding the environment within emplacement and access drifts will be addressed with this model (see Hardin et al., 1998; Meike, 1996).

5.5.2 Abiotic Models

Currently two modeling packages form the foundation of the chemical modeling efforts in this area. One code, EQ3NR/6 is a chemical-modeling package. The other, OS3D/GIMRT is a reactive-transport code.

5.5.2.1 EQ3/6

The EQ3/6 geochemical-modeling package (e g , Wolery, 1992a and b; Wolery and Daveler, 1992) uses process-level algorithms and a data base of fundamental thermodynamic parameters and user-supplied reaction-rate parameters to simulate the chemical evolution of a system The EQ3NR/EQ6 software package is composed of three executable programs (EQPT, EQ3NR and EQ6) and a number of data bases that are used at the modeler's discretion EQPT formats data bases to be readable by EQ3NR and EQ6 The input file for EQ3NR contains the analytical composition of the solution (including total concentrations of dissolved components, pH, Eh, and oxygen fugacity). The code calculates the distribution of chemical species, using thermodynamic data located in the selected data base. The output consists of an output and a pickup file, which is used to initialize the EQ6 input file EQ6 models the reaction of the aqueous solution with a set of minerals and gases, as well as fluid mixing and temperature changes.

The output of the simulations are pH, Eh, mineral assemblages, and water chemistry (chemical speciation) as a function of time (reaction progress) These simulations provide important information to establish·

- The mechanisms responsible for contrasts in chemical properties of different systems (e g , why pH differences are observed between fixed and unfixed gas phase (fCO_2 and fO_2) cases).
- Steady-state conditions between the water chemistry and solid-phase assemblage, which represents an endpoint for the evolution of the system
- Whether desired chemical conditioning is achieved during an approach to steady-state transient, or equilibrium, conditions

The results of the EQ3/6 simulations are used to select the significant chemical properties of the system. These properties are then used in the OS3D/GIMRT reactive transport code, which has reduced the maximum number of chemical species that can be involved in a simulation to streamline the simulations.

5.5.2.2 OS3D/GIMRT

The OS3D/GIMRT reactive-transport package is a first-principles reactive-transport code (Steefel and Lasaga, 1994; Steefel and Yabusaki, 1995) that simulates chemical changes in an aqueous fluid as the fluid moves through a porous medium. OS3D/GIMRT also determines the evolution of mineralogy and porosity as the aqueous fluid reacts with the porous medium, thus providing a model of the time-dependent evolution of the physical framework of the flow field. As mentioned previously, the simulations rely on first-principles chemical modeling (e.g., EQ3/6) for the selection of appropriate input parameters. The output of the simulations shows spatial and temporal chemical and mineralogical changes due to the reactive transport of water through a saturated permeable material. Spatial simulation shows

reaction fronts and time-sequence evolution as a function of flow rate, thermal gradient, and water chemistry. Although the precipitation of solids is simulated, the formation of an impermeable layer, or crust, is not part of the simulation Nevertheless, the formation of a crust may have a great impact on hydrology and depends on grain size, ratio of the components and reaction rates. The formation and impact of such a crust will be evaluated at a later date.

5.5.2.3 Thermochemical Data Bases

5 5 2 3 1 Standard Geochemical Data Bases

Five data bases are usually supplied with the EQ3/6 modeling package. Three of these (COM, SUP and NEA) may be used with either the Davies equation, or the B-dot equation to calculate the activity coefficients. Their use is restricted to rather dilute solutions (ionic strength less than that of sea water (i.e., ~0 7 molal) (Garrels and Christ, 1965). The two other data files (HMW, PIT) use Pitzer's equations (Pitzer, 1979) and are suitable for the modeling of high concentrations solutions. These data bases are outlined below.

- SUP data base. Designed entirely from the SUPCRT92 program (Johnson et al , 1992), this data base has a high level of internal consistency. The data base covers a wide range of chemical species. However, for the purpose of drift-scale chemical modeling, it does not contain necessary data related to calcium–silicate–hydrate species that might be formed in cements at temperatures between 60° and 300°C.
- NEA data base. This data base was produced by the Data Bank of the Nuclear Energy Agency of the European Community (Grenthe et al., 1992) and is specifically tailored to conduct uranium studies
- HMW data base. This data base is founded on the use of Pitzer's activity coefficient expressions, which were used by Harvie, Moller and Weare (Harvie, 1980, Harvie et al , 1984). HMW can be applied to both dilute solutions and concentrated brines, at 25°C. It has also a very high degree of internal consistency but it only treats the components present in the sea-salt-water system. Important elements for the modeling of cement in a geologic repository, such as aluminum and silicon, are not included in this data base.
- PIT data base This data base is designed primarily from data summarized by Pitzer (1979). This data file can also be applied to concentrated brines between 25° and 100°C. PTT covers a larger set of species than the HMW data base, but it does not address the silica and inorganic carbon species that are necessary to model cement in a geologic repository. In addition, it has the same attributes and limitations as HMW More details of the HMW and PIT data bases are provided by Jackson (1988) and Jackson and Wolery (1985).
- COM data base. This data set represents a melange of data found in the SUP and NEA data sets, as well as data from the HMW data set. Other data in COM have been obtained by correlation or interpolation. This set therefore offers the least assurance of internal consistency. However, it is the only means available to model problems with a high degree of compositional complexity.

5 5.2.3 2 Data Availability for Modeling Cementitious Materials

To predict chemical properties over a long period of time, we need models that are based on the fundamental properties of the appropriate materials These kinds of models are well developed in geology, where long periods of time are frequently addressed. Similarly, the

fundamental properties are often better known for geological materials, because the interest in very-long-term chemical prediction has existed for decades. An interest in the long-term degradation of fabricated materials is relatively recent and is most common in relation to radioactive-waste-disposal efforts. Previous efforts in the area of fabricated materials have focused on optimizing fabrication conditions, which is unnecessary for predicting processes in which the environment will not be controlled. Therefore, users of an application-driven program find themselves in need of generating fundamental data.

Examination of the ability to model aqueous systems of interest to the YMP repository has revealed that, historically, there has been a deficit in the ability to model complex water–materials systems that contain ordinary portland cement (OPC) (e g , Bruton et al , 1994, Meike et al , 1994). The ability to conduct this kind of modeling has become more critical as repository designers begin to consider the incorporation of OPC materials in the emplacement drifts The YMP is unique among the high-level radioactive-waste repository projects in the world in the need to understand and predict processes in excess of 100°C.

Much emphasis in the concrete literature is placed on the hydration of the wet cement paste into the cured solid product. These data are not useful to the YMP because they either represent an insignificant amount of time (in the case of cast-in-place concrete) or are irrelevant (in the case of precast concrete). Our goal is different We wish to model the interaction between water and well-cured concretes, which may have undergone extensive transformation in the solid state due to a thermal pulse

Most of the hydrous phases of cured cement and the anhydrous and hydrous solid solutions lack calorimetric data Calcium–silicate hydrate (or C-S-H) is the major constituent of a cement paste and is characteristically poorly crystalline or nearly amorphous in a young cement paste C-S-H can also be synthesized by reaction between $Ca(OH)_2$ and silicic acid, or between solutions of sodium silicate and a soluble calcium salt In this manner, quasi-crystalline varieties can be obtained, two of them, known as C-S-H(I) [$0.8 < Ca/Si < 1\ 3$] and C-S-H(II) [$Ca/Si > 1.5$] can be compared structurally to tobermorite and jennite, respectively The somewhat variable structure and composition of C-S-H gel and its relation to thermodynamics, solubility, and aging of the material are summarized in Clodic and Meike (1997) and Hardin et al. (1998).

The kinetics of transformation of C-S-H into other phases at its upper temperature limit is significant to predictions of cement behavior in the repository, which will stay at 80° to 120°C for an extended time. Of prime importance for 25°C performance modeling are calorimetric data for ettringite and tobermorite and well-characterized solid solutions of these phases. The prediction of chemical reactions at greater temperatures requires more data than are presently available. Geochemical codes are also useful, in the absence of these data, for conducting a sensitivity analysis to determine the solid solutions or end-member phases that are critical for calorimetry. The original ΔH of formation (20°C) from CaO and silica-gel thermodynamic data for all Ca_2SiO_4 phases are evaluated by Haas et al. (1981). Qualitative rate information has been obtained for ettringite components (Majling et al , 1985) Except for an enthalpy of dehydration (Maycock et al., 1974) and heat-capacity data (Ederova and Satava, 1979) obtained over the range of 273 to 333 K, thermochemical data for ettringite are calculated (Sarker et al , 1982; Babushkin et al., 1985). The only experimental data for monosulfate (C_4ASH_{12}, or AFm) located so far date is heat-capacity data from 273 to 353 K (Ederova and Satava, 1979). As discussed previously, the kinetics of the relevant reactions are even less well understood.

Comparisons of cement leachates with calculations performed using available data and standard thermochemical tables (Barnes and Roy, 1983) suggest the best agreement with the solutions buffered by tobermorite and possibly gyrolite. The most successful chemical models to date have been achieved by working with a limited number of equations that include C-S-H solid solutions, monosulfate solid solution, and ferrite solid solution. Glasser et al. (1985) analyze a simplified cement system as the ternary $CaO–SiO_2$ H_2O Barret and Bertrandie (1986) make a similar analysis of the system $CaO–Al_2O_3–CO_2·H_2O$ Incorporation of aggregate into repository concrete will increase the complexity of geochemical modeling Calculations that include portland cement, special cements, and concretes that incorporate blast-furnace slag, fly ash, and silica fume (Berner, 1987) have achieved some success for equilibrium-solid-phase and pore-solution-composition data obtained from experiment, but they do not readily take reaction progress into account

The use of numerical simulations to integrate the effects of the variables complements experimental and historical investigations. Eventually, coupled chemical effects that are difficult or inaccessible through experiment can be examined. However, even the present chemical data base (Sarker et al., 1982; Babushkin et al , 1985), although limited, can be manipulated to obtain insight into some effects that may be expected due to man-made materials. Conversely, the data base will be enhanced over time by incorporation of new thermodynamic data from the experimental and historical investigations

5.5.2.4 Development of a Data Base Dedicated to Modeling Concrete Dissolution at 25°C

The set of thermodynamic data we usually use (and discussed in Section 5.5.2 3 2) has been developed to study natural rock–groundwater interaction and does not contain some of the thermodynamic information necessary for modeling the cementitious systems in a natural environment (e.g , Bruton et al , 1994, Meike et al., 1994). Our aim has been to develop this capability in the area of aqueous chemistry. In addition to acquiring new thermodynamic data, we have incorporated extant data bases for cement systems (Read, 1991, Atkins et al , 1992, Berner, 1987, 1988, 1990) into one of the standard geologic data bases. Clodic and Meike (1997) describe the construction of the data base CEM.R27, which was accomplished by starting with a simple three-component system and building progressively more complex chemical systems from data in the literature (primarily CEMCHEM), with additional single-component increments. CEMCOMP R28 contains the thermodynamic data from COM R27 and the data from CEM.R27.

As a consequence of working in this area, it has been necessary to be conversant in the symbolism of both cement chemistry and standard chemistry. The symbolism of both fields is used in this report. For a lexicon of cement chemistry notation, refer to Taylor (1990).

5.5.2.5 Cement-Water Interaction Models

The data bases, codes and sources of models for cement–water interaction (Berner, 1987, 1988, 1990, Glasser et al., 1987; Atkins et al., 1992, Bennett et al., 1992) are discussed further in Clodic and Meike (1997). The data bases for these models and simulations encompass a restricted chemical system and include phases found in young concretes. The simulations are oriented toward modeling concrete under normal conditions, at lower temperatures, and for younger, non-thermally-treated concrete than the present purpose.

5.5.2.6 Generation of New Data for Data Bases

5.5.2.6.1 Measurement

The work that has been conducted in generating more thermodynamic data has focused on phases that are expected to be part of the drift-scale chemical system at elevated temperatures if OPC is a major element of drift construction As described by Meike (1996), much of the data required for long-term modeling of the same quality that presently allows us to predict the chemical interactions of the natural system is unavailable A program was begun to obtain that data. Synthesis of Ca-Si-H_2O phases had been completed and measurement of thermodynamic data had just begun when the program was halted in November, 1995. Heat-capacity and entropy measurements were obtained for 11-Å-tobermorite using heat-pulse calorimetry, but the data has not yet been analyzed The work on other phases was halted Plans are in progress to reinitiate thermochemical experiments.

5 5 2.6.2 Calculation of Thermodynamic Data from First Principles

Given the difficulties inherent in direct measurement of the thermodynamic parameters of these phases, we have undertaken a set of first-principles electronic-structure calculations To provide a means of verifying experimental data, and ultimately of developing a means to calculate necessary thermodynamic parameters and better understand the relation between relative humidity and the stability of Ca-Si H_2O phases, a program was initiated to conduct electronic structure calculations of Ca-Si–hydrates (Sterne and Meike, 1995).

The goal of this modeling effort was to determine the energetics of hydration for crystalline Ca-Si–hydrate phases The work performed to date represents an initial step in this direction The initial results for the first phases undertaken for phases representing the water-poor end-members, wollastonite ($CaSiO_3$) and xonotlite ($Ca_6Si_6O_{17}(OH)_2$) The results, reported in Sterne and Meike (1995), are summarized below

The calculated ground-state properties of wollastonite and xonotlite agree with experiment, and provide equilibrium lattice parameters within 1–1 4% of the experimentally reported values The roles of the different types of oxygen atoms, which are fundamental to understanding the energetics of crystalline Ca-Si–hydrates, examined in terms of their electronic-state densities, appear to agree with experiment for the lattice parameters and internally consistent when comparisons are drawn between the two structures. The exercise, completed with wollastonite and xonotlite, demonstrates the applicability of these electronic-structure methods in calculating the fundamental properties of these phases. The electronic-structure calculation methods are demonstrated to give reliable results, even for the relatively large wollastonite and xonotlite unit cells. Thus, the application of this new approach to the study of calcium–silicate hydrates appears to be fruitful not only in terms of the ability to calculate heats of formation, but also by virtue of the insight that it can provide into the nature of hydration and dehydration.

5 5.2.6.3 Generation of Kinetic Data from Multicomponent Experiments

The need for kinetic data is similar to that described above for thermodynamic data, but measurement of this data was also halted in November 1995. However, in the process of conducting the diesel-fuel experiments described above, we have obtained some data regarding the degradation of cementitious material, specifically Fibercrete™. In all experiments containing Fibercrete™ (DF3, DF4, and DF6), 11-Å-tobermorite formed. Thus,

11-Å-tobermorite appears to be a stable, or at least metastable, phase at 200°C. As is observed in experiment DF6, the precipitation of 11-Å-tobermorite, calcite and cristobalite may control geochemistry and effect porosity and permeability for waters contacting both cements and Topopah Spring tuff. The importance in the dissolution and precipitation kinetics can be seen in the slow changes in solution pH and dissolved-silica concentrations and in the small fraction of the initial starting material dissolved to form secondary precipitates at the Fibercrete™ and Topopah Spring tuff surfaces In the absence of Fibercrete™, cristobalite appears to be the dominant secondary mineral formed in Topopah Spring tuff experiments, in agreement with previous studies (Knauss et al , 1985; Knauss and Peifer, 1986; Knauss et al , 1987).

Calculations using the current data base appear to be contradictory. Aqueous chemical-modeling results suggest that mesolite should precipitate from the solution. They predict that the chemical system is saturated with respect to quartz and calcite after 20 days of reaction and undersaturated with respect to 11-Å-tobermorite. Zeolites were not detected in any of the experiments, suggesting either that the thermodynamic data is not correct, that zeolite nucleation from solution has a very large activation energy, or that zeolite precipitate rates are very slow even in very supersaturated solutions. Given the lack of thermodynamic and kinetic data pertinent aqueous degradation of Ca-Si-H_2O phases, the first option is very likely. Thermodynamic data for Ca-Si-H_2O phases are sparse and contradictory (Vieillard and Rassineux, 1992, Bruton et al., 1994, Meike et al., 1994) The constant 11-Å-tobermorite saturation index after 40 days of reaction and the identification of 11-Å-tobermorite in the final solid material indicate that the solubility of 11-Å-tobermorite is overestimated in the current data base Previous experiments that have investigated the stability of various phases typically lasted only a couple of days (Lea, 1971). Atkins et al (1991) determined the solubility of cement-hydrate phases after four weeks of reaction at 25°C Clearly, longer reaction periods are required for the crystalline phases to reach equilibrium

From the present work, it is possible to calculate a 11-Å-tobermorite solubility constant K at 200°C to be 1039 7(±0 6), using the experimental ion activity product IAP for the following solubility expression for each aqueous sample after 20 days of reaction:

$$Ca_5(SiO_2)_6(OH)_{10} \bullet 0\,5\,H_2O + 10\,H^+ = 5\,Ca^{2+} + 6\,SiO_2 + 10\,5\,H_2O \qquad (5\,5\text{-}1)$$

and

$$IAP(200^\circ C) = \left(Ca^{2+}\right)_5 (SiO_2)_6 / \left(H^+\right)_{10} \quad , \qquad (5.5\text{-}2)$$

assuming $a_{H2O} = 1$ and unit activity of the solid phase. This simplifying assumption is also taken that only crystalline tobermorite of pure composition is involved in the chemical reaction. In the absence of other data, this IAP may prove to be a useful guide However, the derivation does not allow for the interaction of complexes or other amorphous or crystalline Ca-Si-H_2O phases that are known to precipitate under these conditions. This calculation thus requires verification using independent checks for internal consistency.

5.5.3 Biotic Models

To model the impact of microbes, we need to establish two types of parameters. First, we need to establish the boundary conditions within which microbes operate (for example, water availability and temperature). These conditions we consider to be the "on and off switches"

for microbial processes in the model The second type of parameter relates to processes impacted by microbial activity. Our purpose is to determine whether these metabolic activities are ongoing in both perturbed and unperturbed microbial communities, to assess the magnitude and rates of those reactions, and to establish boundary conditions for microbial survival and activity. Approaches to modeling microbially mediated processes are summarized in Hardin et al. (1998)

5.6 Modeling Plan: Simulations of the Interaction between Water and Mechanical Support Material

Previous publications (Glassley and Meike, 1997, Van Konynenburg et al., 1997, McCright, 1996) have touched on the chemical impact of iron alloys and our ability to predict their chemical impact, primarily that of carbon steel Should steel sets be selected for mechanical support in the emplacement drifts, our analysis would be developed similarly to the discussion of the iron component of the backfill in those reports In the previous analysis, we established that hematite (for which adequate data exists for modeling) represented the most significant solid phase in contact with water over geologically significant periods of time (see Section 2.1) and examined the chemical conditioning effects of hematite on water in a closed and an open system. We demonstrated that the greatest chemical impact is observed in a closed environment, where the further degradation of the iron phase can deplete oxygen in the atmosphere. In an open environment, there is little significant impact on the water chemistry, although these materials are recognized as a significant potential source of colloids (see discussion in Hardin et al , 1998)

In the present report, we focus on concrete, which represents a potentially more complex evolution of the solid material and potentially more sensitivity to important variables in the evolution of the repository.

Our modeling efforts are organized in three phases. In our preliminary phase, we outlined a method for representing both the evolution of the solid concrete and various possible chemical scenarios. This preliminary set of simulations was also conducted to provide a foundation for large-scale corrosion tests The next phase is another purely chemical-modeling step in which we use the same strategy on a complete matrix of solid assemblages representing three possible evolutions as a result of different gas chemistries In the last phase, we will attempt to incorporate the inherent heterogeneity of the drift environment by using reactive-transport models In each of these phases, we define reactant compositions as a function of time and construction materials For example, we expect the characteristics of a concrete immediately after closure of the repository to be different than that of a concrete exposed to a thermal pulse and a large volume fraction of CO_2 gas. We tailor our reactants to be idealized representations (mineral assemblages) of the materials at significant points in their evolution. With each of these original reactants, we have used EQ3/6 and the time-appropriate water chemistries to simulate time- and material-specific steady-state chemistries. The steady-state chemistry is important because it represents a chemical bounding condition with respect to flow rate. Given that the flow rate of water entering the repository is not exactly known, the extent to which water will react with the materials it contacts is not clear. Thus, we will provide bounding calculations. The extent of the water-solid reactions will be inversely related to the flow rate. If the flow is slow enough, the water can achieve a steady state (i.e., no further chemical change) with respect to the material with which it is in contact Our calculations represent that slow-flow bounding condition. The other bound, which represents a flow rate fast enough that water composition is subject to no significant chemical effect, of course, is the composition of the water itself.

5.6.1 Preliminary Calculations of Water–Grout Interaction

Steady-state chemical simulations have been completed for the determination of a water chemistry to use in the large scale corrosion test (McCright, 1996). During this preliminary phase, we used a QA-approved GEMBOCHS data base, COM.R27 with EQ3/6 to simulate the reaction between representative minerals that might evolve from a cured and thermally treated grout (without additives or aggregate) and water to obtain the chemical composition of a water. The purpose was to develop a formulation for water that could be used in the large-scale corrosion tests (see Section 2 2) and that might represent a somewhat thermally evolved concrete.

The simulations were conducted using J-13 well water (see Section 5 6.2 2) and mineralogies representative of thermally treated grouts that also could be found in a data base that is in standard usage within YMP (COM R27). Although the original reactants could differ from those in the data base (as long as the dissolution laws are defined), the precipitated phases are only those that are present in the data base We chose to conduct all of our work within the framework of the data base. We derived two mineralogies, the "old carbonated cement" file described in Table 5.6-1 and the "old sulfate-rich cement" file described in Table 5.6-2 The reactant compositions were derived from a bulk compositional analysis of type II grout from Taylor (1990) This analysis was converted into a set of soluble solid phases, primarily ettringite, a silica phase, and calcite, which are expected to be major components of a grout exposed to an atmosphere rich in carbon dioxide CO_2 was used for charge balance, and amorphous silica was chosen as the silica phase to provide a relatively high concentration (conservative) of silica to the simulated solution (see Table 5 6-1) A sulfate-rich composition was formulated similarly from the high-sulfate composition provided by Taylor (1990) (compare Table 5.6-2)

Table 5.6-1. **Calculation for carbonated, thermally treated grout.**

From Taylor (1990)	g	mol	Contribution to phases	mol
Na_2O	0 2	00322	thermonatrite	00322
MgO	1 2	0298	brucite	.0298
Al_2O_3	5 6	110	ettringite gibbsite	.0216 .0882
SiO_2	21.0	349	amorphous silica	349
SO_3	2 6	0325	ettringite	0108
K_2O	0 4	.00425	potassium carbonate hydrate	00425
CaO	65 4	1 17	ettringite calcite	.0649 1 10
TiO_2	0 3	00376	ilmenite	.00376
Fe_2O_3	3 1	048	ilmenite goethite	.00375 3 51
CO_2	0.7	016	calcite	

Table 5.6-2. Calculation for sulfate-rich, thermally treated grout.

From Taylor (1990)	g	mol	Contribution to phases	mol
MgO	2 7	067	brucite	067
Al_2O_3	8 4	0824	ettringite gibbsite	0516 0417
SiO_2	14 6	.243	amorphous silica	243
SO_3	12 4	155	ettringite	0516
CaO	57 6	1 03	ettringite calcite	31 771
Fe_2O_3	1 6	01	goethite	02

For the simulation exercise, it was necessary to use the QA-approved data base, due to the nature of the experiments that would use these simulations as a basis for a water chemistry. This data base is more limited than the subsequently developed data base, and therefore the scope of the calculations were limited, as were the minerals that could be formed in the simulation The results are summarized in Hardin et al (1998)

As steady state was approached in the simulations (see Hardin et al , 1998), the pH of the solution approached a value below that which might be expected of a young grout that contained excess portlandite and alkali hydroxides This result reflects the preconversion of the reactants for the simulation, the Ca and alkali hydroxides, to carbonates or other minerals. This type of solid-state conversion is expected to occur over a long period of time in the proposed repository setting Hydrothermal experiments, field experiments and analog studies, such as those described in Section 5.3, will help us to represent those evolved solid phases with increasing accuracy

Reducing uncertainty related to the pH of water in contact with concrete is discussed further in Section 5 8 4.

5.6.2 Chemical Modeling of Water–Concrete Interaction

To represent concrete in our simulations requires an additional level of complexity over the preliminary simulations because it contains aggregate and additive components as well as the grout. For this phase of simulations, newly constructed data bases (CEM.R27 and CEMCOMP.R28) have been used The assembly of these data bases and their advantages over COM.R27 are discussed in Clodic and Meike (1997) and Hardin et al (1998). In addition, a more detailed suite of idealized mineral assemblages have been developed to represent various environmentally determined factors. The results presented in this section are from simulations representative of part of that matrix

5.6.2.1 Data Base

The process by which thermodynamic data available from the literature has been incorporated into a data base that can be utilized by EQ3/6, the geochemical-modeling code, is described in Section 5.5.2.3. Three data bases were constructed. The first, CEM.R27, represents a data used in a model dedicated strictly to simulating cement water interaction at 25°C. CEMCOMP.R28 contains additional phases selected from the COM data base (for EQ3/6) that belong to the cement mineral system. These two data bases are used to test the

internal robustness of the more limited Ca-Si-Al-SO_3-H_2O chemical system that represents the most significant phases found in Portland cement. The data base used in the calculations below, is CEMCOMP.R28, which incorporates the CEM.R27 data base with the COM data base to facilitate the modeling of a much larger chemical system Because it is new, the CEMCOMP R28 data base has not undergone the rigorous testing of the standard set of EQ3/6 data bases. It will be necessary to test the results of this data base against experimental and historical analog results to understand its limitations and utility. The simulations presented here represent the initiation of this assessment

5.6.2.2 EQ3 Calculations: Speciation of Incoming Water and Additional Constraints

During any one simulation, the incoming water chemistry is prepared (the chemistry is actually distributed into the appropriate aqueous species) by EQ3. The incoming water chosen for these simulations is a J-13 well-water chemistry by Harrar et al (1990) that has been used historically as the point of departure for simulations of rock–water interaction at YM. Recently, there has been some discussion about the accuracy of some details of this water composition (e.g , the actual pH of J-13 water may differ by one pH unit). However, for the purpose of the present simulations, because we are interested in a steady-state product of the interaction of the water with the concrete, and because the incoming J-13 water is quite dilute and near-neutral, other choices in the set-up of this simulation are far more crucial to the outcome than the chemistry of the J-13 water.

The modeler chooses a temperature for the EQ3 part of the simulation and also chooses other constraints that apply to the entire EQ3/6 simulation In the present simulations, we have chosen to precondition the water at the temperature of the EQ6 simulation to maintain a consistent simulation methodology throughout the set of simulations that span a temperature range from 25° to 150°C. All elements that will appear in the simulation must be represented in the input J-13 chemistry in at least trace quantities. For the purpose of the present simulations, the addition of trace species was not necessary. However, if the water-chemistry results of this simulation were reacted with a waste form that contains a different group of elements, the J-13 water would need to be preconditioned to contain very trace quantities of these elements.

The input files for all of the runs in this set of simulations were identical with the exception of the selected temperature.

5.6.2.3 EQ6: Interaction of Water with Solid Phases

5.6 2 3.1 Calculation of the Evolving Concrete Solids

A high-level radioactive-waste repository is outside the realm of normal construction experience, due to the elevated temperatures, evolving gas chemistry and long period of time during which the chemistry of water in contact with concrete needs to be understood and predicted. We do know that the conditions of the repository are similar to those that have been characterized in geology as low-grade metamorphism. During low-grade metamorphism, metastable phases evolve by processes such as phase transformation (a solid-state process in which one mineral transforms into another, such as graphite into diamond), dissolution and precipitation, and the addition and subtraction of water from crystal structures (contributing to or subtracting from the overall liquid- and vapor-water budget). Those solid phases that are metastable with respect to each other evolve into a more stable assemblage (Figure 5.6-1). With this concept in mind, we have developed five mineral assemblages that are intended to represent the solid concrete at different points in its

evolution and under different chemical conditions The basis for the chemical composition is described in more detail in Section 5.3.

Figure 5.6-1. Conditions under which solid minerals develop from a grout in response to a thermal pulse and a range of gas compositions.

The difference between the two concretes before the thermal pulse is in the representation of the sulfate-bearing phase. In the case of young concrete, this phase is represented as ettringite In the case of AFm concrete, it is represented as monosulphate (AFm). During the present simulation, the impact of this distinction is small, because relative rates are being used (see subsequent sections). However, as the input data is improved and we develop a basis for distinctions in solubilities, this may govern the concentration of sulfur species in solution

As our understanding of thermally treated concrete improves with experiment and the examination of historical analogs, the representation of these mineral assemblages will become more accurate. However, given the present understanding of these minerals, a more accurate representation of the mineralogy will not improve the prediction of water chemistry Because the dissolution rates of the important minerals are not known, they must be chosen somewhat arbitrarily based on the best guess and scientific insights of the modeler. Thus, at present, our simulations are conducted in titration mode, and the mineralogical input is a vehicle for getting the solid components into the water (see Section 5 6 2 3.3 for a description of the various test modes). The real work of the simulation is to determine, based on the information in the data base, which minerals are supersaturated and therefore should be precipitated, and the resultant chemistry of the solution

5 6 2 3 2 Idealized Mineral Assemblages Representative of Grout Evolution

The calculation of concrete-reactant files is more complex than the preliminary exercises for several reasons First, we are representing a concrete, which has components in addition to grout, and we must represent each of these components in appropriate proportionality to each other Second, in the Total System Performance Assessment we are calculating mineralogical formulations for three distinct materials that may evolve from the original precast concrete as a result of repository conditions

Using information from the literature and our hydrothermal experiments and the repository-design specifications, we calculate a composition for one young grout and two old, thermally treated grouts. Each of the old grout formulations represents a material that has been exposed to one of two different gas environments that represent extremes in concrete vapor-phase alteration. the oxygen-rich case and the CO_2-rich case. Ultimately, the simulations will use a full concrete formulation that will include the grout assemblages described below, the appropriate aggregate, and the appropriate additives

A first approximation of the quantity of cementitious material in the repository drift per linear meter is given by Tang (1997). Our calculations use, as a basis for the original chemical composition of the grout, the Type V (Table 5.6-3) composition supplied by Tang (1997). The chemical composition of the grout is given as charge-balanced oxides of the analyzed cation, it is therefore not necessary to conserve oxygen in our calculations. We note that important compositional aspects of the concrete, such as sulfate, can vary from type to type (Table 5 2-4) and to a lesser extent between formulations that fit the classification of a single type.

Table 5.6-3. Calculation of the chemical composition of starting materials: grout per meter.

Type V grout	wt% dry	Wt. (lb)	Amount per meter			
			lb	kg[a]	Molec. wt	Cation (mol)
SiO_2	25	3,380	845	383	60 1	6,378
Al_2O_3	3 4	3,380	114	52 1	102	1,022
Fe_2O_3	2 8	3,380	94 6	42 9	160	538
CaO	64 4	3,380	2176	987	56 1	17,603
MgO	1 9	3,380	64 2	29 1	40 3	723
SO_3	1 6	3,380	54 1	24 5	80 1	306
Total				2,135		60,805

[a] The difference between this calculation and those in Table 5 2-1 is due to rounding difference between total weight given in pounds (used as the basis of calculation in Table 5 2-2) and in kg (used as the basis of calculation in Table 5 2-1)

In the calculation of the young grout composition (Table 5.6-4), all water is conserved either as liquid or solid form. We also conserve moisture from the aggregate. The calculation thus derived may possibly overestimate the amount of liquid water in the pores, because some small portion of the water is expected to be lost due to "bleeding" during the hydration of the concrete For the case of precast concrete segments, the water lost in this way would not be present in the repository However, this is not the case for cast-in-place concrete, which would lose water to the repository rock During the construction of the ESF, much of the introduced water was labeled with a LiBr tracer, because the LiBr tracer caused accelerated setting in the Fibercrete™ and concrete, the tracer was not added to the water in these materials Therefore, it is not possible to distinguish water derived from the "bleeding" of cementitious materials and natural water in the ESF at this time In these calculations, we assume that 50% of the silicon from the silica fume is available for the formation of C-S-H gel

The calculation of the three old-concrete compositions only conserves water bound in solid phases. We assume that pore water would be driven from the material during the thermal pulse. In these calculations, we assume that 100% of the silicon from the silica fume is available for the formation of C-S-H gel.

Young Grout

The formulation was balanced first on the available sulfate. In the first calculation (Table 5.6-4a), all available sulfate is accounted for in ettringite, and, in the second calculation (Table 5.6-4b), it is accounted for in monosulfate (an AFm phase). The remaining aluminum is accounted for in hydrogarnet Iron is also accounted for in a hydrogarnet phase. These are tabulated separately, in reality, the aluminum and iron hydrogarnets would probably be present as a solid solution. The available silicon from the grout and half the silicon from the silica fume is calculated into C-S-H gel. The chosen representative C-S-H composition is 1.7Ca: Si: $2H_2O$. Portlandite is formed from the remaining calcium, and magnesium hydroxide is formed from the remaining magnesium

Table 5.6-4. Calculation of mineral assemblage per meter in young grout.

a. Ettringite as sulfate phase.

Constituent		kg/m	Molec. wt.	Phase (mol)	H_2O (mol)	Ca (mol)	Al (mol)	H_2O (wt%)
C-S-H gel	Ca-Si H_2O	5,496	86 2	6,377	12,756	10,842		33 79
Ettringite	$[Ca_3Al(OH)_6\ 12H_2O]_2(SO_4)_3\ 2H_2O$	1,282	1,255	102	2,655	613	204	7 03
Hydrogarnet	$Ca_3[Al(OH)_6]_2$	1,547	378	409	409	1,227	818	1 08
Hydrogarnet	$Ca_3[Fe(OH)_6]_2$	1,179	436	269	269	806		
Portlandite	$Ca(OH)_2$	790	74 1	1,067	1,067	1,067		2 83
	$Mg(OH)_2$	421	58 3	723	723			
	Total grout hydration	10,709						
C-S-H gel	contribution from silica fume (excess CaOH, surface reaction)	1,545	86 2	1793	3585	3,047		
	Total dry components	12,254						
Liquid water	H_2O	2,301	18 0	12,772	12,772			
Liquid water	add H_2O from aggregate	1,458						
	Total liquid water	3,759						55 27
Total					31,768			100 00

b. AFm as sulfate phase.

Constituent		kg/m	Molec. wt	Phase (mol)	H_2O (mol)	Ca (mol)	Al (mol)	Fe (mol)
C–S–H gel	1 7Ca-Si $2H_2O$	5,496	86 2	6,377	1,276	10,842		
AFm (C_4ASH)	$Ca_3Al(OH)_6Ca(SO_4)\ 12H_2O$[a]	1,843	601	306	4,595	503	306	
Hydrogarnet	$Ca_3[Al(OH)_6]_2$	1,354	379	358	2,148	1,074	716	
Hydrogarnet	$Ca_3[Fe(OH)_6]_2$	1,172	436	269	1,613	807		538
	$Ca(OH)_2$	985	74 1	1,330	1,330	1,330		
	$Mg(OH)_2$	421	58 3	723	723			
	Total grout hydration	11,272			23,164	14,555	1,022	538
C–S–H gel	contribution from silica fume (excess CaOH, surface reaction)[b]	1,545	86 2	1,793	3,585	3,047		
	Total dry components	12,817			26,749	17,603	1,022	538
Liquid water	H_2O	1,349	18 0	7,487	7,487			
Liquid water	add H_2O from aggregate	1,458	18 0					
	Total liquid water	2,807	18 0					

[a] Mg is accounted for as solid solution in AFm phase

[b] Destruction of 50 wt%

Thermally Treated Grout

Oxygen-Rich Environment: This formulation is composed assuming the reactive gas composition is close to atmospheric (Table 5.6-5). The formulation was balanced first on the available sulfate. All available sulfate is accounted for in ettringite. The remaining aluminum is accounted for in gehlenite hydrate. The available silicon is converted to tobermorite Magnesium is accounted for as solid solutions in tobermorite. Iron is not included in this calculation, but could also be included in the tobermorite solid solution. The remaining calcium is converted to calcite.

Table 5.6-5. Calculation of mineral assemblage per meter in thermally treated concrete: O_2-rich environment (O_2 close to or above atmospheric).

Constituent		kg/m	Molec. wt	Phase (mol)	H_2O (mol)	Ca (mol)	Si (mol)	Al (mol)
Ettringite	$[Ca_3Al(OH)_6 \cdot 12H_2O]_2(SO_4)_3\ 2H_2O$	125	1,228	102	2,655	306		102
Tobermorite	$[Ca_5(Si_5O_{16}H_2)]Ca\ 4H_2O$[a]	1,382	727	1,901	9,503	8,780	9,503	
Gehlenite hydrate	$Ca_2Al_2SiO_7\ 8H_2O$	192	418	460	3,681	920	460	920
Calcite	$CaCO_3$	760	100	7,596		7596		
"Structural" H_2O		285	18 0					
Total					15,839	17,603	9,963	1,022

[a] Mg is accounted for as solid solution in tobermorite

Carbon-Dioxide–Rich Environment: This formulation is composed assuming that the reactive gas contains more CO_2 than the normal atmospheric composition (Table 5.6-6). In this calculation, the sulfate is accounted for in the carbonate phase, thaumasite The aluminum is converted into hemicarboaluminate. The silicon is converted into tobermorite, and includes magnesium in solid solution Iron is not included in this calculation, but could also be included in the tobermorite solid solution The remaining calcium is converted into calcite

Table 5.6-6. Calculation of mineral assemblage per meter in thermally treated concrete: CO_2-rich environment (CO_2 above atmospheric).

Constituent		kg/m	Molec. wt.	Phase (mol)	H_2O (mol)	Ca (mol)	Si (mol)	Al (mol)
Thaumasite	$[Ca_3Si(OH)_6\ 12H_2O](SO_4)(CO_3)$	191	622	306	4,595	919	306	
Hemicarbo-aluminate	$Ca_{3.5}Al_2C_{0.5}H_{20}O_{18}$	318	623	511	5,111	1,789		1,022
Calcite	$CaCO_3$	597	100	5,961		5,961		
Tobermorite	$[Ca_5(Si_5O_{16}H_2)]Ca\ 4H_2O$[a]	1,404	727	1,931	1,931	8,934	9,657	
"Structural" H_2O		210	18 0					
Total					11,638	17,603	9,963	1,022

[a] Mg is accounted for as solid solution in tobermorite

Carbon-Dioxide–Rich Environment (CO_2 Only): This formulation is composed assuming that the only reactive gas present is CO_2 (Table 5.6-7). In this calculation, the sulfate is

accounted for in the carbonate phase, thaumasite The aluminum is converted into tricarboaluminate. Silicon is converted into an SiO_2 phase, either chalcedony or microcrystalline quartz. The remaining iron and magnesium are converted to carbonates

Table 5.6-7. Calculation of mineral assemblage per meter in thermally treated concrete: CO_2-rich environment (CO_2 only).

Constituent		kg/m	Molec. wt	Phase (mol)	H_2O (mol)	Ca (mol)	Si (mol)	Al (mol)
Thaumasite	$[Ca_3Si(OH)_6\ 12H_2O](SO_4)(CO_3)$	190	622	306	4,595	919	306	
Tricarbo-aluminate	$Ca_6Al_2C_3H_{60}O_{45}$	568	1,111	511	15,334	3,067		1,022
Calcite	$CaCO_3$[a]	1,363	100	13,616		13,617		
Chalcedony	SiO_2[b]	580	60 0	9,656			9,657	
Siderite	$FeCO_3$							
Magnesite	$MgCO_3$[a]							
"Structural" H_2O		359	18 0					
Total					19,929	17,603	9,963	1,022

[a] Use as solid solution in modeling (moles ($CaCO_3$ + $MgCO_3$) = moles high-Mg calcite)
[b] Or microcrystalline quartz

Other Additives

The chemical compositions of all concrete components listed in Table 5 2-5 (excerpted from Meike et al , 1997a) were based on the information given by Tang (1997) where possible. For example, the aggregate, both coarse and fine, is specified as tuff, which is given an average composition based on a previous report (Wilder, 1996) (Table 5.6-8) A comparable steel-fiber composition was obtained from manufacturer's specifications for steel fibers used in Fibercrete™ in the ESF (Meike 1996)

Table 5.6-8. Calculation of the chemical composition of additives per meter.

Additive	wt% dry	Wt. (lb)	lb	kg	Molec. wt.	H_2O%	H_2O (kg)	Cation (mol)
Liquid H_2O		1,360	1,360	617	18 0			34,235
Silica fume (SiO_2)	95	500	475	215	60 1			3,585
Water-reducing agent		25						
Superplasticizer		60						
Steel fiber		330						
Fine aggregate		8,520	256	116		3 0	3 5	
Coarse aggregate		6,600	66	29 9		1 0	0 3	

Aggregate: A concrete differs from a grout in the addition of aggregate, usually in two sizes, fine and coarse. Our simulations use a formulation of tuff as the aggregate. We diverge from the standard tuff formulation that is found in the EQ3/6 library to incorporate the mineralogy given in the Tang (1997) report. Comparison of the two shows some differences,

but they are probably insignificant to the present simulation. Coarse and fine aggregate are not distinguished by mineralogy, but rather by grain size. This difference in grain size translates in the simulation to a difference in surface area, which should be reflected in reaction rate (see next subsection) Although it would be preferable to simulate this physical difference directly in the simulation, it bears no impact on the present result because relative rates must be imposed on the grout mineralogy. In the future, when the grout mineralogy can be more adequately characterized, it will make sense to represent the two grain sizes more accurately. At present we have included a single representative of each mineral with the intention that the contribution of both mineral sizes to the water chemistry will be represented by an average relative dissolution rate

Silica Fume and Other Additives: Of the other additives to the original concrete formulations, only silica fume is represented. It is assumed, for the sake of the simulation, that only part of the silica fume is consumed in the curing of young and AFm concrete The silica is thus incorporated in other minerals in that assemblage, and the remaining silica fume is represented as amorphous silica It is assumed that all of the silica fume is reacted in the thermally treated mineral assemblages, and thus that all of the silica is incorporated into other minerals Superplasticizers and other additives are not represented in this simulation and will need to be incorporated, as determined to be appropriate in future simulations.

Dissolution Rates

Real time cannot be simulated in the present exercise, because only the dissolution rates of some the mineral phases represented are known As a consequence, it is not useful to include the real reaction rates of any of the phases in the simulation We have therefore represented the dissolution of the minerals as relative rates For these preliminary simulations we have made a gross approximation that the grout components dissolve twice as fast as the aggregate components

Resultant Reactant Files

The mineral assemblages discussed in the previous sections, and detailed in Tables 5 6-3 through 5.6-7, have been modified slightly to reflect phases that are actually present in the data base. The actual reactants used are presented in Table 5.6-9. This choice was intended to simplify the present discussion. However, the mineral assemblages presented previously can be used as input. Those minerals that are not represented in the data base can be incorporated (and dissolved) as special reactants The more fundamental problem is that phases that are not represented in the data base cannot be precipitated in the simulation. Thus, all solid phases that are expected to be a significant part of the chemical process must be represented in the data base.

Table 5.6-9. **Solid reactants used in EQ6 simulations at 25°C (by run/file name). Identical simulations have been conducted at 60° and 150°C.**

Constituent		Amount (moles/m)				
		25_ Young	25_ Young AFm	25_ Thermal O_2	25_ Thermal O_2/CO_2	25_ Thermal CO_2
CSH1 7gel	1 7Ca-Si $2H_2O$	5,970	6,020			
Tobermorite	$[Ca_5(Si_5O_{16}H_2)]Ca$ $4H_2O$			1,990	1,970	
Ettringite	$[Ca_3Al(OH)_6$ $12H_2O]_2(SO_4)_3$ $2H_2O$	102		102	102	102
Monosulfate	$Ca_3Al(OH)_6Ca(SO_4)$ $12H_2O$		306			
Gehlenite hydrate	$Ca_2Al_2SiO_7$ $8H_2O$	409	358			
Hydrogarnet	$Ca_3Al_2O_6$ $6H_2O$			409		
Hematite	Fe_2O_3	269	269	269		
Portlandite	$Ca(OH)_2$	3,990	3,400	3,810	1,680	
Brucite	$Mg(OH)_2$	723	723	723		
Calcite	$CaCO_3$				1,680	14,200
Hemicarboaluminate	$Ca_{3.5}Al_2C_{0.5}(H_{20}O_{18})$				511	
Tricarboaluminate	$Ca_6Al_2C_3H_{60}O_{45}$					511
Hydromagnesite	$Mg_5(CO_3)_4(OH)_2$ $4H_2O$				145	
Artinite	$Mg_2CO_3 \cdot 3H_2O$					361
Hematite	Fe_2O_3				134	
Siderite	$FeCO_3$				269	538
Chalcedony	SiO_2 or microcrystalline quartz					9,860
Silica Fume		**1/3 reacted**	**1/3 reacted**	**100% reacted**	**100% reacted**	**100% reacted**
Silica fume	SiO_2	1790	1790	0	0	0
"Aggregate, Fine"						
Annite		17 0	17 0	17 0	17 0	17 0
Phlogopite		7.87	7 87	7 87	7.87	7 87
Sanidine-high		4,120	4,120	4,120	4,120	4,120
Albite		774	774	774	774	774
Anorthite		334	334	334	334	334
Pyrophyllite		105	105	105	105	105
Quartz		7,290	7,290	7,290	7,290	7,290
Cristobalite		16,200	16,200	16,200	16,200	16,200
"Aggregate, Coarse"						
Annite		22 2	22 2	22.2	22.2	22 2
Phlogopite		10 3	10 3	10 3	10 3	10.3

Constituent		Amount (moles/m)				
		25_ Young	25_ Young AFm	25_ Thermal O_2	25_ Thermal O_2/CO_2	25_ Thermal CO_2
Sanidine-high		5,380	5,380	5,380	5,380	5,380
Albite		1,010	1,010	1,010	1,010	1,010
Anorthite		436	436	436	436	436
Pyrophyllite		137	137	137	137	137
Quartz		9,530	9,530	9,530	9,530	9,530
Cristobalite		21,100	21,100	21,100	21,100	21,100

5.6.2.3 3 Gas Constraints: Modeling the Emplacement-Drift Gas Environment

Physically, the exposure of the WPs to oxygen and other atmospheric gases is limited by two possibilities Either the drifts are ventilated by an engineered ventilation system or by natural rock fractures, or the drifts are unventilated The implication of this distinction is profound because it means the distinction between a system in which the gas composition and fugacities remain constant over time, and a system in which the gas composition evolves These physical possibilities are simulated by setting two modeling options First, the system parameters are set using the terminology "open," "closed," "titration," or "flow-through," which determine the means by which reactants and precipitated phases enter and leave the system, and the duration for which the phases can react with the aqueous phases. All simulations in the present study were conducted in titration mode, implying that aliquots of reactants are added to 1 kg of water and allowed to react and that precipitated minerals remain in the system and continue to be potential reactants with the aqueous phase. Second, the gas-ugacity parameters are set as either fixed, which means the fugacity remains constant throughout the simulation (equivalent to a ventilated system) or unfixed, which allows the fugacities to evolve over time. In these simulations, the fugacities for the fixed case were set at atmospheric values.

Three cases are examined for each mineral assemblage In the first case, O_2 and CO_2 fugacities are fixed at an approximation of atmospheric values. In the second case, CO_2 and O_2 values are fixed, but CO_2 is set at a value far below atmospheric. In the third case, the gas composition is not fixed. Because it is necessary to set a value for the maximum volume of gas in the simulation (the "gas reservoir") and because reaction rates are not well constrained, CO_2 is consumed to form calcite and, in all cases, CO_2 is eventually depleted

5 6 2 3.4 Redox Conditions

These preliminary simulations have been conducted without a control on the redox state other than the atmospheric conditions (note the production of pyrite in the unfixed-gas case). Because the contribution of iron to the composition of the water is so small (less than 10^{-9} in most of the simulations), we have not judged such control to be necessary in this phase of the simulations. It will, however be included in future simulations. In the simulations in Section 5.7, the amount of product hematite is constant throughout the simulation.

5 6.2 3 5 Temperature Conditions

Simulations were conducted at 25°, 60° and 150°C. We stress that the 60° and 150°C simulations require additional interpretation and examination because in some cases the new data is only applicable at 25°C.

5 6.2 3 6 Suppressed Phases.

The EQ3 part of the simulation allows the modeler the opportunity to suppress the precipitation of minerals that would not be expected to form under the temperature conditions of the simulation It is quite common to suppress the precipitation of quartz, for example, at low temperatures The present simulations have been conducted with the intent to judge the simulation capabilities provided by the data base Our preliminary assessment included the progressive suppression of mineral phases until some of the newly introduced phases began to precipitate The intent is to provide a somewhat independent test of the relation among the newly added phases and between the new and the old phases, by testing the sensitivity of the simulation to CO_2(gas), a relation that is not implicit in the thermodynamic input. The following phases were suppressed maximum microcline, low-albite, k-feldspar, ordered dolomite, grossular garnet, prehnite, muscovite, paragonite, dolomite, talc, epidote, ordered epidote, high albite, andradite, tremolite diopside and wollastonite Quartz was not suppressed because it is a reactant phase in the EQ6 run Instead, the precipitation rate was set to a very low value

5.7 Modeling Results and Discussion

We have presented a conceptual model for the prediction of the chemistry of water in contact with concrete during the evolution of a potential repository at YM Our approach is to select representative points in time for which mineral assemblages representing the evolving solid concrete can be described. Thus a complete simulation represents various aspects of a short duration over which many of the parameters do not change

We have also presented a specific case and modeling scenarios as a point of departure from which modifications and improvements will be made as our understanding of environmental factors and their impact on the evolution of solids in concrete improves Because of the need for brevity in this report, only three of the many simulation results at 60°C and two at 25°C have been selected for discussion (Figures 5 7-1 through 5 7-5); the complete matrix of simulations tested is shown in Table 5 7-1 For the sake of emphasizing the new data base, we concentrate on the young concrete results.

Table 5.7-1. **Matrix of chemical simulations of water–concrete interaction. Figure numbers designate plots of simulations selected for presentation in this report. X's designate simulations that have been conducted but are not presented in this report.**

Conditions		Reactant file				
Gas condition	Temp (°C)	Young concrete	Young AFm concrete	Thermal concrete	Thermal CO_2/O_2	Thermal CO_2
Unfixed	25	Figure 5 7-2 a,b	X	X	X	X
CO_2 fixed normal	25	X	X	X	X	X
CO_2 fixed low	25	Figure 5 7-1 a,b	X	X	X	X
Unfixed	60	Figure 5 7-5 a,b	X	X	X	X
CO_2 fixed normal	60	Figure 5 7-3 a,b	X	X	X	X
CO_2 fixed low	60	Figure 5 7-4 a,b	X	X	X	X
Unfixed	150	X	X	X	X	X
CO_2 fixed normal	150	X	X	X	X	X
CO_2 fixed low	150	X	X	X	X	X

Figure 5.7-1. 25°C, fixed low CO_2.

a. Reaction progress versus mineral precipitation.

b. Reaction progress versus elemental concentration.

Figure 5.7-2. 25°C, unfixed gas.

a. Reaction progress versus mineral precipitation.

b. Reaction progress versus elemental concentration.

Figure 5.7-3. 60°C, fixed atmospheric CO_2.

a. Reaction progress versus mineral precipitation.

b. Reaction progress versus elemental concentration.

Figure 5.7-4. 60°C, fixed low CO_2.

a. Reaction progress versus mineral precipitation.

b. Reaction progress versus elemental concentration.

Figure 5.7-5. 60°C, unfixed gas.

a. Reaction progress versus mineral precipitation.

b. Reaction progress versus elemental concentration.

For each scenario two plots are presented. One is a plot of reaction progress versus elemental concentration in the aqueous phase. The other plot presents the precipitation of

solid phases as a function of reaction progress (and within the precipitation constraints defined by the model). The precipitated minerals are presented to allow the reader to identify the reactions controlling the water chemistry. With respect to the fixed-gas composition cases, an increase in pH represents the point at which the gas reservoir of the model has been depleted At the moment, we do not give any physical significance to the depletion of the model's gas reservoir, and only note that a significant shift occurs in the identity of the precipitated phases and some of the aqueous species with the change in pH. For the purpose of determining bounding conditions for the concentration of aqueous species, it is appropriate to consider only the part of the fixed-gas scenarios that occur before the depletion of the CO_2 gas

Each of these scenarios (fixed at atmospheric values, fixed at low CO_2 values and unfixed) can be related to a physical situation The fixed cases represent open drifts in which the evolution of the solids have no impact on the gas composition Given that our strategy has been to select representative points in time to conduct simulations (which is different from the evolutionary context that is being used in most of the modeling strategies), it is logical to choose a fixed-gas scenario. The unfixed case relates to the evolution of a gas-impermeable emplacement drift. This is the only case in which the evolution of the gas composition might be treated as a part of a time-dependent physical model

Generally, it is clear that the aqueous chemistry is dependent on gas composition, which in these simulations is directly linked to pH. Certain preliminary observations can be made about the sensitivity of aqueous species to pH Examine, for example, concentration of aluminum species in solution, which is greater at higher pH values, other species, such as magnesium, are less sensitive. It is possible, therefore, to develop a first-order estimate of the concentration of these less sensitive elements in solution, for this scenario The concentrations of the more sensitive species can be bounded within an envelope of uncertainty that encompasses the range of values represented in the simulation The concentration of a particular species in solution is directly related to the solid phases that are precipitated Further reaction progress is required to determine an upper bound for species such as nitrogen, sulfur, and potassium concentrations, because they are still increasing at the end of the simulations This is because, as solids continue to be added and dissolved in the solution, saturation has not been reached with respect to a mineral that contains a large enough percentage of these elements. These simulations are only as good as the data base, which contains the phases and the thermodynamic data that allows the phases to precipitate. Phases from the new data base are precipitated in these simulations. More of them are apparent at 25°C (Figure 5 7-1 and Figure 5 7-2).

The case in which gas composition is fixed at close to atmospheric values (Figure 5.7-3) does not suffer a depletion in CO_2 gas from the model reservoir until near the end of the simulation, when the pH and the gas-fugacity values change sharply. Elemental concentrations in the aqueous phase before that point depend on the precipitation of calcite, but also kaolinite, diaspore and anhydrite. The relation between the formation of calcite and the fugacity of CO_2 is more clear at 25°C (Figure 5 7-1 and Figure 5.7-2)

The case in which gas composition is fixed, but for which the CO_2 fugacity is fixed at a low value, (Figure 5.7-1 and Figure 5.7-4) similarly does not suffer a depletion in CO_2 gas from the model reservoir until near the end of the simulation, when, again, the pH and the gas-fugacity values are affected. The range of concentrations of the various species contrasts with the first simulation. For example the concentration of silicon species in solution varies over a range from 10^{-3} to 10^{-6} molal, whereas in the atmospheric case it ranged from 10^{-3} to $10^{-4.5}$ molal.

The unfixed case (Figure 5.7-2 and Figure 5.7-5) does not seem to be physically achievable in a repository at YM, except during certain episodes in which gas permeability decreases to zero during the thermal pulse, because gas exchange will most likely occur along fractures. However, it is an important reference case that may be helpful to establish bounding concentrations for some chemical species. For example, a lower bound can be suggested for magnesium at roughly 10^{-9} molal. In the unfixed case, even portlandite becomes supersaturated and begins to precipitate. In all cases, potassium and sulfur concentrations increase over the course of the simulation, even though sulfur-bearing phases such as ettringite and anhydrite begin to form later in the simulation.

5.8 The Influence of Construction Materials on WP Performance

Modifications of the natural environment due to construction of an underground repository would, in themselves, alter the natural chemistry, some aspects of which may be critical to the robustness of the WP or to the chemistry of the fluid leaving the repository However, once the materials are emplaced, given defined extrinsic properties, the chemical evolution of the repository would be fixed to a specific path and hypothetically predictable

The ability to model these processes depends on our understanding of the processes, on our ability to develop equations to describe those processes or adapt existing models to our purpose, and on the availability of the appropriate data to feed those models

5.8.1 Solid-State Evolution as a Function of Gas Composition and Temperature

The addition of cementitious materials widens boundary conditions and increases uncertainty. With increased temperature, Ca-Si·H_2O gel and other metastable phases will undergo solid-state transformations into more crystalline and ultimately less hydrous and more stable crystalline phases Ultimately, portlandite will be destroyed in favor of carbonates and sulfates. However, the path of that evolution depends on the environmental conditions and may lead through the family of Ca-Si·H_2O phases that shrink and swell with changing relative humidity and temperature. These physical changes lead to mechanical instabilities and extreme changes in surface area of the original concrete material

5.8.2 Water-Chemistry Evolution

It has not been established that the more crystalline and less hydrous Ca-Si·H_2O phases also are in equilibrium with water at such elevated pH. In fact, there is evidence to the contrary. Hillebrandite and wollastonite, water-poor end-members of the Ca-Si·H_2O system, do not produce such elevated pH.

5.8.3 Microbiological Considerations

In general, the microbial use of protons serves to reduce pH This is beneficial for the microorganism, because it tends to solubilize solids and, thus, provide nutrients. The pH of water in contact with concrete in the presence of microbes can be quite acidic (in the range of 2–3 pH units) (Horn and Meike, 1995)

5.8.4 Design Options that can Reduce Uncertainty (e.g., original concrete formulation and pretreatments)

There are a few engineering options that can reduce modeling uncertainty The pH of the water in contact with concrete is not expected to increase during the evolution of the

proposed repository. Therefore, the upper bound of the range of uncertainty can be reduced significantly by using a "low pH" formulation, even though this is a relative term, because the value of a "low pH" formulation could be about 9.5 or 10.0 (new formulations may bring this value down even further). The real value is in the reduction of uncertainty Minimization of the volume of portlandite in the set cement not only controls the reaction of $Ca(OH)_2$ with sulfate to form gypsum or ettringite (and thus reduces cracking and increased surface area exposed to degradation), but also controls the pH. Sulfate-resistant cements (Taylor, 1990), which are formulated with low aluminum content to minimize the possibility of forming ettringite after the cement has set, can also reduce the sulfate concentration in the aqueous phase. Increasing the reactive silica content of the formulation can also reduce the amount of unreacted portlandite in the cured cement This uncertainty can be reduced even further if the concrete is pre-treated so as to change the mineralogy to calcite, an engineering possibility using a supercritical CO_2 treatment (Rubin et al , 1997). The pH of this concrete would be reduced even further, to near-neutral values, depending on the completeness of the treatment.

There are a few engineering options that can reduce modeling uncertainty The pH of the water in contact with concrete is not expected to increase during the evolution of the proposed repository. Therefore, the upper bound of the range of uncertainty can be reduced significantly by using a "low pH" formulation, even though this is a relative term, because the value of a "low pH" formulation could be about 9.5 or 10.0 (new formulations may bring this value down even further). The real value is in the reduction of uncertainty Minimization of the volume of portlandite in the set cement not only controls the reaction of $Ca(OH)_2$ with sulfate to form gypsum or ettringite (and thus reduces cracking and increased surface area exposed to degradation), but also controls the pH Sulfate-resistant cements (Taylor, 1990), which are formulated with low aluminum content to minimize the possibility of forming ettringite after the cement has set, can also reduce the sulfate concentration in the aqueous phase Increasing the reactive silica content of the formulation can also reduce the amount of unreacted portlandite in the cured cement This uncertainty can be reduced even further if the concrete is pre-treated so as to change the mineralogy to calcite, an engineering possibility using a supercritical CO_2 treatment (Rubin et al., 1997) The pH of this concrete would be reduced even further, to near-neutral values, depending on the completeness of the treatment

5.9 Future Plans

The complete matrix of chemical simulations will be completed by the end of 1998. Then, reactive-transport modeling, which requires the results of the chemical modeling, will be initiated. We will attempt to link the water-material interactions into reaction paths using OS3D/GIMRT, or X1T over defined possible water pathways, such as the following (where WP indicates waste package and WF indicates waste form):

- Incoming water → concrete liner → WP → WF → invert → rock wall
- Incoming water → steel set → WP → WF → invert → rock wall
- Incoming water → salt crust → WP → WF → invert → rock wall
- Incoming water → concrete liner → backfill → WP → WF → invert → rock wall
- Incoming water → steel set → backfill → WP → WF → invert → rock wall
- Incoming water → salt crust → backfill → WP → WF → invert → rock wall

These exercises may be conducted in two halves, representing water flow toward and away from the WPs, depending on the availability of data inputs.

Iterative chemical modeling will be conducted as significant data base improvements are made, and as we improve our understanding of reactant formulations, their evolution and the dissolution laws relating to their components.

The effects of factors such as microbes, heating, and partial pressure of CO_2 above ambient have not been well established and therefore cannot be well constrained. Their impacts are discussed in previous sections, and a general assessment of the uncertainty is discussed in Section 5.8 4.

5.10 References for Section 5

Atkins, M , F P Glasser, A Kindness, and D E. Macphee (1991). *Solubility Data for Cement Hydrate Phases (25°C).* (DOE/HMIP/RR/91/032) Washington, DC U S. Department of Energy

Babushkin, V I., G. M. Matveyev, and O. P. Mchedlov-Petrossyan (1985) *Thermodynamics of Silicates.* Berlin, Germany: Springer-Verlag [NNA.19920401.0112]

Barnes, M W., and D. M. Roy (1983). "The Buffering Mechanisms in Leaching of Composites of Cement with Radioactive Water." *Mater Res Soc Symp. Proc.* **15**:159–166 [NNA 19920131 0250]

Barr-Kumarakulasinghe, S. A. (1994). "Modelling the Thermal Oxidative Degradation Kinetics of Polyethylene Film Containing Metal Pro-oxidants " *Polymer* 35·995-1003

Barret, P , and D. Bertrandie (1986) "Fundamental Hydration Kinetic Features of the Major Cement Constituents· Ca_3SiO_5 and b-Ca_2SiO_4." *J Chem Phys* 83·765–775

Bennett, D G , D Read, M Atkins, and F. P. Glasser (1992). "A Thermodynamic Model for Blended Cements II Cement Hydrate Phases, Thermodynamic Values and Modelling Studies." *J Nucl. Mater* **190**.315–325

Berner, U R (1987) "Modelling Porewater Chemistry in Hydrated Portland Cement." *Mater Res Soc Symp Proc* **84**·319–330

Berner, U. R. (1988) "Modelling the Incongruent Dissolution of Hydrated Cement Minerals " *Radiochim Acta* **44/45**:387–393.

Berner, U.R (1990). *A Thermodynamic Description of the Evolution of Pore Water Chemistry and Uranium Speciation during Degradation of Cement* (PSI Bericht Nr 62) Villigen, Switzerland· Paul Scherrer Institut.

Bruton, C. J., W. E. Glassley, and A. Meike (1995) *Geothermal Areas as Analogues to Chemical Processes in the Near Field and Altered Zone of the Potential Yucca Mountain, Nevada, Repository* (UCRL-ID-119842) Livermore, CA· Lawrence Livermore National Laboratory

Bruton, C. J., B. L. Phillips, A. Meike, S. Martin, and B. E. Viani (1994). "Cement Minerals at Elevated Temperature: Thermodynamics and Structural Characteristics." *Mater Res Soc. Proc.* **133**:327–333. (UCRL-JC-115796) [NNA.19940318.0008]

Burnay, S. G. (1990). "A Practical Model for Prediction of the Lifetime of Elastomeric Seals in Nuclear Environments." In proceedings from *ACS Symposium Series: Radiation Effects on Polymers.* R.L. Clough and S.W. Shalaby, eds. Washington, DC: American Chemical Society. pp. 524–533.

Burnett, N C., R D. Hooton, R. B. Heimann and M Onofrei (1985) "The Development of Durable Cementitious Materials for Use in a Nuclear Fuel Waste Disposal Facility " *Mat Res Soc. Symp Proc.* **50**:461-468

Burton, B L. (1993). "The Thermooxidative Stability of Cured Epoxy Resins." *Int J Appl Polym Sci* **47**.1821-1837.

Clodic, L , and A Meike (1997) *Thermodynamics of Calcium–Silicate Hydrates Phase I Development of a Database Dedicated to Modeling Concrete Dissolution at 25°C* Milestone report for the CRWMS Management and Operating Contractor, U S Department of Energy (SPLG1EM4) Livermore, CA Lawrence Livermore National Laboratory [MOL 19971217.0321]

Ederova, J , and V Satava (1979) "Heat Capacities of C_3AH_6, C_4ASH_{12} and $C_6AS_3H_{32}$ " *Thermochim Acta* **31** 126–128

Garrels, R M , and C. L Christ (1965) *Solutions, Minerals, and Equilibria* San Francisco, CA W H Freeman & Co [HQS 19880517.1981]

Garrett, R W , D J T. Hill, T T. Le, K A Milne, J H. O'Donnell, S. M C. Perera, and P J Pomery (1990) *Temperature Dependence of the Radiation Chemistry of Polymers* Washington, DC: American Chemical Society.

Gillen, K. T , and R. L. Clough (1989) "Time-Temperature-Dose Rate Superposition: A Methodology for Extrapolating Accelerated Radiation Aging Data to Low Dose Rate Conditions " *Polym Degrad Stab* **24** 137–168

Glasser, F P , E E Lachowski, and D E MacPhee (1987) "Compositional Model for Calcium–Silicate Hydrate (C-S-H) Gels, Their Solubilities, and Free Energies of Formation " *Am Ceram Soc J* 70(7) 481–485

Glasser, F. P., M J Angus, C. E McCulloch, D MacPhee, and A A Rahman (1985) "The Chemical Environment in Cements " *Mater Res Soc Symp Proc* 44.849–858 [NNA.910207 0039]

Glassley, W E , and A Meike (1997) *Chemical Modeling of Backfill Composed of Quartz Sand, Lime and an Fe-phase* (UCRL-ID-124631) Livermore, CA Lawrence Livermore National Laboratory [MOL.19971217.0351]

Grassie, N. and G. Scott (1985). *Polymer Degradation and Stabilisation* Cambridge, UK. Cambridge Univerisity Press

Grenthe, I , J Fuger, R J. M Konings, R J. Lemire, A. B. Muller, C Nguyen-Trung, and H. Wanner (1992). *Chemical Thermodynamics, Vol 1 Chemical Thermodynamics of Uranium*. Amsterdam: North Holland. [NNA.19940415.0009]

Haas, J. L. J , G. R. J. Robinson, and B. S. Hemingway (1981). "Thermodynamic Tabulations for Selected Phases in the System CaO-Al_2O_3-H_2O at 101.32 kPa (1 atm) between 273 15 and 1800 K." *J Phys Chem Ref Data* **10**.575–669.

Hardin, E. L., S. C. Blair, T. A. Buscheck, D. A. Chesnut, L. D. DeLoach, W. E. Glassley, J. W. Johnson, R. B. Knapp, K. Lee, A. Meike, K. Myers, J. J. Nitao, C. E. Palmer, L. L. Rogers, N. D. Rosenberg, B E. Viani, H. F. Wang, C Wittwer, and T. J. Wolery (1998). *Near-Field/Altered-Zone Models Report* Milestone report for the CRWMS Management and Operating Contractor, U.S. Department of Energy.

(SP3100M3) Livermore, CA Lawrence Livermore National Laboratory (UCRL-ID-129179 DR)

Harrar, J , J. F. Carley, W. F. Isherwood, and E Raber (1990) *Report of the Committee to Review the Use of J-13 Well Water in Nevada Nuclear Waste Storage Investigations* (UCRL-ID-21867) Livermore, CA Lawrence Livermore National Laboratory. [NNA.910131.0274]

Harvie, C. E., and J. H Weare (1980) "The Prediction of Mineral Solubilities in Natural Waters: The Na-K-Mg-Ca-Cl-SO_4-H_2O System from Zero to High Concentration at 25°C " *Geochim Cosmochim Acta* 44(7).981–997

Harvie, C E , N. Moller, and J. H. Weare (1984). "The Prediction of Mineral Solubilities in Natural Waters: The Na–K–Mg–Ca–H–Cl–SO_4–OH–HCO_3–CO_3–CO_2–H_2O System to High Ionic Strengths at 25°C " *Geochim Cosmochim Acta* 48(4):723–751 [NNA 19891006.0190]

Haveman, S A., S. Stroes-Gascoyne, and C. J. Hamon (1996). *Biodegradation of a Sodium Sulphonated Naphthalene Formaldehyde Condensate by Bacteria Naturally Present in Granitic Groundwater* (Technical Record: TR-721, COOG-95-547) Atomic Energy of Canada Ltd

Heimann, R B (1988a) "Interaction of Cement and Radioactive Waste Forms in Multicomponent Systems Tests at 200°C. Part 1: Leaching and Sorption of Cesium, Strontium, and Actinides " *Cem Concr. Res* 18 389–400 [NNA.19920506.0048]

Heimann, R B (1988b) "Interaction of Cement and Radioactive Waste Forms in Multicomponent Systems Tests at 200°C Part 2· Mineralogical Changes of Cement." *Cem. Concr. Res* 18:554–560 [NNA.19920506.0049]

Heimann, R. B., and R. D. Hooton (1986) "Mineralogical Changes of Various Cement Formulations during Reaction with Groundwater in the Presence of Ca and Na-Bentonite at 150°C " *Can Min* 24 289-302 (Also issued as AECL-8895, Atomic Energy of Canada Ltd)

Heiner, M , T T Gonzaga, S. Nordick, S. Bailey, K Herold, J. W. Willis, and J. L Naaf (1994) *Package 2C, TS North Ramp Steel Sets and Lagging Elevation* (engineering drawing, BABEAB000-01717-2100-41101-03) Las Vegas, NV. Civilian Radioactive Waste Management System Management and Operating Contractor. TRW Environmental Safety Systems, Inc. October 28, 1994. [MOL 19960109.0081]

Horn, J M., and A Meike (1995). *Microbial Activity at Yucca Mountain, Part I Microbial Metabolism, Adaptation and the Repository Environment.* Position Paper resulting from the Workshop on Microbial Activity at Yucca Mountain, Lafayette, California, April 10–12, 1995. (UCRL-ID-122256) Livermore, CA: Lawrence Livermore National Laboratory. [222145]

Jackson, K. J (1988). *Verification and Validation Studies of the Addition of Pitzer's Equations to the EQ3/6 Brine Model.* (UCRL-53841) Livermore, CA: Lawrence Livermore National Laboratory. [NNA.19910326 0060]

Jackson, K. J , and T. J. Wolery (1985). "Extension of the EQ3/6 Computer Codes to Geochemical Modeling of Brines." In proceedings from *Scientific Basis for Waste*

Management VIII. Boston, MA: Materials Research Society. 44:507–514. [NNA.19891006.0198]

Johnson, J. W., E H. Oelkers, and H C. Helgeson (1992). "SUPCRT92: A Software Package for Calculating the Standard Molal Thermodynamic Properties of Minerals, Gases, Aqueous Species, and Reactions from 1 to 5000 bars and 0°C to 1000°C." *Comput Geosci* 18·899–947 (UCRL-JC-107907) [234273]

Kaplan, M L (1991). "Solvent Penetration in Cured Epoxy Networks " *Poly Eng Sci* 31(10):689–698

Kenny, J M , L. Torre, and L Nicolais (1993) "Short-Term and Long-Term Degradation of Polymer-Based Composites " *Thermochim Acta* 227.97–106.

Knauss, K G., W J. Beiriger, D W. Peifer, and A. J. Piwinskii (1985). *Hydrothermal Interaction of Solid Wafers of Topopah Spring Tuff with J-13 Water and Distilled Water at 90, 150, and 250°C, Using Dickson-Type, Gold-Bag Rocking Autoclaves* (UCRL-53645) Livermore, CA Lawrence Livermore National Laboratory [NNA 19900207 0282, HQS.19980517.2482]

Knauss, K G , and D W. Peifer (1986). *Reaction of Vitric Topopah Spring Tuff and J-13 Ground Water Under Hydrothermal Conditions, Using Dickson-Type, Gold-Bag Rocking Autoclaves* (UCRL-53795) Livermore, CA Lawrence Livermore National Laboratory. [NAA 891102 0117]

Knauss, K G , W J Beiriger, and D W Peifer (1987) *Hydrothermal Interaction of Solid Wafers of Topopah Spring Tuff with J-13 Water and Distilled Water at 90 and 150°C Using Dickson-Type, Gold-Bag Rocking Autoclaves Long-Term Experiments* (UCRL-53722) Livermore, CA Lawrence Livermore National Laboratory [NNA.19870713 0081, 203013]

Komarneni, S and D M Roy (1983) "Hydrothermal Interactions of Cement or Mortar with Zeolites or Montmorillonites " *Mat Res Soc Symp Proc* 15 55-62

Kosmatka, S H., and W. C Panarese (1994) *Design and Control of Concrete Mixtures* Skokie, IL Portland Cement Association (Thirteenth edition)

Lea, F. M (1971) *The Chemistry of Cement and Concrete.* New York, NY· Chemical Publishing Co. Inc. [NNA.19890713.0195]

Leedy, W. T., and R. J. Watters (1994). "Assessment of Rock Bolt Systems for Underground Waste Storage." In proceedings from *High-Level Radioactive Waste Management Conference* Las Vegas, NV· Am. Nucl Soc , Inc

Livingston, R. A , P. E. Stutzman, R. Mark and M. Eridik (1992) "Preliminary Analysis of the Masonry of the Hagia Sophia Basilica, Istanbul." *Mat Res Soc Symp Proc* 267.721-735.

Majling, J , V. Tomkova, and E. Istenikova (1985). "Calorimetric Study of Reactions in the System C_4A_3S-CH-CS-H." *Thermochim. Acta* 85·219–222.

Martin, S. I , B Viani, and A. Meike (1996). *Water Adsorption by Okenite ($Ca_{10}Si_{18}O_{46}·18H_2O$) at Ambient Temperature.* Livermore, CA: Lawrence Livermore National Laboratory. [MOL 19960223 0336]

Maycock, J. N., J Skalny, and R. S. Kalyoncu (1974). "Thermal Decomposition of Cementitious Hydrates." R. S. Porter and J. F. Johnson, eds. *Analytical Calorimetry* New York, NY: Plenum Press [NNA.19920506.0051]

McCright, R D (1996). *Engineered Materials Characterization Report* (UCRL-ID-119564, Rev 0) Livermore, CA: Lawrence Livermore National Laboratory. [MOL 19961022.0024]

McNeil, M. B , D W. Mohr, and B. J. Little (1990) "Correlation of Laboratory Results with Observations on Long-Term Corrosion of Iron and Copper Alloys." In proceedings from *Symposium on Materials Science in Archeology* San Francisco, CA Materials Research Society (1990 Spring Meeting) [NNA.19920506 0038]

Meike, A. (1996) *Introduced Materials Synthesis Report 1993–1996* Yucca Mountain Project internal report for the CRWMS Management and Operating Contractor, U S Department of Energy. Livermore, CA Lawrence Livermore National Laboratory. [MOL 19961108.0016]

Meike, A , K. Myers, M Spragge, and A. Barr (1997a). *Calculation of Quantities, Masses, and Chemical Compositions of Steel Set and Concrete Liner Mechanical Support Components for Emplacement Drifts* Report for deliverable reports WP26809 and WP26815 for the CRWMS Management and Operating Contractor, U.S Department of Energy. Livermore, CA Lawrence Livermore National Laboratory [MOL.19980109 0258]

Meike, A , M Onofrei, C J Bruton, and B. E Viani (1994) "Progress in Understanding the Structure and Thermodynamics of Calcium–Silicate Hydrates " In proceedings from *Fifth Annual International High-Level Radioactive Waste Management Conference* Las Vegas, NV. American Nuclear Society, La Grange Park, IL pp 2590–2596 (Also UCRL-JC-116358) [NNA 19940517 0130]

Meike, A , M Spragge, and C. Aracne-Ruddle (1997b) *Hydrothermal Alteration of Concrete First Batch.* Deliverable report for the CRWMS Management and Operating Contractor, U.S. Department of Energy Livermore, CA· Lawrence Livermore National Laboratory [MOL.19970507 01957]

Meike, A , W. L. Bourcier, M. Alai, D L. Haldeman, P. S. Amy, and T. Lagadinos (1995) *Potential Long-Term Chemical Effects of Diesel Fuel Emissions on a Mining Environment A Preliminary Assessment Based on Data from a Deep, Subsurface Tunnel at Rainier Mesa, Nevada Test Site.* Livermore, CA Lawrence Livermore National Laboratory. (UCRL-ID-121046) [MOL19950406.0141]

Milestone, N B , T. Sugama, L E. Kukacka, and N. Carciello (1987). "Carbonation of Geothermal Grouts—Part 3 CO_2 Attack on Grouts Containing Bentonite." *Cem Concr. Res* **17**:295–306 [NNA.902506.0052]

Mor, E D , and A. M. Beccaria (1975). "Behaviour of Copper in Artificial Sea Water Containing Sulphides." *Br. Corrosion J* **10**(1):33–38. [NNA.19920506.0040]

Myers, K , and A. Meike (1997). *Hydrothermal Alteration of Concrete Second and Third Batches.* Milestone report for the CRWMS Management and Operating Contractor, U.S. Department of Energy. (SPLGDM4; SPLGEM4) Livermore, CA· Lawrence Livermore National Laboratory. [MOL.19980114.0113]

O'Donnell, J.H. (1990). "Chemistry of Radiation Degradation of Polymers." R L Clough and S W. Shalaby, eds. *Radiation Effects on Polymers.* Washington, DC: American Chemical Society.

Pitzer, K. S (1979). "Theory: Ion Interaction Approach." R M Pytkowicz, ed. *Activity Coefficients in Electrolyte Solutions* Boca Raton, FL: CRC Press [NNA 19891996 0194]

Pollard, A M , R G Thomas, and P A Williams (1989) "Synthesis and Stabilities of the Basic Copper (II) Chlorides Atacamite, Paratacamite, and Botallackite " *Mineral Mag* 53 57–563 [NNA 19920401 0111]

Prater, M , and K K Bhattacharyya (1998) *Committed Repository Materials Document Control Action Request for Addendum D* (BCA000000-01717-5705-00005-0, part K) Las Vegas, NV· Civilian Radioactive Waste Management System Management and Operating Contractor· TRW Environmental Safety Systems, Inc. [MOL.19980420.0867]

Ravanetti, G P , and M Zini (1992). "A Study on the Thermal-Degradation Kinetics of Syndiotactic Polystyrene by Thermogravimetric Analysis " *Thermochim Acta* 207.53–64.

Read, D T (1991). *Chemval Project Report on Stages 3 and 4 Testing of Coupled Chemical Transport Models* (DOE/HMIP/RR/91/003) London, UK U K Department of Energy

Rhoderick, J E (1981) *Examination of Samples of Grout After 63 Years Exposure Underground* (ONWI-248) Springfield, VA. U S Department of Commerce

Roy, D M , and C A Langton (1989) *Studies of Ancient Concrete as Analogs of Cementitious Sealing Materials for a Repository in Tuff* (LA-11527-MS) Los Alamos, NM Los Alamos National Laboratory. [HQX.19890608 0033]

Roy, D. M , and C. A. Langton (1983). *Characterization of Cement Based Ancient Building Materials in Support Seal Materials Study* (MI/ONWI-523) Columbus, OH Battelle Memorial Institute/Office of Nuclear Waste Isolation [SRX.19840127 0146]

Rubin, J. B , J W. Carey, and D. M. V. Taylor (1997) *Enhancement of Cemented Waste Forms by Supercritical CO_2 Carbonation of Standard Portland Cements* (LA-UR-97-1859) Los Alamos, NM: Los Alamos National Laboratory.

Russell, C , R. Jacobsen, D. L. Haldeman, and P. S. Amy (1994) "Heterogeneity of Deep Subsurface Microorganisms and Correlations to Hydrogeological and Geochemical Parameters." *Geomicrobiology J.* 12:37-51.

Sarker, A. K , M. W. Barnes, and D M Roy (1982). *Longevity of Borehole and Shaft Sealing Materials· Thermodynamic Properties of Cements and Related Phases Applied to Repository Sealing* (ONWI-201) Springfield, VA: U.S. Department of Commerce. [NNA.19900316.0016]

Scott, D A (1985). "Periodic Corrosion Phenomena in Bronze Antiquities." *Studies in Conservation* 30:49–57. [NNA.920401.0108]

Smirnov, V. V., and E. B. Dubova (1992). "Characteristics of the Radiation Modification of High-Density Polyethylene in the Presence of Solvents." *High Energy Chem.* 26(3) 173–177.

Steefel, C I, and A. C. Lasaga (1994). "A Coupled Model for Transport of Multiple Chemical Species and Kinetic Precipitation/Dissolution Reactions with Application to Reactive Flow in Single-Phase Hydrothermal Systems." *Am J Sci* 294·529–592 [235372]

Steefel, C I, and S B. Yabusaki (1995). *OS3D/GIMRT Software for Modeling Multicomponent-Multidimensional Reactive Transport* Richland, WA Pacific Northwest Laboratory, Battelle Memorial Institute

Sterne, P. A., and A Meike (1995). *Electronic Structure Calculations of Calcium–silicate hydrates* (UCRL-JC-121437) Livermore, CA· Lawrence Livermore National Laboratory (For submittal to Mater Res. Soc Fall Meeting, Boston, MA, November 27–December 1, 1995) [235671]

Tang, D. (1997) *Emplacement Drift Ground Support* May 23, 1997 Yucca Mountain Project report. (BCAA00000-01717-0200-00003, Rev. 00B) Las Vegas, NV: prepared by the Civilian Radioactive Waste Management System, Management and Operating Contractor, for the U.S. Department of Energy.

Taylor, H F W (1990) *Cement Chemistry* New York, NY Academic Press

Van Konynenburg, R A (1984). *Radiation Doses in Granite around Emplacement Holes in the Spent Fuel Test - Climax* (Final Report, UCRL-53580) Livermore, CA Lawrence Livermore National Laboratory [HQS 19880517 2558]

Van Konynenburg, R A., R D. McCright, A K Roy, and D. Jones (1997) *Engineered Materials Characterization Report* (UCRL-ID-119564) Livermore, CA· Lawrence Livermore National Laboratory (Rev 1) [MOL 19960402 0552]

Vieillard, P., and F Rassineux (1992). "Thermodynamic and Geochemical Modelling of the Alteration of Two Cement Matrices " *Appl Geochem Suppl* 1.125–136

West, K A (1988) *Nevada Nuclear Waste Storage Investigations Exploratory Shaft Facility Fluids and Materials Evaluation* (LA-11398-MS) Los Alamos, NM: Los Alamos National Laboratory. [NNA 890926 0014]

Wilder, D G. (1996). *Near-Field and Altered-Zone Environment Report, Volume II* (UCRL-LR-124998, Vol. II) Livermore, CA: Lawrence Livermore National Laboratory. [MOL 19961212.0121, MOL 19961212.0122]

Wilski, H. (1990). "Radiation Stability of Polymers Radiation Physics and Chemistry." *Int J Rad Appl Instrument. Part C.* 35(1–3)·186–189.

Wolery, T J (1992a). *EQ3NR, A Computer Program For Geochemical Aqueous Speciation-Solubility Calculations Theoretical Manual, User's Guide, and Related Documentation* (UCRL-MA-110662) Livermore, CA: Lawrence Livermore National Laboratory. (Version 7 0) [NNA 19921218.0010]

Wolery, T. J. (1992b). *EQ3/6, A Software Package for Geochemical Modeling of Aqueous Systems: Package Overview and Installation Guide* (UCRL-MA-110662) Livermore, CA: Lawrence Livermore National Laboratory. (part 1) [NNA.19921023 0028]

Wolery, T. J., and S. A. Daveler (1992). *EQ6, A Computer Program for Reaction Path Modeling of Aqueous Geochemical Systems· Theoretical Manual, User's Guide, and Related Documentation (Version 7 0)*. (UCRL-MA-110662) Livermore, CA Lawrence Livermore National Laboratory (part 4) [MOL 19980218 0570]

5.11 Appendix A for Section 5

Table 5.11-1. Quantities of selected construction materials to be used in proposed Yucca Mountain repository, based on the current design (provided by Norman Kramer, Repository Design). All quantities are estimates.

ID	Item	CL	Quantity	Unit	Material	System	Location	Est. service life	Description
37	Air locks	T	150,000	kg	steel	ventilation systems	east main	21–30	
38	Air locks	T	150,000	kg	steel	ventilation systems	west main	21–30	
39	Rock bolt	P	980	each	steel	ground support	PC drifts	51–100	Super Swellex bolt 3 m long
40	Wire mesh	P	1,290	m^2	steel	ground support	PC drifts	51–100	WWF 3 × 3
41	Drift invert	P	7,520	each	concrete	ground support	PC drifts	51–100	
42	Rock bolt	P	48,375	each	steel	ground support	PC drifts	51–100	Super Swellex bolt 3 m long
43	Wire mesh	P	56,770	m^2	steel	ground support	PC drifts	51–100	WWF 3 × 3
44	Steel sets	P	1,747,300	kg	steel	ground support	PC drifts	51–100	5 5-m dia , W8 × 31, 2020 sets
45	Lagging	P	968,000	kg	steel	ground support	PC drifts	51–100	C8 × 11 5 × 4 ft long, 46,300 ea
46	Cast-in-place concrete	P	145	m^3	concrete	ground support	PC drifts	51–100	5,000 psi
47	Metal	P	20,000	kg	steel	ground support	PC drifts	51–100	Frame
48	Rock bolt	P	2,580	each	steel	ground support	alcoves	51–100	Super Swellex bolt 1 5 m long
49	Wire mesh	P	3,660	m^2	steel	ground support	alcoves	51–100	WWF 3 × 3
50	Cast-in-place concrete	P	22,430	m^3	concrete	ground support	north ramp	101–150	5,000 psi
51	Cast-in-place concrete	P	17,780	m^3	concrete	ground support	south ramp	101–150	5,000 psi
52	Cast-in-place concrete	P	18,150	m^3	concrete	ground support	south ramp extension	101–150	5,000 psi
53	Cast-in-place concrete	P	11,930	m^3	concrete	ground support	north ramp extension	101–150	5,000 psi

ID	Item	CL	Quantity	Unit	Material	System	Location	Est. service life	Description
54	Cast-in-place concrete	P	22,800	m^3	concrete	ground support	east main	101–150	5,000 psi
55	Cast-in-place concrete	P	27,890	m^3	concrete	ground support	west main	101–150	5,000 psi
56	Cast-in-place concrete	P	9,100	m^3	concrete	ground support	north main	101–150	5,000 psi
57	Cast-in-place concrete	P	12,110	m^3	concrete	ground support	east main north extension	101–150	5,000 psi
58	Cast-in-place concrete	P	40,750	m^3	concrete	ground support	exhaust main	101–150	5,000 psi
59	Pipe	P	2,804	m	steel	utility systems	north ramp	51–100	8 in air pipe
60	Pipe	P	2,223	m	steel	utility systems	south ramp	51–100	8 in air pipe
61	Pipe	P	2,269	m	steel	utility systems	south ramp extension	51–100	8 in air pipe
62	Pipe	P	1,491	m	steel	utility systems	north ramp extension	51–100	8 in air pipe
63	Pipe	P	2,850	m	steel	utility systems	east main	51–100	8 in air pipe
64	Pipe	P	3,486	m	steel	utility systems	west main	51–100	8 in air pipe
65	Pipe	P	1,137	m	steel	utility systems	north main	51–100	8 in air pipe
66	Pipe	P	1,514	m	steel	utility systems	east main north extension	51–100	8 in air pipe
67	Pipe	P	5,094	m	steel	utility systems	exhaust main	51–100	8 in air pipe
68	Pipe	P	2,804	m	steel	utility systems	north ramp	51–100	6 in water supply line
69	Pipe	P	2,223	m	steel	utility systems	south ramp	51–100	6 in water supply line
70	Pipe	P	2,269	m	steel	utility systems	south ramp extension	51–100	6 in water supply line
71	Pipe	P	1,491	m	steel	utility systems	north ramp extension	51–100	6 in water supply line
72	Pipe	P	2,850	m	steel	utility systems	east main	51–100	6 in water supply line
73	Pipe	P	3,486	m	steel	utility systems	west main	51–100	6 in water supply line

ID	Item	CL	Quantity	Unit	Material	System	Location	Est service life	Description
75	Pipe	P	1,137	m	steel	utility systems	north main	51–100	6 in water supply line
76	Pipe	P	1,514	m	steel	utility systems	east main north extension	51–100	6 in water supply line
77	Pipe	P	5,094	m	steel	utility systems	exhaust main	51–100	6 in water supply line
78	Pipe	P	2,804	m	steel	utility systems	north ramp	51–100	6 in waste water line
79	Pipe	P	2,223	m	steel	utility systems	south ramp	51–100	6 in waste water line
80	Pipe	P	2,269	m	steel	utility systems	south ramp extension	51–100	6 in waste water line
81	Pipe	P	1,491	m	steel	utility systems	north ramp extension	51–100	6 in waste water line
82	Pipe	P	2,850	m	steel	utility systems	east main	51–100	6 in waste water line
83	Pipe	P	3,486	m	steel	utility systems	west main	51–100	6 in waste water line
84	Pipe	P	1,137	m	steel	utility systems	north main	51–100	6 in waste water line
85	Pipe	P	1,514	m	steel	utility systems	east main north extension	51–100	6 in waste water line
86	Pipe	P	5,094	m	steel	utility systems	exhaust main	51–100	6 in waste water line
87	Electrical wire	P	2,804	m	other metal	utility systems	north ramp	51–100	3/c 15 KV 500 MCM cable
88	Electrical wire	P	2,223	m	other metal	utility systems	south ramp	51–100	3/c 15 KV 500 MCM cable
89	Electrical wire	P	2,269	m	other metal	utility systems	south ramp extension	51–100	3/c 15 KV 500 MCM cable
90	Electrical wire	P	1,491	m	other metal	utility systems	north ramp extension	51–100	3/c 15 KV 500 MCM cable
91	Electrical wire	P	2,850	m	other metal	utility systems	east main	51–100	3/c 15 KV 500 MCM cable
92	Electrical wire	P	3,486	m	other metal	utility systems	west main	51–100	3/c 15 KV 500 MCM cable
93	Electrical wire	P	1,137	m	other metal	utility systems	north main	51–100	3/c 15 KV 500 MCM cable

ID	Item	CL	Quantity	Unit	Material	System	Location	Est service life	Description
94	Electrical wire	P	1,514	m	other metal	utility systems	east main north extension	51–100	3/c 15 KV 500 MCM cable
95	Electrical wire	P	5,094	m	other metal	utility systems	exhaust main	51–100	3/c 15 KV 500 MCM cable
96	Electrical wire	P	2,804	m	other metal	utility systems	north ramp	51–100	power system
97	Electrical wire	P	2,223	m	other metal	utility systems	south ramp	51–100	power system
98	Electrical wire	P	2,269	m	other metal	utility systems	south ramp extension	51–100	power system
99	Electrical wire	P	1,491	m	other metal	utility systems	north ramp extension	51–100	power system
100	Electrical wire	P	2,850	m	other metal	utility systems	east main	51–100	power system
101	Electrical wire	P	3,486	m	other metal	utility systems	west main	51–100	power system
102	Electrical wire	P	1,137	m	other metal	utility systems	north main	51–100	power system
103	Electrical wire	P	1,514	m	other metal	utility systems	east main north extension	51–100	power system
104	Electrical wire	P	5,094	m	other metal	utility systems	exhaust main	51–100	power system
105	Electrical—other	P	2,804	m	other metal	utility systems	north ramp	51–100	trolly system
106	Electrical—other	P	2,223	m	other metal	utility systems	south ramp	51–100	trolly system
107	Electrical—other	P	2,269	m	other metal	utility systems	south ramp extension	51–100	trolly system
108	Electrical—other	P	1,491	m	other metal	utility systems	north ramp extension	51–100	trolly system
109	Electrical—other	P	2,850	m	other metal	utility systems	east main	51–100	trolly system
110	Electrical—other	P	3,486	m	other metal	utility systems	west main	51–100	trolly system
111	Electrical—other	P	1,137	m	other metal	utility systems	north main	51–100	trolly system
112	Electrical—other	P	1,514	m	other metal	utility systems	east main north extension	51–100	trolly system

ID	Item	CL	Quantity	Unit	Material	System	Location	Est service life	Description
113	Electrical—other	P	5,094	m	other metal	utility systems	exhaust main	51–100	trolly system
114	Rail	P	658,940	kg	steel	excavated openings	north ramp	51–100	115 lb/yd @ 2,804 m
115	Rail	P	522,400	kg	steel	excavated openings	south ramp	51–100	115 lb/yd @ 2,223 m
116	Rail	P	533,220	kg	steel	excavated openings	south ramp extension	51–100	115 lb/yd @ 2,269 m
117	Rail	P	350,390	kg	steel	excavated openings	north ramp extension	51–100	115 lb/yd @ 1,491 m
118	Rail	P	669,750	kg	steel	excavated openings	east main	51–100	115 lb/yd @ 2,850 m
119	Rail	P	819,210	kg	steel	excavated openings	west main	51–100	115 lb/yd @ 3,486 m
120	Rail	P	267,200	kg	steel	excavated openings	north main	51–100	115 lb/yd @ 1,137 m
121	Rail	P	355,790	kg	steel	excavated openings	east main north extension	51–100	115 lb/yd @ 1,514 m
122	Rail	P	1,197,090	kg	steel	excavated openings	exhaust main	51–100	115 lb/yd @ 5,094 m
123	Electrical—other	P	2,804	m	other metal	utility systems	north ramp	31–40	leaky feeder cable
124	Electrical—other	P	2,223	m	other metal	utility systems	south ramp	31–40	leaky feeder cable
125	Electrical—other	P	2,269	m	other metal	utility systems	south ramp extension	31–40	leaky feeder cable
126	Electrical—other	P	1,491	m	other metal	utility systems	north ramp extension	31–40	leaky feeder cable
127	Electrical—other	P	2,850	m	other metal	utility systems	east main	31–40	leaky feeder cable
128	Electrical—other	P	3,486	m	other metal	utility systems	west main	31–40	leaky feeder cable
129	Electrical—other	P	1,137	m	other metal	utility systems	north main	31–40	leaky feeder cable
130	Electrical—other	P	1,514	m	other metal	utility systems	east main north extension	31–40	leaky feeder cable
131	Electrical—other	P	5,094	m	other metal	utility systems	exhaust main	31–40	leaky feeder cable
132	Electrical—other	P	5,608	m	plastic	utility systems	north ramp	31–40	fiber-optic cable

ID	Item	CL	Quantity	Unit	Material	System	Location	Est. service life	Description
133	Electrical—other	P	4,446	m	plastic	utility systems	south ramp	31–40	fiber-optic cable
134	Electrical—other	P	4,538	m	plastic	utility systems	south ramp extension	31–40	fiber-optic cable
135	Electrical—other	P	2,982	m	plastic	utility systems	north ramp extension	31–40	fiber-optic cable
136	Electrical—other	P	5,700	m	plastic	utility systems	east main	31–40	fiber-optic cable
137	Electrical—other	P	6,972	m	plastic	utility systems	west main	31–40	fiber-optic cable
138	Electrical—other	P	2,274	m	plastic	utility systems	north main	31–40	fiber-optic cable
139	Electrical—other	P	3,028	m	plastic	utility systems	east main north extension	31–40	fiber-optic cable
140	Electrical—other	P	10,188	m	plastic	utility systems	exhaust main	31–40	fiber-optic cable
141	Cast-in-place concrete	P	179	m^3	concrete	excavated openings	development shaft	101–150	
142	Cast-in-place concrete	P	2,269	m^3	concrete	excavated openings	development shaft	101–150	
143	Pipe	P	335	m	steel	utility systems	development shaft	51–100	6 in water supply line
144	Pipe	P	335	m	steel	utility systems	development shaft	51–100	6 in waste water line
145	Electrical wire	P	335	m	other metal	utility systems	development shaft	51–100	3 c 15 KV 500 MCM cable
146	Pipe	P	335	m	steel	utility systems	development shaft	51–100	8 in air piping
147	Electrical equipment	P	1	each	steel	utility systems	development shaft	51–100	power center
148	Electrical—other	P	335	m	other metal	utility systems	development shaft	51–100	power system
149	Metal	P	335	m	steel	utility systems	development shaft	101–150	ladder
150	Cast-in-place concrete	P	179	m^3	concrete	excavated openings	emplacement shaft	101–150	

ID	Item	CL	Quantity	Unit	Material	System	Location	Est. service life	Description
151	Cast-in-place concrete	P	2,792	m^3	concrete	excavated openings	emplacement shaft	101–150	
152	Pipe	P	410	m	steel	utility systems	emplacement shaft	51–100	6 in water supply line
153	Pipe	P	410	m	steel	utility systems	emplacement shaft	51–100	6 in waste water line
154	Electrical wire	P	410	m	other metal	utility systems	emplacement shaft	51–100	3/c 15 KV 500 MCM cable
155	Pipe	P	410	m	steel	utility systems	emplacement shaft	51–100	8 in air pipe
156	Electrical equipment	P	1	each	steel	utility systems	emplacement shaft	51–100	power center
157	Electrical—other	P	410	m	other metal	utility systems	emplacement shaft	51–100	power system
158	HEPA filter	P	4	each	steel	ventilation systems	emplacement shaft	51–100	
159	Metal	P	410	m	steel	excavated openings	emplacement shaft	51–100	Ladder
160	Pipe	P	3 440 200	kg	steel	ventilation systems	exhaust main	51–100	72-in dia duct
161	Metal	P	102,000	kg	steel	ventilation systems	ventilation raises	51–100	exhaust structure @ 1,000 kg ea
165	Rock bolt	P	34,300	each	steel	ground support	east main turnouts	51–100	Super Swellex bolts 3 m
166	Rock bolt	P	34,300	each	steel	ground support	west main turnouts	51–100	Super Swellex bolts 3 m
167	Wire mesh	P	45,150	m^2	steel	ground support	east main turnouts	51–100	WWF 3 × 3
168	Wire mesh	P	45,150	m^2	steel	ground support	west main turnouts	51–100	WWF 3 × 3
169	Cast-in-place concrete	P	29,370	m^3	concrete	ground support	east main turnouts	51–100	5 000 psi
170	Cast-in-place concrete	P	29,370	m^3	concrete	ground support	west main turnouts	51–100	5,000 psi
171	Rail	P	824,380	kg	steel	excavated openings	east main turnouts	51–100	115 lb/yd @ 3,508 m
172	Rail	P	824,380	kg	steel	excavated openings	west main turnouts	51–100	115 lb/yd @ 3,508 m

ID	Item	CL	Quantity	Unit	Material	System	Location	Est service life	Description
173	Electrical—other	P	3,508	m	other metal	utility systems	east main turnouts	51–100	trolly system
174	Electrical—other	P	3,508	m	other metal	utility systems	west main turnouts	51–100	trolly system
175	Pipe	P	3,508	m	steel	utility systems	east main turnouts	51–100	6 in air line
176	Pipe	P	3,508	m	steel	utility systems	west main turnouts	51–100	6 in air line
177	Pipe	P	3,508	m	steel	utility systems	east main turnouts	51–100	4 in water supply line
178	Pipe	P	3,508	m	steel	utility systems	west main turnouts	51–100	4 in. water supply line
179	Pipe	P	3,508	m	steel	utility systems	east main turnouts	51–100	4 in waste water line
180	Pipe	P	3,508	m	steel	utility systems	west main turnouts	51–100	4 in waste water line
181	Electrical—other	P	3,508	m	other metal	utility systems	east main turnouts	51–100	leaky feeder cable
182	Electrical—other	P	3,508	m	other metal	utility systems	west main turnouts	51–100	leaky feeder cable
183	Electrical wire	P	3,508	m	other metal	utility systems	east main turnouts	51–100	power system
185	Electrical wire	P	3,508	m	other metal	utility systems	west main turnouts	51–100	power system
186	Electrical—other	P	7,016	m	plastic	utility systems	east main turnouts	51–100	fiber-optic cable
187	Electrical—other	P	7,016	m	plastic	utility systems	west main turnouts	51–100	fiber-optic cable
188	Shielding door	P	510,000	kg	steel	ventilation systems	east main turnouts	51–100	@ 5,000 kg each
189	Shielding door	P	510,000	kg	steel	ventilation systems	west main turnouts	51–100	@ 5,000 kg each
190	Precast concrete lining	P	454,470	m^3	concrete	ground support	emplacement drifts	101–150	5,000 psi, 113,617 m long
191	Grout	P	340,850	ft^3	concrete	ground support	emplacement drifts	101–150	
192	Rail	P	$10\,8 \times 10^6$	kg	steel	waste package handling equipment	emplacement drifts	101–150	90 lb/yd @ 113,617 m

ID	Item	CL	Quantity	Unit	Material	System	Location	Est service life	Description
193	Metal	P	302,980	each	steel	waste package handling equipment	emplacement drifts	101–150	rail mounting device
194	Electrical wire	P	113,600	m	other metal	utility systems	emplacement drifts	31–40	leaky feeder cable
195	Electrical—other	P	113,600	m	other metal	utility systems	emplacement drifts	51–100	gantry power system
196	Cast-in-place concrete	P	920	m^3	concrete	excavated openings	ventilation raises	101–150	5,000 psi @ 102 ea × 10 m @ 0 9 cm/m
197	Rock bolt	P	6,260	each	steel	ground support	alcoves	51–100	Super Swellex bolt 3 m long
198	Wire mesh	P	8,240	m^2	steel	ground support	alcoves	51–100	WWF 3 × 3
199	Cast-in-place concrete	P	3,150	m^3	concrete	ground support	alcoves	51–100	5,000 psi
200	Electrical wire	P	640	m	other metal	utility systems	alcoves	51–100	power system
201	Electrical wire	P	640	m	other metal	utility systems	alcoves	51–100	3/c 15KV 500 MCM cable
202	Pipe	P	640	m	steel	utility systems	alcoves	51–100	8 in air piping
203	Pipe	P	640	m	steel	utility systems	alcoves	51–100	6 in water supply line
204	Pipe	P	640	m	steel	utility systems	alcoves	51–100	6 in waste water line
205	Electrical—other	P	640	m	other metal	utility systems	alcoves	51–100	trolly system
206	Rail	P	150,400	kg	steel	excavated openings	alcoves	51–100	115 lb/yd @ 640 m
207	Electrical wire	P	640	m	other metal	utility systems	alcoves	51–100	leaky feeder cable
208	Electrical—other	P	640	m	plastic	utility systems	alcoves	31–40	fiber-optic cable
209	Precast concrete invert	P	1,050	each	concrete	ground support	PC drifts	101–150	5,000 psi
210	Rock bolt	P	6,770	each	steel	ground support	PC drifts	101–150	Super Swellex bolts 3 m long
211	Wire mesh	P	7,940	m^2	steel	ground support	PC drifts	101–150	WWF 3 × 3

ID	Item	CL	Quantity	Unit	Material	System	Location	Est. service life	Description
212	Steel sets	P	244,795	kg	steel	ground support	PC drifts	101–150	5 5-m dia , W8 × 31 — 283 sets
213	Lagging	P	135,470	kg	steel	ground support	PC drifts	101–150	
214	Cast-in-place concrete	P	36	m^3	concrete	ground support	PC drifts	101–150	5,000 psi
215	Rock bolt	P	645	each	steel	ground support	PC alcoves	101–150	Super Swellex bolts 3 m long
216	Wire mesh	P	915	m^2	steel	ground support	PC alcoves	101–150	WWF 3 × 3
217	Air locks	T	150,000	kg	steel	ventilation systems	exhaust main	21–30	

CL = Class
P = Permanently installed item
PC = Performance confirmation
T = Temporarily installed item

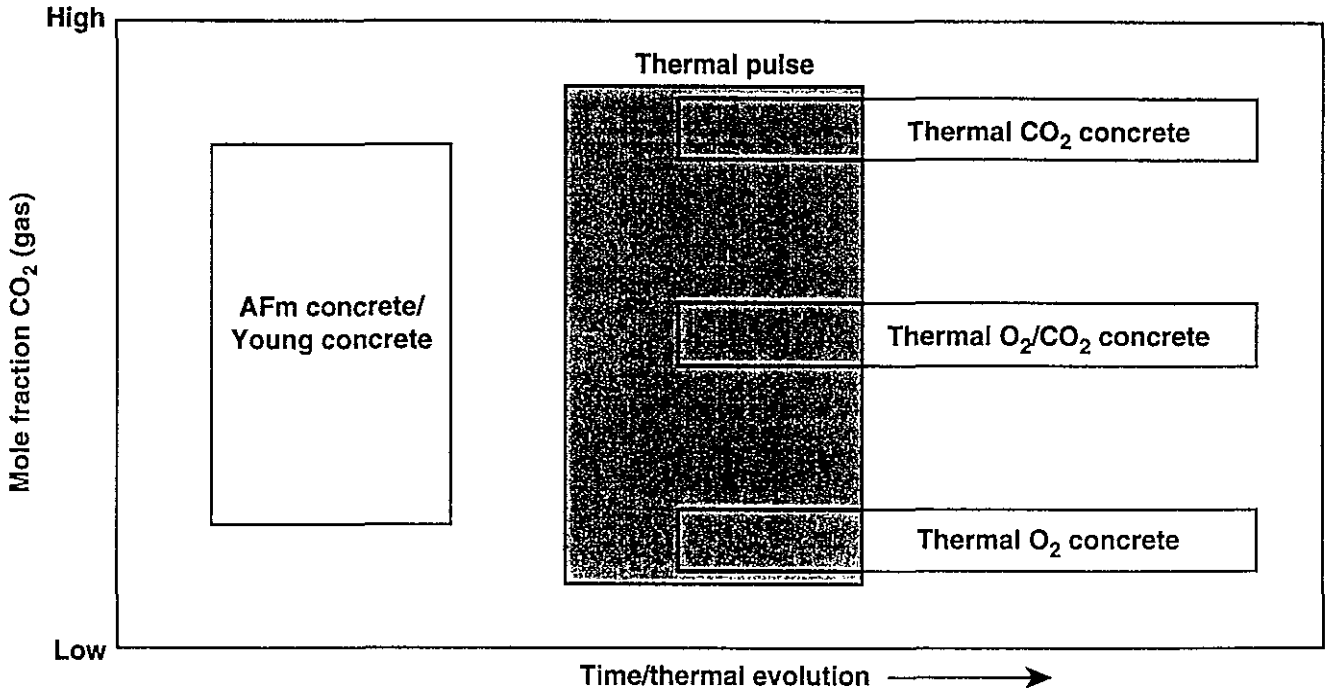

Figure 5.6-1. Conditions under which solid minerals develop from a grout in response to a thermal pulse and a range of gas compositions

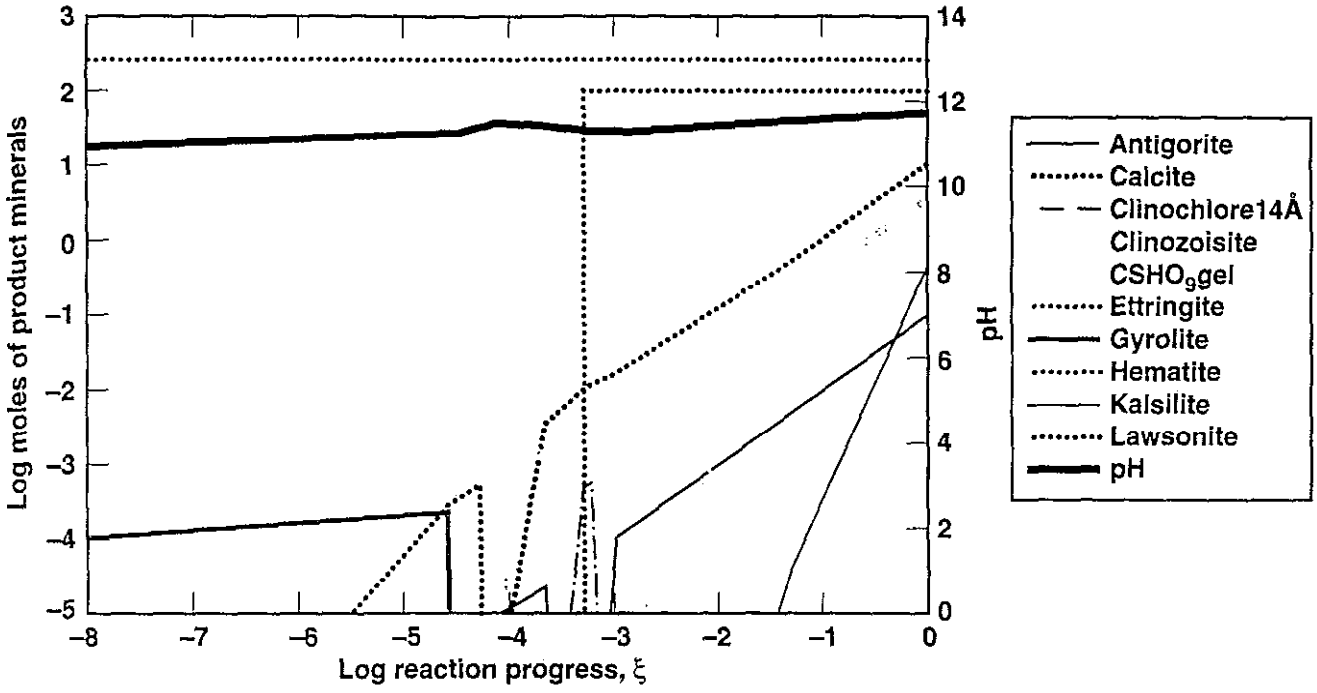

Figure 5.7-1a 25°C, fixed low CO_2 Reaction progress versus mineral precipitation

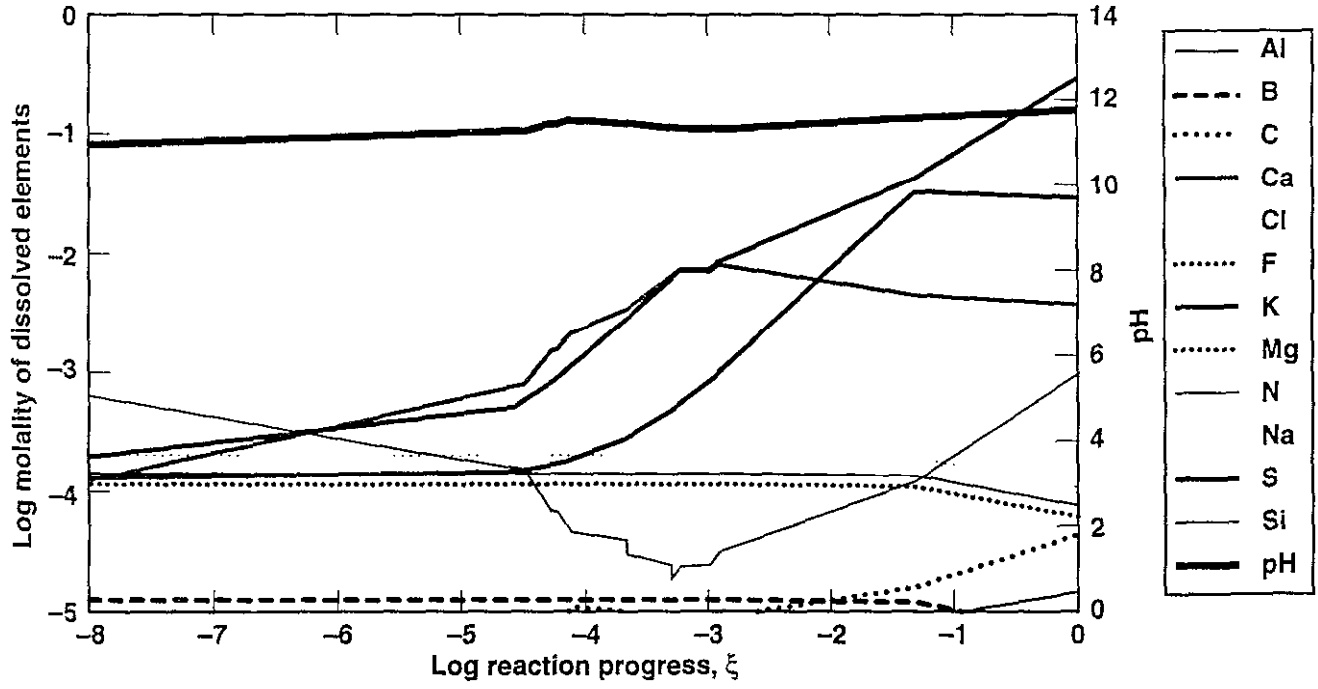

Figure 5 7-1b. 25°C, fixed low CO_2 Reaction progress versus elemental concentration

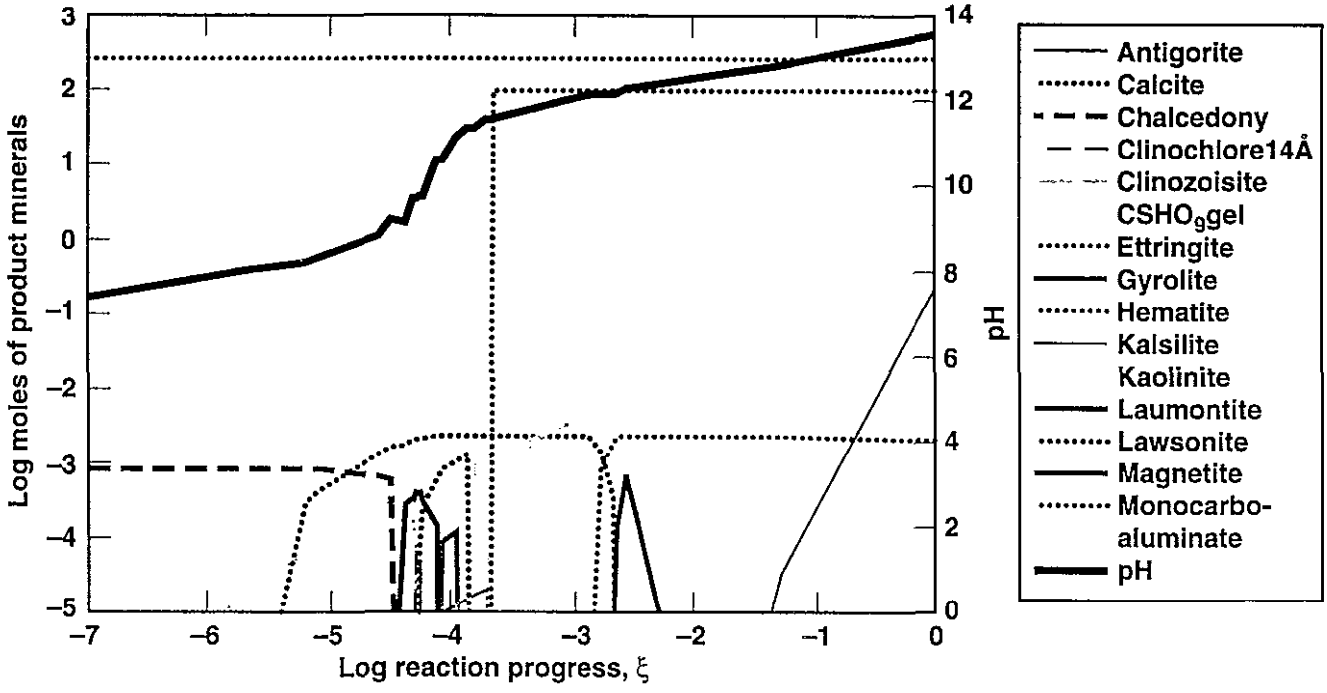

Figure 5.7-2a. 25°C, unfixed gas Reaction progress versus mineral precipitation

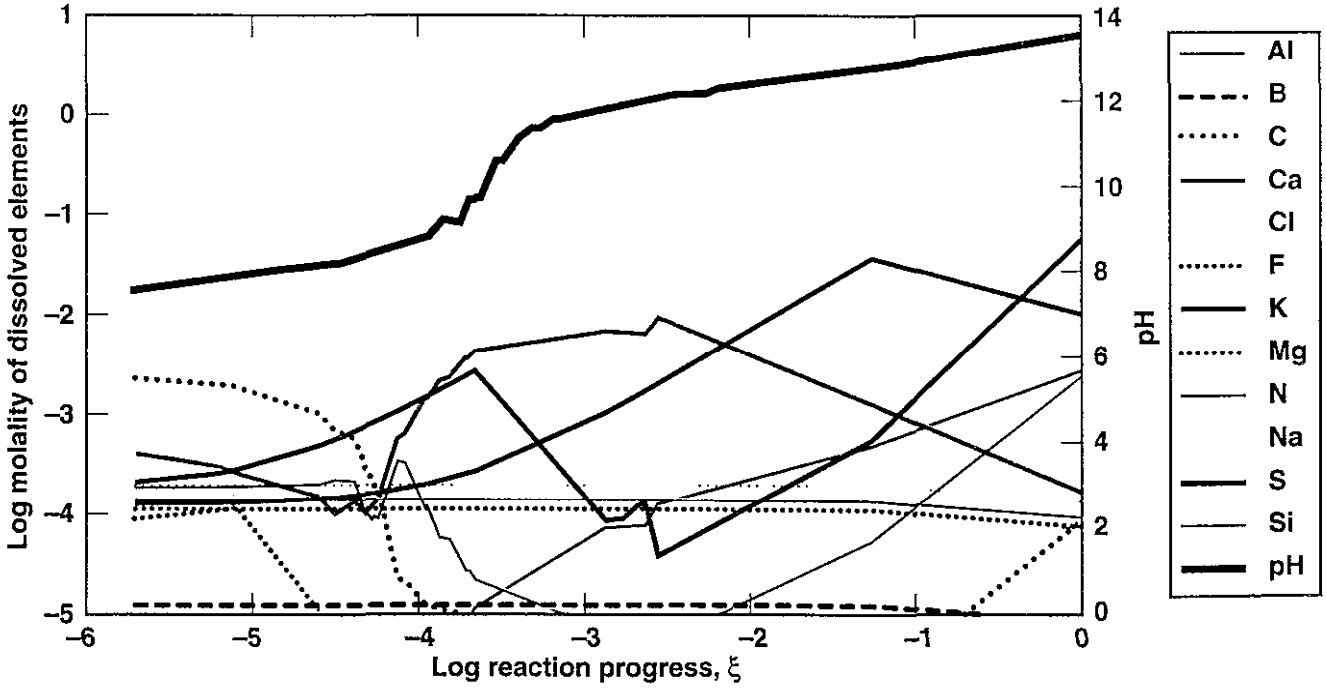

Figure 5.7-2b 25°C, unfixed gas Reaction progress versus elemental concentration

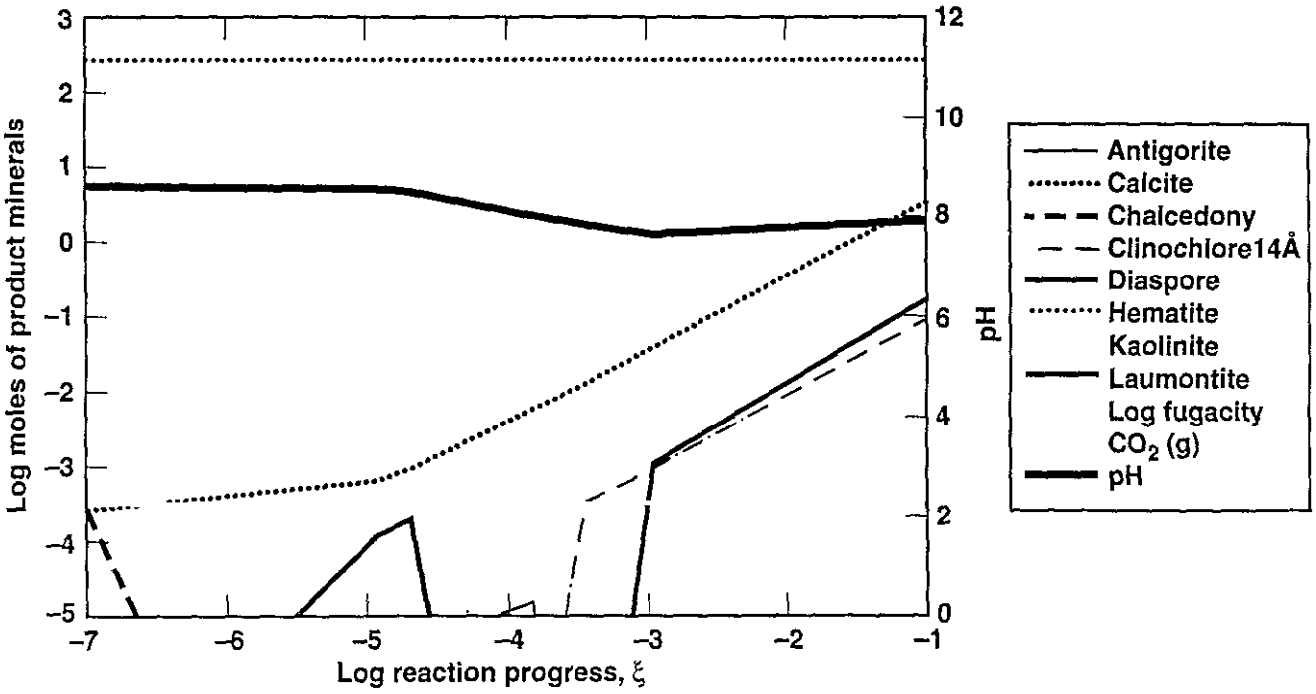

Figure 5.7-3a. 60°C, fixed atmospheric CO_2 Reaction progress versus mineral precipitation

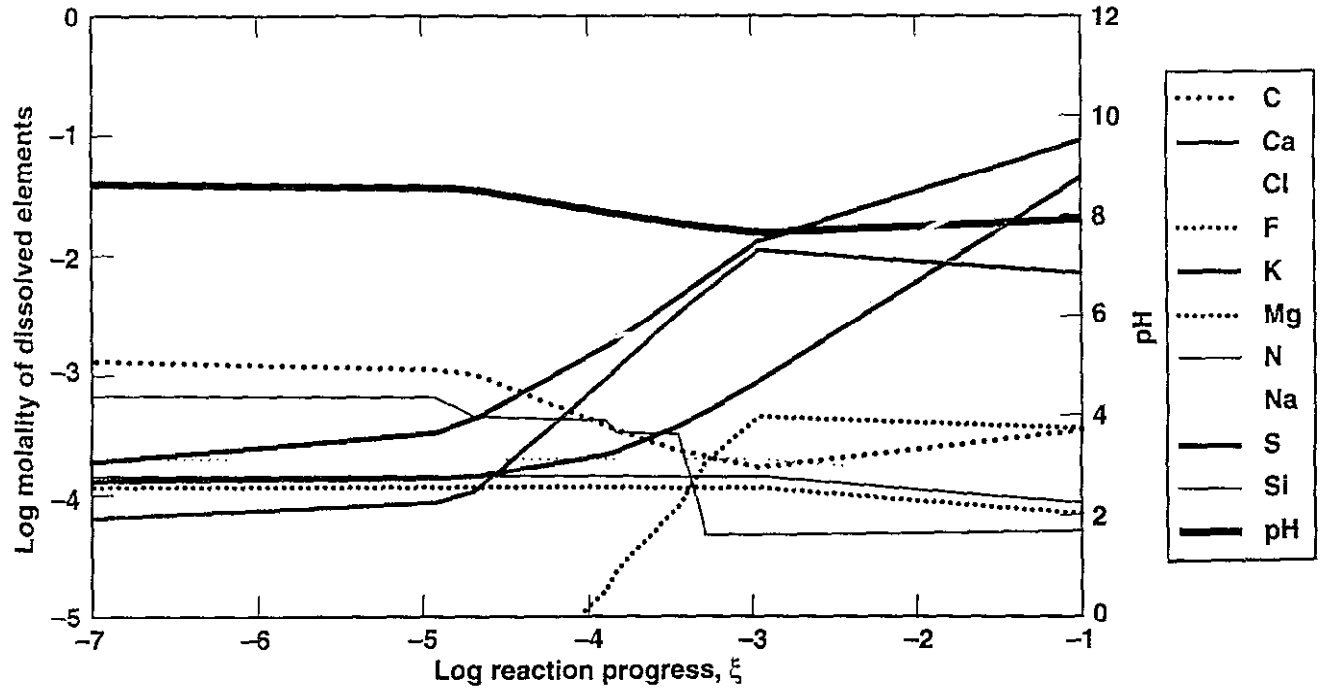

Figure 5 7-3b. 60°C, fixed atmospheric CO_2 Reaction progress versus elemental concentration

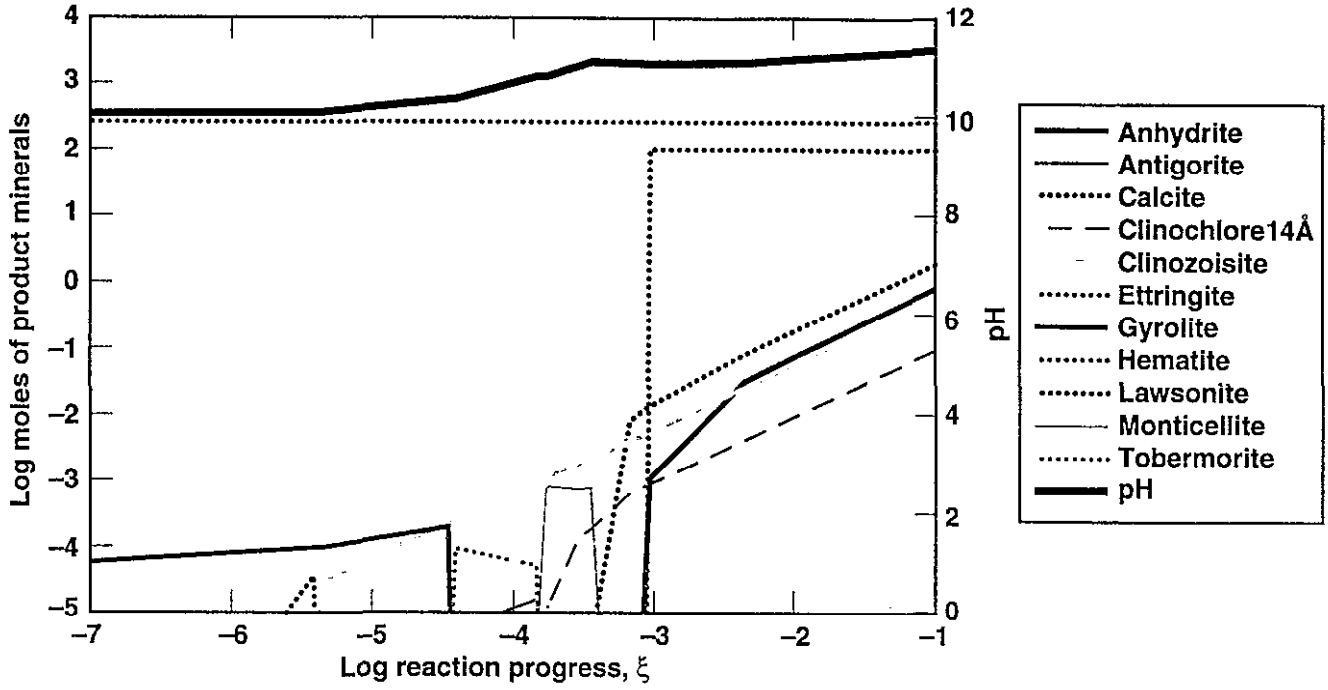

Figure 5 7-4a 60°C, fixed low CO_2 Reaction progress versus mineral precipitation

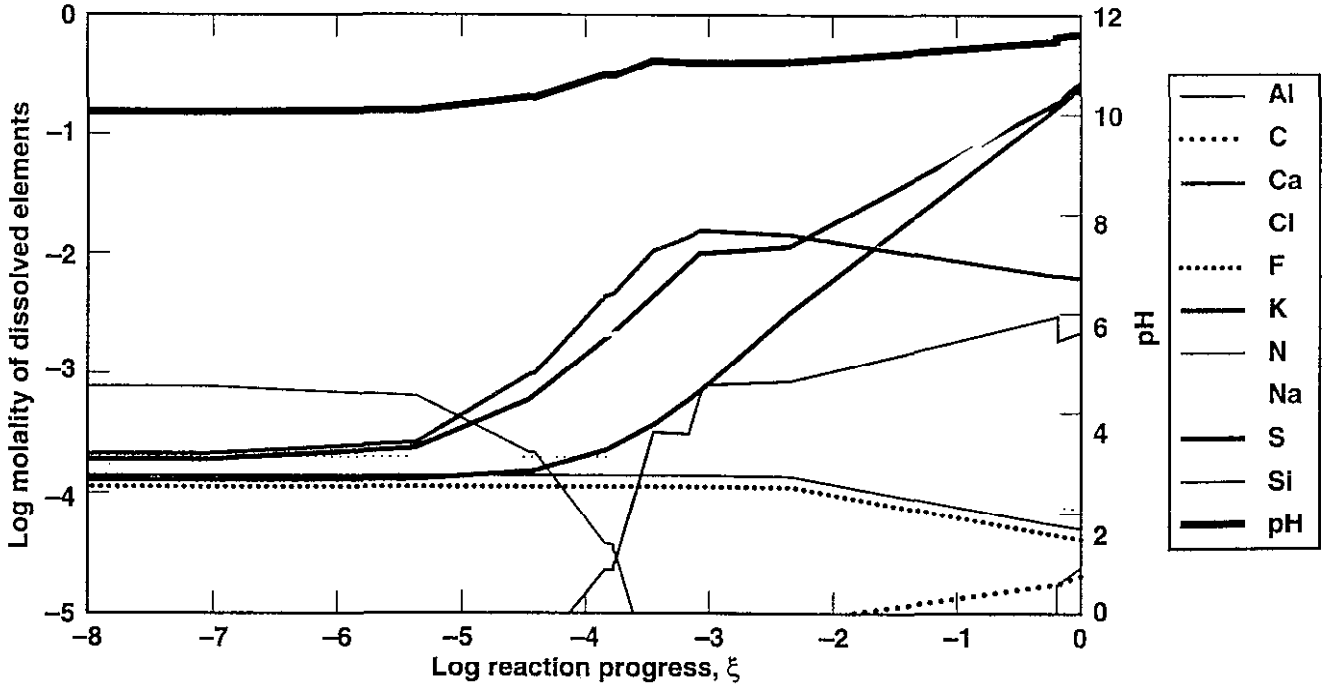

Figure 5.7-4b. 60°C, fixed low CO_2 Reaction progress versus elemental concentration

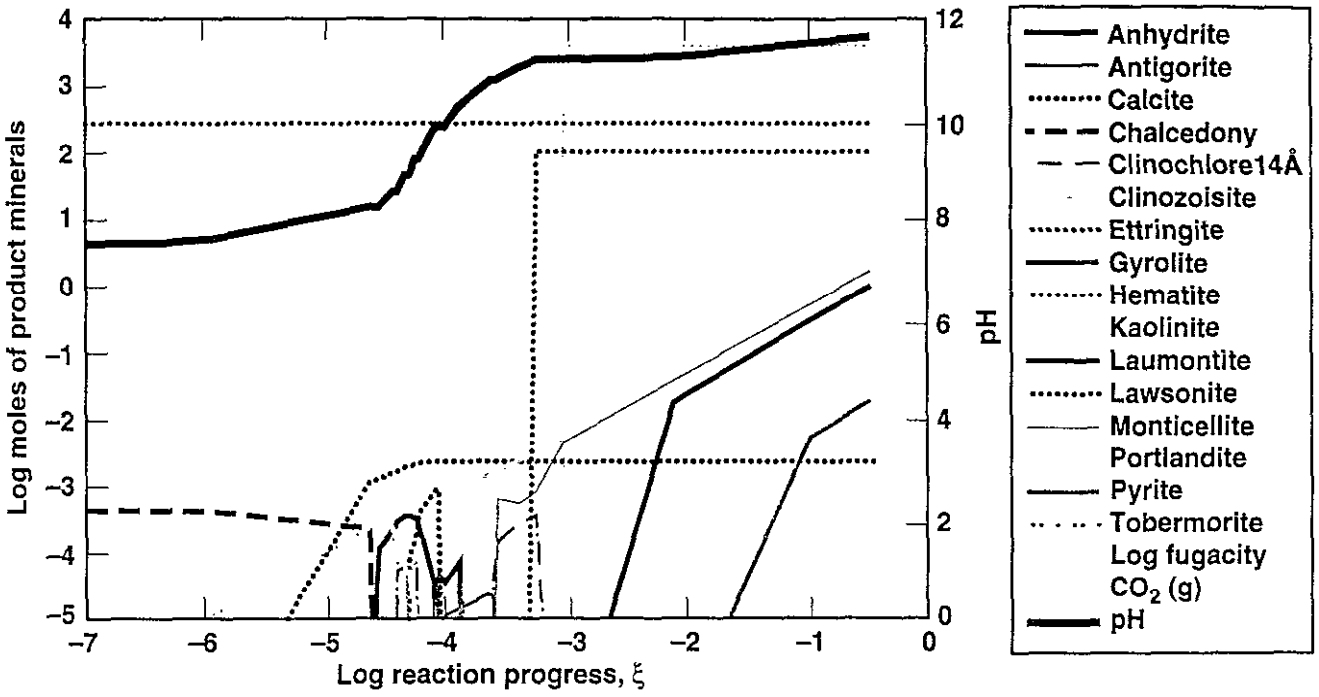

Figure 5 7-5a. 60°C, unfixed gas Reaction progress versus mineral precipitation

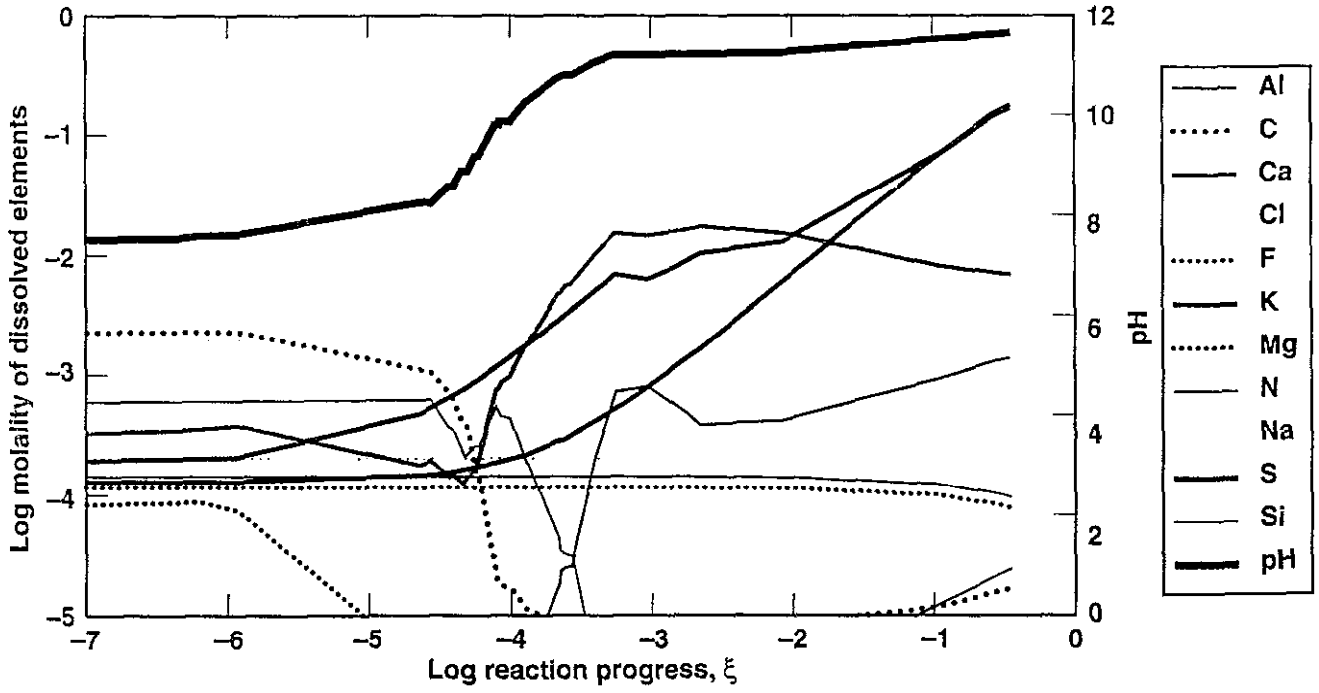

Figure 5.7-5b. 60°C, unfixed gas Reaction progress versus elemental concentration

Appendix A. Quality Assurance Information

The tables presented in this section address the acceptance criteria for the Level 3 deliverable *Engineered Materials Characterization Report, Volume 3, Revision 1 1.* **Table A-1** is the required "roadmap" that indicates where the criteria are met in this report **Table A-2** is a list of the codes used for calculations discussed in this report, including the versions used and whether the codes are qualified

Table A-3 lists the significant data used in this revision and the related data-tracking numbers (DTNs) from the Technical Data Management System

Table A-1. "Roadmap" table identifying where deliverable-acceptance criteria are met in the *Engineered Materials Characterization Report.*

Criterion	Section	Comment
The EMCR-VA includes the most recent test data	2 1, 2 2, 2 3, 2 4, 2 5, 2 6, 2 7, 3 0, 4 0, 5 0	These sections cover progress made in the experimental work Sections 2 1 through 2 7 cover the metallic barriers Section 3 covers ceramic coatings on the metallic barriers Section 4 covers basket materials, internal parts of spent-fuel waste packages Section 5 covers invert and other EBS materials outside the waste package
The EMCR-VA includes the most recent model development	2 8, 3 0, 5 0	Section 2 8 covers modeling development for the metallic barriers The experimental basis for this is found in Sections 2 1 through 2 7 Sections 3 and 5 contain both experimental and modeling activities
Data and process models will be assembled from all of the engineered materials tasks, both short-duration and long-duration tasks	2 8, 3 0, 5 0	Section 2 8 covers modeling development for the metallic barriers The experimental bases for these are found in Sections 2 1 through 2 7 Sections 3 and 5 contain both experimental and modeling activities
The collected data and process models will be synthesized along with that obtained from the literature and degradation-mode surveys	Entire report	Section 2 8, notably, consists of extensive comparisons and analyses of data and process models for the metallic barriers
EBS components shall, as a minimum, include the reference material as identified in the Waste Package Materials Selection Analysis Report	Entire report, see especially Section 1	

Criterion	Section	Comment
Process models and supporting test data for each application component/material combination shall, as a minimum, be provided for each applicable performance parameter identified in the Waste Package Development Technical Document and be consistent with applicable environmental conditions as identified in site investigation plans		
PERFORMANCE PARAMETERS		
Metallic Container		
• Phase Transformations	2 6 2	
• Oxidation Rates	2 8 2 1	
• General Corrosion Rates	2 1 4, 2 1 7, 2 2 6, 2 2 7, 2 8 2 2, 2 8 2 4	
• MIC Rates	2 5 7	
• E_{crit} for Pitting	2 3 1, 2 3 2, 2 8 4 6	
• E_{prot} for Crevice	2 3 1, 2 8 4 6	
• Pit Penetration Rates	2 8 4 7	
• Crevice Penetration Rates	2 8 3 8, 2 8 3 9	
• Crack Propagation Rates	2 4 2, 2 8 6 7	
• Threshold Stress Intensity Factors	2 4 2, 2 8 5 1, 2 8 5 7	
Non-Metallic Container (Ceramic Coating)		
• Fracture Toughness	3 3 4	
SNF Basket		
• Boron Concentration	4 2	
Emplacement Drift Invert		
• Hydrothermal Alteration	5 3 2 2, 5 6 2	
• Microbial Degradation	5 3 6 5, 5 6 2	
Q and non-Q data used and cited in this deliverable shall be appropriately noted and clearly identified	Appendix A	All test data generated at LLNL and sub-contractors are governed by Scientific Investigation Plans and Activity Plans and are therefore considered Q Data taken from literature sources are generally non Q Derived data, such as that outputted from modeling activities, is not considered Q Further identification of data QA is given in Table A-3
Every effort was made to assure that qualified data are used in this deliverable as specified in Supplement III, 2 5 "Data Usage "	Sections 2 through 5	

Criterion	Section	Comment
Technical data contained within the deliverable and not already incorporated in GENISES is submitted, if appropriate, for incorporation in accordance with YAP-SIII 3Q Verification of submittal compliance is demonstrated by including as part of the deliverable a copy of the TDIF and of the transmittal letter to the GENISES administrator	Appendix B	Data actually used in this report are identified in Appendix A Where these data are not incorporated in the automated data-tracking system, TDIFs have been submitted, as demonstrated by the records included in Appendix B
Record accession numbers and Automating Tracking numbers are included, as appropriate, for all data used and/or cited in this deliverable	Sections 1 through 5 Appendix A	Accession numbers are given in the reference lists Data-tracking numbers are given in Table A-3
The EMCR-VA shall have completed internal M&O reviews	Entire report	
((The document need not complete a YAP-30 12 review)		

Table A-2. Simulation codes and chemical databases used in the *Engineered Materials Characterization Report.*

Section	Code	Version	Description	Application	Qualified?	Reference
2 2	PLC Ladder Logic Software and Man-Machine Interface (MMI) Configuration Software	Rev 0	Operational software	Maintain temperature and liquid level control in Long-Term Corrosion Test Facility vessels	no, commercial	Individual software plan, ISP-CM-01 Green, 1997
2 2	Microsoft Access	MS Office 97	Data base manager	Weight-loss data from Long-Term Corrosion Test Facility	no, commercial	Gdowski, 1998
2 8	Microsoft FORTRAN Compiler	5 0 for DOS	General calculational and data analyses	Projection of corrosion-rate data for various corrosion models	no, commercial	Sample outputs in Farmer and McCright, 1998, see also Scientific Notebook 00334
5 5	EQ3/6	7 2b	Thermo-dynamic and reaction-path model	Equilibrium water composition and reaction path modeling	yes	Wolery, 1992a and 1992b, Wolery and Daveler, 1992

Section	Code	Version	Description	Application	Qualified?	Reference
5 5	GEMBOCHS	V 6	Thermo-dynamic data base and maintenance software	Derive, enter, and test thermodynamic data files	no	Wolery, 1992a and 1992b
5 5	OS3D / GIMRT	1 0	Reactive transport simulator	Altered-zone water composition, reference case for evaluating coupled processes	no, commercial software	Steefel and Yabusaki, 1995

Table A-3. Summary of significant data used in the *Engineered Materials Characterization Report*.

Table	Data description	Interpretive report	LLNL data?	Related DTNs	QA/ NQA
2-1	Composition and designation of candidate container materials	SAE, 1993	no	LL980704605924 035 (see Appendix B)	NQA
2 1-1	Composition of J-13 water	Harrar et al , 1990	yes	none	QA
2 1-3	Aqueous solution concentration for some salts	Duly, 1950	no	none (reference data)	NQA
2 1-4	RH, water partial pressure and nitric acid partial pressures	Perry and Chilton, 1973	no	none (reference data)	NQA
2 2-2 through 2 2-5	Water compositions used in long-term corrosion test	This report and TIPs cited in the associated text	yes	LL980704605924 035 (see Appendix B)	QA
2 2-6	Dissolved-oxygen content	This report	yes	LL980704605924 035 (see Appendix B)	QA
2 2-7	Ratio of CO_2 concentrations	This report	yes	LL980704605924 035 (see Appendix B)	QA
2 2-8 through 2 2-10	Corrosion rate of corrosion-resistant materials, corrosion-allowance materials, and intermediate materials	This report	yes	LL980704605924 035 (see Appendix B)	QA
Section 2 2 6 Supple-ment 1	Weight-loss results	This report	yes	LL980704605924 035 (see Appendix B)	QA
2 4-1	Results of SCC tests	This report	yes	LL980704605924 035 (see Appendix B)	QA

Table	Data description	Interpretive report	LLNL data?	Related DTNs	QA/ NQA
2 5-1	Compositions of 1x J-13 well water, M9 medium, and experimental results	This report	yes	LL980704605924.035 (see Appendix B)	QA
2 5-2	Composition of 10x J-13 well water and altered macronutrient formulas	This report	yes	LL980704605924 035 (see Appendix B)	QA
2 5-3	Endpoint ICP analyses of spent media	This report	yes	none	QA
2 8-3 through 2 8-7	Regression analyses data for corrosion of A516 carbon steel	Section 2 2 6 Supplement 1 Weight Loss Data for A516 steel	yes, derived data	LL980704605924 035 (see Appendix B)	NQA
2 8-8	Mechanical properties of ceramic coatings	Thornton and Colangelo, 1985	no	none (handbook data)	NQA
2 8-10	Passive corrosion data for Alloy C-22 Regression analyses from long term corrosion facility	Section 2 2 6 Supplement 1 Weight Loss Data for Alloy C-22	yes, derived data	LL980704605924 035 (see Appendix B)	NQA
2 8-11	Passive corrosion data for Alloy C-22 Regression analyses from various data sources	Section 2 3 and other sources given in Section 2 8 2 4	yes, in part, but derived data	none (derived data)	NQA
2 8-12	Data for passive corrosion of Alloy C-4 in saturated brines	Smialos et al , 1986, Shoesmith, 1998	no	none (reference data)	NQA
2 8-13	Estimates of CDFs for passive corrosion of Alloy C-22 with dripping	Compilation of Tables 2 8-10 through 2 8-12	yes, in part, but derived data	none	NQA
2 8-18	Parameter values used in probabilistic pitting model	Henshall, 1996	yes, but derived data	none (derived data)	NQA
2 8-19	Expected electrochemical potentials in repository	Compiled from Section 2 3, in part, plus Roy et al , 1996, 1997a, 1997b	yes, but derived data	none (derived data)	NQA
2 8-20	Potentiostatic polarization of alloy C-22 in acidic salt solutions	Roy et al , 1997a	yes	none (reference data)	QA

Table	Data description	Interpretive report	LLNL data?	Related DTNs	QA/ NQA
2 8-21	Pit stifling based on flux of dissolved oxygen	Calculations in Section 2 8 4 7 and information from Andresen, 1998	no	none (reference data)	NQA
2 8-23 and 2 8-24	Solubilities of various compounds responsible for passivation of Alloy C-22	Calculations in Section 2 8 4 7 and information from Pourbaix, 1996	no	none (reference data)	NQA
2 8-25	Maximum pit depths in Alloy C-22	Calculations in Section 2 8 4 7 and Tables 2 8-21 through 2 8-24	no	none (reference data)	NQA
2 8-27 and 2 8-28	Measure values of stress intensity and critical flaw size to initiate stress corrosion cracking	Table 2 4-1, plus calculations in Section 2 8 5 6	yes, but derived data	LL980704605924 035 (see Appendix B)	NQA
2 8-29	Predicted segregation of phosphorus at grain boundaries of carbon steel	Huang, 1998, and calculations in Section 2 8 6	no	none (reference data)	NQA
3 5-1	Mechanical properties of ceramic coatings	Thornton and Colangelo, 1985	no	none (handbook data)	NQA
4 1-1	Selected corrosion and pH results from candidate basket materials scoping test	Van Konynenburg et al , 1998	yes	LL980704605924 035 (see Appendix B)	QA
4 2-1	Composition of candidate materials in long term corrosion test	Vendor-supplied analyses and confirmation analyses	no	none	QA
5 2-4	Typical compositions of portland cements	Kosmatka and Panarese, 1994	no	none (reference data)	NQA
5 6-1 and 5 6-2	Calculations for thermally treated grout	GEMBOCHS data base and Taylor, 1990	no	Under submission	NQA
5 6-3 and 5 6-4	Calculations of mineral assemblage in young grout	EQ3/6 code and Tang, 1997	no	Under submission	NQA
5 6-5 through 5 6-9	Calculations of mineral assemblage in thermally treated concrete	EQ3/6 code and Tang, 1997	no	Under submission	NQA

References

Andresen, P. L. (1998) *Assessment of Corrosion Rate Properties for the Hastelloy C-22 Inner Barrier, An Environment for Waste Packages, Background Information for Consideration* General Electric Research Center

Duly, S. J (1950). "The Corrosion of Steel by Sea Salt of Given Moisture Content " *J Soc Chem Ind.* 69.304.

Farmer, J C , and R D. McCright (1998) *Crevice Corrosion and Pitting of High-Level Waste Containers Integration of Deterministic and Probabilistic Models* (UCRL-ID-127980 and UCRL-JC-127980-PT-1) Also Paper No 98160, Symposium 98-T-2A in proceedings from *Corrosion/98* San Diego, CA. March 22–27, 1998 Houston, TX National Association of Corrosion Engineers. [MOL 19980113.0389]

Gdowski, G. E (1998) *Yucca Mountain Project Activity Plan, Long-Term Corrosion Studies* (MB SIP Activity E-20-50, Rev. 4) Livermore, CA· Lawrence Livermore National Laboratory. [MOL.19980105.0583]

Green, R (1997) *Yucca Mountain Project Individual Software Plan, Individual Software Plan for the Programmable Logic Controller* (ISP-CM-01 Rev. 0) Livermore, CA Lawrence Livermore National Laboratory

Harrar, J , J. F. Carley, W. F. Isherwood, and E Raber (1990). *Report of the Committee to Review the Use of J-13 Well Water in Nevada Nuclear Waste Storage Investigations* (UCRL-ID-21867) Livermore, CA. Lawrence Livermore National Laboratory [NNA 910131 0274]

Henshall, G A (1996) *Modeling Pitting Degradation of Corrosion Resistant Alloys.* (UCRL-ID-125300) Livermore, CA Lawrence Livermore National Laboratory [MOL 19970122 0131]

Huang, J S (1998) *Stress Corrosion Cracking in Canistered Waste Package Containers Welds and Bare Metals* (UCRL-ID-120063) Livermore, CA: Lawrence Livermore National Laboratory. [MOL.19980126 0559, 234846]

Kosmatka, S H., and W C Panarese (1994). *Design and Control of Concrete Mixtures* (13th edition) Chicago, IL: Portland Cement Association

Perry, R H., and C. H. Chilton, eds. (1973). *Chemical Engineers' Handbook* Fourth edition New York, NY. McGraw-Hill

Pourbaix, M (1966) *Atlas of Electrochemical Equilibria in Aqueous Solutions* (English Translation by J A Franklin) New York, NY· Pergamon Press; Cebelcor [NNA 19891005.0098]

Roy, A K., D L. Fleming, and S. R Gordon (1996) "Localized Corrosion of Container Materials in Anticipated Repository Environments " In proceedings from *189th Meeting of The Electrochemical Society, Inc* Los Angeles, CA May 5–10, 1996 (Also UCRL-JC-122861 for Lawrence Livermore National Laboratory, Livermore, CA) [MOL.19960708 0433]

Roy, A K , D. L Fleming, and B Y. Lum (1997a) *Electrochemical and Metallographic Evaluation of Alloy C-22 and 625* (UCRL-ID-127355) Livermore, CA Lawrence Livermore National Laboratory. [MOL 19980114 0137]

Roy, A K ,D L. Fleming, and B. Y Lum (1997b) *Effect of Environmental Variables on Localized Corrosion of High-Performance Container Materials* (UCRL-JC-125329) Livermore, CA. Lawrence Livermore National Laboratory [MOL.19971217.0031]

SAE (1993) *Metals & Alloys in the Unified Numbering System.* (6th edition) Warrendale, PA Society of Automotive Engineers and American Society for Testing and Materials (SAE HS 1086-93; ASTM DS-56E)

Shoesmith, D W (1998) "Elicitation Summary " In proceedings from *Waste Package Degradation Expert Elicitation Panel* San Francisco, CA. March 14, 1998 San Francisco, CA. Geomatrix Consultants, Inc.

Smailos, E , W Schwarzkopf, and R. Koster (1986) *Corrosion Behaviour of Container Materials for the Disposal of High-Level Wastes in Rock Salt Formations* (DUR 10400) Nuclear Science and Technology, Commission of the European Communities

Steefel, C I , and S B Yabusaki (1995). *OS3D/GIMRT Software for Modeling Multicomponent-Multidimensional Reactive Transport* Richland, WA. Pacific Northwest National Laboratory, Battelle Memorial Institute.

Tang, D (1997) *Emplacement Drift Ground Support* May 23, 1997 Yucca Mountain Project report (BCAA00000-01717-0200-00003, Rev 00B) Las Vegas, NV prepared by the Civilian Radioactive Waste Management System, Management and Operating Contractor, for the U.S Department of Energy

Taylor, H F W (1990) *Cement Chemistry.* London, UK· Academic Press.

Thornton, P A , and V J Colangelo (1985) *Fundamentals of Engineering Materials* Englewood Cliffs, NJ Prentice Hall

Van Konynenburg, R A., P G Curtis, and T S E Summer (1998) *Scoping Corrosion Tests on Candidate Waste Package Basket Materials for the Yucca Mountain Project* (UCRL-ID-130386) Livermore, CA Lawrence Livermore National Laboratory.

Wolery, T J (1992a) *EQ3/6, A Software Package for Geochemical Modeling of Aqueous Systems Package Overview and Installation Guide* (UCRL-MA-110662) Livermore, CA Lawrence Livermore National Laboratory. (part 1) [NNA.19921023 0028]

Wolery, T J (1992b) *EQ3NR, A Computer Program For Geochemical Aqueous Speciation-Solubility Calculations· Theoretical Manual, User's Guide, and Related Documentation* (UCRL-MA-110662) Livermore, CA Lawrence Livermore National Laboratory (Version 7.0) [NNA 19921218 0010]

Wolery, T J , and S A Daveler (1992) *EQ6, A Computer Program for Reaction Path Modeling of Aqueous Geochemical Systems Theoretical Manual, User's Guide, and Related Documentation (Version 7 0)* (UCRL-MA-110662) Livermore, CA Lawrence Livermore National Laboratory (part 4) [MOL.19980218 0570]